INVESTIGATING THE REMAINING FATIGUE RELIABILITY OF AN AGING ORTHOTROPIC STEEL PLATE DECK

by

Justin N. Clarke

Submitted in partial fulfilment of the requirements
for the degree of Master of Applied Science

at

Dalhousie University
Halifax, Nova Scotia
December 2014

Table of Contents

List of Tables

List of Figures

Abstract

The A. Murray MacKay Bridge is an aging structure which opened to traffic over 40 years ago. With many of our structures aging, the ability to make confident management decisions supported by reliable engineering has become increasingly important. Evaluating existing structures using the design code approach contains uncertainty which affects management decisions. This thesis explores an alternate method that used structural health monitoring (SHM) coupled with laboratory testing to reduce uncertainty in these decisions.

The MacKay is the first suspension bridge in North America to have an orthotropic steel plate deck (OSPD), which contains three fatigue prone details of interest. A planning decision is required for when to replace the OSPD, thus the remaining fatigue reliability of the OSPD is needed. During the summer of 2010, sections of the OSPD near the expansion joints on the MacKay were replaced and 29 specimens from the former deck were obtained for laboratory testing. These specimens were subjected to various stress ranges and number of load cycles to obtain the remaining life S-N curve. Concurrently, key details on the MacKay were instrumented with strain gauges to obtain the in-situ strain range from vehicle loads in the deck for a one year period.

Numerical models were developed to determine necessary factors to adjust strain readings for both geometric location and the stress state at the fatigue details. After a limit state equation was defined for the fatigue limit state (FLS), probability distributions were used to model each variable in the limit state equation. Using the Rackwitz-Fiessler procedure, the reliability index was calculated over time for each gauge location. System reliability theory was used to combine all component reliabilities and determine the fatigue reliability of the whole OSPD.

List of Abbreviations and Symbols Used

AASHTO	American Association of State Highway and Transportation Officials
ADTT	Average Daily Truck Traffic
AISC	American Institute of Steel Construction
ASTM	American Society for Testing and Materials
B&T	Buckland and Taylor Ltd.
CAFL	Constant Amplitude Fatigue Limit
CDF	Cumulative Distribution Function
CHBDC	Canadian Highway Bridge Design Code
CSA	Canadian Standards Association
DAL	Dalhousie University
DCB	Dartmouth Cable Bent
DMT	Dartmouth Main Tower
FEM	Finite Element Model
FLS	Fatigue Limit State
GAF	Geometric Adjustment Factor
GVW	Gross Vehicle Weight
HCB	Halifax Cable Bent
HHB	Halifax Harbour Bridges
HMT	Halifax Main Tower
HSS	Hollow Structural Section
KTM	KTM Services Group Inc.
LRFD	Load Resistance Factor Design
NCHRP	Nation Cooperative Highway Research Program
OSPD	Orthotropic Steel Plate Deck
PDF	Probability Density Function
SHM	Structural Health Monitoring
SLS	Serviceability Limit State
SSAF	Stress State Adjustment Factor
S-N	Stress-Life
ULS	Ultimate Limit State

A	fatigue detail coefficient
A_c	cross sectional area
A_{design}	design value of fatigue detail coefficient
a	current age of the bridge in years
a_i	limit state constant
b	total number of range bins
c	new value for variable or constant
d	base case value for variable or constant
C_L	correction factor for the fatigue truck weight
D	damage fraction
E	modulus of elasticity
e	measurement error factor
F_X	cumulative distribution function of X
F_i	force in shell i
F_s	shunt calibration factor
F_{sr}	fatigue stress range resistance for the detail
F_{srt}	CAFL determined by the detail category
f_X	probability distribution function of X
$f_{DL\ comp.}$	unfactored compressive stress due to dead load at the detail under consideration
f_{sr}	fatigue stress range calculated at the detail concerned due to the passage of the CL-W Truck, as specified in clause 3.8.3.2 of CHBDC
G	load path factor
G_i	component i of limit state partial derivative column vector
g	estimated percentage annual traffic growth rate
I	importance factor
I_{yy}	moment of inertia about y-axis

k	window width
M	bending moment
m	fatigue strength exponent defining slope of S-N curve, taken as 3.0
m_{Nf}	mean number of cycles to failure
m_{Nn}	mean number of applied cycles
$m_{\ln(\varepsilon_m)}$	mean of natural logarithm of measured strain
$m_t^{(k)}$	median of neighbouring data points
m_{ε_m}	mean measured strain
N	total cumulative number of cycles
N_a	number of applied cycles
N_c	specified number of design cycles
N_i	number of cycles to cause failure at stress range i
N_f	number of cycles to failure
N_t	greater of y or 100 years
N_{2010}	number of cycles for year 2010
N_{2013}	number of cycles recorded for year 2013
n	number of stress range cycles per truck passage
n_i	number of cycles occurring at stress range i
n_j	number of cycles in bin j
n_t	total number of cycles
$n_t^{(k)}$	set of neighbouring data points
P	axial load
P_f	probability of failure
Q	load effect
Q_f	fatigue serviceability index
R	load resistance

R_R	resistance factor of the specified fatigue life level assessment
R_f	redundancy factor
R_P	multiple presence factor
R_s	stress range estimate partial load factor
R_{sa}	analysis partial load factor
R_{st}	truck-weight partial load factor
S	stress range
S_{max}	maximum magnitude stress in any shell
S_{re}	equivalent stress range
S_{ri}	i^{th} stress range
t	deck plate thickness
V_{Nf}	coefficient of variation of number of cycles to failure
V_{Nn}	coefficient of variation of number of applied cycles
w_{eff}	effective width
X	specimen type (A, B, or C)
X_i	uncorrelated random variable
x	distance away from point under consideration in outlier detection
x^*	design point
Y	year reliability analysis is being calculated
YY	stiffening rib number (given in Figure 5.6)
y	remaining finite fatigue life of a fatigue prone detail in years
y_n	set of data points
y_t	data point under consideration
Z	gauge number (Table 5.1)
Z_Q	reduced variable for load;
Z_R	reduced variable for resistance

z	perpendicular distance from neutral axis to stress point
z_i^*	reduced variable i
α	traffic growth rate per year
β	reliability index
Δ	Miner's critical damage accumulation index
Δf	calculated or measured estimated stress range using Palmgren-Miner's rule
ε_m	measured field strain
ε_{mj}	mid-point strain in bin j
ε_n	field strain noise
ε_{xx}	strain in the x-axis (longitudinal)
ε_{yy}	strain in y-axis (transverse)
ζ	standard deviation of natural logarithm of random variable
λ	mean of natural logarithm of random variable
μ_A	mean of fatigue detail coefficient
μ_Q	mean of load
μ_R	mean of resistance
μ_X^e	equivalent normal mean
$\mu_{\ln(A)}$	mean of the natural logarithm of fatigue detail coefficient
$\mu_{\ln X}$	mean of $\ln(X)$
ν	Poisson's ratio, taken as 0.3
σ_Q	standard deviation of load
σ_R	standard deviation of resistance
σ_X^e	equivalent normal standard deviation
$\sigma_{\ln(A)}$	standard deviation of the natural logarithm of fatigue detail coefficient
$\sigma_{\ln X}$	standard deviation of $\ln(X)$

$\sigma_{\ln(\varepsilon_m)}$	standard deviation of the natural logarithm of measured strain
σ_{xx}	stress in the x-axis (longitudinal)
$\sigma_{xx,a}$	longitudinal axial stress
$\sigma_{xx,b}$	longitudinal bending stress
σ_{yy}	transverse stress
σ_{ε_m}	standard deviation of measured strain
τ	threshold for outlier
Φ	cumulative distribution function for the standard normal distribution
ϕ	probability distribution function for the standard normal distribution
φ_i	fraction of cycles from stress range i to the total number of cycles applied
γ	fatigue life constant determined from Table 10.4 in the CHBDC (CAN/CSA S6-06)
Ψ_g	geometric adjustment factor
Ψ_{ss}	stress state adjustment factor
$(ADTT)_{SL}$	average daily truck traffic in a single lane averaged for the entire fatigue life
$(\Delta f)_{eff}$	effective stress range
$(\Delta f)_{tension}$	factored tensile portion of the stress range caused by the passage of a fatigue truck
$[(ADTT)_{SL}]_P$	present average daily truck traffic in a single lane
$\{\alpha\}$	sensitivity vector

Acknowledgements

First, I would like to acknowledge NSERC for providing funding to conduct this research. I would like to thank Halifax Harbour Bridges for allowing me the opportunity to use the data contained in this thesis; without their consent, this thesis would not be possible. Cooperation with Buckland and Taylor Ltd. was also important to the success of this project. Both Halifax Harbour Bridges and Buckland and Taylor Limited provided reports and drawings not available to the public; these have been referenced in text as (courtesy of B&T) or (courtesy of HHB). Where the drawings have been modified, they are referred as (adapted from B&T).

I would like to thank my supervisor, Dr. John Newhook for his advice, guidance, and encouragement throughout this thesis, as well as providing me the opportunity to work on this project. Thank you to my committee members, Dr. Yi Liu and Dr. George Jarjoura, for taking the time to review this research project.

For their aid in the field, I would like to thank KTM Services Group Inc.

For their assistance in the laboratory testing, I would like to thank Phil Vickers, Brian Liekens, Blair Nickerson, Brian Kennedy, and Chris Gagnon.

Finally, I would like to thank my family and my girlfriend Katie for the encouragement and support to complete this thesis.

Chapter 1: Introduction

Much of the infrastructure in Canada was constructed decades ago, meaning maintenance has become an increasingly important issue. The ability to make confident management decisions supported by reliable engineering is essential. However, using design codes in the evaluation of existing structures contains a level of uncertainty. This thesis presents an alternate method using structural health monitoring (SHM) coupled with laboratory testing to reduce uncertainty in these decisions.

1.1 Project Background

Halifax Harbour Bridges (HHB), owner and operator of both the A. Murray MacKay Bridge (MacKay Bridge) and the Angus L. Macdonald Bridge (Macdonald Bridge) in Halifax Nova Scotia, is currently in the final preparatory stages for a complete re-decking project on the Macdonald Bridge, scheduled to begin in 2015. The MacKay Bridge will soon require a similar re-decking of its orthotropic steel plate deck (OSPD). HHB wishes to assess the current fatigue reliability of the OSPD, and obtain an estimate for an eventual deck replacement. Buckland & Taylor Ltd. (B&T) was contracted to perform the fatigue reliability assessment on the OSPD. B&T developed a fatigue assessment strategy that coupled a laboratory testing component with SHM. Dalhousie University (DAL) and KTM Services Group Inc. (KTM) were contracted to supply and install a SHM system on specific fatigue details located on the OSPD. DAL was also contracted to perform fatigue testing on specimens extracted from the MacKay Bridge OSPD.

The Canadian Highway Bridge Design Code (CHBDC) is used for the design and evaluation of bridges throughout Canada. However, the CHBDC has been developed with conservative load models to encompass all locations where the code could be used, all while ensuring the target reliability index is met. Instrumenting key fatigue details on the OSPD of the MacKay allows site-specific data to be extracted at a variety of locations. With this data, the need to use conservative load models within the CHBDC to predict stress levels is eliminated.

Further, predefined stress-life (S-N) curves are available in the CHBDC. Using these S-N curves on an existing structure introduces two sources of uncertainty. Firstly, the S-N curves defined in the CHBDC were constructed from new steel specimens which do not represent the current aging OSPD on the MacKay Bridge. Secondly, the loading history of stress cycles on the MacKay Bridge for the past 40-plus years is unknown. Therefore assumptions are needed about the number of loading cycles during the past 40-plus years in order to theoretically estimate the current fatigue state of the OSPD. Creating an S-N curve developed from specimens extracted from the OSPD on the MacKay eliminates both uncertainties.

1.2 Objectives

The primary objective of this research was to assess the fatigue reliability of the OSPD on the MacKay Bridge, using SHM to help support and inform this analysis. During the summer of 2010, sections of the OSPD near the expansion joints on the MacKay were replaced and 29 specimens from the former deck were obtained for laboratory testing. These specimens were subjected to various stress ranges and number of load cycles to obtain the remaining life S-N curve. Concurrently, key details on the MacKay were instrumented with strain gauges to obtain the in-situ strain range from vehicle loads on the deck for a one year period. Numerical models were constructed to provide necessary adjustments to both the laboratory and the field monitoring data. A limit state equation defining the fatigue failure of a single monitored joint was developed and used to predict the reliability of the joint. Ultimately, the reliability at each location was combined to give an overall system reliability of the OSPD.

Two secondary objectives existed for this research: 1) to understand the behaviour of the OSPD fatigue details and determine the loading type of concern, and 2) to examine the impact deterioration from corrosion has on the fatigue life of the deck. A literature review examined previous research on OSPDs and their behaviour. Field testing of the SHM system allowed strain data to be collected under a known load. Through the laboratory testing, several specimens were identified as corroded and the results were able to be compared to the non-corroded specimens from the same fatigue detail.

1.3 Thesis Layout

The thesis begins with a brief history of suspension bridges and their components, including the different deck types. A detailed description of OSPDs is given. Chapter Two also contains a review of the relevant theory in fatigue, SHM, and reliability of structures. In Chapter Three, a literature review on the fatigue of OSPD is completed, along with the current codes and papers which attempt to assess the fatigue life of an existing bridge structure. Chapter Four describes the MacKay Bridge, while Chapters Five and Six detail the installation and field testing of the SHM system on the MacKay. In Chapter Seven, the laboratory testing is documented, including the analysis of the results. Chapter Eight discusses the data processing for the collected SHM data. Adjustments to the strain gauge readings for both the laboratory and the field gauges were found through the numerical modeling presented in Chapter Nine. After all parameters are defined and summarized in Chapter Ten, the reliability analysis for the OSPD is completed in Chapter Eleven. Finally, Chapter Twelve presents the conclusions as well as the recommendations from this research.

Chapter 2: Literature Review – General Background and Theory

This chapter presents the background theory about suspension bridges, fatigue, and structural health monitoring.

2.1 Suspension Bridges

It is unknown when the first suspension bridge was constructed, but isolated regions in South America and Africa show the primitive idea of the suspension bridge, consisting of as little as a single vine (Kawada, 2010). The use of iron chain in suspension bridge construction dates back over 2000 years in China and India (Harazaki et al., 2000). The iron suspension bridge, assumed to have originated in the Eastern world, appeared in Europe during the 16th century and was developed in the 18th century (Harazaki et al., 2000).

The concept of modern suspension bridges as seen today was developed over 200 years ago and stemmed from the same idea as the first suspension bridges with a cable as the main load carrying member. The first modern suspension bridge, Jacob's Creek Bridge located in Pennsylvania, was built by James Finley in 1801. Finley's bridge consisted of five unique features noted in his patent application: installed anchorages and towers, separation of the main cables from the deck, identical angle of the main cables as they diverge from both sides of the tower tops, suspended hangers extending from the main cables, and attachment of the deck to the suspenders (Kawada, 2010). Since Finley's bridge was constructed, the main concept of the suspension bridge has not changed, but the development of stronger materials and a better understanding of suspension bridge behaviour has allowed the span of suspension bridges to continually increase over the past 200 years. When constructed, the Jacob's Creek Bridge had a main span of 21 metres. Today, the world's longest suspension bridge, the Akashi Kaikyo Bridge in Japan, has a main span of 1991 metres. With increasing span, the design and construction of suspension bridges introduces challenges never seen before in bridge engineering. Even with the gap between suspension and cable-stayed bridges closing, the suspension bridge still remains the most suitable choice for a long span crossing (Kawada, 2010).

2.1.1 Components of a Suspension Bridge

A suspension bridge consists of four main elements: the deck (which includes the stiffening girder/truss), the cable system supporting the deck, the pylons (or towers) supporting the cable system, and the anchorages supporting the cable system. These elements are shown in Figure 2.1. With the aid of the stiffening girder/truss system, the deck directly supports the traffic load. To support the deck, suspender cables (also called hanger ropes) hanging from the main cables are attached to the deck at the edge of the stiffening girder/truss system. The main cables suspend from the pylons and attach to the anchorage system at each end of the bridge. The pylons transfer the load from the main cables to the foundation of the bridge. Depending on the type of anchorage, the load may also be then transferred into the ground (earth anchored), or through the deck of the bridge (self-anchored). For earth anchored systems, the load is resisted by either the mass of the anchorage block, or by adequate geotechnical conditions allowing the main cable to be anchored into the ground. For self-anchored systems, the cable is anchored to the deck at the ends of the bridge, however, these anchorages are not typically found in suspension bridges as the deck in a suspension bridge is not typically capable of resisting the large compressive loads applied.

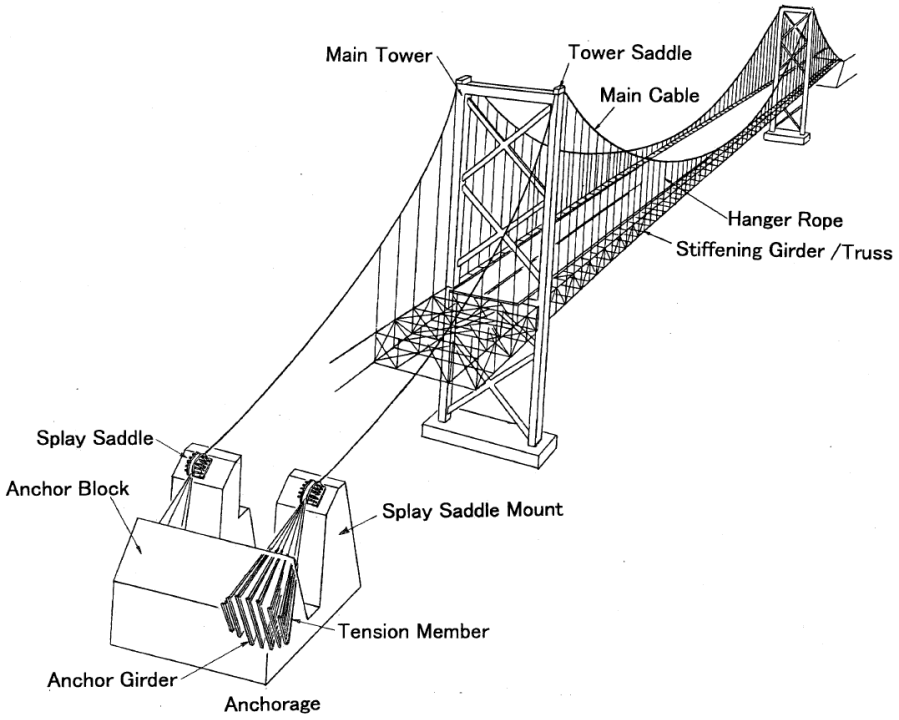

Figure 2.1: Components of a suspension bridge (Harazaki et al., 2000).

2.1.1.1 Stiffening Girder/Truss

In current suspension bridge design, there are typically three types of longitudinal stiffening girders that will provide the required amount of stiffness for aerodynamic stability. These include a plate girder system, a truss system, and a box girder system, all shown in Figure 2.2. As the span of a suspension bridge increases, a truss or box girder system is typically adopted as the plate girder system becomes disadvantageous due to its aerodynamic instability at longer spans and its lack of torsional stiffness, as seen in the 1940 collapse of the Tacoma Narrows Bridge. The truss system typically consists of longitudinal trusses, a deck system between the top chords of the longitudinal trusses, and a lateral truss system along the bottom chord of the longitudinal trusses. This structural system completes a pseudo-box cross section giving the system torsional stiffness. The box girder system consists of a single steel box section with longitudinal ribs to provide stiffening. Since the section is a closed shape, it is naturally torsionally stiff. Traditionally, the truss system is associated with American style suspension bridges, with the box girder system being characteristic of European style suspension bridges (Kawada, 2010).

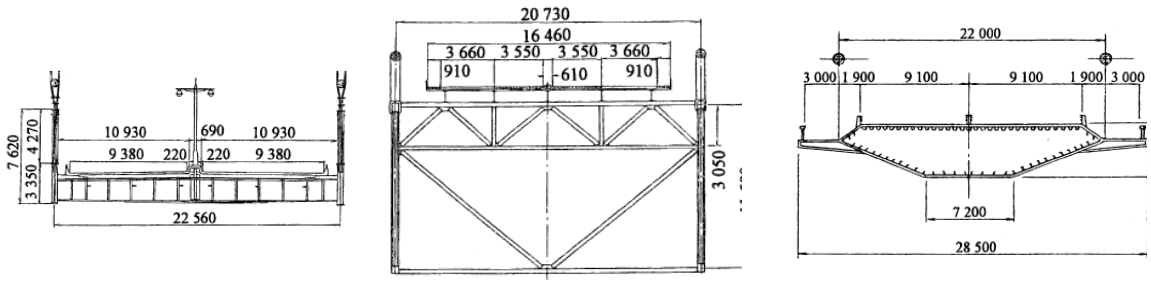

(a) (b) (c)

Figure 2.2: Three type of stiffening girders (a) plate girder, (b) truss, (c) box girder (Harazaki et al., 2000).

2.1.1.2 Deck

The deck, which forms the top driving surface for the plate girder, truss, and box girder systems, directly supports the traffic load acting on the suspended structure. It must be able to provide flexural stiffness in the vertical direction to carry load between the suspender connection points, and to distribute concentrated loads to multiple suspenders (Gimsing & Georgakis, 2012). Further, the deck must also provide flexural stiffness in the transverse direction to resist and distribute bending from wind load. Additionally, the deck needs some degree of torsional stiffness for aerodynamic stability.

There are several different deck types for a bridge, which include reinforced concrete, precast deck panels, prestressed cast-in place decks, post-tensioned concrete panels, steel grid, and orthotropic decks (Keever & Fujimoto, 2000). Since this research is concerned with an orthotropic deck, this is the only deck type discussed further.

An OSPD is comprised of a thin steel deck plate, accompanied by longitudinal stiffening ribs spanning between transverse floor beams. The ribs can either be of opened or closed shape. Open-ribs are torsionally soft and do not have favourable load distribution properties when compared to closed-ribs. For this reason, closed ribs are more common on OSPDs.

A lower mass, ductile behaviour, shallower sections, rapid installation, and cold-weather constructions are all reasons orthotropic decks are common. In seismic zones, the lower mass of the deck means reduced earthquake forces the bridge must resist. For example, the Golden Gate Bridge had an original deck comprised of reinforced concrete, weighing 508

kg/m^2 (Mangus & Sun, 2000). When the Golden Gate Bridge was re-decked using an OSPD in 1985, the weight of the new deck was 386 kg/m^2, resulting in a 24 percent reduction in deck weight (Mangus & Sun, 2000).

OSPDs are found in all three girder systems. For the truss system, the OSPD is typically found alongside the top chord of the longitudinal stiffening truss. The OSPD thus forms the top chord of the torsional resisting pseudo-box shape. In the box girder system, the OSPD forms the top of the box section itself. Figure 2.3 shows both open and closed stiffening ribs for an OSPD in the plate girder system. To connect the stiffening ribs to the deck plate, welding is used, which is a process that produces defects susceptible to fatigue.

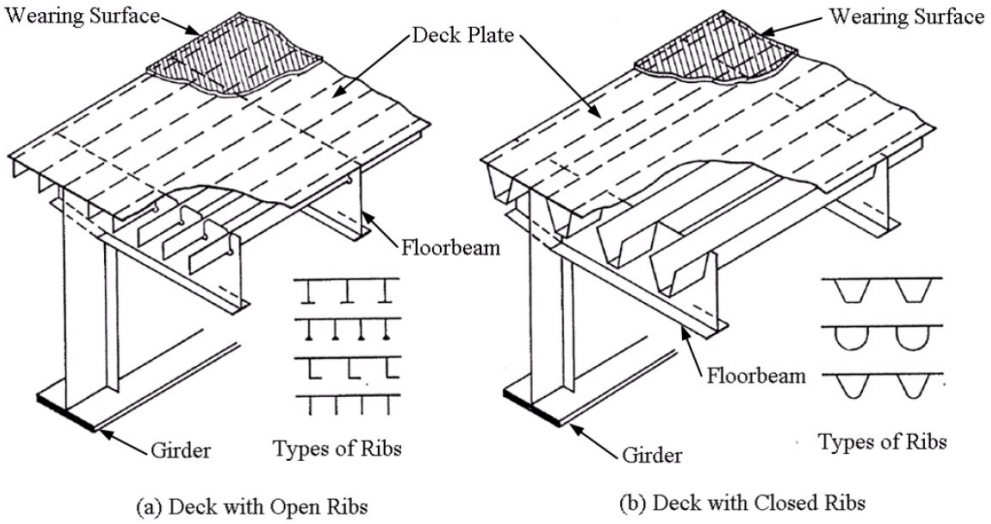

Figure 2.3: Orthotropic deck (AISC, 1963).

2.2 Fatigue

As stated by Wirsching (1998) "fatigue is perhaps the most important failure mode in mechanical and structural systems because over 80% of observed service failures are due to fatigue." This highlights the need to thoroughly evaluate fatigue in both the design and inspection of structures.

Fatigue is defined as the initialization and propagation of cracks under the repetitive action of varying loads. The stress causing fatigue crack growth is normally significantly lower

than the static design stress, and a large number of cycles are required before significant fatigue cracking is observed. If a crack is allowed to grow, fracture of the member can occur due to a decrease in cross sectional area.

Fatigue of structures considers two separate types of fatigue: load-induced fatigue and distortion-induced fatigue. The first, load-induced fatigue, occurs due to loads normally calculated and accounted for in the design of a structure. For bridge structures, the loading of concern is live load, and more specifically, truck loading. Hence load-induced fatigue is normally referred to as live-load-induced fatigue. The second, distortion-induced fatigue occurs when bridge components move relative to each other such to cause large strains in a localized area. Distortion-induced fatigue is not normally calculated in the design of a structure (CAN/CSA S6.1-06, 2006). To handle distortion-induced fatigue, structures are normally detailed to eliminate any potential problems. Live-load-induced fatigue is the concern of this research.

Fatigue crack growth can potentially occur in every steel structure but because of the large number of load cycles required for significant crack growth to occur, only certain structures are evaluated for fatigue. Buildings are an example of a steel structure that is typically exempted (barring any atypical details) from a fatigue investigation, even though buildings undergo the repetitions of wind loading. Structures that are typically evaluated for fatigue include bridges, cranes, ships, and towers, with many more structures undergoing a large number of stress cycles requiring analysis.

Rolled steel sections fall into the base metal fatigue category and are not normally a concern due to the high number of cycles needed at a large stress range before a fatigue failure will occur. However, fatigue needs to be considered in a fabricated structure because of the inherent flaws, defects, or discontinuities due to the manufacturing process of steel or fabrication process, causing stress concentrations in the fabricated components. The difference between defects and flaws should be quickly noted. Defects are defined as imperfections that need repairing, whereas flaws are imperfections that do not need repair due to their small size (Kulak & Grondin, 2010). In the examination of a fillet weld, flaws include partial penetration and lack of fusion, porosity and inclusions, undercut or micro-

flaws at the weld toe, and cracking or inclusions around a weld repair or at start-stop locations or at arc strikes (Kulak & Grondin, 2010). Some of these flaws are shown in Figure 2.4. Though the steel fabricator is responsible for inspecting the steel fabrication, inspection will only minimize the amount of flaws in the fabricated steel structure. It is impossible to completely eliminate flaws involved in the fabrication process. The use of mechanical connections, such as bolts, can help reduce the amount of flaws found due to welding, but realistically, welding can never be eliminated from a structure. These flaws and discontinuities are locations where fatigue needs evaluation, therefore welds need evaluation for fatigue.

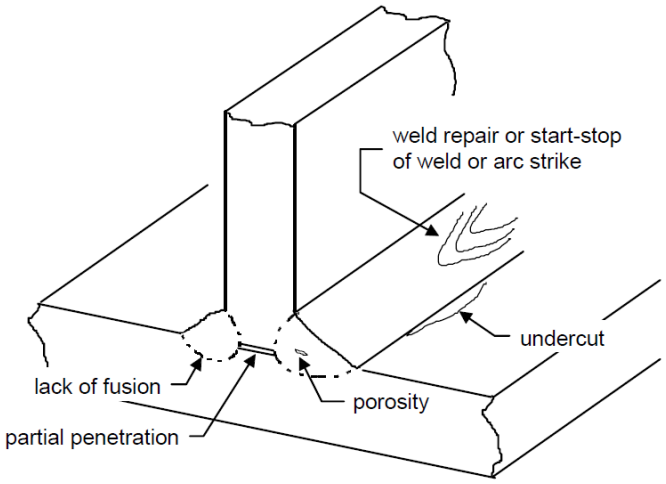

Figure 2.4: Typical weld flaws for a fillet weld (Fisher et al., 1998).

Through laboratory testing of many welded details in fabricated steel structures, researchers determined there are three principle factors that affect fatigue life: number of loading cycles, the type of detail, and the stress range at the detail (Fisher et al. 1998). In calculating the stress range at a fatigue detail, basic mechanics of materials is applied and the nominal stress range is found. The inclusion of a stress concentration due to the weld geometry is accounted for in the selection of the detail type. Eight detail categories are given in the CHBDC, which provides guidance in selecting the appropriate fatigue detail.

2.2.1 Cracking Modes and Crack Propagation

Before describing the design process for fatigue, the process of crack propagation through

a metal component and the different cracking modes should be defined. A total of three cracking modes exist for fatigue cracking. Mode I is the opening mode and is most common in engineering applications (Stephens et al., 2001). Mode II is the in-plane shearing mode, and mode III is the tearing or anti-plane shearing mode (Stephens et al., 2001). All three modes are shown in Figure 2.5.

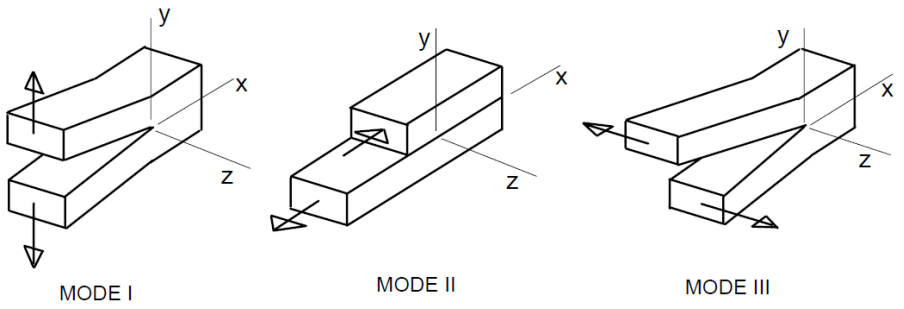

Figure 2.5: Cracking modes (Fisher et al., 1998).

A crack will grow in a metal component under the repetitive action of varying loads. For each load cycle that is applied to a metal part or a welded component, a discontinuity or initial crack will grow a small amount. Crack growth occurs at the crack tip. Initially, the crack tip is sharp, which causes a large stress concentration. Plastic deformation occurs at the crack tip due to this stress concentration, even under low loads. Continued plastic deformation results in a blunted crack tip and the crack grows a small amount. Once the metal component is unloaded, the crack tip will become sharp again. This process is called fatigue crack growth, and it occurs during every load cycle. (Kulak & Grondin, 2010). Figure 2.6 shows a typical crack in a metal component.

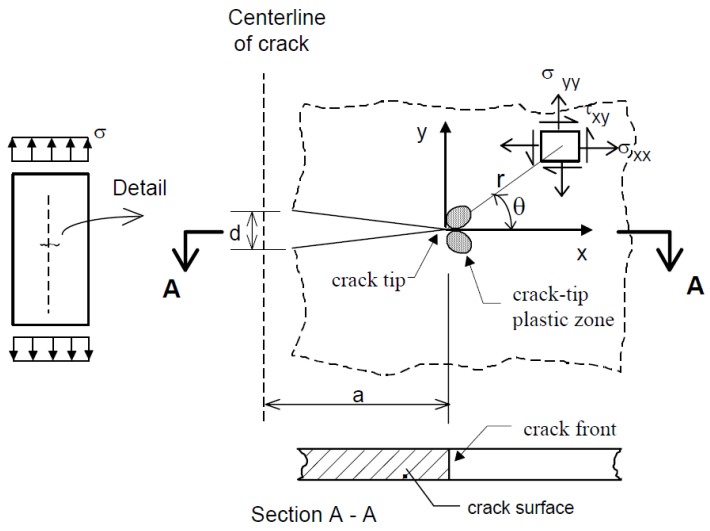

Figure 2.6: Crack in an infinitely wide plate (Fisher et al. 1998).

2.2.2 Stress-Life (S-N) Fatigue

The stress-life method (S-N method) is the most commonly used method in industry standards, such as the CHBDC. In this method, a stress range versus number of cycles to failure curve is utilized to predict the number of cycles associated with an applied stress range. The S-N method treats all strains as elastic, therefore this method is only valid for high cycle fatigue where plastic strains are very small. The S-N method is not appropriate for low cycle fatigue as applied strains have a large plastic component. The division between low and high cycle fatigue depends on the material under consideration, but is between 10 and 10^5 cycles (Bannantine et al., 1990). The S-N method also does not differentiate between the crack initiation and the crack propagation phases.

A large database has been compiled of stress-life fatigue data since 1970, which includes Fisher et al. (1970), Fisher et al. (1974), Schilling et al. (1978) and Fisher et al. (1983). The first study included 800 full-scale bridge details and formed the basis for the AASHTO Specifications published in 1974. The latter two studies explore the effect of variable amplitude loading. A study completed by Keating and Fisher (1986) evaluated the available fatigue tests for welded details and the fatigue design criteria in the AASHTO Specifications. Over 1500 additional data points were added to the original study by Fisher

et al. (1970), which expanded the current fatigue detail database. Keating and Fisher (1986) proposed new curves for each detail, all with the same slope of -3.0. The current stress-life curves used in the latest version of the CHBDC are shown in Figure 2.7.

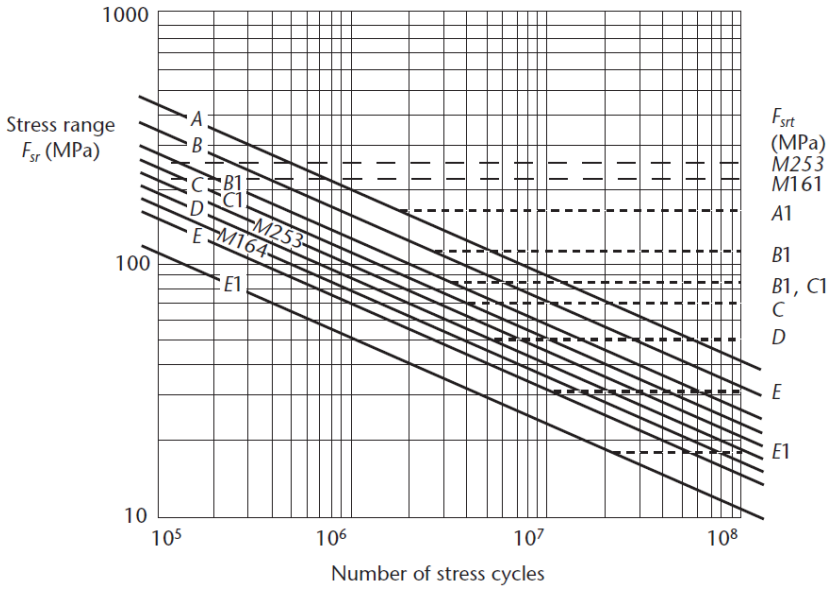

Figure 2.7: Current stress-life curves available in the current edition of the CHBDC Commentary (CAN/CSA S6.1-06, 2006).

From the significant amount of fatigue testing on welded components, the stress-life relationship has been found to be linear on a log-log scale, until reaching the constant amplitude fatigue limit (CAFL), which is represented by a horizontal line extending to infinity stress cycles. The CAFL is the level below which cracks will not grow under constant amplitude loading. The stress-life relationship can thus be modeled by Equation [2.1], or alternatively Equation [2.2]:

$$\log N_f = \log A - m \log S \qquad [2.1]$$

$$N_f = AS^{-m} \qquad [2.2]$$

where: N_f = number of cycles to failure;

A = fatigue detail coefficient;

m = fatigue strength exponent defining slope of S-N

curve (typically 3.0);

S = stress range.

2.2.3 CSA S6-06 – CHBDC – Fatigue Provisions

Fatigue design of bridges in Canada is considered under clause 10.17 in the CHBDC and is almost identical to the AASHTO Standard. With distortion-induced fatigue being a detailing concern, only calculations for load-induced fatigue are presented. The CHBDC uses the stress-life approach in determining fatigue life of a bridge component. Calculation of the stress range at the detail under consideration is completed using ordinary elastic analysis and the principles of mechanics of materials. More detailed analysis is only required for cases that are not covered in the detail category tables presented in Table 10.7 and Table 10.8 of the CHBDC. In locations of compressive stress due to dead load, fatigue need not be considered if the compressive stress is at least twice as large as the maximum tensile stress caused by live load. In calculating the fatigue loading, specified loads are used.

In the design of fatigue details not occurring on the bridge deck, Equation [2.3] applies:

$$0.52 C_L f_{sr} < F_{sr} \quad [2.3]$$

where: C_L = correction factor for the fatigue truck weight;

f_{sr} = fatigue stress range calculated at the detail concerned due to the passage of the CL-W Truck, as specified in clause 3.8.3.2;

F_{sr} = fatigue stress range resistance for the detail.

For the design of load-induced fatigue in bridge decks, Equation [2.4] applies:

$$0.62 f_{sr} < F_{sr} \quad [2.4]$$

In Equation [2.4], f_{sr} is the fatigue stress range calculated at the detail concerned due to the passage of a tandem set of 125 kN axles spaced 1.2 m apart and with a transverse wheel spacing of 1.8 m.

Equation [2.3] and Equation [2.4] contain factors of 0.52 and 0.62 respectively. These factors account for the difference between the design truck, the CL-625, and the trucks that cause fatigue (CAN/CSA S6.1-06, 2006). Loads at the design truck level will be present on the structure for very few loading cycles, but smaller trucks will cause a large number of cycles at a lower stress level (CAN/CSA S6.1-06, 2006). These smaller trucks are the main concern for fatigue as the number of cycles is much greater. Since decks are governed by tandem axles rather than the entire CL-625 truck, the factor is 0.62 instead of 0.52 for decks.

The right-hand side of the both Equation [2.3] and Equation [2.4] is equal to the fatigue stress range resistance, which is defined by Equation [2.5] below:

$$F_{sr} = (\gamma / N_c)^{1/3} \geq F_{srt}/2 \qquad [2.5]$$

where: γ = fatigue life constant determined from Table 10.4 in the CHBDC;

N_c = specified number of design cycles;

F_{srt} = CAFL determined by the detail category.

The right-hand side of Equation [2.5] represents one-half the CAFL because the stress range applied to a bridge detail is actually of variable amplitude and can occasionally be twice as large as the value calculated for the specified fatigue load (CAN/CSA S6.1-06, 2006). Additional details on determining the necessary parameters in Equation [2.3] through Equation [2.5] are presented in clause 10.17 of the CHBDC.

2.2.4 Variable Amplitude Loading

Actual structural details in field conditions undergo variable amplitude loading rather than constant amplitude loading, thus a relationship between constant amplitude loading and variable amplitude loading must be introduced. It has been shown by Tilly and Nunn (1980) that an infinite fatigue life exists if all stress ranges are below the CAFL. Two studies by Fisher et al. (1983) and Fisher et al. (1993) showed that under variable amplitude testing, fatigue damage will occur if as little as one out of 2000 cycles exceeds the CAFL; the fatigue damage follows a straight line extension of the resistance curve below the CAFL

(Fisher & Roy, 2011). Dual-slope S-N curves are used in CSA S16-09 to account for variable amplitude loading above and below the CAFL, but no such diagram has been adopted in the current edition of the CHBDC.

To account for the fatigue damage caused by variable amplitude loading, several methods exist. These methods include both linear and non-linear damage theories, however, only one linear damage theory is discussed as it is the most widely accepted and used theory in civil engineering (Fisher et al., 1998). The linear damage theory was first developed by Palmgren in 1924 (Palmgren, 1924) and then later developed further by Miner in 1945 (Miner, 1945). The rule is commonly called Palmgren-Miner's rule. The rule states that the damage fraction at any stress range is a linear function of the number of cycles at the stress range (Fisher et al. 1998). The total damage at a detail is the sum of all stress range occurrences, as written below in Equation [2.6]:

$$\sum \frac{n_i}{N_i} = D \qquad [2.6]$$

where: n_i = number of cycles occurring at stress range i;

N_i = number of cycles to cause failure at stress range i;

D = damage fraction.

A damage fraction of 1.0 is typically considered 'failure', meaning the permissible fatigue life of the detail has been exhausted. Using Palmgren-Miner's rule, an equivalent stress range can also be written, which represents the equivalent constant amplitude stress range for the same total number of applied cycles. Equation [2.7] presented below shows the equivalent stress range:

$$S_{re} = \left[\sum (\varphi_i S_{ri}^3)\right]^{1/3} \qquad [2.7]$$

where: S_{re} = equivalent stress range;

φ_i = fraction of cycles from stress range i to the total number of cycles applied;

S_{ri} = i^{th} stress range.

The derivation of Equation [2.7] is presented in Fisher et al. (1998).

2.2.5 Residual Stress

The process of welding steel components together causes residual stresses to form in the welded component due to the shrinkage of the weld material and expansion of the base metal. The pattern of the residual stress distribution depends on many factors such as the material strength of both the weld metal and the steel, the geometry of the joint, and the size of the weld with respect to the components being welded (Fisher et al., 1998). The important concept to note is that the residual stresses in welded components can reach the magnitude of the yield stress of the material (Fisher et al., 1998). Due to these high residual stresses, the mean stress becomes an insignificant effect in the fatigue strength of a welded joint, and only the stress range is considered. Figure 2.8 shows both the transverse and longitudinal residual stress pattern in a flat plate. Figure 2.9 shows the approximate residual stress distribution on an OSPD.

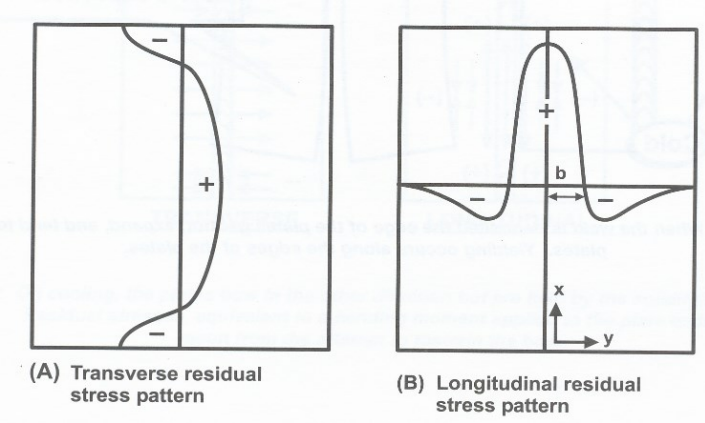

Figure 2.8: Residual stress pattern along a weld (CWB, 2006).

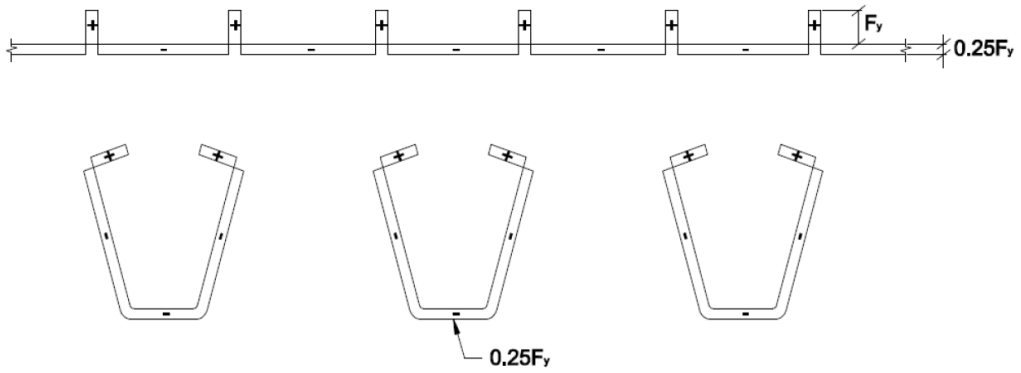

Figure 2.9: Approximate longitudinal residual stress distribution on an OSPD (FHWA, 2012).

A tensile residual stress reduces the fatigue strength of a component when compared to a mean stress of zero. The opposite is true for a compressive residual stress, where the fatigue strength is increased when compared to a mean stress of zero.

Additional residual stresses will also be present in a component when sub-assemblies are connected, due to improper fit-up and distortions (Maddox, 2000). If a specimen is cut-out from a large component, the residual stresses from the improper fit-up will be relieved (Fricke & Feltz, 2013). In a study by Fricke and Feltz (2013), small specimens 600 mm by 60 mm were extracted from a steel panel in a ship hull. The panel measured 1600 mm by 3200 mm by 4 mm thick. Before removing the small-scale specimens, the large panel was instrumented with strain gauges, 40 mm away from the weld, to determine the relieved stresses. Stresses in the range of -320 MPa to 200 MPa were observed when the small-scale specimens were removed. A compressive residual at the weld will results in a longer fatigue life, whereas a tensile residual stress will result in a shorter fatigue life when compared to the small-scale specimens. More details about the differences in the residual stresses for small-scale versus large-scale specimens can be found in Fricke and Feltz (2013). Unfortunately, no literature has been published on the residual stress distribution in an OSPD from improper fit-up.

2.2.6 Damaging Cycles

A conflicting view exists in literature on exactly which type of cycles cause fatigue damage in welded structures. Maddox (2000) states that due to the very high tensile residual

stresses, up to the yield stress at a welded detail, only the applied stress range is of concern, even if this is a compressive stress range. Since there is a tensile residual stress, the net stress range will be tensile. This follows the view of European design codes. Both the Eurocode 3 EN 1993-1-9 and the BS5400 Part 10 (replaced by Eurocode 3) suggest that when welded components are examined, all stress ranges, whether compressive or not, should be considered as damaging. In contrast, North American design codes state compressive stress ranges do not cause damage; only tensile and reversing stress ranges are damaging. The AAHSTO Bridge Design Specifications, the AISC Steel Construction Manual, the CHBDC, and CSA S16-09 all consider compressive stress range cycles as non-damaging. Fisher et al. (1998) states there are no known cases of load-induced fatigue cracking that has occurred in bridge structures when the stress range is totally in compression. Further, it is also argued by Fisher et al. (1998) that if fatigue cracking were to occur under compressive loading in the tensile residual stress region, the cracking would stop once outside the tensile residual stress region. The European code developers state it may be dangerous when a crack growing from a welded joint is subjected to fully compressive stress ranges as testing has shown some welded elements failing due to crack growth under fully compressive cyclic loading (Fisher et al., 1998).

2.2.7 CHBDC Fatigue Detail Category Statistics

Moses et al. (1987) reports the mean stress range and the design stress range at two million cycles for seven detail categories. The data is presented in Table 2.1, which included the calculation of the fatigue detail coefficient.

Table 2.1: Mean and design stress range at two million cycles for CHBDC categories (adapted from Moses et al., 1987).

Fatigue Detail Category	Mean Stress Range	Design Stress Range	Mean Fatigue Detail Coefficient	Design Fatigue Detail Coefficient
	MPa	MPa	MPa^3	MPa^3
A	227	160	23.5×10^{12}	8.17×10^{12}
B	157	125	7.75×10^{12}	3.88×10^{12}
B'	124	100	3.82×10^{12}	1.99×10^{12}
C	115	90	3.05×10^{12}	1.44×10^{12}
D	90	71	1.44×10^{12}	715×10^{9}
E	65	56	561×10^{9}	348×10^{9}
E'	50	40	244×10^{9}	128×10^{9}

Since the mean and standard deviation of the natural logarithm of the fatigue detail coefficients were not directly reported by Moses et al. (1987), these values were calculated. Equation [2.8] is a direct relationship between lognormal and non-lognormal statistics. Equation [2.9] is a rearrangement of the design fatigue detail coefficient calculation, two standard deviations below the mean on a logarithmic scale. Solving these two equation simultaneously allows the mean and standard deviation to be found, as presented in Table 2.2.

$$\mu_A = e^{\mu_{\ln(A)} + \frac{1}{2}\sigma_{\ln(A)}^2} \quad [2.8]$$

where: μ_A = mean of fatigue detail coefficient;

$\mu_{\ln(A)}$ = mean of the natural logarithm of fatigue detail coefficient;

$\sigma_{\ln(A)}$ = standard deviation of the natural logarithm of fatigue detail coefficient.

$$\mu_{\ln(A)} = \ln\left(A_{design}\right) + 2\sigma_{\ln(A)} \quad [2.9]$$

where: A_{design} = design value of fatigue detail coefficient.

Table 2.2: Fatigue detail coefficient statistics.

Fatigue Detail Category	$\mu_{ln(A)}$	$\sigma_{ln(A)}$
A	30.7	0.473
B	29.6	0.321
B'	28.9	0.302
C	28.7	0.346
D	27.9	0.323
E	27.0	0.226
E'	26.2	0.302

2.3 Structural Health Monitoring

Structural health monitoring (SHM) is the non-destructive process of examining an existing structure using a variety of sensors to provide information on the structural performance, condition, or health (ISIS, 2006). These sensors provide data which is collected and analyzed to give information about the behaviour of the structure.

As early as the 1990s, SHM systems were implemented in bridges in Canada, the United States, China, Hong Kong, Japan, and across Europe for long-term monitoring purposes (Xu & Xia, 2012). As of 2005, over 40 long-span bridges in mainland China and Hong Kong contain long-term SHM systems (Sun et al., 2007). In Canada, the Confederation Bridge contains a long-term SHM system with over 10 different sensor types installed on the bridge (Cheung et al., 1997). This SHM system was implemented when the bridge was being constructed. The incorporation of SHM systems in the design of bridge structures is becoming more common in practice.

2.3.1 Components of a SHM System

A typical SHM system consists of six components including: acquisition of data, communication of information, intelligent processing and analyzing of data, storage of processed data, diagnostics, and retrieval of information as required (ISIS, 2006). Figure

2.10 shows the relationship and order between each of the components.

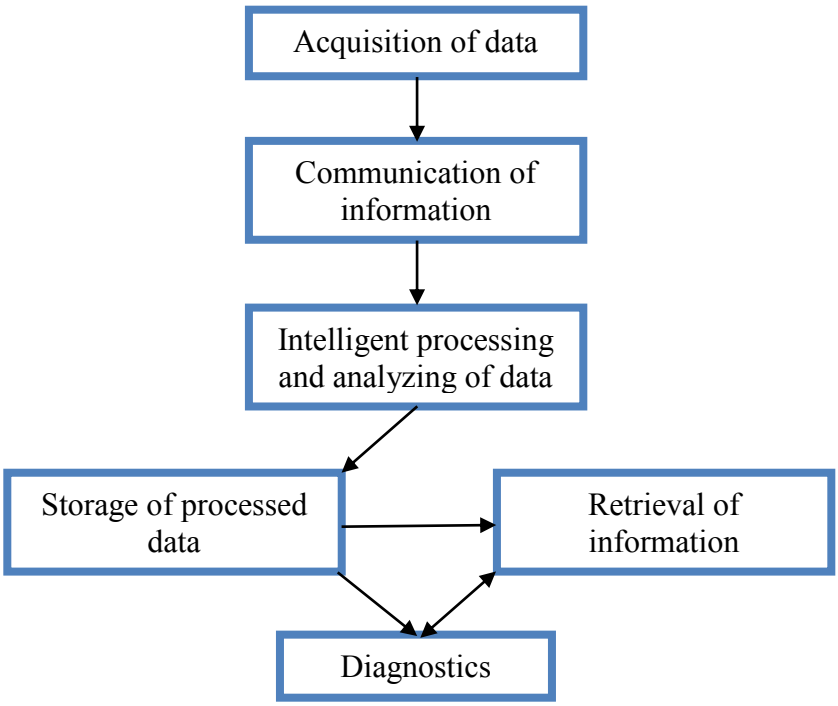

Figure 2.10: Flowchart of six components found in a SHM system (adapted from ISIS, 2006).

Sensors and the data acquisition system make up the first component, the acquisition of data. The data acquisition system, also known as the datalogger, is the system located onsite to extract, condition and store the measured data before transferring the data to another location for analysis. The desired response, which may include strains, deformations, accelerations, temperature, moisture, and loads, will determine which sensors should be installed to acquire the desired data. The entire system works together to capture data. First sensors receive an input signal. The resulting output signal is received by the data acquisition system which converts this raw signal into meaningful engineering terms. At this point, the data is fit for transfer to a separate location so further analysis can be conducted.

The second component is communication of information. Effective communication of the data allows remote monitoring to take place and no site visit to download data is necessary. Most SHM systems now make use of remotely transferring data through the internet, or

wireless technologies such as cellular transmission.

Once the data is received at the analysis location, further processing is required before any analysis of the data can be made. This is the third component, intelligent processing and analyzing of data. The data collected by sensors in a SHM system will possibly include extraneous data and noise in the data which has no relevance to SHM. Being able to remove the extraneous data and noise prior to completing the analysis will save time and avoid later complications in interpretation. This can also include removing any unwanted effects in the data before analysis, such as thermal effects. Filters can be used on the data acquisition system itself to remove certain unwanted data, but sometimes not all extraneous data can be eliminated in the recorded data. Further, filtering after the data had been collected and transferred allows the preservation of the raw data collected. Having the raw data can be useful in fully understanding how each sensor is functioning.

When the data is properly processed, it should be stored in a logical place that can be accessed for many years in the future. Further, it is important to ensure the data stored is easy to understand since additional analysis could take place many years in the future, or a future engineer could look to use the processed data. Commonly, the raw data is deleted and only processed or analyzed data is saved, which decreases the amount of data needing to be stored. The drawback to deleting the original data is that it is not available for later reinterpretation.

One of the most important components of a SHM system is the further interpretation of the processed data. This component takes expert knowledge and understanding of how the structure behaves, and how damage and deterioration can affect the analysis. Diagnostics takes the processed data and derives meaningful information about the response and health of the structure. It is not uncommon in the diagnostics component that a numerical model is constructed and calibrated against the field data obtained so further information can be gathered about the structure.

The final component, retrieval of information, refers to selecting the appropriate data to store for retrieval. Significance and confidence in the data and the analysis should be considered, as well as the volume of data obtained.

2.3.2 Advantages of SHM

As previously mentioned, SHM allows the monitoring of the performance and health of a structure under in-service conditions. This means a SHM system provides real time data about the safety of the structure. Reliability of the structural performance is significantly increased with this information. Further, SHM can take the information obtained from the data and incorporate these findings into future maintenance and planning strategies for the structure. Also, SHM allows damage in the structure to be identified and subsequently rectified on a real time basis. By providing useful information to the engineers and owners of the structure, SHM reduces the down time needed for repairs and maintenance of a structure. Ultimately, SHM improves the safety and reliability of the structure while at the same time reducing maintenance costs (ISIS, 2001).

2.4 Structural Safety Analysis

This section explains how to quantify safety and reliability of a structure. After defining terms, methods for calculating the reliability of structural components are given.

2.4.1 Limit State

Failure is defined differently by different people. One could define failure when a structure is unable to perform its intended function, which is a very vague definition. To be more specific, failure could be defined as the loss of load carrying capacity, or the loss of normal function due to vibrations or deflections. Many other definitions for failure can also be defined. To assist in the definition of failure, a limit state is used. A limit state defines a boundary between satisfactory and unsatisfactory performance of a structure. A limit state function is often used to mathematically represent this boundary.

In structural safety analysis, the three limit states of concern include, the ultimate limit state (ULS), the serviceability limit state (SLS), and the fatigue limit state (FLS). ULSs cover the loss of load-carrying capacity. SLSs cover gradual deterioration, user comfort, and maintenance costs. FLSs cover the loss of strength under repetitive loading. In this research, the FLS is the limit state of concern.

2.4.1.1 Limit State Function

A simple limit state function can be defined as given in Equation [2.10].

$$g(R, Q) = R - Q \quad [2.10]$$

where: R = load resistance;

Q = load effect.

The boundary between satisfactory and unsatisfactory performance is given when Equation [2.10] equals zero. When Equation [2.10] is greater or equal to zero, the structure is safe; when Equation [2.10] is less than zero, the structure is not safe. The probability of occurrence of the latter case is given by Equation [2.11], which mathematically defines the probability of failure.

$$P_f = P(R - Q < 0) \quad [2.11]$$

where: P_f = probability of failure.

If R and Q are continuous random variables, then a probability density function (PDF) can represent each, as shown in Figure 2.11, which also gives R – Q as its own PDF.

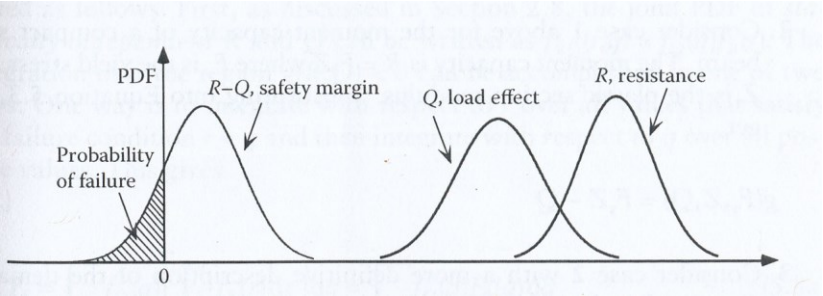

Figure 2.11: PDFs for load and resistance (Nowak & Collins, 2013).

The limit state function can be much more complex and become a function of more than one variable, including load components, resistance parameters, material properties, and analysis factors to name a few. Therefore, it is often difficult to directly calculate the probability of failure using Equation [2.11], so the term reliability index is used to quantify the safety of a structure, which is discussed in Section 2.4.2.

2.4.1.2 State Variables

State variables are the load and resistance parameters used in the limit state function. If the limit state function is constructed with two state variables, resistance R and load effect Q, then the space of state variables is two-dimensional as given in Figure 2.12. A three-dimensional joint PDF for R and Q can be defined as shown in Figure 2.13. To calculate the probability of failure, this joint PDF is integrated over the failure region, which can be extremely difficult, if not impossible to calculate.

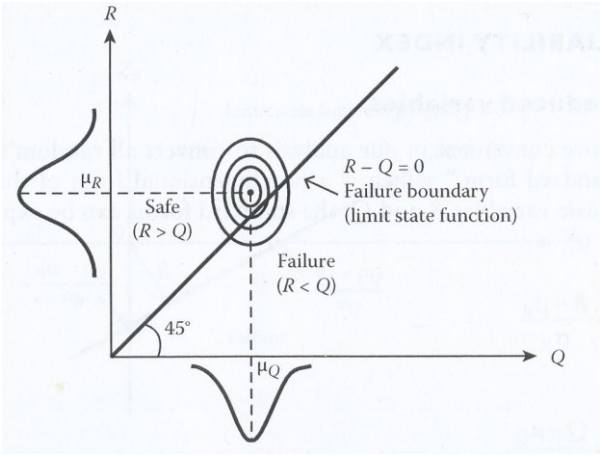

Figure 2.12: Failure boundary in state space (Nowak & Collins, 2013).

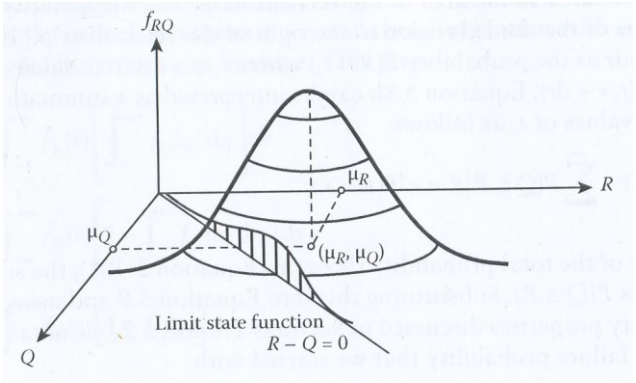

Figure 2.13: Joint PDF for load and resistance (Nowak & Collins, 2013).

2.4.2 Reliability Index

The reliability index is used to quantify the safety of a structure. In defining the reliability

index, it is convenient to convert R and Q to their non-dimensional form. This is shown in Equation [2.12] and Equation [2.13], which can be rearranged to form Equation [2.14] and Equation [2.15].

$$Z_R = \frac{R - \mu_R}{\sigma_R} \quad [2.12]$$

where: Z_R = reduced variable for resistance;

μ_R = mean of resistance;

σ_R = standard deviation of resistance.

$$Z_Q = \frac{Q - \mu_Q}{\sigma_Q} \quad [2.13]$$

where: Z_Q = reduced variable for load;

μ_Q = mean of load;

σ_Q = standard deviation of load.

$$R = \mu_R + Z_R \sigma_R \quad [2.14]$$

$$Q = \mu_Q + Z_Q \sigma_Q \quad [2.15]$$

Using the failure boundary of Equation [2.10] equal to zero, the reliability index is defined as the shortest distance from the origin to the failure boundary line. This definition is shown in Figure 2.14 and was introduced by Hasofer and Lind (1974). It can be shown through geometry that the reliability index is given by Equation [2.16].

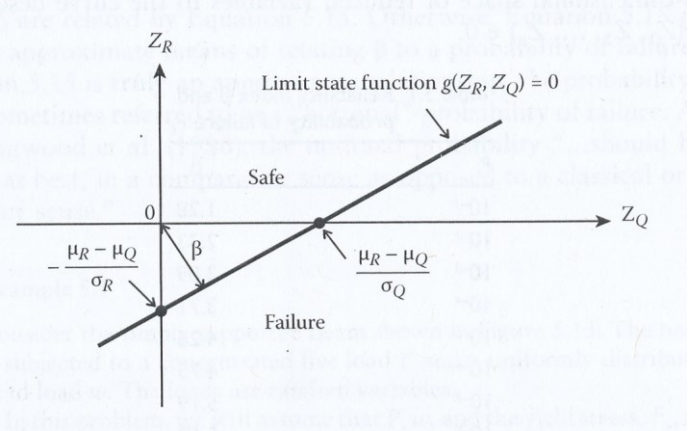

Figure 2.14: Reliability index shown visually.

$$\beta = \frac{(\mu_R - \mu_Q)}{\sqrt{{\sigma_R}^2 + {\sigma_Q}^2}} \qquad [2.16]$$

where: β = reliability index.

If both R and Q are normally distributed random variables, the reliability index can be related to probability of failure by Equation [2.17]. If R and Q are non-normal, Equation [2.17] is only an approximation. Table 2.3 presents the variation of reliability index with probability of failure.

$$P_f = \Phi(-\beta) \qquad [2.17]$$

where: Φ = cumulative distribution function of the standard normal distribution.

Table 2.3: Relationship between reliability index and probability of failure.

Probability of Failure	Reliability Index
10^{-1}	1.28
10^{-2}	2.33
10^{-3}	3.09
10^{-4}	3.71
10^{-5}	4.26
10^{-6}	4.75
10^{-7}	5.19
10^{-8}	5.62
10^{-9}	5.99

2.4.2.1 Methods of Calculation

Several methods exist to calculate the reliability index for a given limit state function. Three methods are discussed briefly in this thesis, which include first-order, second-moment; Hasofer-Lind; and Rackwitz-Fiessler procedure.

2.4.2.1.1 First-Order, Second-Moment Reliability Index

In this method, only the mean and standard deviation of the variables are required to calculate the reliability index. For a simple linear limit state function, such as the function given in Equation [2.18], the reliability index is calculated from Equation [2.19].

$$g(X_1, X_2, \ldots, X_n) = a_0 + \sum_{i=1}^{n} a_i X_i \qquad [2.18]$$

where: a_i = limit state constant;

X_i = uncorrelated random variable.

$$\beta = \frac{a_0 + \sum_{i=1}^{n} a_i \mu_{Xi}}{\sqrt{\sum_{i=1}^{n} (a_i \sigma_{Xi})^2}} \qquad [2.19]$$

However, if the limit state function is non-linear, an approximate answer is obtained by

linearizing the function using a Taylor series expansion, in which only the first term of the expansion is used. Details on calculating the reliability index for non-linear limit state functions is given in Nowak and Collins (2013).

Though this method is simple and does not require knowledge of the probability distribution of each variable, it does have two major disadvantages. First, if the tails of the variable's distribution cannot be approximated by the normal distribution, the results are not accurate. Second, this method contains an invariance problem and the reliability index depends on the form of the limit state function.

2.4.2.1.2 Hasofer-Lind Reliability

Hasofer and Lind proposed an alternate reliability index which did not have an invariance problem. Instead of evaluating the limit state function at the mean values of the variables as the first-order, second-moment method did, the limit state function is evaluated at a design point. This design point is a point on the failure boundary. Since the design point is usually not known, iteration is required to solve for the reliability index. The interactive procedure involves solving (2n + 1) variables using one of two solution procedures: simultaneous equation procedure or matrix procedure. These procedures are detailed in Nowak and Collins (2013). The iterations stop when the reliability index and the design point converge.

2.4.2.1.3 Rackwitz-Fiessler Procedure

If information about the distribution for each random variable is known, a more accurate calculation of the reliability index can be made. The Rackwitz-Fiessler procedure essentially calculates equivalent normal values for the mean and standard deviation of each variable. To obtain the equivalent mean and equivalent standard deviation, the cumulative distribution function (CDF) and the PDF of the actual function needs to equal the normal CDF and PDF at the design point on the failure boundary. Since the design point is not known, this procedure also requires iteration. The detailed method of calculating the reliability index using a modified matrix procedure, as well as a graphical method is given in Nowak and Collins (2013).

2.4.3 System Reliability

Thus far this chapter has discussed methods for calculating the reliability of a single structural component. A structure normally consists of many components put together to form a structural system. Differentiating between the component reliability and the system reliability is important, and is detailed herein.

Two ideal systems exist in system reliability, a series system and a parallel system. In a series system, the system fails when one element of the system fails. This is similar to a chain in that if one link fails, the whole chain fails. A parallel system is the other extreme, requiring all elements of the system to fail before the system fails. This is similar to a cable with parallel wires in which all wires have to fail before the cable fails. In most cases, a real structural system is a combination of both series and parallel systems. In calculating the reliability of a structural system, probability of failure is calculated and the reliability index can then be determined using Equation [2.17]. The calculated reliability index is only the true reliability index if all variables are normally distributed, otherwise it is only an approximation.

2.4.3.1 Reliability of a Series System

The probability of failure for a series system can be calculated depending on the level of correlation between elements. If each element in a series system is statistically independent, or if each element is fully correlated, the probability of failure is calculated easily, only requiring the probability of failure for each element. These two cases represent the bounds for the probability of failure of the whole system, as shown in Equation [2.20]. The left side of Equation [2.20] represents perfect correlation and the right side represents no correlation. However, if the correlation between elements lies somewhere between no correlation and full correlation, the system reliability is difficult, if not impossible to calculate (Nowak & Collins, 2013).

$$\max\{P_{fi}\} \leq P_f \leq 1 - \prod_{i}^{n}[1 - P_{fi}] \qquad [2.20]$$

2.4.3.2 Reliability of a Parallel System

For a parallel system, the probability of failure can be calculated similar to a series systems, with different bounds. The bounds for the probability of failure of the system are given in Equation [2.21]. The left side of Equation [2.21] represents if each element in the system were uncorrelated and the right side represents perfect correlation between elements.

$$\prod_{i}^{n}[P_{fi}] \leq P_f \leq min\{P_{fi}\} \quad [2.21]$$

2.4.4 Definition of Failure

It is important in this research to define 'failure'. For this situation, a single fatigue crack on the OSPD is considered a 'failure'. Though it does not result in the overall failure of the deck, it does present an issue requiring an unwanted repair. This makes the OSPD consistent with a series system, in which the 'failure' of one member results in the failure of the entire system.

Chapter 3: Literature Review – Fatigue Evaluation of Steel and OSPD

The literature review performed for this research reviews the fatigue of OSPDs, and the fatigue evaluation of steel structures, both using code approaches and recent research using SHM.

3.1 Fatigue of Orthotropic Decks

OSPDs are fabricated using several welded details to connect the various steel components, thus OSPDs are prone to fatigue. Two of the most common fatigue details are shown in Figure 3.1(a) and Figure 3.1(b), which show the rib-to-deck welded joint and the rib-to-floor beam joint respectively. A third joint is present on the MacKay Bridge due to the addition and subsequent removal of stiffeners between adjacent stiffening ribs, shown in Figure 3.1(c).

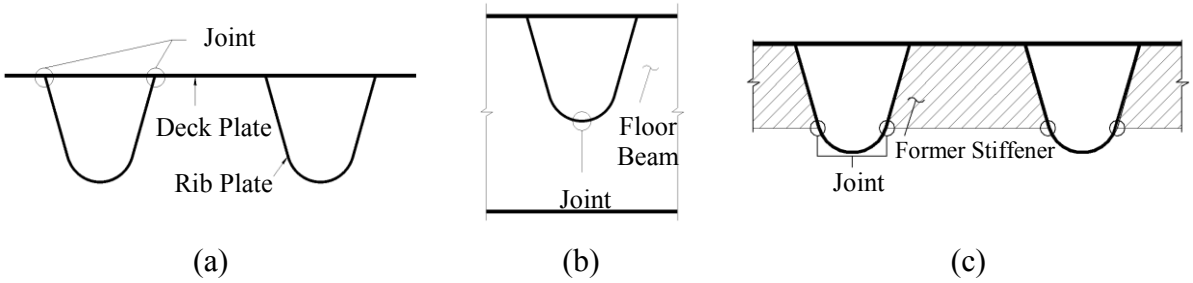

Figure 3.1: Three joints under investigation: (a) rib-to-deck joint, (b) rib-to-floor beam joint, and (c) former stiffener between adjacent stiffening ribs.

Wolchuk (1990) was one of the first researchers to investigate fatigue cracking of OSPD. Cracking in both the rib-to-deck weld and the rib-to-floor beam weld on three different OSPD bridges was documented. The three bridges, the Haseltal Bridge, the Sinntal Bridge and the Severn Bridge, all were constructed with closed stiffening ribs. Wolchuk (1990) discovered that much of the cracking is due to the fabrication procedure and developed several rules for good practice. For the rib-to-floor beam connection, the ribs should be continuous through the floor beam, meaning a cut-out should be made in the floor beam. For the rib-to-deck connection, the welds should have the maximum penetration possible, with at least 80 percent penetration. Further, proper cutting and fitting of the ribs onto the deck plate before welding is essential to eliminate gaps. Also for the rib-to-deck joint, a

thicker deck plate should be used to reduce bending moments in the rib web. An additional fatigue detail existed on the bridges investigated by Wolchuk (1990); this detail was on attachments welded to the bottom of the ribs. The recommendation by Wolchuk was to not permit welded attachments to the ribs or deck plate for erection, support of utilities, or for any other reason. This investigation highlights the importance of proper detailing and fabrication procedures to reduce fatigue issues in OSPD bridges.

3.1.1 Rib-to-Deck Joint (Type A)

Extensive research has been completed on the longitudinal stiffening rib-to-deck plate joint (FHWA, 2012). Through this research, the response of the rib-to-deck weld was determined to be dependent on individual wheel loads rather than axles or gross vehicle weight (GVW) (FHWA, 2012). The joint carries load due to transverse bending and axial stress in the deck plate. An important observation was noted by Freitas et al. (2012) which confirms the stresses of concern are transverse to the welded joint. In the study, Freitas et al. (2012) examined a rehabilitated OSPD in the Netherlands which bonded a second flat steel plate to the original plate. The deck was monitored both before and after the rehabilitation and the maximum principal stress found in the deck plate acts transverse to the welded joint. It has also been determined by Pfeil et al. (2005) and Ya and Yamada (2008) that this joint is dominated by transverse bending moment and the in-plane axial component is small. In a numerical study of an OSPD, it was discovered that the axial stress component was always less than 10 percent of the total stress, and in some critical components, only 3 percent of the total stress (Ya & Yamada, 2008). It is apparent that the stress transverse to the rib-to-deck joint is of concern for fatigue damage. A small amount of the stress in this joint is due to the global effects of the OSPD, however, these effects are usually small and occur in a direction parallel to the rib-to-deck joint, and therefore do not typically present a concern for the fatigue limit state (FHWA, 2012). Four potential fatigue cracks exist at this welded joint and include:

A. A crack propagating from the weld root through the deck plate, called root-deck cracking;

B. A crack propagating from the weld root through the weld throat, called root-weld cracking;

C. A crack propagating from the weld toe in the deck plate through the deck plate, called toe-deck cracking;

D. A crack propagating from the weld toe in the rib web through the rib web, called toe-rib cracking.

These potential fatigue crack locations are shown in Figure 3.2.

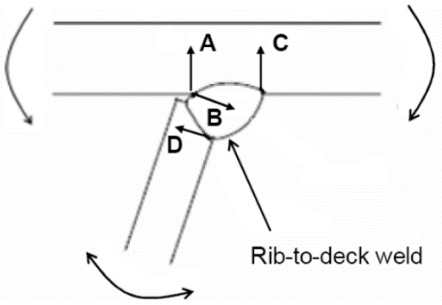

Figure 3.2: Potential fatigue cracks for the rib-to-deck joint; (A) root-deck cracking, (B) root-weld cracking, (C) toe-deck cracking, (D) toe-rib cracking (FHWA, 2012).

Fatigue cracks that initiate at the weld root have a lower fatigue resistance than fatigue cracks initiating at the weld toe (FHWA, 2012). To prevent root cracking, an adequate amount of penetration and proper fit-up are the governing factors in the resistance. It has been shown recently that if the fit-up gap is controlled carefully prior to welding, cracking that initiates at the root can be prevented (Wright, 2011).

A study by Connor and Fisher (2001) observed the response of the rib-to-deck joint through two strain measurements made on the rib and the deck plate close to the joint. Under a truck loading of known axles, each individual axle can be identified in Figure 3.3, which shows how the rib-to-deck detail is impacted by individual wheel loads. Also observed in the study by Connor and Fisher (2001) was the impact of transverse position of the wheel loads on the deck plate. Figure 3.4 shows the observed response of a rib gauge due to the passage of two different trucks. One of the trucks produces a tensile stress range, whereas the other truck produces a compressive stress range. The observed response was witnessed in all rib and deck gauges, showing the impact of transverse wheel positioning. The observed strain response of a deck or rib gauge was either tensile or compressive, depending on the transverse positioning of the truck.

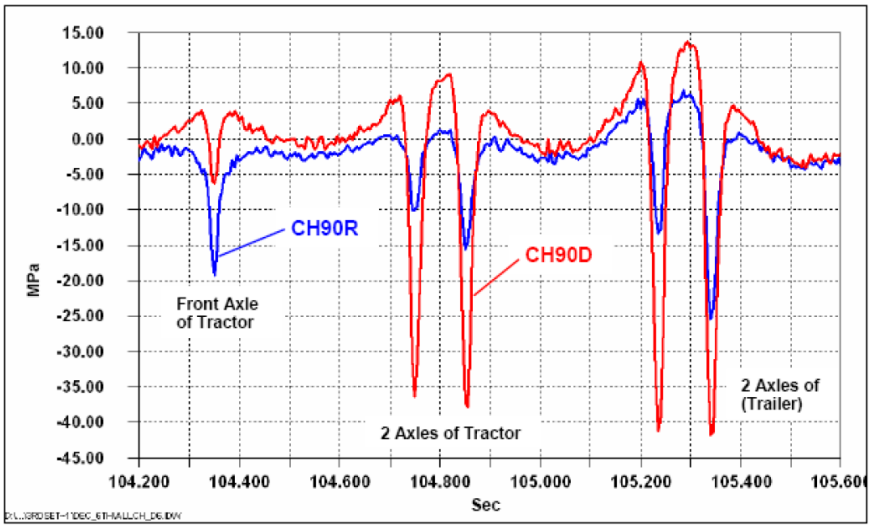

Figure 3.3: Measured strain of two gauges on the rib and deck plate as a five-axle truck passed (Connor & Fisher, 2001).

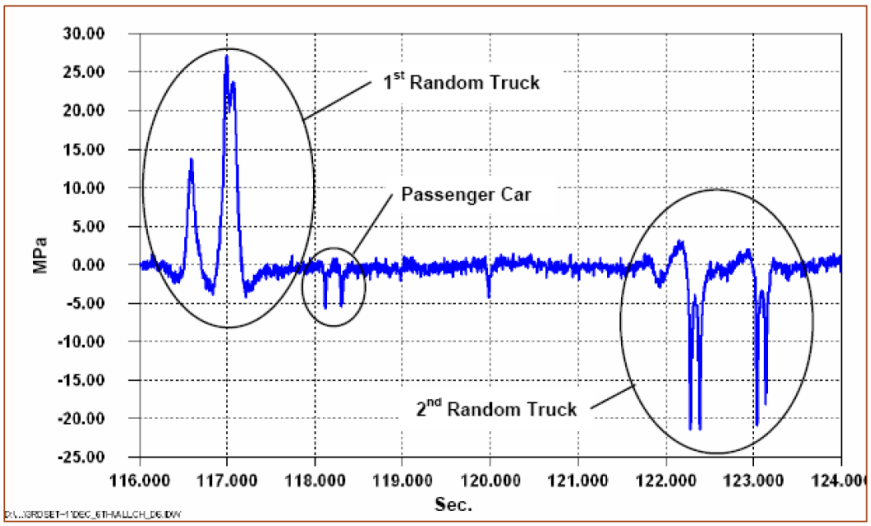

Figure 3.4: Measured strain of rib gauge due to passage of two random trucks (Connor & Fisher, 2001).

In a study by Xiao et al. (2008), a 3-dimensional numerical model of an OSPD was constructed with a 12 mm thick deck plate, 8 mm thick closed trapezoidal ribs 250 mm in height and a width of 320 mm at the deck plate level. Shell elements were used in the model, approximately 20 mm by 20 mm in size. It was assumed the asphalt was capable of distributing the wheel loads at a 1:1 slope through the 70 mm pavement thickness, thus the asphalt was not modeled. In the study, the transverse position of the wheel load with respect

to the rib-to-deck joint was studied. Three separate transverse driving locations were used in the analysis: centred over the rib, centred between ribs, and centred over the rib-to-deck joint. The wheel load was also placed at 30 different longitudinal locations, 29 of which were located on a single span between floor beams. In most cases, the wheel load centred over the rib-to-deck joint produced the highest stress at the rib-to-deck joint. The worst longitudinal position was at the one-eighth span point. It was also found that the stresses in the rib plate are smaller than the stresses found in the deck plate. These results are shown in Table 3.1, where the stress was taken at different section locations as marked in Figure 3.5

Table 3.1: Results from FEM of OSPD (Xiao et al., 2008).

Range of transverse stresses (MPa) under the action of 100 kN wheel load

Location of stress investigation		Over-rib loads	In-between-ribs loads	Riding-rib wall loads
Section A (Bottom face)	X=0	94.7	47.4	91.0
	$X = -300$ (L/8)	77.3	74.6	104.8
	$X = -600$ (L/4)	76.2	73.2	103.6
	$X = -900$ (3L/8)	74.3	72.1	101.6
	$X = -1200$ (L/2)	72.1	71.5	99.8
Section B (Bottom face)	$X = -300$ (L/8)	86.3	88.7	118.3
	$X = -600$ (L/4)	84.9	87.4	117.5
	$X = -900$ (3L/8)	82.2	86.8	115.2
	$X = -1200$ (L/2)	79.1	86.5	113.0
Section C (Outside face)	$X = -300$ (L/8)	9.1	34.9	22.6
	$X = -600$ (L/4)	14.7	39.7	23.4
	$X = -900$ (3L/8)	18.1	40.9	21.7
	$X = -1200$ (L/2)	18.1	40.8	20.1

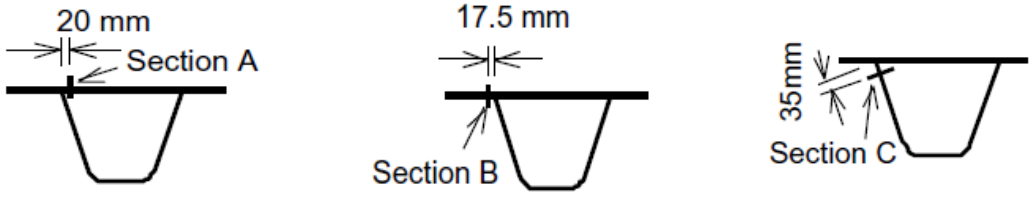

(a) (b) (c)

Figure 3.5: Investigation locations for FEM of OSPD (Xiao et al., 2008).

The longitudinal placement of the wheel load was also explored by Ya and Yamada (2008). In this study, a 3-dimensional numerical model was also developed, and similarly used shell elements and only modeled the load distribution characteristics of the pavement. The wheel load was applied at the same three transverse locations given in Xiao et al. (2008).

The critical location for the rib-to-deck joint was examined between transverse floor beams and found to be located at the one-quarter span point. However, the authors note the difference between the one-quarter and the one-half span points were so small that fatigue cracking could occur in either location first.

Several parametric studies have taken place through numerical modeling (Pfeil et al., 2005, Ya & Yamada, 2008, Xiao et al., 2008). The results of these studies have arrived at the conclusion that the most effective way to increase the fatigue life of the rib-to-deck joint is by increasing the thickness of the deck plate, which significantly reduces the stress range at the rib-to-deck joint. Further, the wearing surface has been found to play a significant role in the stress range by distributing the wheel loads over a much larger area. This was confirmed by Connor and Fisher (2000) who found the addition of pavement reduced the stress range by 25 to 50 percent on a prototype OSPD installed on the Williamsburg Bridge. The data collected by Connor and Fisher (2000) was from a controlled load test both before and after the application of pavement on the OSPD. A wearing surface that is maintained in good condition will elongate the fatigue life of the rib-to-deck joint.

3.1.2 Rib-to-Floor beam (Type B)

Several different rib-to-floor beam details have been used in OSPD across the world. These details include fitted and continuous ribs between floor beams, with and without internal bulkheads, with and without internal stiffeners, different weld types, and different plate sizes. In the case that includes a cut-out, an additional cope-hole in the floor beam web, located at the bottom of the rib plate, has been studied extensively. Figure 3.6 shows the connection with and without an additional cope-hole, as well as the welding detail for fitted versus continuous stiffening ribs.

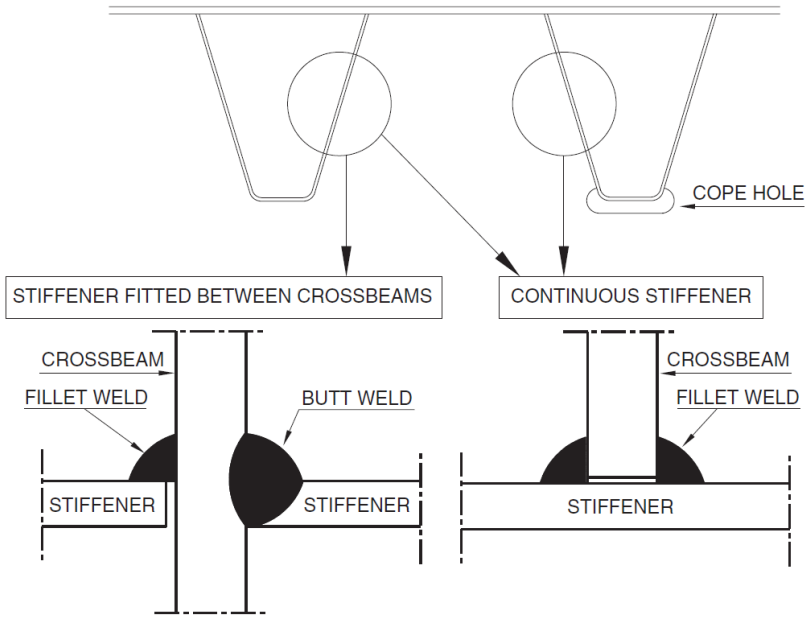

Figure 3.6: Typical geometry for rib-to-floor beam connection (Kolstein, 2007).

The connection of the rib plate to the floor beam has two main types; the first has stiffening ribs passing through the floor beam via a cut-out in the floor beam web. The second has discontinuous ribs fitted between floor beams. The first type can either be tight fitting or contain a cope-hole in the floor beam web, near the bottom of the rib plate; a detail containing a cope hole is easier to fabricate (Kolstein, 2007). The second type, with stiffening ribs fitted between floor beams, was used in early designs. Though this detail was good for reducing the chance of cracking in the floor beam, the connecting weld has a low fatigue strength. This design was abandoned in most bridge applications, except for short-life bridges and other atypical designs (Kolstein, 2007).

The stress observed in the floor beam web plate is a result of combined in-plane and out-of-plane loading. The in-plane loading is a result of flexure and shear from the floor beam spanning along the top chord of the transverse stiffening truss. The out-of-plane loading is due to the rib rotation, causing out-of-plane flexure of the floor beam, which can vary from rib to rib depending on the stiffness of the OSPD and the transverse position of the wheel load.

For continuous ribs with a tight fitting cut-out in the floor beam, the connection is

completed with fillet welds on both sides of the floor beam web to connect the two components. In this joint, there is three types of fatigue cracking:

A. A crack propagating from the weld root through the weld throat, called root-weld cracking;

B. A crack propagating from the weld toe through the rib plate, called toe-rib cracking;

C. A crack propagating from the weld toe through the floor beam, called toe-web cracking.

The most likely crack location for continuous ribs welded all around the rib plate is at the bottom of the rib at the weld toe (Kolstein, 2007). The stress at this location is due to the bending moment in the rib from the application of a wheel load some distance away from the floor beam (out-of-plane bending).

Research completed by Connor and Fisher (2004) examined the response of the rib-to-floor beam joint on a prototype OSPD installed on the Bronx-Whitestone Bridge. This detail contained a cope-hole. From controlled load testing, the in-plane and out-of-plane stresses were observed from the passage of a three-axle truck. Figure 3.7 shows the in-plane and out-of-plane behavior at the gauged locations noted in the figure. Though the out-of-plane stress observes every axle, it has been observed that this particular detail does not receive stress cycles from every axle passing. The passage of a truck will produce one primary stress cycle, which is not governed by the GVW, but rather a single or group of axles spaced closely together. Figure 3.8 shows the response of different rib-to-floor beam gauges subjected to a five-axle truck. The gauge steady near zero is a deck plate gauge, which observes each axle for comparison.

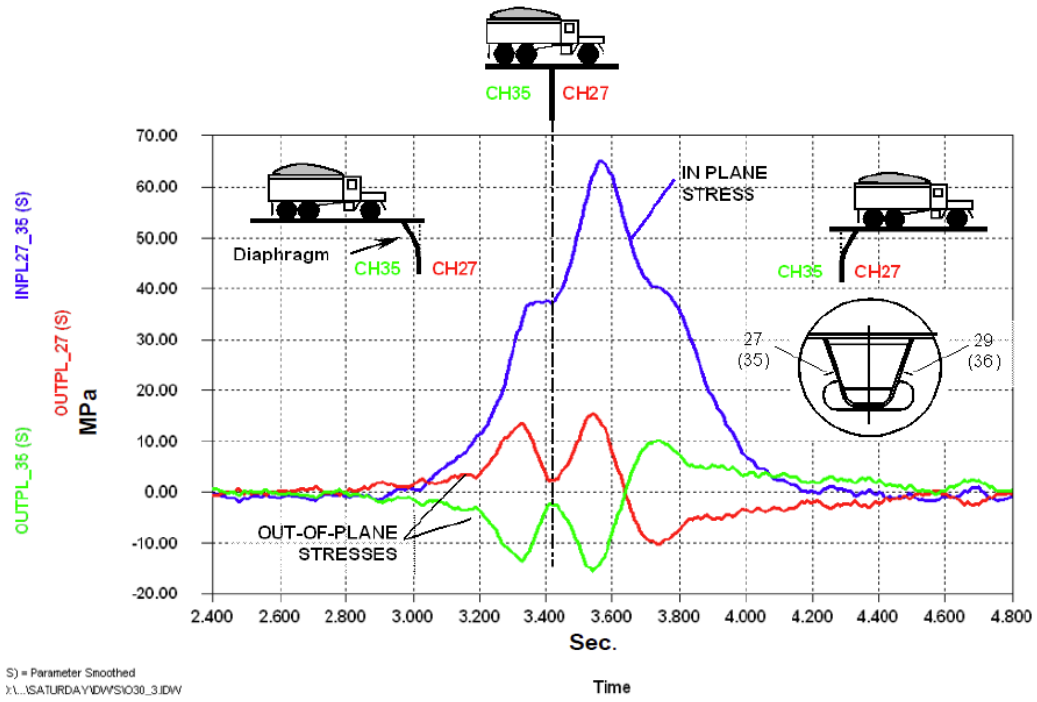

Figure 3.7: In-plane and out-of-plane behavior of rib-to-floor beam joint (Connor & Fisher, 2004).

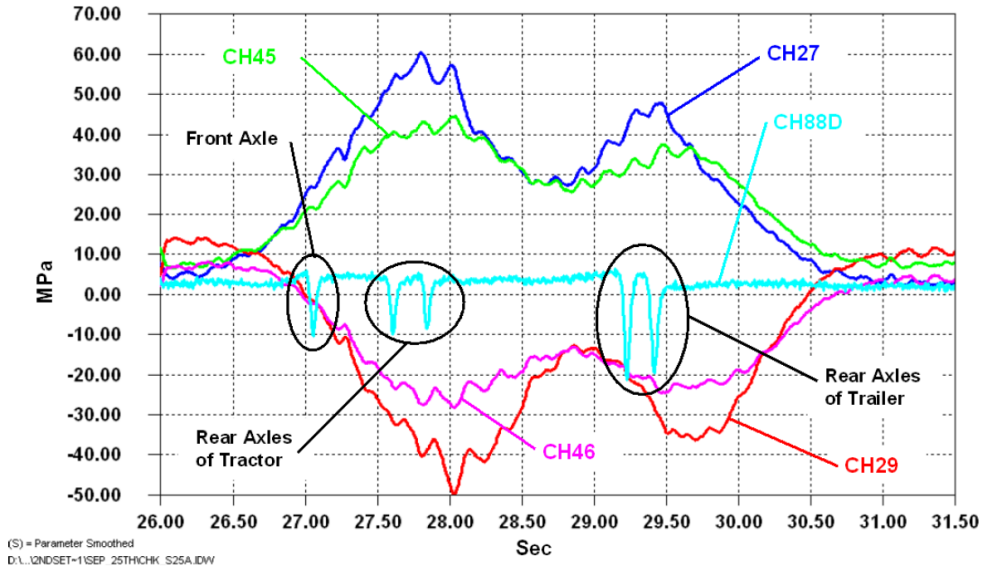

Figure 3.8: Response of rib-to-floor beam connection subjected to a five axle truck loading (Connor & Fisher, 2004).

Several studies exist (Connor & Fisher, 2000, Tsakpoulos & Fisher, 2003, Tsakpoulos & Fisher, 2005a, Tsakpoulos & Fisher, 2005b, Connor & Fisher, 2005) which examine the

rib-to-floor beam connection on two New York bridges; the Williamsburg Bridge and the Bronx-Whitestone Bridge. In these studies, the cope hole in the floor beam web was studied to provide the best detail possible for a new OSPD being installed on each bridge. A prototype deck panel installed on the Williamsburg Bridge was instrumented to monitor the response of the details under random traffic. Controlled load testing also took place. Concurrent with the field monitoring, laboratory testing of full-scale deck panels took place in the laboratory. It was observed that stresses in the floor beam were dominated by in-plane stress for both the field and laboratory testing. Improvements of the detail were made and laboratory testing of new panels was completed before installation on the Williamsburg Bridge. In the laboratory testing of the Bronx-Whitestone Bridge, the use of internal bulkheads and internal stiffeners were examined. Different weld options were also studied. Unfortunately, the exact detail examined by these studies does not match the research being conducted on the rib-to-floor beam detail on the MacKay Bridge. The OSPD on the MacKay has the stiffening rib passing through the floor beam web via a tight fitting cut-out; no additional cope-hole is provided.

3.1.3 Type C (former stiffeners)

When the former stiffeners were present on the OSPD, they created a distortion-induced fatigue problem at the bottom of the stiffener due to out-of-plane displacements. This is the reason they were removed. Now that the stiffeners have been removed, the type C detail is a load-induced fatigue problem.

The type C detail is unique and not typically found in OSPD. For that reason, no literature is available on this detail. However, the behavior of this detail would be similar to a welded rib splice. The ribs carry shear and bending moment from passing wheel loads. Essentially the ribs behave as bending members, with a small amount of torsional moment (FHWA, 2012). The transverse position of a wheel load significantly influences the response. When gauged, the response of the rib under axle groups can be observed; individual axles within an axle group cannot be identified (FHWA, 2012). Connor and Fisher (2004) document the field measurements made on a prototype orthotropic deck installed on the Bronx-Whitestone Bridge in New York. The instrumentation included uniaxial strain gauges installed on the bottom of select stiffening ribs. During controlled load testing, a three-axle

truck was driven over the gauged OSPD. Figure 3.9 shows the resulting response of several stiffening rib gauges. Though the response is small, both axles on the rear tandem are observed on the two rib gauges closest to the wheel loads. The additional small stress cycle has a negligible contribution to overall fatigue damage. The corresponding strain range is approximately 20 microstrain. Further, these gauges are installed on the bottom of the stiffening rib where bending stress is the highest. The type C fatigue detail under consideration is located approximately 66 mm above the bottom of the stiffening rib, meaning the stress from each axle would be even more difficult to distinguish.

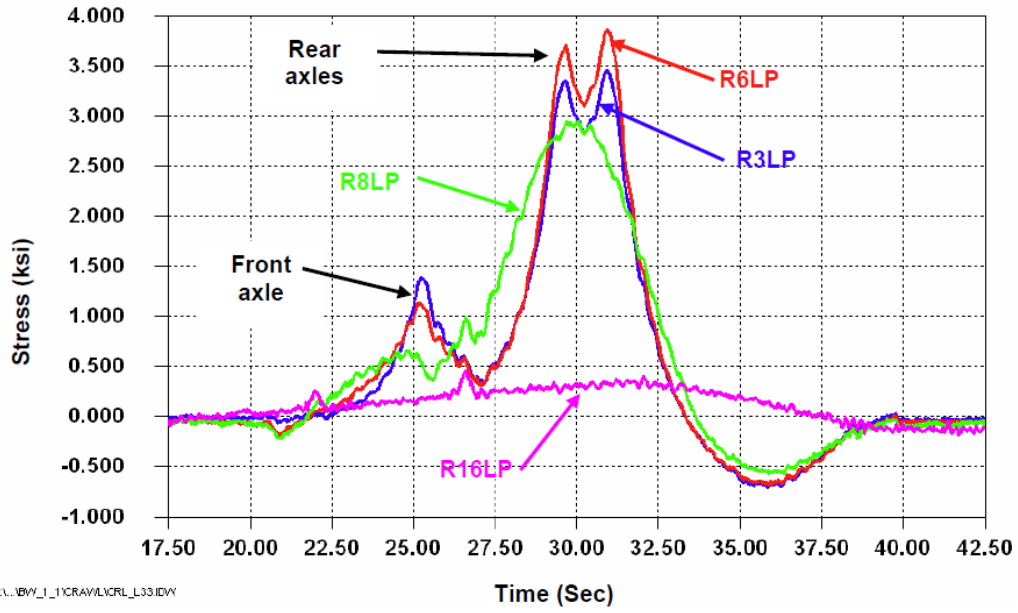

Figure 3.9: Response of longitudinal ribs (Connor & Fisher, 2004).

3.1.4 Laboratory Testing

Many laboratory studies have been undertaken to investigate the behaviour of the rib-to-deck joint, as well as the rib-to-floor beam web joint. A summary of the fatigue testing of OSPD fatigue details can be found in Kolstein (2007), which attempts to provide a detail classification for several fatigue details in an OSPD. Tests documented included small-scale tests of the rib-to-deck joint and the rib-to-floor beam web joint. Large-scale testing of entire OSPD panels has been mentioned previously, and include: Connor and Fisher (2000), Connor and Fisher (2001), Tsakpoulos and Fisher (2003), Tsakpoulos and Fisher (2005a), Tsakpoulos and Fisher (2005b), Connor and Fisher (2005). The main focus of

these studies was on the rib-to-floor beam web joint, which contained a cope-hole. In the case of small-scale and large-scale testing, there is no research that attempts to determine the fatigue life of an OSPD by obtaining specimens from an aging in-service deck which has the imprinted fatigue damage from the in-service loading and testing the specimens until failure.

3.2 Fatigue Evaluation of Steel Bridges

Provisions for the evaluation of steel bridges are found in many codes, and many papers contain methods for determining the remaining life of a steel bridge. This section outlines these published methods which have been incorporated into various design codes, and other relevant publications.

3.2.1 CSA S6-06 – CHBDC – Fatigue Evaluation

In the CHBDC, the evaluation of existing structures is covered under Section 14 – Evaluation. The evaluation under the fatigue limit state is covered under Clause 14.18, which states any fatigue prone detail, or detail that shows evidence of fatigue-related defects, shall be assessed for fatigue at the fatigue limit state using appropriate methods. The load factors for the load combinations used in the assessment shall be as specified in Section 3 of the CHBDC. No specific methods are given in Section 14 of the CHBDC, however, the Commentary to the CHBDC suggests an evaluator could use one of three methods: the actual stress measured through field monitoring, Moses' approach in NCHRP Report 299 (Moses et al., 1987), or Albrecht and Rubeiz (1987). With Albrecht and Rubeiz (1987) proving extremely difficult to be located, most designers would turn to NCHRP Report 299. It can be assumed that the loading model for the evaluation to be the same as prescribed for fatigue design in Clause 10.17 of the CHBDC.

3.2.2 AASHTO Manual for Bridge Evaluation 2011 Edition

Section 7 of the Manual for Bridge Evaluation is entitled "Fatigue Evaluation of Steel Bridges". The development of this section was based on NCHRP Report 299, as well as the AASHTO Guide Specification for Fatigue Evaluation of Existing Steel Bridges 1990 Edition. This manual has restrictions on its use and does not apply to details that are already cracked. Additionally, it is explicitly stated that when more refined analysis is performed,

or site-specific data is used, uncertainty is removed and lower partial load factors can be used.

Three different levels of fatigue life exist in this manual, all associated with different probabilities of failure. In order of increasing probability of failure, the three different fatigue life levels are the minimum expected life (two standard deviations below the mean in log-log space), the evaluation life (one standard deviation below the mean in log-log space), and the mean life. These represent approximately 2 percent, 16 percent, and 50 percent probability of failure respectively. The fatigue resistance can be calculated based on either of these three lives. The minimum expected life is conservative for design, the evaluation life is conservative for evaluation of an existing structure, and the mean life is the most likely fatigue life (AASHTO, 2011). The procedure for evaluating the fatigue life of steel bridges is detailed below.

3.2.2.1 Stress Range

In determining the effective stress range, either a calculated estimated stress range or a measured estimated stress range is multiplied by the stress range partial load factor. The calculated estimated stress range is found by:

- Using 75 percent of the fatigue truck specified in AASHTO LRFD Design Article 3.6.1.4;
- Using an effective truck weight estimated through a weigh-in-motion study;
- Using an effective truck weight estimated through a truck survey.

The measured estimated stress range is determined through field measurements of strains at the detail in question. Equation [3.1] shows how the effective stress range is determined:

$$(\Delta f)_{eff} = R_s \Delta f \qquad [3.1]$$

where: $(\Delta f)_{eff}$ = effective stress range;

R_s = stress range estimate partial load factor;

Δf = calculated or measured estimated stress range using Palmgren-Miner's rule.

Two sources of uncertainty exist in determining the effective stress range; uncertainty associated with the analysis used, represented by an analysis partial load factor, R_{sa}, and uncertainty associated with the assumed effective truck weight, represented by a truck-weight partial load factor, R_{st}. These two factors are multiplied together to give the stress range estimate partial load factor, R_s. Table 3.2 shows the partial load factors for calculating the evaluation or minimum fatigue life. All partial load factors equal one for the mean fatigue life.

Table 3.2: Load factors (reproduced from AASHTO, 2011).

Fatigue Life Evaluation Method	Analysis Partial Load Factor, R_{sa}	Truck Weight Partial Load Factor, R_{st}	Stress Range Estimate Partial Load Factor, R_s
Stress range calculated using simplified analysis, truck weight from LRFD Design Article 3.6.1.4	1.0	1.0	1.0
Stress range calculated using simplified analysis, truck weight from weigh-in-motion study	1.0	0.95	0.95
Stress range calculated using refined analysis, truck weight from LRFD Design Article 3.6.1.4	0.95	1.0	0.95
Stress range calculated using refined analysis, truck weight from weigh-in-motion study	0.95	0.95	0.90
Stress range calculated using field measured strains	N/A	N/A	0.85

3.2.2.2 Determining Fatigue-Prone Details

A detail only incurs fatigue damage if it experiences a net tensile stress. Therefore, the

detail only needs to be evaluated further if Equation [3.2] applies.

$$2R_s(\Delta f)_{tension} > f_{DL\ comp.} \quad [3.2]$$

where: $(\Delta f)_{tension}$ = factored tensile portion of the stress range caused by the passage of a fatigue truck;

$f_{DL\ comp.}$ = unfactored compressive stress due to dead load at the detail under consideration.

3.2.2.3 Infinite-Life Check

The fatigue detail under consideration has an infinite fatigue life if the CAFL is greater or equal to the maximum expected stress range at the detail. Otherwise, the finite fatigue life must be calculated according to Section 3.2.2.4.

3.2.2.4 Estimating Finite Fatigue Life

As mentioned previously, three different levels of fatigue life exist, the minimum expected life, the evaluation life, and the mean life. The three fatigue life levels have different resistance factors used in the calculation for remaining fatigue life. To calculate the remaining fatigue life of a detail, in years, Equation [3.3] is used.

$$y = \frac{R_R A}{365n(ADTT)_{SL}[(\Delta f)_{eff}]^3} - a \quad [3.3]$$

where: y = remaining finite fatigue life of a fatigue prone detail in years;

R_R = resistance factor of the specified fatigue life level assessment;

n = number of stress range cycles per truck passage;

$(ADTT)_{SL}$ = average daily truck traffic in a single lane averaged for the entire fatigue life;

a = current age of the bridge in years.

In calculating the number of cycles per truck passage, three options are presented, which include the use of LFRD Design Table 6.6.1.2.5-2, the use of influence lines, and through the use of field measurements.

The $(ADTT)_{SL}$ is as specified in LRFD Design Article 3.6.1.4.2. A plot has been included in the AASHTO Manual for Bridge Evaluation (Figure C7.2.5.5-1) to assist in estimating this value over the life of the structure.

The R_R values for each fatigue detail category are presented in Table 3.3 for all three fatigue life levels.

Table 3.3: Resistance factor for specified fatigue level assessment for each fatigue detail category.

Fatigue Detail Category	R_R		
	Evaluation Life	Minimum Life	Mean Life
A	1.7	1.0	2.8
B	1.4	1.0	2.0
B'	1.5	1.0	2.4
C	1.2	1.0	1.3
C'	1.2	1.0	1.3
D	1.3	1.0	1.6
E	1.3	1.0	1.6
E'	1.6	1.0	2.5

3.2.2.5 Strategies to Increase the Remaining Fatigue Life

If the fatigue life calculated is not acceptable, this manual presents options available to the engineer. Recalculating the fatigue life is suggested by either accepting greater risk, or through more accurate data. Retrofitting the critical details is the other option available if the fatigue life is still not acceptable after recalculation.

3.2.3 NCHRP Report 721: Fatigue Evaluation of Steel Bridges

The NCHRP Report 721 by Bowman et al. (2012) makes suggested changes to Section 7 of the AASHTO Manual for Bridge Evaluation written in 2011. This includes the introduction of a fatigue serviceability index used to measure the fatigue performance of a structural detail. The proposed changes are outlined in the sections below.

3.2.3.1 Stress Range

A slight modification to the effective stress range has been made from Section 7. A multiple presence factor, R_p, has been included to account for the effect of trucks being present at the same time in multiple traffic lanes. A complex equation is presented in NCHRP Report 721 to calculate the multiple presence factor. Equation [3.4] is used to calculate the effective stress range.

$$(\Delta f)_{eff} = R_p R_s \Delta f \qquad [3.4]$$

where: R_P = multiple presence factor.

The stress range can still be estimated through field measurements at the location of the fatigue prone detail.

3.2.3.2 Estimating Finite Fatigue Life

This report suggests four levels of fatigue life, all associated with different probabilities of failure. In order of increasing probability of failure, the four different fatigue life levels are the minimum expected life (two standard deviations below the mean in log-log space), the evaluation 1 life (one standard deviations below the mean in log-log space), the evaluation 2 life (one-half of a standard deviation below the mean in log-log space), and the mean life. These correspond to approximately 2 percent, 16 percent, 33 percent, and 50 percent probability of failure respectively. The four fatigue life levels have different resistance factors used in the calculation for remaining fatigue life. To calculate the remaining fatigue life of a detail, in years, Equation [3.5] is used, which has been modified from Section 7 to include traffic growth rate and the present average daily truck traffic (ADTT) in a single lane.

$$y = \frac{\log\left[\frac{R_R A}{365n[(ADTT)_{SL}]_P\left[(\Delta f)_{eff}\right]^3} g(1+g)^{a-1} + 1\right]}{\log(1+g)} - a \qquad [3.5]$$

where: $[(ADTT)_{SL}]_P$ = present average daily truck traffic in a single lane;

g = estimated percentage annual traffic growth rate.

The R_R values for each fatigue detail category are presented in Table 3.3 for all fatigue life levels.

Table 3.4: Resistance factor for specified fatigue level assessment for each fatigue detail category.

Fatigue Detail Category	R_R			
	Minimum Life	Evaluation 1 Life	Evaluation 2 Life	Mean Life
A	1.0	1.5	2.2	2.9
B	1.0	1.3	1.7	2.0
B’	1.0	1.3	1.6	1.9
C	1.0	1.3	1.7	2.1
C’	1.0	1.3	1.7	2.1
D	1.0	1.3	1.7	2.0
E	1.0	1.2	1.4	1.6
E’	1.0	1.3	1.6	1.9

3.2.3.3 Fatigue Serviceability Index

A fatigue serviceability index is presented to measure the performance of a structural detail with respect to the fatigue resistance. The fatigue serviceability index is calculated using Equation [3.6].

$$Q_f = \left(\frac{y-a}{N_t}\right) G R_f I \qquad [3.6]$$

where: Q_f = fatigue serviceability index;

N_t = greater of y or 100 years;

G = load path factor;

R_f = redundancy factor;

I = importance factor.

Values for G, R_f, and I are tabulated in Bowman et al. (2012). Based on the fatigue

serviceability index calculated, recommended actions are given and are presented below in Table 3.5:

Table 3.5: Recommended actions based on fatigue serviceability index (Bowman et al., 2012).

Fatigue Serviceability Index	Fatigue Rating	Assessment Outcome
< 0.00	Critical	Consider retrofit, replacement or reassessment
0.00 – 0.10	Poor	Assess frequently
0.10 – 0.20	Fair	Increase inspection frequency
0.20 – 0.35	Moderate	Continue regular inspection
0.35 – 0.50	Good	Continue regular inspection
0.50 – 1.00	Excellent	Continue regular inspection

3.2.4 Issues with Code Methods

Several issues arise when using the code methods presented above. First, these codes do not account for any degradation of the bridge components over time. It is explicitly stated that the codes are not applicable to a bridge component having any degradation. The resistance to fatigue loading is derived from brand new steel specimens that were tested until failure. Second, these codes contain partial load factors to account for uncertainty in using these methods. These factors have been calibrated for any bridge structure an engineer might evaluate and are not specific to characteristics of the bridge or loading it is subjected to. Finally, predicting the traffic over the lifetime of a bridge structure is extremely difficult as truck loading can change over the typical 75 year design life. Though the code methods allow the calculation of remaining fatigue life, they still contain a large amount of uncertainty.

3.2.5 Fatigue Life Assessment using SHM

SHM has been used in the fatigue evaluation of existing structures by many researchers. Examples include Szersen et al. (1999), Kim et al. (2001), Abdou et al. (2003), Li et al. (2003), Alampalli & Lund (2006), Battista et al. (2008), Tong et al. (2008), Battista et al. (2008), Liu et al. (2009), Liu et al. (2010), Kwon & Frangopol (2010), Kashefi et al. (2010),

Guo & Chen (2011), Freitas et al. (2012), Ye et al. (2012), Freitas et al. (2012), and Soliman et al. (2013). The details of notable fatigue assessments are documented below.

A fatigue load model for a short 10.5 metre span steel girder bridge structure that uses weigh-in-motion data was developed by Szerszen et al. (1999). The model was calibrated against field data obtained from in-situ strain gauges. Strain gauges were attached at mid-span on the bottom flange of each of the 10 steel girder on the bridge. Strain data was collected and stored using rainflow counting for a one week period. The equivalent stress range was calculated using Miner's rule to determine the applied loading (shown in Equation [2.6]). The resistance model used in the reliability analysis was developed based on a small number of applicable fatigue tests from Fisher et al. (1974). A limit state function was defined as shown in Equation [3.7].

$$N_f - N_a = 0 \qquad [3.7]$$

where: N_a = number of applied cycles.

Assuming the load and resistance were lognormal random variables, a reliability analysis was performed and the reliability index was calculated for the 10 equivalent stress ranges for each girder as a function of time using Equation [3.8]. Figure 3.10 shows the considerable variation in the reliability index as the equivalent stress range varies.

$$\beta = \frac{\ln(m_{Nf}/m_{Nn})}{\sqrt{{V_{Nf}}^2 + {V_{Nn}}^2}} \qquad [3.8]$$

where: m_{Nf} = mean number of cycles to failure;

m_{Nn} = mean number of applied cycles;

V_{Nf} = coefficient of variation of number of cycles to failure;

V_{Nn} = coefficient of variation of number of applied cycles.

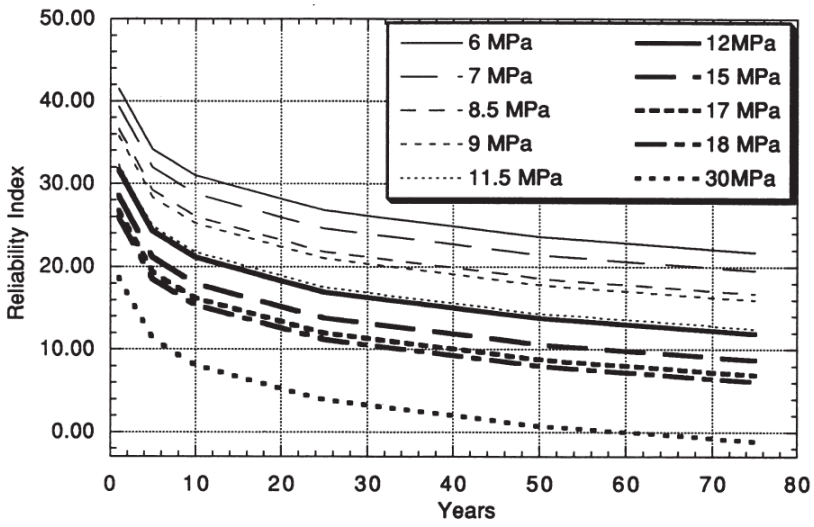

Figure 3.10: Reliability index over time for various effective stress ranges (Szerszen et al., 1999).

The impact of the monitoring period length was revealed by Abdou et al. (2003) in a study that used SHM and numerical modeling to make modifications to the floor beam cut-out on the orthotropic deck of the Triborough Bridge, and ultimately predict the fatigue life of the OSPD. It was found in this study that a longer monitoring period produced a more precise estimate for the fraction of truck traffic, and the distribution of truck traffic in each lane. The three monitoring periods used in this study were four hours, 24 hours, and 30 days.

The field instrumentation of two separate OSPD bridges, the Williamsburg Bridge and the Bronx-Whitestone Bridge, is documented by Connor and Fisher (2005). The primary focus of the project was the rib-to-floor beam connection and to provide the best fatigue detail possible. In these particular orthotropic decks, cope-holes were used at this detail. At several different locations, the region surrounding this connection was heavily strain gauged. Further, gauges were also installed transverse to the rib-to-deck weld to monitor this detail. The rib-to-deck welds governed the sampling rate of the system because these gauges responded to individual wheel loads occurring at a high load rate. Both data from controlled load tests and long-term monitoring under random traffic loading were collected. For the long-term monitoring, video monitoring was triggered by the logger, allowing identification of truck configuration and position. The system used ensures any

high-cycle strain occurrences are linked to a vehicle type, configuration, location, and number of vehicles.

A fatigue life assessment was completed by Battista et al. (2008) using numerically simulated stress histograms based on SHM data collected from an OSPD bridge on the Rio-Niteroi highway. Cracks in the bridge have been observed in numerous locations. A reinforced concrete slab was installed on the bridge to rehabilitate the bridge deck. Gauges were installed on the bridge at various locations where fatigue was deemed likely to occur, both before and after the rehabilitation work to understand the behaviour before and after the rehabilitation. A numerical model was also constructed for both the pre and post-rehabilitated bridge and calibration with the field monitoring results was completed. Stress histograms were numerically simulated and the remaining fatigue life was calculated at select details. The fatigue resistance of the details were based on S-N curves given in BS5400. In this study, the difficulty in completing a fatigue assessment of welded joints in slender decks was realized due to sensitivity to many factors, such as tire radius, tire pressure, and transverse location of tire contact area.

A probabilistic method to calculate the remaining fatigue life is proposed by Kwon and Frangopol (2010). Equation [3.9] is defined as the limit state function for the fatigue reliability analysis.

$$g(X) = \Delta - e \cdot \frac{N \cdot {S_{re}}^{m}}{A} = 0 \qquad [3.9]$$

where: Δ = Miner's critical damage accumulation index;

e = measurement error factor;

N = total cumulative number of cycles.

In this reliability model, the equivalent stress range, the fatigue detail coefficient, Miner's critical damage accumulation index, and the measurement error are all treated as random variables. In determining the equivalent stress range, field monitoring was used and three separate probability density functions were fit to the observed field stresses; lognormal, Weibull, and Gamma. The lognormal distribution was the best fit for the field data and

used in the analysis. The fatigue detail coefficient was modeled with a lognormal distribution with mean and variance determined from data reported in Keating and Fisher (1986). Miner's critical damage accumulation index is assumed to be lognormally distributed with a mean of 1.0 and a coefficient of variation of 0.3, as taken from Wirsching (1984). The measurement error is assumed to be lognormally distributed with a mean of 1.0 and a coefficient of variation of 0.03 for a typical monitoring system. The number of stress cycles was predicted using ADTT (cycles per day), a traffic growth rate, and the number of years. Once the mean and standard deviation of all random variables were determined, the reliability index is easily calculated using Equation [3.10] since all random variables are lognormally distributed.

$$\beta = \frac{\lambda_\Delta + \lambda_A - (\lambda_e + m\lambda_{S_{re}} + \ln(N))}{\sqrt{{\zeta_\Delta}^2 + {\zeta_A}^2 + {\zeta_e}^2 + (m\zeta_{S_{re}})^2}} \qquad [3.10]$$

where: λ = mean of natural logarithm of random variable;

ζ = standard deviation of natural logarithm of random variable.

This method of reliability analysis was applied to two bridges, the Neville Island Bridge and the Birmingham Bridge. The reliability index over time is shown in Figure 3.11 for one gauged location on the Birmingham Bridge; the effect of traffic growth rate is also shown. The fatigue assessment method has shown the ability to use reliability theory in the analysis of existing structures, accounting for various uncertainties, and allowing the analysis to achieve a consistent reliability. This method is further demonstrated by Guo & Chen (2011), who examined a retrofit fatigue detail on the Throgs Neck Bridge in New York.

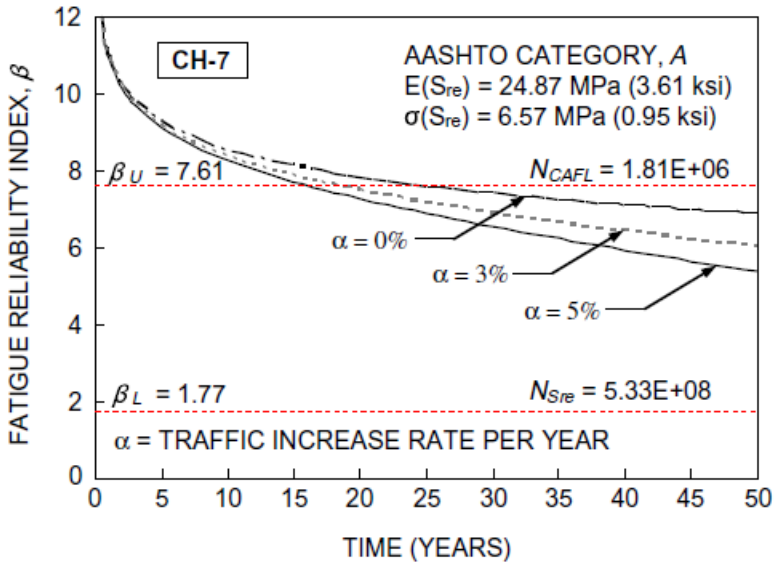

Figure 3.11: Reliability index over time for different traffic growth rates (α) for two separate gauge locations for the Birmingham Bridge (Kwon & Frangopol 2010).

Liu et al. (2010) uses SHM and numerical modeling to develop a factor to account for not placing the strain gauge at the exact location of maximum stress. For various reasons, the strain gauges may not be able to be placed at the critical locations. In this research, the fatigue assessment of a retrofitted fatigue detail is calculated. Strain gauges were installed at various locations around the retrofitted fatigue detail. Numerical models were then constructed to explore the relationship between the stress ranges recorded at the sensor locations and the critical locations. This results in the definition of a spatial adjustment factor, which is defined as the ratio between the maximum stress at the critical location and the stress at the corresponding sensor location. The spatial adjustment factor can then be multiplied by the measured stress ranges at the gauged locations to give an equivalent stress range at the critical location. The reliability assessment can then be calculated at the critical location using the proper stress range values.

Kashefi et al. (2010) attempts to find the remaining fatigue life of an OSPD on an existing bridge in Tehran, Iran. The study couples SHM and laboratory testing to find the result. It was determined the bottom flange of the main girders for the bridge would see the largest stress range, therefore strain gauges were installed at these locations, mid-span of each girder. Strain data was collected from these gauges for a period of eight days. Using the

AASHTO LRFD, the fatigue life estimate was determined to be infinite for each of the gauged locations. For further investigation, fatigue testing of coupons took place. The coupons were retrieved from an identical bridge which was being taken out of service. The coupons were taken from locations on the bottom flange/web of the main girder where the author states no fatigue damage occurred throughout the life of the structure. The T-shape specimens were then tested in a loading frame under pure axial load. The failure level for all six specimens validated the results found, confirming an infinite fatigue life. This is the only study which extracts specimens from an existing structure for fatigue testing, however, no imprinted fatigue damage is present on these specimens.

Chapter 4: A. Murray MacKay Suspension Bridge

The A. Murray MacKay Bridge (MacKay Bridge) was constructed between 1966 and 1969, opening to traffic in 1970 to provide a vehicular crossing over Halifax Harbour. It contains four traffic lanes, two for each travel direction. No bicyclists or pedestrians are permitted on the MacKay Bridge; they must use the other Halifax Harbour bridge, the A. L. Macdonald Bridge (Macdonald Bridge). The Macdonald Bridge is the other vehicular crossing across the Halifax Harbour, however, vehicles over 3200 kg are not permitted to cross the bridge, and must therefore take the MacKay Bridge, which has no restriction on truck traffic. On an average workday, the MacKay Bridge carries approximately 65,000 vehicle crossings.

4.1 Description of the MacKay Bridge

The MacKay Bridge consists of two approach spans which total 495 m, along with 739.5 m of suspended spans, making the MacKay Bridge approximately 1235 m long. The Halifax Approach is a three-span continuous steel box girder measuring 114 m. The Dartmouth Approach measures 381 m and is of the same structural form as the Halifax Approach. The suspended spans consists of two 156.4 m side spans, and a 426.7 m main span.

Figure 4.1: A. Murray MacKay Bridge (Chowdhury & Eppell, 2014).

4.1.1 Main Towers

The Halifax Main Tower (HMT) and the Dartmouth Main Tower (DMT) support the

suspended spans of the bridge. The towers are constructed of stiffened steel plate, with each leg formed into a cruciform shape. The towers are a truss type configuration, with four sets diagonal bracing, along with horizontal members located at the top of the main towers, and below the deck level. The tower reach approximately 95 metres above sea level.

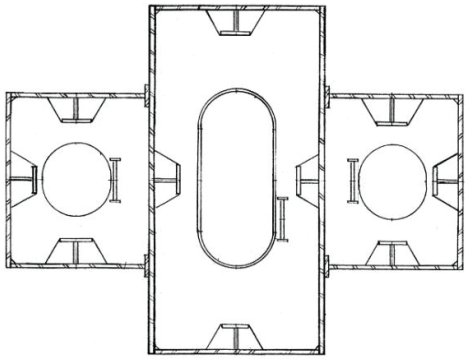

Figure 4.2: Main tower leg (Levy, 2011).

4.1.2 Cables

The two main cables suspending the spans are 364 mm in diameter and consist of 61 strands of 40 mm diameter galvanized wire rope in the shape of a hexagon, as shown in Figure 4.3. Cedar fill is placed on the flat sides of the hexagon to make the cable a circular shape. The entire cable is then wrapped in galvanized wire prior to painting.

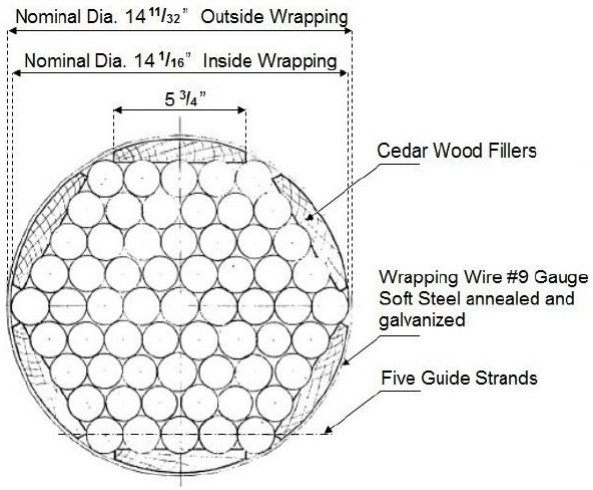

Figure 4.3: Cross section through main cable (Chowdhury & Eppell, 2014).

The suspender cables that hang from the main cable are made of six galvanized strands twisted together to make a 54 mm diameter cable. The suspender cables pass over the main cable and anchor at the deck level only.

4.1.3 Deck System

The MacKay Bridge is the first suspension bridge in North America to use an OSPD (Troitsky, 1987). When the bridge was designed, there were no Canadian codes that covered the design of OSPD or long-span bridges. The deck system on the MacKay Bridge consists of an OSPD, two longitudinal deck trusses, and transverse stiffening trusses upon which transverse floor beams sit. The deck system is shown in Figure 4.4. The OSPD consists of a 9.525 mm flat thick steel plate with 6.35 mm thick longitudinal closed ribs that are 279 mm deep and spaced at 305 mm on centre. The OSPD spans between transverse stiffening trusses. The floor beam of the deck is located along the top chord of the transverse stiffening truss, with a maximum depth of 533 mm at the centre of the deck. The floor beam is tapered to provide an approximate 1% grade for the road surface. Transverse stiffening trusses are 2896 mm deep and located every 4896 mm along the length of the bridge. The longitudinal stiffening truss is 2896 mm deep with the suspender cables attached every 9652 mm along the length.

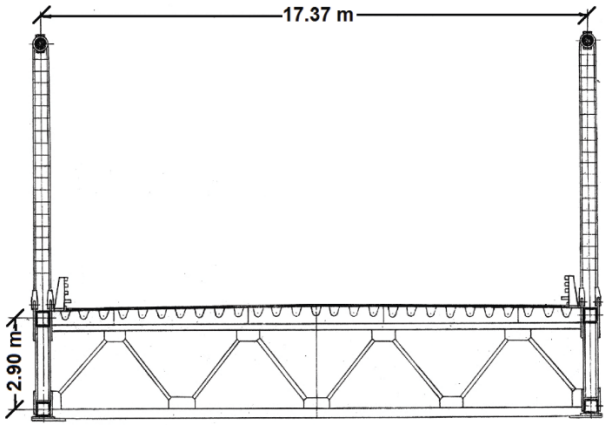

Figure 4.4: Deck system (Levy, 2011).

The focus of this thesis is on the OSPD which remains on the MacKay Bridge today and has been subjected to many vehicle crossings; over 18 million vehicle crossings were recorded in 2009. It is well known that OSPDs contain certain welded details prone to structural fatigue. These are the longitudinal welds connecting the deck plate to the rib plate (type A), as well as the weld at the intersection of the rib and the web of the floor beam (type B), as shown in Figure 4.5(a) and Figure 4.5(b) respectively. The MacKay Bridge also contains one additional detail not typically found on OSPDs; this detail was caused by the addition and then removal of transverse stiffeners between adjacent ribs on the deck (type C), shown in Figure 4.5(c) and Figure 4.5(d).

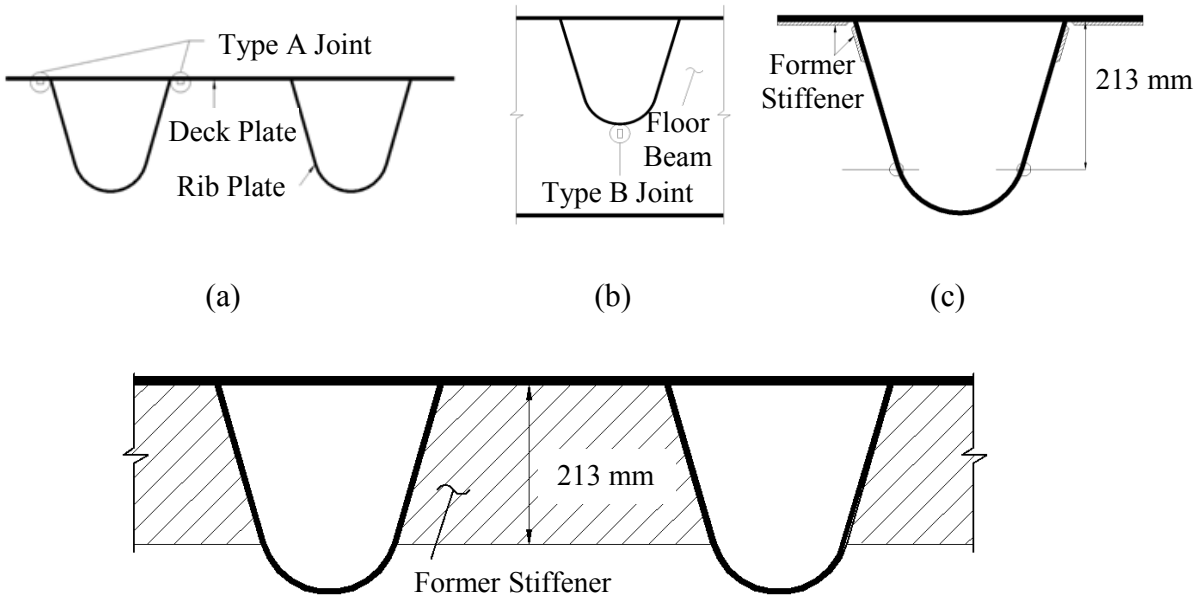

Figure 4.5: OSPD connection types and strain gauge locations (a) type A, (b) type B, (c) type C, and (d) type C showing former stiffener.

Chapter 5: Structural Health Monitoring System

This chapter documents the SHM system installed on the MacKay Bridge to collect the in-situ fatigue loading, which is necessary in assessing the fatigue state of the OSPD. It has been shown by Abdou et al. (2003) that a longer monitoring period will better predict heavy truck traffic, which is the primary loading concern for fatigue. In order to obtain an adequate amount of data for use in the fatigue life prediction, a collection period of one year was selected. This collection period was 11 months longer than the lengthiest monitoring period completed in the study by Abdou et al. (2003).

5.1 Gauge Locations

In August 2010, the expansion joints on the MacKay Bridge were replaced. As part of this project, the OSPD panels adjacent to the expansion joints were also replaced. The specimens used in the laboratory component of this thesis were taken from these removed deck panels. Since the new panels had a thicker deck plate, this panel was not representative of the rest of the OSPD. The panel adjacent to the new panel has a unique boundary condition due to its connection to the new panel. Therefore, the third deck panel away from the HMT in the centre span, as shown in Figure 5.1 and Figure 5.2, was selected and outfitted with a total of 82 strain gauges. These included 16 uniaxial strain gauges for each of the type A and type B fatigue locations, along with 16 – 45° strain gauge rosettes for the type C fatigue locations, and two dummy gauges used for temperature effects. These dummy gauges are mechanically isolated from the bridge and are identical to the two gauge types being used for the fatigue details. These gauges measure only temperature strains and can be used to assess both thermal effects and long-term drift in the system. Corrections could then be applied as required.

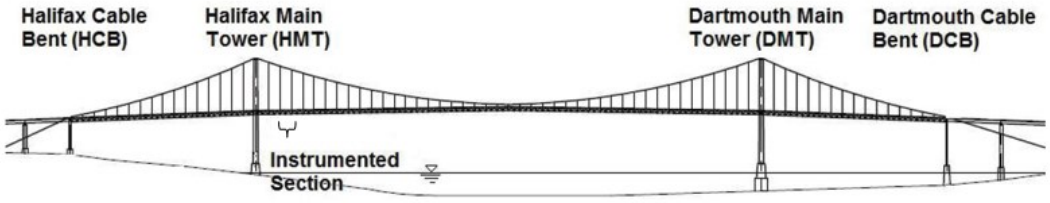

Figure 5.1: Profile of bridge with location of instrumented panel (adapted from B&T).

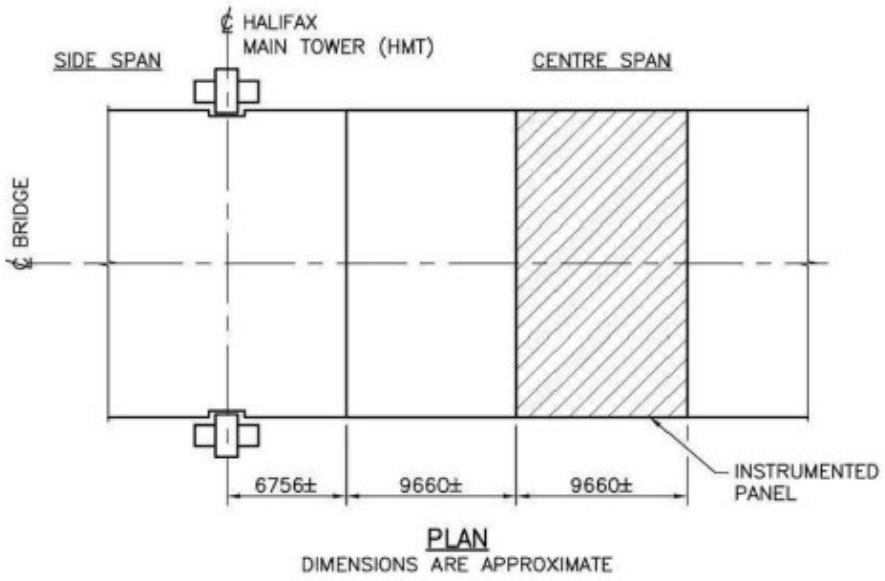

Figure 5.2: Location of instrumented panel (courtesy of B&T).

The placement for each gauge depended on the detail. The first detail, the type A detail examining the longitudinal weld connecting the deck plate and the rib plate has uniaxial strain gauges placed perpendicular to the weld axis. The gauges are installed in pairs on each side of the closed rib plate, as shown in Figure 5.3. The second detail, the type B detail exploring the weld at the intersection of the stiffening rib and the web of the floor beam also uses uniaxial gauges placed perpendicular to the weld axis at the bottom of rib plate, as shown in Figure 5.4. These gauges are also installed in pairs with a gauge on each side of the floor beam web. For the type A and type B details, the gauges were placed approximately 10 mm from the toe of the weld to the centre of the gauge. The third detail, the type C detail examining the impact of former stiffeners uses strain gauge rosettes located 213 mm from the underside of the deck plate. These gauges are placed in pairs on both sides of the stiffening rib, as shown in Figure 5.5.

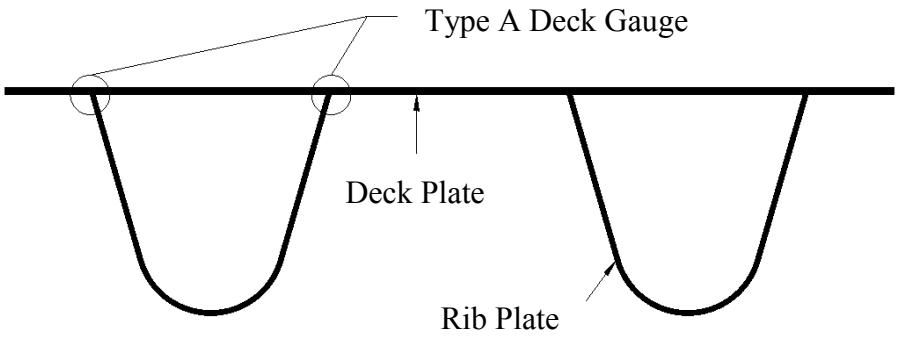

Figure 5.3: Type A fatigue detail.

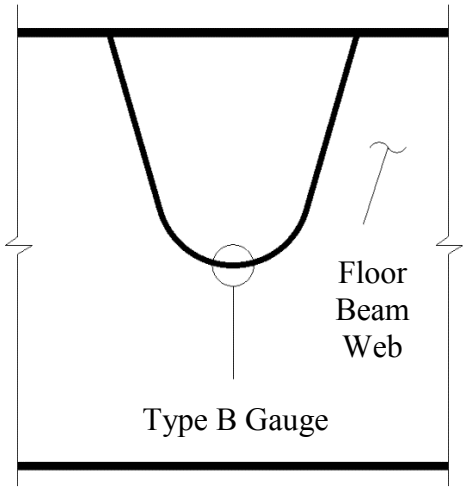

Figure 5.4: Type B fatigue detail.

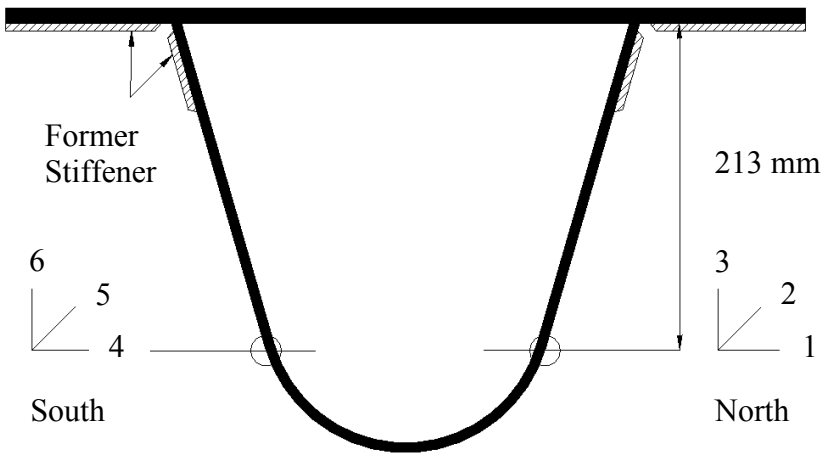

Figure 5.5: Type C fatigue detail.

The gauges are located in each of the four traffic lanes, underneath each wheel path. During installation, two type A gauges were moved due to the presence of a deck splice in the original location. These two gauges are marked with a blue box. The gauge placement locations are given in Figure 5.6.

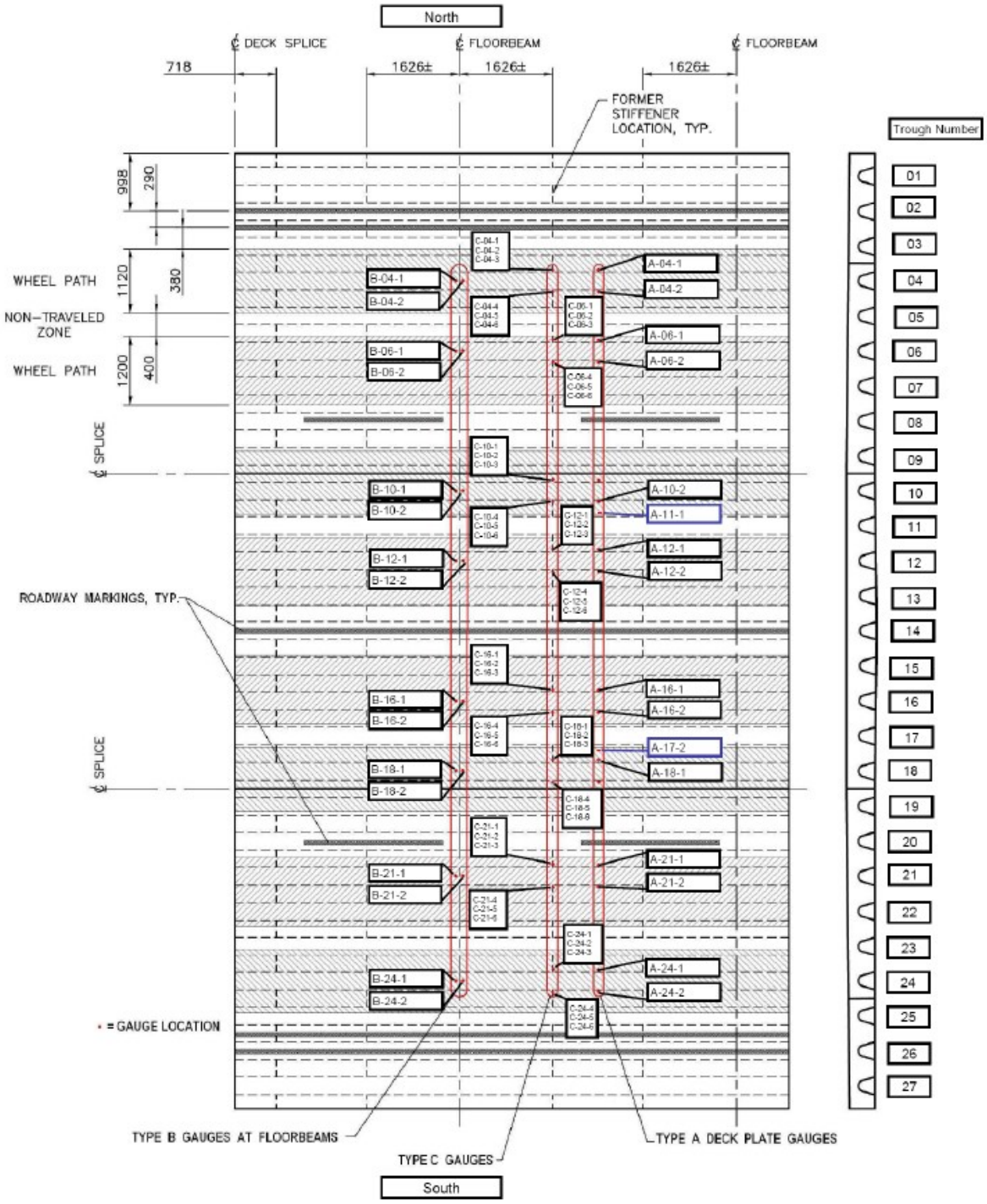

Figure 5.6: Gauge locations (adapted from B&T).

The labeling scheme used is explained using Equation [5.1] and Table 5.1. The datalogger channel wiring to each gauge is given by Table 5.2.

$$X - YY - Z \qquad [5.1]$$

where: X = specimen type (A, B, or C);

YY = stiffening rib number (given in Figure 5.6);

Z = gauge number (Table 5.1).

Table 5.1: Gauge numbering.

Gauge Type	Side	Gauge	Gauge Number
Type A	North	-	1
Type A	South	-	2
Type B	West	-	1
Type B	East	-	2
Type C	North	Longitudinal	1
Type C	North	Diagonal	2
Type C	North	Vertical	3
Type C	South	Longitudinal	4
Type C	South	Diagonal	5
Type C	South	Vertical	6

Table 5.2: Datalogger channel wiring.

Channel	Gauge	Channel	Gauge
1	A-04-1	42	C-16-4
2	A-04-2	43	C-18-1
3	A-06-1	44	C-18-4
4	A-06-2	45	C-21-1
5	A-10-2	46	C-21-4
6	A-11-1	47	C-24-1
7	A-12-1	48	C-24-4
8	A-12-2	49	Dummy 1 (A)
9	A-16-1	50	Dummy 2 (C)
10	A-16-2	51	C-04-2
11	A-18-1	52	C-04-3
12	A-17-2	53	C-04-5
13	A-21-1	54	C-04-6
14	A-21-2	55	C-06-2
15	A-24-1	56	C-06-3
16	A-24-2	57	C-06-5
17	B-04-1	58	C-06-6
18	B-04-2	59	C-10-2
19	B-06-1	60	C-10-3
20	B-06-2	61	C-10-5
21	B-10-1	62	C-10-6
22	B-10-2	63	C-12-2
23	B-12-1	64	C-12-3
24	B-12-2	65	C-12-5
25	B-16-1	66	C-12-6
26	B-16-2	67	C-16-2
27	B-18-1	68	C-16-3
28	B-18-2	69	C-16-5
29	B-21-1	70	C-16-6

Channel	Gauge	Channel	Gauge
30	B-21-2	71	C-18-2
31	B-24-1	72	C-18-3
32	B-24-2	73	C-18-5
33	C-04-1	74	C-18-6
34	C-04-4	75	C-21-2
35	C-06-1	76	C-21-3
36	C-06-4	77	C-21-5
37	C-10-1	78	C-21-6
38	C-10-4	79	C-24-2
39	C-12-1	80	C-24-3
40	C-12-4	81	C-24-5
41	C-16-1	82	C-24-6

Details on the gauge installation, system wiring, data acquisition, and shunt calibration are all found in Appendix A.

5.2 Rainflow Program

A standard Campbell Scientific rainflow counting program was used to collect strain cycles. Details on the rainflow program can be found in Campbell Scientific (2012) and Downing and Socie (1982).

During normal data collection, the datalogger collects strain data at 200 Hz and a rainflow program on the datalogger takes this strain data and sorts it into mean bins and range bins. Every hour, the datalogger produces a rainflow histogram for each gauge recording data. In total, 50 gauges are recording rainflow histograms; 16 type A gauges, 16 type B gauges, and 16 longitudinal type C gauges, with an additional two dummy gauges.

In order for the rainflow program to run, numerous parameters need to be set. Several different values for these parameters in the rainflow program were used before the final parameters were selected for the duration of the monitoring program. Table 5.3 shows the different parameter trials, whereas Table 5.4 shows the time each trial was active. Trial 4 parameters were selected for normal operation.

Table 5.3: Parameter trials for rainflow program.

Trial Number	Mean Bins	Amplitude Bins	Lower Limit	Upper Limit	Minimum Amplitude
			με	με	με
1	1	20	-400	400	30
2	8	16	-400	400	40
3	45	45	-400	500	70
4	10	45	-400	500	70
5	10	45	-400	500	40

Table 5.4: Active running times for each trial.

Trial Number	Start Date	End Date
1	October 4, 2012 – 04:00hrs	October 25, 2012 – 13:00hrs
2	October 25, 2012 – 14:00hrs	October 31, 2012 – 16:00hrs
3	October 31, 2012 – 17:00hrs	November 30, 2012 – 08:00hrs
2	November 30, 2012 – 08:00hrs	December 21, 2012 – 22:00hrs
4	December 22, 2012 – 00:00hrs	Present*
5	February 27, 2013 – 01:00hrs	February 28, 2013 – 00:00hrs

* Except for trial number 5 used for a gauge investigation (see Report #3A)

Chapter 6: Field Calibration of SHM System

Once the SHM system was installed on the MacKay Bridge, the functionality of the system needed confirmation. To do this, full-scale calibration testing was performed. To test the SHM system, the bridge was closed on October 4, 2012 between midnight and 5:30 am. While the bridge was closed, field testing was completed both statically and dynamically using a calibration truck with known axle loads.

6.1 Calibration Truck

The calibration truck consisted of a small two-axle dump truck loaded with a fill material. The loaded calibration truck was weighed at a provincial scale on the night of October 3, 2012, just prior to the calibration testing performed on the morning of October 4, 2012. The axle loads reported by the weigh station are shown in Figure 6.1, with the tire and axle spacing shown in Figure 6.2.

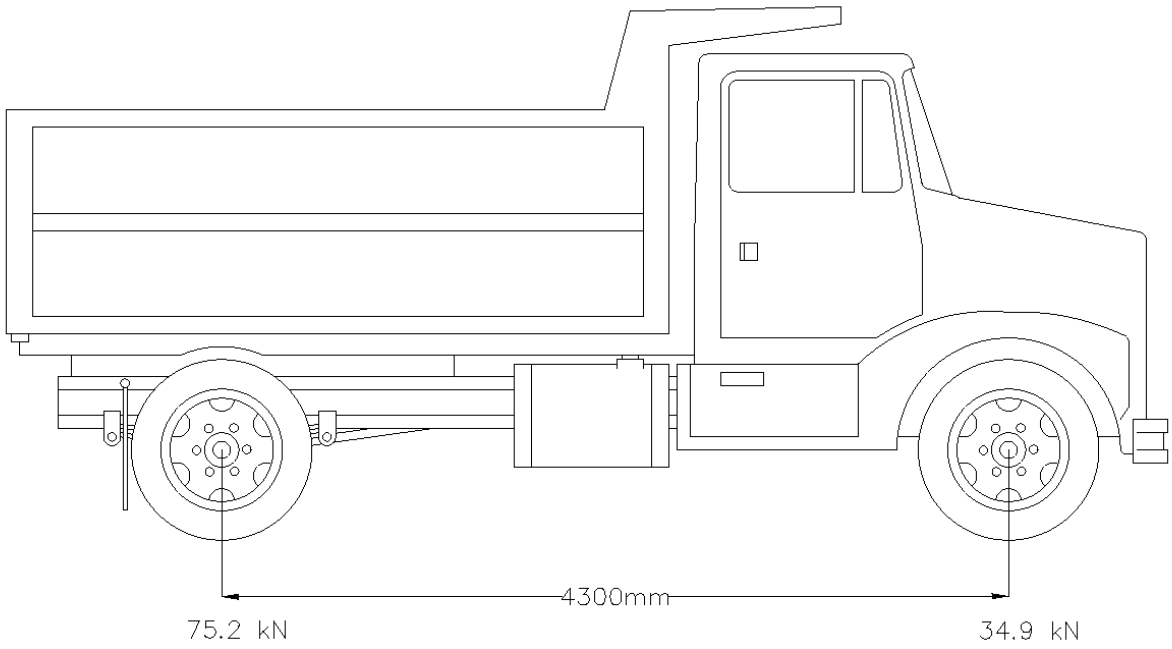

Figure 6.1: Calibration truck.[1]

[1] Drawing modified from http://www.autocad-drawing.com/

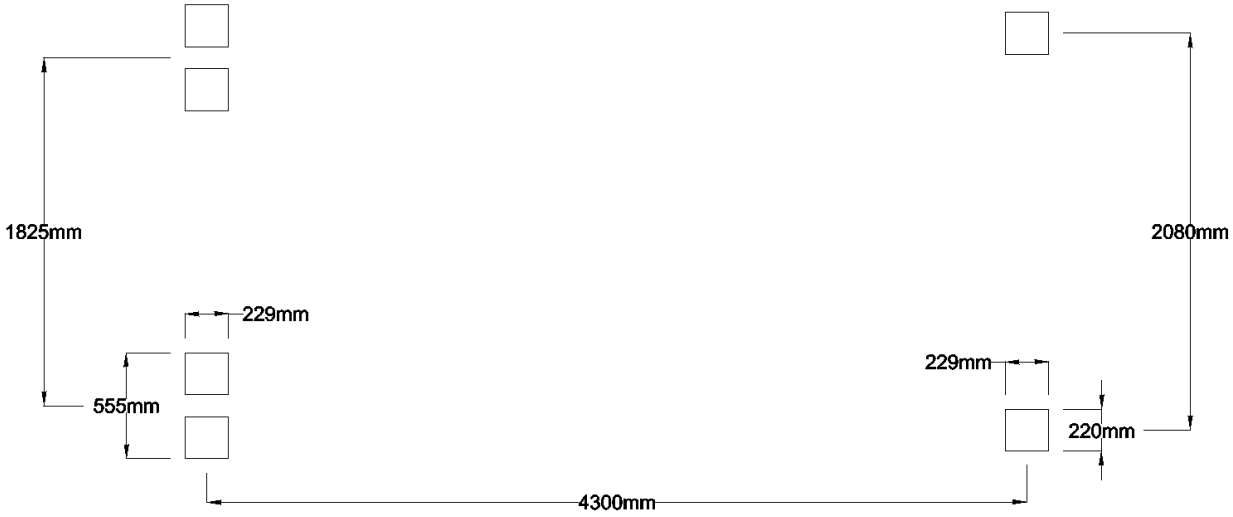

Figure 6.2 : Calibration truck footprint and wheel spacings.

6.2 Static Test

For the static test, the calibration truck was stopped at several locations marked on the deck surface. These locations corresponded to the intersection of transverse and longitudinal lines marked on the bridge deck. The two transverse lines across the deck are at the type A and type C gauge locations. The first line, along the type C gauge line, was approximately 1626 mm from the centreline of the floor beam containing the type B gauges. The second line, along the type A gauges, was approximately mid-span between the two transverse floor beams, or 2413 mm from the centreline of the floor beam containing the type B gauges. The longitudinal lines, called travel lines, defined the stopping locations, and were located along the centreline of the stiffening ribs, as given in Figure 6.3 and Figure 6.4. Either the left ('L' in Figure 6.3 and Figure 6.4) or right ('R' in Figure 6.4) rear tire was placed at the stopping locations with the tire centred over the marked location on the deck surface. For travel lines 1 to 7, both transverse lines were used to define stop locations. From transverse line 8 to 12, only the type A transverse line was used to define stop locations. A total of 19 stopping locations were used in the static test with the calibration truck always facing Dartmouth. The location of the travel lines is shown in Figure 6.3 and Figure 6.4.

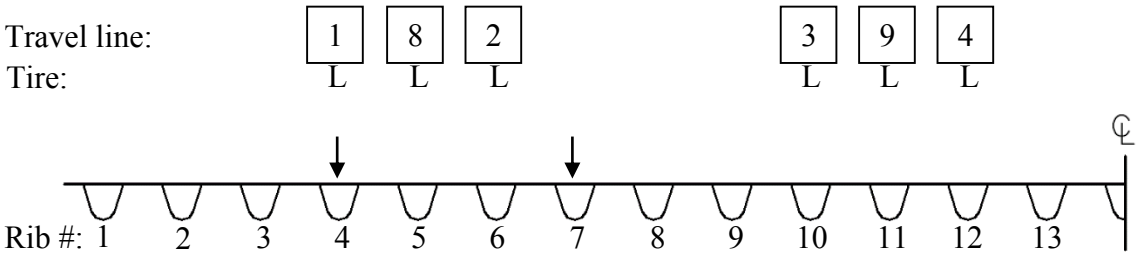

Figure 6.3: North side of bridge, static positions; wheel loads shown for longitudinal travel line 1.

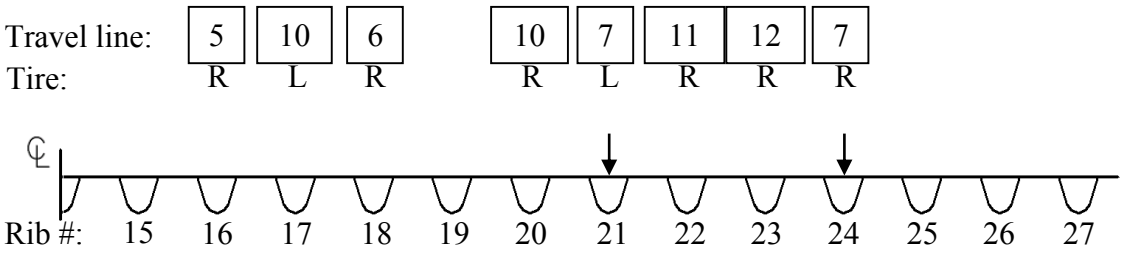

Figure 6.4: South side of bridge, static positions; wheel loads shown for longitudinal travel line 7.

To mark the stop locations, the locations of all type B gauges were transferred onto the deck surface. From these markings, the stop positions for the static test were marked. Figure 6.5 and Figure 6.6 show the stop locations marked on the deck. The travel line number was labelled with pink chalk. Figure 6.7 shows the position of the calibration truck during the static test. Positioning was similar for each stopping location.

Figure 6.5: Static test stop locations across the bridge deck.

Figure 6.6: Static stop locations 7A, 7C, and 12A.

Figure 6.7: Positioning of calibration truck for static testing.

6.2.1 Results

During testing, data was recorded through a direct connection from a laptop to the datalogger. Data collected from the static test was zeroed based on an initial zero reading taken while the bridge was closed to traffic. The strain gauge readings for each stopping position are found in Appendix B. The maximum strain values observed during the static test, compressive or tensile, are given in Table 6.1 for the type A, type B and longitudinal type C gauges.

Table 6.1: Maximum strain readings, compressive or tensile, for gauges during static test.

Gauge	Travel Line	Transverse Line	Strain
			με
A-04-1	1	A	-155
A-04-2	1	A	-140
A-06-1	8	A	-145
A-06-2	1	A	-243
A-10-2	9	A	-134
A-11-1	3	A	-119
A-12-1	9	A	-160
A-12-2	3	A	-199
A-16-1	6	A	-154
A-16-2	10	A	-40
A-18-1	6	A	-193
A-17-2	10	A	-210
A-21-1	12	A	-211
A-21-2	7	A	-193
A-24-1	12	A	-53
A-24-2	7	A	-111
B-04-1	1	C	88
B-04-2	1	C	-143
B-06-1	2	C	70
B-06-2	2	C	-113
B-10-1	3	C	65
B-10-2	3	C	-104
B-12-1	4	C	61
B-12-2	4	C	-104
B-16-1	5	C	70
B-16-2	5	C	-103
B-18-1	6	C	56

Gauge	Travel Line	Transverse Line	Strain
			με
B-18-2	6	C	-117
B-21-1	7	C	49
B-21-2	7	C	-96
B-24-1	7	C	81
B-24-2	7	C	-138
C-04-1	1	C	155
C-04-4	1	C	173
C-06-1	2	C	152
C-06-4	2	C	141
C-10-1	3	C	144
C-10-4	3	C	154
C-12-1	4	C	130
C-12-4	4	C	158
C-16-1	5	C	185
C-16-4	5	C	142
C-18-1	6	C	52
C-18-4	6	C	145
C-21-1	7	C	137
C-21-4	7	C	130
C-24-1	7	C	164
C-24-4	7	C	147

The type B gauge readings consist of two components, axial strain and bending strain. The type B gauge pairs in Table 6.1 do not match because of these components. A breakdown of the axial strain and bending strain for the static test is given in Table 6.2. Adding or subtracting the bending strain from the axial strain will give both gauge 1 (west) and gauge 2 (east) readings respectively. A tensile axial strain is defined as positive, whereas a compressive axial strain is defined as negative. Positive bending strain is defined as gauge 1 (west) in tension and gauge 2 (east) in compression.

Table 6.2: Type B strain components.

Gauge Pair	Axial Strain	Bending Strain
	με	με
B-04	-28	116
B-06	-22	92
B-10	-20	85
B-12	-22	83
B-16	-17	87
B-18	-31	87
B-21	-24	73
B-24	-29	110

6.3 Dynamic Test

To observe the dynamic response of the bridge under moving vehicle loads, a dynamic test was completed. The calibration truck was driven across the bridge in each of the four traffic lanes (see lane numbering in Figure 6.8) and strain data was recorded continuously. The lateral positioning of the calibration truck within the traffic lane was not recorded.

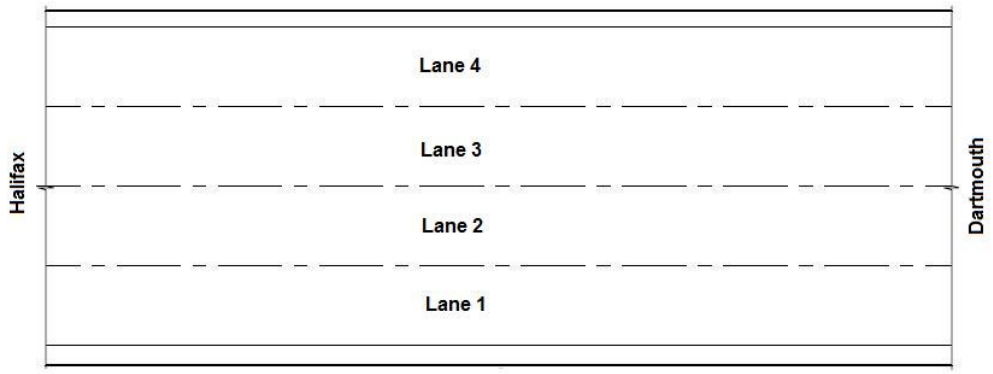

Figure 6.8: Lane numbering (Levy, 2011).

The posted traffic speed limit of 70 km/h was attempted during this test, however, the calibration truck was only able to reach 50 km/h. This speed of 50 km/h was then used for all dynamic tests. Data was collected continuously from the time the truck began on the approach spans until the truck reached the opposite approach. Since data was collected at

a frequency of 200 Hz, the data file was saved after the calibration truck ran through each lane to reduce the amount of meaningless data. The data file was then restarted when the calibration truck was approaching the bridge for the next lane of the dynamic test. The calibration truck was driven in the following lane order: 4, 2, 3, 1.

6.3.1 Results

Figure 6.9 through Figure 6.13 show the response from all gauges along stiffening rib 21, with the calibration truck travelling in lane 1.

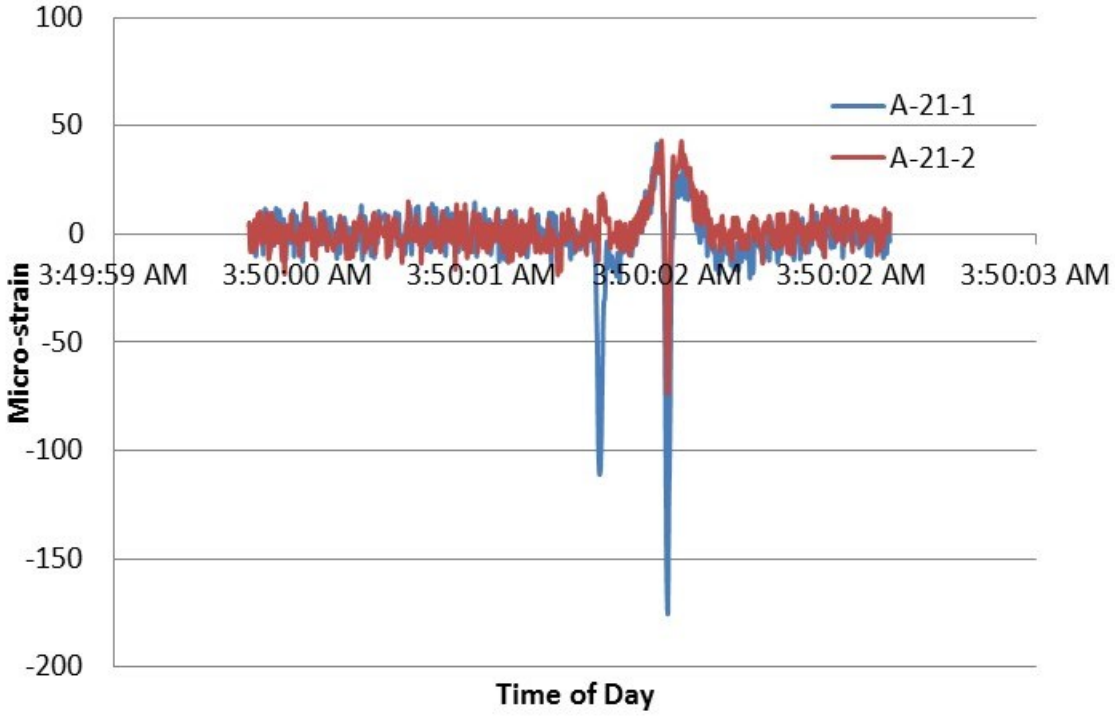

Figure 6.9: Lane 1 – A-21 gauge response for the dynamic test.

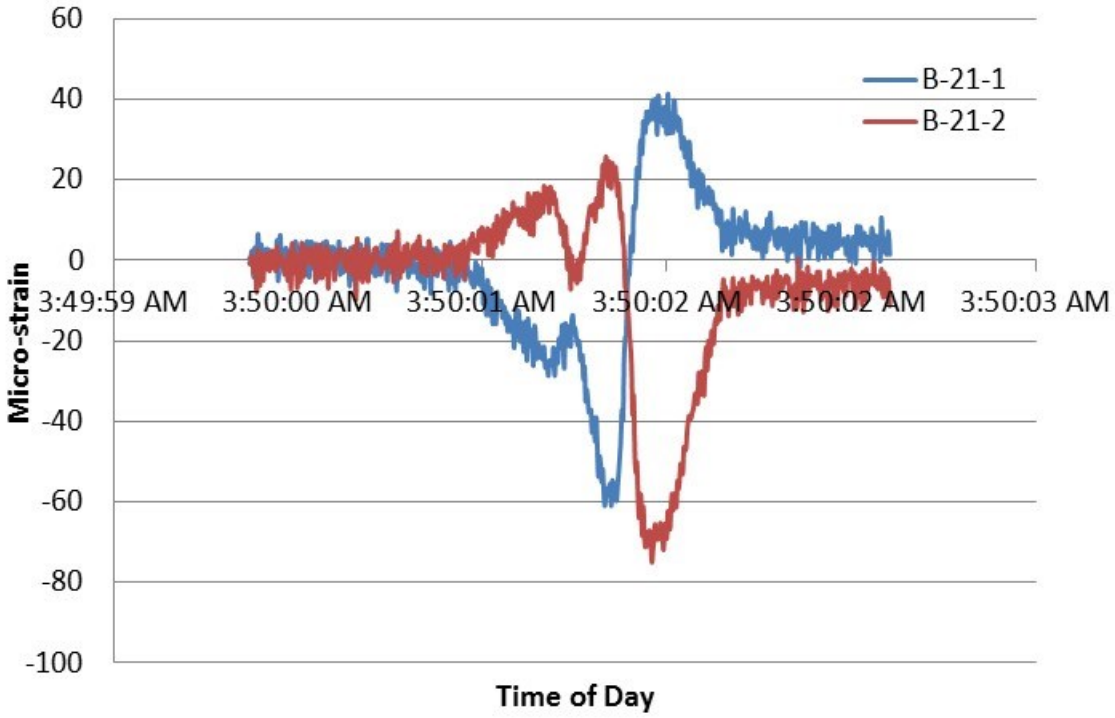

Figure 6.10: Lane 1 – B-21 gauge response for the dynamic test.

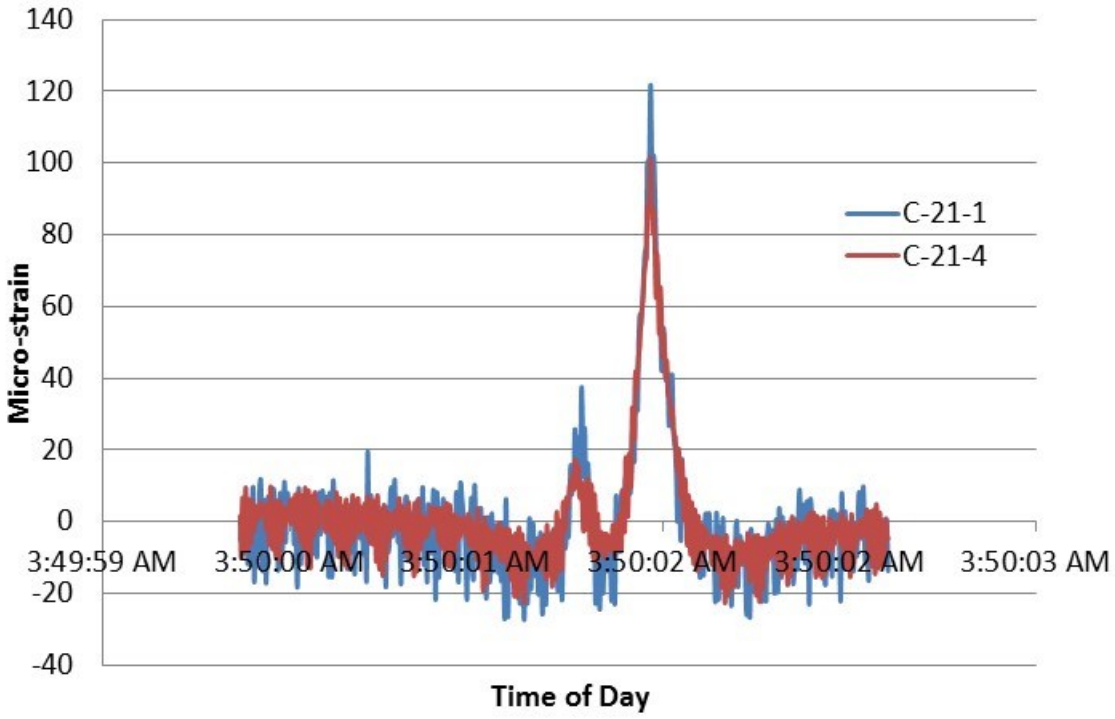

Figure 6.11: Lane 1 – C-21 longitudinal gauge response for dynamic test.

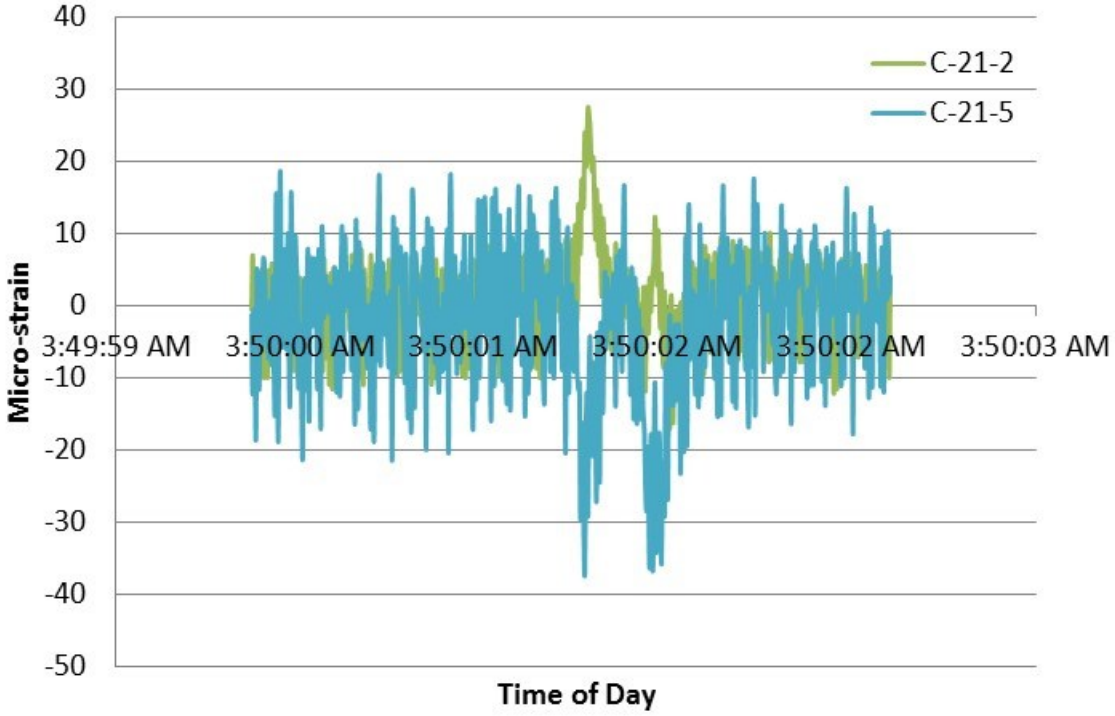

Figure 6.12: Lane 1 – C-21 diagonal gauge response for dynamic test.

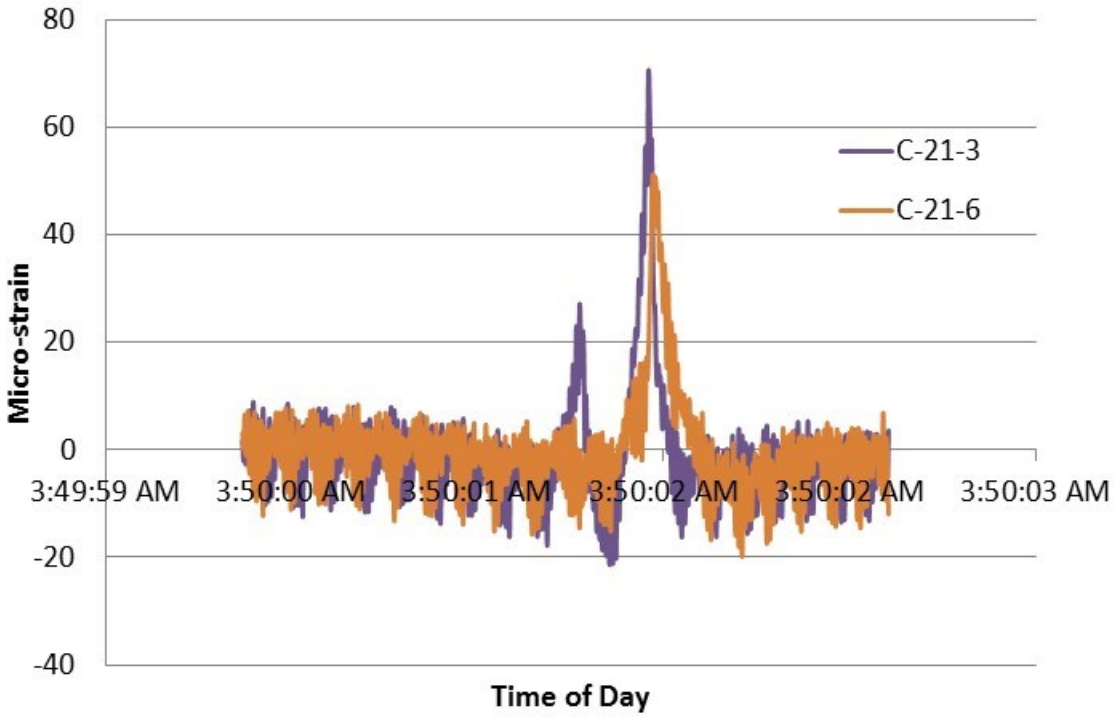

Figure 6.13: Lane 1 – C-21 vertical gauge response for dynamic test.

A comparison of the components in the type B strain values was also made in the dynamic test results. Figure 6.14 shows both the axial strain and bending strain components for the gauge pair B-21 with the calibration truck travelling in lane 1. Positive and negative strains are as defined in the static test results.

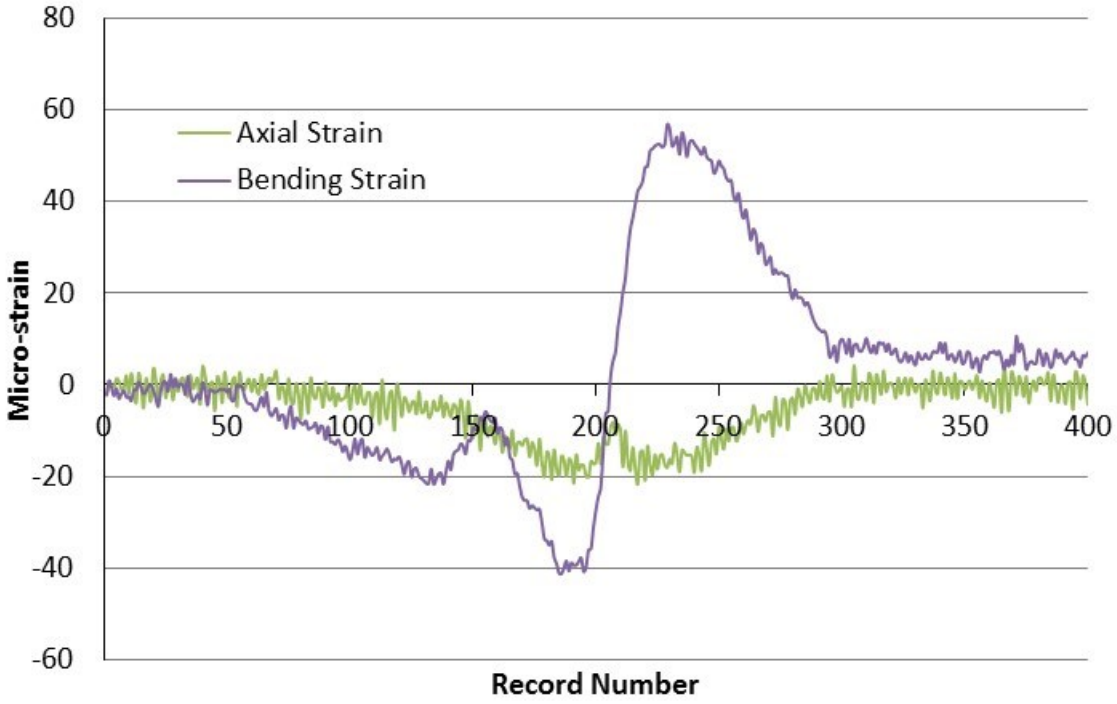

Figure 6.14: Components of B-21 gauge pair during dynamic test with truck travelling in lane 1.

6.4 Discussion of Results

In examining the dynamic test data for the type A detail, each axle of the calibration truck can be identified. The behaviour confirms the findings from Connor and Fisher (2001) presented in Section 3.1.1. Considering the calibration truck only had two axles compared to the five axles used in Connor and Fisher (2001), the behaviour shown in Figure 6.9 matches Figure 3.3. It is clear that the type A detail is influenced by each individual axle.

Out-of-plane bending drives the stress range at the type B detail. From the dynamic test, two strain cycles are counted from the passage of the calibration truck, meaning both axles induce a strain range at the detail location. When compared to a study by Connor and Fisher

(2004), the same number of cycles are observed for out-of-plane behavior when a three-axle truck was used. It should be noted that this detail was instrumented at a different location since the rib-to-floor beam joint contained a cope-hole. It appears as though the type B detail is influenced by axle groups rather than individual axles, but more data is needed to support this finding.

Each axle on the type C longitudinal gauge can be seen for the dynamic test. This excludes GVW as the loading of concern. Due to the calibration truck consisting of two axles, it is not possible to establish if the type C detail is sensitive to individual axles, or axle groups. However, it has been found in previous work that axle groups are of concern (FWHA, 2012). The influence of individual axles is very small (Connor & Fisher, 2004).

Chapter 7: Laboratory Testing

Conducting full-scale testing of an entire deck panel, similar to Taskopoulos and Fisher (2003 & 2005), would require an extremely large testing facility. Instead, small specimens for each of the three fatigue details have undergone testing. A description of the test setup, specimen geometry, and test results for these specimens is presented in this chapter.

7.1 Specimen Locations

As noted above, the specimens were taken from critical fatigue details. In total, three fatigue details were examined, type A, type B, and type C, as noted in Section 5.1. The breakdown of the 29 specimens extracted from the OSPD include 10 type A specimens, 10 type B specimens, and 9 type C specimens. Only nine type C specimens were obtained due to an error during cutting at the steel fabrication facility where specimens were cut to the appropriate dimensions so they could be tested in the laboratory.

7.2 Testing Methodology

For each fatigue detail, testing was conducted to obtain an S-N curve. The testing was separated into three main phases with a preliminary component to develop and confirm the test setup. Originally each phase required three specimens to be tested at a predetermined stress range as documented in Table 7.1. However, as testing progressed, adjustments were made to subsequent phases based on the results obtained in the preceding phase(s). The final test breakdown differed for each specimen type. Since only the preliminary type B specimen was tested, no changes are noted. The final breakdown for the type A and type C details is contained in Section 7.3.8 and Section 7.5.7 respectively.

Table 7.1: Initial testing breakdown.

Phase	Number of Specimens	Nominal Stress Range	Predicted Number of Stress Cycles
		MPa	
Preliminary	1	250	370000
1	3	250	370000
2	3	175	1000000
3	3	100	6000000

7.3 Type A Specimen

In order to differentiate between sides of the type A specimen, the terms north, south, east, and west are used. These directions are based on the compass directions of the specimen while being tested in the laboratory. The directions have no relation to the location of the specimen sides when removed from the MacKay Bridge.

7.3.1 Specimen Geometry

Figure 7.1 shows the type A specimen after being cut to size for testing. The nominal dimensions for the specimen are shown in Figure 7.2. It is impossible to cut specimens to the nominal dimensions exactly, therefore the measured dimensions are given in Table 7.2. Specimens A21 and A27 have a measured length much smaller than the nominal length. This is due to the available pieces removed from the OSPD having a smaller length. This was deemed acceptable, recognizing the load required to achieve the target stress in these two specimens would be less than a full length specimen.

Figure 7.1: Type A specimen cut to size for testing.

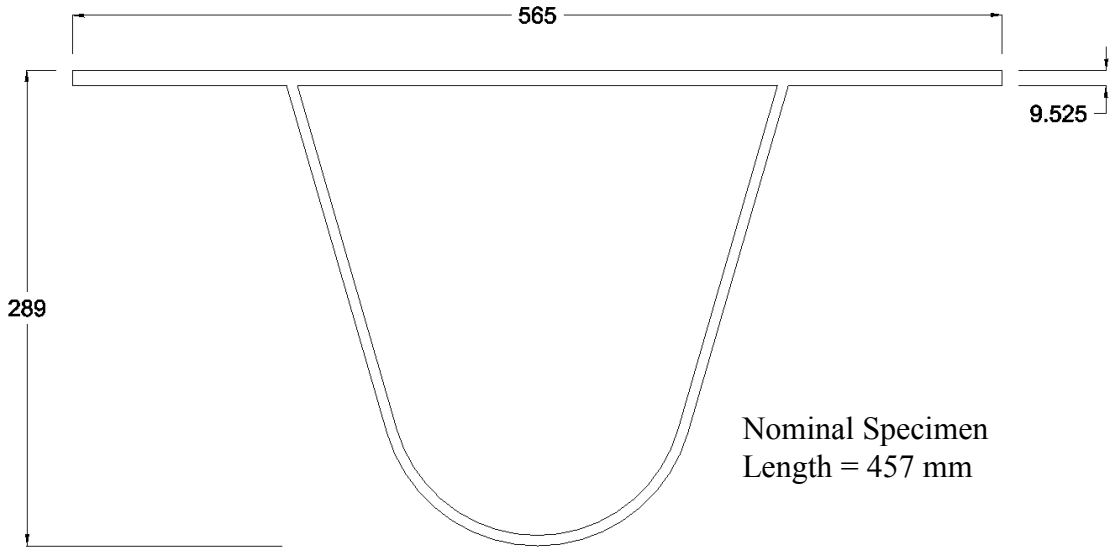

Figure 7.2: Nominal dimensions for the type A specimen (all dimensions in mm).

Table 7.2: Measured dimensions for type A specimens.

Phase of Testing	Specimen Identification	Measured Length Parallel to Stiffening Rib	Measured Width Perpendicular to Stiffening Rib
		mm	mm
Preliminary	A1	455	550
1	A5	457	562
1	A7	456	560
1	A8	461	565
2	A6	457	564
2	A2	457	553
2	A3	456	565
3	A11	456	562
3	A21	304	583
3	A27	299	528

To characterize the variation in deck plate thickness, calipers were used to measure the deck plate thickness along the marked locations given in Figure 7.3 for each specimen. Table 7.3 documents the thickness readings. Some corrosion was noticed on the deck plate, resulting in slightly lower thickness readings than the nominal 9.525 mm thickness. No buildup of surface corrosion was present, therefore the larger than nominal thickness readings were a result of a thicker deck plate being used in the original fabrication.

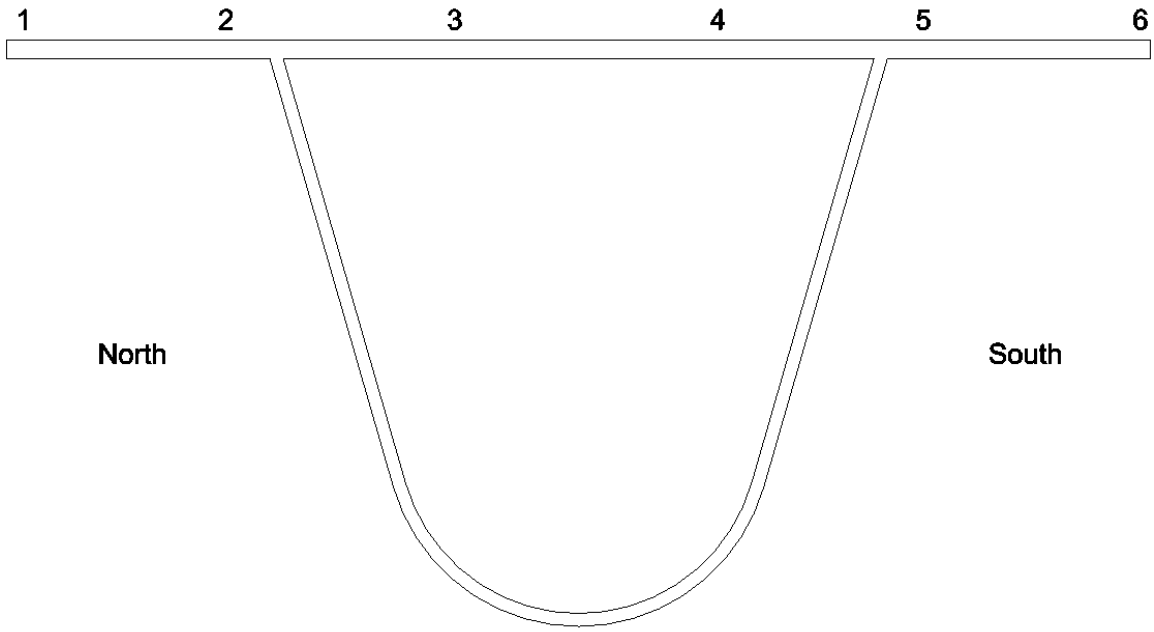

Figure 7.3: Locations of thickness measurement of deck plate.

Table 7.3: Thickness measurements of deck plate.

Specimen Identification	Thickness					
	1	2	3	4	5	6
	mm	mm	mm	mm	mm	mm
A1	9.72	9.76	9.87	9.78	9.82	9.86
A5	10.05	10.07	9.01	8.78	9.97	9.98
A7	9.40	9.27	9.38	9.28	9.31	9.27
A8	9.55	9.61	9.47	6.57	8.96	9.95
A6	10.38	10.25	10.18	10.11	10.25	10.33
A2	10.83	10.81	10.69	10.25	10.62	10.58
A3	10.06	10.16	9.08	9.18	10.03	10.01
A11	10.15	10.12	10.18	10.20	10.17	10.22
A21	9.83	9.34	9.27	9.75	9.44	9.82
A27	10.04	9.73	9.52	10.00	9.97	9.88

7.3.2 Test Setup

Figure 7.4 shows the standard fatigue test setup for type A specimens. The specimens were tested in a vertical reaction frame that has a maximum capacity of 1000 kN. A simple test support was fabricated to simulate bending about the weld that connects the deck plate to the underlying stiffening rib. Small rollers were placed along the axis of the weld on both sides of the specimen to induce bending about the weld. To prevent the sample from slowly moving during cyclic loading, vice clamps were attached to the supports as seen in Figure 7.4. The nominal dimensions of the test support can be seen below in Figure 7.5.

Figure 7.4: Standard fatigue test setup for type A specimens.

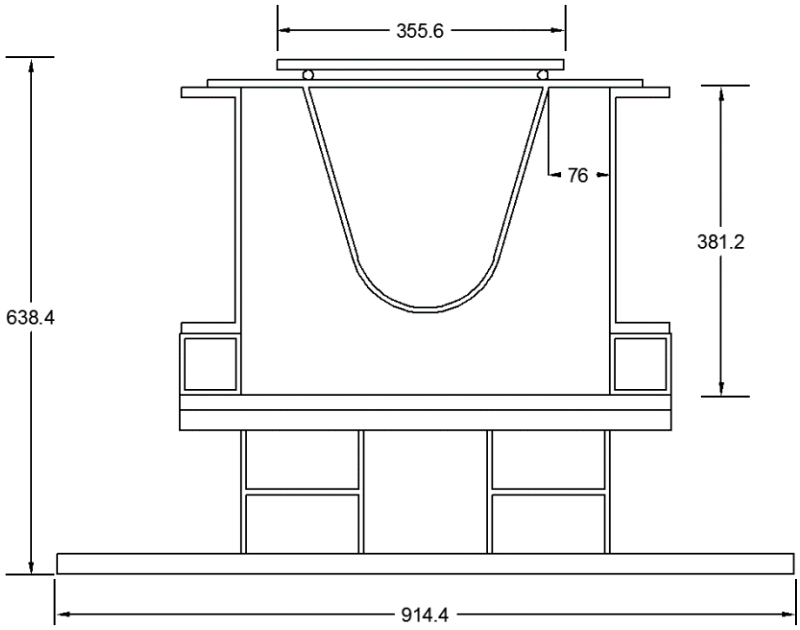

Figure 7.5: Test layout for type A specimen (all dimension in mm).

7.3.3 Test Procedure

Daily short cycle tests and periodic static tests were performed at a high scan rate to confirm the specimen was loading equally on both sides, as well as to capture the minimum and maximum strains during a cycle to ensure the correct stress range was being achieved. Adjustments were made to load or displacement input parameters to account for any change in specimen stiffness or the stiffness of the testing fixture. Once the setup and loading was confirmed, normal cyclic testing was performed. Applied load and measured strain were recorded throughout the testing. The data collection rate depended on the type of testing, and the phase of testing. The collection and testing frequency are given in Table 7.4 below. This testing procedure continued until failure or the desired number of cycles was applied. Failure of the specimens occurred when the specimen was incapable of maintaining the load applied during normal testing. Both load control and displacement control were used in the testing of the type A specimens. In load control, parameters are entered into the controller which tell the actuator what load to apply, whereas in displacement control, parameters are entered into the controller which tell the actuator what displacement to apply.

Table 7.4: Breakdown of testing frequencies and modes for type A specimens.

Phase	Normal Cyclic Data Collection Frequency	Static and Short Cyclic Data Collection Frequency	Cyclic Loading Frequency	Actuator Control Mode
	Hz	Hz	Hz	
Preliminary	5	50	0.5	Load
1	5	50	0.5	Load
2	4	35	0.5/0.7*	Load & Displacement*
3	4	40	0.5	Load

* Specimen A2 and A3 were tested at 0.7 Hz using displacement control

7.3.4 Strain Gauge Instrumentation

Strain gauges were attached to the underside of the deck plate, perpendicular to the weld connecting the deck to stiffening rib. Figure 7.6, along with Table 7.5, show the location of the centre of the strain gauges with respect to the toe of the rib-to-deck weld. One uniaxial gauge was installed on both the north and south side of the deck plate, located at one half the total length of the specimen. All strain gauges used were Vishay CEA-06-125UW-350 having a gauge length of 3.18 mm.

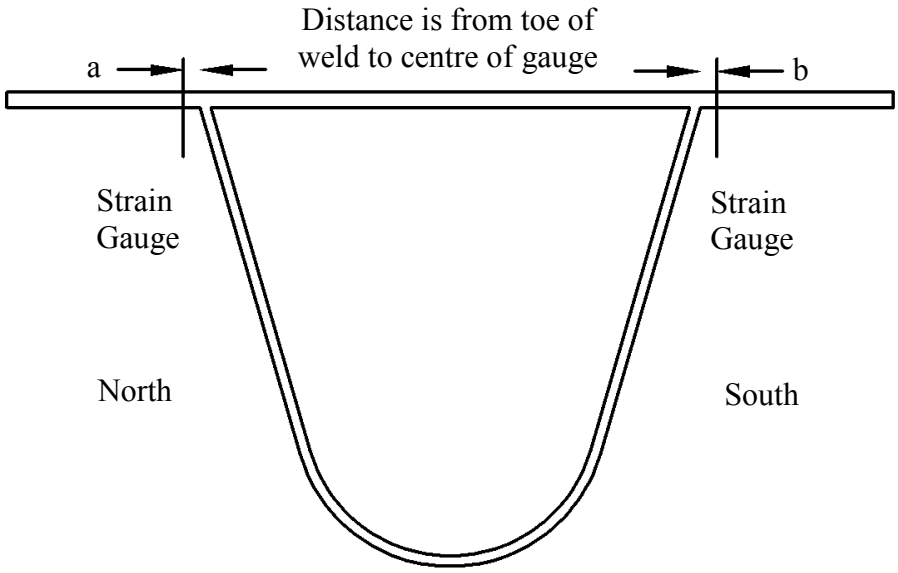

Figure 7.6: Location of strain gauges for type A specimens.

Table 7.5: Distance from toe of weld to centre of gauge.

Specimen Identification	Distance 'a'	Distance 'b'
	mm	mm
A1	9	8
A5	7	7
A7	8	9
A8	9	12
A6	7	5
A2	5	5
A3	6	5
A11	4	4
A21	4	5
A27	4	4

7.3.5 Short Cycle Analysis

To ensure the required stress range was being achieved during cyclic loading, short cycle testing was performed at a high scan rate to capture maximum and minimum strains acting on a specimen. Figure 7.7 shows an example of the stress range associated with one load cycle of specimen A5. The minimum stress, maximum stress, and stress range for each of the specimens is given in Table 7.6. The load for testing each specimen is given in Table 7.7. All measured strains were converted to stresses using a modulus of elasticity of 181 GPa, which was determined from tension coupon testing documented in Appendix C. The stress was also multiplied by a geometric adjustment factor (GAF) to account for measuring the strain some distance away from the weld toe. Determination of the GAF is given in Section 9.2.1.

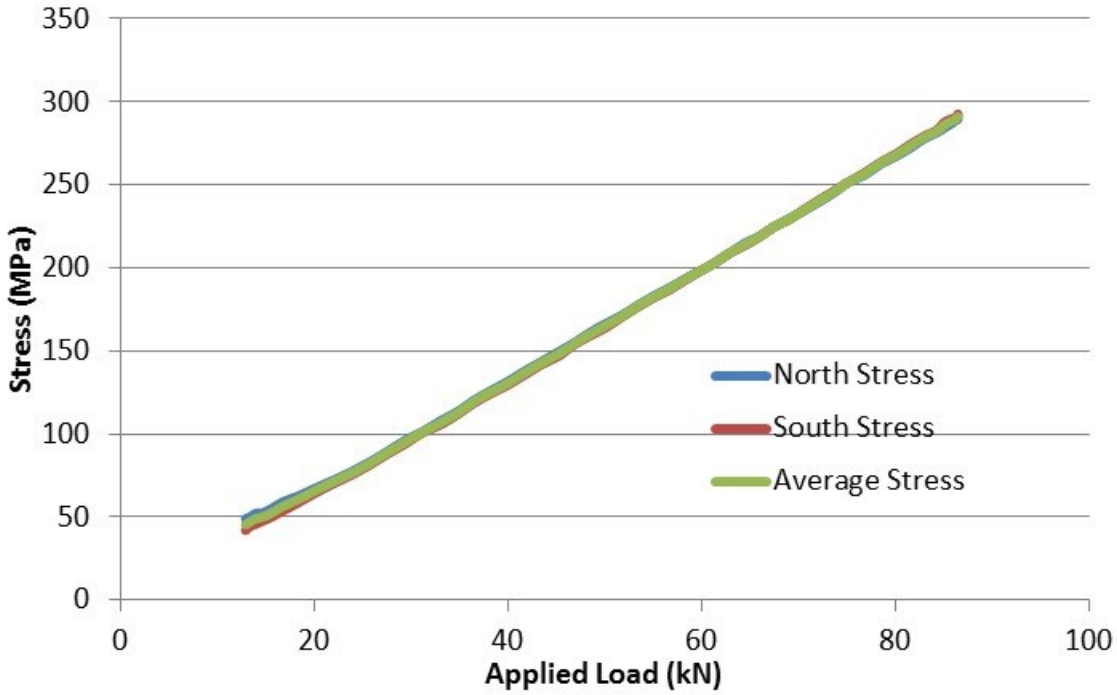

Figure 7.7: Stress range during one load cycle for specimen A5.

Table 7.6: Stress range for type A specimens

Specimen Identification	North Side			South Side		
	Minimum Stress	Maximum Stress	Stress Range	Minimum Stress	Maximum Stress	Stress Range
	MPa	MPa	MPa	MPa	MPa	MPa
A1	59	321	262	58	315	257
A5	49	290	241	42	293	251
A7	54	229	245	47	320	273
A8	57	309	252	58	368	310
A6	43	207	164	55	215	160
A2	35	198	163	33	190	157
A3	20	176	156	23	177	154
A11	12	213	201	7	209	202
A21	14	213	199	13	215	202
A27	-	-	-	-	-	-

Table 7.7: Load range for type A specimens.

Specimen Identification	Minimum Load	Maximum Load	Load Range
	kN	kN	kN
A1	8	82	74
A5	13	86	73
A7	9	76	67
A8	11	81	70
A6	8	54	46
A2	6	60	54
A3	3	46	43
A11	2	48	46
A21	1	26	25
A27	-	-	-

7.3.6 Test Results

Figure 7.8, developed from specimen A5, shows an example of how the strain varies throughout the test. Little variation in the strain readings occur over time, except when the specimen approached failure. Plots for other specimens are given in Appendix D. The number of cycles applied to each specimen, as well as whether the specimen failed or was stopped (classified as a run-out) is given in Table 7.8.

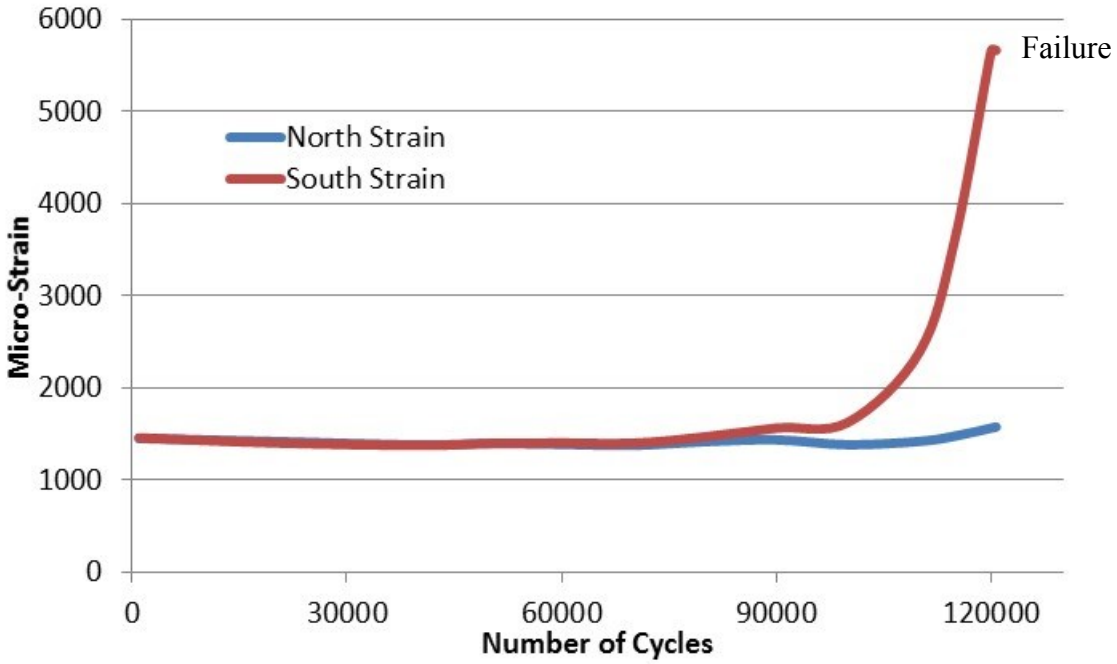

Figure 7.8: Specimen A5 strain over time at 83kN.

Table 7.8: Cycle counts for type A specimens.

Specimen Identification	Stress Range	Number of Cycles	Failure or Run-out
	MPa		
A1	260*	145 761	Failure
A5	251	120 677	Failure
A7	245	146 472	Failure
A8	252	90 211	Failure
A6	164	1 000 000	Run-out
A2	163	1 000 000	Run-out
A3	156**	682 160	Failure
A11	202	300 000	Run-out
A21	199	300 000	Run-out
A27	-	-	-

* Maximum stress range taken since both sides failed

** Maximum stress range taken since corrosion failure

7.3.7 Re-testing Run-out Specimens

After initial testing had been completed for some time, a custom MTS actuator with a capacity of 100 kN became functional for dynamic testing. This presented the opportunity to re-test type A specimens that did not fail. A higher frequency was achieved with the new actuator which allowed testing to be completed much quicker. The test setup remained the same, except rotated 90 degrees. The north side of the specimen faced east and the south faced west.

Figure 7.9: New actuator installed in testing frame.

Table 7.9 summarizes the collection and testing frequencies for the re-tested specimens. Table 7.10 provides the minimum stress, maximum stress, and stress range for each of the re-tested specimens given by short cycle testing. The load range for re-testing each specimen is given in Table 7.11. As previously stated, all measured strains were converted to stresses using a modulus of elasticity of 181 GPa. Each specimen was tested until failure. The number of cycles completed during the re-testing portion is documented in Table 7.12. It should be noted that specimen A27 was not a true re-test as it was never tested in the other testing frame.

Table 7.9: Breakdown of testing frequencies and modes for re-tested type A specimens.

Specimen Identification	Normal Cyclic Data Collection Frequency	Static and Short Cyclic Data Collection Frequency	Cyclic Loading Frequency	Actuator Control Mode
	Hz	Hz	Hz	
A6	16	32	3.8	Load
A2	16	32	2.5	Load
A11	16	32	6.5	Load
A21	16	32	2/3.5/7.8*	Load
A27	16	32	7.8	Load

* Frequency was increased after frame braces were installed

Table 7.10: Stress range for re-tested type A specimens.

Specimen Identification	North/East Side			South/West Side		
	Minimum Stress	Maximum Stress	Stress Range	Minimum Stress	Maximum Stress	Stress Range
	MPa	MPa	MPa	MPa	MPa	MPa
A6	27	259	232	21	245	224
A2	36	261	225	30	256	226
A11	25	256	231	19	250	231
A21	14	213	199	13	215	202
A27	20	232	212	14	224	210

Table 7.11: Load range for re-tested type A specimens.

Specimen Identification	Minimum Load	Maximum Load	Load Range
	kN	kN	kN
A6	5	63	59
A2	11	73	62
A11	4	58	54
A21	1	26	25
A27	3	34	31

Table 7.12: Cycle counts for re-tested specimens.

Specimen Identification	Stress Range	Number of Cycles
	MPa	
A6	232	1 019 221
A2	225	815 820
A11	231	2 585 617
A21	199	6 631 929
A27	212	1 169 980

7.3.8 Equivalent Test Results

Four of the nine specimens used in the development of the stress-life curve were subjected to variable amplitude loading. During re-testing, the stress range was increased to reduce number of cycles and hence time until failure of the re-tested specimens. Therefore, the specimens were subjected to variable amplitude loading in the laboratory. To combine the variable amplitude data, Equation [2.6] was used to give an equivalent stress range for the number of total cycles. The final laboratory results for development of the stress-life curve are given in Table 7.13.

Table 7.13: Equivalent stress range for total number of cycles.

Specimen Identification	Equivalent Stress Range	Total Number of Cycles
	MPa	
A1	260	145 761
A5	251	120 677
A7	245	146 472
A8	252	90 211
A6	204	2 019 221
A2	196	1 815 820
A3	156	682 160
A11	228	2 885 617
A21	199	6 931 929
A27	212	1 169 980

7.3.9 Failures

Three different failure modes were observed during testing. The first mode, the most common mode, was toe-deck cracking, defined by 'C' in Figure 3.2. Figure 7.10 shows specimen A5 which failed from toe-deck cracking. The second mode was a hybrid mode in which toe-deck cracking was present with root-weld cracking. Figure 7.11 and Figure 7.12 shows the only specimen showing this failure, specimen A21. Two weld passes were present on specimen A21, shown in Figure 7.13, starting approximately 50 mm to the north side of the strain gauge, and ending at the south face of the specimen. The failure root-weld failure is believed to be a result of lack of penetration of the weld, which is shown in Figure 7.14. The third failure mode was due to corrosion of the underside of the deck plate, specifically inside the stiffening rib, on the deck plate. Only one specimen failed due to pitting corrosion and is shown in Figure 7.11. The specimen breakdown of which side failed and in what mode is given in Table 7.14.

Figure 7.10: Toe-deck cracking on specimen A5.

Figure 7.11: Root-weld cracking on Specimen A21.

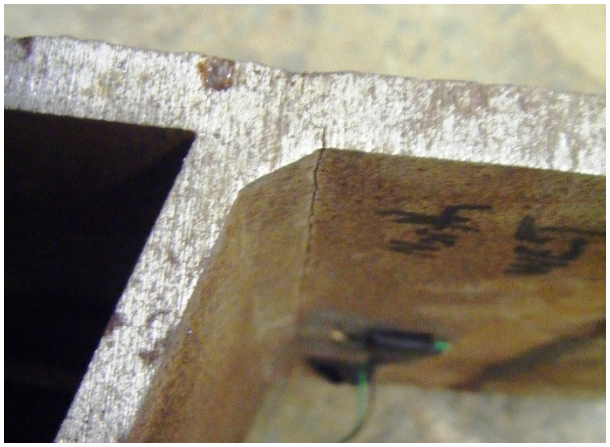

Figure 7.12: Toe-deck cracking that accompanied weld-root cracking on Specimen A21.

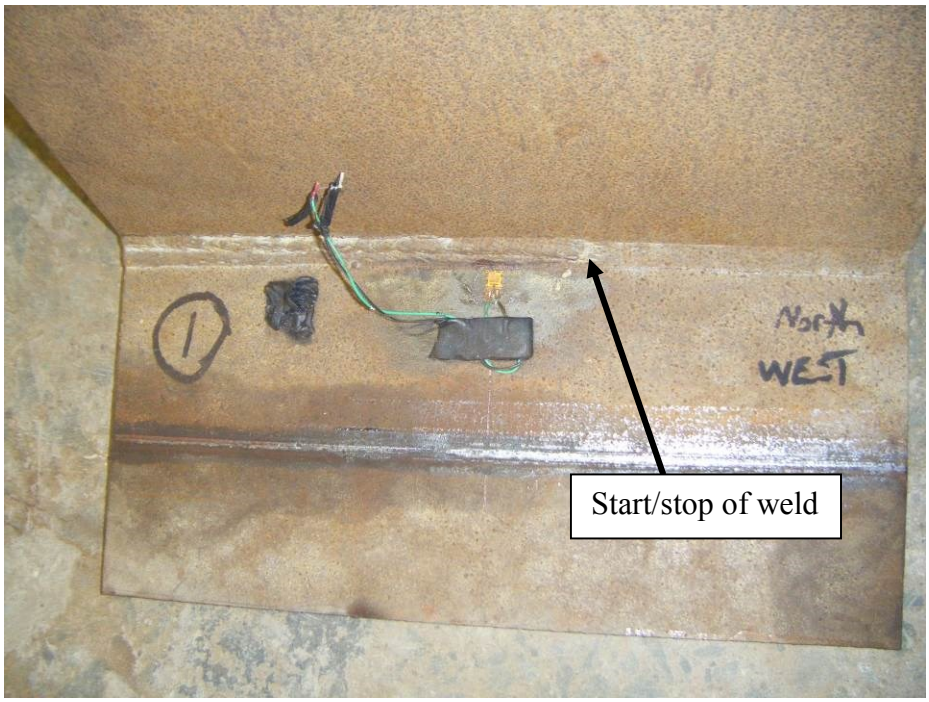

Figure 7.13: Start/stop position of second weld pass on specimen A21.

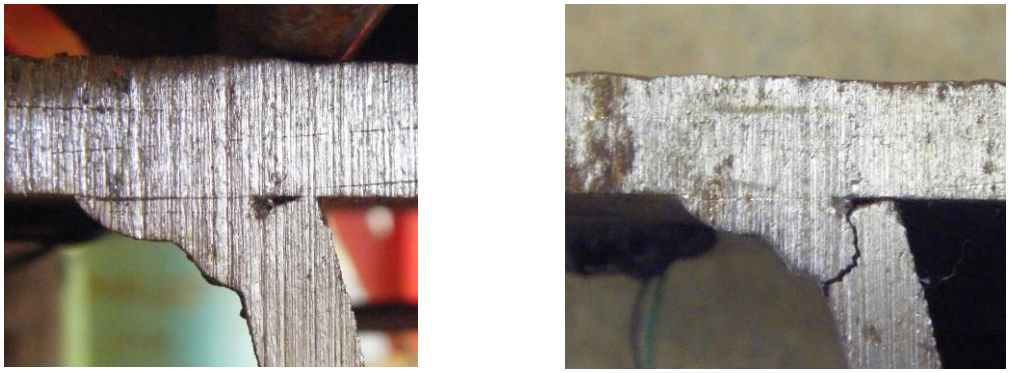

(a) (b)

Figure 7.14: Lack of penetration of rib-to-deck weld before (a) and after (b) failure

Figure 7.15: Specimen A3 failure due to pitting corrosion of deck plate.

Table 7.14: Crack failure modes.

Specimen Identification	Crack Failure Mode	Failure Side
A1	Toe-deck	North & South
A5	Toe-deck	South
A7	Toe-deck	North
A8	Toe-deck	North
A6	Toe-deck	North/East
A2	Toe-deck	North/East
A3	Corrosion	-
A11	Toe-deck	South/West
A21	Toe-deck & root-weld	North/East
A27	Toe-deck	North/East

7.4 Type B Specimen

Type B samples were used to investigate the intersection of the stiffening rib and the web of the floor beam with specific focus on the weld at the bottom of the stiffening rib. Only the preliminary specimen, with specimen identification B9, has been tested. In this preliminary phase of testing, the specimen was tested using cyclic loading to create an approximate 250 MPa stress range.

7.4.1 Specimen Geometry

Specimens were produced from sections removed from the MacKay Bridge and then cut to nominal dimensions. Figure 7.16 shows a sample after being cut to size at a steel fabrication facility. It was decided to further cut down the specimen at Dalhousie to reduce the overall weight of the specimen, which is shown in Figure 7.17. Figure 7.18 shows the nominal dimensions of the specimen. The width of the specimen was 461 mm.

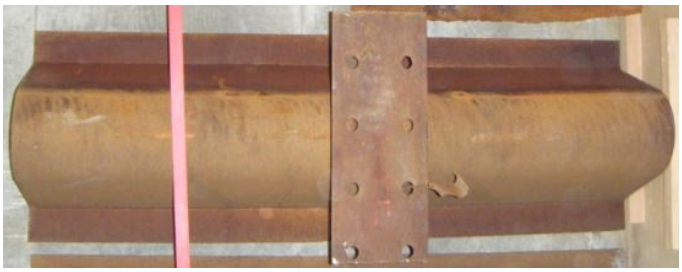

Figure 7.16: Type B specimen after cutting at steel fabrication facility.

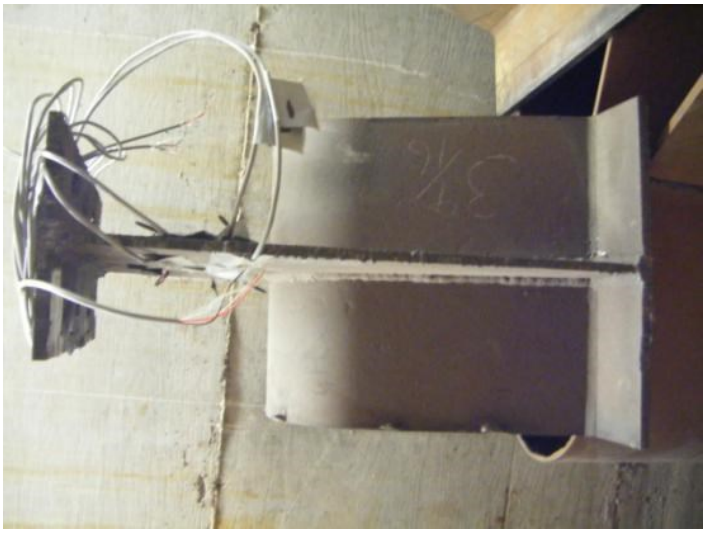

Figure 7.17: Specimen B9 after further cutting at DAL.

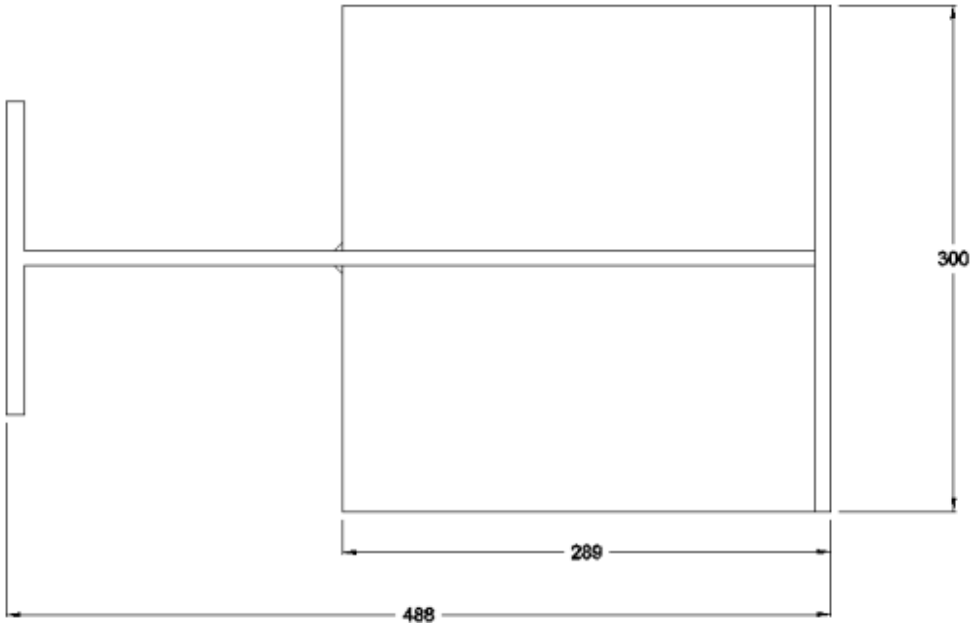

Figure 7.18: Dimensions of specimen B9.

7.4.2 Test Setup

Figure 7.19 shows the fatigue test setup for the type B specimen. The specimen was tested in a vertical reaction frame that had a maximum capacity of 1000 kN. Two steel HSS pedestals were used to bring the sample to a working height of approximately 1.5 metres. A 51 mm diameter floor bolt was bolted through a 13 mm thick steel plate placed on the bottom of the sample, through both pedestals, and finally through the concrete floor. The sample was then sandwiched between the bottom steel plate, and another steel plate placed on top of the sample through the use of four 22 mm bolts. The nominal dimensions of the test support are shown below in Figure 7.20.

Figure 7.19: Fatigue test setup for type B specimens.

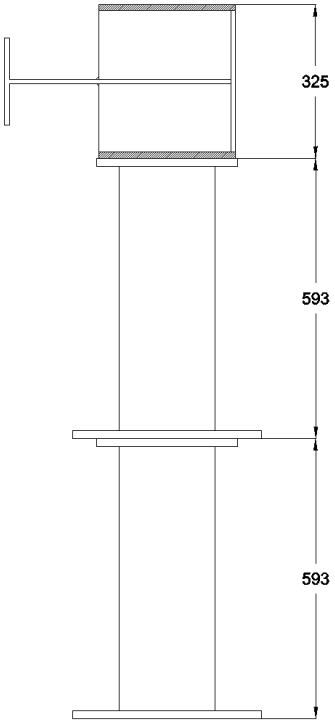

Figure 7.20: Test setup for type B specimens (all dimensions in mm).

7.4.3 Test Procedure

The testing regime consisted of daily static tests and short cycle tests at a high scan rate to confirm the specimen was loading equally on the top and bottom, as well as to capture the minimum and maximum strains during a cycle to ensure the correct stress range was being achieved. Adjustments were made to load or displacement input control parameters to account for any change in specimen stiffness or stiffness of the test setup. Once the setup and loading was confirmed, normal cyclic testing was performed. Applied load and measured strain were recorded throughout the testing. During normal cyclic loading, data was collected at a scan rate of eight scans per second. Twelve scans per second were used during daily static testing as well as daily short 50 or 100 cycle tests to capture maximum and minimum loads during a cycle to ensure the correct stress range was being achieved. For approximately the first 90000 cycles, cyclic loading was performed at a frequency of 1.0 Hz, however the frequency was changed to 0.9 Hz for the remainder of the test as the stress range remained more consistent at this new frequency. All cyclic testing was performed in displacement control.

7.4.4 Strain Gauges

Strain gauges were attached to both sides of the web of the floor beam, next to the weld connecting the trough to the web. Both gauges were located 6 mm from the toe of the weld to the centre of the gauge. Figure 7.21 shows the location of the strain gauges with respect to the toe of the rib-to-web weld. All strain gauges used were Vishay CEA-06-125UW-350 having a gauge length of 3.18 mm.

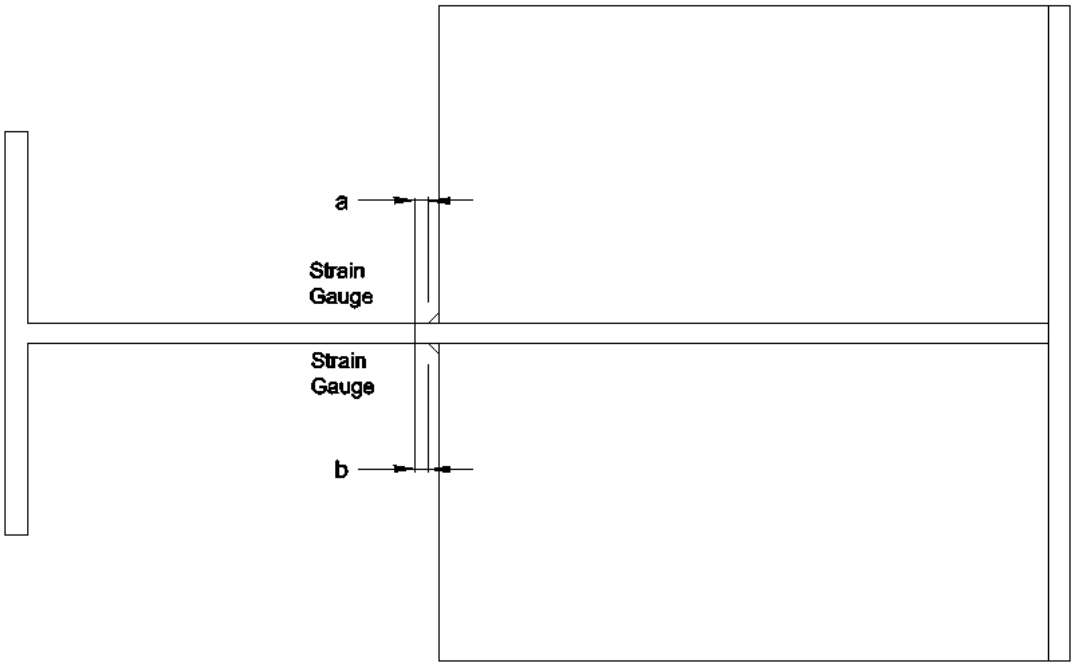

Figure 7.21: Location of strain gauges.

7.4.5 Short Cycle Analysis

Figure 7.22 shows the stress range associated with one load cycle of specimen B9. A small amount of rotation of the specimen was noticed when the load was applied. The rotation meant a small amount of axial stress accompanied the large bending stress at the gauge locations. The stress range and load range for all specimens are given in Table 7.15 and Table 7.16. All measured strains were converted to stresses using a modulus of elasticity of 181 GPa (Appendix C).

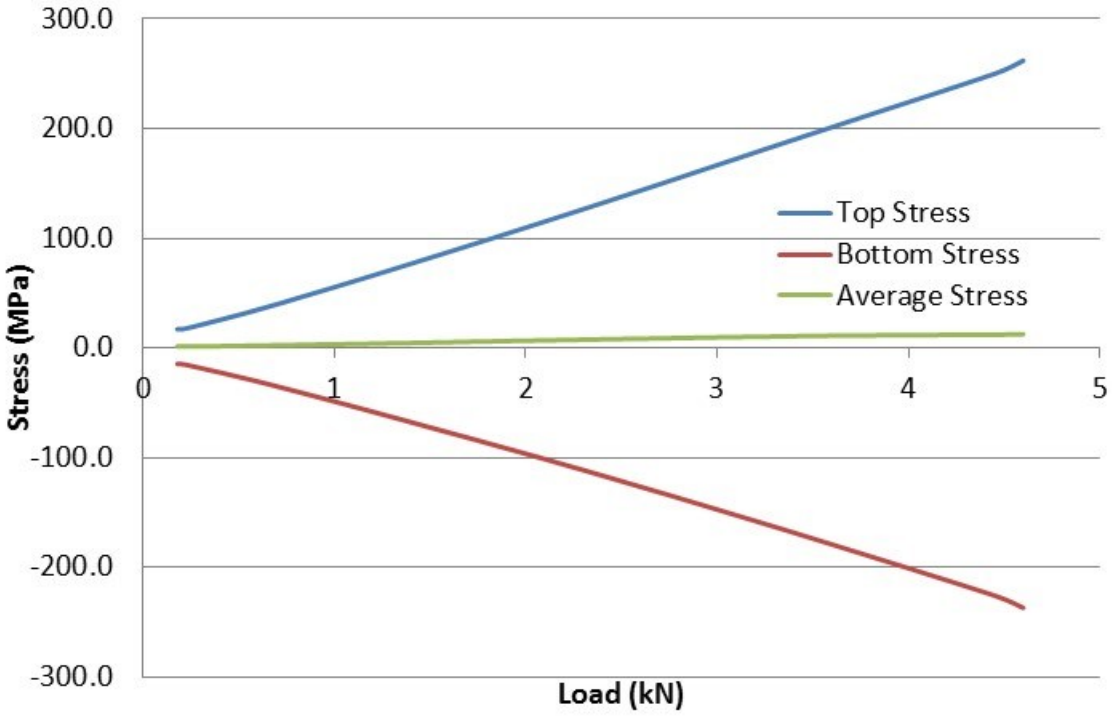

Figure 7.22: Stress range during one load cycle for specimen B9.

Table 7.15: Stress range for type B specimen.

Specimen Identification	Top Gauge			Bottom Gauge		
	Minimum Stress	Maximum Stress	Stress Range	Minimum Stress	Maximum Stress	Stress Range
	MPa	MPa	MPa	MPa	MPa	MPa
B9	17	262	245	-237	-14	223

Table 7.16: Load range for type B specimen.

Specimen Identification	Minimum Load	Maximum Load	Load Range
	kN	kN	kN
B9	0.2	4.6	4.4

7.4.6 Test Results

Figure 7.23 shows how the strain varied throughout testing. The varying nature of the strain versus number of cycles in Figure 7.23 is an artifact of conducting the testing in displacement control. Each group of cycles would have the same displacement but as the specimen response softened, the strain would reduce. The static test would permit a re-adjustment of the displacement setting followed by another softening; this repeated for each group of cycles. The specimen was tested for 370 000 cycles and failure did not occur. Since the specimen reached the 370 000 cycle target without failure, testing on the specimen stopped.

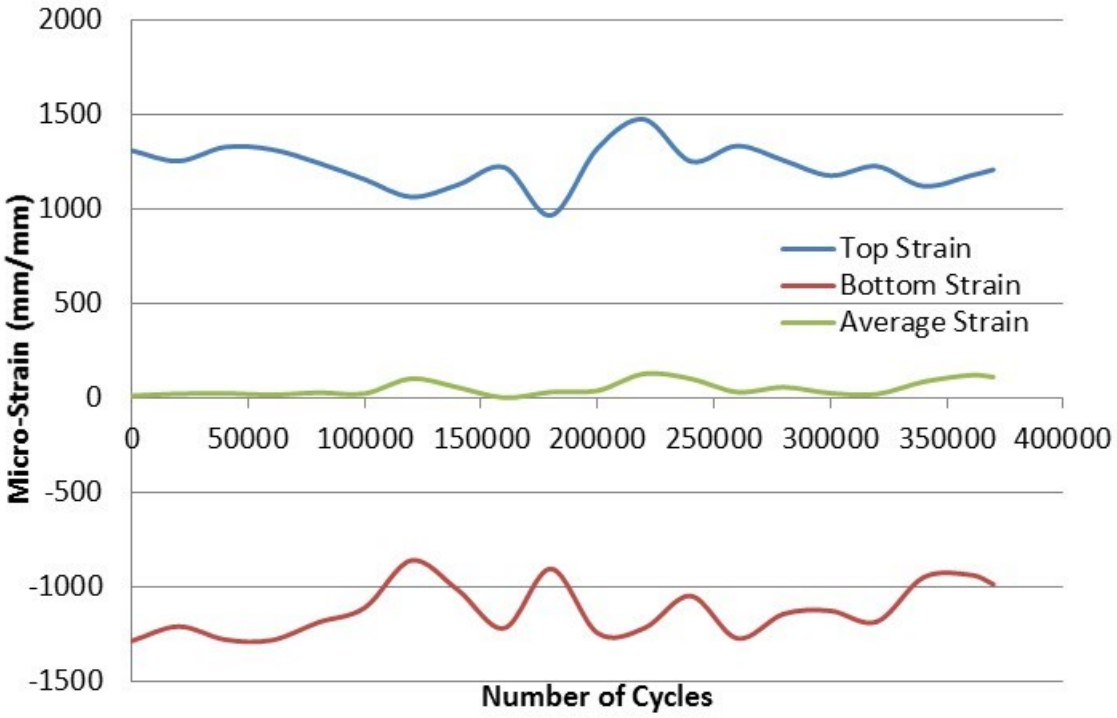

Figure 7.23: Specimen B9 strain over time at 4.5 kN.

Due to the limitations of the testing frequency and the problems with displacement control testing, it was not practical to continue testing with this frame. Therefore, the remaining type B specimens have not been tested. The new actuator documented in Section 7.3.7 will allow the testing of these specimens to be completed in the future.

7.5 Type C Specimen

This specimen was used to examine the impact of a former stiffener which was installed between adjacent stiffening ribs and subsequently removed when it was discovered to have caused a fatigue hot-spot, while adding very little stiffness to the OSPD. Though the detail has been removed, the impact due to the welding of the stiffener is still a concern for fatigue. A brief description of the test setup, specimen geometry, testing procedure, and strain gauge instrumentation for the type C specimens is presented below.

7.5.1 Specimen Geometry

Figure 7.24 shows the type C specimen after being cut to size for testing. The nominal dimensions for the specimen are shown in Figure 7.25 as well as Table 7.17. It is impossible to cut specimens to the nominal dimensions exactly, therefore the measured dimensions are given in Table 7.18.

Figure 7.24: Type C specimen after cutting.

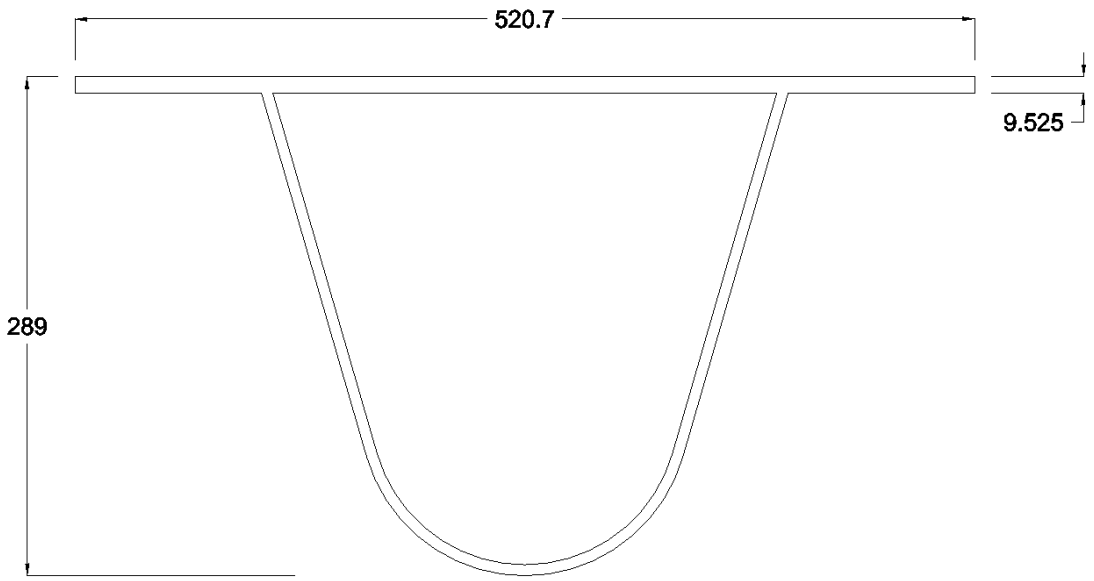

Figure 7.25: Nominal dimensions for type C specimen (all dimensions in mm).

Table 7.17: Nominal section properties for type C specimen.

Length Parallel to Stiffening Rib	Width Perpendicular to Stiffening Rib	Area	Neutral Axis from Bottom of Rib	Moment of Inertia
mm	mm	mm^2	mm	mm^4
1480	520.7	9252	209	92.34×10^6

Table 7.18: Measured dimensions for type C specimens.

Phase of Testing	Specimen Identification	Measured Length Parallel to Stiffening Rib	Measured Width Perpendicular to Stiffening Rib
		mm	mm
Preliminary	C8	1476	519
1	C7	1488	522
1	C1	1473	516
1	C9	1484	521
2	C10	1483	519
2	C4	1480	522
2	C5	1480	511
3	C6	1483	521
3	C2	1485	521

Due to the significant corrosion observed on the inside of the rib plate for many specimens, the thickness was measured at nine different sections using digital calipers. If the specimen failed during testing, the thickness was measured on the failure plane. For specimens that did not fail, the thickness was measured at the end of the specimen. Figure 7.26 in conjunction with Table 7.19 give the measured thickness for all specimens tested.

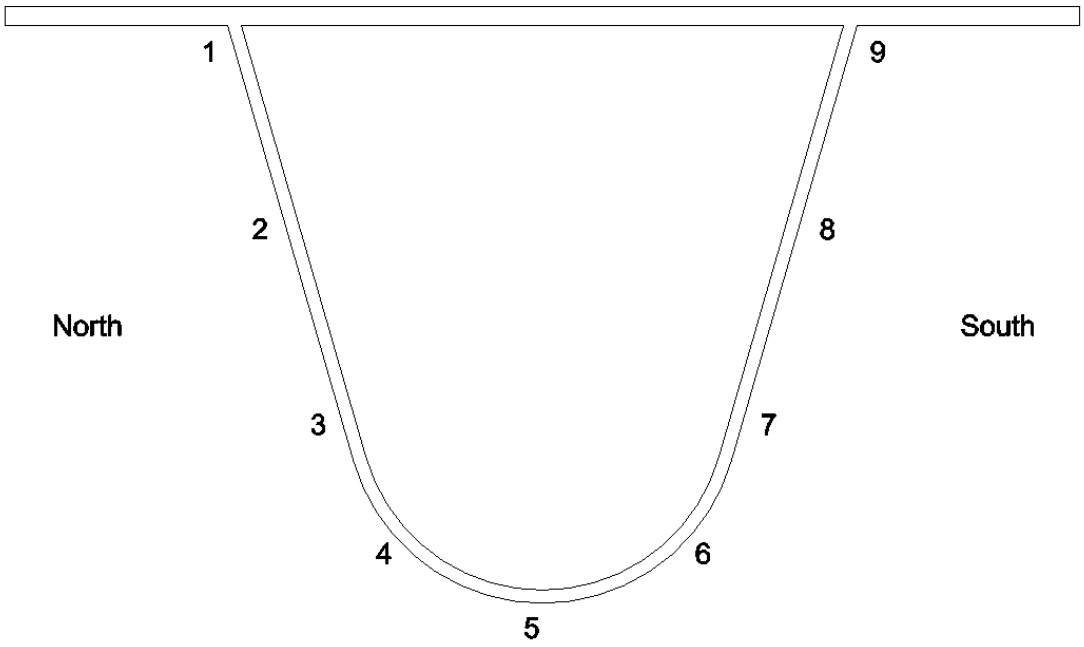

Figure 7.26: Measured thickness locations along cross section.

Table 7.19: Measured thickness of specimens.

Specimen Identification	Section Thickness									
	1	2	3	4	5	6	7	8	9	Average
	mm	mm	mm	mm	mm	mm	mm	mm	mm	mm
C8	6.75	6.67	6.21	6.57	6.40	6.51	6.51	6.64	6.88	6.57
C7	6.76	6.72	6.71	6.71	6.73	6.83	6.79	6.79	6.92	6.77
C1	4.03	1.75	1.71	5.67	5.04	2.72	2.68	2.70	2.71	3.22
C9	6.13	5.36	6.07	4.31	5.74	4.92	5.54	5.43	5.61	5.46
C10	6.77	6.72	4.88	1.06	5.47	0.94	5.66	6.03	6.73	4.92
C4	6.14	6.66	6.57	6.34	5.28	6.42	6.87	6.78	6.82	6.43
C5	4.82	6.27	6.00	6.23	3.96	6.44	6.21	6.44	6.39	5.86
C6	6.51	6.56	6.51	6.37	6.22	6.49	6.46	6.49	6.52	6.46
C2	6.94	6.86	6.63	6.74	6.59	6.76	6.47	7.22	7.00	6.80

7.5.2 Condition Assessment

Since significant corrosion was noticed on the inside of the rib plate for many specimens, all specimens were visually inspected prior to testing. The condition of the rib varied and included specimens which saw significant corrosion, including pinholes completely through the rib thickness, to specimens which looked pristine. Figure 7.27 through Figure 7.30 show the range of specimen condition. A condition inspection for each specimen is included in Appendix D.

Figure 7.27: Inside rib plate, specimen C10.

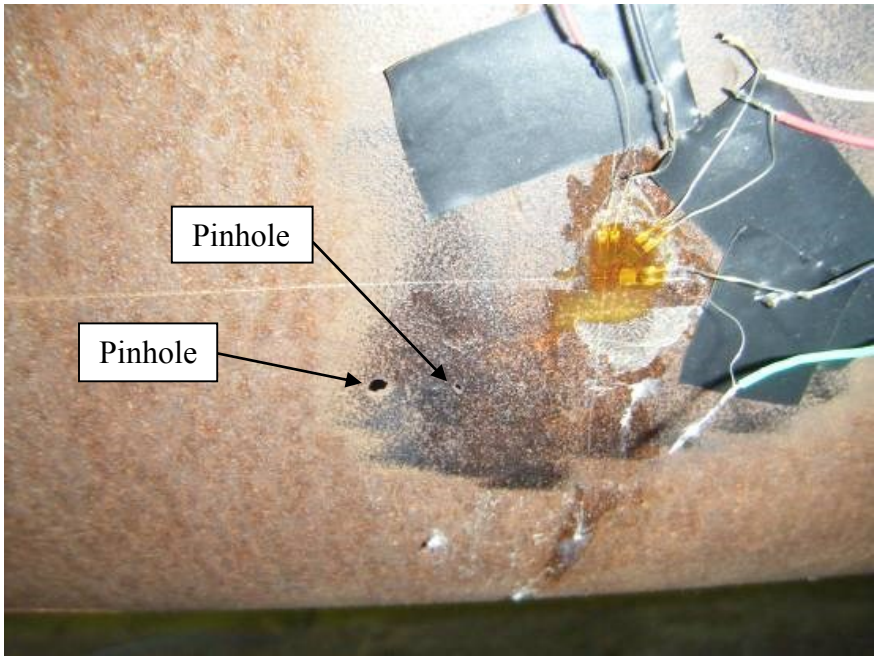

Figure 7.28: Pinholes located on south side of specimen C10.

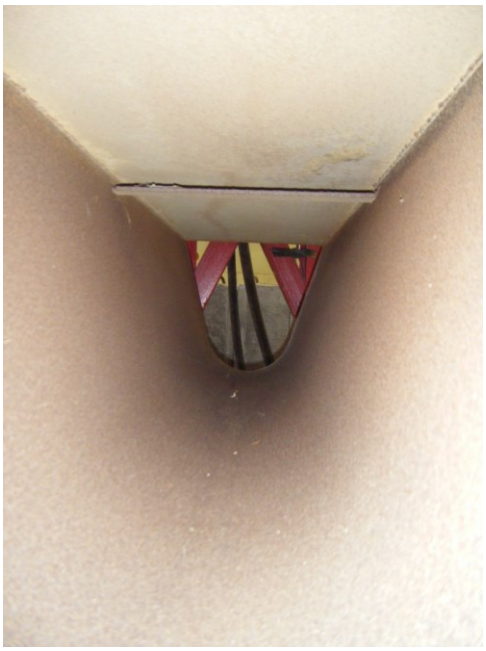

Figure 7.29: Inside rib plate, specimen C6.

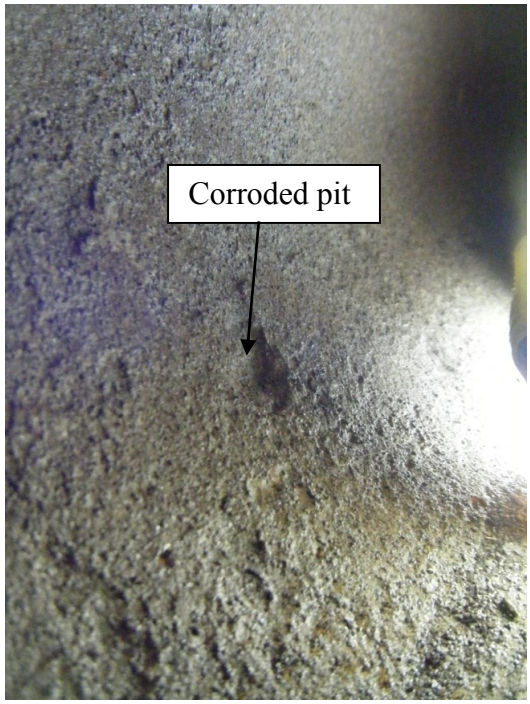

Figure 7.30: Corroded pit on north side in close proximity to strain gauge, specimen C2.

7.5.3 Test Setup

Figure 7.31 shows the standard fatigue test setup for type C specimens. The three-point bending test setup is applied to achieve maximum moment at mid-span, where the critical fatigue detail is located. Testing took place in a vertical reaction frame that has maximum capacity of 1000 kN. Profiled supports were fabricated to simulate simply supported boundary conditions. Due to varying rib dimensions, it was required to shim voids between the specimen and supports to ensure proper contact during testing. The profiled supports are shown in Figure 7.32. The nominal dimensions of the test support can be seen below in Figure 7.33.

Figure 7.31: Standard fatigue test setup for type C specimens.

Figure 7.32: Profiled supports.

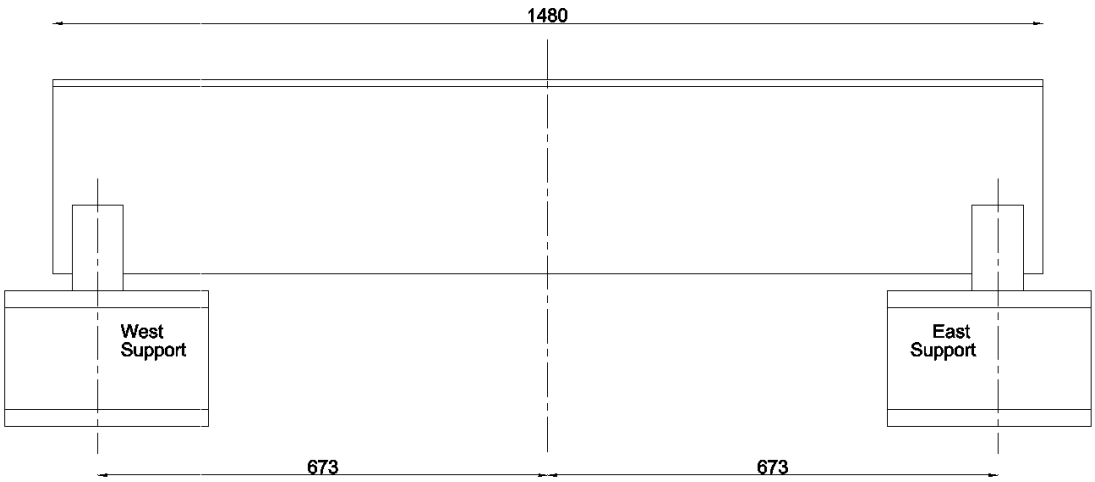

Figure 7.33: Test layout for type C specimens (all dimensions in mm).

7.5.4 Test Procedure

The testing regime consisted of daily static tests and short cycle tests at a high scan rate to confirm the specimen was loading equally on both sides, as well as to capture the minimum and maximum strains during a cycle to ensure the correct stress range was being achieved. Adjustments were made to load or displacement input parameters to account for any change in specimen stiffness or stiffness of the test setup. Once the setup and loading was confirmed, normal cyclic testing was performed. Applied load and measured strain were recorded throughout the testing. The data collection rate depended on the type of testing, and the phase of testing. The collection and testing frequency are given in Table 7.20 below. This testing procedure continued until failure or the desired number of cycles was applied.

Table 7.20: Breakdown of testing frequencies and modes for type A specimens.

Phase	Normal Cyclic Data Collection Frequency	Static and Short Cyclic Data Collection Frequency	Cyclic Loading Frequency	Actuator Control Mode
	Hz	Hz	Hz	
Preliminary	5	50	1	Load
1	5	50	1	Load
2	5	50	1	Load
3	15	25	0.9	Load

7.5.5 Strain Gauge Instrumentation

A 45-degree strain gauge rosette was attached to both sides of the rib plate, 213 mm below the deck plate. All gauges were located at mid span where the former stiffeners existed. All rosette gauges used were Omega SGD-1/350-RYT21 having a gauge length of 1.6 mm. Figure 7.34 shows an example of a strain rosette used for this testing and Figure 7.35 shows the gauge location with respect to the cross section of the specimen, along with the numbering system used for data collection. Gauge one and four were longitudinal, gauge two and five were diagonal, and gauge three and six were vertical.

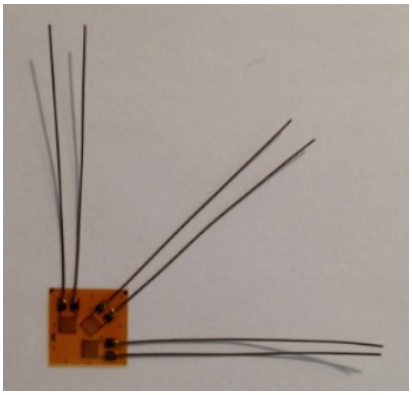

Figure 7.34: Strain gauge rosette used in laboratory testing.

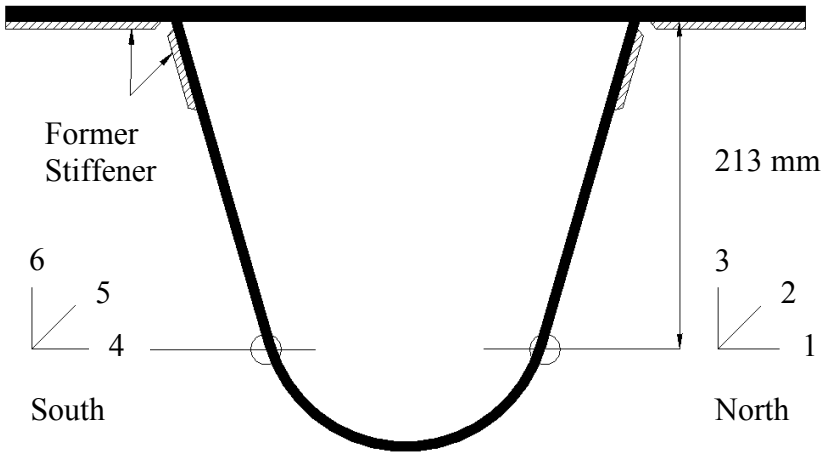

Figure 7.35: Strain gauge rosette location and numbering system.

7.5.6 Short Cycle Analysis

Figure 7.36 shows the stress range associated with one load cycle of specimen C10. The stress range and load range for all specimens are given in Table 7.21 and Table 7.22. All measured strains were converted to stresses using a modulus of elasticity of 181 GPa.

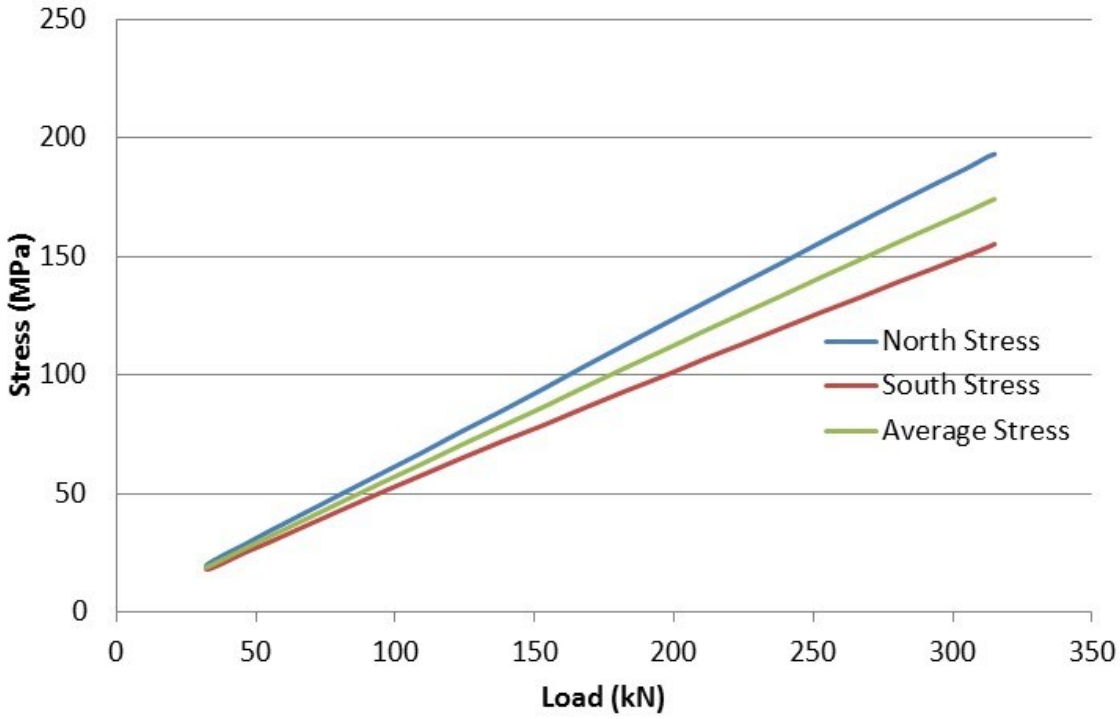

Figure 7.36: Principal stress range during one load cycle for specimen C10.

Table 7.21: Principal stress range for type C specimens.

Specimen Identification	North Side			South Side		
	Minimum Stress	Maximum Stress	Stress Range	Minimum Stress	Maximum Stress	Stress Range
	MPa	MPa	MPa	MPa	MPa	MPa
C8	43	244	201	29	276	247
C7	32	300	268	29	241	212
C1	92	547	455	41	290	249
C9	31	303	272	36	315	279
C10	20	193	173	17	157	140
C4	48	230	182	26	191	165
C5	25	212	187	16	182	166
C6	28	232	204	16	227	211
C2	42	365	323	16	225	209

Table 7.22: Load range for type C specimens.

Specimen Identification	Minimum Load	Maximum Load	Load Range
	kN	kN	kN
C8	61	455	394
C7	50	451	401
C1	51	340	289
C9	39	469	430
C10	32	315	283
C4	38	222	184
C5	23	218	195
C6	34	359	325
C2	35	364	329

7.5.7 Test Results

Figure 7.37, developed from specimen C10, shows an example of how the strain varied throughout testing. Little variation in the strain readings occur over time, except when the specimen approached failure. The longitudinal stress does not vary significantly from the principal stress until approaching failure, meaning the principal stress axis is very close to the longitudinal axis, as expected for a bending member. Plots for other specimens are given in Appendix D. The number of cycles applied to each specimen, as well as whether the specimen failed or was stopped (classified as a run-out) is given in Table 7.23, which gives the maximum stress range as well.

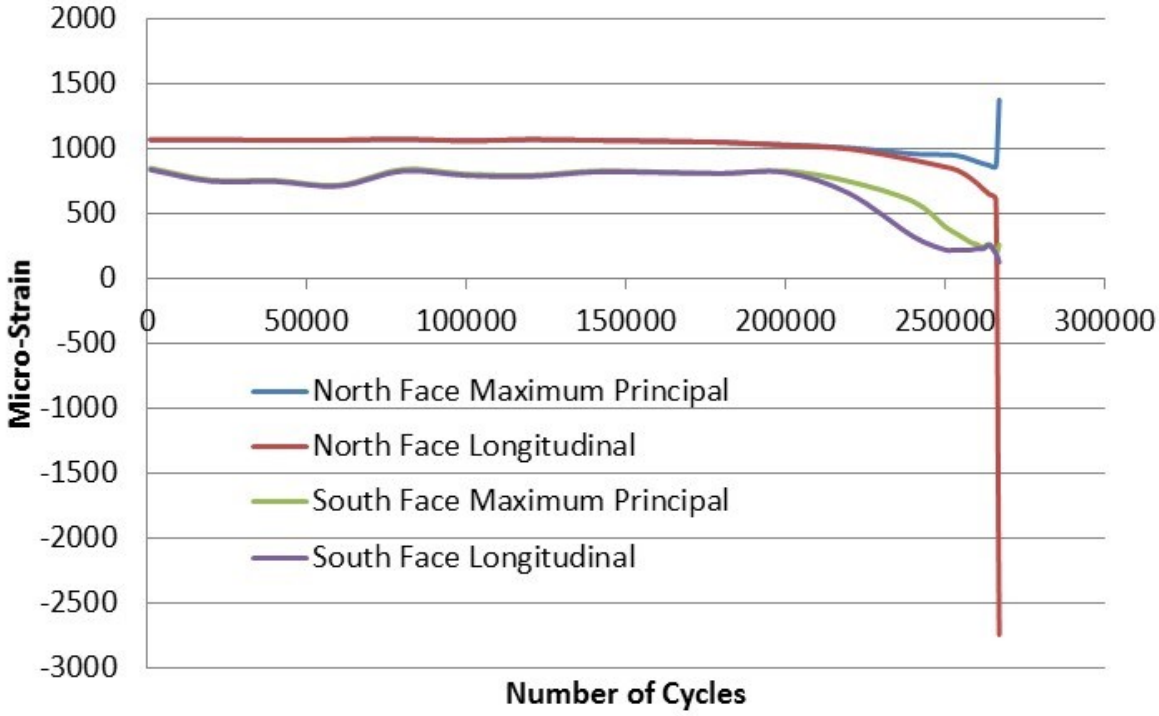

Figure 7.37: Specimen C10 strain over time at 313 kN.

Table 7.23: Cycle counts for type C specimens.

Specimen Identification	Stress Range	Number of Cycles	Failure or Run-out
	MPa		
C8	247	72 032	Failure
C7	268	767 396	Run-out
C1	455	78 163	Failure
C9	279	125 822	Failure
C10	173	267 042	Failure
C4	182	1 000 000	Run-out
C5	187	1 000 000	Run-out
C6	211	300 000	Run-out
C2	323	300 000	Run-out

7.5.8 Failures

The failure locations were documented for all specimens that failed. The location of the initial failure is documented in Table 7.24 for the north and south sides respectively. Figure 7.38 through Figure 7.40 show the failure initiation locations on the specimens. The former stiffener ended at a distance of 143 mm below the neutral axis of the section (213 mm from the underside of the deck plate). The initial failure locations do not correspond to the location of the former stiffener welds and are all related to the effect of corrosion, whether a 'pinhole', corroded pit, or reduced wall thickness. This shows that for the specimens extracted and tested, corrosion is more of a concern for the fatigue life of the type C specimens than the former stiffener welds. However, the test specimens are not believed to be representative of the OSPD currently on the MacKay Bridge. The impact of corrosion on the fatigue reliability will be explained further in this thesis, but will not be used in predicting the remaining fatigue life of the in-service OSPD panels. HHB has known the OSPD panel replaced in 2010 had removed sealer plates since the early 1990's, therefore atypical leaking was present at this panel for about 20 years.

Table 7.24: North and south side failure locations.

Specimen Identification	Load	Longitudinal Distance from Loading Point to Failure Location	Distance below Neutral Axis to Initial Failure Location	Max Moment at Loading Point	Moment at Failure Location	Ratio of Moments
	kN	mm	mm	kN-m	kN-m	
North						
C1	339	73	147	114	102	0.89
C9	468	200	203	157	111	0.70
C10	314	32	148	106	101	0.95
South						
C1	339	-	-	114	-	-
C9	468	200	203	157	111	0.70
C10	314	13	146	106	104	0.98

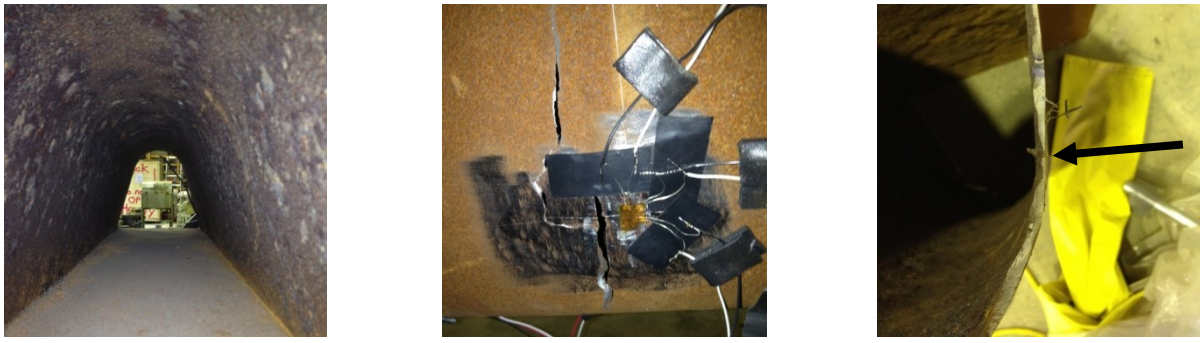

(a) (b) (c)

Figure 7.38: Specimen C1 (a) condition inside section prior to testing, (b) fracture on north face, (c) reduced wall thickness on north face.

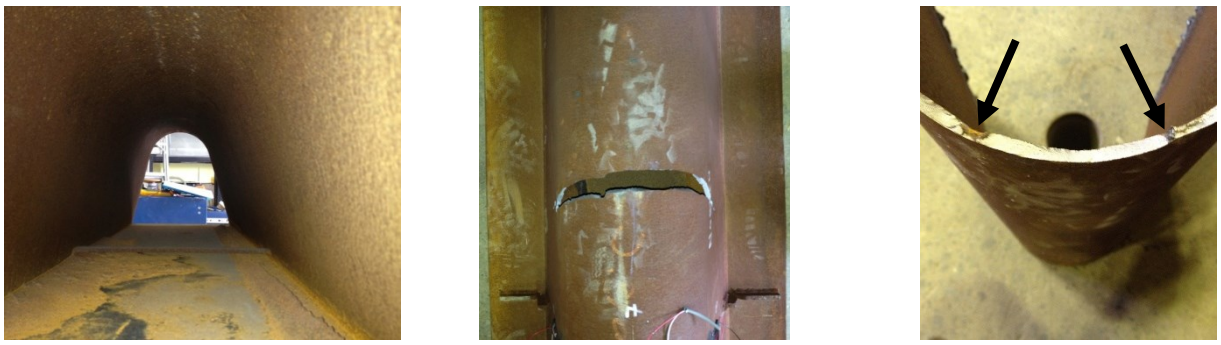

(a) (b) (c)

Figure 7.39: Specimen C9 (a) condition inside section prior to testing, (b) fracture on bottom of rib, (c) corroded pit (left) and "pinhole" (right).

(a) (b) (c)

Figure 7.40: Specimen C10 (a) condition inside section prior to testing, (b) corroded "pinhole" on south face, (c) corroded pit on north face.

7.6 Statistical Analysis

Due to the limited number of specimens available for testing, only the fatigue strength coefficient was estimated from the results. Since the fatigue strength exponent for all fatigue details in the CHBDC is taken at 3.0, it is more important to determine the fatigue detail coefficient, assuming 3.0 fatigue strength exponent is representative for these specimens. If a large number of specimens were available for testing, in the range of 12 to 24 specimens (ASTM E739-10), the fatigue strength exponent could also be estimated. The specimens that were extracted from the former OSPD on the MacKay Bridge were limited, and therefore the fatigue strength exponent given in the CHBDC was used. The analysis of the test data was performed similar to ASTM E739-10, assuming a log-log relationship

between stress range and number of cycles until failure. The logarithm base 10 of the fatigue detail coefficient was calculated for each specimen used in the analysis by rearranging Equation [2.1]. For the type A analysis, specimen A3 was not included because the failure was not characteristic of the failure of concern, which is failure of the rib-to-deck weld. It is believed that the level of corrosion present in specimen A3 is not representative of the rest of the OSPD on the MacKay. The stress range taken in the type A analysis corresponded to the side that failed. Analysis for the type B detail was not performed as only the preliminary specimen has been tested. The type C analysis was broken into two categories, corroded and non-corroded. All specimens that failed were corroded, and therefore all fall into the corroded category. Since the remaining specimens did not fail due to corrosion and were stopped before failure, they fall into the non-corroded category. The non-corroded specimens did not fail, thus this gives only a lower bound of the fatigue resistance. It is believed these non-corroded specimens are more representative of the bridge. The maximum stress range was used for the type C analysis. For both the type A and type C analysis, the preliminary specimen was excluded. The values used in the analysis are given in Table 7.25 through Table 7.26. The final statistics for the type A and type C fatigue details are given in Table 7.28.

Table 7.25: Type A stress-life curve.

Specimen Identification	Equivalent Stress Range	Total Number of Cycles	Log(Sr)	Log(N)	Log(A)
	MPa				
A5	251	120 677	2.40	5.08	12.28
A7	245	146 472	2.39	5.17	12.33
A8	252	90 211	2.40	4.96	12.16
A6	204	2 019 221	2.31	6.31	13.23
A2	196	1 815 820	2.29	6.26	13.13
A11	228	2 885 617	2.36	6.46	13.53
A21	199	6 931 929	2.30	6.84	13.73
A27	212	1 169 980	2.33	6.07	13.05

Table 7.26: Type C non-corroded stress-life curve.

Specimen Identification	Stress Range	Total Number of Cycles	Log(Sr)	Log(N)	Log(A)
	MPa				
C7	267	767 396	2.43	5.89	13.16
C4	182	1 000 000	2.26	6.00	12.78
C5	188	1 000 000	2.27	6.00	12.82
C6	211	300 000	2.32	5.48	12.45
C2	324	300 000	2.51	5.48	13.01

Table 7.27: Type C corroded stress-life curve.

Specimen Identification	Stress Range	Total Number of Cycles	Log(Sr)	Log(N)	Log(A)
	MPa				
C1	455	78 163	2.66	4.89	12.87
C9	279	125 822	2.45	5.10	12.44
C10	173	267 042	2.24	5.43	12.14

Table 7.28: Statistics for type A and type C specimens.

Detail	μ_{logA}	σ_{logA}	μ_{lnA}	σ_{lnA}
Type A	12.9	0.602	29.8	1.39
Type C – Non-corroded	12.8	0.269	29.6	0.620
Type C – Corroded	12.5	0.365	28.7	0.841

7.7 Discussion of Results

In general, the type A and type C details tested above the expected fatigue strength, especially considering the imprinted fatigue damage from 40-plus years of in-service loading. Unfortunately, the type B specimens were not tested so no discussion of results is provided for this detail.

7.7.1 Type A

In five cases, the fatigue testing was stopped at a pre-defined number of cycles in order to complete testing on other specimens. Once the opportunity presented itself to re-test the five specimens, a large number of cycles at a high stress range was needed before the specimens failed.

Failure of all type A specimens, except specimen A3, were a result of toe-deck cracking, with one case of toe-deck cracking present with root-deck cracking. These failures indicate good weld quality in the rib-to-deck joint; a large number of root-weld cracks would

indicate poor weld quality. Specimen A3 failed as a result of corrosion.

Though only eight specimens were used in the statistical analysis, some general conclusions can be drawn. The mean of the type A detail, classified as a category C fatigue detail according to the CHBDC, tests to a level higher than that of the category C detail. The type A detail tests closer to a category B' detail, even with the imprinted fatigue damage of 40-plus years of loading. However, a large variation exists within the eight specimens used in the analysis; a much smaller standard deviation is found in the CHBDC fatigue details as these are based on thousands of fatigue tests. A larger number of type A specimens would reduce the variation and provide better fitting distribution parameters (mean and standard deviation) in the analysis. Unfortunately, since all specimens were obtained from sections of OSPD being replaced on the MacKay Bridge, limited specimens were available and no more specimens at this fatigue damage level can be tested.

7.7.2 Type C

The eight type C specimens were broken into corroded and non-corroded specimens after testing was performed. Corrosion played a significant role in the failure of all specimens, which significantly decreased the fatigue life. The corroded specimens are not believed to be representative of the condition of the OSPD on the MacKay Bridge, and therefore the non-corroded results are used in the reliability analysis.

The mean of the three corroded specimens tests close to that of the category C fatigue detail from the CHBDC, which is surprising considering the imprinted fatigue damage, as well as the significant corrosion that occurred to these specimens. However, large variation between specimens existed due to the very low number of specimens. Therefore, significant conclusions cannot be drawn from such a small dataset.

The mean from the five non-corroded specimens tested above the category C fatigue detail, close to the type A specimen mean. However, smaller variation in the type C results is noticed when compared to the type A, but a large variation is still present when compared to the CHBDC categories in Section 2.2.7. It is important to remember the type C specimens were stopped at pre-defined number of cycles, calculated from previous results, thus the variation is artificially small. The non-corroded specimens did not fail and only

represent a lower bound to the fatigue resistance of the type C fatigue detail. The non-corroded type C specimens cannot be re-tested similar to the type A specimens because of the load level required.

Chapter 8: SHM Data Processing

Once the SHM data was collected from the datalogger, it was imported into MATLAB for analysis. The data was processed through an outlier detection filter to remove any outliers in the data before the data was totaled for each channel. Further adjustments were made to the data and are detailed in the subsequent sections.

8.1 Outlier Detection

Basu and Meckensheimer (2007) define an outlier as "a data point in a time series that is significantly different from the rest of the data points". The potential causes for recording an outlier in a SHM application include an extreme loading event, a change in structural behaviour, sensor and equipment failure, sensor reconfiguration, and a change in system noise. Outliers can significantly affect the analysis of the collected data, thus it is important to identify any outliers. Upon identification, the outliers of a data set were explored in more detail to determine if the flagged data point is a legitimate data point that should be included in the data set or not.

8.1.1 The Median Method

The median method was proposed by Basu and Mackensheimer (2007) as a technique to detect and identify outliers in a data set. The method is based on the principle that data points in a close vicinity are correlated. Data points in this vicinity are then used to predict the expected value of the data point under consideration.

Two variations of the median method were presented by Basu and Mackensheimer (2007), which include the two-sided median method and the one-sided median method. In the two-sided median method, an equal number of points before and after the data point under consideration are used to determine if the particular data point is an outlier or not. The one-sided median method is a slight variation of the two-sided median method and uses only data points before the data point under consideration to determine if the particular data point is an outlier. The one-sided median method is ideal for real time monitoring as it can operated in real time while the data is being collected and outliers can be actively identified. In the analysis of the rainflow data collected from the MacKay Bridge, the two-sided median method is better suited since the data is being processed for outliers after data

collection. The advantage for using the two-sided median method in the analysis of the rainflow data is the ability to use more data points in the prediction of the data point under consideration. The observed trend in the rainflow data follows the peak traffic hours on the bridge. The cycle counts will increase from a low count to a high count, and back to a low count over a period of several hours. Using both points before and after allows for more data to be used in the prediction. If the one-sided median method were used, as the data points got farther away from the data point under consideration, the less correlation between the points exist and a less accurate prediction will be made. Using the two-sided median method allows for double the amount of points as the one-sided median method, while maintaining the same distance away from the point under consideration, thus the same level of correlation. Figure 8.1 shows the number of data points used for the one-sided and two-sided median methods for a distance 'x' away from the point under consideration. The distance away 'x' corresponds to how correlated the points are to the point under consideration; the smaller the distance 'x' the greater the correlation between the points.

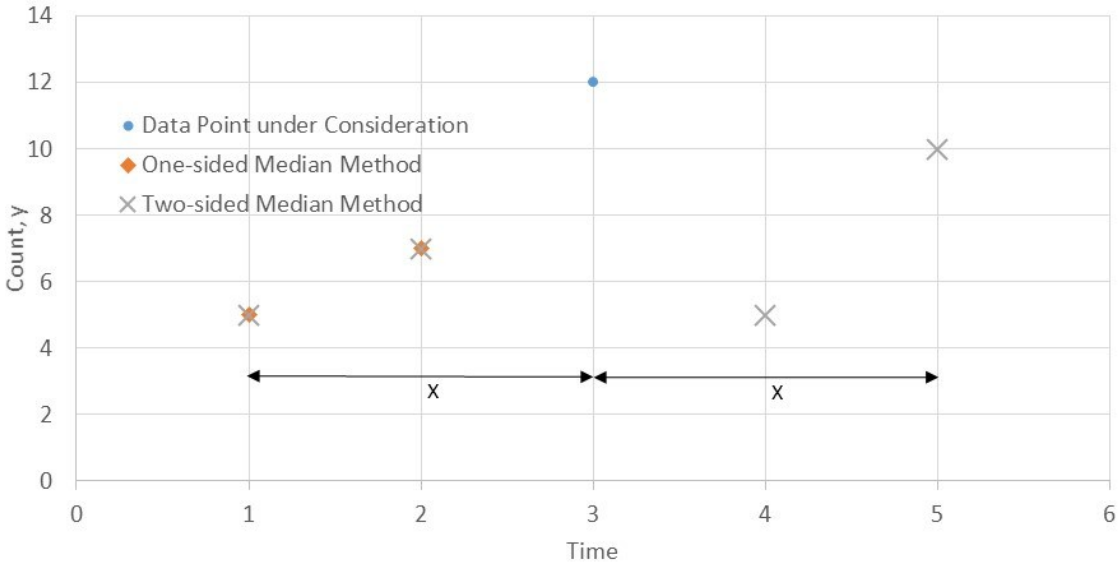

Figure 8.1: Comparison of points included in distance 'x' away from point under consideration for one-sided and two-sided median method.

8.1.2 Two-sided Median Method

Since the two-sided median method is used in the analysis of the rainflow data, it is

described further in this section. The method is illustrated with real data. For a given time series of y_1, y_2, …, y_n, a set of neighbouring data points is defined as $n_t^{(k)} = \{y_{t-k}, \ldots, y_{t-1}, y_{t+1}, \ldots, y_{t+k}\}$, where the neighbouring window size is 2k, which starts at t-k and ends at t+k. The median of $n_t^{(k)}$ is calculated and defined as $m_t^{(k)}$, which is then compared to y_t. The error is defined by the absolute value of the difference between $m_t^{(k)}$ and y_t. This is then compared to a specified threshold, τ, to determine if y_t is an outliner. If the error exceeds the threshold, y_t is flagged as an outlier, as shown by Equation [8.1].

$$\left| y_t - m_t^{(k)} \right| \geq \tau \qquad [8.1]$$

Using rainflow data from August 10, 2013 and August 11, 2013 on channel 1 (gauge A-04-1), the two-sided median method is explored in more detail. The comparison of the predicted values to the actual values are shown in Figure 8.2. It is obvious in this set of data that an outlier exists at 22:00 hours that does not fall within the general trend of the data series. If this cycle count is not identified and investigated, the total cycle counts for this particular gauge could be incorrect by a significant margin. In this case, the error is 620, which is a significant amount of extra cycles that could be included in the analysis. Figure 8.3 shows how the two-sided median method examines $y_{22:00}$ using a window width of k = 2, the width used in the complete analysis. It is clearly seen that the error exceeds the shaded band of threshold, therefore the point is identified as an outlier.

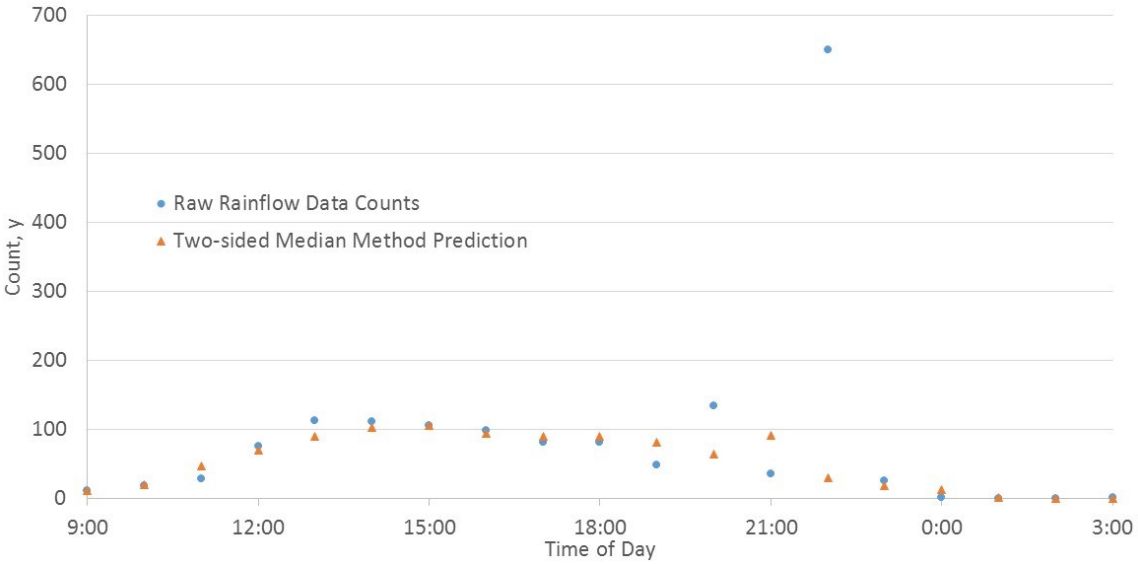

Figure 8.2: Comparison of actual bin counts to the predicted bin counts using the two-sided median method.

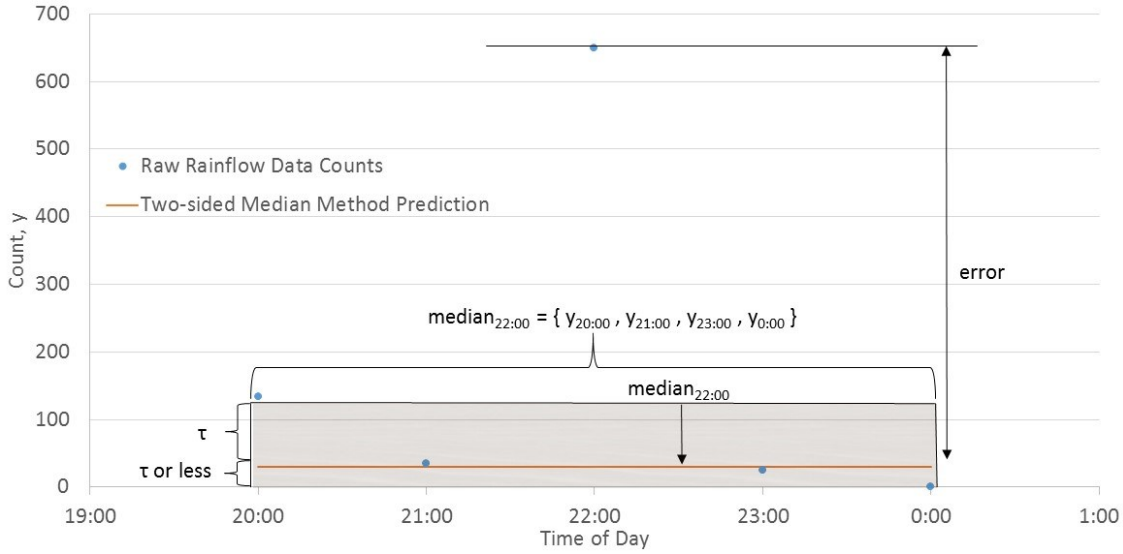

Figure 8.3: Two-sided median method analysis on selected rainflow counts.

Different thresholds were used for the three different gauge types. The thresholds were determined from manually checking seven weeks of data spread out throughout the year 2013. The thresholds for each gauge type is given in Table 8.1.

Table 8.1: Thresholds for outlier detection.

Gauge Type	Count Threshold
A	100
B	50
C	80

Once a data point was identified as an outlier, the occurrence was investigated manually. If the data point occurred during a traffic peak and was of realistic magnitude, the data point was accepted as a real data point that belonged in the data set. However, if the data point was deemed unreasonably large and did not fall within the trend of the data, the data point was classified as an anomaly and was either replaced or deleted. Deletion occurred when an anomaly was detected in multiple gauges for the same hour. When only a single gauge was deemed an anomaly, the count was replaced with the predicted value, $m_t^{(k)}$. A total of 224 hours were deleted from the 2013 data set, which is less than three percent data loss. In the analysis it is assumed that the cleaned data is representative for the entire year, and therefore the totals for each gauge were multiplied by a factor to give the yearly total. The factor was calculated as the ratio of hours in a year to the hours contained in the cleaned data (8760 hours / 8536 hours), resulting in a factor of 1.026.

8.2 Adjustment Factor

For the type C fatigue detail, only the longitudinal gauge on the strain gauge rosette recorded a rainflow histogram. However, two issues arise when only the longitudinal gauge is considered. First, the principal strain (or principal stress) is actually of interest because it is larger and occurs at a different angle than the longitudinal strain. This issue is shown in Figure 8.4. The strain gauge rosettes were located on the stiffening ribs at the bottom of the former stiffener. The former weld connecting the stiffening plate to the stiffening rib was a continuous weld that started on one side of the stiffening plate, wrapping around the bottom and up the other side of the plate. This means that all stress vectors at the rosette location are perpendicular to the weld axis. If histograms were recorded on each arm of the rosette, they could not be related to one another to give an equivalent principal strain histogram. The only way to obtain the principal strain histogram directly is by recording strain from all three arms of the rosette and calculating the principal strain, all while

running the datalogger at 200 Hz. This would overwhelm the data acquisition system.

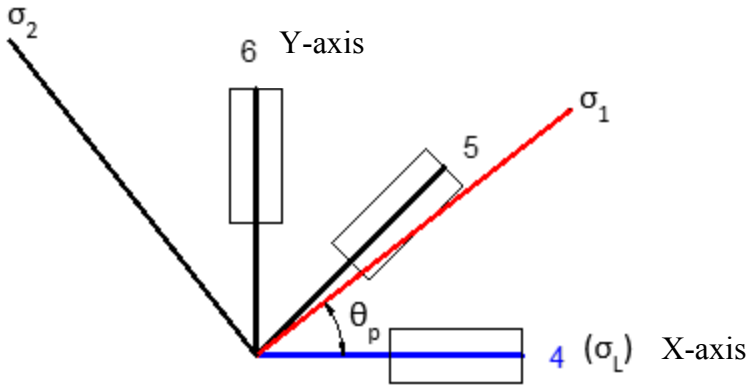

Figure 8.4: Principal stress location from longitudinal stress.

The second issue occurs when converting the strains to stresses. Uniaxial Hooke's law, Equation [8.2], is valid when stress is only present in the axis under consideration. For the type C detail, a condition of multi-axial stress exists, therefore uniaxial Hooke's law cannot be used in converting the strains to stresses. The full 2-dimensional state of stress, Equation [8.3], is needed for converting from strains to stresses.

$$\sigma_{xx} = E\varepsilon_{xx} \qquad [8.2]$$

where: σ_{xx} = stress in the x-axis (longitudinal);

E = modulus of elasticity;

ε_{xx} = strain in the x-axis (longitudinal).

$$\sigma_{xx} = \frac{E}{1-\nu^2}\left(\varepsilon_{xx} + \nu\varepsilon_{yy}\right) \qquad [8.3]$$

where: ν = Poisson's ratio;

ε_{yy} = strain in y-axis (transverse).

To account for the combined effects of both principal axis and the stress conversion, a simple adjustment factor was calculated to convert the data from the longitudinal gauge to the principal stress. The adjustment factor is defined as the ratio of the principal stress

calculated from 2-dimensional stress state (Equation [8.3]) to the longitudinal uniaxial Hooke's law stress (Equation [8.2]). Table 8.2 shows the adjustment factor associated with specimen C10 in the laboratory testing. At both the minimum and the maximum load recorded during testing, the adjustment factor is very close to unity. However, due to much more complex loading in the field, an adjustment of close to unity does not transfer to field loading. Table 8.3 and Table 8.4 show the combined errors, as well as the adjustment factor for each gauge during the static test. The need for an adjustment factor is further shown in Figure 8.5, which displays the dynamic test data for C-21-4 gauge.

Table 8.2: Specimen C10 stress calculation for minimum and maximum load from laboratory testing.

	North Side			South Side		
Load	**Longitudinal Stress from Uniaxial Hooke's Law**	**Principal Stress from 2D Stress State**	**Adjustment Factor**	**Longitudinal Stress from Uniaxial Hooke's Law**	**Principal Stress from 2D Stress State**	**Adjustment Factor**
kN	MPa	MPa		MPa	MPa	
32	19.7	19.6	1.00	18.1	17.3	0.96
315	193	193	1.00	155	157	1.01

Table 8.3: North rosette stress calculation from static test.

Gauge Number	North			
	Equivalent Longitudinal Stress from Uniaxial Hooke's Law	Equivalent Principal Stress from 2D Stress State	Percent Error	Adjustment Factor
	MPa	MPa		
C-04-1	28.1	45.5	38%	1.62
C-06-1	27.5	48.9	44%	1.78
C-10-1	26.1	45.8	43%	1.76
C-12-1	23.5	24.8	5%	1.05
C-16-1	33.5	53.6	38%	1.60
C-18-1	9.4	28.1	66%	2.98
C-21-1	24.8	42.9	42%	1.73
C-24-1	29.5	49.1	40%	1.67

Table 8.4: South rosette stress calculation from static test.

	South			
Gauge Number	**Equivalent Longitudinal Stress from Uniaxial Hooke's Law**	**Equivalent Principal Stress from 2D Stress State**	**Percent Error**	**Adjustment Factor**
	MPa	MPa		
C-04-4	31.3	54.2	42%	1.73
C-06-4	25.5	44.7	43%	1.75
C-10-4	27.9	49.8	44%	1.79
C-12-4	28.6	48.5	41%	1.70
C-16-4	25.7	46.4	45%	1.81
C-18-4	26.2	64.5	59%	2.46
C-21-4	23.5	41.6	43%	1.77
C-24-4	26.6	46.0	42%	1.73

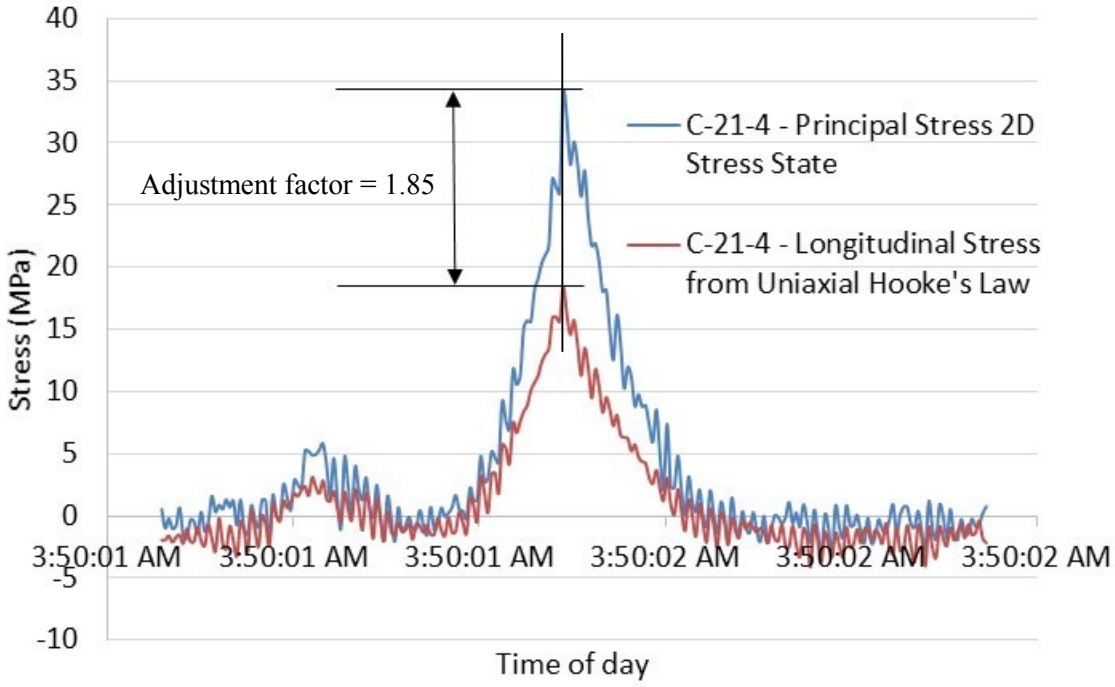

Figure 8.5: Dynamic test results for C-21-4 rosette.

Since the bridge is subjected to random traffic loading, the adjustment factor will vary. Raw gauge readings on all arms of the rosettes were collected for a nominal one hour time period during the morning traffic rush hour on two separate occasions; April 17, 2014 and June 4, 2014. Two dates were needed so the data acquisition system was not overwhelmed. It took in excess of six hours to download the entire raw data file. Once the raw data was obtained, the readings were split into each individual rosette. The data was then put through a peak picking filter to obtain the peak strains. Strain readings that were below the threshold of 70 με on the longitudinal gauge were not included in the analysis. The adjustment factor was then calculated for each of the remaining readings. Figure 8.6 explores the correlation between the adjustment factor and the recorded strain, which can only be described as random. Therefore, a normal probability density function was used to describe the adjustment factor, shown in Figure 8.7.

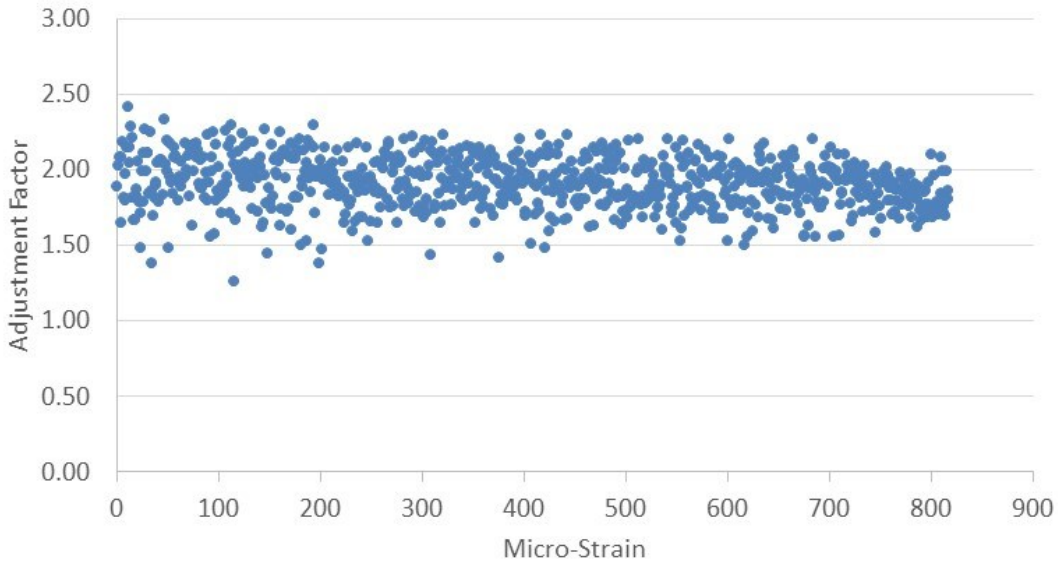

Figure 8.6: Adjustment factor for C-21-4 rosette at varying levels of strain.

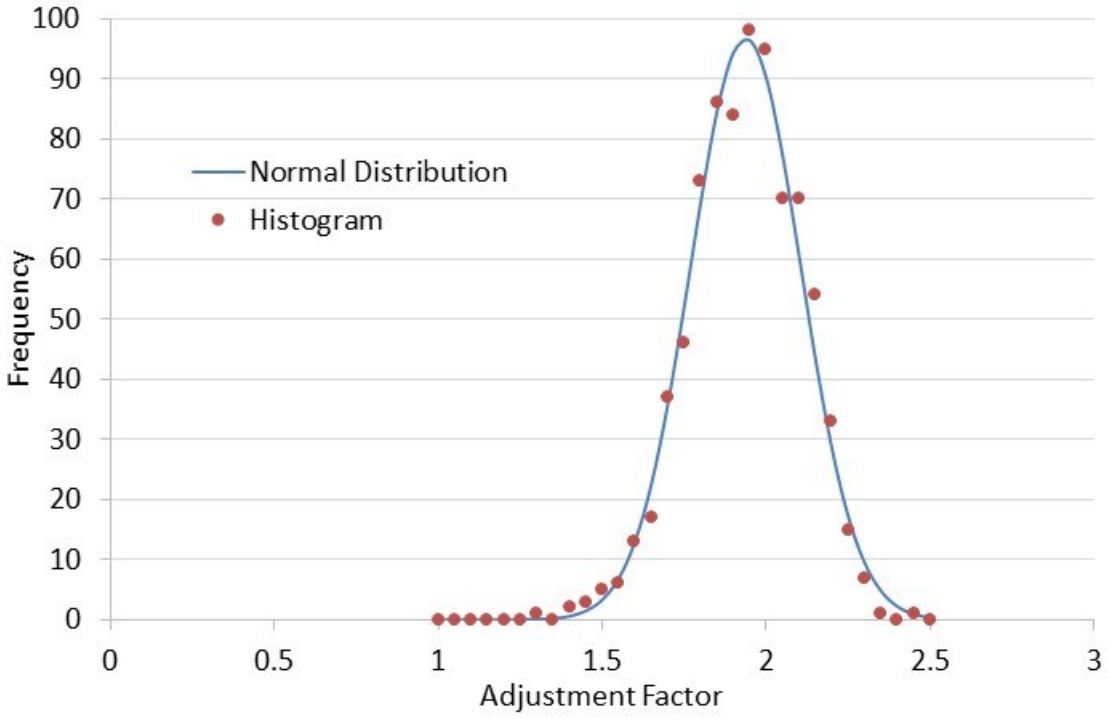

Figure 8.7: Normal distribution used to describe the adjustment factor for C-21-4 rosette.

Table 8.5: Adjustment factor statistics.

Gauge	Static Test	Raw 200 Hz Data	
		Mean	Coefficient of Variation
C-04-1	1.62	1.44	0.298
C-04-4	1.73	1.68	0.286
C-06-1	1.78	1.86	0.149
C-12-4	1.70	1.75	0.178
C-16-1	1.60	1.50	0.193
C-18-4	2.46	1.99	0.185
C-21-1	1.73	1.69	0.128
C-21-4	1.77	1.91	0.119
C-24-1	1.67	1.76	0.207

Unfortunately, not all rosette gauges were functional for a year and a half after the installation date because the system was only designed for a single year. However, the four gauges without adjustment factor statistics have otherwise good data. The particular gauges are documented in Table 8.6. Either the diagonal or vertical arm on the rosette had a broken gauge at the time of 200 Hz adjustment factor data collection, which made adjustment factor calculations impossible. To accommodate the four gauges with no adjustment factor statistics, the distribution statistics were assigned instead of calculated values. Though adjustment factors are available from the static test, a difference between the static test values and the raw 200 Hz data is shown in Table 8.5. The difference is likely due to the randomness of the applied loading which is not captured in the static test. Further, the raw 200 Hz data collected more than a single loading event. For the four rosettes with faulty gauges, the mean adjustment factor used for analysis was taken as the average of all nine gauges that collected raw 200 Hz data, as given in Table 8.5. The mean adjustment factor is calculated as 1.73. Since the value of 1.73 is close to all static results from the four gauges under consideration, it is reasonable to use. The variation of the adjustment factor at these locations is also not known so the maximum coefficient of variation 0.298 (rounded to 0.3) was used. Table 8.6 summarizes the four gauges under consideration and the

adjustment factor statistics used for the analysis.

Table 8.6: Adjustment factors for rosettes with faulty gauges.

Gauge	Static Test	Data for Analysis	
		Mean	Coefficient of Variation
C-06-4	1.75	1.73	0.30
C-10-1	1.76	1.73	0.30
C-10-4	1.79	1.73	0.30
C-24-4	1.73	1.73	0.30

8.3 Noise

During normal data collection, the data acquisition system was scanning at 200 Hz with no averaging to help remove noise in the system. Therefore, noise has been included in the strain readings and needs to be factored into the analysis. On two separate dates, October 4, 2012 and June 6, 2013, raw 200 Hz data was collected for a few minutes on all channels during the re-zeroing procedure, which occurred at midnight. This gave ambient noise readings when essentially no traffic was present on the bridge. The statistics for each channel was calculated and are presented in Appendix E. With the mean of all gauges occurring between -1 με and 1 με, it was assumed a mean of 0 με would be appropriate for all gauges. The average standard deviation for each gauge type was used in further analysis. The standard deviations assigned were 6 με, 4 με, and 5 με for the type A, type B and type C gauges respectively. To eliminate the possibility of counting strain range readings that were simply noise, the minimum amplitude of strain range to be counted was set at 70 microstrain, which is larger than any noise readings observed during the raw 200 Hz data collection.

8.4 Excluded Gauges

Upon processing the SHM data through the outlier detection filter and comparing gauges within each gauge group, numerous gauges gave erroneous results due to abnormal cycle counts and were therefore excluded from the analysis. Including these gauge would

significantly skew the results obtained by the analysis. Abnormal counts were either extremely high, as indicated by a significant number of outliers being detected, or extreme low when compared to the average count for the gauges in that detail type. Abnormal counts also include an extremely different distribution of counts throughout the mean bins, with similar count magnitudes in every mean bin. The abnormal counts could be present for the entire year of data, or for only a few weeks. In either scenario, the data would skew the analysis, therefore the gauges were exclude. The excluded gauges are documented in Table 8.7.

Table 8.7: Gauges excluded from analysis.

Excluded Gauge	Abnormality
A-17-2	Low counts
A-21-1	Bin distribution
A-24-1	Low counts
B-04-2	High counts
B-10-1	High counts
B-24-2	High counts
C-12-1	High counts
C-16-4	Low counts
C-18-1	Low counts

8.5 Gauge Totals

Once all data was filtered and erroneous gauges excluded, the data was totaled on each of the remaining channels, and the gauge statistics were calculated, as shown in Table 8.8 through Table 8.10. Statistics were calculated using Equation [8.4] and Equation [8.5]. The number of cycles recorded is not adjusted for only recording approximately 97 percent of the year. The percentage of compression only cycles was also included since there is some debate as to whether or not compression cycles are damaging. For this analysis, compression cycles were included in the analysis, which is the more conservative option. However, if compression cycles were excluded, the analysis would not change significantly since they only make up approximately 5 percent of the total cycles in the worst case. A

rainflow histogram for gauge C-21-4 is given in Figure 8.8, showing the distribution of cycles into the mean and amplitude bins. The histogram is truncated to only include bins with actual data. Complete histograms are given in Appendix F.

$$m_{\varepsilon_m} = \frac{\sum_{i=1}^{b} n_j \varepsilon_{mj}}{n_t} \quad [8.4]$$

where: m_{ε_m} = mean measured strain;

n_j = number of cycles in bin j;

ε_{mj} = mid-point strain in bin j;

n_t = total number of cycles;

b = total number of range bins.

$$\sigma_{\varepsilon_m} = \sqrt{\frac{\sum_{i=1}^{b} n_i (\varepsilon_{mj} - m_{\varepsilon_m})^2}{n_t - 1}} \quad [8.5]$$

where: σ_{ε_m} = standard deviation of measured strain.

Table 8.8: Type A gauge counts.

Gauge	Number of cycles	Percentage of Compression Cycles	Mean	Coefficient of Variation
		%	με	
A-04-1	833 725	0.7	121	0.490
A-04-2	326 087	0.1	100	0.371
A-06-1	93 337	0.2	107	0.385
A-06-2	1 334 456	2.4	121	0.509
A-10-2	96 952	0.3	98	0.364
A-11-1	40 606	1.6	97	0.609
A-12-1	84 867	0.2	103	0.416
A-12-2	618 611	1.3	111	0.487
A-16-1	242 833	0.2	91	0.275
A-16-2	68 544	0.0	88	0.244
A-18-1	10 160	0.1	90	0.295
A-21-2	1 700 825	1.1	132	0.479
A-24-2	1 180 844	1.6	128	0.447

Table 8.9: Type B gauge counts.

Gauge	Number of cycles	Percentage of Compression Cycles	Mean	Coefficient of Variation
		%	με	
B-04-1	437 389	0.8	139	0.465
B-06-1	271 570	1.2	127	0.411
B-06-2	306 121	1.5	131	0.437
B-10-2	194 878	2.6	119	0.421
B-12-1	265 707	2.8	112	0.409
B-12-2	265 160	3.1	112	0.416
B-16-1	125 747	2.8	93	0.242
B-16-2	84 920	3.1	91	0.222
B-18-1	47 754	2.6	92	0.253
B-18-2	129 605	5.5	93	0.236
B-21-1	55 479	1.8	118	0.383
B-21-2	615 802	1.3	122	0.396
B-24-1	557 939	1.9	130	0.464

Table 8.10: Type C gauge counts.

Gauge	Number of cycles	Percentage of Compression Cycles	Mean	Coefficient of Variation
		%	με	
C-04-1	686 906	3.5	123	0.409
C-04-4	662 399	1.4	118	0.420
C-06-1	383 429	0.6	118	0.369
C-06-4	429 058	0.6	119	0.370
C-10-1	256 218	0.6	118	0.398
C-10-4	169 879	0.7	116	0.362
C-12-4	216 692	0.5	120	0.406
C-16-1	99 360	1.2	92	0.303
C-18-4	69 129	2.9	91	0.290
C-21-1	764 471	1.4	117	0.352
C-21-4	757 225	0.7	119	0.340
C-24-1	427 590	1.4	111	0.341
C-24-4	649 842	1.2	118	0.364

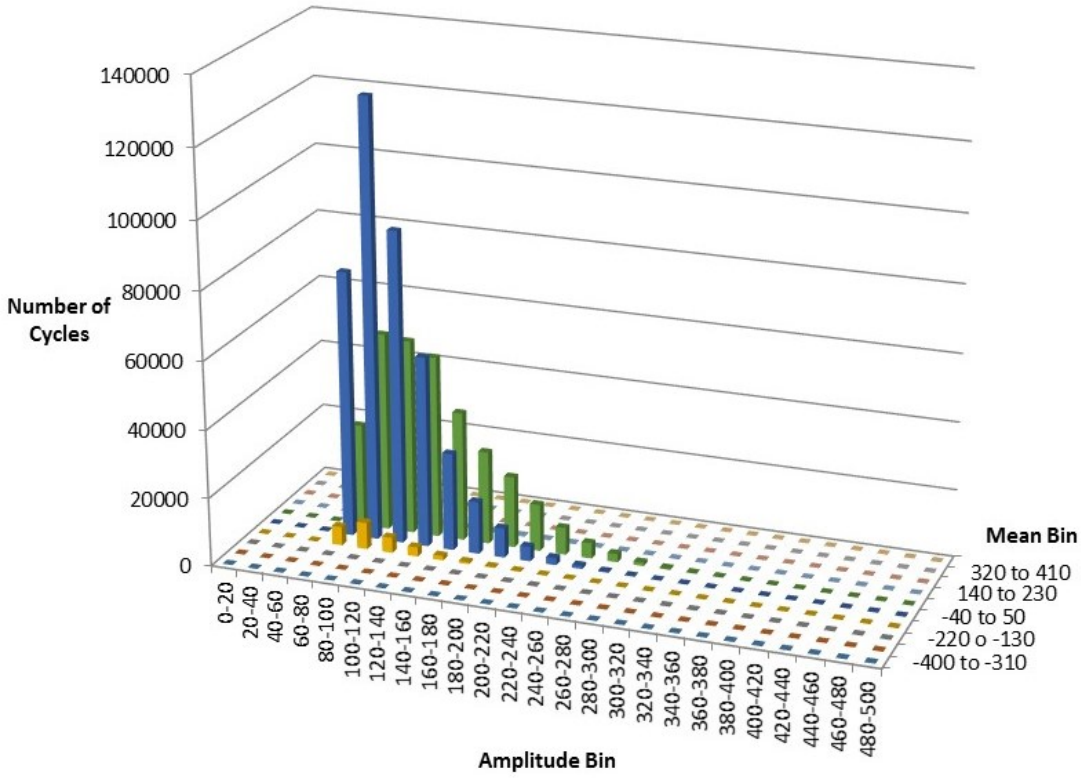

Figure 8.8: C-21-4 rainflow histogram for 2013.

Chapter 9: Finite Element Studies

Finite element models (FEMs) are needed to compliment both the laboratory and field testing components due to each of their limitations. This section details the finite models developed to remove these limitations.

9.1 Type A Laboratory Model

The type A fatigue detail examines the rib-to-deck weld. The strain gauges applied to each side of the deck plate were only able to be located a certain distance from the centre of the gauge to the toe of the weld, which varied from 4 mm to 12 mm. The location of the strain gauge does not allow it to capture the strain at the toe of the weld, therefore an extrapolation is needed to obtain the strain at the toe of the weld. The strain at the toe of the weld is desired as this is where the stress concentration is the largest, and where most laboratory specimens show failure. To extrapolate, a ratio between the transverse strain at the weld toe and the transverse strain at the gauge location is used. The ratio is called a geometric adjustment factor (GAF).

The laboratory type A specimen was modeled using the finite element program ADINA. A 3-dimensional, linear elastic model of the type A specimen was created using 4-noded shell elements. All elements were approximately 5 mm wide. Figure 9.1 shows the mesh used for the 3-dimensional type A model. The boundary conditions applied were vertical restraints were placed parallel to the weld axis on both sides of the stiffening rib, approximately 76 mm from the toe of the weld. No other restraints were applied. A total loading of 50 kN was applied using two pressures above each weld location. The pressure was applied over an area 3 mm wide, by the complete length of the specimen, 457 mm.

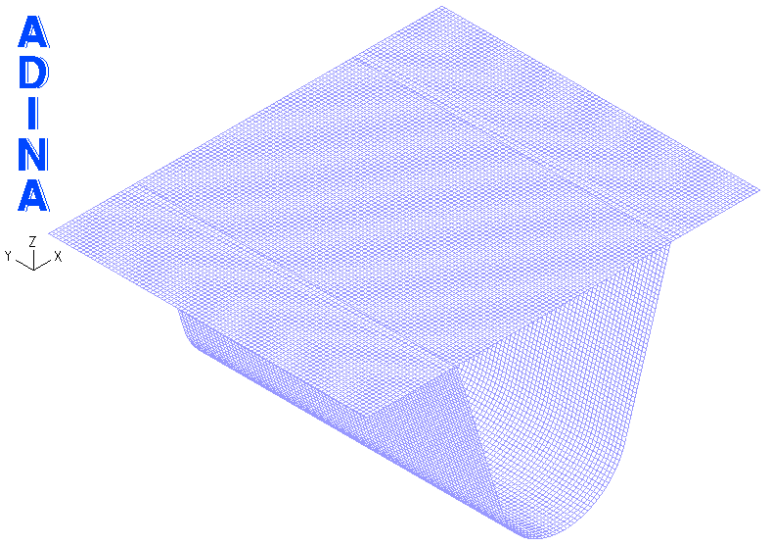

Figure 9.1: Type A specimen 3-dimensional mesh.

To accompany the 3-dimensional model, 2-dimensional plane stress and plane strain models were also built since a heavier mesh density can be constructed in the vicinity of the weld and strain gauge. Half symmetry was used in creating the 2-dimensional models, with the mesh shown in Figure 9.2. In all models, a modulus of elasticity of 181 GPa was used.

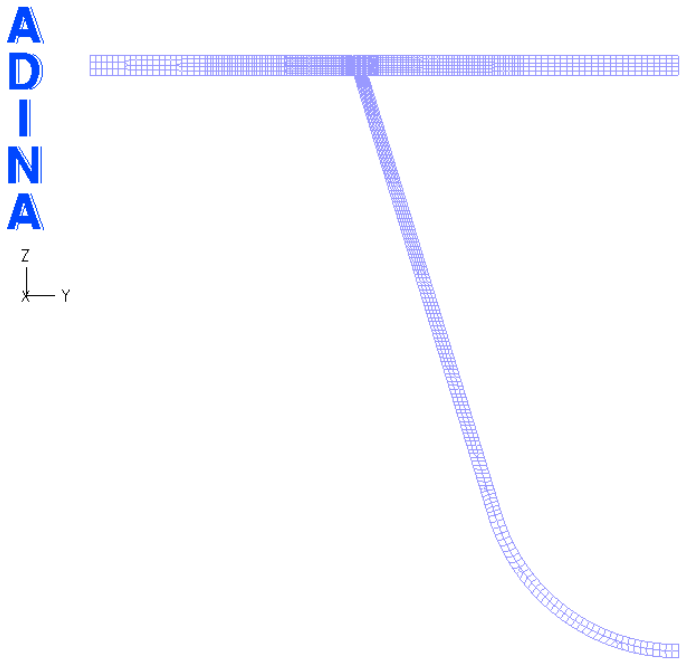

Figure 9.2: Type A specimen 2-dimensional mesh.

The models were compared to determine which of the 2-dimensional models best represented the real 3-dimensional test. In comparing the models, the vertical displacement and the strain transverse to the weld axis were examined. The transverse strain was able to be compared to the laboratory strain results at 50 kN. The comparison for the left-hand side of the models is given in Figure 9.3 and Figure 9.4. These plots show that neither the plane stress nor the plane strain case match the 3-dimensional behaviour of the type A specimen; the actual behaviour is between the two models. A closer look at the 3-dimensional model showed that neither the longitudinal stress nor the longitudinal strain are equal to zero. The three models are compared to the laboratory results from specimen A11 in Table 9.1. The average of the two sides was used for the laboratory results at a load of 50 kN.

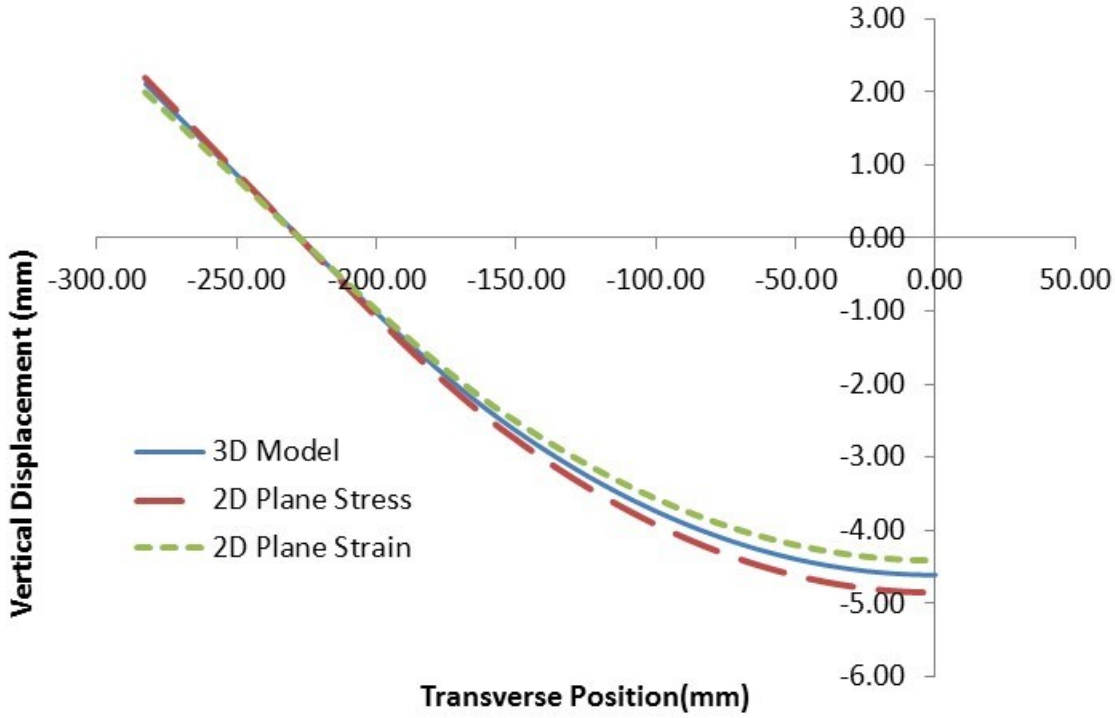

Figure 9.3: Comparison of vertical displacement.

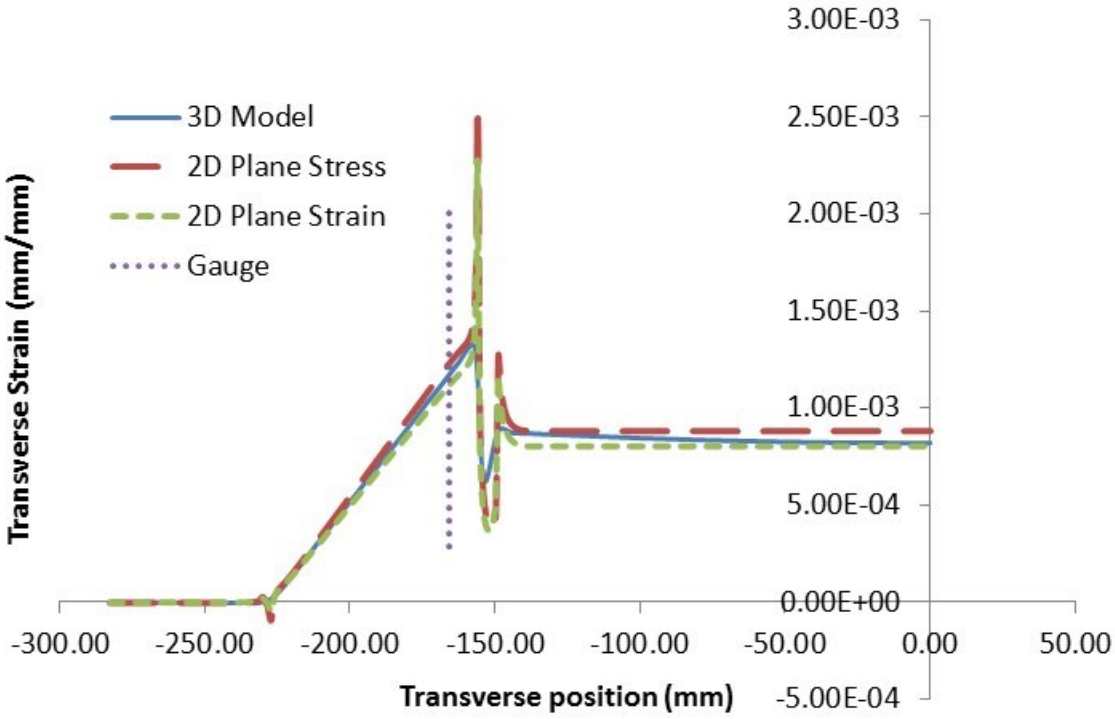

Figure 9.4: Comparison of transverse strains.

Table 9.1: Error for each model.

Model/Lab	Strain at Gauge	Percent Error
	με	%
3D Shell	1168	3
2D Plane Stress without Weld	1230	9
2D Plane Strain without Weld	1119	1
Lab Specimen A11	1130	-

The purpose of this analysis is to find the GAF, which has been compared for the different models in Table 9.2. For the laboratory specimen A11, the gauge to weld toe distance was 4 mm for both sides. The average strain reading of the two sides was used for the laboratory results at a load of 50 kN. It is interesting to note that no matter the model, the GAF is consistently the same value. Table 9.3 shows the GAF for the largest gauge to weld toe distance of 12 mm.

Table 9.2: GAF comparison for 4 mm gauge distance to weld toe.

Model/Lab	Strain at Gauge	Strain at Weld Toe	GAF
	με	με	
3D Shell	1168	1244	1.06
2D Plane Stress without Weld	1230	1309	1.06
2D Plane Strain without Weld	1119	1192	1.06
Lab Specimen A11	1130	-	-

Table 9.3: GAF comparison for 12 mm gauge distance to weld toe.

Model/Lab	Strain at Gauge	Strain at Weld Toe	GAF
	με	με	
3D Shell	1017	1244	1.22
2D Plane Stress without Weld	1071	1309	1.22
2D Plane Strain without Weld	975	1192	1.22

The GAF for each type A laboratory specimen has been summarized in Table 9.4. These factors have been applied to each laboratory specimen appropriately to obtain the strain values at the weld toe.

Table 9.4: GAF for each type A laboratory specimen.

Specimen Identification	Gauge Distance		GAF	
	North	South	North	South
	mm	mm		
A1	9	8	1.15	1.13
A5	7	7	1.11	1.11
A7	8	9	1.13	1.15
A8	9	12	1.15	1.22
A6	7	5	1.11	1.08
A2	5	5	1.08	1.08
A3	6	5	1.09	1.08
A11	4	4	1.06	1.06
A21	4	5	1.06	1.08
A27	4	4	1.06	1.06

9.2 Type A Field Model

Two limitations exist with the monitoring of the type A details. The first limitation is similar to that of the laboratory specimens; the gauge could only be located so close to the toe of the rib-to-deck weld. However, the loading in the field is different. In the field the

loading is applied via a tire pressure. The tire location can also vary, leading to variation in the GAF for the field gauges. The second limitation is the stress state at the type A gauges since only uniaxial strain gauge were used at this detail. In the laboratory, stress was only applied perpendicular to the rib-to-deck weld. In the field, stress exists in the longitudinal direction of the weld due to global bending of the OSPD. The longitudinal stress influences the transverse strain readings. If the transverse direction is defined as the y-axis, and the longitudinal direction is defined as the x-axis, it can be seen in Equation [9.1] that the longitudinal stress effects the strain in the transverse axis. For this case, a stress state adjustment factor (SSAF) is defined in Equation [9.2] to adjust uniaxial Hooke's law stress.

$$\varepsilon_{yy} = \frac{1}{E}\left[\sigma_{yy} - \nu\sigma_{xx}\right] \qquad [9.1]$$

where: σ_{yy} = transverse stress;

σ_{xx} = longitudinal stress.

$$\Psi_{ss} = \frac{\sigma_{yy}}{E\varepsilon_{yy}} \qquad [9.2]$$

where: Ψ_{ss} = stress state adjustment factor.

9.2.1 Geometric Adjustment Factor

A 3-dimensional linear elastic model of the OSPD was constructed using 4-noded shell elements. The finite element program ADINA was used to construct and analyze this model. The OSPD spans between transverse floor beams, a span of 4826 mm, however, the floor beams were not modeled and fixed supports were used at the ends of the panel. The panel was modeled nine stiffening ribs wide, with the edges of the model remaining free. Figure 9.5 shows the meshing of the OSPD. The mesh size used varied from 5 mm at mid-span in the vicinity of the rib-to-deck joint, to 40 mm at the ends of the model. The modulus of elasticity used in the model was 181 GPa.

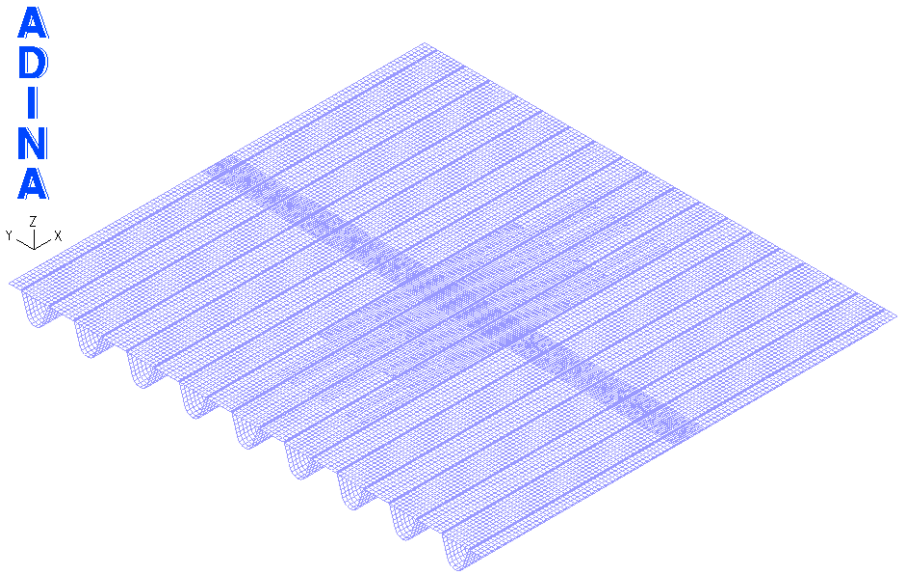

Figure 9.5: OSPD mesh.

A load of 37.6 kN, the rear wheel load from the calibration truck, was applied in the model. Since the loaded truck footprint could not be measured accurately, the load was distributed over the wheel contact area provided in the CHBDC for the CL-625 design truck. The contact area measures 250 mm (in the longitudinal direction of the stiffening ribs) by 600 mm (in the transverse direction). However, the pavement on the bridge provides some load distribution, increasing the loaded area on the OSPD surface. Assuming a load distribution angle of 45 degrees through a 50 mm thick asphalt pavement, the new loaded area becomes 350 mm by 700 mm, resulting in a pressure of 0.153 MPa applied to the OSPD.

Four joints were identified for comparison of the FEM to the static field test results. These joints are shown in Figure 9.6. The tire pressure was centred over rib 5 in the model, and the transverse strains were extracted from the model at these joints. The model strains are compared to the field strains in Table 9.5. Away from the load, at joint 3 and joint 4, the FEM agrees well with the field results. Under the load, at joint 1 and joint 2, it is expected that the FEM does not match as well due to load interaction effects in close proximity to these joints. Further, the 4-noded shell elements used in this analysis can only transfer load through axial force and bending, whereas the actual OSPD can accommodate through thickness shear effects. The very local effects of the weld were not captured by the FEM, including any additional stiffening effect the weld may have. Figure 9.6 shows how the

transverse strain under joint 1 and joint 2 change very rapidly, meaning if the strain gauge is even a few millimetres further away from the weld toe than reported (average reported as 10 mm from weld toe to centre of gauge by KTM) the strain can be largely different. The strain does not change as rapidly around the other joints.

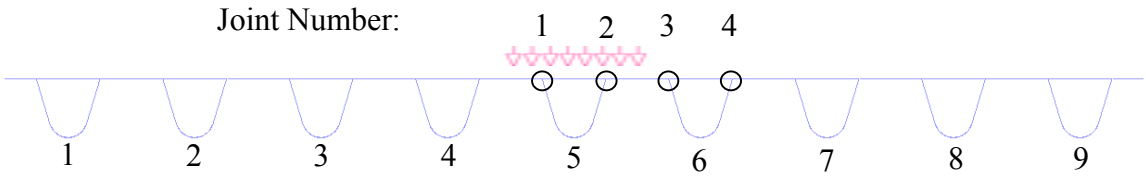

Figure 9.6: Joint and stiffening rib numbering for FEM.

Table 9.5: Comparison of transverse field strains and FEM strains.

Joint Number	Number of Field Readings	Average Field Strain	FEM Strain	Percent Error
		με	με	%
1	16	-127	-197	59
2	16	-127	-197	59
3	17	-142	-156	10
4	17	33	34	3

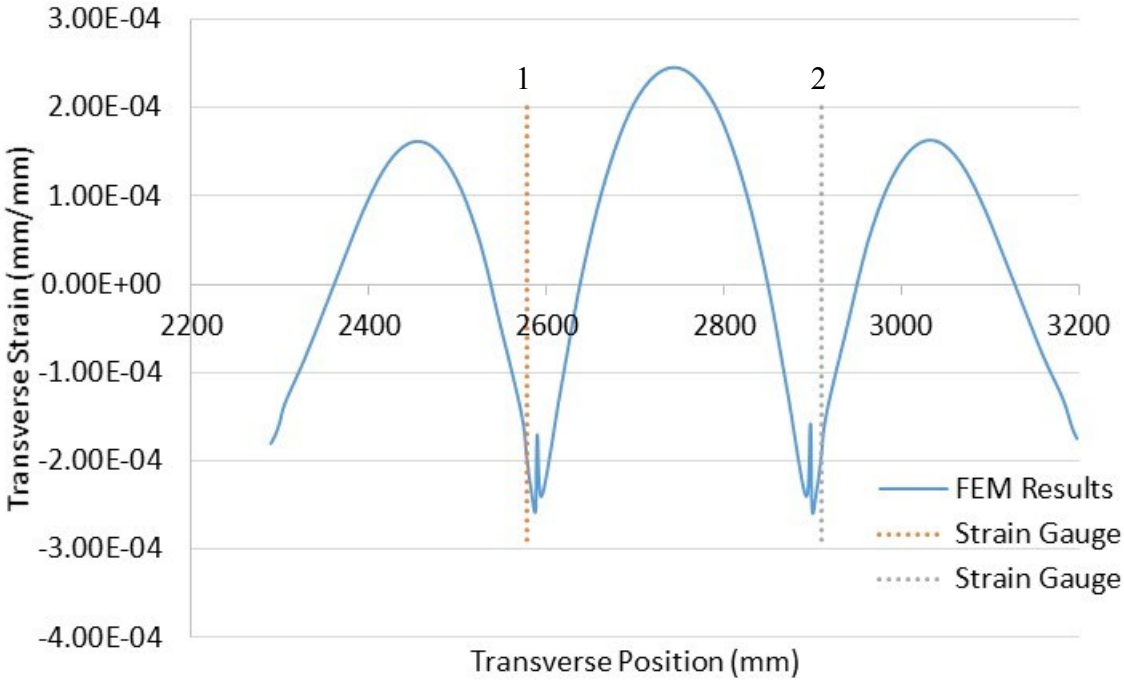

Figure 9.7: Transverse strain on bottom of deck plate for rib 5.

Each of the strain gauges installed for the field monitoring were installed underneath a wheel path; each wheel path is approximately 1200 mm wide. If the load is applied to the centre of the wheel path, each gauge could be represented by a load case, as given in Figure 9.8 through Figure 9.10, and by joint number, given in Figure 9.6.

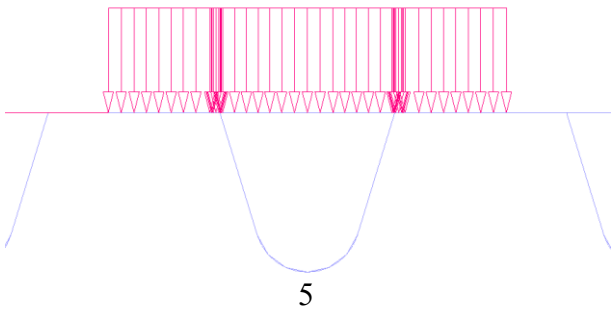

Figure 9.8: Load case 1; pressure centred over stiffening rib 5.

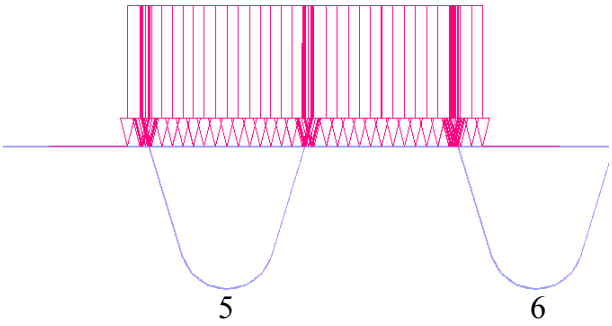

Figure 9.9: Load case 2; pressure centred over joint 1.

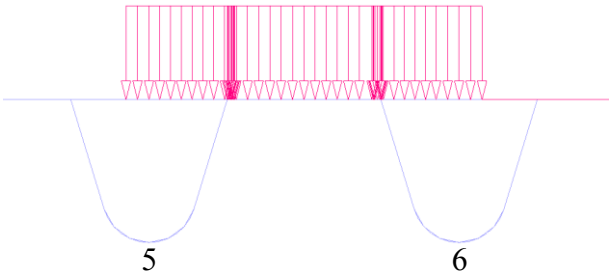

Figure 9.10: Load case 3; pressure centred between rib 4 and rib 5.

From the FEM, the transverse strain was obtained at the gauge location (10 mm away from the weld toe) and at the weld toe. Using these strain values, the GAF was calculated for each of the field gauges as shown in Table 9.6. It is important to note that this is the GAF for the mean position of a truck tire in the wheel path and that variation in the GAF takes place due to variation of the wheel position within the wheel path. To account for this variation, the average GAF and the coefficient of variation for the GAF is calculated based on all gauges.

Table 9.6: GAF for field gauges.

Gauge	Load Case	Joint Number	Strain at Gauge	Strain at Weld Toe	GAF
			με	με	
A-04-1	1	1	-197	-256	1.30
A-04-2	1	1	-197	-256	1.30
A-06-1	3	1	-356	-377	1.06
A-06-2	3	2	-260	-325	1.25
A-10-2	2	1	-72	-93	1.28
A-11-1	2	5	-45	-46	1.02
A-12-1	2	1	-72	-93	1.28
A-12-2	2	2	-275	-342	1.24
A-16-1	2	2	-275	-342	1.24
A-16-2	2	1	-72	-93	1.28
A-18-1	2	1	-72	-93	1.28
A-17-2	2	5	-45	-46	1.02
A-21-1	3	2	-260	-325	1.25
A-21-2	3	1	-356	-377	1.06
A-24-1	1	1	-197	-256	1.30
A-24-2	1	1	-197	-256	1.30
Mean					**1.22**
C.O.V.					**0.0884**

9.2.2 Stress State Adjustment Factor

A 3-dimensional linear elastic grillage model of the OSPD was constructed using beam elements. The deck trusses were modeled using truss elements. The model was created in the finite element software, S-FRAME. Creating a grillage model reduced the amount of modeling required. Section properties for the different members were calculated and input into the model. Figure 9.11 shows the constructed grillage model. A total of five OSPD panels were modeled, with the instrumented OSPD panel located in the middle. The model

is supported on one end by simple supports, as this end is attached to the tower via bearings. The other end remains free. Transverse trusses are spaced at 4.826 m. Hangers are spaced 9.652 m apart and are modeled as springs with an equivalent stiffness. The total length of the model is 48.26 m, with an approximate width of 17.37 m.

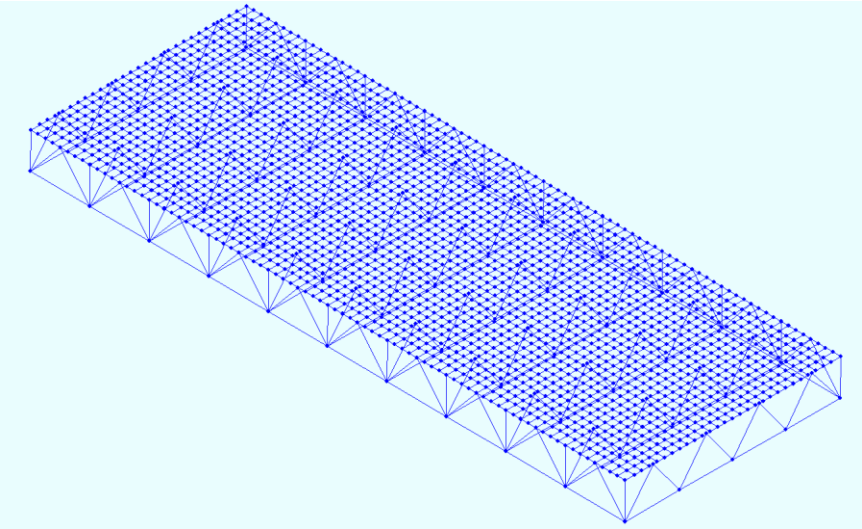

Figure 9.11: Grillage model.

All wheel loads were applied as point loads to the grillage model in each of the 19 static test positions. The load effects from the model were then extracted at the type A gauge locations for any static position with a field strain greater than the threshold of 70 microstrain. Since beam members were used to model all elements of the OSPD, including the stiffening ribs, calculations are required to extract the stress at the gauge location. The longitudinal stress at the gauge was calculated using Equation [9.3] with the section properties given in Table 9.7. The transverse strain is obtained from the field data, which allows the true stress state to be calculated by rearranging Equation [9.1]. The SSAF is then calculated using Equation [9.2]. The results for the SSAF are given in Table 9.8.

$$\sigma_{xx} = \sigma_{xx,a} + \sigma_{xx,b} = \frac{P}{A} + \frac{Mz}{I_{yy}} \qquad [9.3]$$

where: $\sigma_{xx,a}$ = longitudinal axial stress;

$\sigma_{xx,b}$ = longitudinal bending stress;

P = axial load;

A_c = cross sectional area;

M = bending moment;

z = perpendicular distance from neutral axis to stress point;

I_{yy} = moment of inertia about y-axis.

Table 9.7: Section properties used to calculate longitudinal stress.

Area	**Moment of Inertia**	**Distance from Neutral Axis to Stress Point**
mm^2	mm^4	mm
11 846	104.96 x10^6	-53.8

Table 9.8: SSAF results.

Gauge	Static Path	$\sigma_{xx,b}$	$\sigma_{xx,a}$	σ_{xx}	ε_{yy}	σ_{yy}	E × ε_{yy}	SSAF
		MPa	MPa	MPa	με	MPa	MPa	
A-04-1	1	-13.5	-0.5	-14.0	-155	-32.3	-28.1	1.15
A-04-2	1	-13.5	-0.5	-14.0	-140	-29.5	-25.3	1.17
A-04-2	8	-1.2	-0.5	-1.7	-116	-21.6	-21.1	1.02
A-06-1	2	-13.7	-0.3	-14.0	-85	-19.6	-15.4	1.27
A-06-1	8	-1.5	-0.4	-1.9	-145	-26.8	-26.2	1.02
A-06-2	1	-1.5	-0.4	-1.8	-242	-44.4	-43.8	1.01
A-06-2	2	-13.7	-0.3	-14.0	-137	-29.0	-24.8	1.17
A-10-2	3	-13.6	-0.1	-13.7	-115	-24.9	-20.8	1.20
A-10-2	9	-1.4	-0.1	-1.5	-134	-24.7	-24.3	1.02
A-12-1	4	-13.8	-0.1	-13.9	-148	-31.0	-26.9	1.15
A-12-1	9	-1.6	-0.1	-1.7	-160	-29.4	-28.9	1.02
A-12-2	3	-1.5	-0.1	-1.6	-199	-36.4	-35.9	1.01
A-12-2	4	-13.8	-0.1	-13.9	-141	-29.6	-25.5	1.16
A-12-2	5	-1.5	-0.1	-1.6	-86	-16.1	-15.6	1.03
A-12-2	5	-1.5	-0.1	-1.6	-111	-20.5	-20.0	1.02
A-16-1	4	-1.5	-0.1	-1.6	-79	-14.7	-14.2	1.03
A-16-1	4	-1.5	-0.1	-1.6	-98	-18.3	-17.8	1.03
A-16-1	5	-13.8	-0.1	-13.9	-181	-37.0	-32.8	1.13
A-16-1	6	-1.5	-0.1	-1.7	-154	-28.4	-27.9	1.02
A-18-1	6	-13.6	-0.2	-13.8	-193	-39.0	-34.9	1.12
A-18-1	10	-1.5	-0.2	-1.7	-174	-32.0	-31.5	1.02
A-21-1	7	-13.6	-0.4	-14.1	-78	-18.3	-14.1	1.30
A-21-1	10	-1.4	-0.3	-1.7	-140	-25.8	-25.3	1.02
A-21-1	12	-1.6	-0.4	-2.0	-211	-38.7	-38.1	1.02
A-21-2	7	-13.6	-0.4	-14.1	-193	-39.1	-34.9	1.12
A-21-2	11	-1.6	-0.4	-1.9	-115	-21.3	-20.7	1.03
A-24-2	7	-13.5	-0.7	-14.1	-111	-24.3	-20.1	1.21
Mean								**1.09**
C.O.V.								**0.0810**

9.3 Type B Field Monitoring

Similar to the type A detail, the type B detail also contained two limitations in monitoring. The type B detail required both a GAF and a SSAF. The GAF exists because the gauge could only be located so close to the toe of the rib-to-floor beam web weld. However, the GAF for the type B detail does not vary with load position. The GAF for the type B field gauges are much more consistent with the type A laboratory GAF, with the weld subjected to a simple moment.

Due to the global, in-plane behavior of the transverse floor beam, both axial and bending longitudinal stresses are present in the floor beam. These stresses affected the strain reading recorded at the gauges. To accommodate this, a SSAF was used.

An important simplification was made in all modeling for the type B detail. The floor beam was modeled as one continuous section, without the stiffening ribs passing through the floor beam web. All section properties were calculated on a section with no missing material. Further, the actual floor beam on the MacKay Bridge is tapered to accommodate an approximate one percent slope from the centre of the bridge to the edge of the deck. In modeling, the average depth of floor beam was used, approximately 490 mm. The maximum depth is 533 mm, and the minimum depth is 447 mm.

9.3.1 Geometric Adjustment Factor

The behavior of this joint is very similar to the type A laboratory loading situation, with a linear moment through the web height. Figure 9.12 shows the loading, with Figure 9.13 showing the stress observed in the floor beam web. Instead of constructing a new model, the type A laboratory results were be used, with a distance from the centre of the gauge to the weld toe of 10 mm. The resulting average GAF is 1.17. To represent the variability in placement of the gauge, a coefficient of variation of 0.4 is used, obtained from the laboratory results.

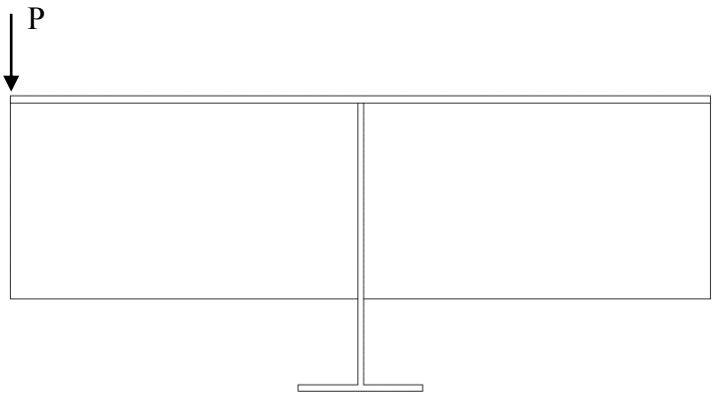

Figure 9.12: Type B loading in field.

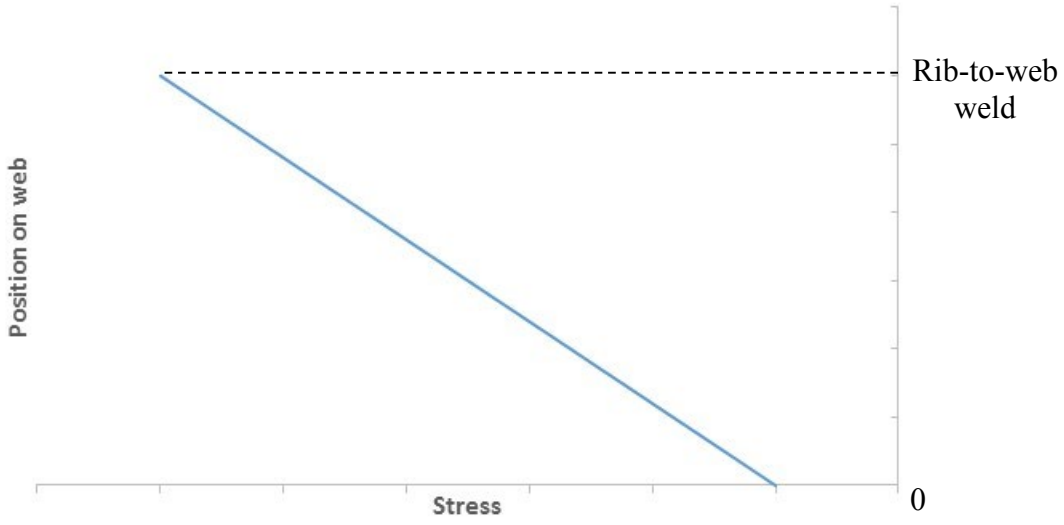

Figure 9.13: Linear pattern of stress along web, below rib-to-web weld.

9.3.2 Effective Width of Deck Plate

Before completing the analysis for the SSAF, the section properties for the floor beam was needed. Since the top flange of the floor beam is formed by the deck plate, an effective width required calculation. A simple linear elastic model was constructed of the floor beams and deck plate using shell elements in S-FRAME, as shown in Figure 9.14. Each deck shell element is 603.25 mm wide and 9.525 mm thick. Vertical point loads, 10 kN in magnitude, were placed at each joint directly above the middle floor beam.

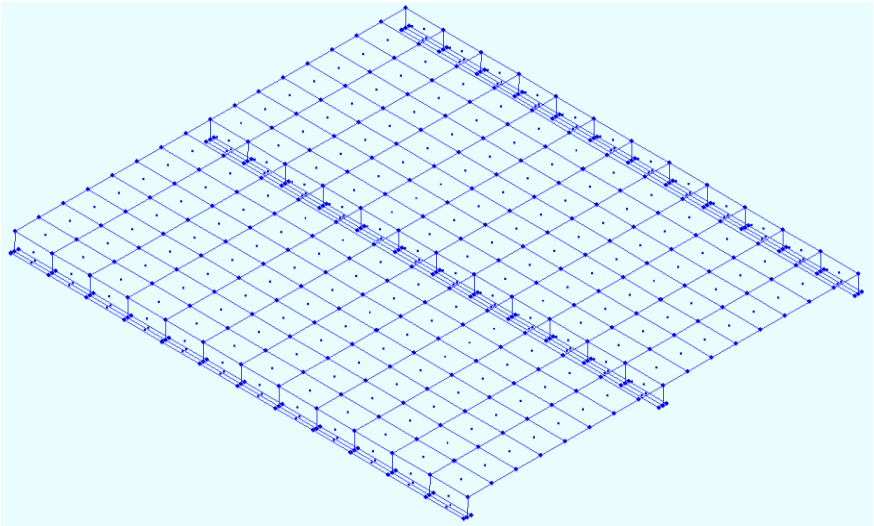

Figure 9.14: Effective width model.

In determining the effective width, the stress at the mid-plane of the deck plate was taken at mid-span of the floor beam and is given in Table 9.9. The resultant force was then calculated. To determine the effective width, Equation [9.4] was used and gives a value of 4537 mm.

Table 9.9: Effective width calculation for half of deck.

Shell	Stress	Force
	MPa	N
1	-0.51	-2908
2	-1.46	-8405
3	-2.56	-14732
4	-3.81	-21897
5	-5.22	-29970
6	-6.79	-39007
7	-8.54	-49050
8	-10.46	-60123

$$w_{eff} = \frac{\sum_{i=1}^{8} F_i}{S_{max} t} \quad [9.4]$$

where: w_{eff} = effective width;

F_i = force in shell i;

S_{max} = maximum magnitude stress in any shell;

t = deck plate thickness.

9.3.3 Stress State Adjustment Factor

In determining the SSAF, the grillage from Section 9.2.2 was used. Since the floor beam is bolted to the top chord of the transverse stiffening truss (see Figure 9.15), it was assumed composite action is not achieved and each member takes load based on their respective section properties; the longitudinal moment is distributed based on moment of inertia, and the axial load is based on gross cross sectional area. The floor beam and top chord are shown together in Figure 9.15, with cross section properties given in Table 9.10.

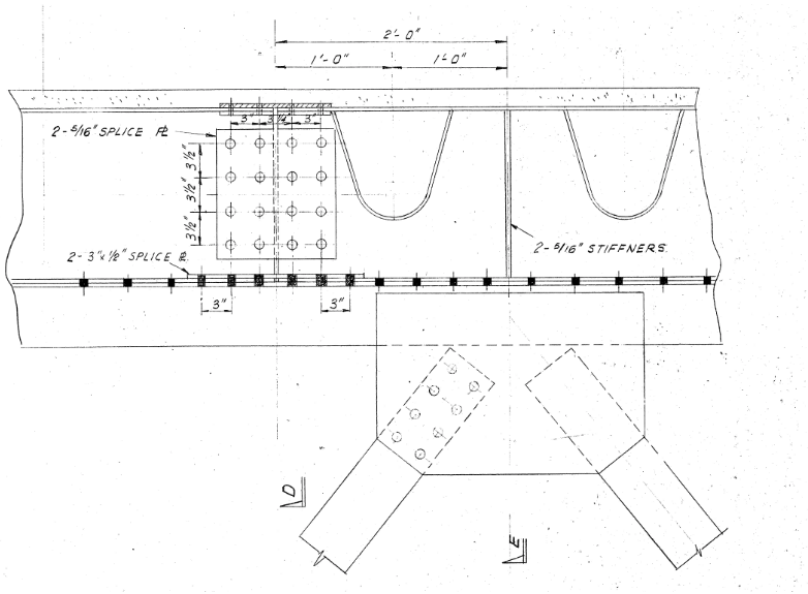

Figure 9.15: Floor beam connected to top chord of truss (courtesy of B&T).

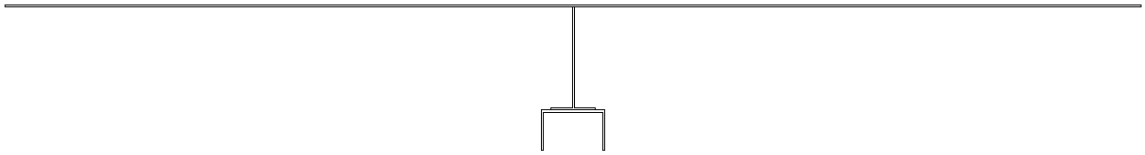

Figure 9.16: Floor beam with effective width and top truss chord.

Table 9.10: Section properties for floor beam and top chord.

Section	Moment of Inertia	Area
	mm^4	mm^2
Floor beam	616×10^6	48646
Top Chord	14.3×10^6	5323
Total	630×10^6	53969

The type B SSAF calculation proceeded similar to the type A SSAF, except requiring the extra step of splitting the total top chord moment and axial force values according to the percentage of the total moment of inertia and area respectively. The resulting statistical parameters for the SSAF are given in Table 9.11.

Table 9.11: Statistics for type B SSAF.

Statistical Parameter	Value
Mean	1.00
Coefficient of Variation	0.111
Number of Points	32

Chapter 10: Summary of Results

This chapter summarizes the analysis completed thus far before proceeding to the fatigue reliability analysis. Figure 10.1 gives a summary of the contributions of each research component.

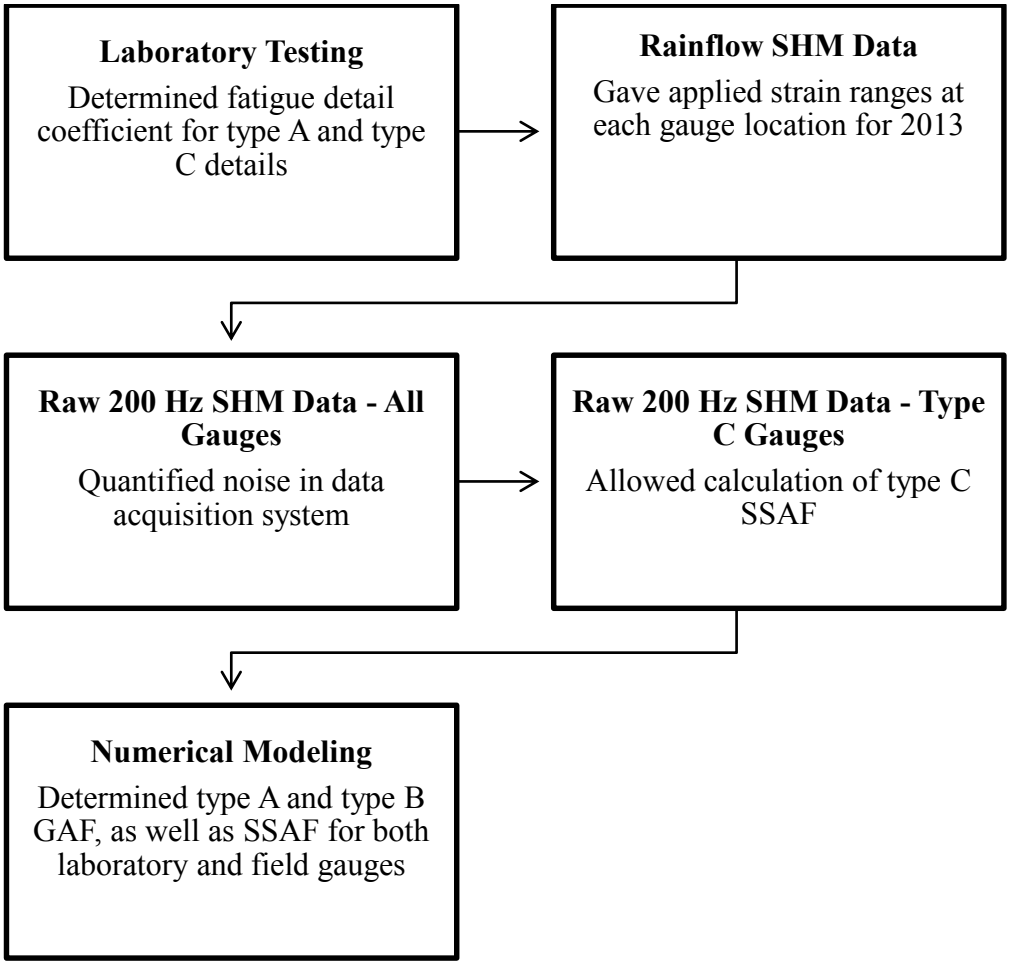

Figure 10.1: Flowchart of research components.

10.1 Fatigue Detail Coefficient

The laboratory testing component of this research determined the fatigue detail coefficient for the type A detail, as well as a corroded and non-corroded category for the type C detail. The type B detail was not tested so the CHBDC category C fatigue detail was used. Table 10.1 summarizes the statistics for each gauge type.

Table 10.1: Summary of statistics for fatigue detail coefficient.

Detail	μ_{logA}	σ_{logA}	μ_{lnA}	σ_{lnA}
Type A	12.9	0.602	29.8	1.39
Type B – CHBDC Category C	12.5	0.150	28.7	0.346
Type C – Non-corroded	12.8	0.269	29.6	0.620
Type C – Corroded	12.5	0.365	28.7	0.841

10.2 Adjustment Factor

Two different adjustment factors have been determined in this research. The first adjustment factor, the GAF, adjusts the strain readings at the strain gauge location to give the strain at the toe of the weld. The second adjustment factor, the SSAF, adjusts the Hooke's law stress calculation since a state of uniaxial stress does not exist. The GAF applies to the type A and type B fatigue details, and the SSAF applies to all three fatigue details. The GAF is summarized in Table 10.2 and the SSAF is given in Table 10.3 and Table 10.4.

Table 10.2: GAF summary.

Gauge	Mean	Coefficient of Variation
Type A	1.22	0.0884
Type B	1.17	0.400

Table 10.3: SSAF summary for type A and type B details.

Gauge	Mean	Coefficient of Variation
Type A	1.09	0.0810
Type B	1.00	0.111

Table 10.4: SSAF summary for type C gauges.

Gauge	Mean	Coefficient of Variation
C-04-1	1.44	0.298
C-04-4	1.68	0.286
C-06-1	1.86	0.149
C-06-4	1.73	0.300
C-10-1	1.73	0.300
C-10-4	1.73	0.300
C-12-4	1.75	0.178
C-16-1	1.50	0.193
C-18-4	1.99	0.185
C-21-1	1.69	0.128
C-21-4	1.91	0.119
C-24-1	1.76	0.207
C-24-4	1.73	0.300

10.3 Field Strain

Statistics were calculated at all gauge locations, excluding those mentioned in Table 8.7. A sample from each gauge type along stiffening rib 21 is given in Table 10.5.

Table 10.5: Sample of field gauge statistics.

Gauge	Number of cycles	Mean	Coefficient of Variation
		με	
A-21-2	1 700 825	132	0.479
B-21-2	615 802	122	0.396
C-21-4	757 225	119	0.340

10.4 Field Strain Noise

Noise in the data acquisition system was captured and the statistics were completed on each

gauge. The noise was found to be centred about zero, with different standard deviations for each gauge. To describe the noise on each of the fatigue detail type, a mean of zero was used. Standard deviations were assigned by gauge type. Table 10.6 gives a summary of the noise data.

Table 10.6: Noise statistics for each gauge type.

Detail	Mean	Standard Deviation
	με	με
Type A	0	6
Type B	0	4
Type C	0	5

Chapter 11:Fatigue Reliability Analysis

This chapter discusses how the data in the preceding chapters was combined to determine the reliability of the OSPD on the MacKay Bridge. In order to calculate the reliability of the entire OSPD, the reliability of each individual component must be found.

11.1 Limit State Equation

Equation [11.1] defines the failure boundary for an individual component.

$$g(\Delta, \Psi, A, \varepsilon_m, \varepsilon_n) = \Delta - \frac{N(\Psi_g \Psi_{ss} E F_s(\varepsilon_m + \varepsilon_n))^m}{A} \qquad [11.1]$$

where: N = total cumulative number of cycles;

Ψ_g = geometric adjustment factor;

F_s = shunt calibration factor;

ε_m = measured field strain;

ε_n = field strain noise.

Failure occurs when the limit state equation is less than zero. Several methods for calculating the reliability index have been detailed in Section 2.4.2.1. Since data was available for the parameters in Equation [11.1], the Rackwitz-Fiessler procedure was used in the analysis to give a more accurate prediction for component reliability.

11.2 Probability Distributions for Variables

For each variable in the limit state equation, a probability distribution was needed. Probability distributions were determined through analysis of data collected during this research, by using results from previously completed and accepted research, or by reasonable assumptions. The distribution used for each variable is detailed below.

11.2.1 Miner's Damage Accumulation Index

Research completed by Wirsching (1984) states a lognormal distribution provides a good fit to model Miner's damage accumulation index. Wirsching (1998) compares fatigue test results and determines the amount of damage accumulated at failure. Significant variation

is observed in the results. Table 11.1 shows a summary of the test results on welded details. For the reliability analysis of the OSPD, the mean was taken as 1.0 with a coefficient of variation of 0.30. These values are the same taken by Kwon and Frangopol (2010) in a fatigue reliability assessment of two different tied-arch bridges, the Neville Island Bridge and the Birmingham Bridge.

Table 11.1: Welded joint statistics for Miner's damage accumulation index (Wirching, 1998).

Source	Median	Coefficient of Variation
Schilling et al. (1978)	1.15	0.48
Berge & Eide (1981)	1.06	0.40
Eidi & Berge (1984)	0.78	0.19
Gurney (1979)	0.85	0.28
Wirsching (1984)	1.0	0.30

11.2.2 Adjustment Factor

An adjustment factor is used in all three fatigue detail types. The value of the adjustment factor, and even what the adjustment factor adjusts for varies between the detail types.

As previously shown in Section 8.2, the type C adjustment factor follows a normal distribution. The statistics used in the reliability analysis are given in Table 8.5 and Table 8.6.

For the type A and type B fatigue details, two adjustment factors exist; the SSAF and the GAF. No field data could be obtained for the SSAF so it was assumed that the SSAF follows a normal distribution, similar to the type C detail, defined by the mean and coefficient of variation given in Table 10.3. As for the geometric adjustment factor, each distance from the centre of the gauge to the toe of the weld would be needed to perform a distribution analysis on the field gauges. Since this data is not available, the GAF was assumed to follow a normal distribution defined by the mean and coefficient of variation given in Table 10.2.

11.2.3 Measured Field Strain

A distribution identification for the field strains obtained from gauge C-21-4 was completed using MiniTab, however, no distribution fit the data sufficiently. Kwon and Frangopol (2010) performed goodness-of-fit tests for fatigue monitoring data, comparing the lognormal distribution, the Weibull distribution, and the Gamma distribution. Upon completing their analysis, the lognormal distribution provided the best fit. Therefore, the lognormal distribution was used in the analysis of the 2013 field data. A comparison between the two-parameter and three-parameter lognormal distributions was performed, as shown in Figure 11.1. The three-parameter function contained an additional parameter called the cut-off threshold. It was thought this might be appropriate since a cut-off threshold was used in the datalogger rainflow program. However, when the two-parameter and three-parameter lognormal distributions were compared, the two-parameter distribution better fit the large loading event. Therefore, the two-parameter lognormal distribution was used in the reliability analysis.

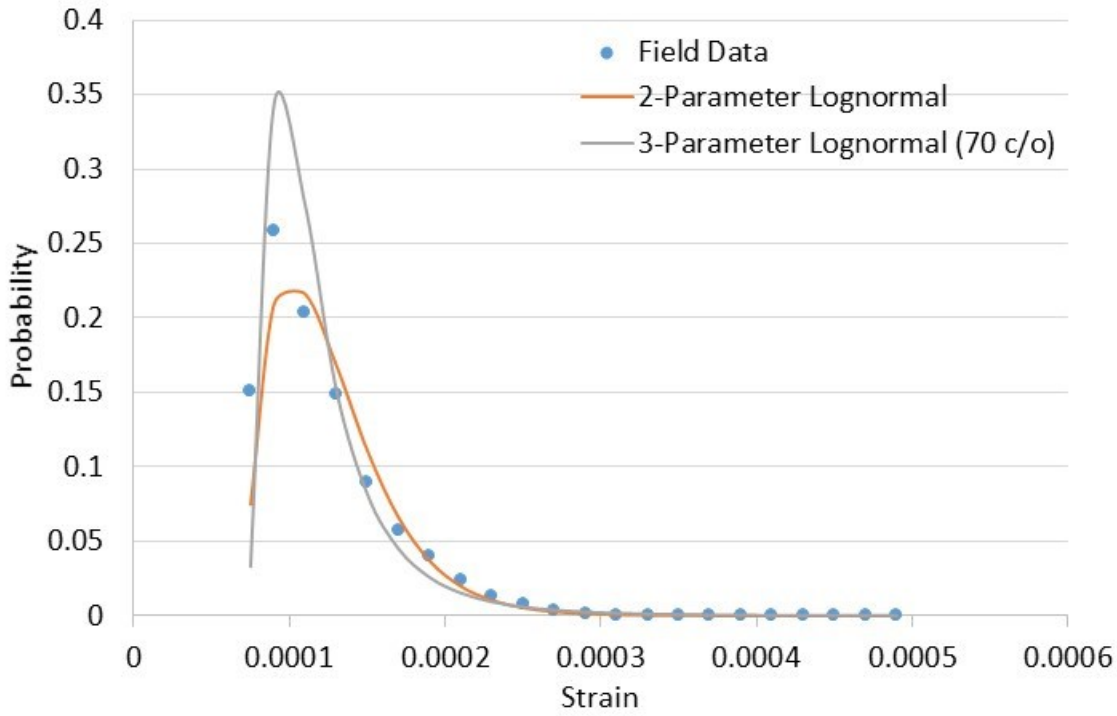

Figure 11.1: Comparison of two-parameter and three-parameter lognormal PDF for field strains on gauge C-21-4.

To obtain the lognormal statistics used in the lognormal PDF, Equation [11.2] and Equation [11.3] were used. The resulting statistics for gauge C-21-4 are presented in Table 11.2. Statistics for all other gauges are presented in Appendix E.

$$m_{\ln(\varepsilon_m)} = \ln\left(m_{\varepsilon_m}\right) - \frac{1}{2}{\sigma_{\ln(\varepsilon_m)}}^2 \qquad [11.2]$$

where: $m_{\ln(\varepsilon_m)}$ = mean of natural logarithm of measured strain;

$\sigma_{\ln(\varepsilon_m)}$ = standard deviation of natural logarithm of measured strain.

$$\sigma_{\ln(\varepsilon_m)} = \sqrt{\ln(1 + \left(\frac{\sigma_{\varepsilon_m}}{m_{\varepsilon_m}}\right)^2)} \qquad [11.3]$$

Table 11.2: Statistics for C-21-4.

Gauge	m_{ε_m}	σ_{ε_m}	$m_{\ln(\varepsilon_m)}$	$\sigma_{\ln(\varepsilon_m)}$
	με	με		
C-21-4	119	40	-9.09	0.331

11.2.4 Strain Noise

As previously analyzed in Section 8.3, the noise was found to be centred about zero, with the standard deviation varying for each gauge. A distribution identification was performed on several gauges using MiniTab, but the noise did not follow any distribution. It was decided to assume a normal distribution to account for the noise. According to the central limit theorem, if a large enough number of data points are collected, the distribution will approach the normal distribution.

11.2.5 Fatigue Detail Coefficient

The laboratory testing component of this research did not contain a large enough sample of data to obtain a distribution for the fatigue detail coefficient. However, a large database exists for thousands of fatigue samples that have undergone testing. Fisher et al. (1970)

performed a large number of these tests, concluding that the logarithmic transformation of the fatigue detail coefficient resulted in a normal distribution at almost every stress level used in the testing program. It is further supported in recent research by Wirsching (1998), Li et al. (2003), and Fisher and Roy (2011). Therefore, a lognormal distribution was used for the fatigue detail coefficient. The statistics for each fatigue detail type is given in Table 10.1.

11.2.6 Constants

Multiple parameters were treated as constants in the reliability analysis. These include the modulus of elasticity, the shunt calibration factor, the fatigue strength exponent, and the traffic growth rate.

The modulus of elasticity testing presented in Appendix C contains five specimens, which makes it difficult to define an accurate probability distribution. Therefore, the mean value of 181 GPa was taken and used as a constant in the reliability analysis.

The shunt calibration factor is a correction applied to the field strain readings. The factor was determined through a shunt calibration procedure detailed in Appendix A, and each gauge has a specific factor used in the analysis.

A large amount of research has been conducted on the fatigue of welded joints, and through such research, it was determined that the fatigue strength exponent is a constant value of 3.0 (Keating & Fisher., 1986). The CHBDC also uses a value of 3.0.

Information contained in the report by HHB (2010) allowed an estimation of a traffic growth rate (α) of two percent per year.

11.2.7 Deterministic Parameters

The number of cycles was classified as a deterministic parameter. Kwon and Frangopol (2010) give an equation to estimate the accumulated number of cycles using the recorded number of cycles and a traffic growth rate. Equation [11.4] gives the estimate of cycles, however, for the SHM on the MacKay Bridge, the data was taken during the year 2013. The laboratory specimens, which ultimately give the resistance, were removed from the bridge in 2010. Equation [11.4] thus needs to accommodate the difference in dates,

therefore Equation [11.5] is substituted into Equation [11.4]. The resulting Equation [11.6] is used to obtain the cumulative cycles on a gauge.

$$N = N_{2010}\frac{(1+\alpha)^{Y-2010}-1}{\ln(1+\alpha)} \quad [11.4]$$

where: N = total cumulative number of cycles;

N_{2010} = number of cycles for year 2010;

α = traffic growth rate per year;

Y = year reliability analysis is being calculated.

$$N_{2010} = \frac{N_{2013}}{(1+\alpha)^3} \quad [11.5]$$

where: N_{2013} = number of cycles recorded for year 2013.

$$N = \left(\frac{N_{2013}}{(1+\alpha)^3}\right)\frac{(1+\alpha)^{Y-2010}-1}{\ln(1+\alpha)} \quad [11.6]$$

11.2.8 Summary

This section provides a helpful summary of the different variables and constants present in the analysis. Table 11.3 shows the variables and constants, as well as deterministic inputs.

Table 11.3: Summary of variables and constants for reliability analysis.

Parameter	Notation	Type	Distribution
Miner's damage accumulation index	Δ	Variable	Lognormal
Number of cycles	N	Deterministic	-
Geometric adjustment factor	Ψ_g	Variable	Normal
Stress state adjustment factor	Ψ_{ss}	Variable	Normal
Modulus of elasticity	E	Constant	-
Shunt calibration factor	F_s	Constant	-
Measured field strain	ε_m	Variable	Lognormal
Field strain noise	ε_n	Variable	Normal
Fatigue strength exponent	m	Constant	-
Fatigue detail coefficient	A	Variable	Lognormal

11.3 Calculation of Reliability Index

The reliability index is calculated for each individual gauge used in the analysis. Gauges excluded from the analysis are documented in Section 8.4. The Rackwitz-Fiessler procedure is used to calculate the reliability index. The calculation takes several steps:

1. Formulate the limit state function and determine probability distributions and associated parameters for all random variables X_i, where $i = 1, 2, \dots, n$.
2. Obtain an initial design point $\{x_i^*\}$ by assuming values for $n - 1$ variables of the random variables X_i. Solve limit state function for $g = 0$ for the remaining random variable.
3. For each non-normal distribution, determine the equivalent normal mean $\mu_{X_i}^e$ and standard deviation $\sigma_{X_i}^e$ using Equation [11.7] and Equation [11.8], which simplify to Equation [11.9] and Equation [11.10] for lognormal variables. For a normal distribution, the equivalent normal parameters are the actual parameters; no adjustment is needed.

$$\mu_X^e = x^* - \sigma_X^e\left[\Phi^{-1}\left(F_X(x^*)\right)\right] \qquad [11.7]$$

where: μ_X^e = equivalent normal mean;

x^* = design point;

σ_X^e = equivalent normal standard deviation;

F_X = cumulative distribution function of X.

$$\sigma_X^e = \frac{1}{f_X(x^*)}\phi\left[\Phi^{-1}\left(F_X(x^*)\right)\right] \quad [11.8]$$

where: ϕ = probability distribution function for standard normal distribution;

f_X = probability distribution function of X.

$$\mu_X^e = x^*[1 - \ln(x^*) + \mu_{\ln X}] \quad [11.9]$$

$$\sigma_X^e = x^*\sigma_{\ln X} \quad [11.10]$$

where: $\mu_{\ln X}$ = mean of $\ln(X)$;

$\sigma_{\ln X}$ = standard deviation of $\ln(X)$.

4. Determine the reduced variables $\{z_i^*\}$ corresponding to the design point $\{x_i^*\}$ using Equation [11.11].

$$z_i^* = \frac{x_i^* - \mu_X^e}{\sigma_X^e} \quad [11.11]$$

where: z_i^* = reduced variable i.

5. Determine the partial derivatives of the limit state function with respect to the reduced variables, using Equation [11.12], and create a column vector using Equation [11.13] and Equation [11.14].

$$\frac{\partial g}{\partial Z_i} = \frac{\partial g}{\partial X_i}\sigma_{X_i} \quad [11.12]$$

$$G_i = -\frac{\partial g}{\partial Z_i}\Big|_{evaluated\ at\ design\ point} \quad [11.13]$$

where: G_i = component i of limit state partial derivative column vector.

$$\{G\} = \begin{Bmatrix} G_1 \\ G_2 \\ \vdots \\ G_n \end{Bmatrix} \quad [11.14]$$

6. Calculate an estimated reliability index using Equation [11.15].

$$\beta = \frac{\{G\}^T\{z^*\}}{\sqrt{\{G\}^T\{G\}}} \quad [11.15]$$

$$\{z^*\} = \begin{Bmatrix} z_1^* \\ z_2^* \\ \vdots \\ z_n^* \end{Bmatrix} \quad [11.16]$$

7. Calculate a column vector, according to Equation [11.17], which contains the sensitivity factors for each variable.

$$\{\alpha\} = \frac{\{G\}}{\sqrt{\{G\}^T\{G\}}} \quad [11.17]$$

where: $\{\alpha\}$ = sensitivity vector.

8. Determine a new design point for $n-1$ of the reduced variables using Equation [11.18].

$$z_i^* = \alpha_i \beta \qquad [11.18]$$

9. Determine the corresponding design point values in original coordinates for $n-1$ variables using Equation [11.19].

$$x_i^* = \mu_{X_i}^e + z_i^* \sigma_{X_i}^e \qquad [11.19]$$

10. Determine the value of the remaining random variable by solving the limit state function for $g = 0$.
11. Repeats steps 3-10 until β and the design point $\{x_i^*\}$ converge.

A flowchart can be seen in Figure 11.2 which shows the steps for calculating the individual component reliability index using the Rackwitz-Fiessler procedure.

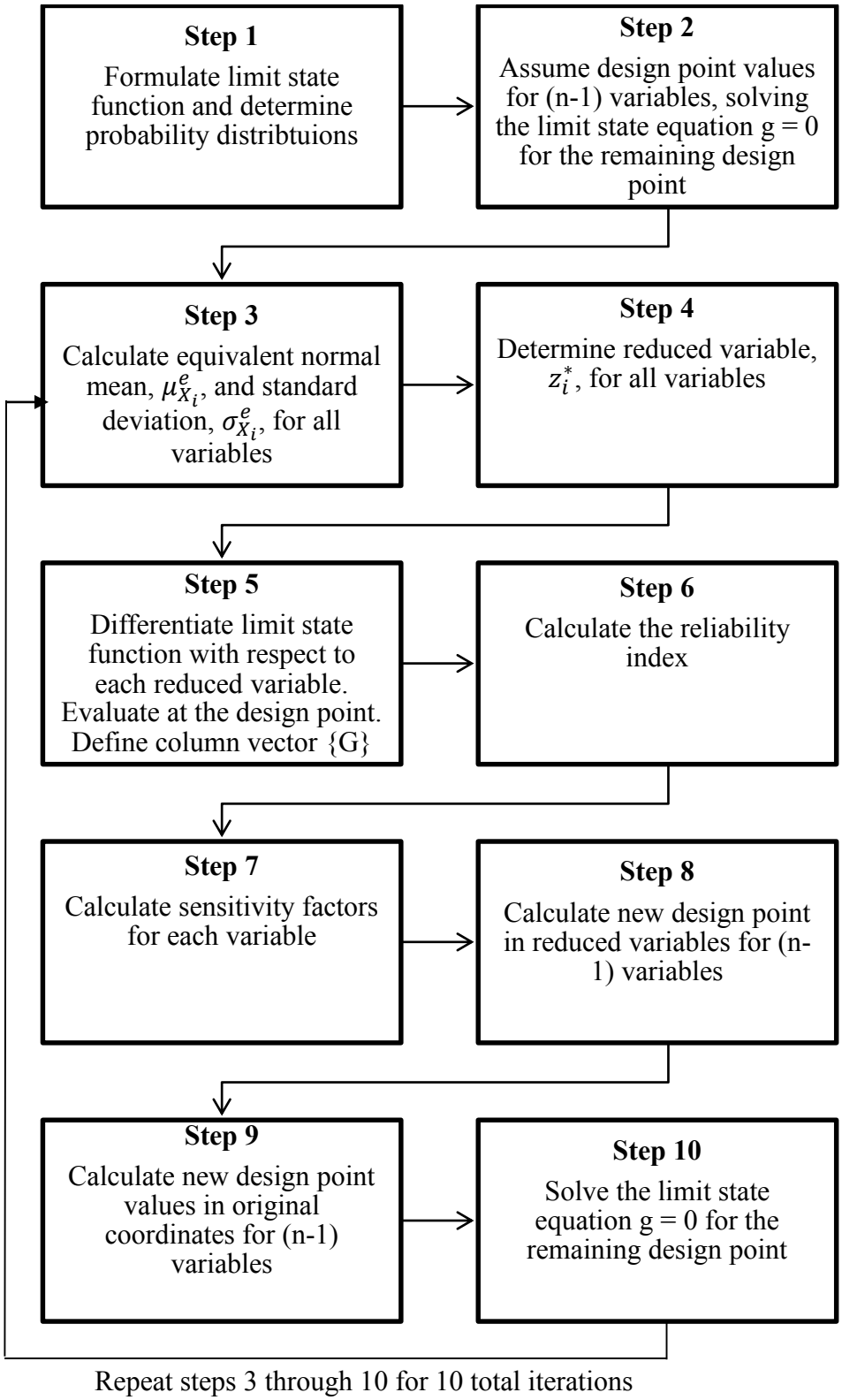

Figure 11.2: Flowchart for Rackowitz-Fiessler procedure using the modified matrix procedure.

11.3.1 Sample Calculation of Reliability Index

To illustrate the Rackwitz-Fiessler procedure, the reliability analysis was performed on gauge C-21-4 for the year 2024. During 2013, C-21-4 recorded 757 225 strain cycles. Applying Equation [11.6] gives 732 275 cycles in 2010. The cumulative cycles at gauge C-21-4 is 11 813 901 in 2024. The shunt calibration factor for gauge C-21-4 is 1.002.

For the type C analysis, a GAF was not necessary and therefore was not included. Miner's damage accumulation index was the variable solved by assuming $g = 0$ after assuming values for the other variables. The results for the first iteration, steps 1 through 4 are shown in Table 11.4.

Table 11.4: First iteration for C-21-4, steps 1 through 4.

Parameter	i	x_i^*	$\mu_{X_i}^e$	$\sigma_{X_i}^e$	z_i^*
Δ	1	0.51	0.83	0.15	-5.09
Ψ_g	2	-	-	-	-
Ψ_{ss}	3	1.5	1.91	0.23	-1.78
ε_m	4	100 x10^{-6}	112 x10^{-6}	33 x10^{-6}	-0.37
ε_n	5	1 x10^{-6}	0	6 x10^{-6}	0.17
A	6	9.0 x10^{12}	6.7 x10^{12}	5.6 x10^{12}	0.41

Steps 5 through 10 were calculated and summarized in Table 11.5. The resulting reliability index was 1.68. A total of 10 iterations were completed with the reliability index converging at 1.80. Ten iterations was standard for all reliability calculations to ensure convergence of the reliability index.

Table 11.5: First iteration for C-21-4, steps 5 through 10.

Parameter	i	G_i	α_i	New z_i^*	New x_i^*
Δ	1	-0.008	-0.23	-	1.00
Ψ_g	2	-	-	-	-
Ψ_{ss}	3	0.013	0.36	0.60	2.05
ε_m	4	0.026	0.76	1.27	154 x10^{-6}
ε_n	5	0.005	0.14	0.23	1 x10^{-6}
A	6	-0.017	-0.48	-0.81	2.24 x10^{12}

11.4 Sensitivity Analysis

A sensitivity analysis was performed for the C-21-4 gauge to determine the impact of the different parameters in the analysis. The base case for all variables used in the analysis is given in Table 11.6. The non-corroded results for the fatigue detail coefficient were used in the sensitivity study as the base case.

Table 11.6: Base case parameters.

Parameter	i	Units	Mean/Constant	Standard Deviation
Δ	1	-	1.00	0.30
Ψ_g	2	-	-	-
Ψ_{ss}	3	-	1.91	0.23
ε_m	4	mm/mm	119 x10^{-6}	40 x10^{-6}
ε_n	5	mm/mm	0 x10^{-6}	6 x10^{-6}
A	6	MPa^3	8.48 x10^{12}	5.80 x10^{12}
E	-	GPa	181	-
m	-	-	3.0	-

Each variable was varied individually through a representative range of possible values, as given in Table 11.7, while all other variables remained constant. Either the mean or standard deviation were varied at one time; not both. The range of variables came from collected field data, laboratory data, and previous research completed by Fisher et al. (1970), Keating and Fisher (1986), Wirsching (1998), and Bowman et al. (2012). In order

to accommodate comparison between different variables on the same figure, the percent difference from the base case was calculated and plotted for each calculation. Equation [11.20] details the calculation of percent difference used in the sensitivity analysis. The results from the sensitivity analysis are shown in Figure 11.3 through Figure 11.5.

Table 11.7: Range of variables and constants.

Parameter	i	Units	Mean/Constant Range	Standard Deviation Range
Δ	1	-	0.4 – 1.2	0.30
Ψ_g	2	-	-	-
Ψ_{ss}	3	-	1.4 – 2.0	0.23
ε_m	4	mm/mm x10^{-6}	90 – 130	20 – 50
ε_n	5	mm/mm x10^{-6}	-	2 – 12
A	6	MPa^3 x10^{12}	2 – 20	0.10 – 10
E	-	GPa	150 – 225	-
m	-	-	2.0 – 4.0	-

$$Percent\ difference = \frac{c - d}{d} \qquad [11.20]$$

where: c = new value for variable or constant;

d = base case value for variable or constant.

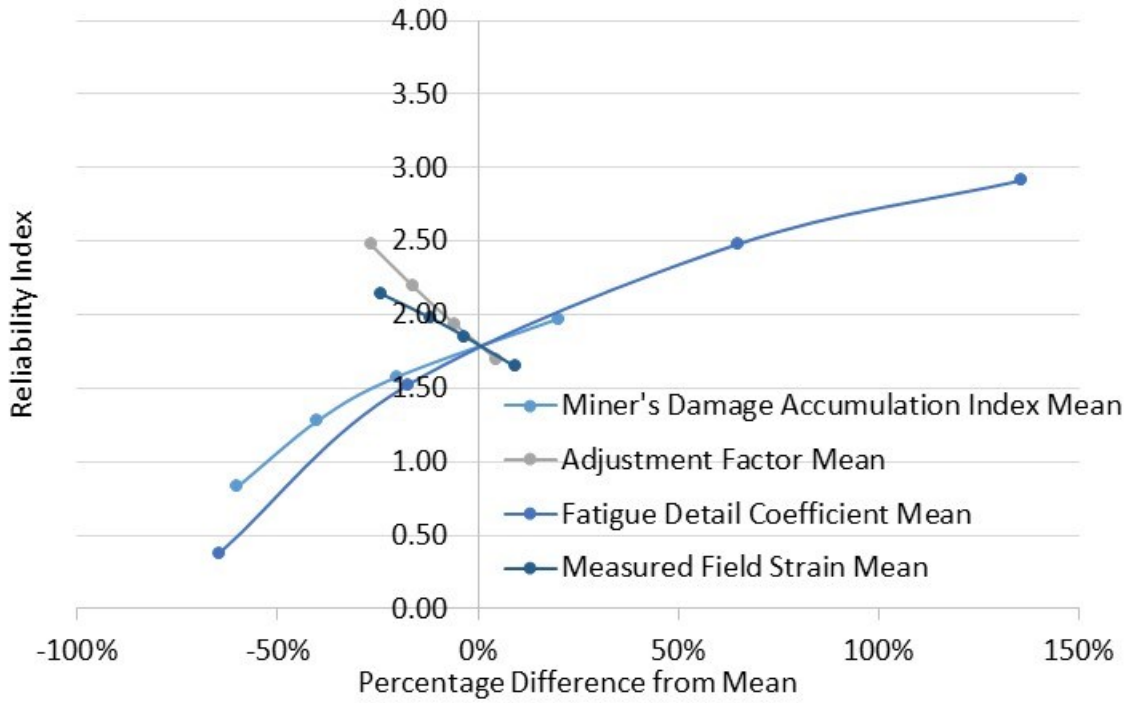

Figure 11.3: Sensitivity to changes in mean values.

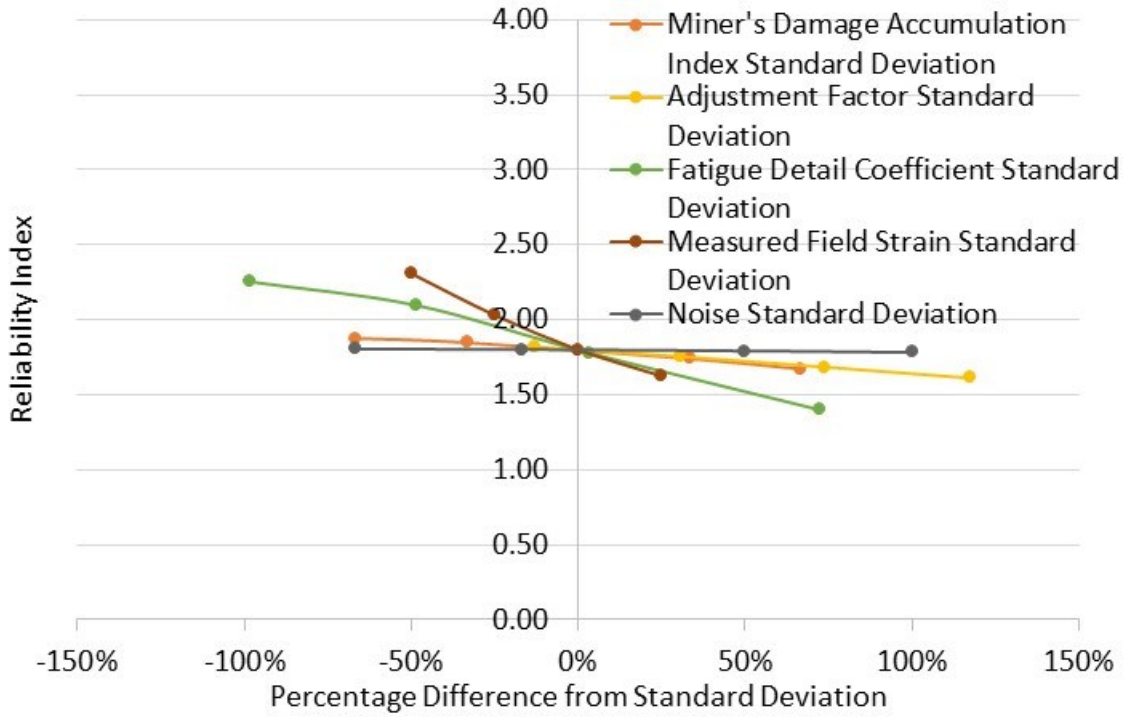

Figure 11.4: Sensitivity to changes in standard deviation values.

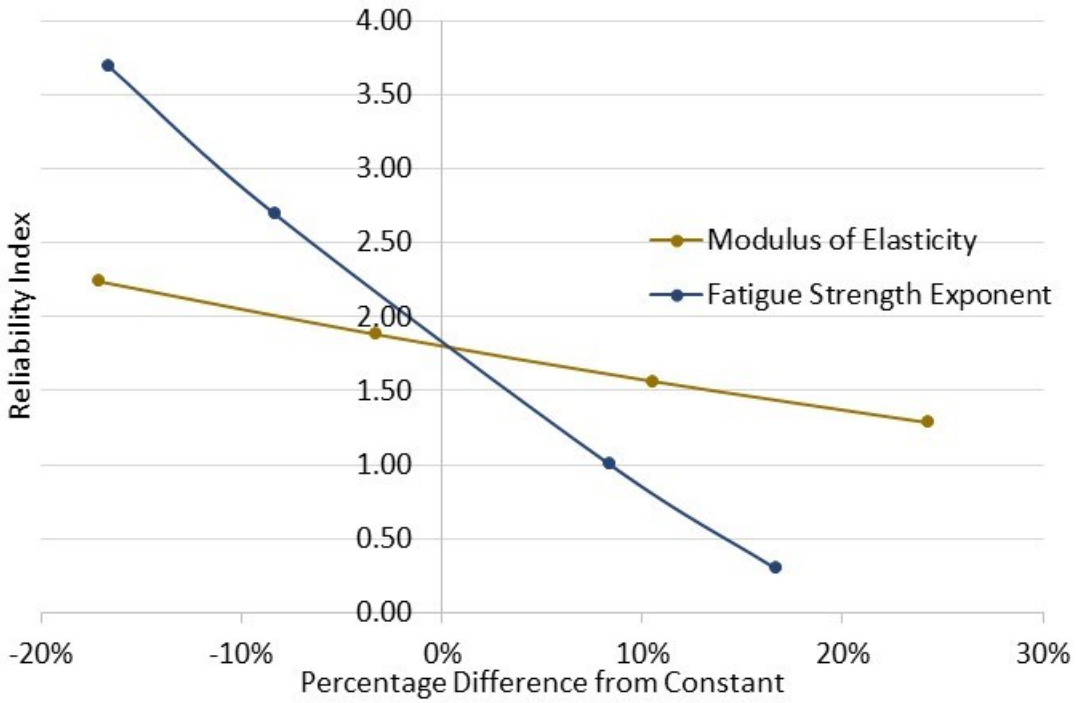

Figure 11.5: Sensitivity to changes in constants.

Some general conclusions can be drawn from the sensitivity analysis. The mean of the input parameters has a larger impact on the reliability index than the standard deviation. It is therefore more important to have a better estimate of the mean in the reliability analysis. Further, the fatigue detail coefficient can vary over a large range of means, which is a reason why it is the largest factor in the reliability calculation, showing the greatest variation in reliability indices. Additionally, the noise observed in the field strain readings has a very minimal impact on the reliability index. One could argue that excluding noise would not affect the reliability analysis. Lastly, the fatigue strength exponent plays a significant role in the reliability calculation. A small change in the fatigue strength exponent results in a large different in reliability index. However, the value of 3.0 used is based on thousands of fatigue tests on different details.

11.5 Reliability over Time

The reliability index was calculated for one gauge location for each fatigue detail from 2012 to 2030. The type A detail used the A-21-2 gauge location, with the resulting reliability plot shown in Figure 11.6. The type B detail used the B-21-2 gauge location.

Since no laboratory results are available for the type B detail, the fatigue detail coefficient was modeled using the category C fatigue detail from the CHBDC. The plot of reliability index over time is given in Figure 11.7. Finally, for the type C detail, a comparison was made since specimens were grouped into two groups, corroded and non-corroded. To compare the impact the corroded specimens had on the reliability, the reliability index was calculated for both the corroded and non-corroded laboratory results from 2012 to 2030 for the C-21-4 gauge location. The CHBDC category C detail was also included for comparison. The reliability over time is shown in Figure 11.8. Appendix G gives the reliability over time for all gauges used in the analysis.

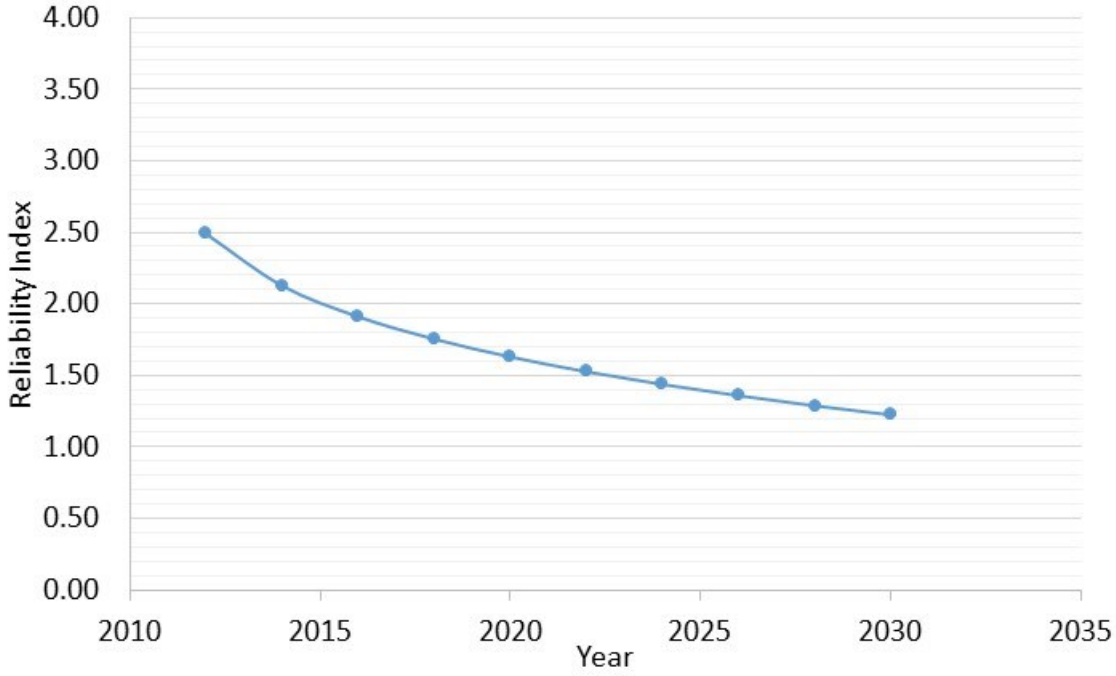

Figure 11.6: Reliability index over time for A-21-2 gauge location.

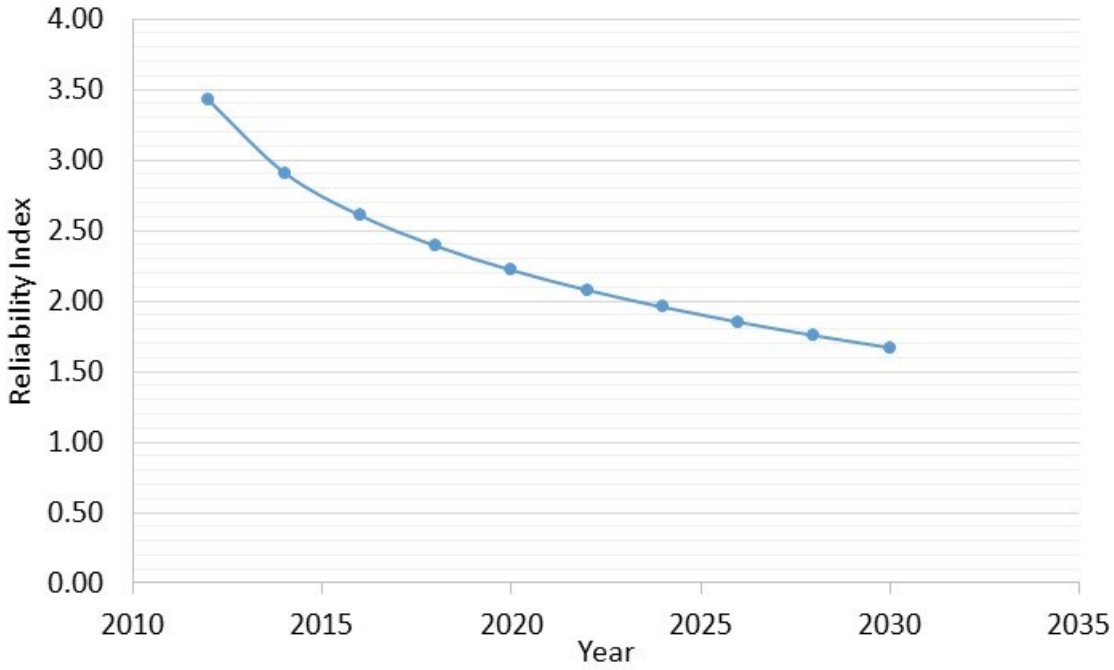

Figure 11.7: Reliability index over time for B-21-2 gauge location.

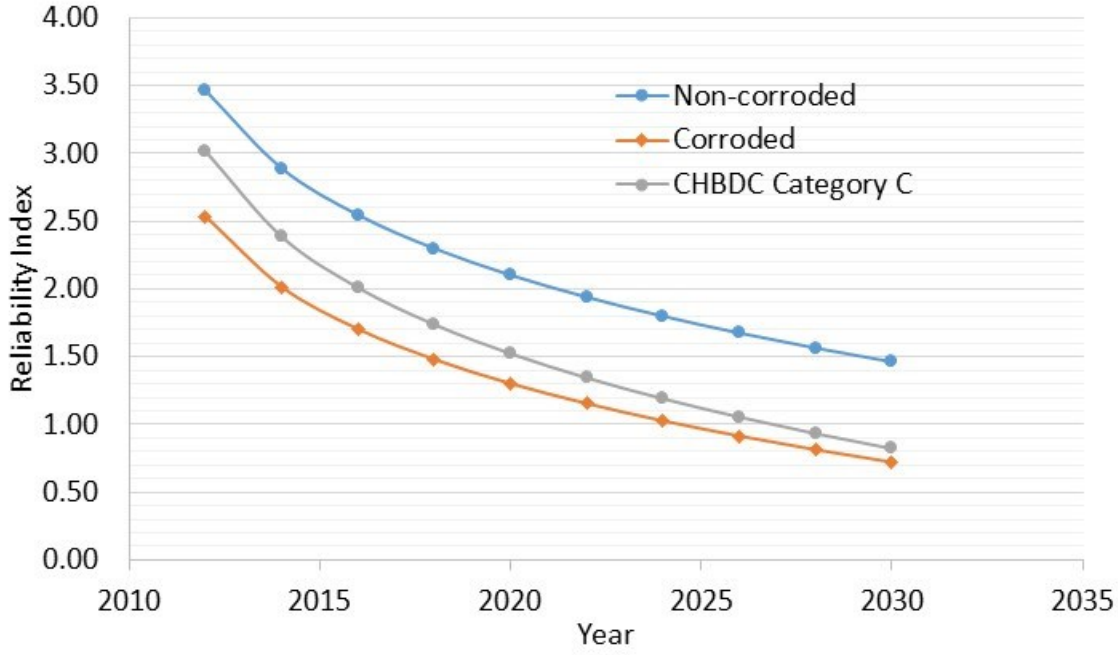

Figure 11.8: Reliability index over time comparison for C-21-4 gauge location.

In examining the C-21-4 location, the non-corroded specimens give the best results for

reliability index for all years whereas the corroded specimens give the worst reliability index. The non-corroded and corroded specimens does not follow the same trend as the CHBDC category C detail over time. This is because of the difference in statistical parameters. The CHBDC category C detail has a much larger database of test specimens and has a much lower standard deviation. It should be noted that the non-corroded results only represent a lower bound to the reliability index over time as the values for the fatigue detail coefficient were based on specimens that did not failure during testing.

11.6 Comparison to AASHTO Manual for Bridge Evaluation

The same three gauge locations were evaluated using the AASHTO Manual for Bridge Evaluation detailed in Section 3.2.2. The analysis proceeded assuming only the field data was available. Hooke's law was used to calculate stress with an assumed modulus of elasticity of 200 GPa. The average SSAF was used in the calculation of the stress at the type C detail. Further, since field data was available, the number of cycles that exceed the CAFL was checked. All three locations had in excess of one out of 2000 cycles over the CAFL, meaning fatigue damage will occur. The details were evaluated at the evaluation life, which represents reliability index of unity. A comparison between the AASHTO method presented Section 3.2.2 and the fatigue reliability analysis presented in Section 11.5 is given in Table 11.8.

Table 11.8: Fatigue reliability comparison

Location	AASHTO Manual for Bridge Evaluation	Fatigue Reliability Analysis
	Year	Year
A-21-2	2016	2038
B-21-2	2162	2052
C-21-4	2003	2041

A few comments should be made. Using the AASHTO method, the C-21-4 location already exceeds the target reliability. Further, the B-21-2 location returns an exceptional large amount of time because of the relatively lower number of cycles present with the low equivalent strain range. However, both the type A and type B locations do not include a

GAF, which has been shown to increase the strain range by approximately 1.20. The Section 11.5 fatigue reliability analysis provides an additional 22 and 38 years for the type A and type C details respectively.

11.7 System Reliability of OSPD

Using the Rackwitz-Fiessler procedure with Equation [11.1] allows for the calculation of the reliability index at each gauged location. The reliability index can be calculated at all accepted gauge locations on the bridge deck for any year desired, however, this does not give the reliability of the whole OSPD system, which was discussed in Section 2.4.3. Since it was determined in Section 2.4.4 that the OSPD represents a series system, the reliability of the deck system can be calculated using Equation [2.20]. It should be reiterated that the reliability index calculated from this equation is only a notional reliability index.

The system reliability was first calculated for each type of fatigue detail. The assumption in the system reliability calculation is that the 13 available data points (detail locations) adequately represents the fatigue detail under consideration on the OSPD. Figure 11.9 through Figure 11.11 plot the bounds of the reliability index of the OSPD for each individual detail type. The upper boundary is defined by the case of perfect correlation between gauge locations for the detail under consideration. The resulting reliability index is the worst individual gauge reliability index for that detail. The lower boundary is defined by the case of no correlation between gauge locations for the detail under consideration. The resulting reliability index is a combination of individual gauge reliability indexes for that detail using Equation [2.20]. The actual reliability index for the OSPD lies between these boundaries. Individual gauge reliability indexes are calculated using the same resistance data for details of the same type. Further, the results from the dynamic test show that multiple gauges respond from a single truck loading event. Therefore, a level of correlation exists between gauge locations. The true reliability index is believed to lie closer to the upper boundary, which represents perfect correlation.

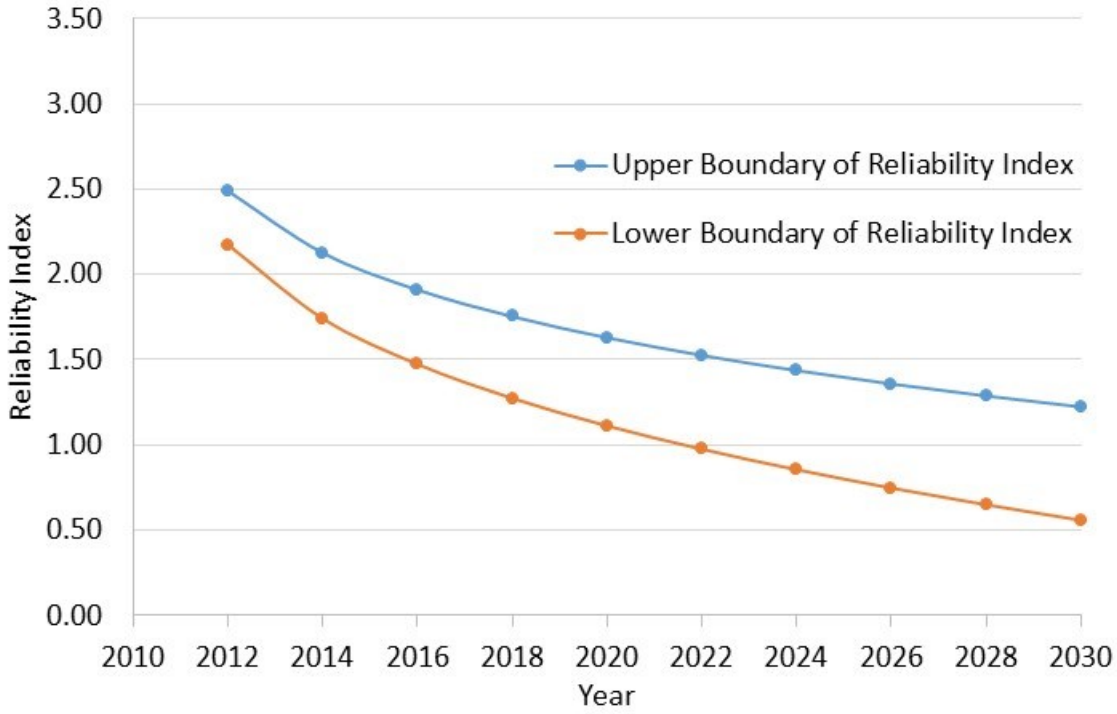

Figure 11.9: System reliability of type A detail over time.

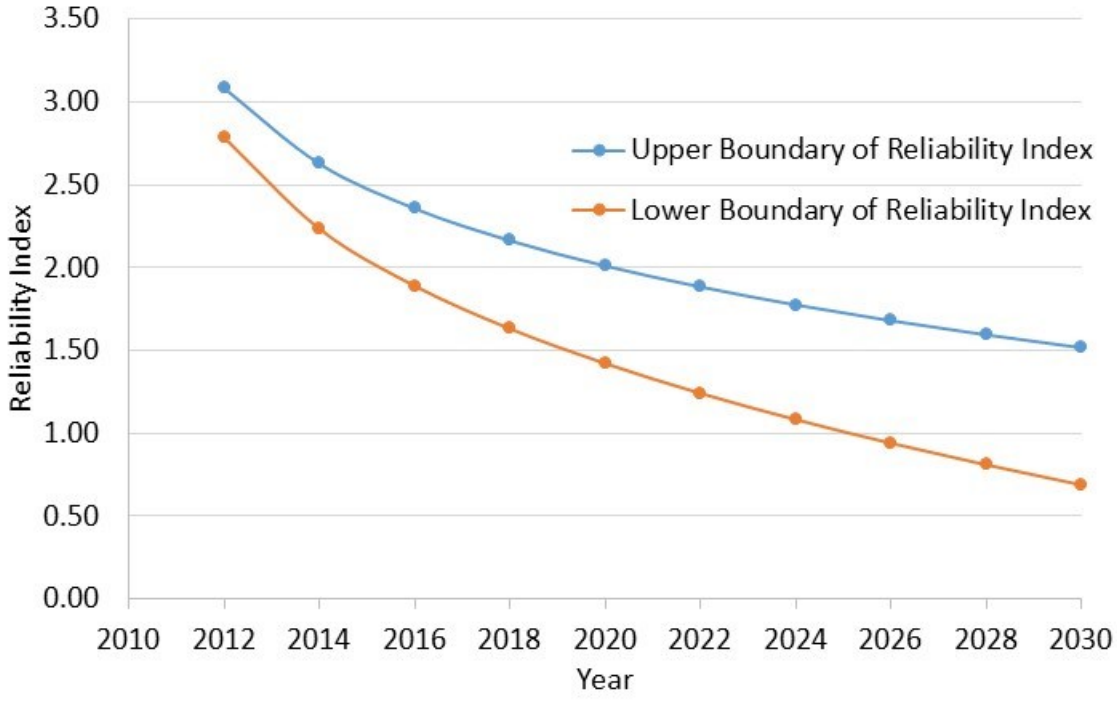

Figure 11.10: System reliability of type B detail over time.

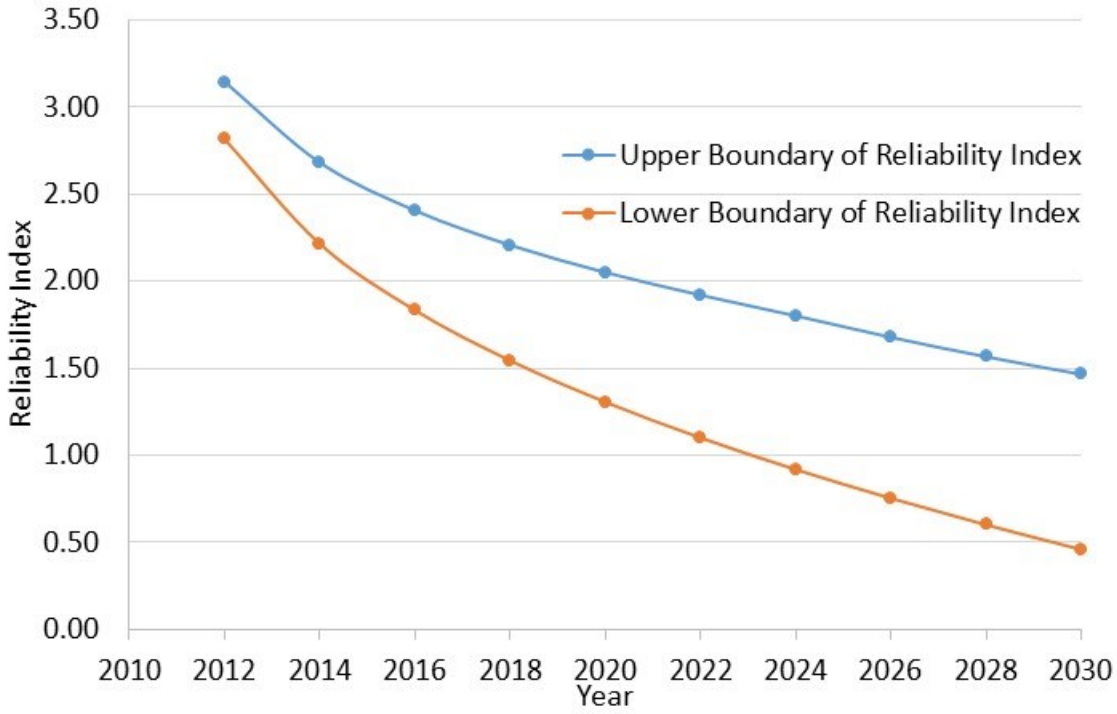

Figure 11.11: System reliability of type C detail over time.

Ultimately the reliability index of the entire OSPD panel is desired. Data from a total of 39 gauge locations was used in the system reliability of the OSPD. Figure 11.12 presents the reliability index over time for the entire OSPD system. Similar to each detail plot, the upper boundary is defined by the case of perfect correlation between all gauge locations. The resulting reliability index is the worst individual gauge reliability index. The lower boundary is defined by the case of no correlation between all gauge locations. The resulting reliability index is a combination of individual gauge reliability indexes using Equation [2.20].

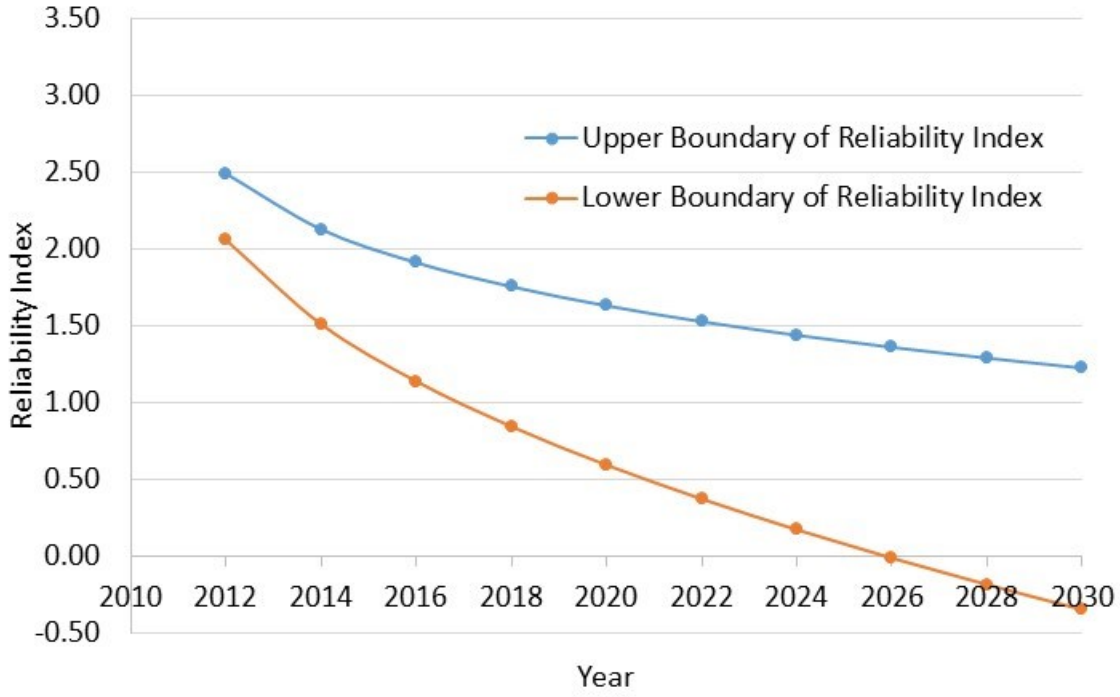

Figure 11.12: System reliability of OSPD over time.

11.8 Discussion of Results

The results from the detail type evaluation are discussed first. All three detail types start with approximately the same difference between the upper and lower boundary. As time increases, the difference between the curves for each detail grows, but at different rates. The type A detail grows at the slowest rate, with the type C detail growing at the fastest rate. The reason the rate of change over time differs for the different detail types comes from when the data is combined for the lower boundary curve. For the type A detail, only a small fraction of the gauge locations see a large number of cycles. The remaining gauge locations see a much lower amount of cycles, which gives a much higher reliability index. When combined, there is only a small fraction of gauges with a low reliability index, resulting in a small deviation from the upper boundary. For the type C detail, a large portion of the gauge locations have a large number of stress cycles, which all give similar reliability indexes. When combined, most gauges have a low reliability index, resulting in a larger deviation from the upper boundary.

For the overall reliability of the OSPD system, the upper boundary follows the type A upper boundary since the type A detail has the lowest reliability of a single monitored point at the A-21-2 gauge location. The lower boundary combines all 39 available data points, assuming no correlation between any points. The actual reliability index of the OSPD is between these two boundaries. With these two boundaries plotted in Figure 11.12, it is difficult to draw conclusions since there is a large range of values the reliability index could take on, however, some general comments can be made.

In evaluating a structure, it is difficult to establish what level of reliability the evaluation should take place. In the CHBDC, guidance is given on selecting the appropriate reliability level, however, no guidance is given on the fatigue evaluation of a bridge structure. In the design of a new bridge according to the CHBDC, the reliability index is 2.0 for fatigue. In the AASHTO Manual for Bridge Evaluation – Section 7, the reliability index used associated with the evaluation of a structure is 1.0. The NCHRP Report 721 by Bowman et al. (2012) introduced a second evaluation reliability level of 0.5. If the first reliability level of 1.0 were used as the target reliability index in this analysis, the OSPD would continue to meet the desired reliability level after 2030 for the upper boundary. For the lower boundary, the target reliability level would be exceeded before 2017.

It is important to remember the system reliability is calculated based on a series system; if one fatigue detail fails, the whole OSPD system fails. However, the OSPD will not catastrophically fail; a fatigue crack will be present on the OSPD. The OSPD has redundancy and the load would be transferred through a different load path. It should also be reiterated that the type C detail is based on a lower bound to the resistance since no specimens actually failed. If testing were to continue on these specimens, the fatigue resistance of this detail would increase, thus increasing the overall system reliability. For the type B specimen only the preliminary specimen has undergone laboratory testing. With no data, it is unable to definitely state what the impact on overall system reliability would be.

On a final note, if the OSPD system is below the target reliability index, whatever value it may be, that does not mean a fatigue crack will be present on the deck. It only represents

that the OSPD system is below the desired level of certainty for the FLS. One of the benefits of the SHM program is that multiple details were monitored across the width of the OSPD and the reliability index for each gauged location is available as a component reliability. The lower component reliability indexes indicate the locations were probability of failure is the highest and where fatigue cracking is most likely to occur. These locations can then be used to focus inspection efforts when the reliability of the OSPD system becomes questionable, minimizing the cost of inspection.

Chapter 12:Conclusions and Recommendations

This research detailed the coupling of a structural health monitoring system and laboratory testing to determine the reliability of a long span bridge in regards to the fatigue limit state. These two components help reduce the uncertainty in evaluating a bridge using a design code approach. The structural health monitoring system allowed collection of site-specific strain at fatigue details of concern, while the laboratory testing reduced the uncertainty in predicting the cumulative fatigue damage in the OSPD prior to 2010. A small component of numerical modeling was used to account for the effect of strain gauge placement, and limitations of uniaxial strain gauges. A limit state function was developed in Equation [11.1] to define fatigue failure of a single fatigue detail. Statistical distributions were developed for all variables based on collected data or previously conducted research. Solving the limit state equation for the reliability index using the Rackwitz-Fiessler procedure allowed the calculation of individual detail reliabilities, called component reliabilities. Using system reliability, all component reliabilities were combined to give a lower and upper boundary to the overall system reliability of the OSPD.

12.1 Conclusions

SHM significantly reduces the uncertainty in the fatigue reliability assessment of an existing structure, which brings more confidence to management decisions.

For the fatigue reliability of the OSPD, several conclusions have been drawn:

- The reliability at monitored details can be calculated precisely, however, the same precision is not achieved in the overall system reliability of the OSPD. Correlation coefficients between the gauged locations are needed to precisely calculate the reliability index for the entire OSPD. Therefore, only lower and upper boundaries can be defined.

- Parameter means have a larger impact on the reliability index when compared to the standard deviations, with the fatigue detail coefficient mean showing the largest impact.

- The noise in the data acquisition system on the MacKay has virtually no impact on the fatigue reliability assessment.

- The fatigue reliability analysis presented in this thesis reduced uncertainties contained in design codes, giving better, more promising results for the reliability of the type A and type C detail when compared to the AASHTO Manual for Bridge Evaluation

The following conclusions have been found for the fatigue detail behaviour and loading of concern:

- The type A detail is influenced by wheel loads rather than axles groups or gross vehicle weight. Further, the transverse wheel position is a significant influence on the strain at the detail.

- To capture fatigue loading events at the type A detail, a high scanning frequency is needed since the loading is applied at such a high rate. With the system on the MacKay, a scan rate of 200 Hz was required. Having such a high scan rate severely limits the number of channels data is collected on, as well as the amount of data processing the datalogger can complete.

- GAF is an important parameter in the fatigue reliability analysis. The average GAF for the type A and type B details is approximately 1.20. When raised to the third power, the net increase in stress range is approximately 1.70.

- Out-of-plane bending drives the stress range at the type B detail. For the literature review and limited field data, it appears that the type B detail is impacted by axle groups, however, additional data is needed to support this finding.

- For the type C detail, the laboratory loading is much simpler when compared to the field load. A complex state of stress exists in the field at the unique type C detail.

To account for only recording the longitudinal strain, a SSAF was derived based on SHM monitoring data collected from all strain gauge rosettes at the type C details.

- Through the review of literature, the type C detail is dominated by axle groups. Though individual axles might be observed, the magnitude of stress caused by each axle is insignificant and contributes minimal to the fatigue life.

Finally, the reliability analysis showed the impact of corrosion on the fatigue reliability:

- Corrosion significantly impacts the fatigue life of the type C detail. All type C failures occurred well below the predicted number of cycles. However, it is difficult to quantify the impact with such a small sample set.

12.2 Recommendations

Recommendations and future work are suggested as developed from the objectives and results from this thesis work, which focus on changes if a similar fatigue assessment program were undertaken.

To improve the field data collection and processing, the following recommendations are made:

- Implementation of outlier detection filter into the rainflow program to reduce amount of post-processing of the data.

- When outlier detection is completed in the post-processing phase, it would be more effective with actual truck traffic counts from the bridge tolls.

- Install a video monitoring system as part of the SHM system. The video monitoring system can then capture and confirm the existence of trucks, as well as the position of trucks within the traffic lanes. Using a similar system to Connor and Fisher (2005) would only record data and video when the strain is above a certain threshold.

The calibration can also be improved by the following:

- Perform calibration test with a truck that contains multiple axle groups to confirm the impact on the type B detail.

- Perform a calibration test during hot and cold temperatures to find the pavement load distribution properties.

- During field testing, place calibration truck at riding-rib and between rib locations to determine impact of eccentric loading about stiffening rib.

- Install rosette gauges at all three fatigue details to obtain the total state of stress. SSAF can easily be calculated from collected data under random traffic.

Recommendations for the laboratory testing are as follows:

- Corrosion significantly impacted the type C results. Obtaining specimens from an additional OSPD panel would eliminate the corrosion issue, as well as provide more specimens for testing, making the analysis more reliable.

- If a small number of specimens are being tested, the testing stress range should remain at the same magnitude. Results can then be directly compared.

Finally, future work can be completed for an improved reliability assessment:

- Another research study is needed to determine the level of correlation between the different gauge locations. Once the correlation coefficients are obtained, the overall system reliability can be more precisely calculated.

References

AASHTO. 2011. *Manual for Bridge Evaluation*. 2nd ed., American Association of State Highway and Transportation Officials, Washington, DC, USA.

Abdou, S., Zhang, W., and Fisher, J.W. 2003. Orthotropic Deck Fatigue Investigation at Triborough Bridge, New York. *Transportation Research Record.* 1845: 153-162.

AISC. 1963. *Design Manual for Orthotropic Steel Plate Deck Bridges.* American Institute of Steel Construction. Chicago, IL, USA.

Alampalli, S., and Lund, R. 2006. Estimating Fatigue Life of Bridge Components Using Measured Strains. *Journal of Bridge Engineering.* American Society of Civil Engineers. 11(*6*): 725-736.

Albrecht, P., and Rubiez, C. 1987. Variable-Amplitude Load Fatigue, Task A – Literature Review, Volume III – Variable-Amplitude Fatigue Behaviour. Report No. FHWA-RD_87_061, Federal Highway Administration, McLean, VA, USA.

ASTM International. 2010. Standard Practice for Statistical Analysis of Linear of Linearized Stress-Life and Strain-Life Fatigue Data. *ASTM E739-10*. American Society for Testing and Materials, West Conshohocken, PA, USA.

Bannantine, J.A., Comer, J.J., and Handrock, J.L. 1990. *Fundamentals of Metal Fatigue Analysis*. Prentice Hall, Upper Saddle River, NJ, USA.

Basu, S., and Meckesheimer, M. 2007. Automatic Outlier Detection for Time Series: an Application to Sensor Data. *Knowledge and Information Systems*, 2(*2*): 137-154.

Battista, R. C., Pfeil, M. S., and Cavalho, E. M. L. 2008. Fatigue Life Estimates for a Slender Orthotropic Steel Deck. *Journal of Constructional Steel Research,* 64: 134-143.

Berge, S., and Eide, O.I. 1981. Residual Stress and Stress Interaction in Fatigue Testing of Welded Joints. *Residual Stress Effects in Fatigue, ASTM STP 776*, American Society for Testing and Materials, 115-131.

Campbell Scientific. 2012. CR9000X Measurement and Control System: Instruction Manual. Retrieved June 2013 from http://www.campbellsci.ca/manuals.

CAN/CSA S6-06. 2006. Canadian Highway Bridge Design Code. Canadian Standards Association. Mississauga, ON, CAN.

CAN/CSA S6.1-06. 2006. Canadian Highway Bridge Design Code Commentary. Canadian Standards Association. Mississauga, ON, CAN.

Cheung, M.S., Tadros, G., Brown, T., Dilger, W., Ghali, A, and Lau, D. 1997. Field Monitoring and Research on Performance of the Confederation Bridge. *Canadian Journal of Civil Engineering.* 24: 951-962.

Chowdhury, A., Eppell, J. 2014. MacKay Suspension Bridge Hanger Replacement and Main Cable Inspection. *CSCE 2014 – 4th International Structural Specialty Conference,* Canadian Society for Civil Engineering, Halifax, NS, CAN.

Connor, R.J., Fisher, J.W., Gatti, W., Gopalaratnam, V., Kozy, B., Leshko, B. McQuaid, D.L., Medlock, R., Mertz, D., Murphy, T., Paterson, D., Sorensen, O., and Yadlosky, J. 2012. *Manaul for Design, Construction, and Maintenance of Orthotropic Steel Deck Bridges.* Federal Highway Administration, Washington, DC, USA.

Connor, R. J., and Fisher, J. W. 2000. In-Service Response of an Orthotropic Steel Deck Compared with Design Assumptions. *Transportation Research Record.* 1696: 100-108.

Connor, R. J., and Fisher, J. W. 2004. Results of Field Measurements made on the Prototype Orthotropic Deck on the Bronx-Whitestone Bridge – Final Report. ATLSS Report Number 04-03. Department of Civil and Environmental Engineering, Lehigh University, Bethlehem, PA, USA.

Connor, R. J., and Fisher, J. W. 2005. Field Testing of Orthotropic Bridge Decks. *Steel Structures.* 5: 225-231.

CWB. 2005. Welding for Design Engineers. Canadian Welding Bureau, Mississauga, ON, CAN.

Eide, O.I., and Berge, S. 1984. Cumulative Damage of Longitudinal Non-Load Carrying Fillet Welds. *Proceedings of the Conference "Fatigue '84".* Warley, England.

Downing, S.D., and Socie, D.F. 1982. Simple Rainflow Counting Algorithms. *International Journal of Fatigue*. 4(*1*): 31-40.

Fisher, J.W., Kulak, G.L., and Smith, I.F.C. 1998. *A Fatigue Primer for Structural Engineers*. National Steel Bridge Alliance, American Institute of Steel Construction.

Fisher, J.W., Albrecht, P.A., Yen, B.T., Klingerman, D.J., and McNamee, B.M. 1974. Fatigue Strength of Steel Beams with Welded Stiffeners and Attachments. NCHRP Report 147. *National Cooperative Highway Research Program*. Transportation Research Board, Washington, DC, USA.

Fisher, J.W., and Roy, S. 2011. Fatigue of Steel Bridge Infrastructure. *Structure and Infrastructure Engineering.* 7(7-8): 457-475.

Fisher, J.W., Frank, K.H., Hirt, M.A., and McNamee, B.M. 1970. Effect of Weldments on the Fatigue Strength of Steel Beams. NCHRP Report 102. *National Cooperative Highway Research Program*. Transportation Research Board, Washington, DC, USA.

Fisher, J.W., Mertz, D.R., and Zhong, A. 1983. Steel Bridge Members under Variable Amplitude Long Life Fatigue Loading. NCHRP Report 267. *National Cooperative Highway Research Program*. Transportation Research Board, Washington, DC, USA.

Fisher, J.W., Nussbaumer, A., Keating, P.B., and Yen, B.T. 1993. Resistance of Welded Details under Variable Amplitude Long-Life Loading. NCHRP Report 354. *National Cooperative Highway Research Program*. Transportation Research Board, Washington, DC, USA.

Freitas, S.T., Kolstein, H., and Bijlaard, F. 2012. Structural Monitoring of a Strengthened Orthotropic Steel Bridge Deck Using Strain Data. *Structural Health Monitoring.* 11(*5*): 558-576.

Fricke, W., and Feltz, O. 2013. Consideration of Influence Factors between Small-Scale Specimens and Large Components on the Fatigue Strength of Thin-Plated Block Joints in Shipbuilding. *Fatigue and Fracture of Engineering Materials and Structures.* 36, 1223-1231.

Gimsing, N.J. and Georgakis, C.T. 2012. *Cable Supported Bridges: Concept and Design*. 3rd ed., John Wiley & Sons Ltd., Chichester, West Sussex, United Kingdom.

Guo, T., and Chen, Y. W. 2011. Field Stress/displacement Monitoring and Fatigue Reliability Assessment of Retrofitted Steel Bridge Details. *Engineering Failure Analysis.* 18: 354-363.

Gurney, T.R. 1979. *Fatigue of Welded Structures*. 2nd ed., Cambridge University Press, New York, NY, USA.

Harazaki, I., Suzuki, S., and Okukawa, A. 2000. "Suspension Bridges." *Bridge Engineering Handbook.* Ed. Wai-Fah Chen and Lian Duan. CRC Press, Boca Raton, FL, USA.

Hasofer, A.M., and Lind N. 1974. An Exact and Invariant First-Order Reliability Format. *Journal of Engineering Mechanics.* American Society of Civil Engineers. 100(*EM1*): 111-121.

HHB. 2010. Annual Report 2009-2010: Planning and Partnerships. Halifax Harbour Bridges. Retrieved November 2014 from http://www.hdbc.ca/publications/

Kashefi, K., Zandi, A. P., and Zeinoddini, M. 2010. Fatigue Life Evaluation through Field Measurements and Laboratory Tests. *Procedia Engineering.* 2: 573-582.

Kawada, T. 2010. In Scott R. (Ed.), *History of the modern suspension bridge: Solving the dilemma between economy and stiffness* (H. Ohashi Trans.). ASCE Press, Reston, Virginia, USA.

Keating, P., and Fisher, J.W. 1986. Evaluation of Fatigue Tests and Design Criteria on Welded Details. NCHRP Report 286. *National Cooperative Highway Research Program*. Transportation Research Board, Washington, DC, USA.

Keever, M.D., and Fujimoto, J.H. 2000. "Bridge Decks and Approach Slabs." *Bridge Engineering Handbook.* Ed. Wai-Fah Chen and Lian Duan. CRC Press, Boca Raton.

Kim, S.H., Lee, S.W., and Mha, H.S. 2001. Fatigue Reliability Assessment of an Existing Steel Railroad Bridge. *Engineering Structures.* 23: 1203-1211.

Kolstein, M.H. 2007. Fatigue Classification of Welded Joints in Orthotropic Steel Bridge Decks. PhD thesis, Delft University of Technology, Faculty of Civil Engineering and Geosciences, Deft, The Netherlands, 485 pp.

Kulak, G.L., and Grondin, G.Y. 2010. *Limit States Design in Structural Steel (9th ed.)*. Canadian Institute of Steel Construction, Markham, ON, CAN.

Kwon, K., and Frangopol, D. M. 2010. Bridge Fatigue Reliability Assessment using Probability Density Functions of Equivalent Stress Range Based on Field Monitoring Data. *International Journal of Fatigue.* 32: 1221-1232.

Levy, J.A. 2011. Application of Structural Monitoring in Management Decisions for Large Infrastructure. MASc thesis, Dalhousie University, Department of Civil and Resource Engineering, Halifax, Nova Scotia, 192 pp.

Li, Z.X., Chan, T.H.T., and Ko, J.M. 2001. Fatigue Analysis and Life Prediction of Bridges with Structural Health Monitoring Data – Part I: Methodology and Strategy. *International Journal of Fatigue.* 23: 45-53.

Liu, M., Frangopol, D. M., and Kim, S. 2009. Bridge Safety Evaluation Based on Monitored Love Load Effects. *Journal of Bridge Engineering.* 14(*4*): 257-269.

Liu, M., Frangopol, D. M., and Kwon, K. 2010. Fatigue Reliability Assessment of Retrofitted Steel Bridges Integrating Monitoring Data. *Structural Safety.* 32: 77-89.

Maddox, S. J. 2000. Fatigue Design Rules for Welded Structures. *Progress in Structural Engineering and Materials.* 2: 102-109.

Mangus, A.R. and Sun, S. 2000. "Orthotropic Deck Bridges." *Bridge Engineering Handbook.* Ed. Wai-Fah Chen and Lian Duan. CRC Press, Boca Raton.

Miner, M.A. 1945. Cumulative Damage in Fatigue. *Transactions of the ASME*. 67: A159-164.

Moses, F., Schilling, C.G., and Raju, K.S. 1987. Fatigue Evaluation Procedures for Steel Bridges. NCHRP Report 299. *National Cooperative Highway Research Program*. Transportation Research Board, Washington, DC, USA.

Moses, M.D., Fu, G., Zhou, Y.E., Connor, R.J., and Godbole, A.A. 2012. Fatigue Evaluation of Steel Bridges. NCHRP Report 721. *National Cooperative Highway Research Program*. Transportation Research Board, Washington, DC, USA.

ISIS. 2001. *Guidelines for Structural Health Monitoring.* ISIS Canada Research Network, Winnipeg, MB, CAN.

ISIS. 2006. *Education Module 5: An Introduction to Structural Health* Monitoring. ISIS Canada Research Network, Winnipeg, MB, CAN.

Nowak, A., and Collins, K.R. 2013. *Reliability of Structures*. 2nd ed., CRC Press, Boca Raton, FL, USA.

Palmgren, A. 1924. Durability of Ball Bearings. *ZVDI*. 86(*14*): 339-341 (in German).

Pfeil, M.S., Battista, R.C., and Mergulhao, A.J.R. 2005. Stress Concentration in Steel Bridge Orthotropic Decks. *Journal of Constructional Steel Research.* 61: 1172-1184.

Schilling, C.G., Klippstein, K.H., Barsom, J.M., and Blake, G.T. 1978. Fatigue of Welded Steel Bridge Members under Variable Amplitude Loading. NCHRP Report 188. *National Cooperative Highway Research Program*. Transportation Research Board, Washington, DC, USA.

Stephens, R.I., Fatemi, A., Stephens, R.R., and Fuchs, H.O. 2001. *Metal Fatigue in Engineering*. 2nd ed., John Wiley & Sons Inc., New York, NY, USA.

Soliman, M., Frangopol, D.M., and Kwon, K. 2013. Fatigue Assessment and Service Life Prediction of Existing Steel Bridges by Integrating SHM into a Probabilistic Bilinear S-N Approach. *Journal of Structural Engineering.* 139(*10*): 1728-1740.

Sun, L., Li, H.N., Ren, L., and Jin, Q. 2007. Dynamic Response Measurement of Offshore Platform Model by FBG Sensors. *Sensors and Actuators A.* 136: 572-579.

Szerszen, M. M., Nowak, A. S., and Laman, J. A. 1999. Fatigue Reliability of Steel Bridges. *Journal of Constructional Steel Research.* 52: 83-92.

Tilly, G.P., and Nunn, D.E. 1980. Variable Amplitude Fatigue in Relation to Highway Bridges. *Proceedings of the Institute of Mechanical Engineers (London)*. 194(*1*), 259-267.

Tong, G., Aiqun, L., and Jianhui, L. 2008. Fatigue Life Prediction of Welded Joints in Orthotropic Steel Decks Considering Temperature Effects and Increasing Traffic Flow. *Structural Health Monitoring.* 7(*3*): 189-202.

Troitsky, M.S. 1987. *Orthotropic Bridges Theory and Design*. 2nd ed., The James F. Lincoln Arc Welding Foundation, Cleveland, OH, USA.

Tsakopoulos, P.A. and Fisher, J.W. 2003. Full-Scale Fatigue Tests of Steel Orthotropic Decks for the Williamsburg Bridge. *Journal of Bridge Engineering,* ASCE, 8: 323-333.

Tsakopoulos, P.A. and Fisher, J.W. 2005a. Fatigue Performance and Design Refinements of Steel Orthotropic Deck Panels Based on Full-Scale Laboratory Tests. *Steel Structures.* 5: 211-223.

Tsakopoulos, P.A. and Fisher, J.W. 2005b. Full-Scale Fatigue Tests of Steel Orthotropic Decks for the Bronx – Whitestone Bridge Rehabilitation. *Bridge Structures*, 1: 55-66.

Vishay. 2007. Tech Note TN-514: Shunt Calibration of Strain Gage Instrumentation. Vishay Micro-Measurements. Retrieved August 2012 from http://www.vishaypg.com/micro-measurements/stress-analysis-strain-gages/technotes-list/.

Wirsching, P.H. 1984. Fatigue Reliability for Offshore Structures. *Journal of Structural Engineering.* American Society of Civil Engineers. 110(*10*): 2340-2356.

Wirsching, P.H. 1998. Fatigue Reliability. *Progress in Structural Engineering and Materials.* 1(*2*): 200-206.

Wolchuk, R. 1990. Lessons from Weld Cracks in Orthotropic Decks on Three European Bridges. *Journal of Structural Engineering*. American Society of Civil Engineers. 116(*1*): 75-84.

Wright, W. 2011. *Orthotropic Deck Discussion Group Meeting.* January 24. Washington, DC, USA.

Xiao, Z.G., Yamada, K., Ya, S., and Zhao, X.L. 2008. Stress Analysis and Fatigue Evaluation of Rib-to-Deck Joints in Steel Orthotropic Decks. *International Journal of Fatigue.* 30: 1387-1397.

Xu, Y.L., and Xia, Y. 2012. *Structural Health Monitoring of Long-Span Suspension Bridges*. Spon Press, New York, NY, USA.

Ya, S., and Yamada, K. 2008. Fatigue Durability Evaluation of Trough to Deck Plate Welded Joint of Orthotropic Steel Deck. *Structural Engineering/Earthquake Engineering, Journal of Japan Society of Civil Engineers.* 25(*2*): 33s-46s.

Ya, S., Yamada, K., Ishikawa, T. 2011. Fatigue Evaluation of Rib-to-Deck Welded Joints of Orthotropic Steel Bridge Deck. *Journal of Bridge Engineering.* 16(*4*): 492-499.

Ye, X.W., Ni, Y.Q., Wong, K.Y., and Ko, J.M. 2012. Statistical Analysis of Stress Spectra for Fatigue Life Assessment of Steel Bridges with Structural Health Monitoring Data. *Engineering Structures.* 45: 166-176.

Appendix A : SHM System

A.1 Gauge Installation

A quarter-bridge configuration is used to measure strain. Linear pattern bondable strain gauges (Vishay Micro-Measurements General Purpose Strain Gauge type CEA-06-125UW-350 with gauge length of 3.18 mm) were installed for type A and type B fatigue details. The gauges are single axis 'foil-type' strain gauges as shown in Figure A.1. Three-Element 45° Strain rosettes (Omega SGD-1/350-RYT21 with gauge length of 1.6 mm) were installed for type C fatigue details. The rosette is shown in Figure A.2. The full bridge was completed with a Campbell Scientific 4 Wire Full Bridge Terminal shown in Figure A.3. Each gauge had independent bridge completion to individual modules within the datalogger. The field installation was completed by KTM according to Micro-Measurement Instruction Bulletin B-127-14 "Strain Gage Installations with M-Bond 200 Adhesive". Both the single-axis and rosette gauges are internally thermally compensated for the steel substrate. The surface of the structure was sanded smooth prior to installation of the gauges to ensure a proper bond.

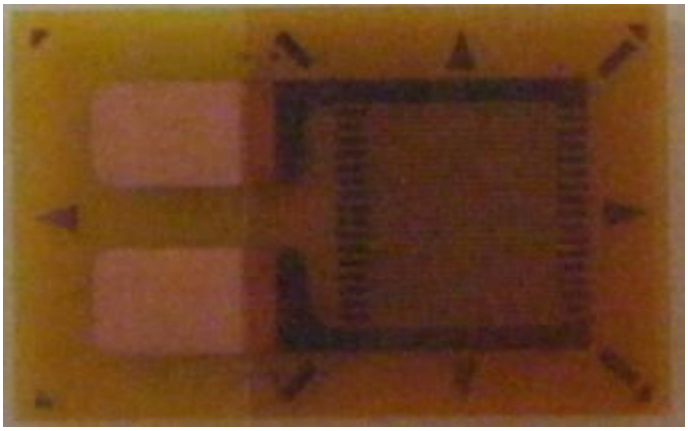

Figure A.1: Type A & B strain gauges.

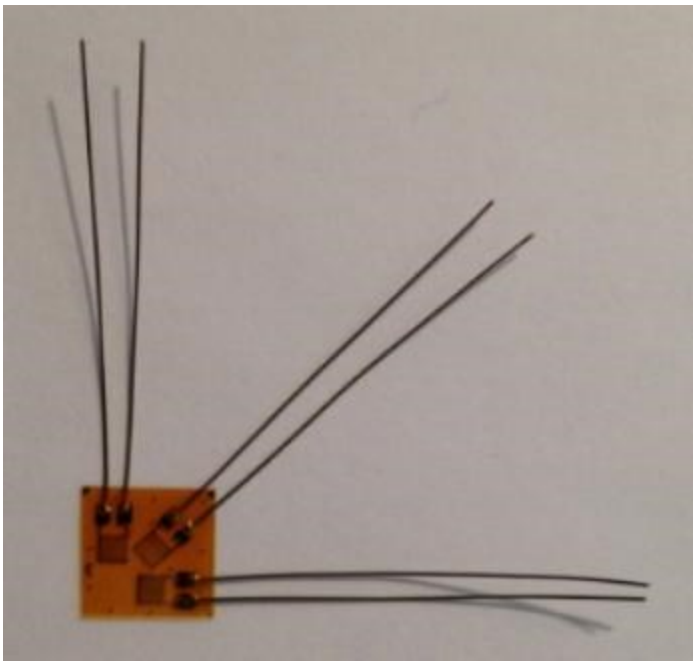

Figure A.2: Type C rosette gauge.

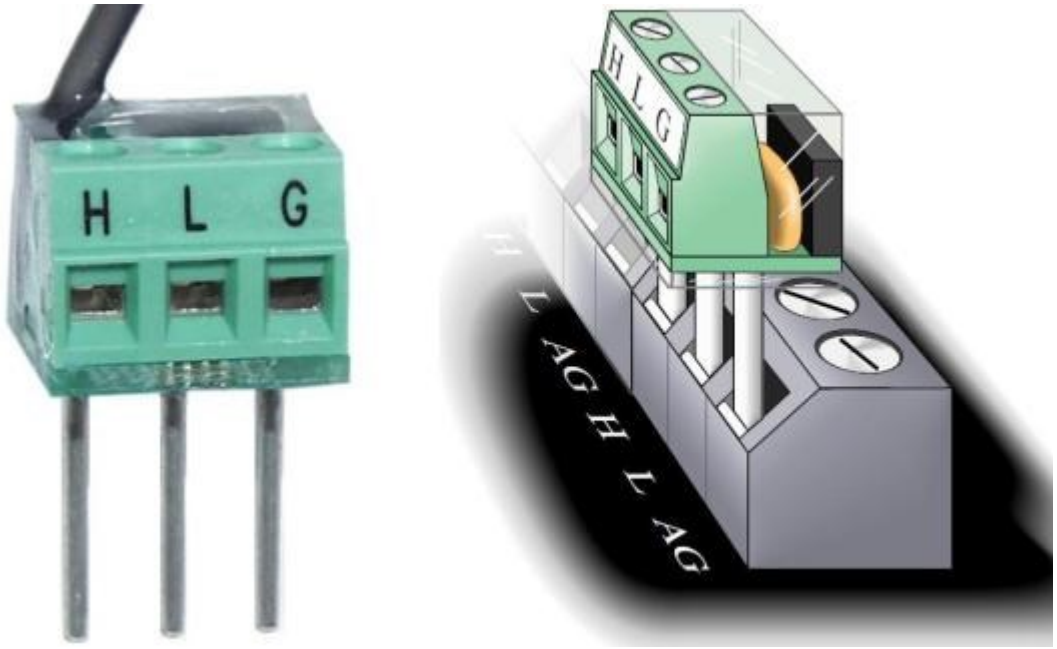

Figure A.3: Full bridge completion terminal (courtesy of Campbell Scientific).

The installed gauges are protected by a system of nitrile rubber, butyl rubber (Vishay M-Coat F), and a yellow waterproofing membrane to provide a moisture barrier and

environmental protection. The layer sequence starts with nitrile rubber, butyl rubber (also used to hold the tails of the leads, which includes a loop to provide strain relief), followed by the waterproofing membrane. Before the application of the waterproofing membrane, the area around the gauge was primed and allowed to cure. The waterproofing membrane was then applied and the edges were sealed with mastic to prevent the corners from lifting. The installation and protection are shown from Figure A.4 through Figure A.6.

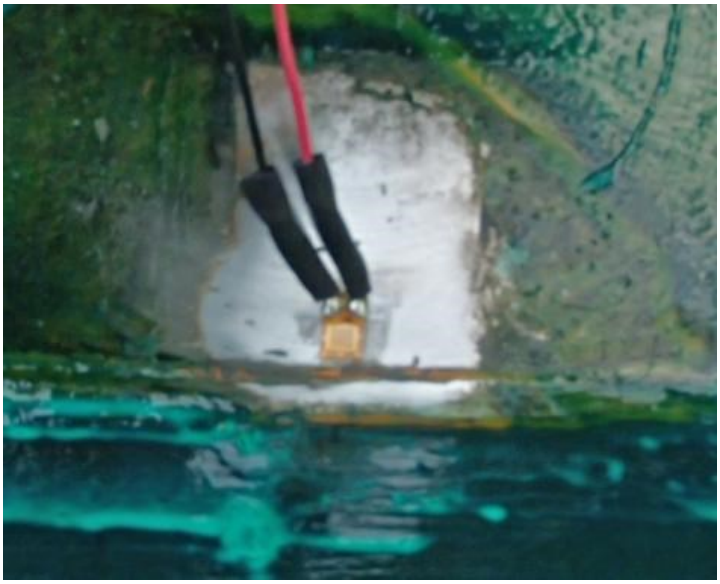

Figure A.4: Type A gauge without any protection (courtesy of KTM).

Figure A.5: Type A gauge before application of waterproofing membrane (courtesy of KTM).

Figure A.6: Type A (left) and type C (right) gauge with waterproofing membrane protection (courtesy KTM).

A.2 System Wiring

A three conductor, jacketed and shielded cable is used for wiring the gauges to the datalogger. The three conductor arrangement reduces noise and thermal influence on the gauge readings due to long cable lengths required to connect the gauges to the datalogger. Stress relief loops were provided at both the location of the gauges and at the datalogger to prevent damage to the gauge or connections from accidental pulls on the cable. The cable was run to the datalogger via a cable tray installed below the floor beam. This is shown in Figure A.7, which also shows the antenna used for data transmission.

After installation of the gauges and cable, each gauge was connected to the datalogger. The shielding wires were grounded to the tower structure to eliminate any build-up of static charge. Figure A.8 shows the completed wiring of the datalogger.

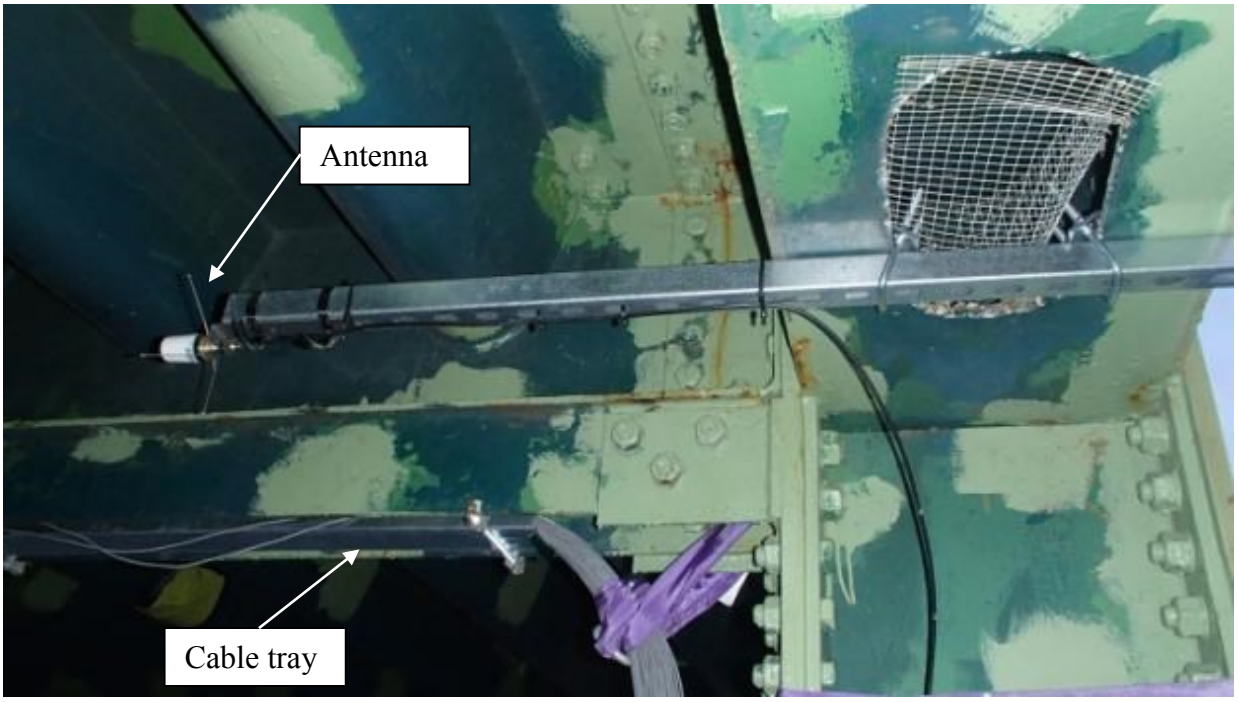

Figure A.7: Cable tray and antenna (courtesy of KTM).

Figure A.8: Datalogger completed wiring.

A.3 Data Acquisition

Data is acquired and stored with a Campbell Scientific CR9000X datalogger (see Figure A.9) contained in a water-resistant enclosure. Data is stored on a 2.0 GB flash card. The Campbell Scientific program LoggerNet: Version 4.0 is used to control data collection and download data to Dalhousie servers automatically, once per hour. Transfer of the data is completed using a wireless modem located at the datalogger.

Figure A.9: CR9000X datalogger (courtesy of Campbell Scientific).

A.4 Shunt Calibration

On October 4, 2012, a manual electronic shunt calibration procedure was completed on the SHM system. Shunt calibration is performed to determine that all the electronics are functioning and to establish an instrument scaling factor for the system. The strain gauge circuitry is shunted with a large precision resistor of a known resistance which simulates a known strain. The strain readings recorded by the instrument are then compared against the expected strain and adjustments can be made to the gain settings or the gauge factor in

the datalogger program to calibrate the strain gauges for instrument, installation and wiring effects. Strain gauges have a gauge factor from the manufacturer, but this is for the gauge only and does not apply to the full instrument and system. More details can be found in Vishay Micro-Measurements Tech Note TN-514.

A.4.1 Equipment

To complete the shunt calibration for each of the strain gauges, an 87.15 kΩ precision resistor was used, as shown in Figure A.10. This resistor should have produced a 2000 micro-strain reading for the 350 Ω strain gauges used for this project.

Figure A.10: Precision resistor used in shunt calibration.

A.4.2 Procedure

The precision resistor was applied to the adjacent dummy arm (to the strain gauge) of the bridge at the datalogger. The displayed strain was recorded before, during, and after applying the resistor to ensure the proper range of values was achieved. This procedure was complete for all 82 channels active on the SHM system.

A.4.3 Results

To determine the expected strain from the shunt calibration, Equation [A.1], provided by Vishay Micro-Measurements (Vishay, 2007) is used:

$$\varepsilon_s = \frac{-R_G}{FG\,(R_G + R_C)} \qquad [A.1]$$

where: ε_s = expected strain = 2000 με

R_G = initial circuit resistance = 350 Ω

FG = system gauge factor = 2.00

R_C = shunt resistance = 87.15 kΩ

A calibrated system gauge factor, and conversion factor for existing data, were determined for each channel and its corresponding gauge using the linear relationship. The gauge factors and conversion factors for each channel are shown in Table A.1. The average gauge factor from is 2.00; therefore no changes to the gauge factor in the datalogger programs were made. The conversion factor can be used to convert measured strain values to the actual strain values.

Table A-1: Calibrated gauge factors and conversion factors for each channel.

Channel	Gauge Factor	Conversion Factor	Channel	Gauge Factor	Conversion Factor
1	1.985	1.008	42	1.997	1.002
2	1.999	1.001	43	1.984	1.008
3	1.998	1.001	44	1.988	1.006
4	1.998	1.001	45	1.997	1.002
5	1.995	1.003	46	1.997	1.002
6	1.998	1.001	47	1.995	1.003
7	1.997	1.002	48	1.994	1.003
8	1.998	1.001	49	1.997	1.002
9	1.996	1.002	50	1.998	1.001
10	2.002	0.999	51	1.997	1.002
11	1.997	1.002	52	1.999	1.001
12	1.998	1.001	53	2.002	0.999
13	2.020	0.990	54	2.002	0.999
14	1.995	1.003	55	2.000	1.000
15	1.999	1.001	56	1.999	1.001
16	1.994	1.003	57	1.998	1.001
17	2.000	1.000	58	1.997	1.002
18	1.998	1.001	59	1.995	1.003
19	1.997	1.002	60	2.051	0.975
20	2.001	1.000	61	1.998	1.001
21	1.984	1.008	62	2.235	0.895
22	1.994	1.003	63	2.004	0.998
23	2.007	0.997	64	1.990	1.005
24	1.989	1.006	65	1.996	1.002
25	2.005	0.998	66	1.996	1.002
26	1.991	1.005	67	1.990	1.005
27	2.005	0.998	68	1.997	1.002
28	1.988	1.006	69	1.996	1.002

Channel	Gauge Factor	Conversion Factor	Channel	Gauge Factor	Conversion Factor
29	2.002	0.999	70	2.009	0.996
30	1.993	1.004	71	1.995	1.003
31	1.999	1.001	72	1.995	1.003
32	1.999	1.001	73	1.997	1.002
33	2.004	0.998	74	1.995	1.003
34	2.000	1.000	75	2.000	1.000
35	2.000	1.000	76	1.997	1.002
36	2.007	0.997	77	1.996	1.002
37	2.000	1.000	78	1.994	1.003
38	1.997	1.002	79	1.994	1.003
39	2.001	1.000	80	1.996	1.002
40	1.997	1.002	81	1.907	1.049
41	1.998	1.001	82	1.994	1.003

Appendix B : Field Testing

Table B-1: Static test results for channels 1 through 6.

Truck Position				Strain_Avg(1)	Strain_Avg(2)	Strain_Avg(3)	Strain_Avg(4)	Strain_Avg(5)	Strain_Avg(6)
Line	Stop	Tire	Time	A-04-1	A-04-2	A-06-1	A-06-2	A-10-2	A-11-1
1	C	T1	1:45:18	59	40	9	-54	-1	-12
	A	T1	1:46:36	-155	-140	25	-242	-1	-13
		T2	1:46:40	-155	-140	26	-243	-1	-15
2	C	T1	1:50:24	6	-27	55	38	21	-31
	A	T1	1:51:33	8	-35	-85	-137	23	-36
3	C	T1	1:54:07	-1	-7	-2	-15	40	-47
	A	T1	1:55:04	0	-6	-1	-14	-115	-119
		T2	1:55:04	0	-6	-1	-14	-115	-119
4	C	T1	1:57:02	0	-4	-2	-10	-32	14
	A	T1	1:57:26	0	-4	-2	-10	-40	26
5	C	T2	2:04:15	-1	-4	-3	-8	-21	-2
	A	T1	2:05:18	-1	-4	-2	-9	-24	-1
6	C	T2	2:07:14	-1	-4	-1	-7	-14	-6
	A	T1	2:08:30	-1	-4	0	-8	-14	-6
		T2	2:08:30	-1	-4	0	-8	-14	-6
7	C	T1	2:12:00	-2	-2	-1	-5	-4	-5
		T2	2:11:59	-1	-3	-1	-5	-6	-5
	A	T1	2:13:25	0	-4	-1	-3	-6	-6
		T2	2:13:14	-1	-2	-1	-4	-5	-5
8	A	T1	2:17:07	27	-116	-145	10	2	-22
9	A	T1	2:20:10	-1	-9	-10	-13	-134	-113
10	A	T1	2:23:52	-2	-5	-4	-6	-10	-7
		T2	2:23:53	-2	-6	-5	-6	-11	-7
11	A	T2	2:27:53	-2	-5	-4	-6	-8	-6
12	A	T2	2:31:24	-2	-4	-3	-5	-8	-7
	=	predicted gauge maximum							

Table B-2: Static test results for channels 7 through 12.

Truck Position				Strain_Avg(7)	Strain_Avg(8)	Strain_Avg(9)	Strain_Avg(10)	Strain_Avg(11)	Strain_Avg(12)
Line	Stop	Tire	Time	A-12-1	A-12-2	A-16-1	A-16-2	A-18-1	A-17-2
1	C	T1	1:45:18	-9	-5	-6	-8	-6	-4
	A	T1	1:46:36	-10	-6	-8	-9	-7	-4
		T2	1:46:40	-10	-7	-8	-8	-6	-4
2	C	T1	1:50:24	-17	-6	-8	-10	-8	-5
	A	T1	1:51:33	-19	-6	-9	-10	-8	-5
3	C	T1	1:54:07	-2	-60	-22	-10	-15	-7
	A	T1	1:55:04	11	-199	-24	-11	-16	-7
		T2	1:55:04	11	-199	-24	-11	-16	-7
4	C	T1	1:57:02	54	37	-79	-5	-24	-3
	A	T1	1:57:26	-148	-141	-98	-5	-26	-3
5	C	T2	2:04:15	10	-86	45	5	-39	15
	A	T1	2:05:18	14	-111	-181	-24	-41	21
6	C	T2	2:07:14	-7	-23	-51	-14	24	-46
	A	T1	2:08:30	-8	-26	-154	-16	-193	-137
		T2	2:08:30	-8	-26	-154	-16	-193	-137
7	C	T1	2:12:00	-5	-7	-9	-17	-8	-19
		T2	2:11:59	-6	-8	-8	-17	-8	-18
	A	T1	2:13:25	-6	-8	-9	-17	-9	-17
		T2	2:13:14	-5	-7	-8	-17	-10	-18
8	A	T1	2:17:07	-15	-6	-8	-15	-12	-6
9	A	T1	2:20:10	-160	-9	-45	-14	-24	-8
10	A	T1	2:23:52	-11	-14	18	-40	-174	-210
		T2	2:23:53	-10	-13	20	-40	-175	-210
11	A	T2	2:27:53	-8	-9	-6	-17	10	-33
12	A	T2	2:31:24	-9	-9	-8	-17	-6	-21
	=	predicted gauge maximum							

Table B-3: Static test results for channels 13 through 18.

Truck Position				Strain_Avg(13)	Strain_Avg(14)	Strain_Avg(15)	Strain_Avg(16)	Strain_Avg(17)	Strain_Avg(18)
Line	Stop	Tire	Time	A-21-1	A-21-2	A-24-1	A-24-2	B-04-1	B-04-2
1	C	T1	1:45:18	-12	-4	-6	-2	88	-143
	A	T1	1:46:36	-11	-5	-7	0	79	-124
		T2	1:46:40	-10	-3	-7	-1	79	-124
2	C	T1	1:50:24	-11	-4	-8	-1	7	-22
	A	T1	1:51:33	-11	-6	-9	0	9	-22
3	C	T1	1:54:07	-15	-6	-9	-1	5	-12
	A	T1	1:55:04	-14	-6	-9	-1	7	-14
		T2	1:55:04	-14	-6	-9	-1	7	-14
4	C	T1	1:57:02	-17	-7	-10	-2	6	-12
	A	T1	1:57:26	-17	-7	-10	-1	7	-14
5	C	T2	2:04:15	-21	-8	-12	-2	5	-11
	A	T1	2:05:18	-22	-8	-12	-2	6	-13
6	C	T2	2:07:14	-29	-5	-13	-1	3	-11
	A	T1	2:08:30	-30	-6	-14	-1	5	-13
		T2	2:08:30	-30	-6	-14	-1	5	-13
7	C	T1	2:12:00	58	51	1	61	0	-8
		T2	2:11:59	57	52	1	61	0	-8
	A	T1	2:13:25	-78	-193	-35	-111	1	-10
		T2	2:13:14	-78	-192	-35	-110	1	-9
8	A	T1	2:17:07	-15	-5	-14	-1	21	-47
9	A	T1	2:20:10	-19	-6	-15	-2	4	-13
10	A	T1	2:23:52	-140	20	-17	-1	3	-11
		T2	2:23:53	-140	19	-17	-1	3	-11
11	A	T2	2:27:53	-23	-115	-22	4	1	-9
12	A	T2	2:31:24	-211	6	-53	41	1	-9
	=	predicted gauge maximum							

Table B-4: Static test results for channels 19 through 24.

Truck Position				Strain_Avg(19)	Strain_Avg(20)	Strain_Avg(21)	Strain_Avg(22)	Strain_Avg(23)	Strain_Avg(24)
Line	Stop	Tire	Time	B-06-1	B-06-2	B-10-1	B-10-2	B-12-1	B-12-2
1	C	T1	1:45:18	16	-28	0	-13	8	-10
	A	T1	1:46:36	20	-34	4	-16	10	-14
		T2	1:46:40	20	-33	3	-15	11	-13
2	C	T1	1:50:24	70	-113	21	-47	6	-8
	A	T1	1:51:33	61	-95	23	-46	8	-11
3	C	T1	1:54:07	0	-3	65	-104	25	-39
	A	T1	1:55:04	1	-5	62	-92	29	-45
		T2	1:55:04	1	-5	62	-92	29	-45
4	C	T1	1:57:02	7	-10	11	-9	61	-104
	A	T1	1:57:26	7	-11	14	-16	58	-92
5	C	T2	2:04:15	6	-10	8	-7	19	-29
	A	T1	2:05:18	7	-11	10	-11	24	-35
6	C	T2	2:07:14	5	-9	9	-10	5	-10
	A	T1	2:08:30	6	-10	11	-13	7	-14
		T2	2:08:30	6	-10	11	-13	7	-14
7	C	T1	2:12:00	2	-6	7	-11	7	-11
		T2	2:11:59	2	-6	7	-11	7	-11
	A	T1	2:13:25	4	-9	7	-12	8	-12
		T2	2:13:14	2	-7	7	-12	7	-13
8	A	T1	2:17:07	22	-39	6	-23	8	-13
9	A	T1	2:20:10	2	-7	23	-30	29	-45
10	A	T1	2:23:52	3	-8	10	-15	8	-14
		T2	2:23:53	4	-8	11	-15	8	-14
11	A	T2	2:27:53	2	-7	8	-13	7	-12
12	A	T2	2:31:24	1	-7	6	-12	6	-12
	=	predicted gauge maximum							

Table B-5: Static test results for channels 25 through 30.

Truck Position				Strain_Avg(25)	Strain_Avg(26)	Strain_Avg(27)	Strain_Avg(28)	Strain_Avg(29)	Strain_Avg(30)
Line	Stop	Tire	Time	B-16-1	B-16-2	B-18-1	B-18-2	B-21-1	B-21-2
1	C	T1	1:45:18	9	-10	8	-13	-1	0
	A	T1	1:46:36	10	-12	9	-14	0	-1
		T2	1:46:40	10	-12	9	-15	1	-3
2	C	T1	1:50:24	10	-11	10	-16	1	-3
	A	T1	1:51:33	12	-14	11	-18	0	-2
3	C	T1	1:54:07	7	-10	10	-16	2	-5
	A	T1	1:55:04	11	-13	11	-18	2	-5
		T2	1:55:04	11	-13	11	-18	2	-5
4	C	T1	1:57:02	22	-28	11	-14	3	-5
	A	T1	1:57:26	25	-32	12	-18	3	-6
5	C	T2	2:04:15	70	-103	12	-19	0	-3
	A	T1	2:05:18	66	-91	15	-24	-1	-4
6	C	T2	2:07:14	28	-38	56	-117	-8	5
	A	T1	2:08:30	30	-42	55	-105	-5	1
		T2	2:08:30	30	-42	55	-105	-5	1
7	C	T1	2:12:00	9	-12	1	-16	49	-96
		T2	2:11:59	12	-13	2	-15	49	-96
	A	T1	2:13:25	12	-14	4	-15	42	-81
		T2	2:13:14	12	-15	4	-16	41	-80
8	A	T1	2:17:07	10	-15	6	-18	-1	-4
9	A	T1	2:20:10	12	-18	12	-20	1	-7
10	A	T1	2:23:52	23	-32	29	-56	8	-22
		T2	2:23:53	23	-32	27	-57	8	-21
11	A	T2	2:27:53	7	-11	12	-37	2	-17
12	A	T2	2:31:24	9	-12	2	-16	9	-28
	=	predicted gauge maximum							

Table B-6: Static test results for channels 31 through 36.

Truck Position				Strain_Avg(31)	Strain_Avg(32)	Strain_Avg(33)	Strain_Avg(34)	Strain_Avg(35)	Strain_Avg(36)
Line	Stop	Tire	Time	B-24-1	B-24-2	C-04-1	C-04-4	C-06-1	C-06-4
1	C	T1	1:45:18	6	-10	155	173	34	38
	A	T1	1:46:36	9	-12	75	79	33	24
		T2	1:46:40	8	-11	75	79	33	24
2	C	T1	1:50:24	5	-9	8	4	152	141
	A	T1	1:51:33	9	-13	6	2	67	59
3	C	T1	1:54:07	8	-13	-2	-2	4	3
	A	T1	1:55:04	11	-17	-3	-3	2	1
		T2	1:55:04	11	-17	-3	-3	2	1
4	C	T1	1:57:02	7	-13	-2	-2	2	2
	A	T1	1:57:26	11	-16	-3	-3	1	1
5	C	T2	2:04:15	7	-13	-3	-2	1	1
	A	T1	2:05:18	9	-16	-3	-3	0	0
6	C	T2	2:07:14	8	-12	-2	-2	1	1
	A	T1	2:08:30	8	-15	-3	-3	0	0
		T2	2:08:30	8	-15	-3	-3	0	0
7	C	T1	2:12:00	81	-138	-2	-2	1	1
		T2	2:11:59	81	-138	-2	-2	0	1
	A	T1	2:13:25	71	-117	-2	-2	2	2
		T2	2:13:14	72	-117	-3	-3	0	0
8	A	T1	2:17:07	7	-13	23	17	31	34
9	A	T1	2:20:10	6	-14	-4	-4	-1	0
10	A	T1	2:23:52	0	-8	-4	-4	-1	0
		T2	2:23:53	1	-9	-4	-4	-1	-1
11	A	T2	2:27:53	2	-9	-4	-4	-1	-1
12	A	T2	2:31:24	24	-42	-5	-5	-2	-1
	=	predicted gauge maximum							

Table B-7: Static test results for channels 37 through 42.

Truck Position				Strain_Avg(37)	Strain_Avg(38)	Strain_Avg(39)	Strain_Avg(40)	Strain_Avg(41)	Ga Strain_Avg(42)
Line	Stop	Tire	Time	C-10-1	C-10-4	C-12-1	C-12-4	C-16-1	C-16-4
1	C	T1	1:45:18	2	5	0	3	1	1
	A	T1	1:46:36	1	5	0	2	0	0
		T2	1:46:40	1	5	-1	2	1	0
2	C	T1	1:50:24	27	30	2	6	2	1
	A	T1	1:51:33	19	28	1	4	0	0
3	C	T1	1:54:07	144	154	32	44	6	6
	A	T1	1:55:04	69	61	30	32	3	4
		T2	1:55:04	69	61	30	32	3	4
4	C	T1	1:57:02	10	10	130	158	24	24
	A	T1	1:57:26	9	9	64	74	21	22
5	C	T2	2:04:15	3	5	20	21	185	142
	A	T1	2:05:18	2	4	19	21	72	72
6	C	T2	2:07:14	1	4	5	7	47	35
	A	T1	2:08:30	-1	3	3	6	32	30
		T2	2:08:30	-1	3	3	6	32	30
7	C	T1	2:12:00	-2	2	-1	3	2	0
		T2	2:11:59	-2	2	-1	3	2	0
	A	T1	2:13:25	-3	1	-2	2	0	-1
		T2	2:13:14	-3	1	-2	2	0	-1
8	A	T1	2:17:07	2	11	-1	3	0	-1
9	A	T1	2:20:10	22	18	25	36	7	8
10	A	T1	2:23:52	-3	2	-1	3	25	19
		T2	2:23:53	-2	1	-1	3	25	19
11	A	T2	2:27:53	-3	1	-3	1	1	-1
12	A	T2	2:31:24	-3	0	-3	1	-2	-2
	=	predicted gauge maximum							

Table B-8: Static test results for channels 43 through 48.

				ıge					
Truck Position				Strain_Avg(43)	Strain_Avg(44)	Strain_Avg(45)	Strain_Avg(46)	Strain_Avg(47)	Strain_Avg(48)
Line	Stop	Tire	Time	C-18-1	C-18-4	C-21-1	C-21-4	C-24-1	C-24-4
1	C	T1	1:45:18	1	3	-5	-4	-2	-1
	A	T1	1:46:36	0	1	-6	-5	-2	-1
		T2	1:46:40	-1	1	-5	-3	-2	-1
2	C	T1	1:50:24	0	2	-5	-4	-3	-2
	A	T1	1:51:33	-1	1	-7	-5	-3	-1
3	C	T1	1:54:07	-1	5	-5	-4	-3	-2
	A	T1	1:55:04	-1	2	-7	-5	-2	1
		T2	1:55:04	-1	2	-7	-5	-2	1
4	C	T1	1:57:02	-1	7	-5	-3	-3	-2
	A	T1	1:57:26	-2	4	-7	-5	-3	-3
5	C	T2	2:04:15	-2	13	-6	-4	-2	-4
	A	T1	2:05:18	-3	9	-8	-5	-3	-4
6	C	T2	2:07:14	52	145	-2	1	-2	-1
	A	T1	2:08:30	36	75	-2	-1	-4	-2
		T2	2:08:30	36	75	-2	-1	-4	-2
7	C	T1	2:12:00	5	6	137	130	164	147
		T2	2:11:59	5	6	135	130	163	147
	A	T1	2:13:25	2	2	57	57	64	72
		T2	2:13:14	3	3	57	56	63	72
8	A	T1	2:17:07	-2	2	-8	-5	-1	-2
9	A	T1	2:20:10	-2	4	-8	-5	-4	-4
10	A	T1	2:23:52	11	40	10	17	-5	-5
		T2	2:23:53	10	41	11	18	-5	-4
11	A	T2	2:27:53	28	23	20	21	1	4
12	A	T2	2:31:24	7	4	18	26	18	24
	=	predicted gauge maximum							

Table B-9: Static test results for channels 49 through 54.

Truck Position				Strain_Avg(49)	Strain_Avg(50)	Strain_Avg(51)	Strain_Avg(52)	Strain_Avg(53)	Strain_Avg(54)
Line	Stop	Tire	Time	Dummy 1 (A)	Dummy 2 (C)	C-04-2	C-04-3	C-04-5	C-04-6
1	C	T1	1:45:18	-2	-2	-5	64	2	97
	A	T1	1:46:36	-2	-2	-18	5	-7	60
		T2	1:46:40	-2	-2	-17	5	-7	60
2	C	T1	1:50:24	-2	-2	-7	-1	4	8
	A	T1	1:51:33	-2	-3	-8	0	4	9
3	C	T1	1:54:07	-2	-3	-2	-4	-2	0
	A	T1	1:55:04	-2	-3	-1	-3	-1	0
		T2	1:55:04	-2	-3	-1	-3	-1	0
4	C	T1	1:57:02	-2	-3	-1	-4	-2	0
	A	T1	1:57:26	-2	-3	-1	-4	-2	0
5	C	T2	2:04:15	-3	-3	-4	-3	-2	-2
	A	T1	2:05:18	-3	-3	-2	-4	-3	-1
6	C	T2	2:07:14	-3	-4	-2	-4	-3	0
	A	T1	2:08:30	-4	-4	-1	-6	-2	1
		T2	2:08:30	-4	-4	-1	-6	-2	1
7	C	T1	2:12:00	-5	-4	-4	-5	-1	-2
		T2	2:11:59	-3	-4	-2	-4	-4	-1
	A	T1	2:13:25	-4	-4	-3	-4	-2	0
		T2	2:13:14	-4	-4	-3	-4	-3	0
8	A	T1	2:17:07	-4	-5	-22	4	11	29
9	A	T1	2:20:10	-4	-4	-2	-5	-3	-2
10	A	T1	2:23:52	-5	-5	-2	-5	-3	0
		T2	2:23:53	-5	-5	-4	-6	-3	-1
11	A	T2	2:27:53	-4	-5	-4	-6	-4	-2
12	A	T2	2:31:24	-4	-5	-3	-5	-3	-2
	=	predicted gauge maximum							

Table B-10: Static test results for channels 55 through 60.

Truck Position				Strain_Avg(55)	Strain_Avg(56)	Strain_Avg(57)	Strain_Avg(58)	Strain_Avg(59)	Strain_Avg(60)
Line	Stop	Tire	Time	C-06-2	C-06-3	C-06-5	C-06-6	C-10-2	C-10-3
1	C	T1	1:45:18	-26	8	20	38	2	0
	A	T1	1:46:36	-16	15	6	29	1	-1
		T2	1:46:40	-16	14	6	30	2	-1
2	C	T1	1:50:24	-19	77	-5	77	16	14
	A	T1	1:51:33	-22	12	-10	47	10	2
3	C	T1	1:54:07	-5	2	-1	2	-31	60
	A	T1	1:55:04	-3	1	-1	1	-26	11
		T2	1:55:04	-3	1	-1	1	-26	11
4	C	T1	1:57:02	-4	0	-1	1	-10	2
	A	T1	1:57:26	-4	0	-1	1	-9	3
5	C	T2	2:04:15	-3	-1	-1	0	-5	1
	A	T1	2:05:18	-4	-1	-1	1	-5	1
6	C	T2	2:07:14	-6	0	-2	1	-3	1
	A	T1	2:08:30	-6	1	-1	1	-3	0
		T2	2:08:30	-6	1	-1	1	-3	0
7	C	T1	2:12:00	-4	1	-1	0	-2	-1
		T2	2:11:59	-6	-2	-2	0	-2	0
	A	T1	2:13:25	-5	-1	-3	0	-2	-1
		T2	2:13:14	-5	-1	-2	0	-2	-1
8	A	T1	2:17:07	1	7	-19	9	2	0
9	A	T1	2:20:10	-5	-1	-1	1	-23	7
10	A	T1	2:23:52	-4	0	-1	0	-2	-1
		T2	2:23:53	-4	0	-2	1	-3	-1
11	A	T2	2:27:53	-5	-1	-1	0	-3	-1
12	A	T2	2:31:24	-5	-2	-1	-1	-3	-2
	=	predicted gauge maximum							

Table B-11: Static test results for channels 61 through 66.

Truck Position				Strain_Avg(61)	Strain_Avg(62)	Strain_Avg(63)	Strain_Avg(64)	Strain_Avg(65)	Strain_Avg(66)
Line	Stop	Tire	Time	C-10-5	C-10-6	C-12-2	C-12-3	C-12-5	C-12-6
1	C	T1	1:45:18	-6	0	-2	-1	-2	-1
	A	T1	1:46:36	-5	0	-3	0	-2	-2
		T2	1:46:40	-6	0	-3	-1	-2	-2
2	C	T1	1:50:24	-27	0	-2	0	-4	-1
	A	T1	1:51:33	-22	-1	-2	0	-4	-2
3	C	T1	1:54:07	3	96	1	-27	17	34
	A	T1	1:55:04	-12	50	6	-18	5	29
		T2	1:55:04	-12	50	6	-18	5	29
4	C	T1	1:57:02	1	10	45	-20	-5	78
	A	T1	1:57:26	1	10	1	-25	-13	47
5	C	T2	2:04:15	-2	4	0	-23	11	21
	A	T1	2:05:18	-2	4	2	-21	9	23
6	C	T2	2:07:14	-3	2	-3	-6	0	1
	A	T1	2:08:30	-3	2	-3	-5	-1	2
		T2	2:08:30	-3	2	-3	-5	-1	2
7	C	T1	2:12:00	-4	0	-4	-3	-4	1
		T2	2:11:59	-4	0	-4	-3	-2	-2
	A	T1	2:13:25	-4	0	-4	-3	-3	-1
		T2	2:13:14	-4	0	-4	-3	-2	-1
8	A	T1	2:17:07	-12	-1	-5	-4	-4	-3
9	A	T1	2:20:10	7	26	1	1	-17	5
10	A	T1	2:23:52	-5	0	-5	-4	-1	1
		T2	2:23:53	-4	0	-5	-6	-2	1
11	A	T2	2:27:53	-4	-1	-5	-5	-3	-1
12	A	T2	2:31:24	-5	0	-5	-4	-2	-1
	=	predicted gauge maximum							

Table B-12: Static test results for channels 67 through 72.

Truck Position				Strain_Avg(67)	Strain_Avg(68)	Strain_Avg(69)	Strain_Avg(70)	Strain_Avg(71)	Strain_Avg(72)
Line	Stop	Tire	Time	C-16-2	C-16-3	C-16-5	C-16-6	C-18-2	C-18-3
1	C	T1	1:45:18	-3	-2	-3	2	-2	0
	A	T1	1:46:36	-2	-3	-4	0	-1	-1
		T2	1:46:40	-2	-3	-4	1	-2	-1
2	C	T1	1:50:24	-3	-2	-4	1	-2	0
	A	T1	1:51:33	-3	-3	-4	0	-1	-1
3	C	T1	1:54:07	-2	0	-8	1	-1	1
	A	T1	1:55:04	-1	-2	-7	0	-1	-1
		T2	1:55:04	-1	-2	-7	0	-1	-1
4	C	T1	1:57:02	12	9	-25	-1	1	2
	A	T1	1:57:26	11	4	-24	-3	1	0
5	C	T2	2:04:15	-8	71	-23	72	4	4
	A	T1	2:05:18	-9	2	-31	39	3	1
6	C	T2	2:07:14	11	24	-28	9	12	95
	A	T1	2:08:30	2	3	-17	10	-8	3
		T2	2:08:30	2	3	-17	10	-8	3
7	C	T1	2:12:00	-9	-4	-2	1	-8	1
		T2	2:11:59	-9	-4	-5	2	-8	1
	A	T1	2:13:25	-8	-5	-5	1	-6	0
		T2	2:13:14	-8	-4	-4	2	-6	0
8	A	T1	2:17:07	-8	-5	-5	1	-3	-2
9	A	T1	2:20:10	-2	-3	-13	-1	-2	-1
10	A	T1	2:23:52	-24	5	8	27	1	6
		T2	2:23:53	-25	5	10	27	2	7
11	A	T2	2:27:53	-10	-4	-4	3	-27	5
12	A	T2	2:31:24	-8	-6	-6	0	-11	0
	=	predicted gauge maximum							

Table B-13: Static test results for channels 73 through 78.

Truck Position				Strain_Avg(73)	Strain_Avg(74)	Strain_Avg(75)	Strain_Avg(76)	Strain_Avg(77)	Strain_Avg(78)
Line	Stop	Tire	Time	C-18-5	C-18-6	C-21-2	C-21-3	C-21-5	C-21-6
1	C	T1	1:45:18	-2	2	-1	-6	-3	-4
	A	T1	1:46:36	-2	1	-1	-6	-2	-4
		T2	1:46:40	-2	1	0	-6	-4	-4
2	C	T1	1:50:24	-3	2	-1	-6	-3	-4
	A	T1	1:51:33	-3	1	-1	-7	-4	-5
3	C	T1	1:54:07	-4	4	-1	-6	-4	-5
	A	T1	1:55:04	-4	1	-1	-8	-4	-5
		T2	1:55:04	-4	1	-1	-8	-4	-5
4	C	T1	1:57:02	-7	5	-1	-7	-5	-4
	A	T1	1:57:26	-6	3	-1	-7	-4	-5
5	C	T2	2:04:15	-13	9	-2	-8	-6	-5
	A	T1	2:05:18	-11	7	-2	-9	-5	-6
6	C	T2	2:07:14	-32	157	-1	-6	-8	-4
	A	T1	2:08:30	-25	59	0	-6	-9	-6
		T2	2:08:30	-25	59	0	-6	-9	-6
7	C	T1	2:12:00	0	8	-22	59	-9	70
		T2	2:11:59	0	8	-22	59	-7	70
	A	T1	2:13:25	-1	4	-20	5	-18	44
		T2	2:13:14	-1	4	-19	4	-18	44
8	A	T1	2:17:07	-4	0	-3	-10	-6	-5
9	A	T1	2:20:10	-6	2	-3	-10	-7	-6
10	A	T1	2:23:52	-20	32	8	-5	-23	-7
		T2	2:23:53	-21	33	8	-5	-22	-8
11	A	T2	2:27:53	12	24	-16	1	0	20
12	A	T2	2:31:24	2	6	2	-5	-21	2
	=	predicted gauge maximum							

Table B-14: Static test results for channels 79 through 84.

Truck Position				Strain_Avg(79)	Strain_Avg(80)	Strain_Avg(81)	Strain_Avg(82)	Strain_Avg(83)	Strain_Avg(84)
Line	Stop	Tire	Time	C-24-2	C-24-3	C-24-5	C-24-6		
1	C	T1	1:45:18	-2	-3	-2	-1	8	NAN
	A	T1	1:46:36	-1	-2	-3	-2	8	NAN
		T2	1:46:40	-1	-3	-2	-2	8	NAN
2	C	T1	1:50:24	-1	-3	-3	-2	9	NAN
	A	T1	1:51:33	-1	-3	-3	-2	10	NAN
3	C	T1	1:54:07	-1	-4	-3	-2	10	NAN
	A	T1	1:55:04	-3	-4	-1	0	10	NAN
		T2	1:55:04	-3	-4	-1	0	10	NAN
4	C	T1	1:57:02	-1	-4	-3	-3	11	NAN
	A	T1	1:57:26	-1	-4	-3	-3	11	NAN
5	C	T2	2:04:15	-1	-4	-4	-4	13	NAN
	A	T1	2:05:18	-2	-5	-3	-4	13	NAN
6	C	T2	2:07:14	-1	-4	-4	-3	13	NAN
	A	T1	2:08:30	-1	-5	-4	-5	14	NAN
		T2	2:08:30	-1	-5	-4	-5	14	NAN
7	C	T1	2:12:00	-4	76	-26	61	15	NAN
		T2	2:11:59	-4	76	-26	61	15	NAN
	A	T1	2:13:25	-13	2	-24	37	15	NAN
		T2	2:13:14	-13	2	-25	37	15	NAN
8	A	T1	2:17:07	-2	-5	-5	-4	16	NAN
9	A	T1	2:20:10	-2	-5	-4	-5	17	NAN
10	A	T1	2:23:52	-1	-6	-5	-6	18	NAN
		T2	2:23:53	-1	-6	-6	-5	18	NAN
11	A	T2	2:27:53	3	-4	-11	-6	19	NAN
12	A	T2	2:31:24	10	-2	-22	-7	21	NAN
	=	predicted gauge maximum							

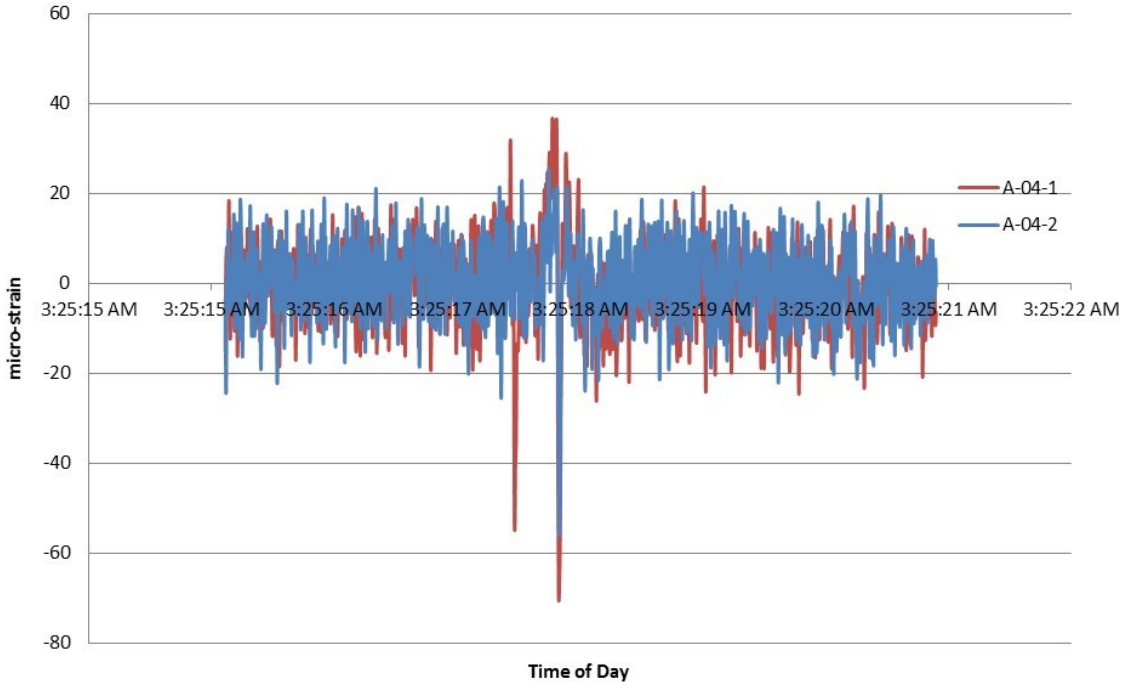

Figure B.1: Dynamic response of A-04 gauges with truck traveling in lane 4.

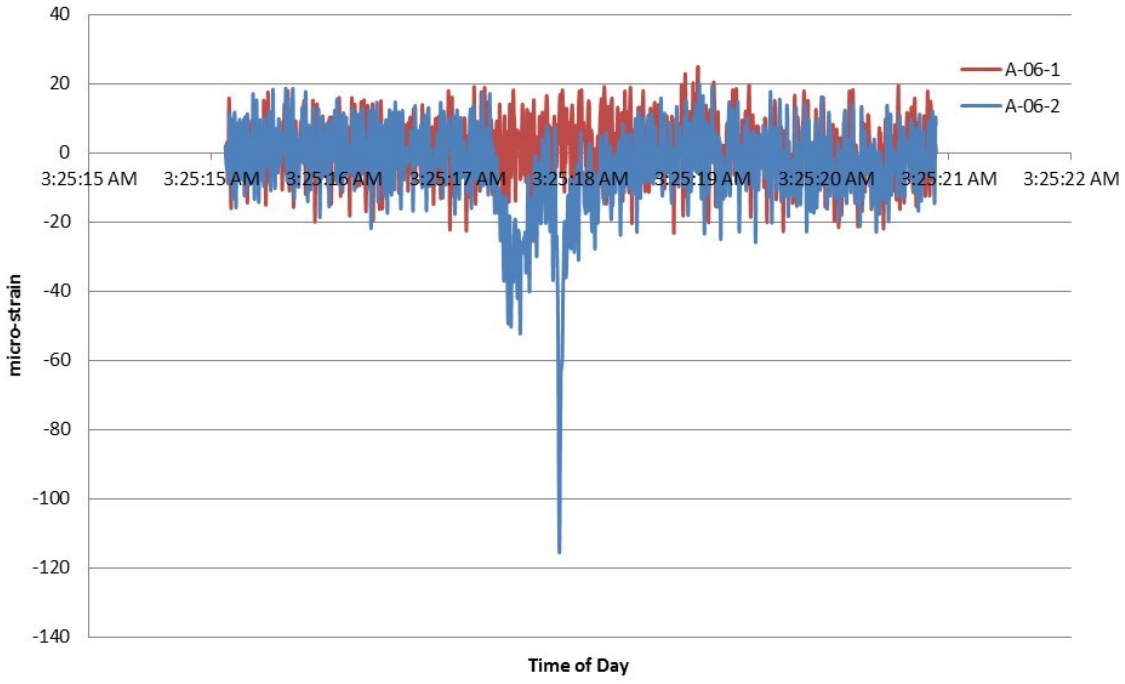

Figure B.2: Dynamic response of A-06 gauges with truck traveling in lane 4.

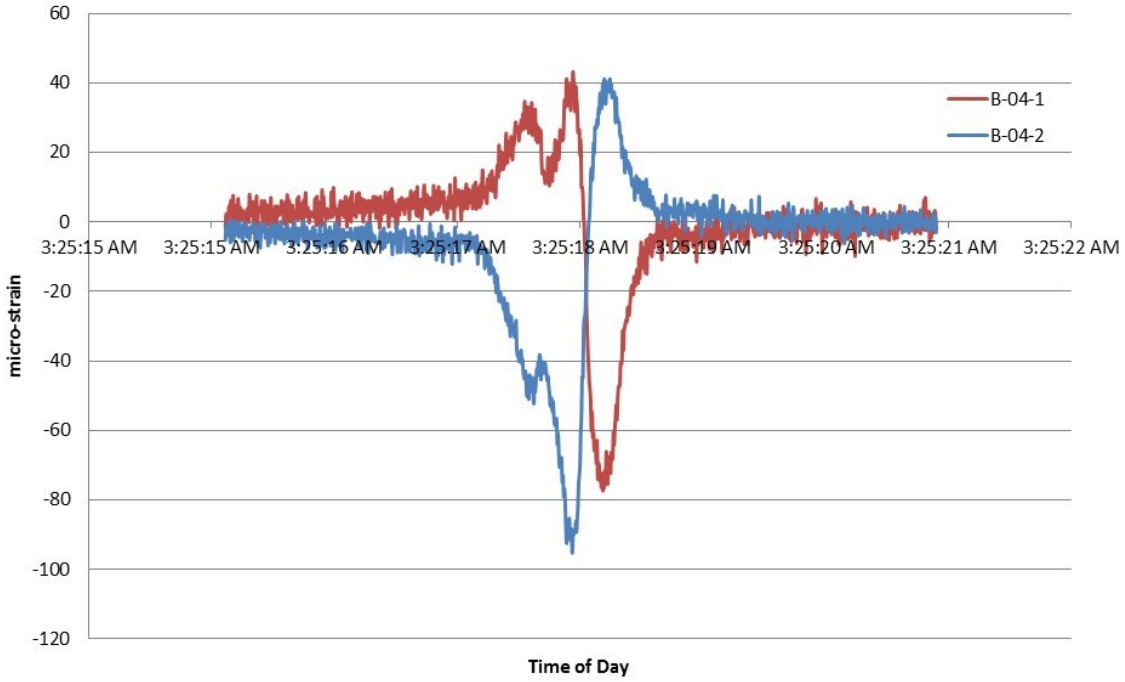

Figure B.3: Dynamic response of B-04 gauges with truck traveling in lane 4.

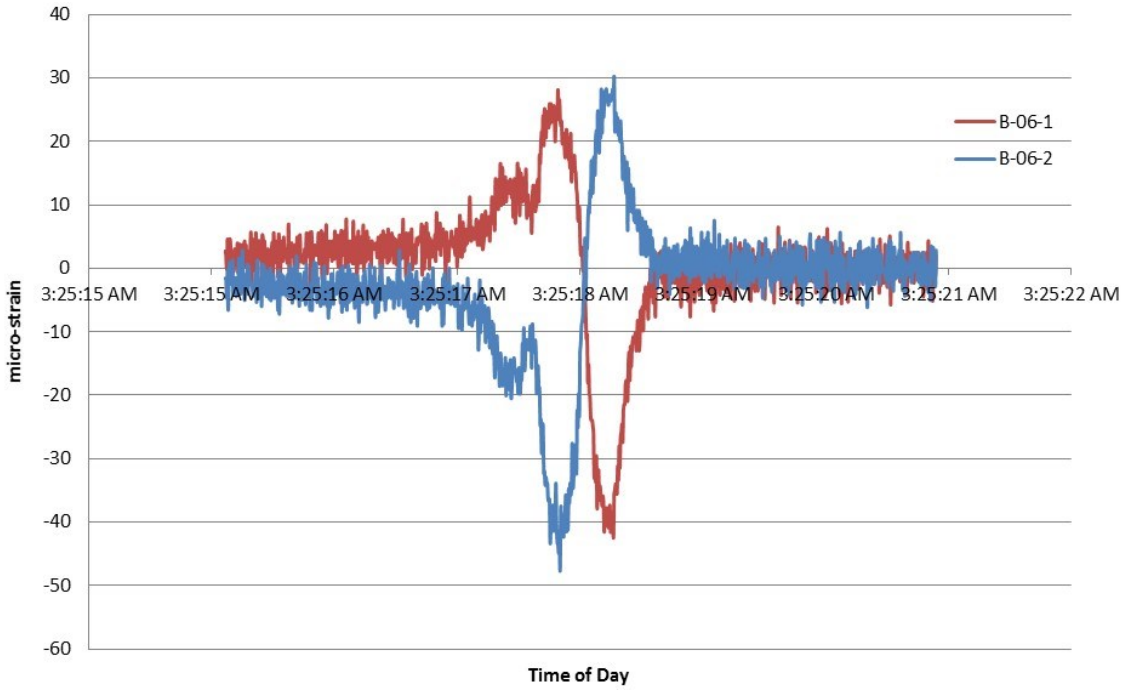

Figure B.4: Dynamic response of B-06 gauges with truck traveling in lane 4.

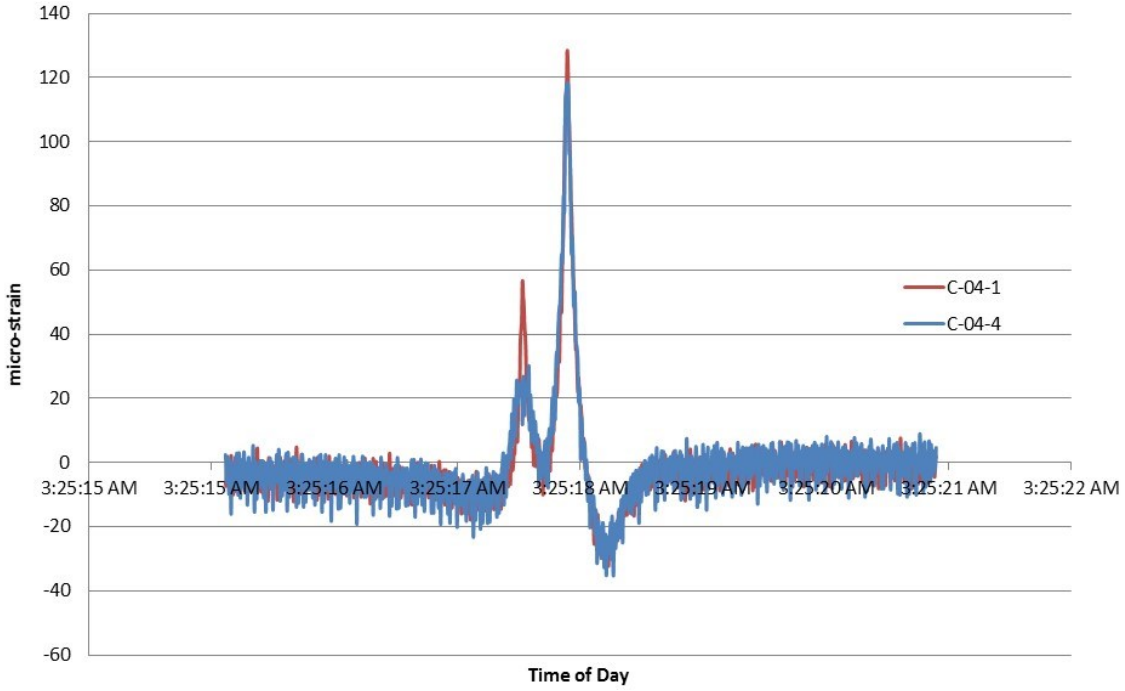

Figure B.5: Dynamic response of C-04 longitudinal gauges with truck traveling in lane 4.

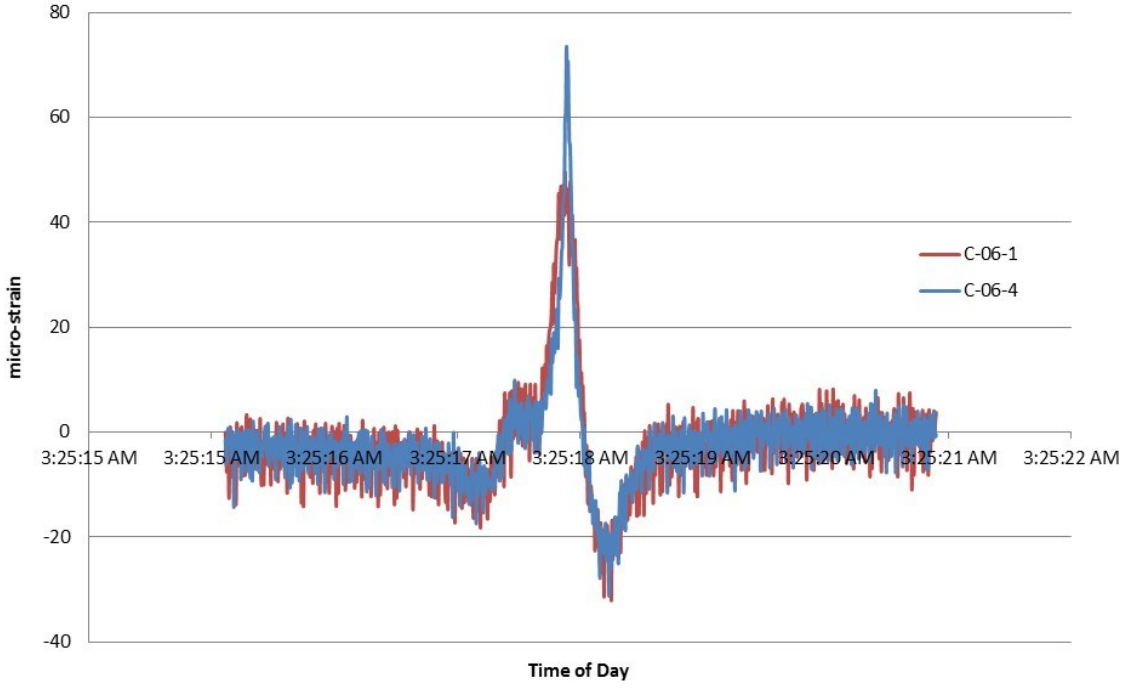

Figure B.6: Dynamic response of C-06 longitudinal gauges with truck traveling in lane 4.

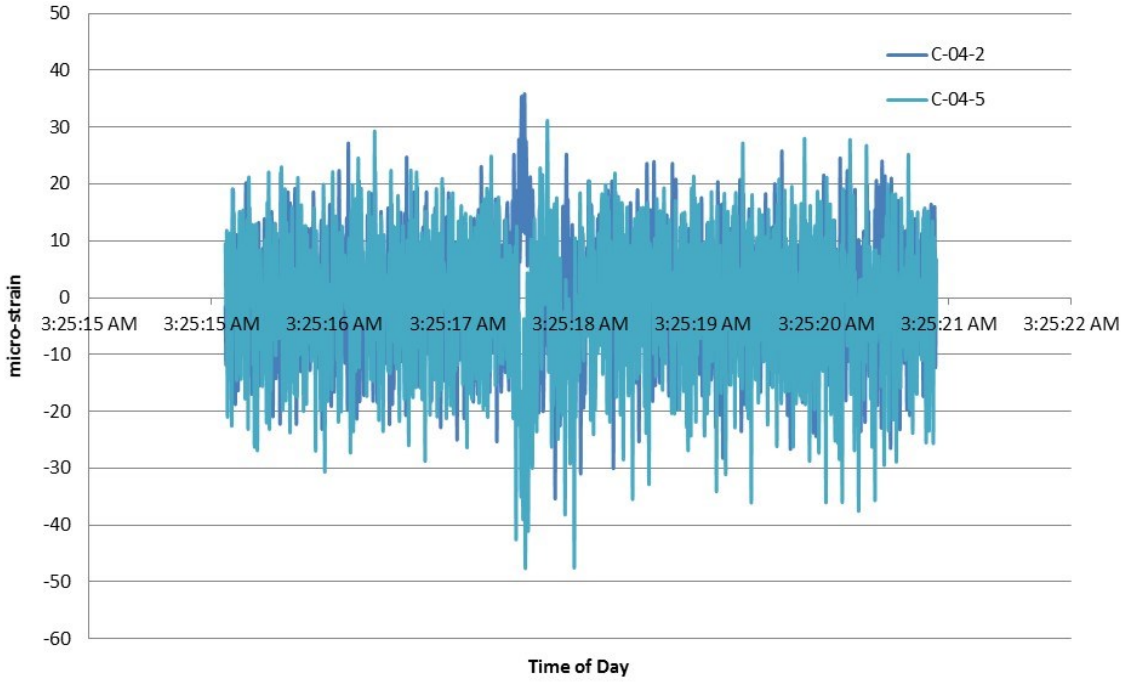

Figure B.7: Dynamic response of C-04 diagonal gauges with truck traveling in lane 4.

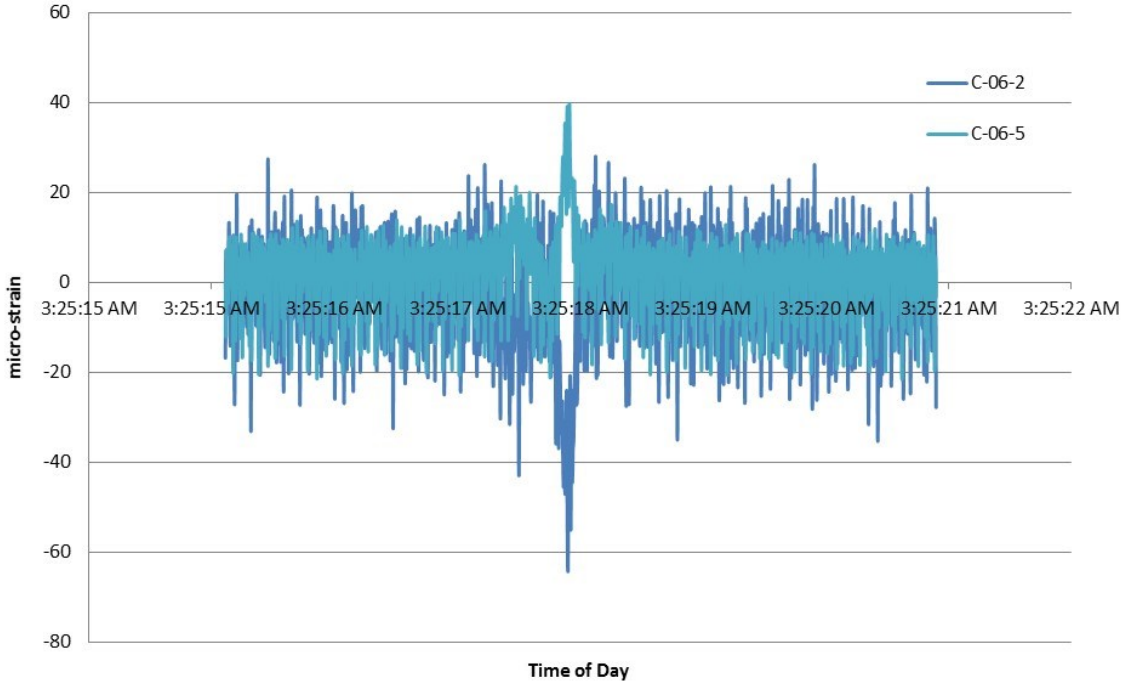

Figure B.8: Dynamic response of C-06 diagonal gauges with truck traveling in lane 4.

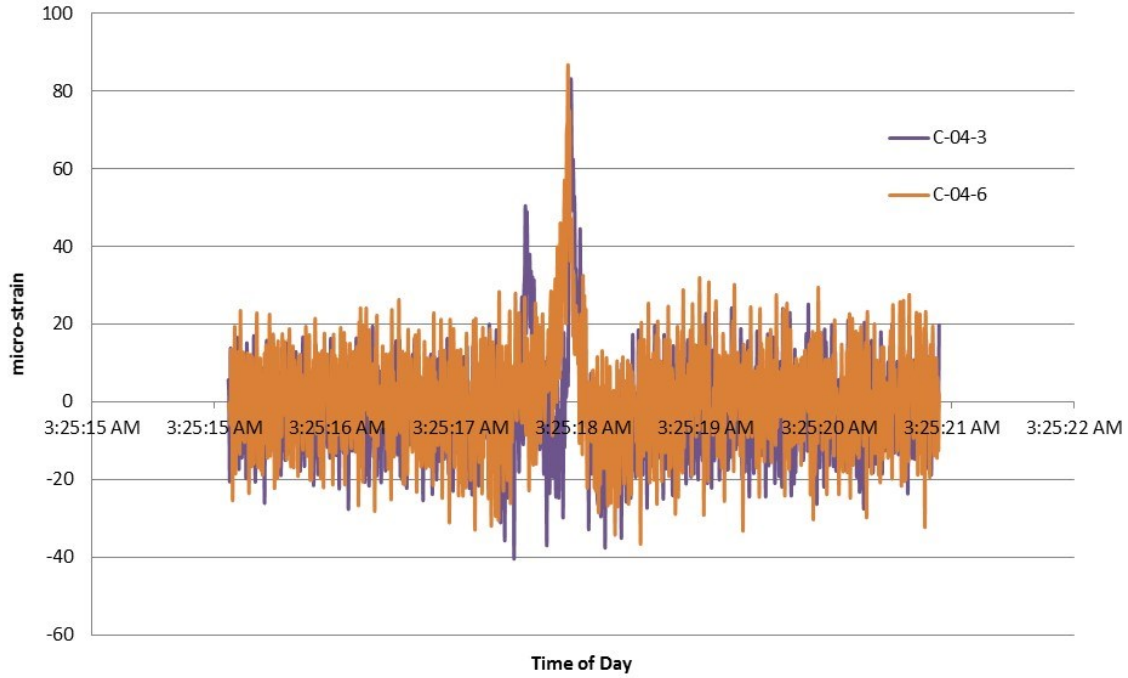

Figure B.9: Dynamic response of C-04 vertical gauges with truck traveling in lane 4.

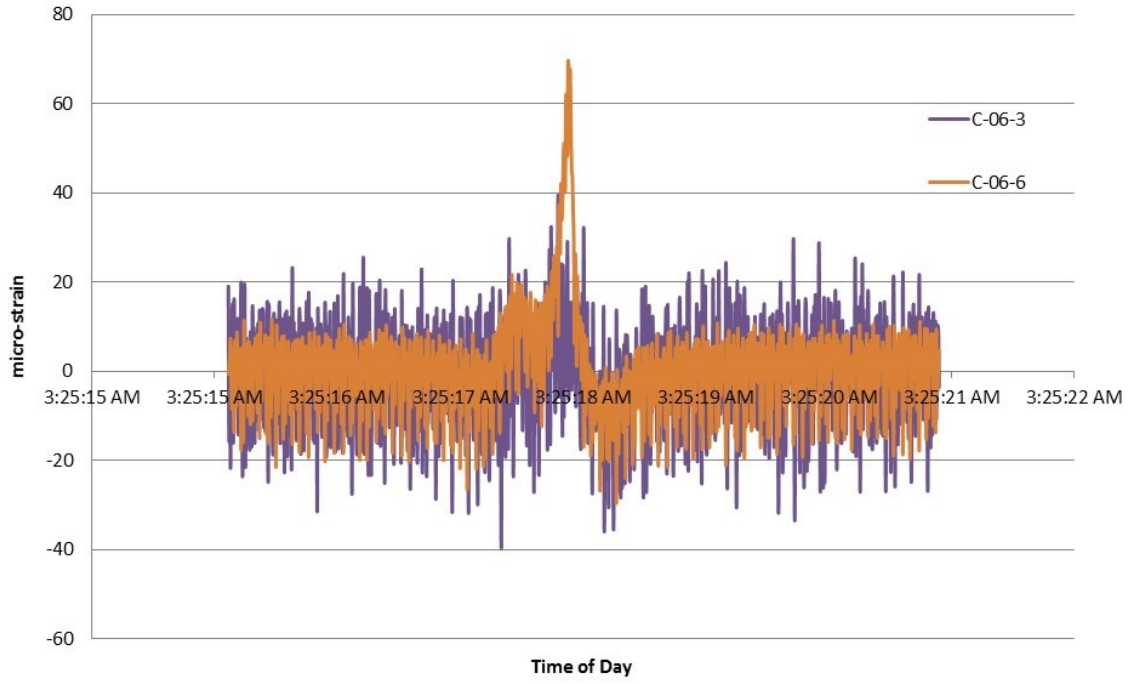

Figure B.10: Dynamic response of C-06 vertical gauges with truck traveling in lane 4.

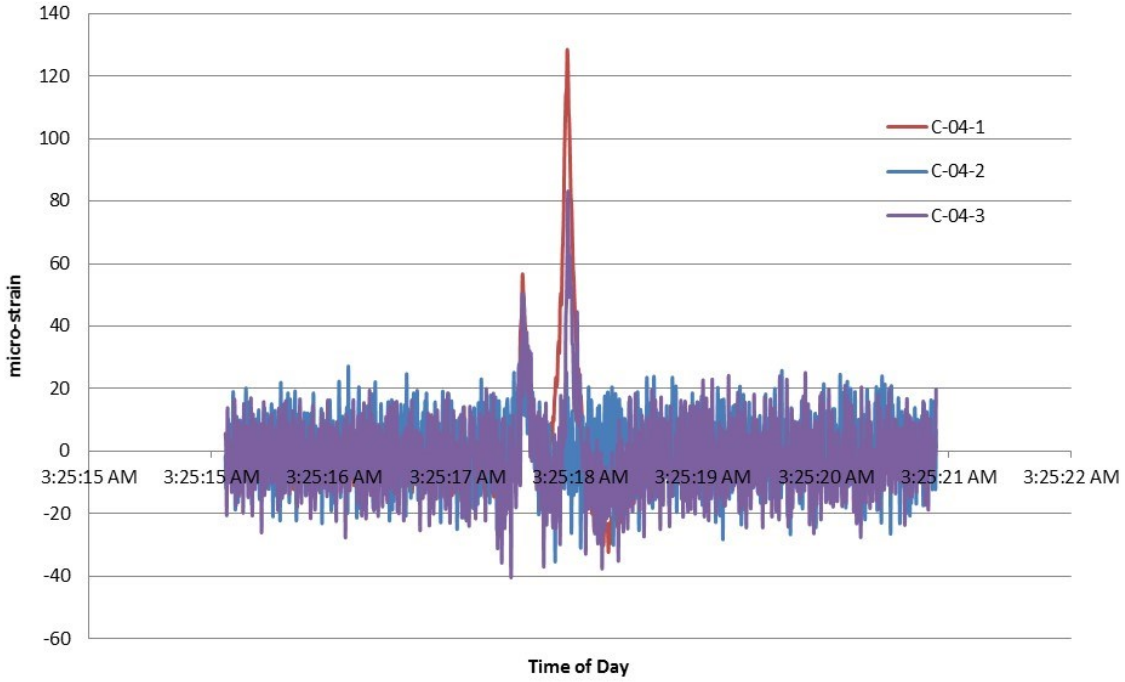

Figure B.11: Dynamic response of C-04-1 rosette with truck traveling in lane 4.

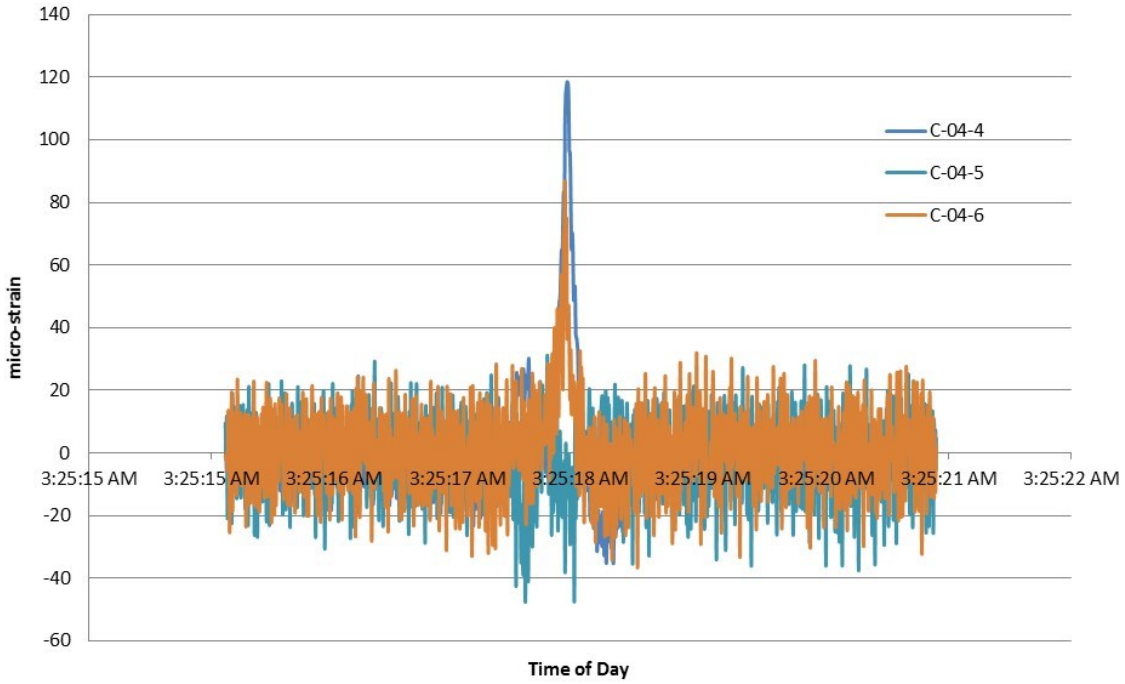

Figure B.12: Dynamic response of C-04-4 rosette with truck traveling in lane 4.

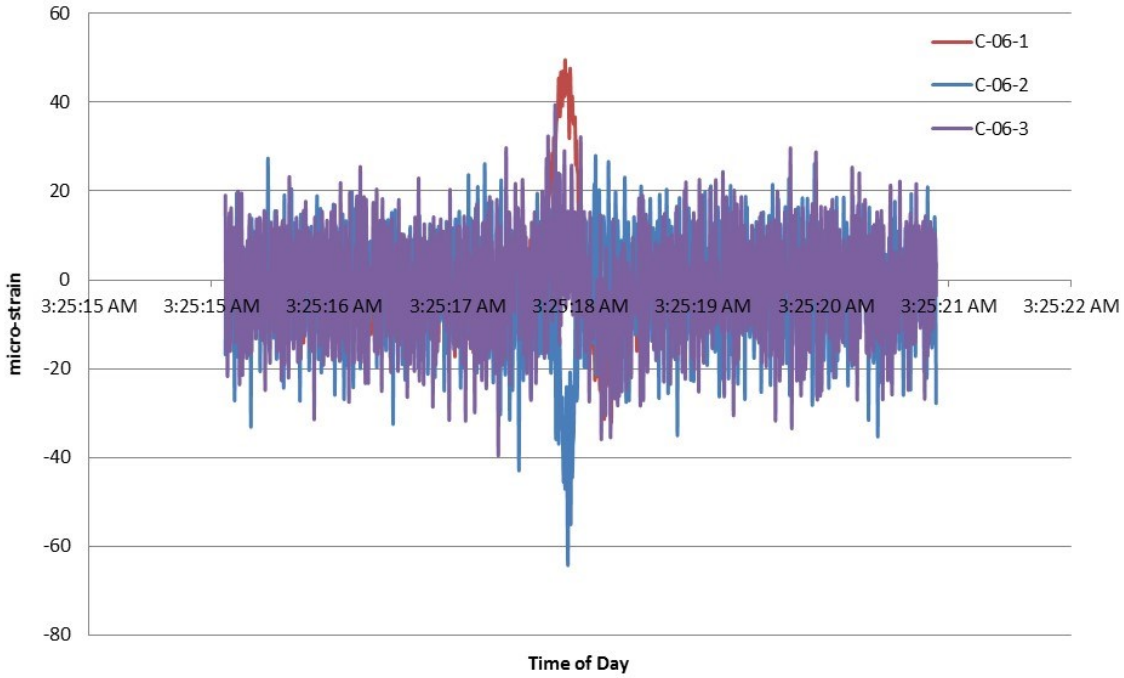

Figure B.13: Dynamic response of C-06-1 rosette with truck traveling in lane 4.

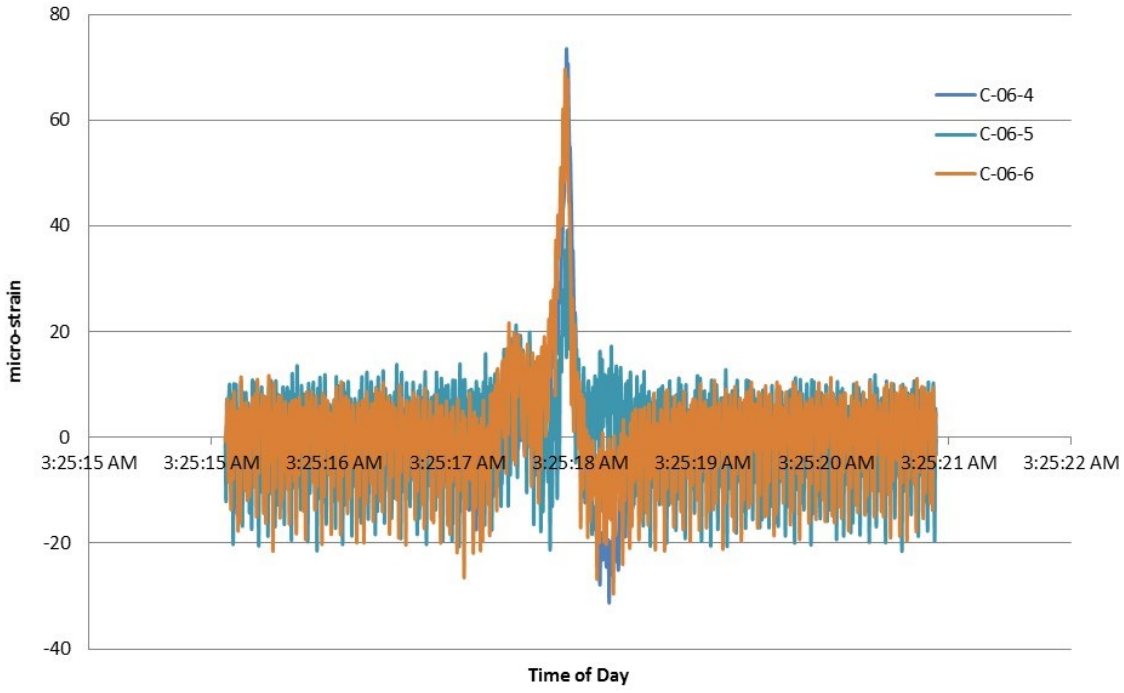

Figure B.14: Dynamic response of C-06-4 rosette with truck traveling in lane 4.

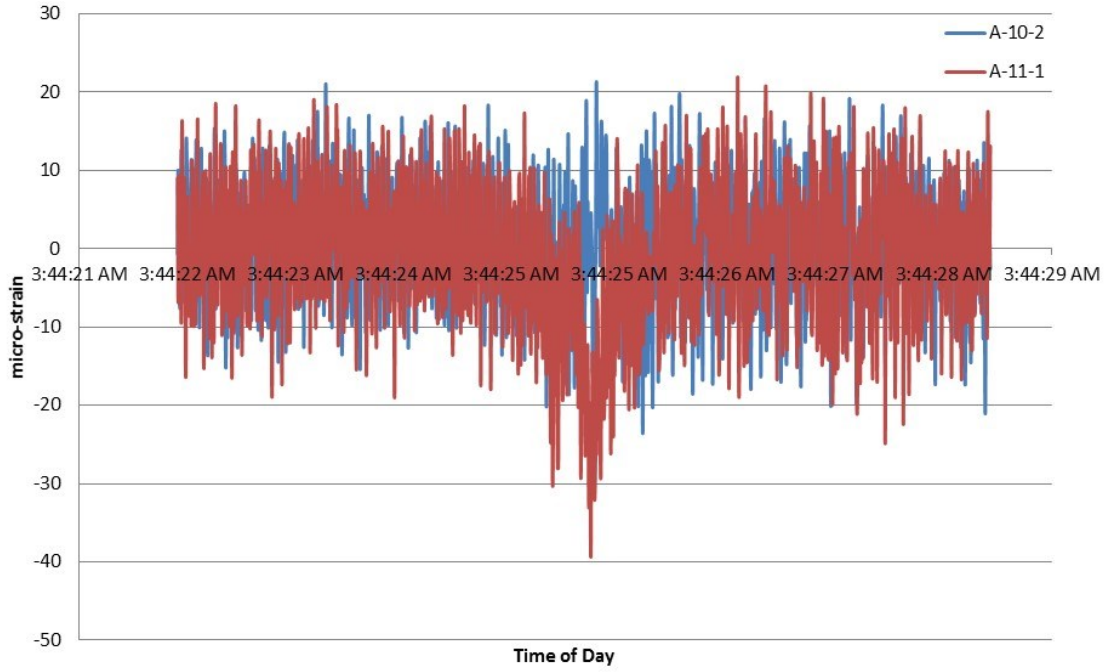

Figure B.15: Dynamic response of A-10/11 gauges with truck traveling in lane 3.

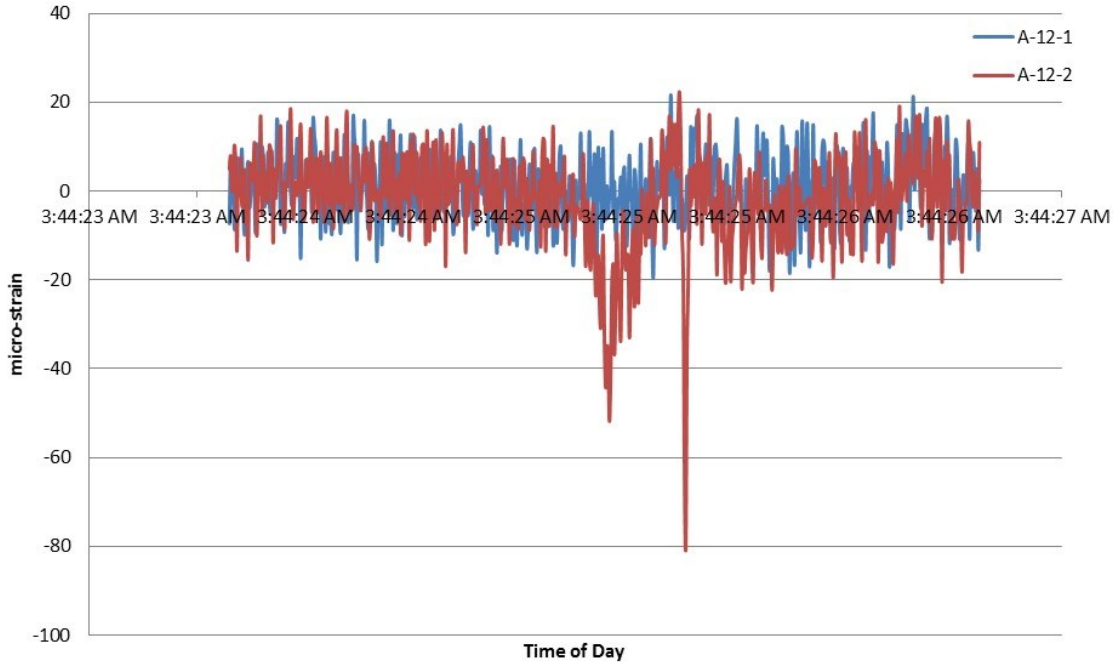

Figure B.16: Dynamic response of A-12 gauges with truck traveling in lane 3.

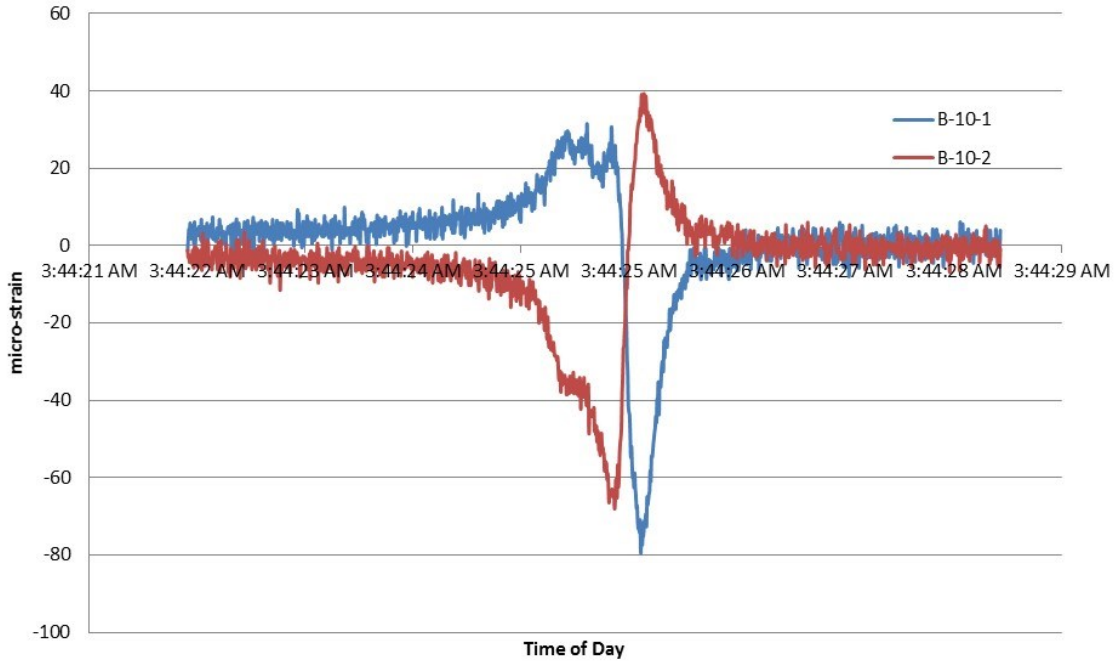

Figure B.17: Dynamic response of B-10 gauges with truck traveling in lane 3.

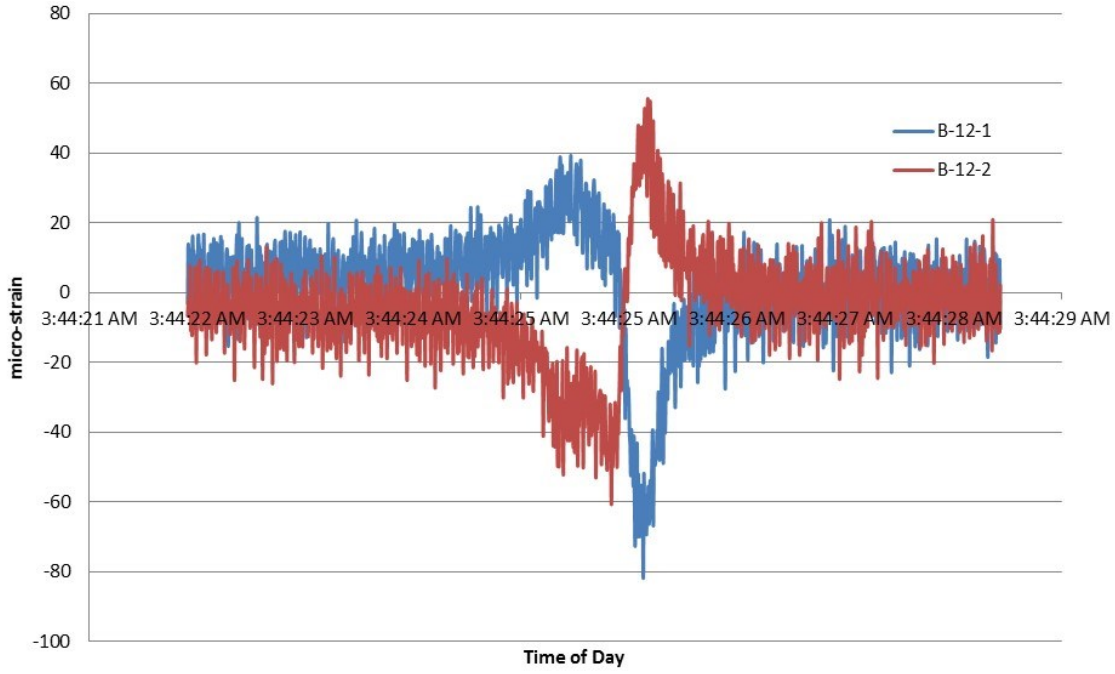

Figure B.18: Dynamic response of B-12 gauges with truck traveling in lane 3.

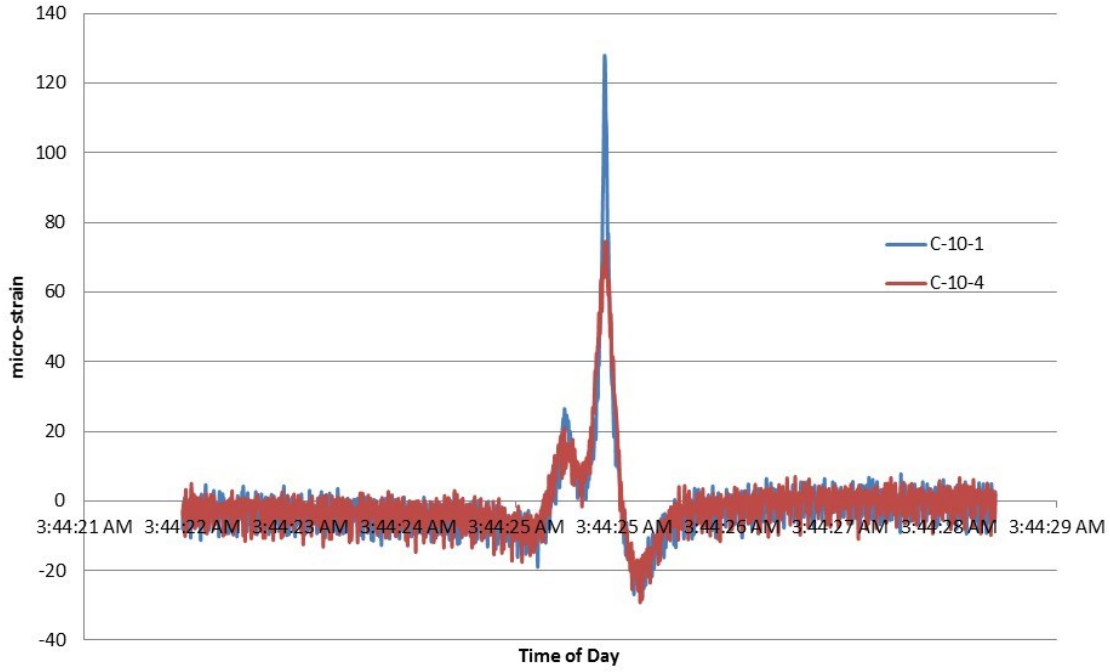

Figure B.19: Dynamic response of C-10 longitudinal gauges with truck traveling in lane 3.

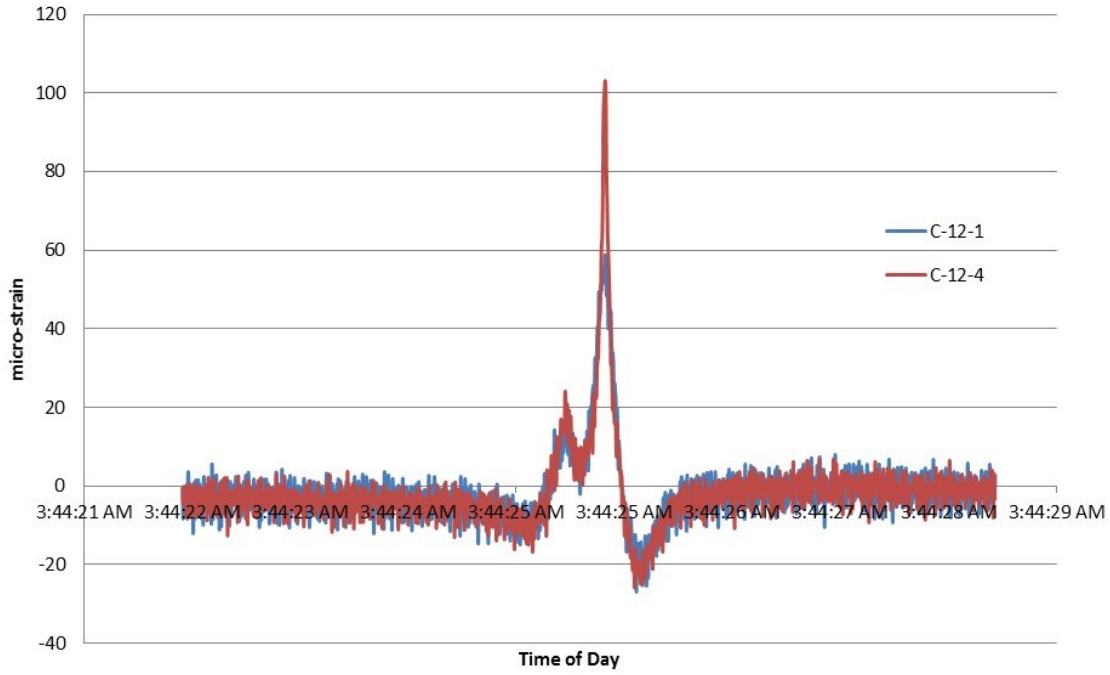

Figure B.20: Dynamic response of C-12 longitudinal gauges with truck traveling in lane 3.

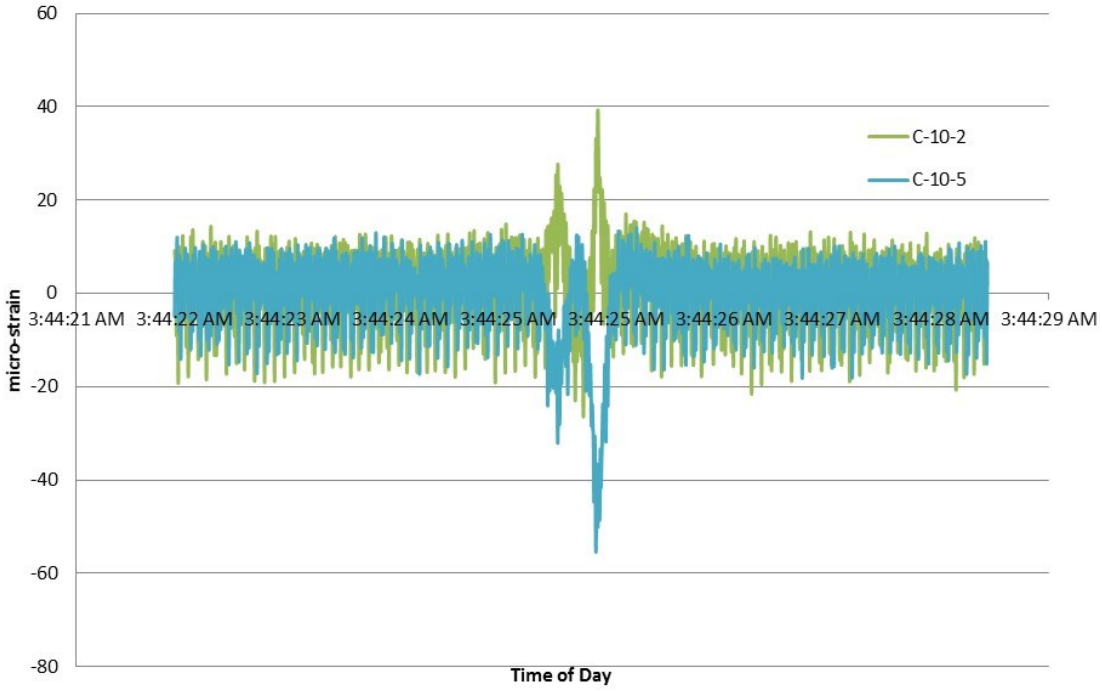

Figure B.21: Dynamic response of C-10 diagonal gauges with truck traveling in lane 3.

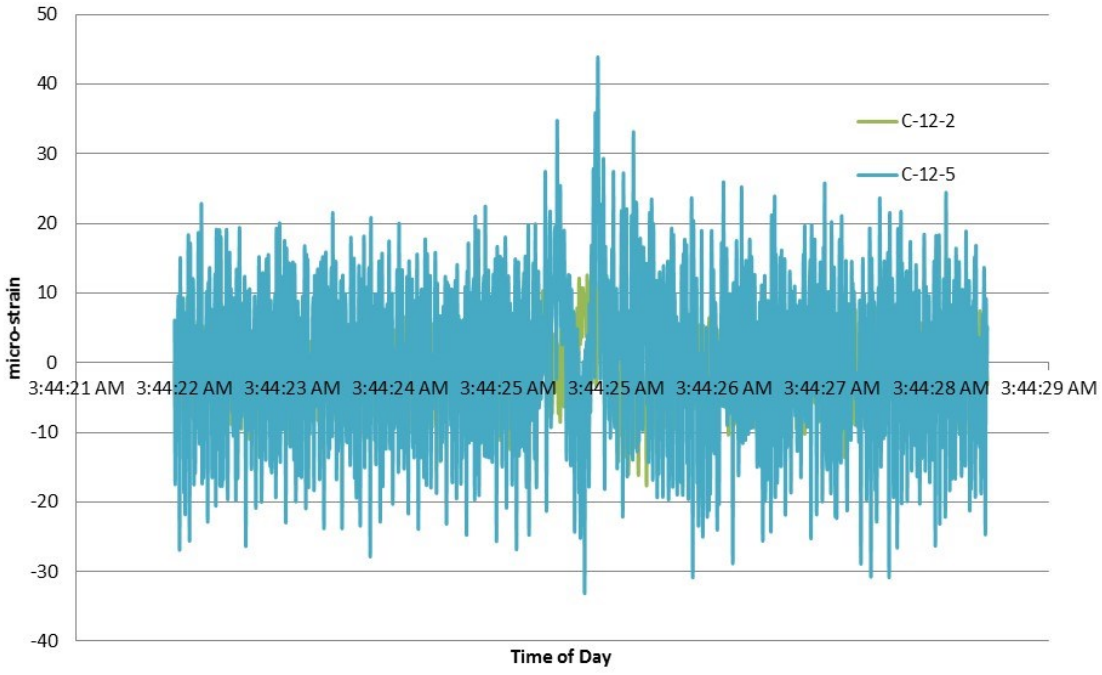

Figure B.22: Dynamic response of C-12 diagonal gauges with truck traveling in lane 3.

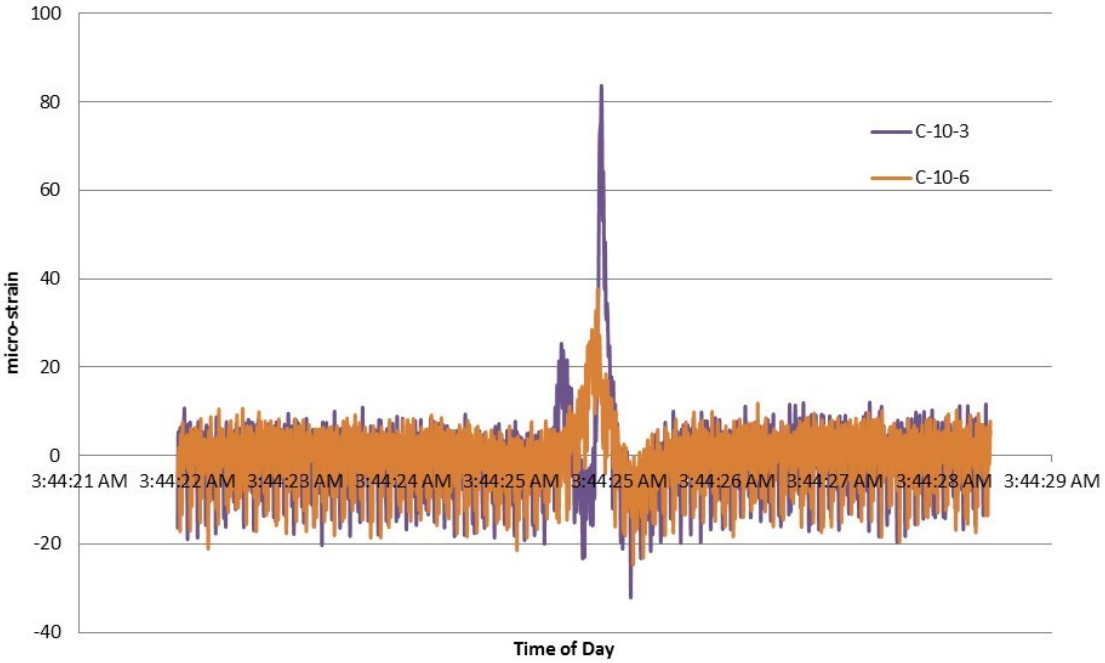

Figure B.23: Dynamic response of C-10 vertical gauges with truck traveling in lane 3.

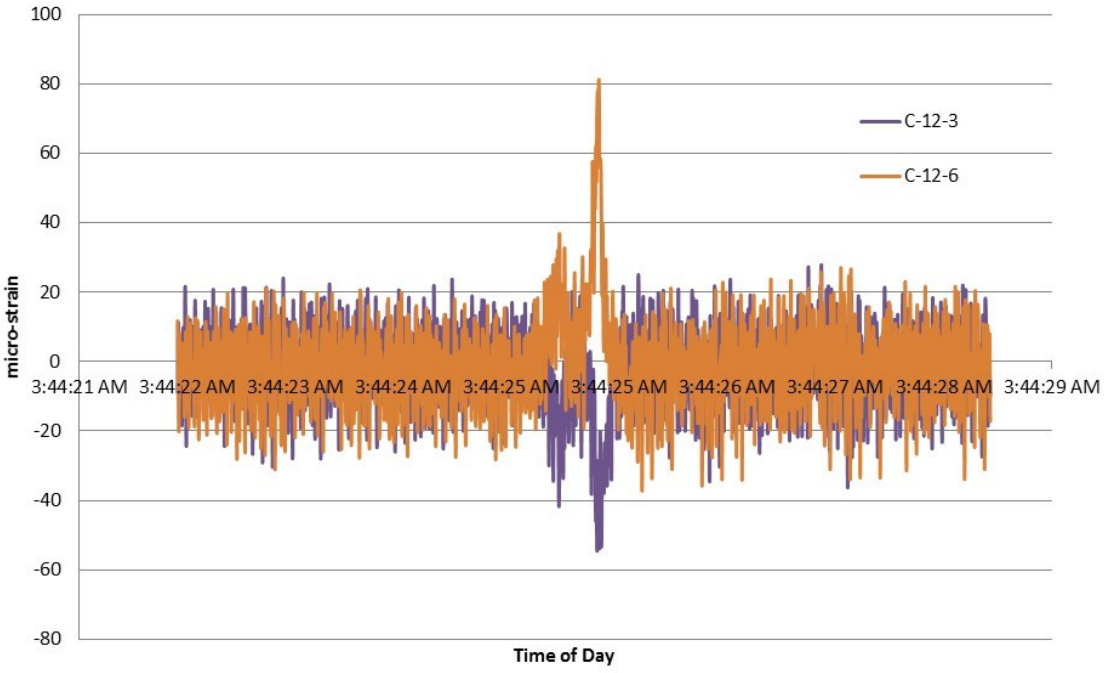

Figure B.24: Dynamic response of C-12 vertical gauges with truck traveling in lane 3.

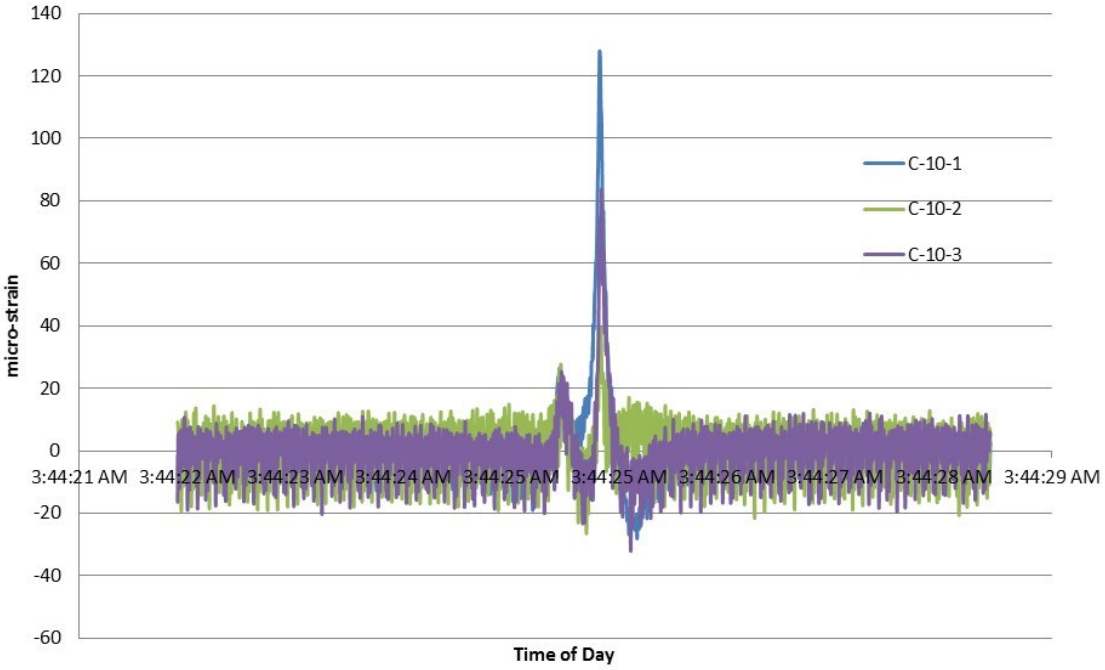

Figure B.25: Dynamic response of C-10-1 rosette with truck traveling in lane 3.

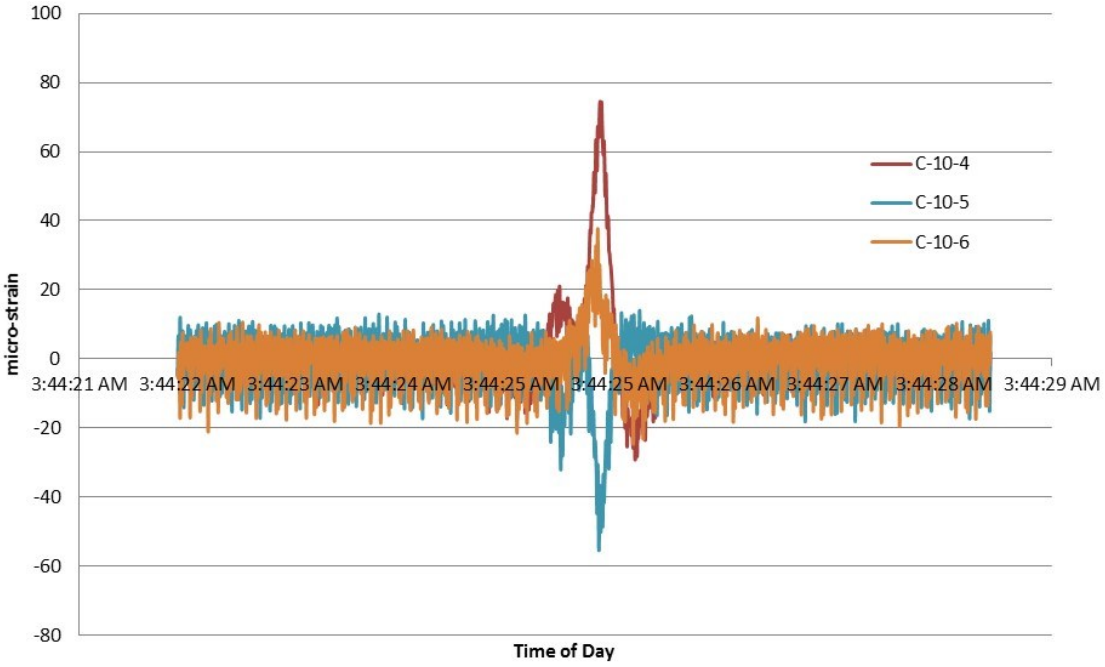

Figure B.26: Dynamic response of C-10-4 rosette with truck traveling in lane 3.

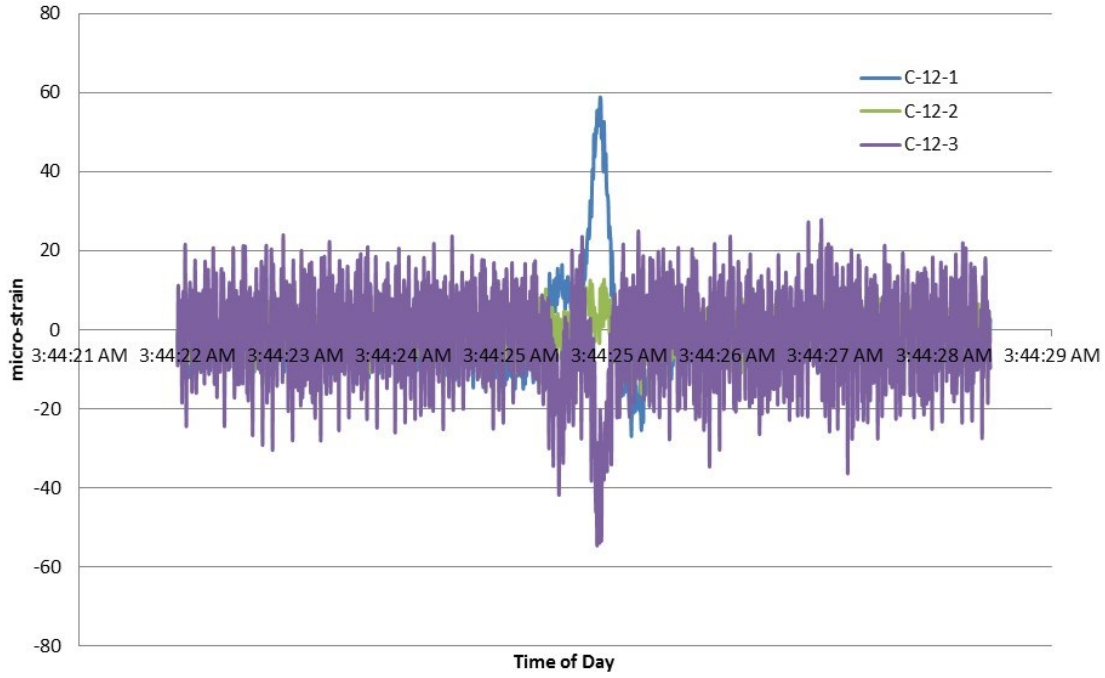

Figure B.27: Dynamic response of C-12-1 rosette with truck traveling in lane 3.

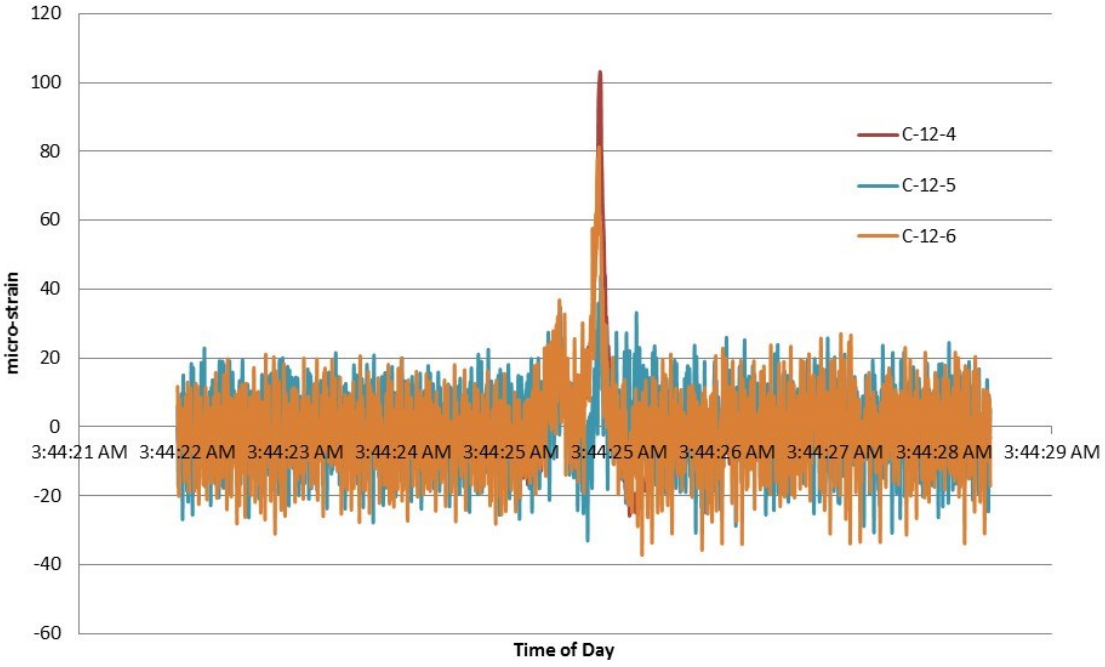

Figure B.28: Dynamic response of C-12-4 rosette with truck traveling in lane 3.

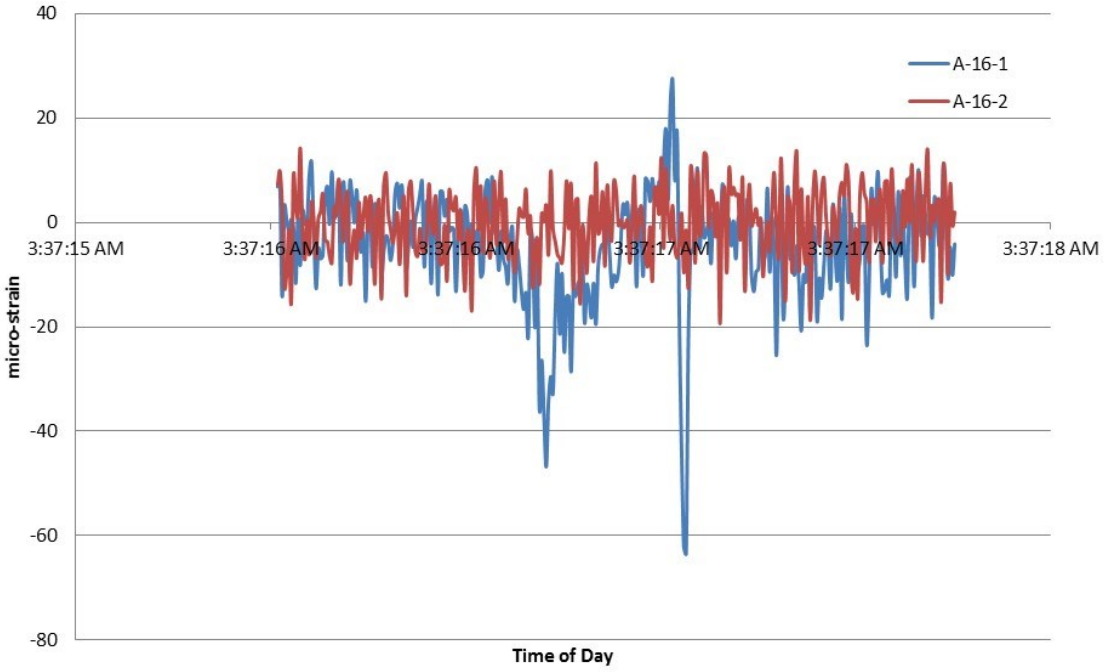

Figure B.29: Dynamic response of A-16 gauges with truck traveling in lane 2.

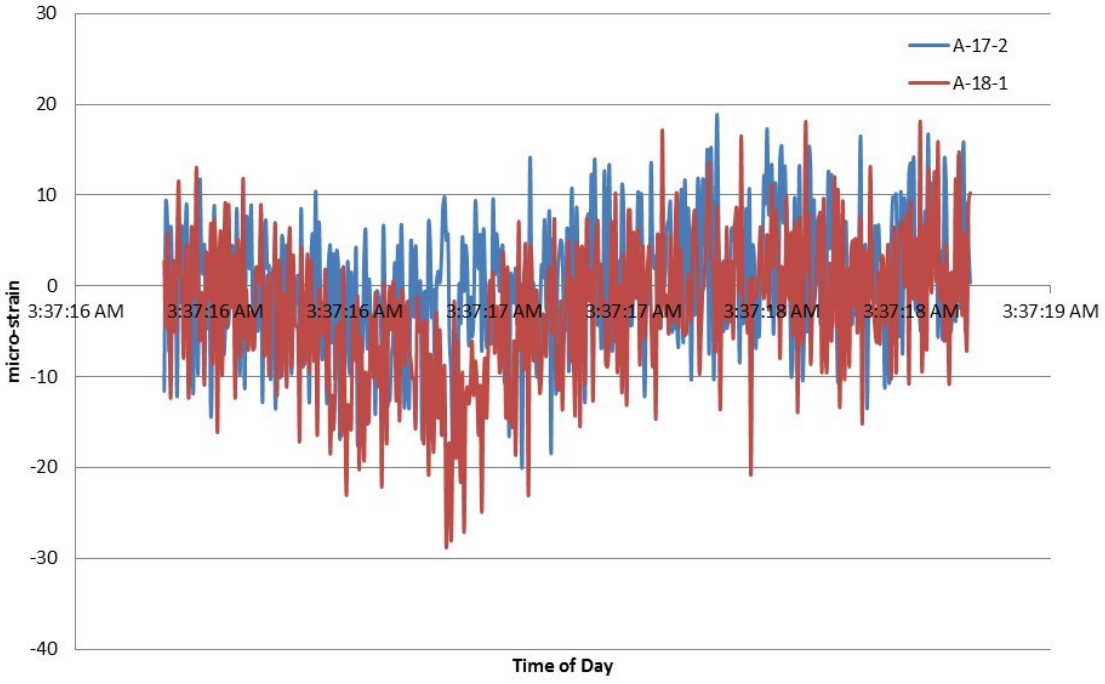

Figure B.30: Dynamic response of A-17/18 gauges with truck traveling in lane 2.

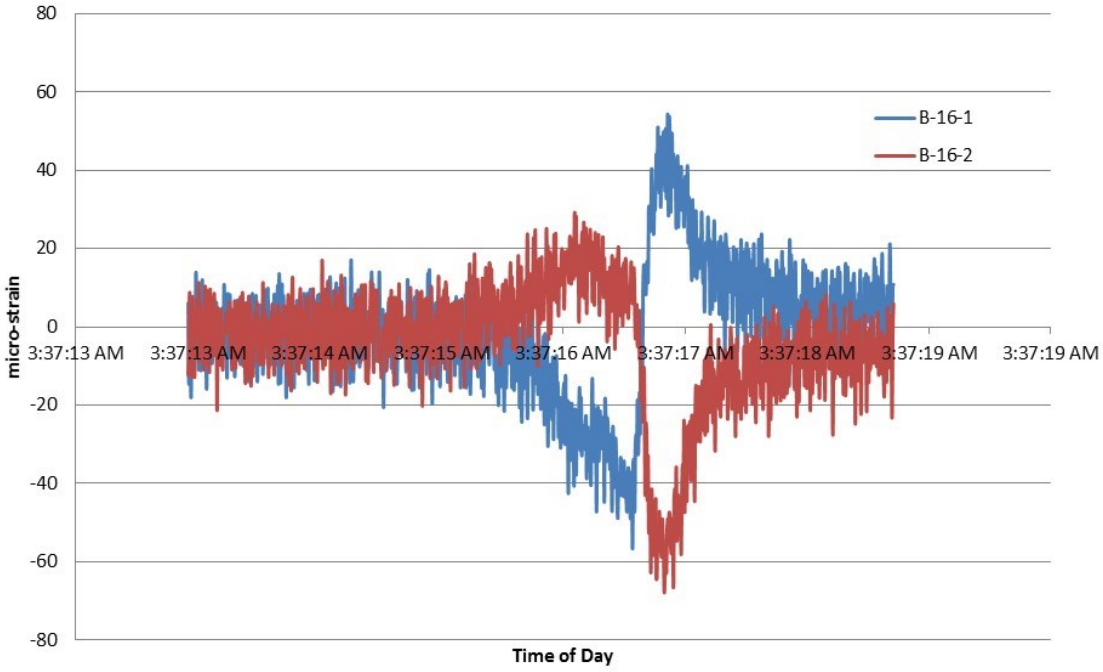

Figure B.31: Dynamic response of B-16 gauges with truck traveling in lane 2.

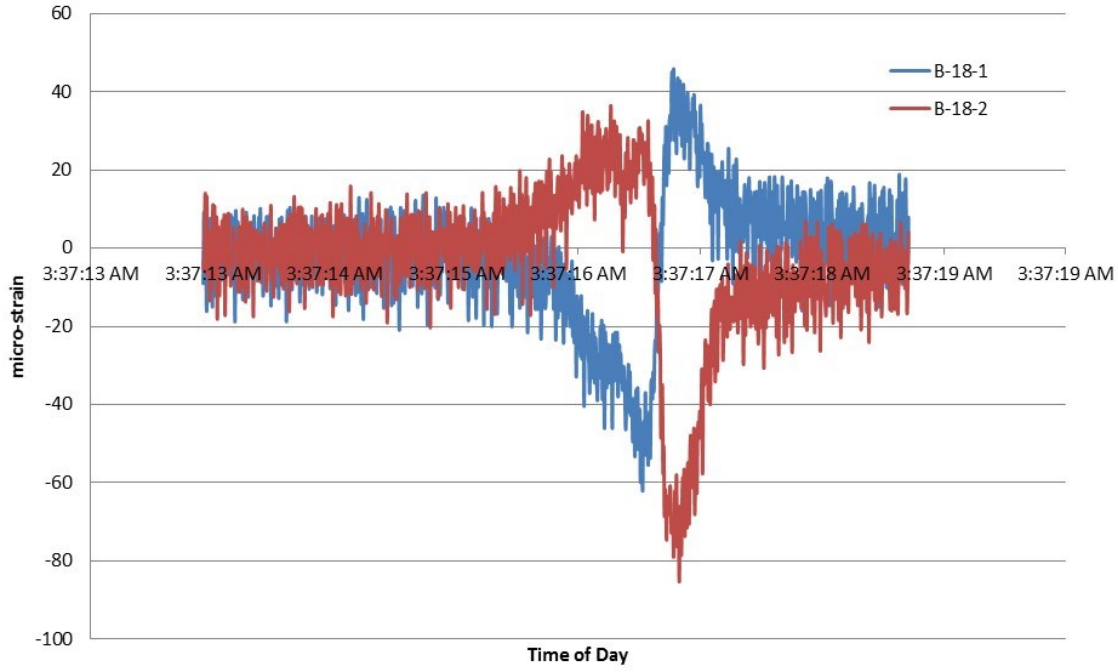

Figure B.32: Dynamic response of B-18 gauges with truck traveling in lane 2.

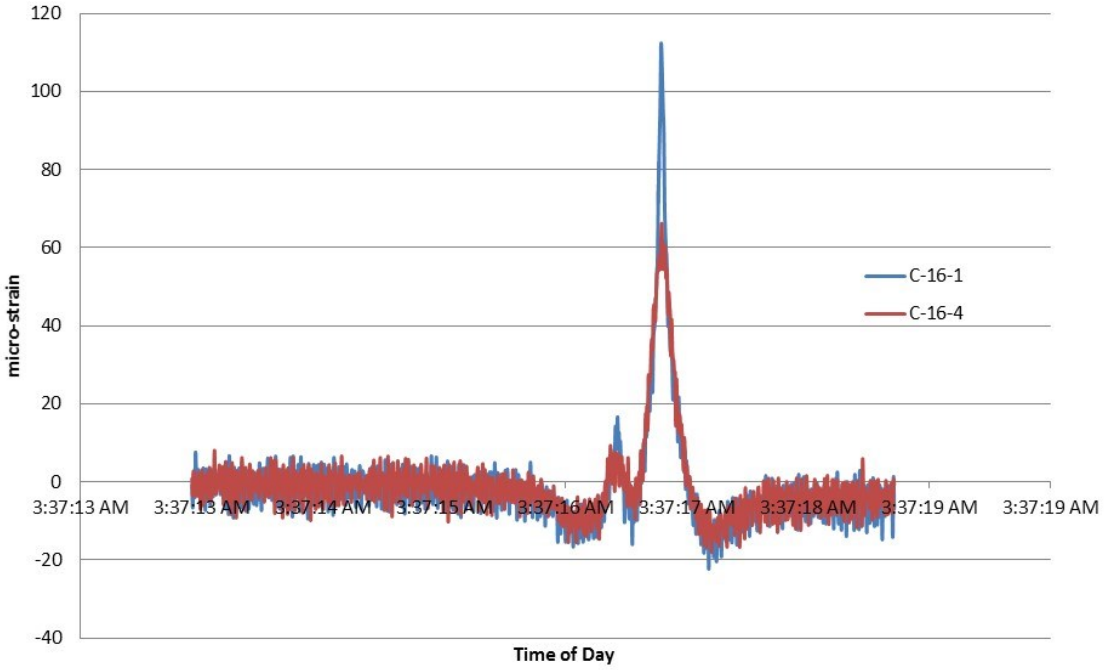

Figure B.33: Dynamic response of C-16 longitudinal gauges with truck traveling in lane 2.

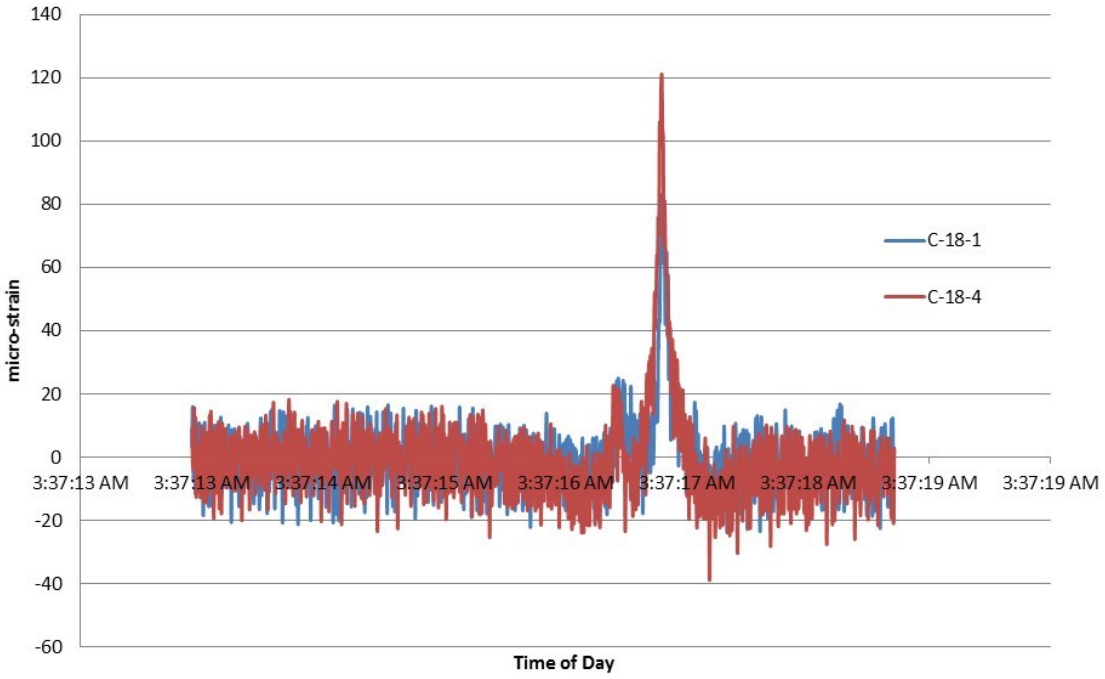

Figure B.34: Dynamic response of C-18 longitudinal gauges with truck traveling in lane 2.

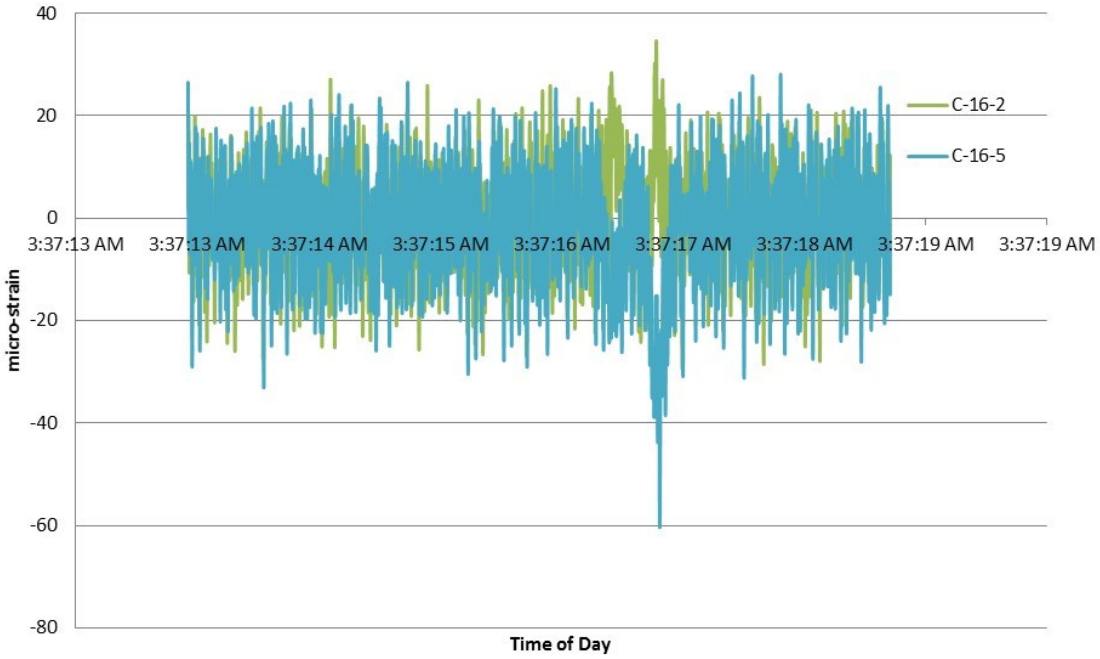

Figure B.35: Dynamic response of C-16 diagonal gauges with truck traveling in lane 2.

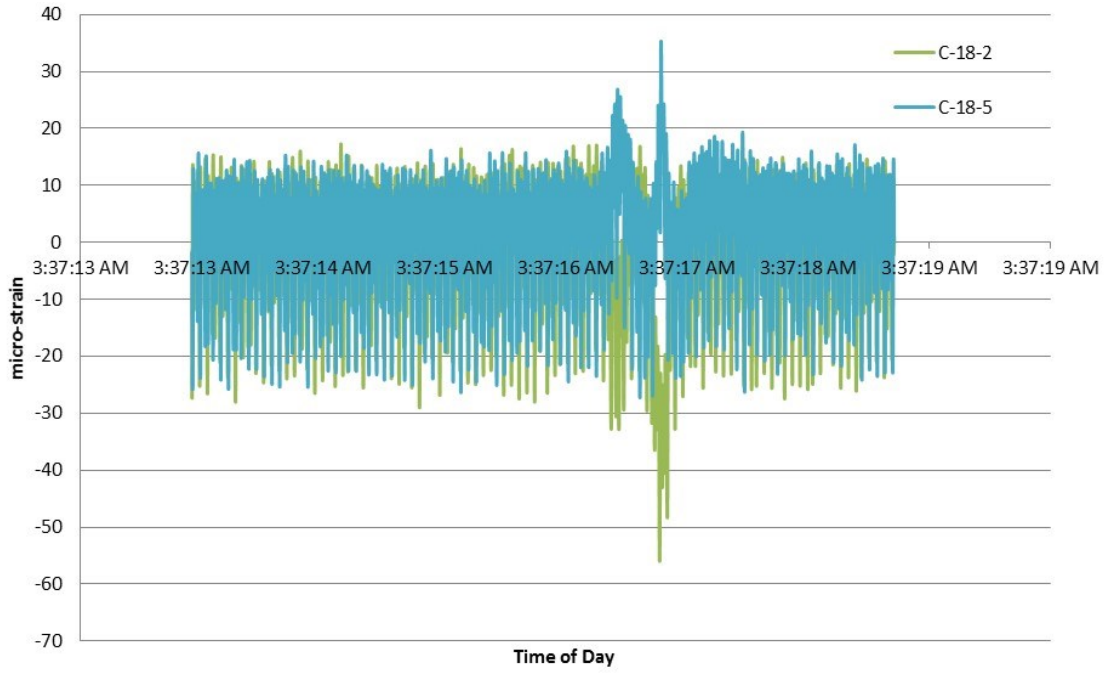

Figure B.36: Dynamic response of C-18 diagonal gauges with truck traveling in lane 2.

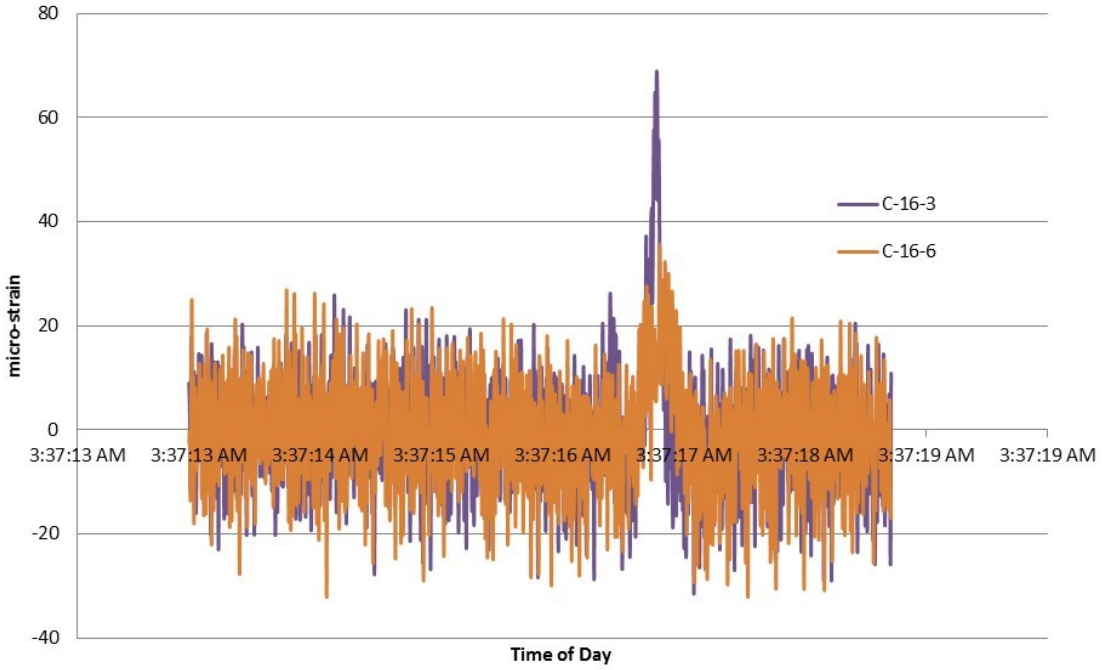

Figure B.37: Dynamic response of C-16 vertical gauges with truck traveling in lane 2.

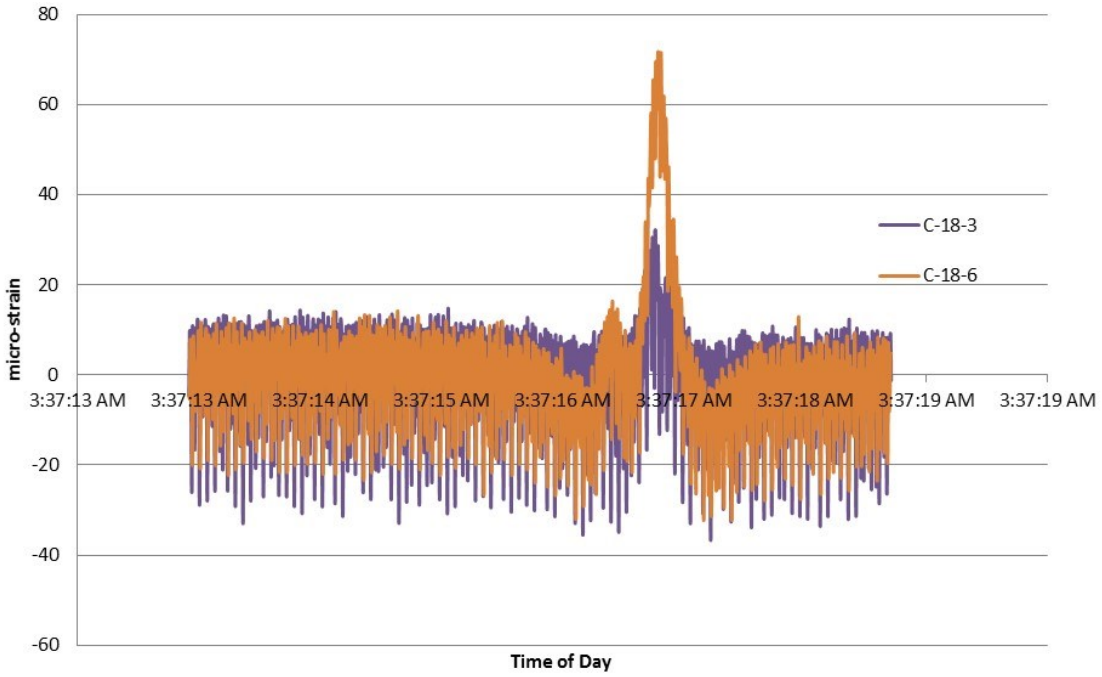

Figure B.38: Dynamic response of C-18 vertical gauges with truck traveling in lane 2.

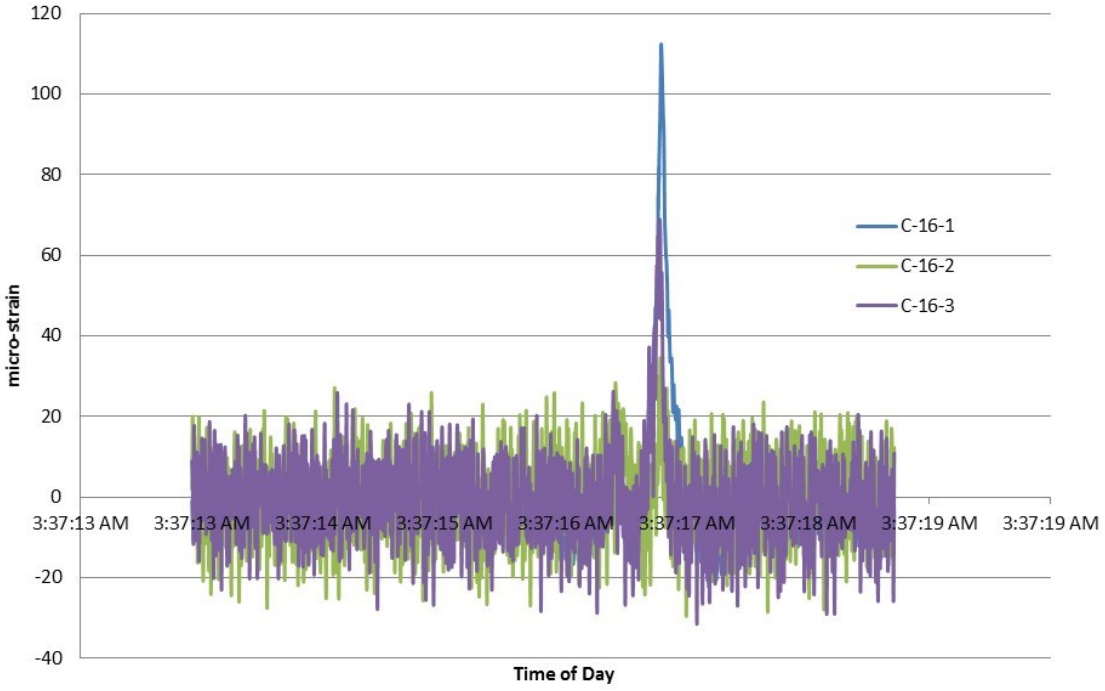

Figure B.39: Dynamic response of C-16-1 rosette with truck traveling in lane 2.

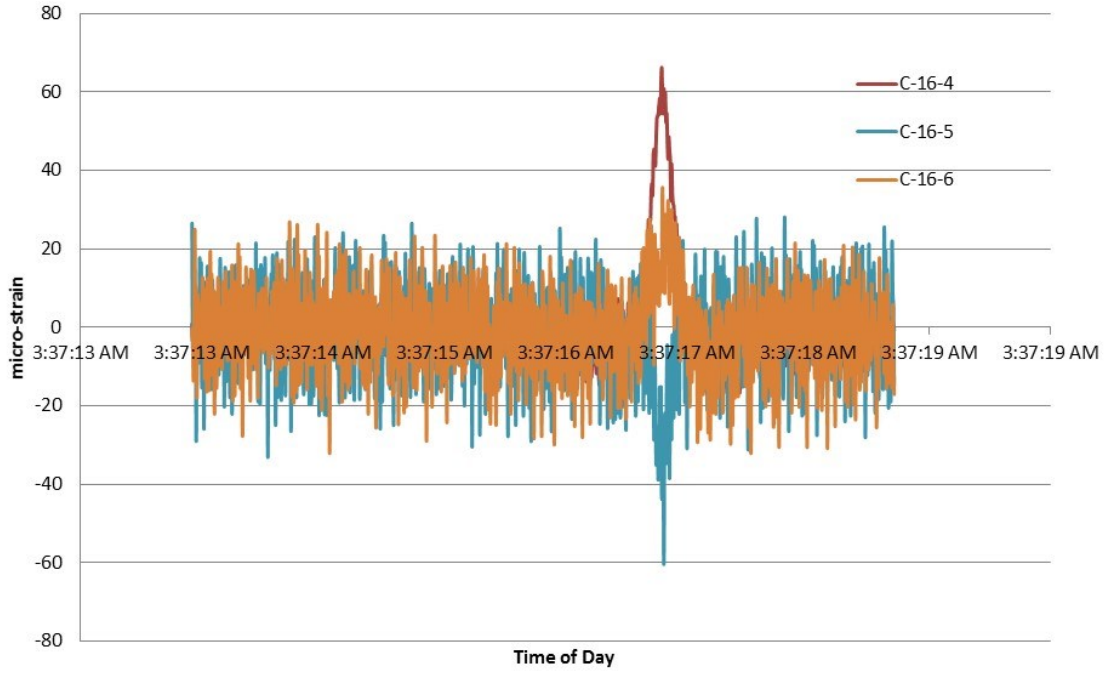

Figure B.40: Dynamic response of C-16-4 rosette with truck traveling in lane 2.

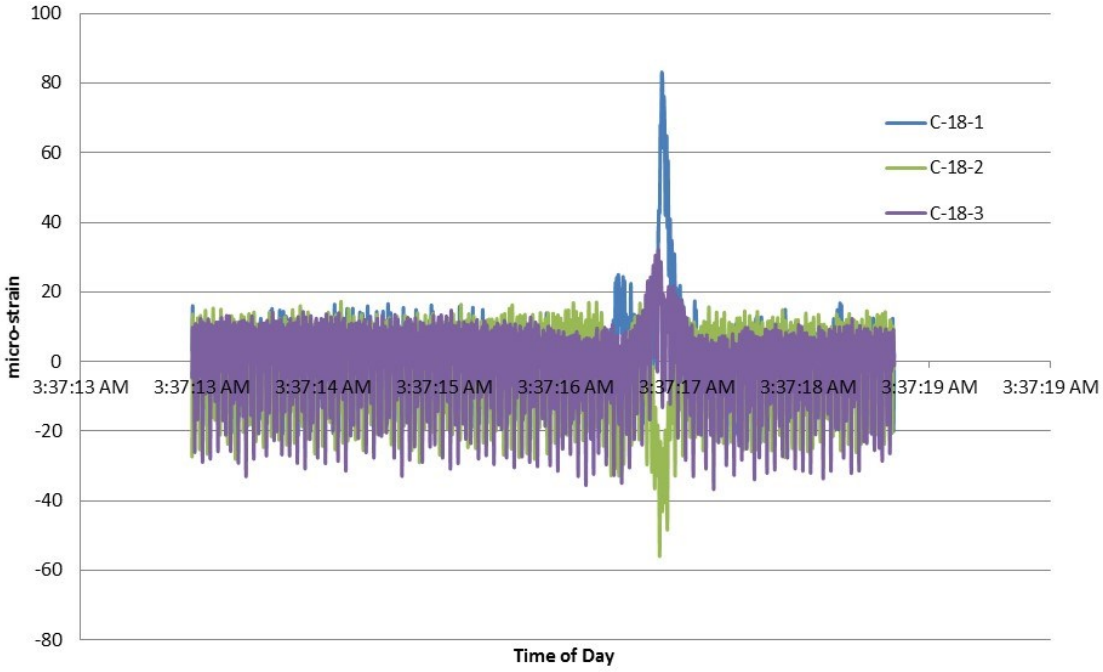

Figure B.41: Dynamic response of C-18-1 rosette with truck traveling in lane 2.

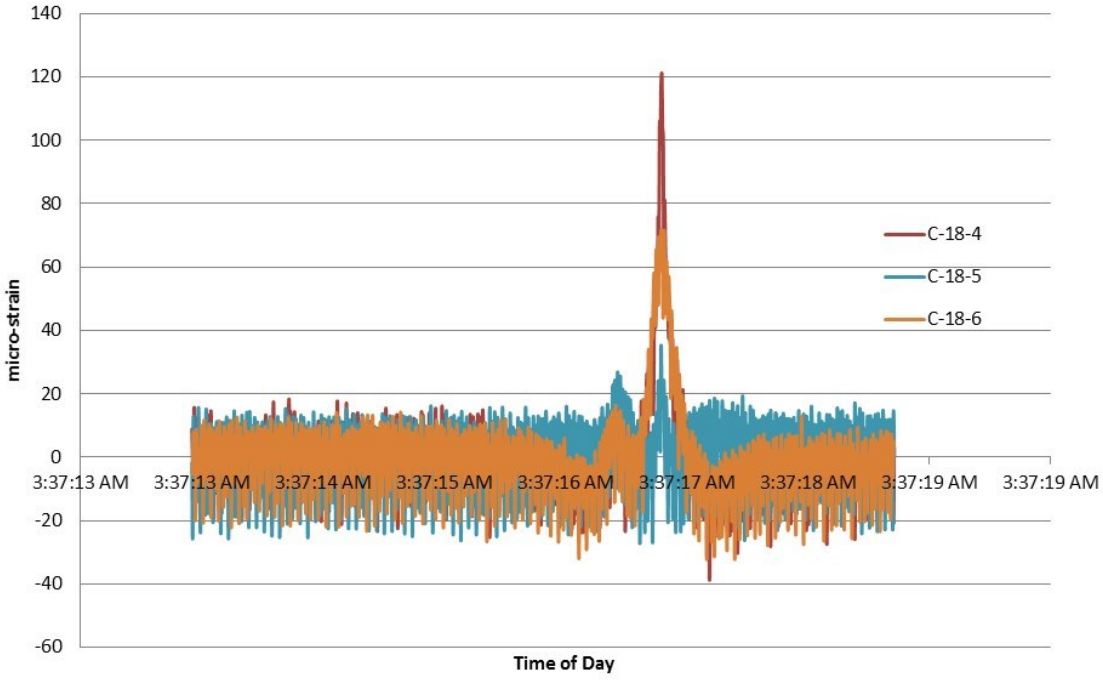

Figure B.42: Dynamic response of C-18-4 rosette with truck traveling in lane 2.

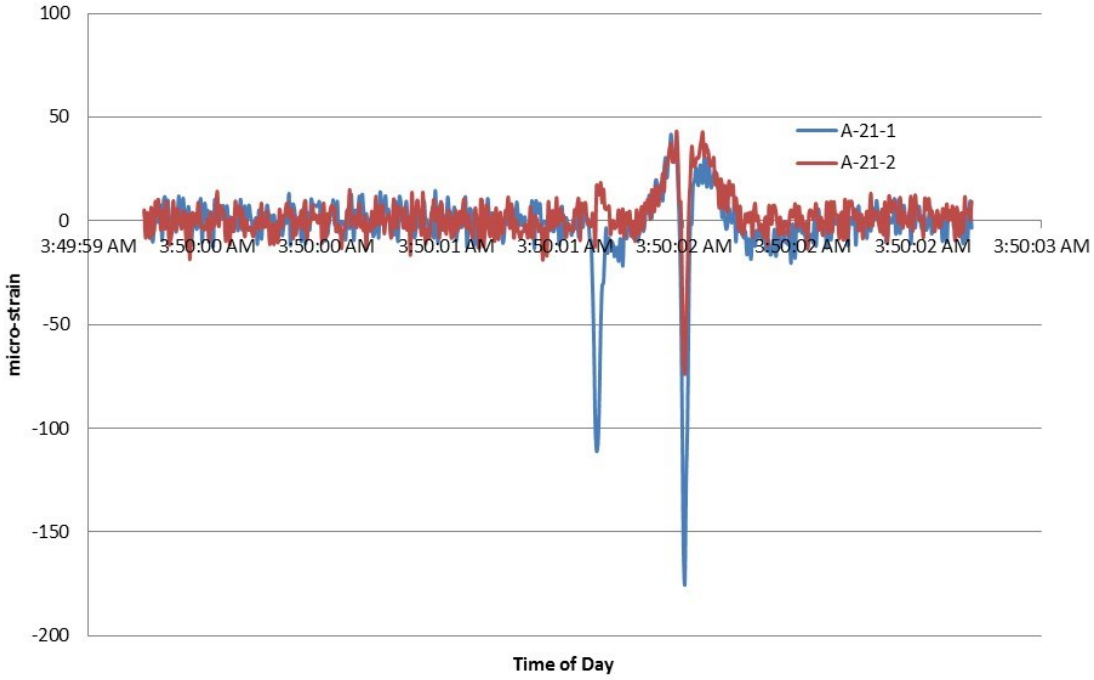

Figure B.43: Dynamic response of A-21 gauges with truck traveling in lane 1.

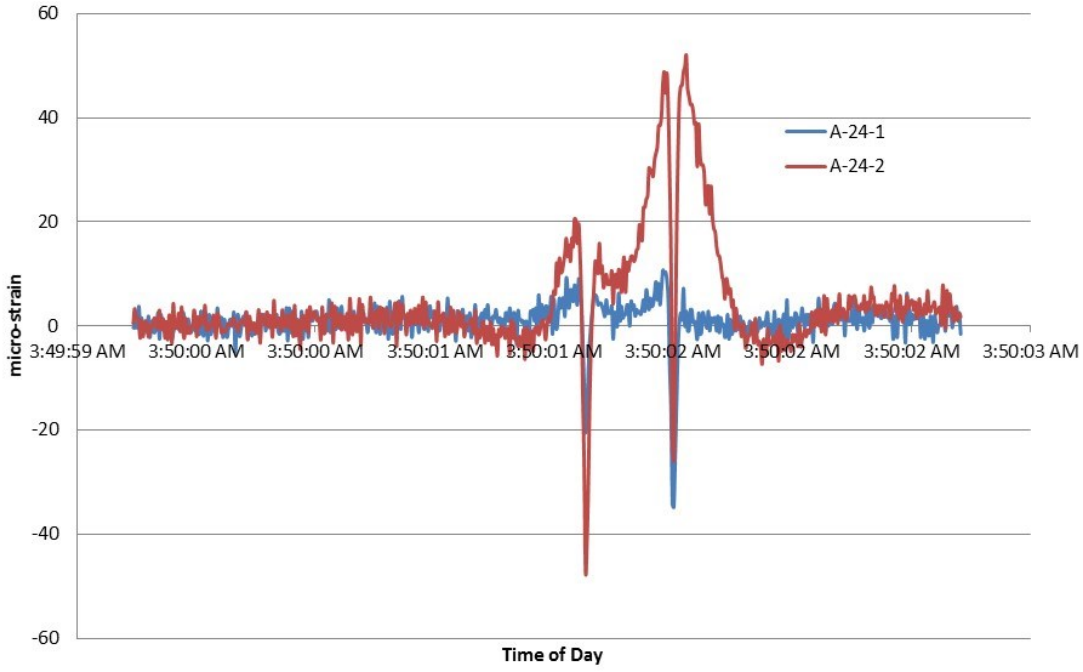

Figure B.44: Dynamic response of A-24 gauges with truck traveling in lane 1.

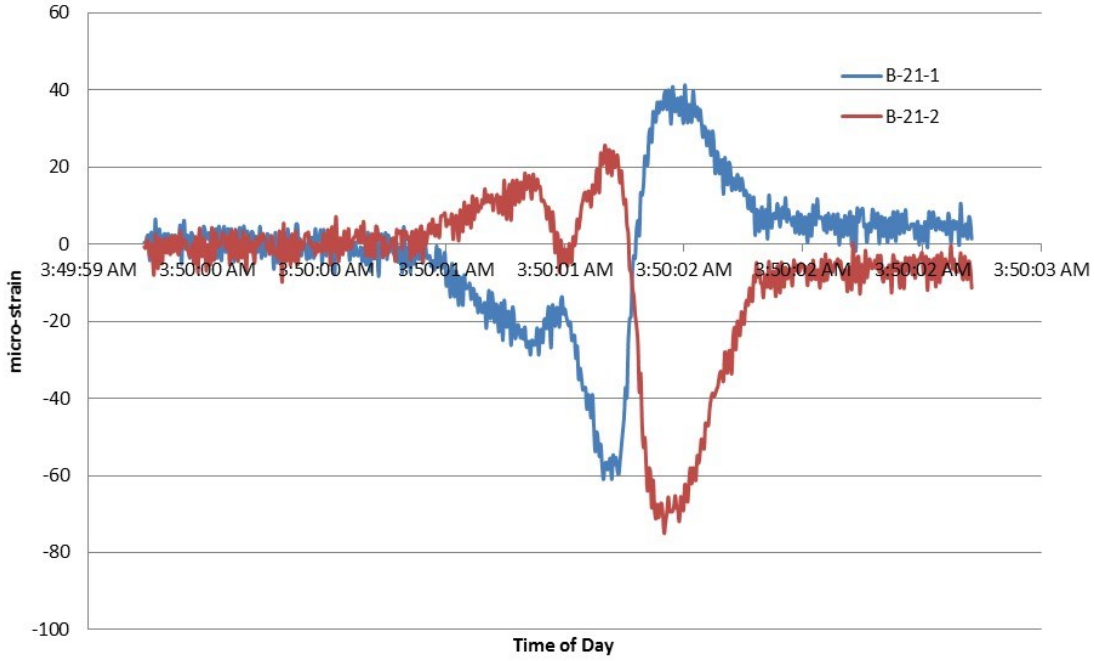

Figure B.45: Dynamic response of B-21 gauges with truck traveling in lane 1.

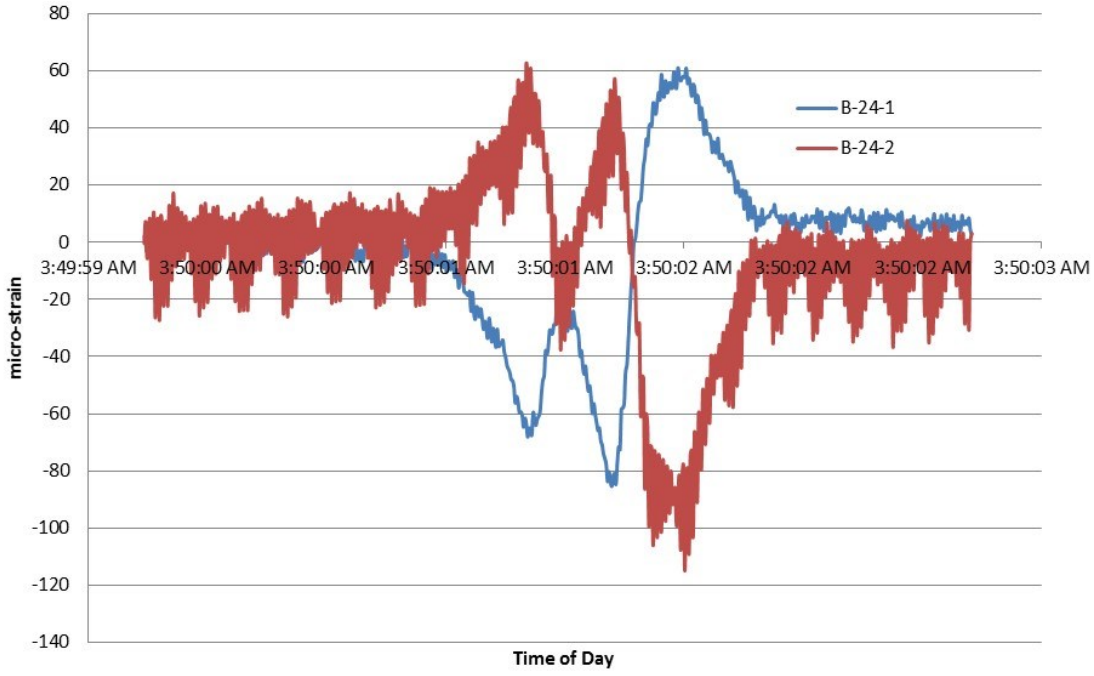

Figure B.46: Dynamic response of B-24 gauges with truck traveling in lane 1.

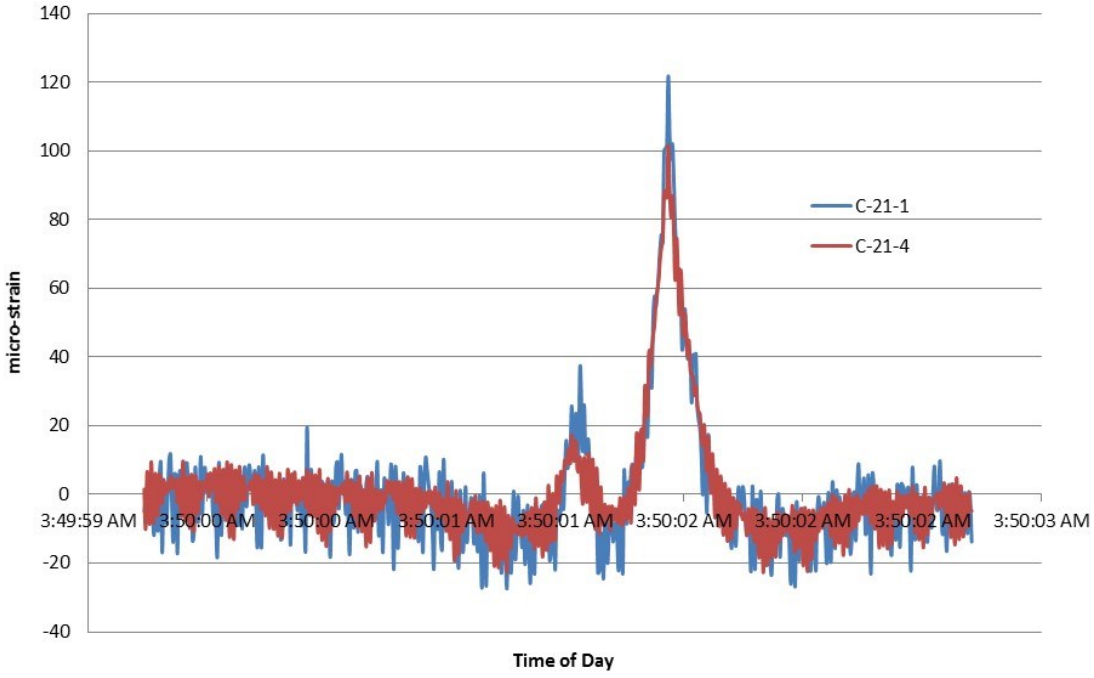

Figure B.47: Dynamic response of C-21 longitudinal gauges with truck traveling in lane 1.

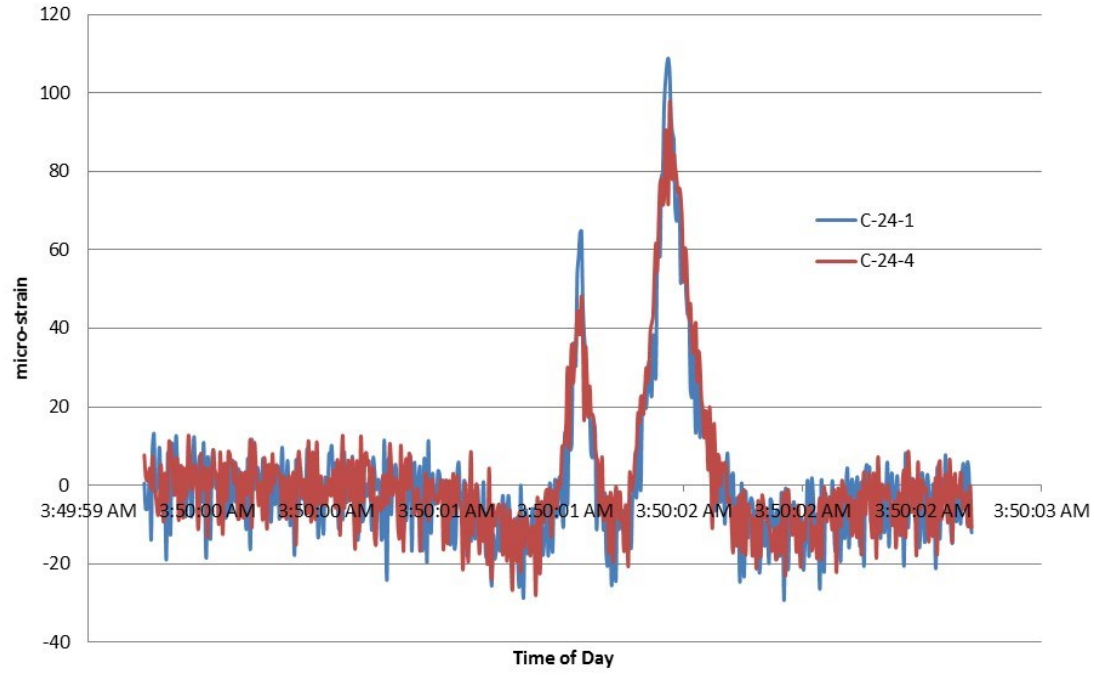

Figure B.48: Dynamic response of C-24 longitudinal gauges with truck traveling in lane 1.

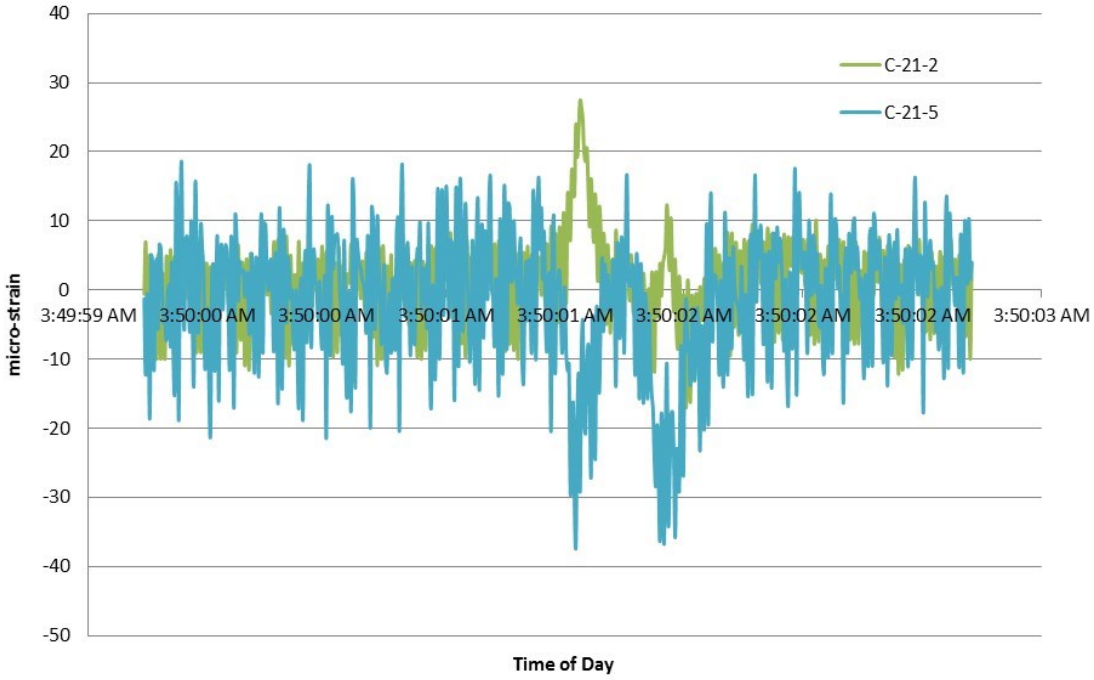

Figure B.49: Dynamic response of C-21 diagonal gauges with truck traveling in lane 1.

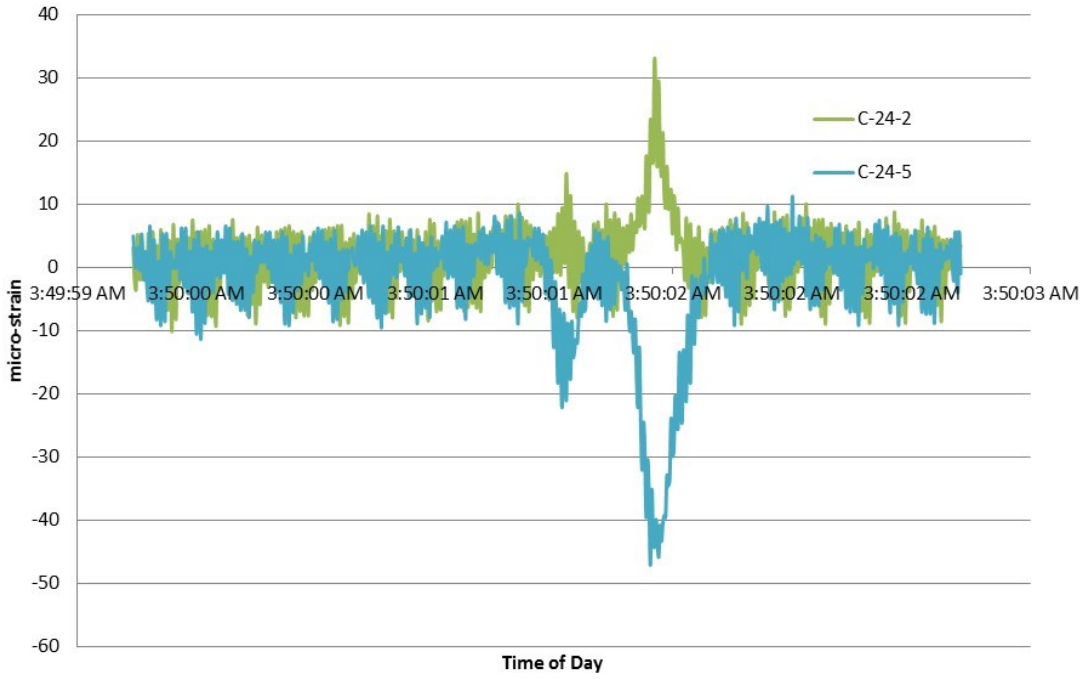

Figure B.50: Dynamic response of C-24 diagonal gauges with truck traveling in lane 1.

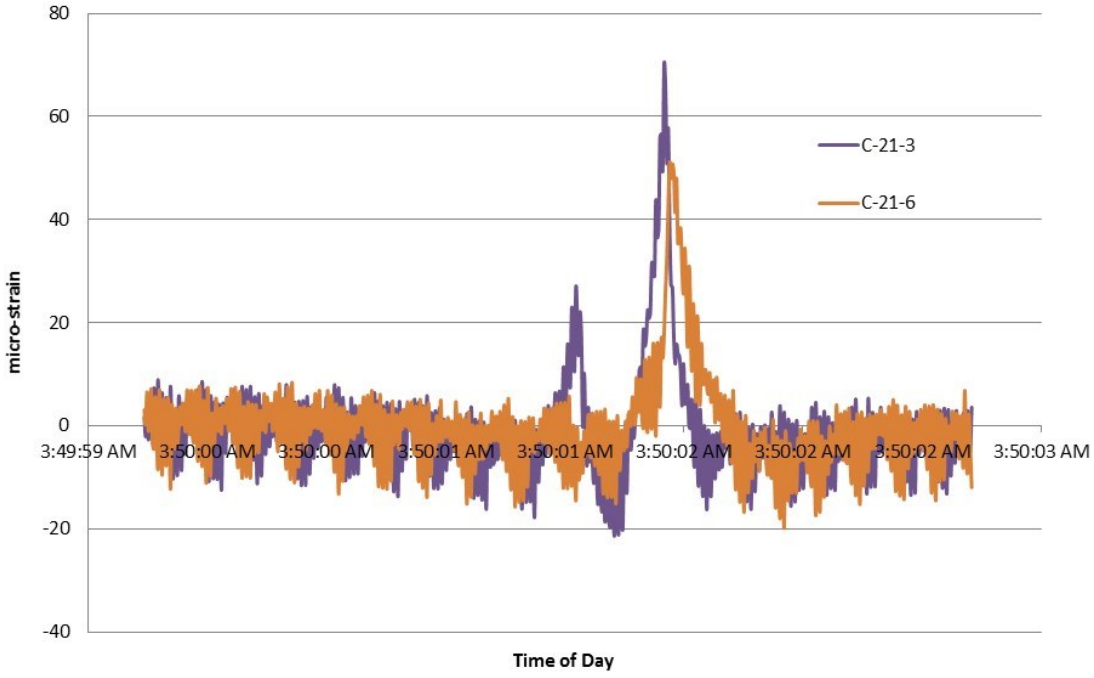

Figure B.51: Dynamic response of C-21 vertical gauges with truck traveling in lane 1.

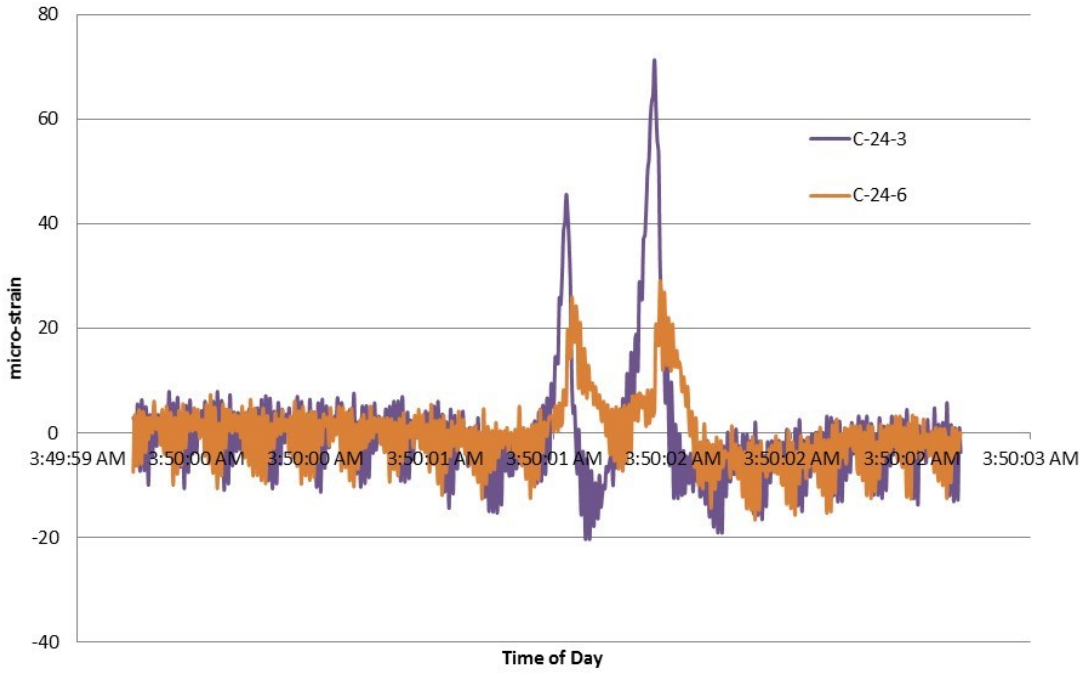

Figure B.52: Dynamic response of C-24 vertical gauges with truck traveling in lane 1.

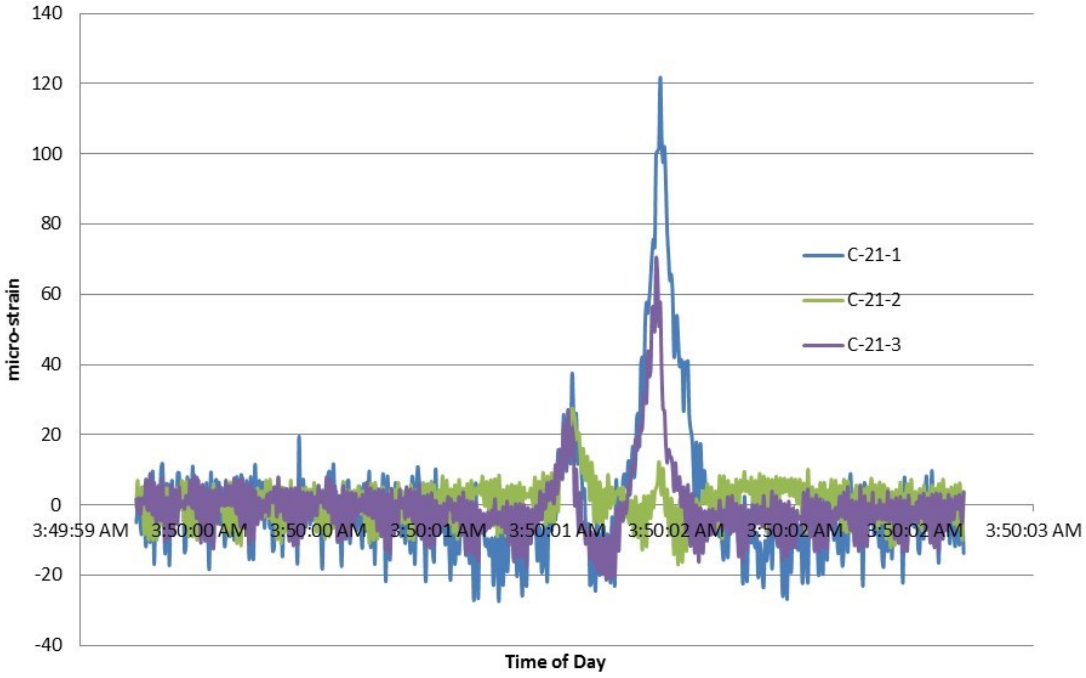

Figure B.53: Dynamic response of C-21-1 rosette with truck traveling in lane 1.

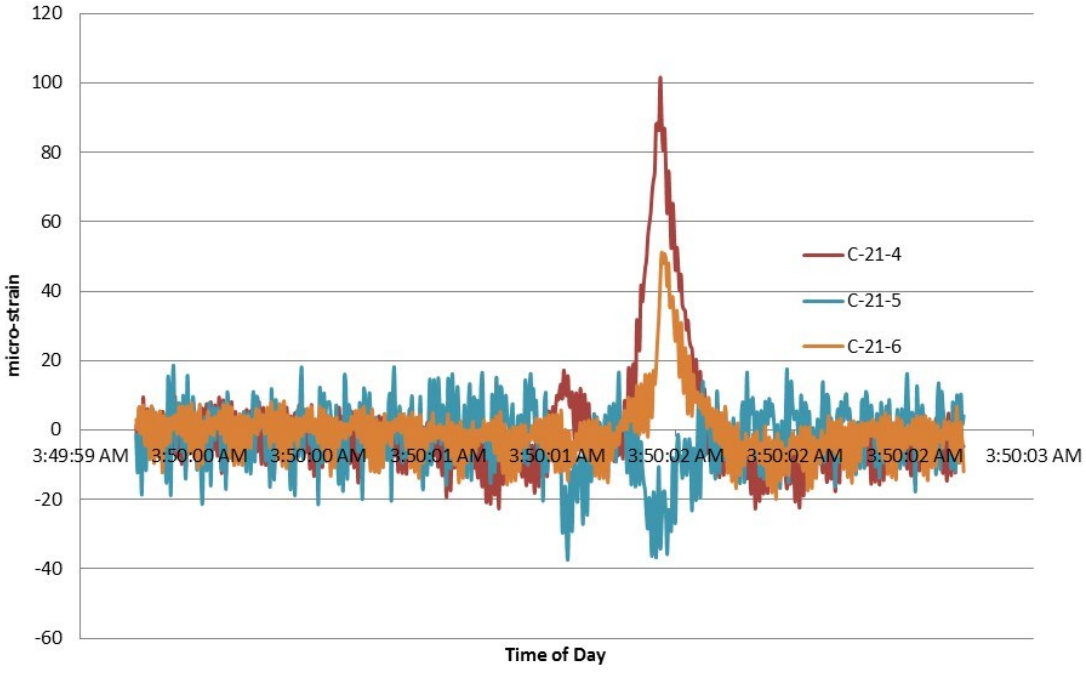

Figure B.54: Dynamic response of C-21-4 rosette with truck traveling in lane 1.

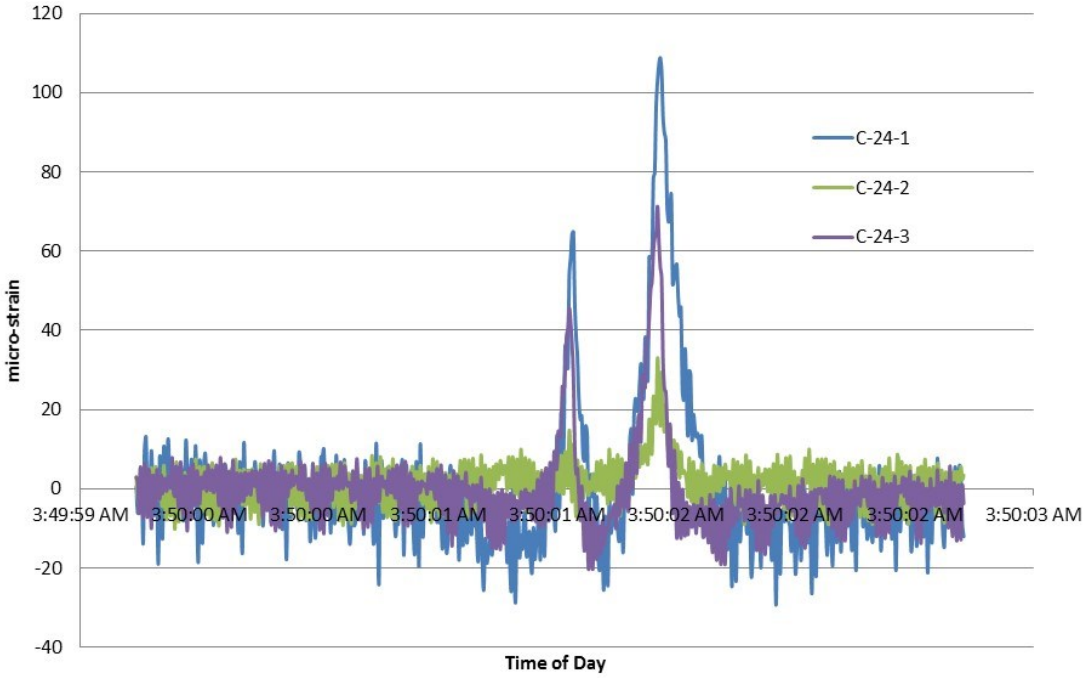

Figure B.55: Dynamic response of C-24-1 rosette with truck traveling in lane 1.

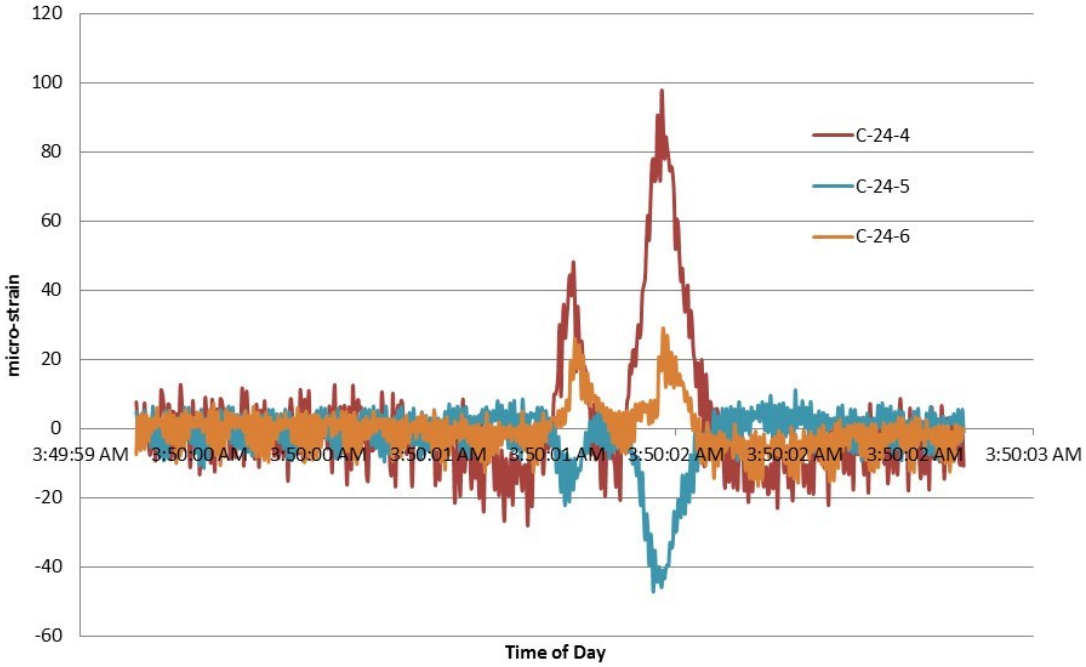

Figure B.56: Dynamic response of C-24-4 rosette with truck traveling in lane 1.

Appendix C : Tension Coupon Testing

Tension coupon testing was performed to determine three material properties: the modulus of elasticity, the yield strength, and the ultimate strength. The testing procedure followed ASTM E8M-13a using sheet-type specimens. An Instron Model 8501 testing machine with a capacity of 200 kN was used to test the coupons. The setup is as shown in Figure C.1. The coupons were tested using position control at a movement rate of 0.75 mm/min while elongation of the coupons was measured from a digital extensometer with a nominal gauge length of 50 mm. Coupons were extracted from the rib plate of specimen C9. A typical stress-strain plot for coupon 2 is given in Figure C.2, with all test results presented in Table C.1. Since no definite yielding plateau was observed, the 0.2% offset method was used to determine the yield strength, as per ASTM E8M-13a.

Figure C.1: Test setup for tension coupons.

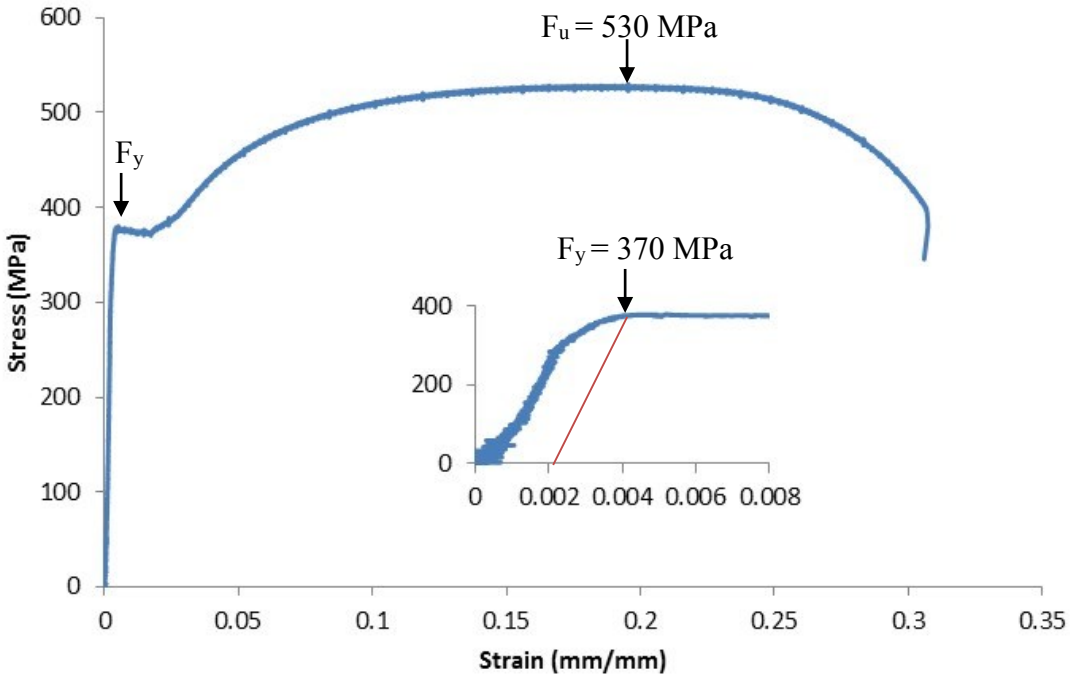

Figure C.2: Stress-strain curve for coupon 2.

Table C-1: Tension coupon results.

Sample Number	Yield Strength	Ultimate Strength	Modulus of Elasticity
	MPa	MPa	GPa
1	375	524	222
2	370	530	154
3	379	530	174
4	383	531	183
5	379	534	172
Average	377	530	181

Appendix D : Laboratory Testing

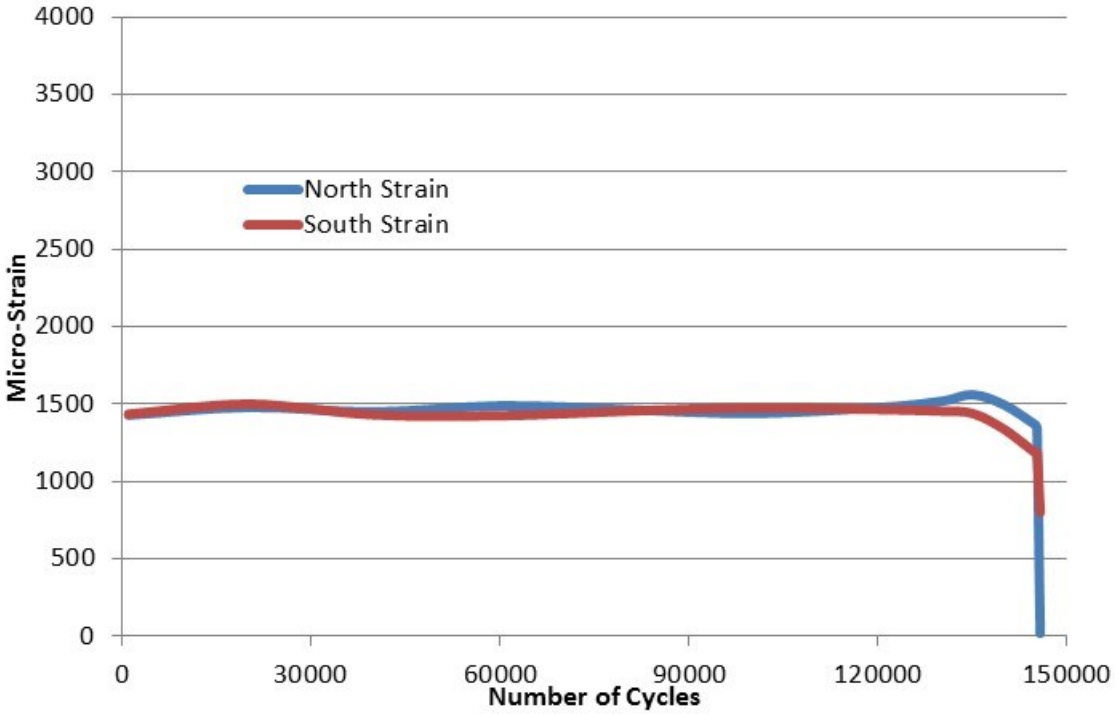

Figure D.1: Specimen A1 strain over time at 79 kN.

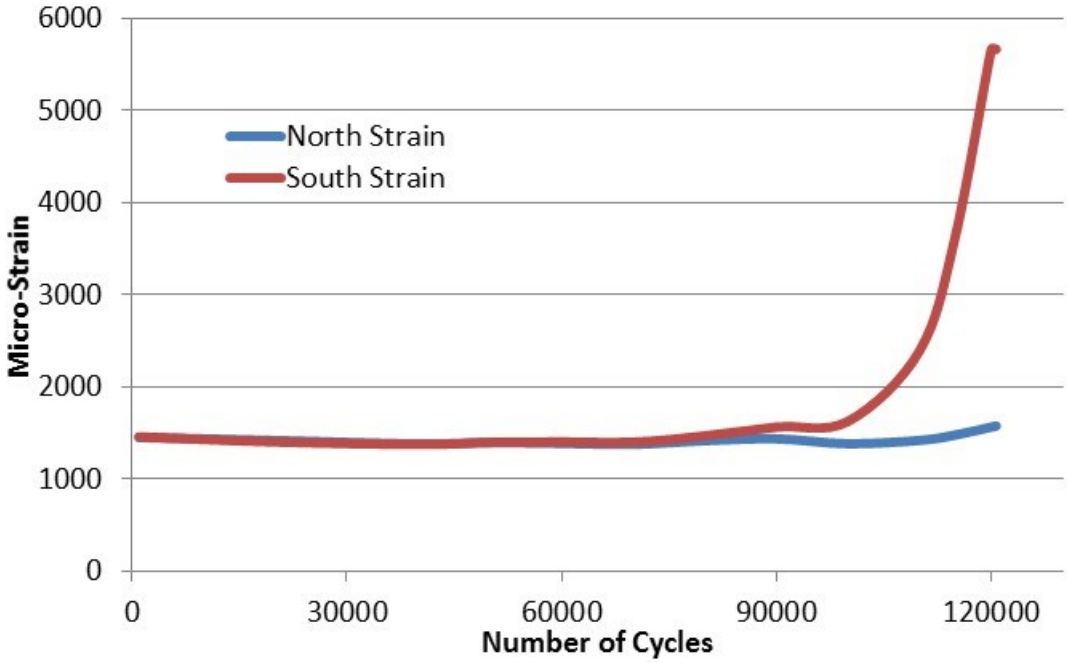

Figure D.2: Specimen A5 strain over time at 83 kN.

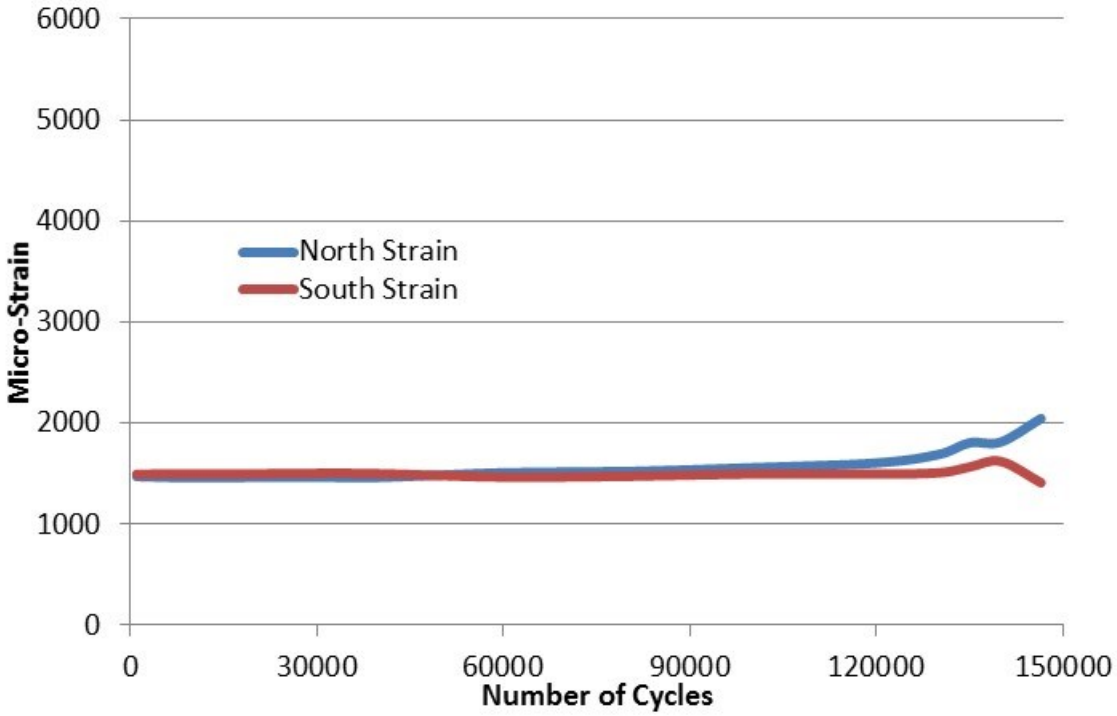

Figure D.3: Specimen A7 strain over time at 74 kN.

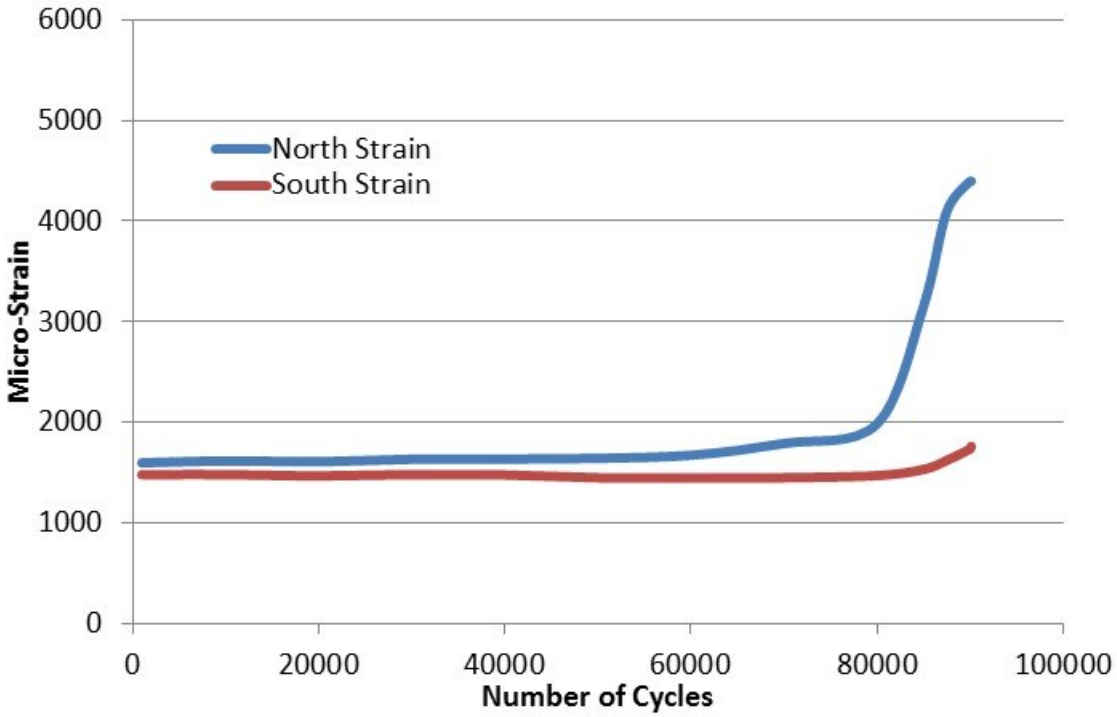

Figure D.4: Specimen A8 strain over time at 77 kN.

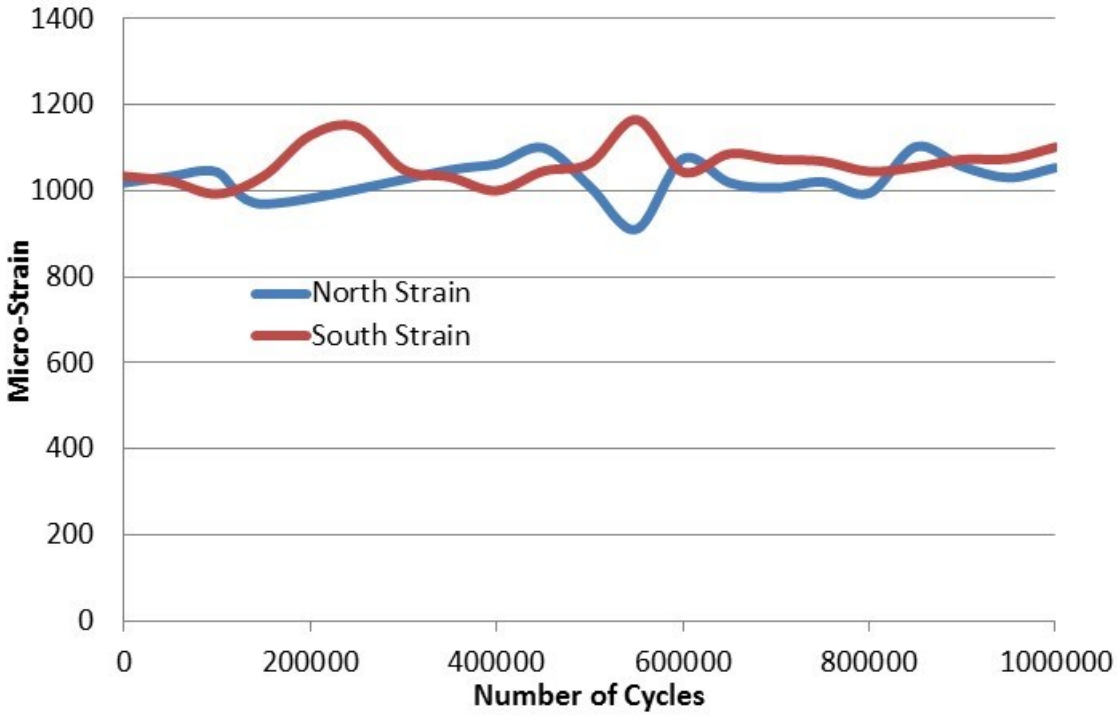

Figure D.5: Specimen A6 strain over time at 52 kN.

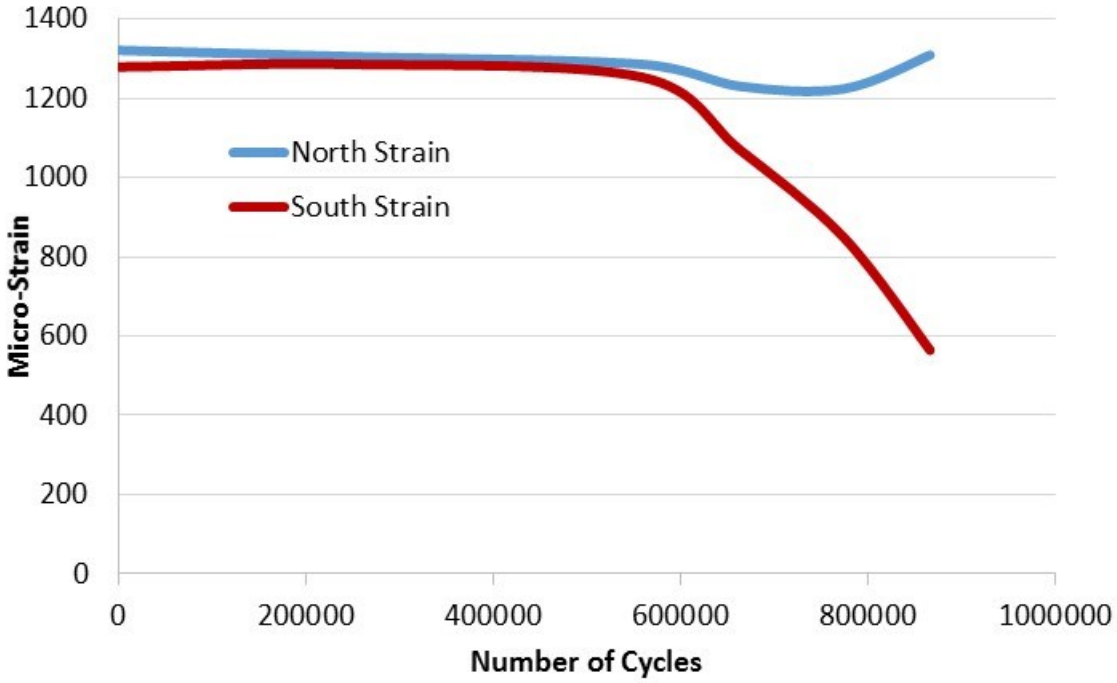

Figure D.6: Specimen A6 re-tested strain over time at 63 kN.

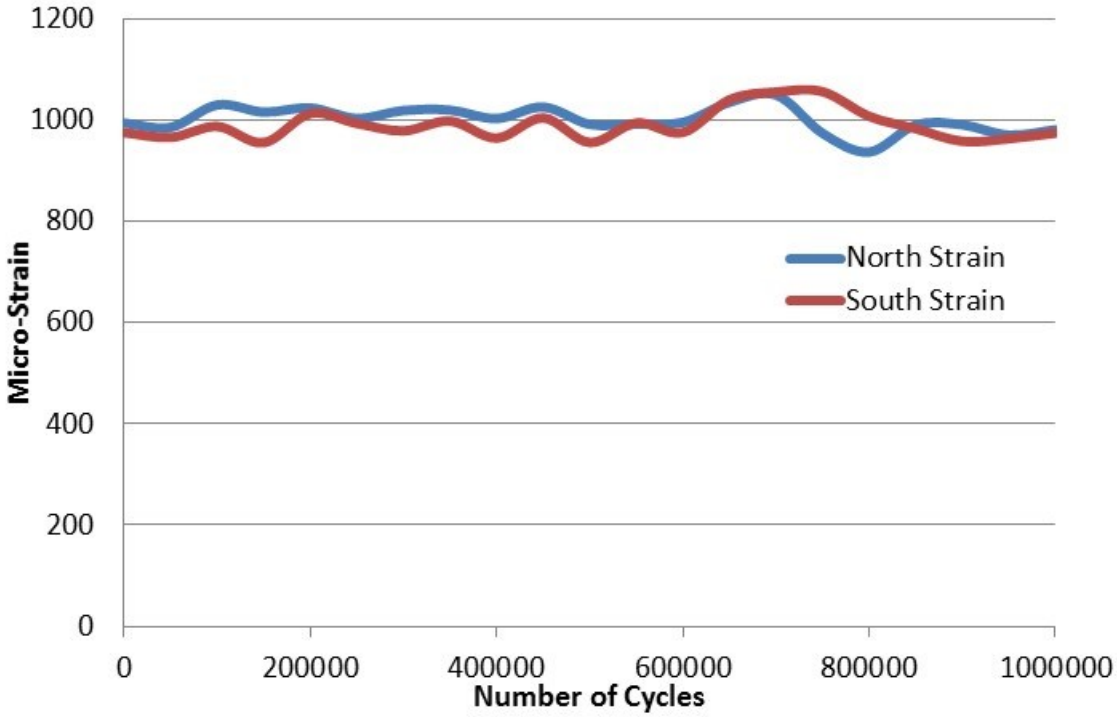

Figure D.7: Specimen A2 strain over time at 57 kN.

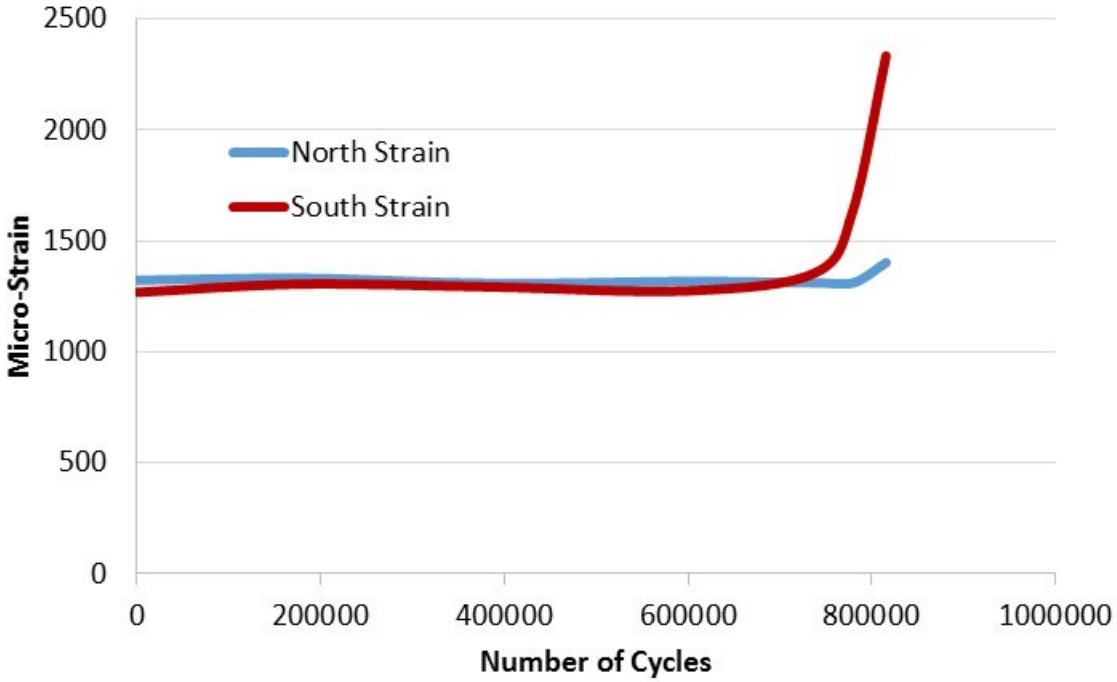

Figure D.8: Specimen A2 re-tested strain over time at 73 kN.

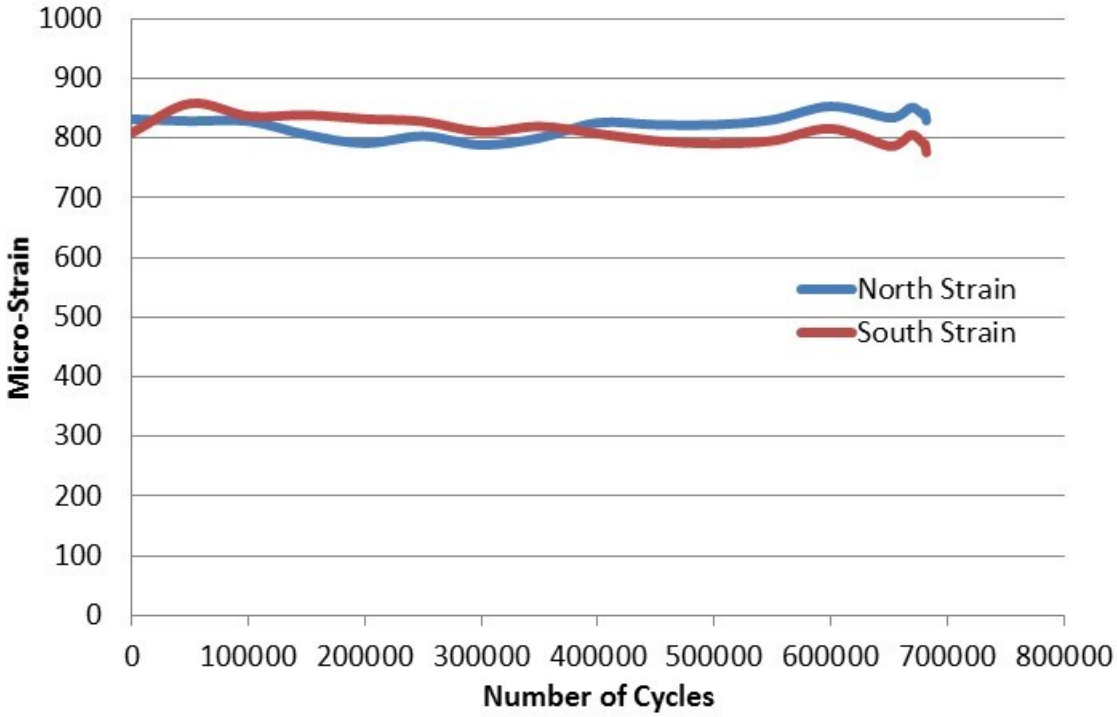

Figure D.9: Specimen A3 strain over time at 41 kN.

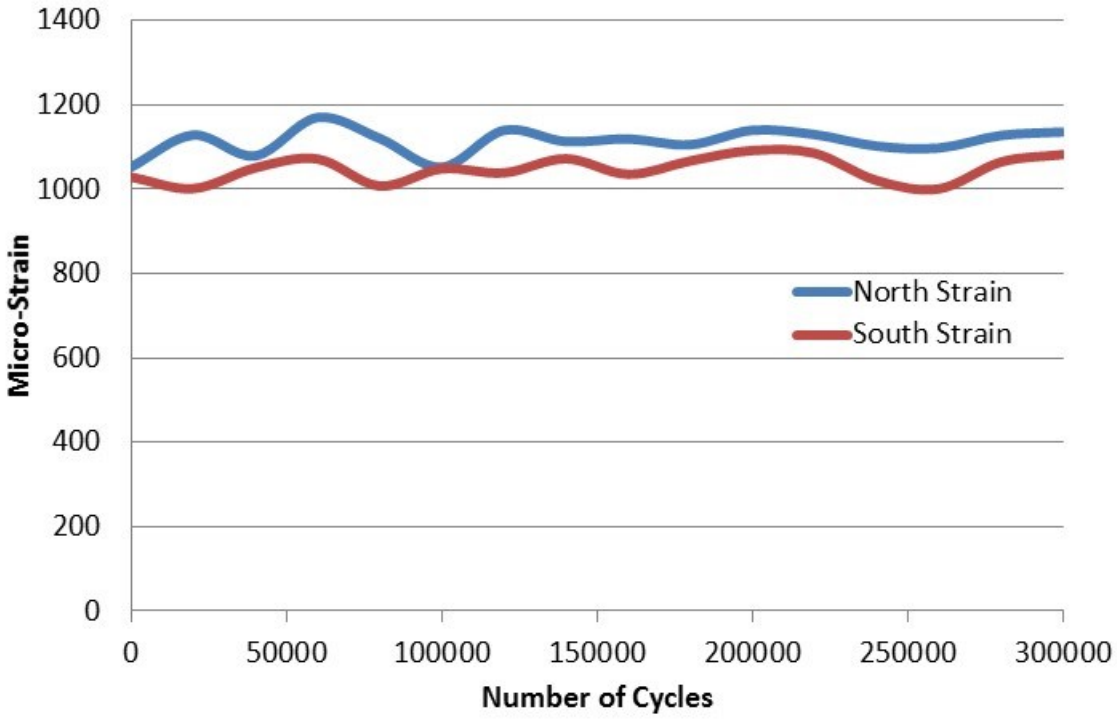

Figure D.10: Specimen A11 strain over time at 45 kN.

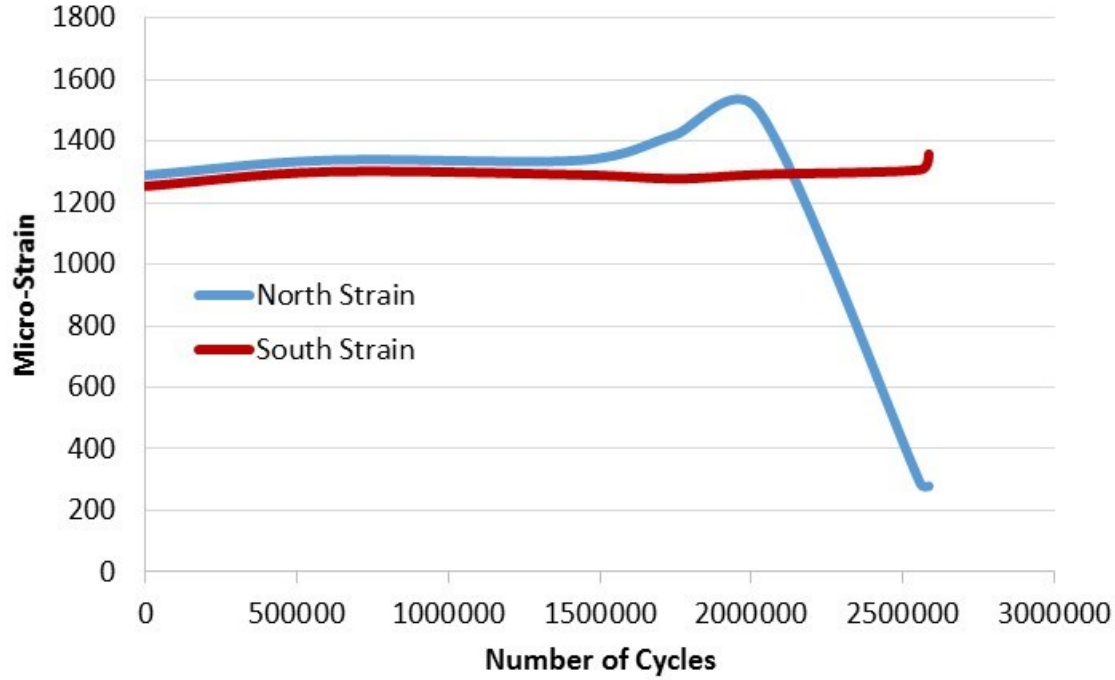

Figure D.11: Specimen A11 strain over time at 55 kN.

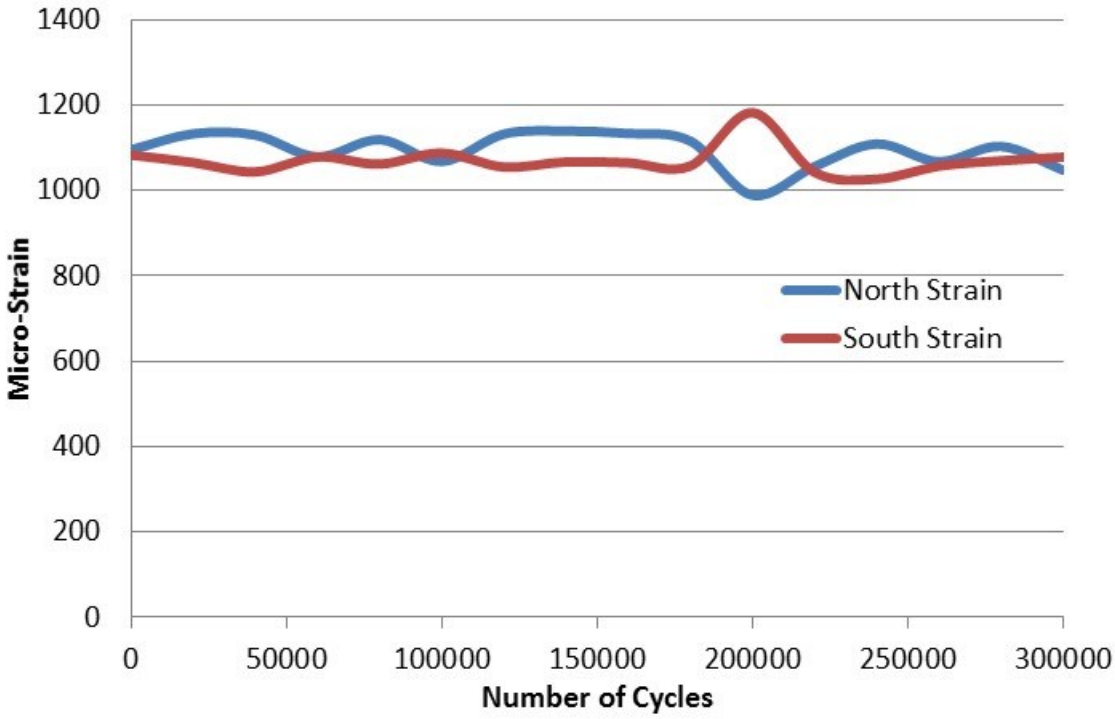

Figure D.12: Specimen A21 strain over time at 25 kN.

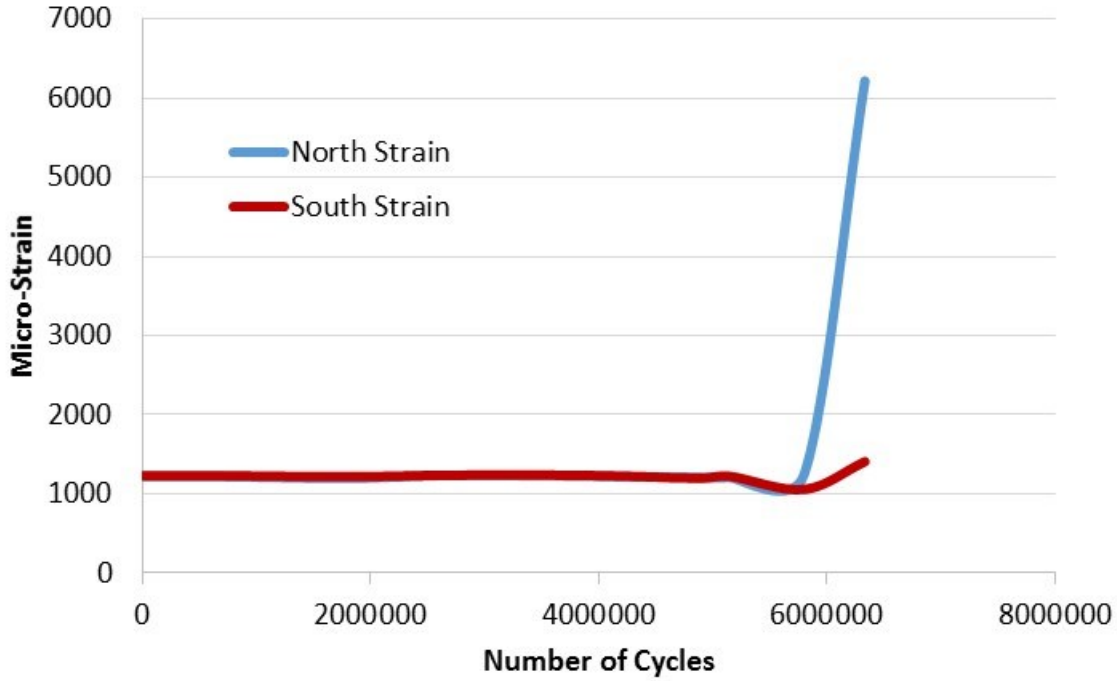

Figure D.13: Specimen A21 re-tested strain over time at 29 kN.

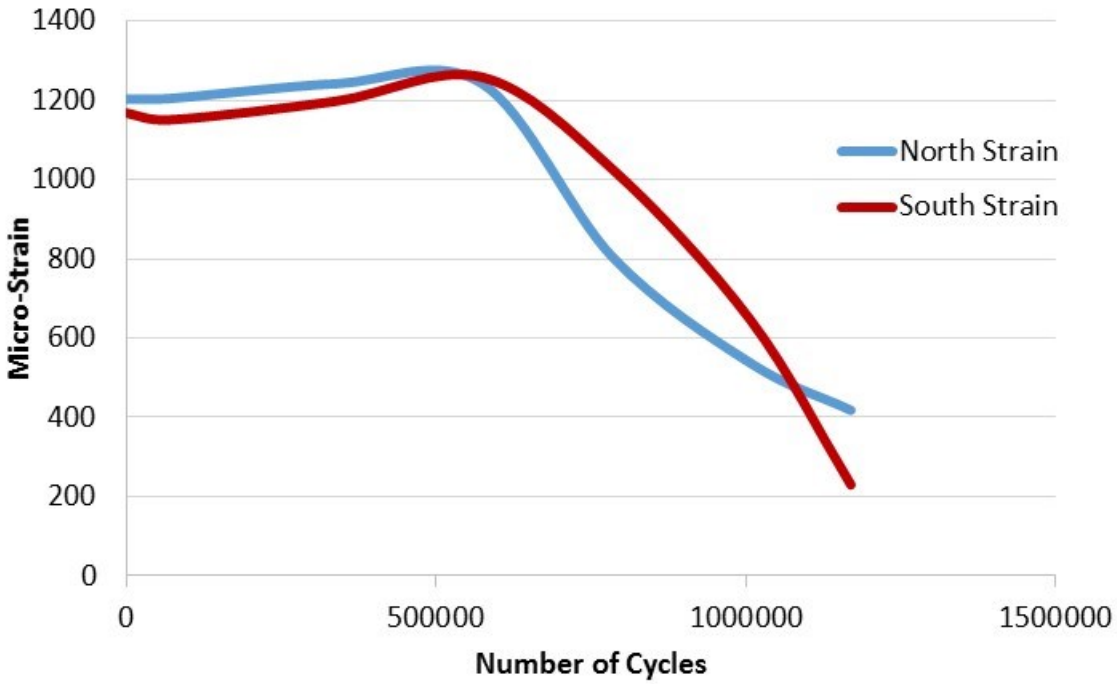

Figure D.14: Specimen A27 strain over time at 34 kN.

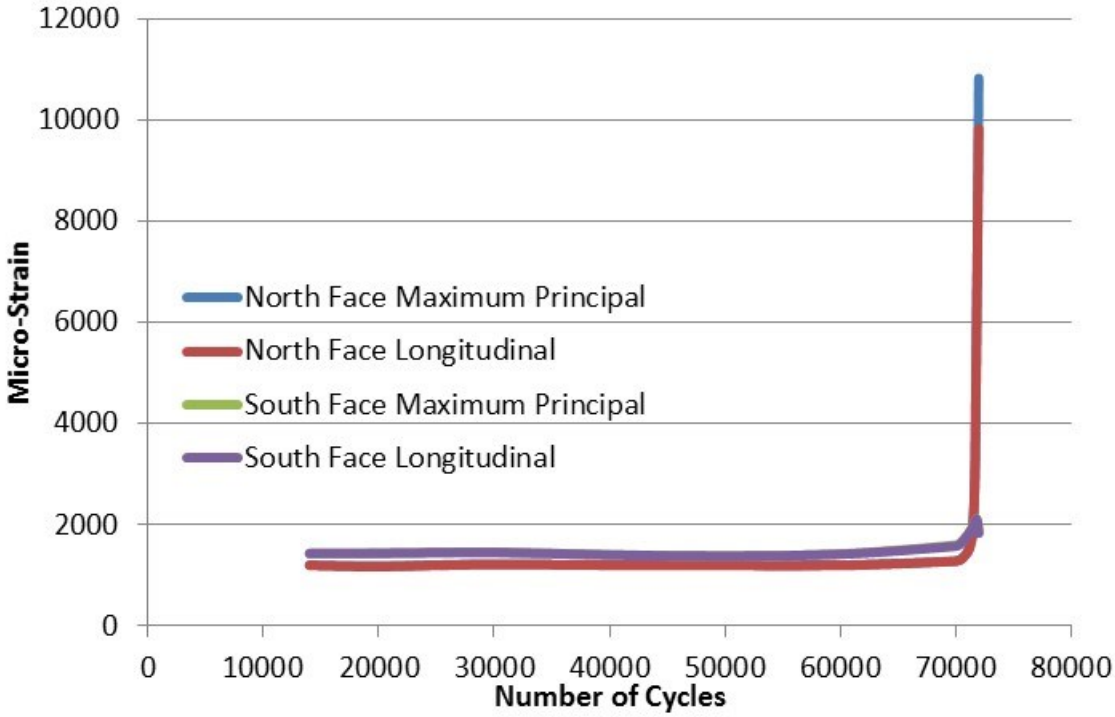

Figure D.15: Specimen C8 strains over time at 430 kN.

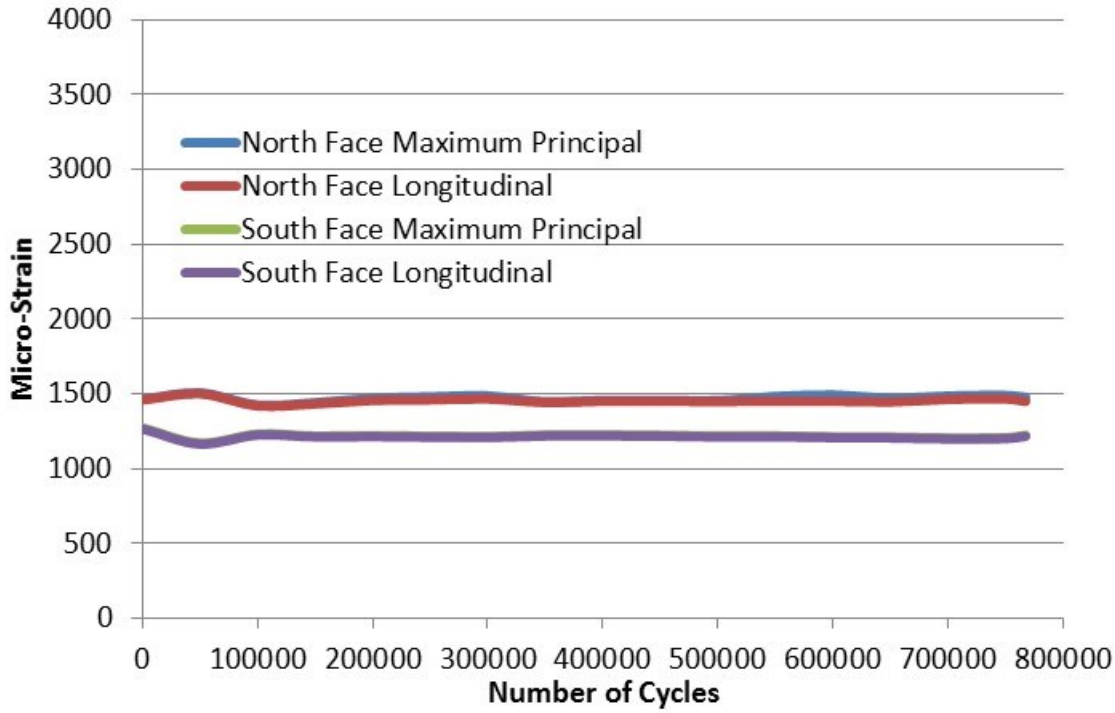

Figure D.16: Specimen C7 strains over time at 450 kN.

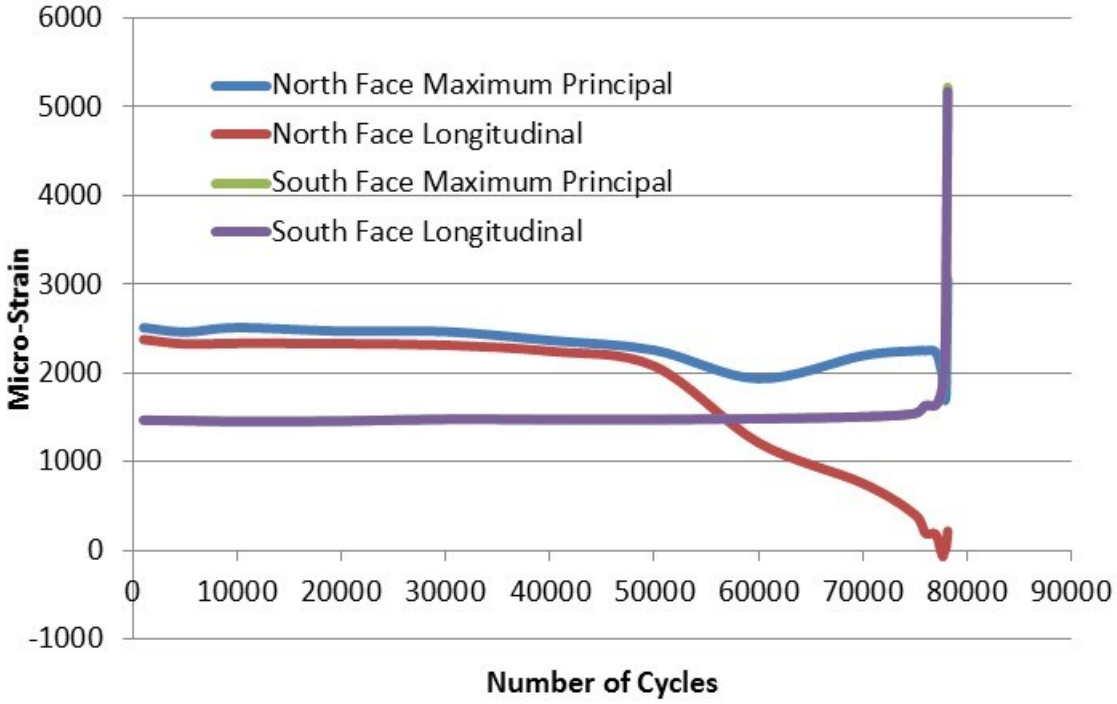

Figure D.17: Specimen C1 strains over time at 330 kN.

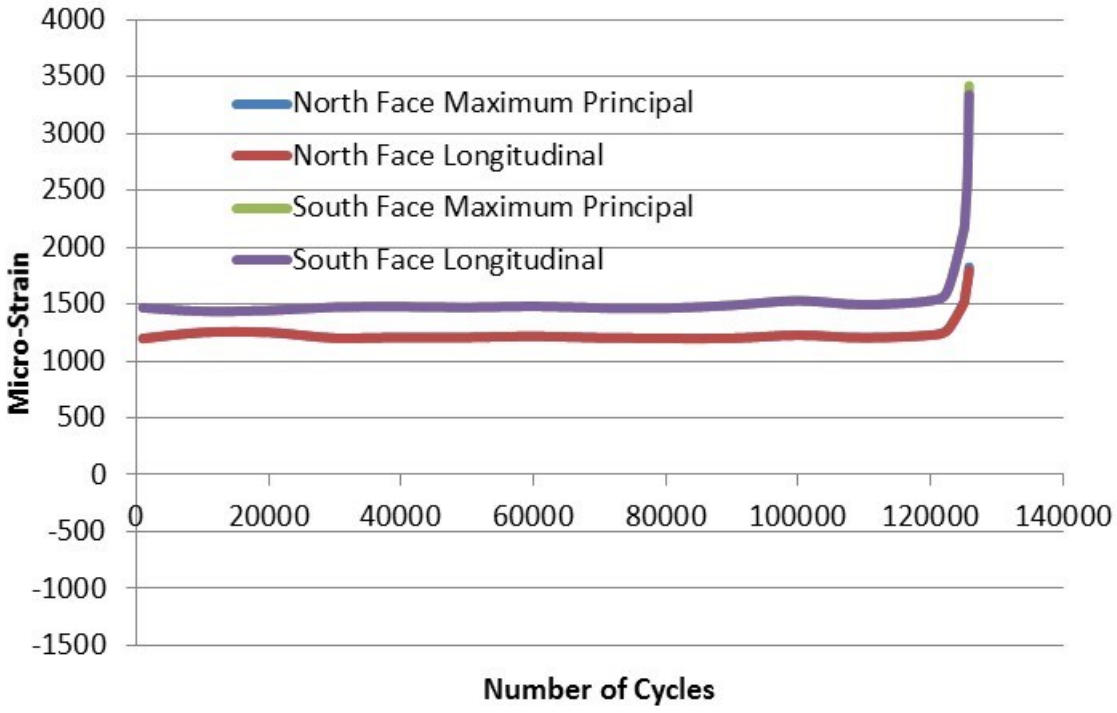

Figure D.18: Specimen C9 strains over time at 435 kN.

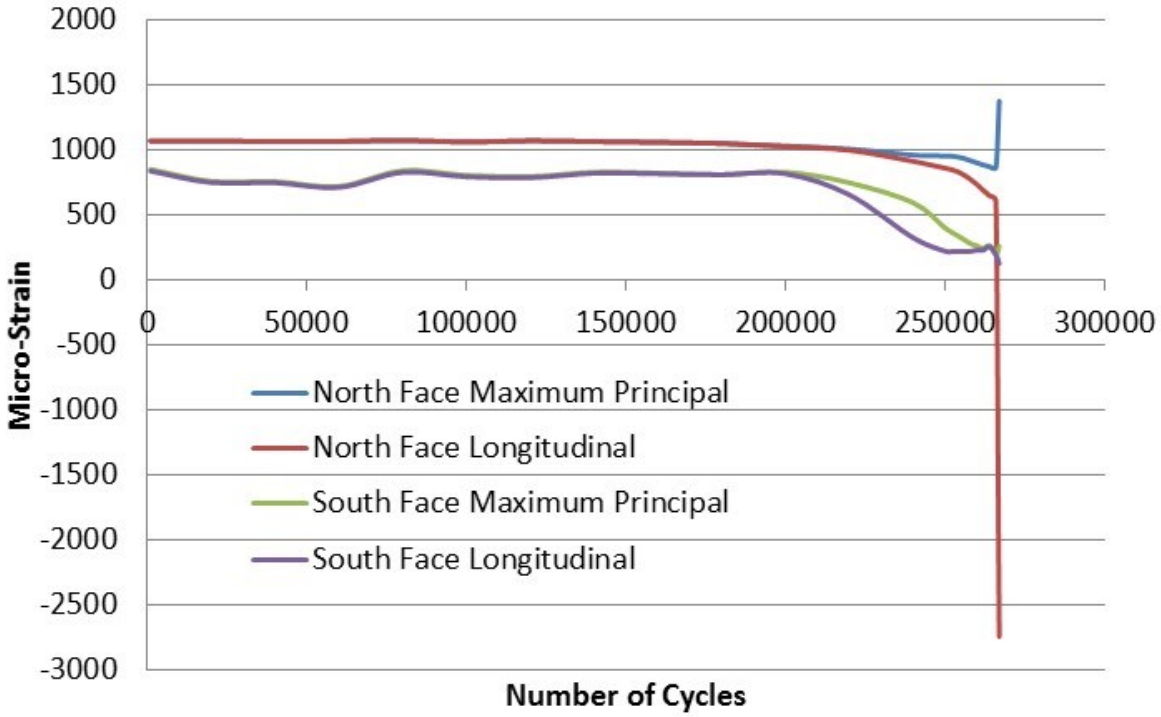

Figure D.19: Specimen C10 strains over time at 313 kN.

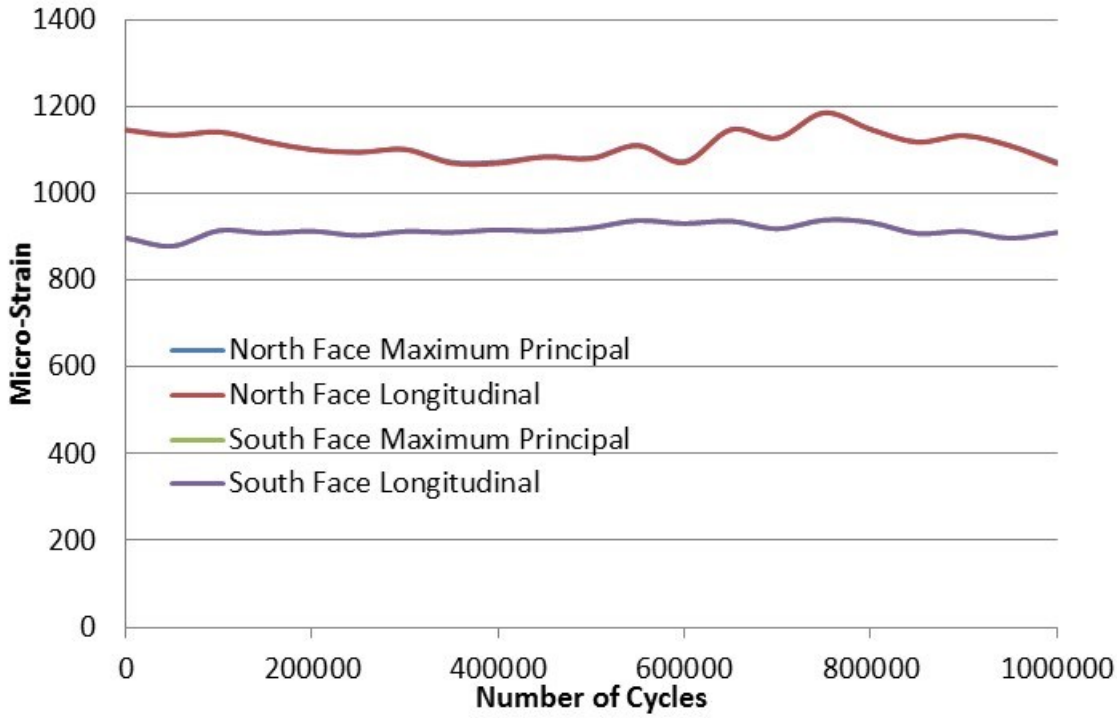

Figure D.20: Specimen C4 strains over time at 217 kN.

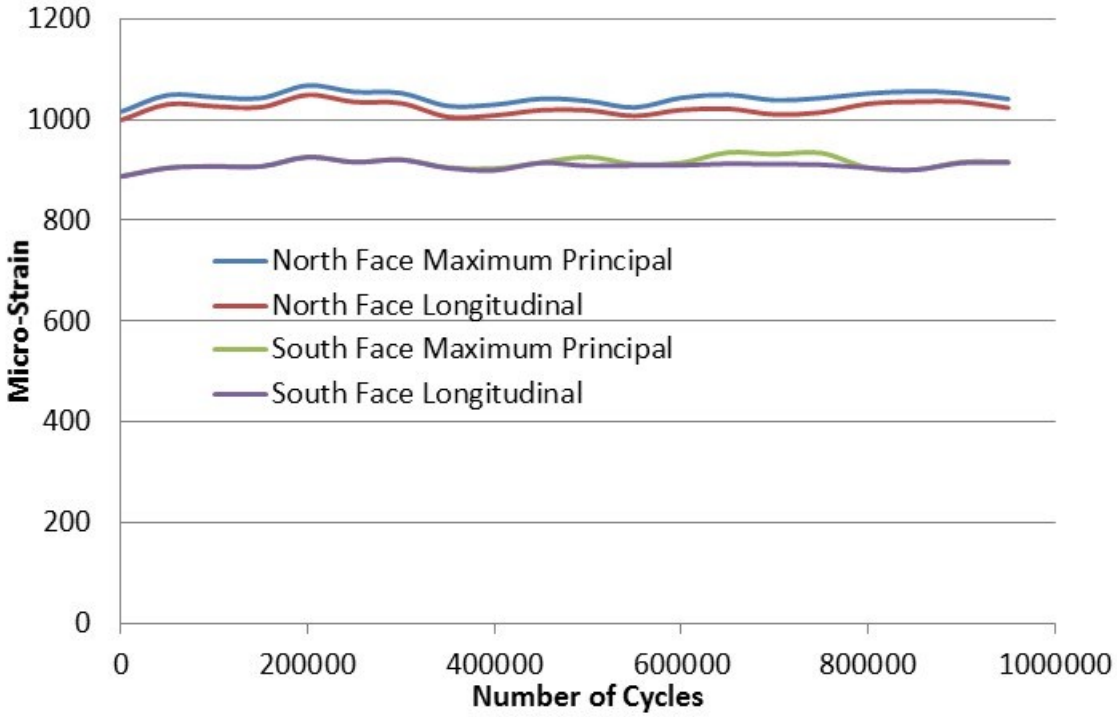

Figure D.21: Specimen C5 strains over time at 218 kN.

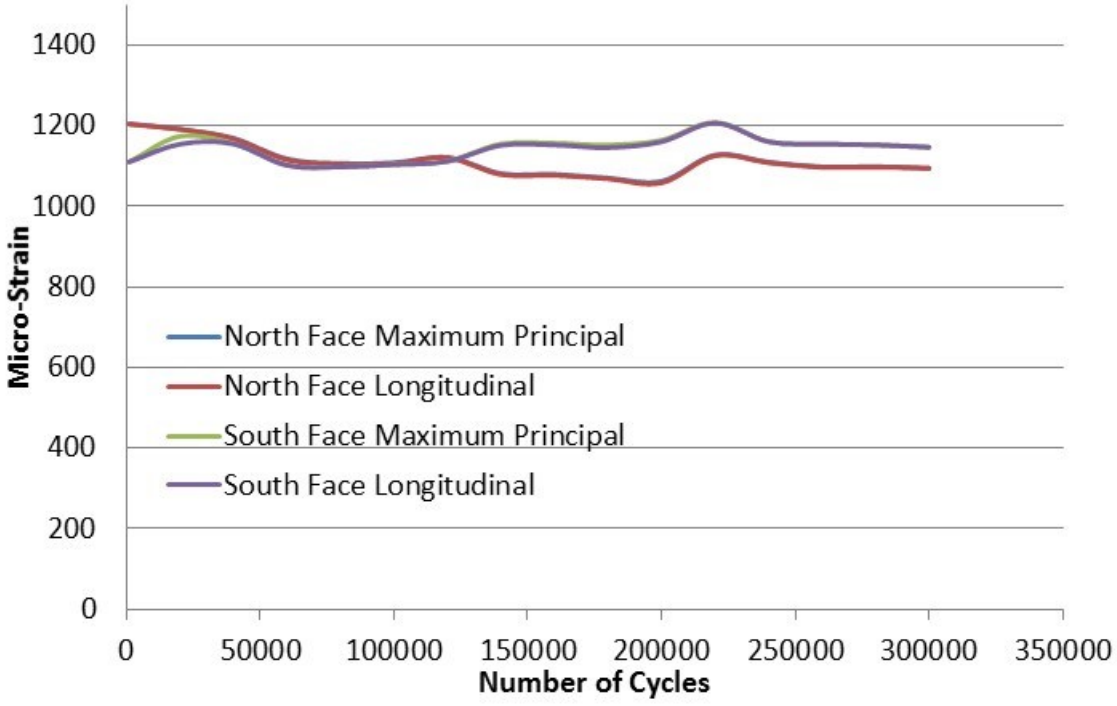

Figure D.22: Specimen C6 strains over time at 348 kN.

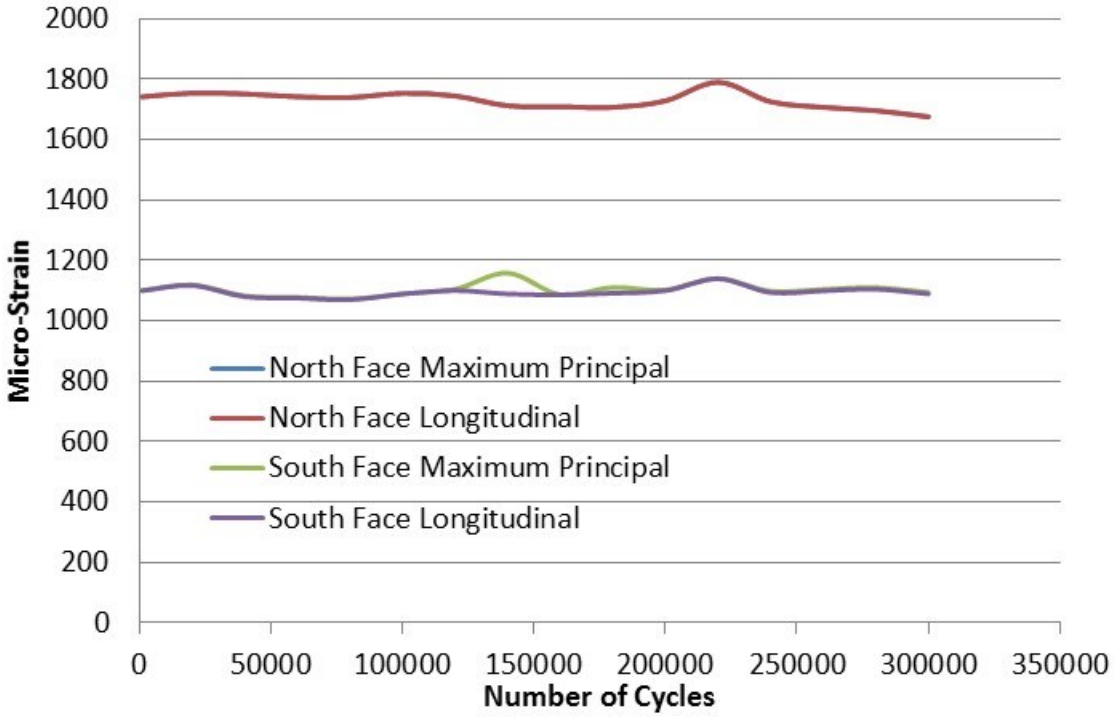

Figure D.23: Specimen C2 strains over time at 351 kN.

D.1 Condition Inspection

Prior to testing, all specimens were inspected for any visible signs of pits or holes due to corrosion. Specimen C7 showed no signs of pitting or corrosion on the outside of the trough. The inside also showed no major signs of corrosion, which can be seen below in Figure D.24. Specimen C1 also showed no signs of pitting or corrosion on the outside of the trough. Figure D.25 shows significant pitting on the inside of the trough prior to testing. Specimen C9 showed no visible signs of corrosion from the outside of the specimen, but the inside of the trough showed signs of moderate corrosion but not as severe as specimen C1. This can be seen below in Figure D.26. Specimen C10 had a total of four corroded pinholes. Three of these pin holes were located on the south side of the specimen, whereas one pinhole was located on the north side of the specimen. Figure D.27 and Figure D.28 show the south side pinholes. Figure D.29 shows the pinhole on the north side. The inside of the trough for specimen C10 shows signs of significant corrosion that can be seen in Figure D.30 and Figure D.31. Specimen C4 and specimen C5 showed no visible holes or corroded areas comparable to specimen C10. Specimen C4 was in very good condition

with the only major areas of corrosion being along the connection of the trough to the deck plate. This can be seen in Figure D.32 and Figure D.33. Specimen C5 showed extensive corrosion along the trough to deck connection. This can be seen below in Figure D.34 and Figure D.35. Specimen C6 showed no visible holes or corroded areas and was in very good condition. This can be seen in Figure D.36. Specimen C2 showed signs of moderate corrosion inside the stiffening rib of the specimen, shown in Figure D.37, including corroded pits, as shown in Figure D.38. A hole was also noted on the east side of the specimen, shown in Figure D.39 and Figure D.40; this is likely a torched hole used to attach an identification tag to the specimen upon being removed from the deck. Figure D.41 shows significant corrosion seen along the cut edge of the specimen, running the length.

Figure D.24: Specimen C7 inside of rib.

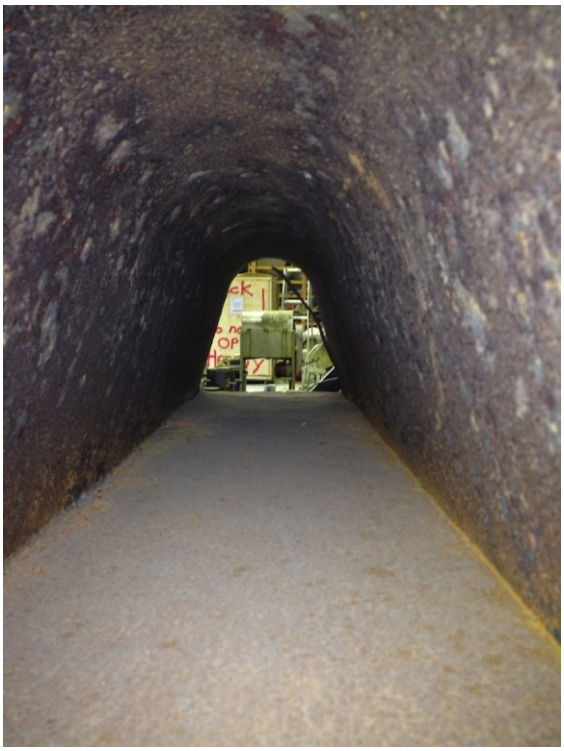

Figure D.25: Specimen C1 inside of rib.

Figure D.26: Specimen C9 inside of rib.

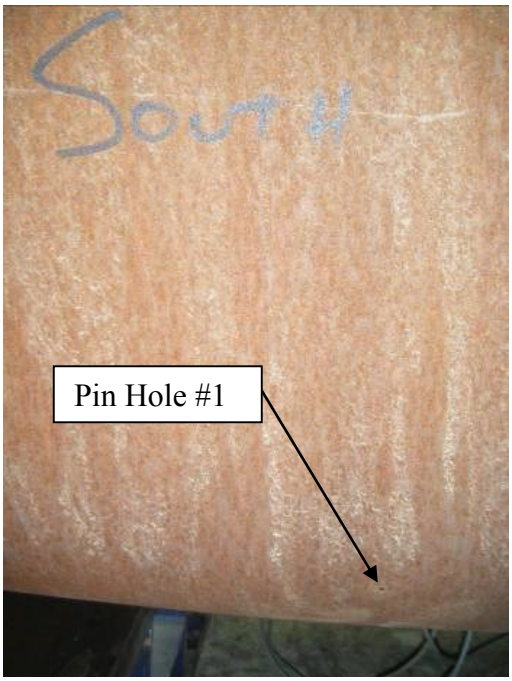

Figure D.27: Specimen C10 pinole #1, located on south face.

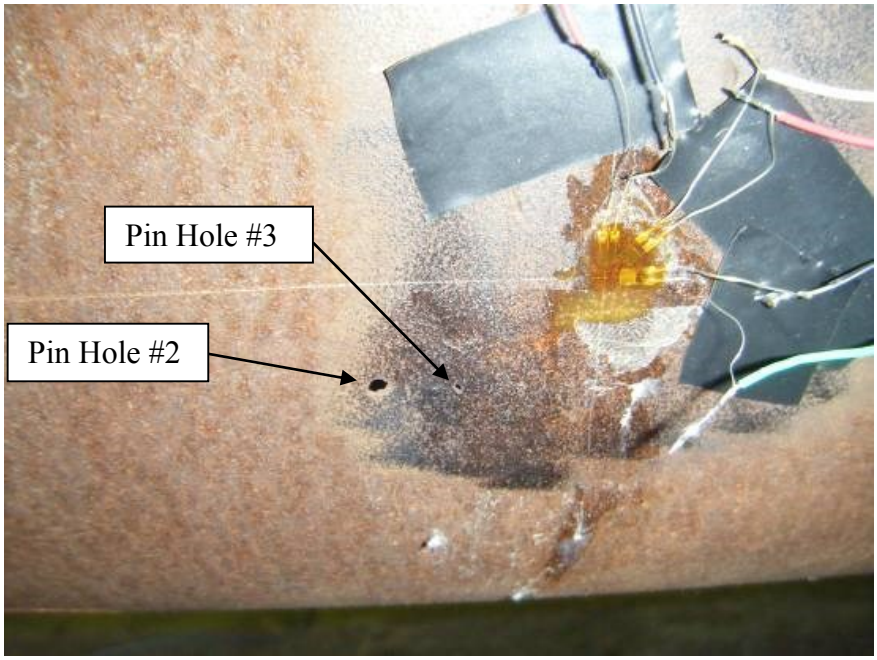

Figure D.28: Specimen C10 pinhole #2 and pinhole #3, located on south face.

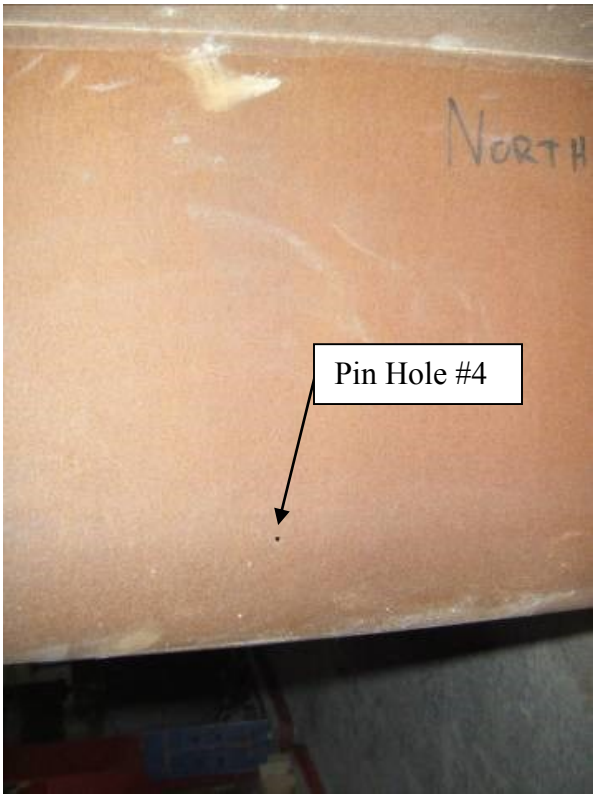

Figure D.29: Specimen C10 pinhole #4, located on north face.

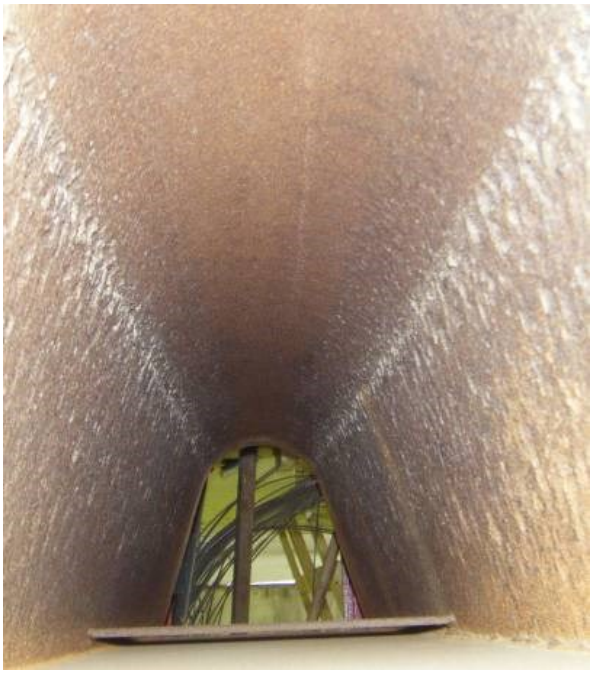

Figure D.30: Specimen C10 inside of rib.

Figure D.31: Specimen C10 bottom of stiffening rib.

Figure D.32: Specimen C4 inside of stiffening rib.

Figure D.33: Specimen C4 bottom of stiffening rib.

Figure D.34: Specimen C5 inside of stiffening rib.

Figure D.35: Specimen C5 deck to stiffening rib connection.

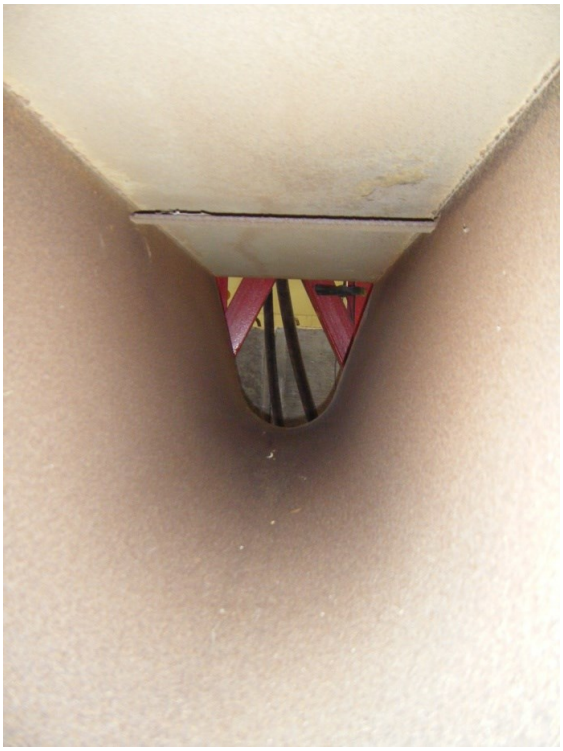

Figure D.36: Specimen C 6 inside of stiffening rib.

Figure D.37: Specimen C2 inside of stiffening rib.

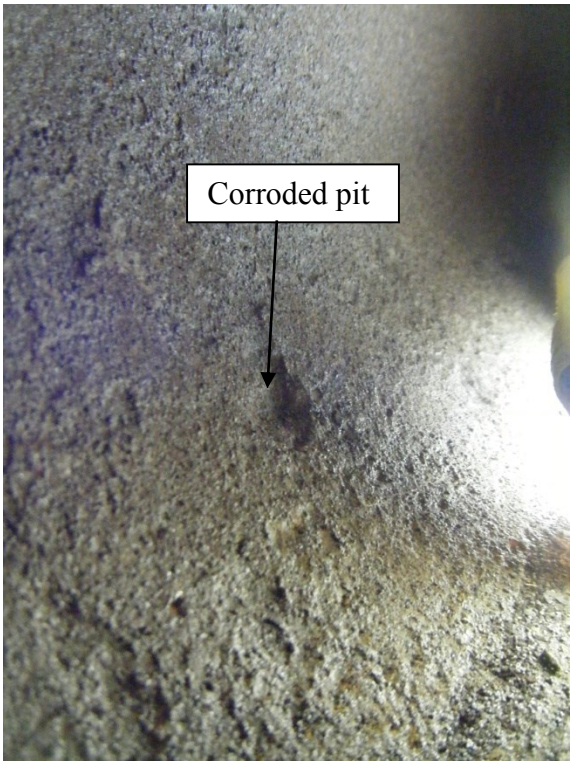

Figure D.38: Specimen C2 corroded pit on north side in close proximity to strain gauge.

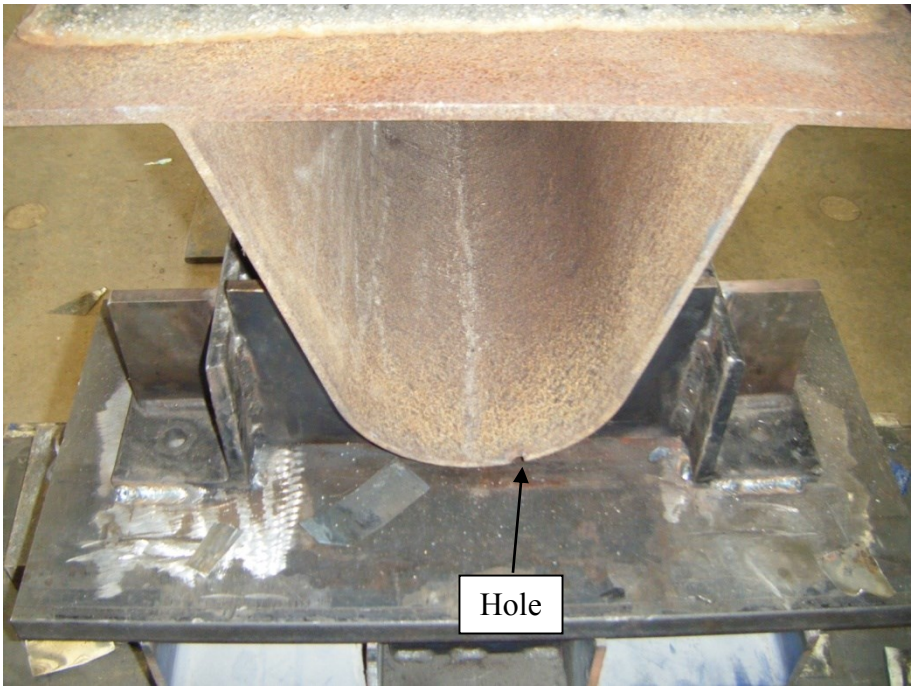

Figure D.39: Specimen C2 hole located on east side.

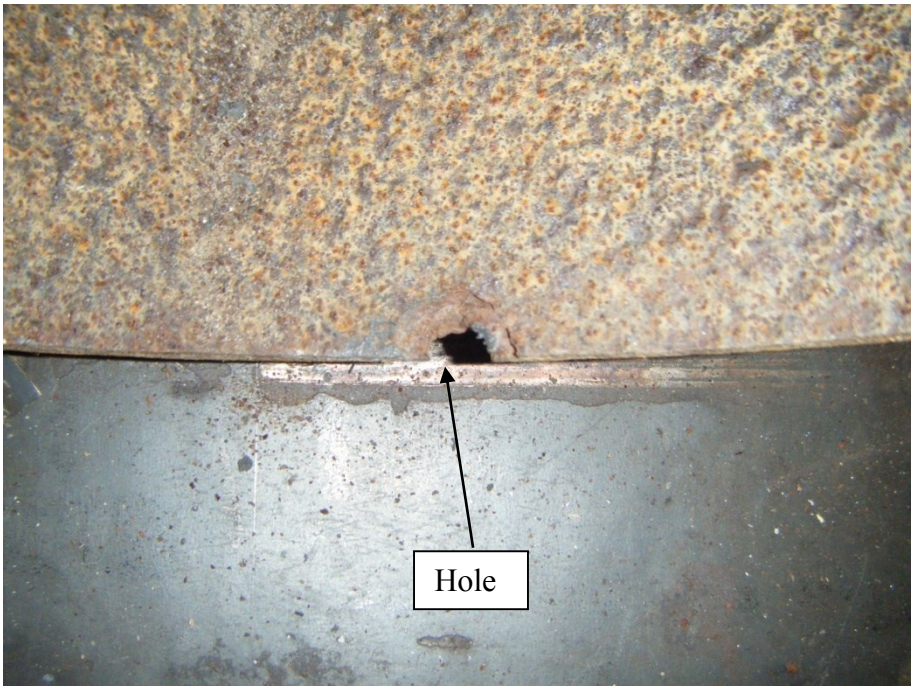

Figure D.40: Specimen C2 close up of hole on east side.

Figure D.41: Specimen C2 corrosion on deck along length of specimen.

Appendix E : Gauge Statistics

Table E-1: Gauge statistics.

Gauge	m_{ε_m}	σ_{ε_m}	$m_{\ln(\varepsilon_m)}$	$\sigma_{\ln(\varepsilon_m)}$	m_{ε_n}	σ_{ε_n}
	με	με			με	με
A-04-1	121	59	-9.13	0.464	0	6
A-04-2	100	37	-9.28	0.359	-1	7
A-06-1	107	41	-9.21	0.372	0	7
A-06-2	121	62	-9.13	0.480	0	7
A-10-2	98	36	-9.29	0.352	-1	6
A-11-1	97	59	-9.40	0.562	-1	6
A-12-1	103	43	-9.26	0.400	0	6
A-12-2	111	54	-9.22	0.461	1	6
A-16-1	91	25	-9.34	0.270	0	6
A-16-2	88	21	-9.37	0.241	0	6
A-18-1	90	27	-9.36	0.289	0	5
A-21-2	132	63	-9.04	0.454	0	5
A-24-2	128	57	-9.06	0.427	0	2
B-04-1	139	64	-8.98	0.442	1	3
B-06-1	127	52	-9.05	0.395	-1	3
B-06-2	131	57	-9.03	0.418	1	3
B-10-2	119	50	-9.12	0.404	0	3
B-12-1	112	46	-9.17	0.393	0	6
B-12-2	112	47	-9.18	0.400	1	7
B-16-1	93	22	-9.32	0.239	0	6
B-16-2	91	20	-9.33	0.220	0	6
B-18-1	92	23	-9.33	0.249	0	6
B-18-2	93	22	-9.31	0.233	0	6
B-21-1	118	45	-9.11	0.370	0	3
B-21-2	122	48	-9.09	0.382	-1	3
B-24-1	130	60	-9.05	0.441	0	2

Gauge	m_{ε_m}	σ_{ε_m}	$m_{\ln(\varepsilon_m)}$	$\sigma_{\ln(\varepsilon_m)}$	m_{ε_n}	σ_{ε_n}
	με	με			με	με
C-04-1	123	50	-9.08	0.393	0	4
C-04-4	118	50	-9.13	0.403	0	6
C-06-1	118	44	-9.11	0.357	0	5
C-06-4	119	44	-9.10	0.362	0	4
C-10-1	118	47	-9.12	0.386	0	4
C-10-4	116	42	-9.12	0.352	0	5
C-12-4	120	49	-9.10	0.391	0	4
C-16-1	92	28	-9.34	0.296	0	4
C-18-4	91	26	-9.34	0.284	0	8
C-21-1	117	41	-9.11	0.342	0	7
C-21-4	119	40	-9.09	0.331	0	6
C-24-1	111	38	-9.16	0.332	0	6
C-24-4	118	43	-9.11	0.352	1	6

Appendix F : Rainflow Plots

Table F-1: Rainflow mean bins.

Number	Range
	με
1	-400 to -310
2	-310 to -220
3	-220 to -130
4	-130 to -40
5	-40 to 50
6	50 to 140
7	140 to 230
8	230 to 320
9	320 to 410
10	410 to 500

Table F-2: Rainflow amplitude bins.

Number	Range	Number	Range	Number	Range
	με		με		με
1	0 to 20	16	300 to 320	31	600 to 620
2	20 to 40	17	320 to 340	32	620 to 640
3	40 to 60	18	340 to 360	33	640 to 660
4	60 to 80	19	360 to 380	34	660 to 680
5	80 to 100	20	380 to 400	35	680 to 700
6	100 to 120	21	400 to 420	36	700 to 720
7	120 to 140	22	420 to 440	37	720 to 740
8	140 to 160	23	440 to 460	38	740 to 760
9	160 to 180	24	460 to 480	39	760 to 780
10	180 to 200	25	480 to 500	40	780 to 800
11	200 to 220	26	500 to 520	41	800 to 820
12	220 to 240	27	520 to 540	42	820 to 840
13	240 to 260	28	540 to 560	43	840 to 860
14	260 to 280	29	560 to 580	44	860 to 880
15	280 to 300	30	580 to 600	45	880 to 900

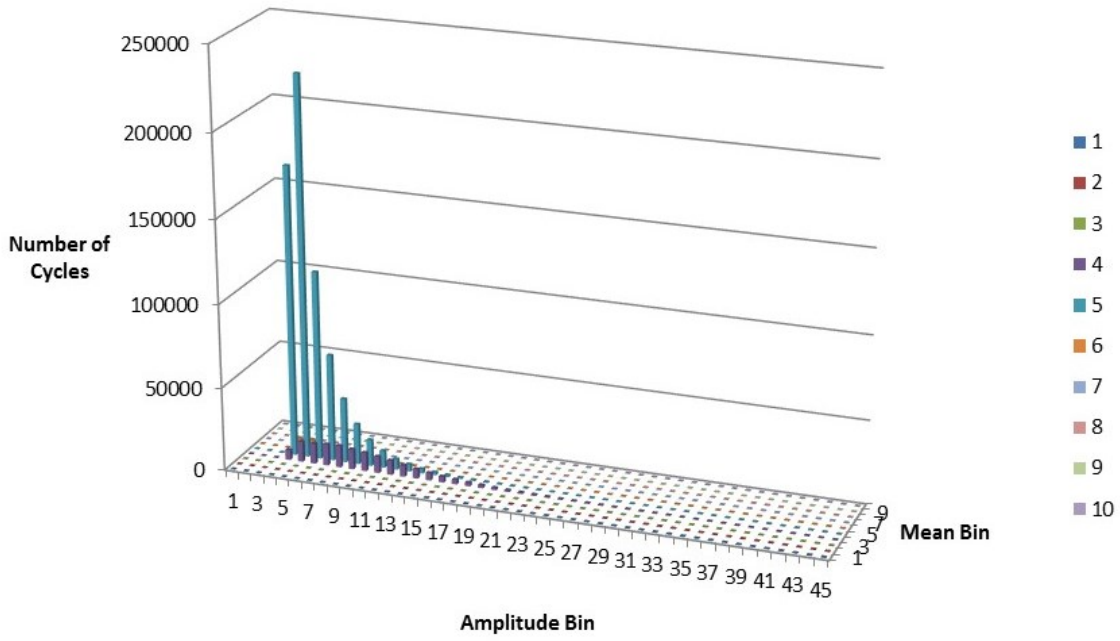

Figure F.1: A-04-1 gauge counts for 2013.

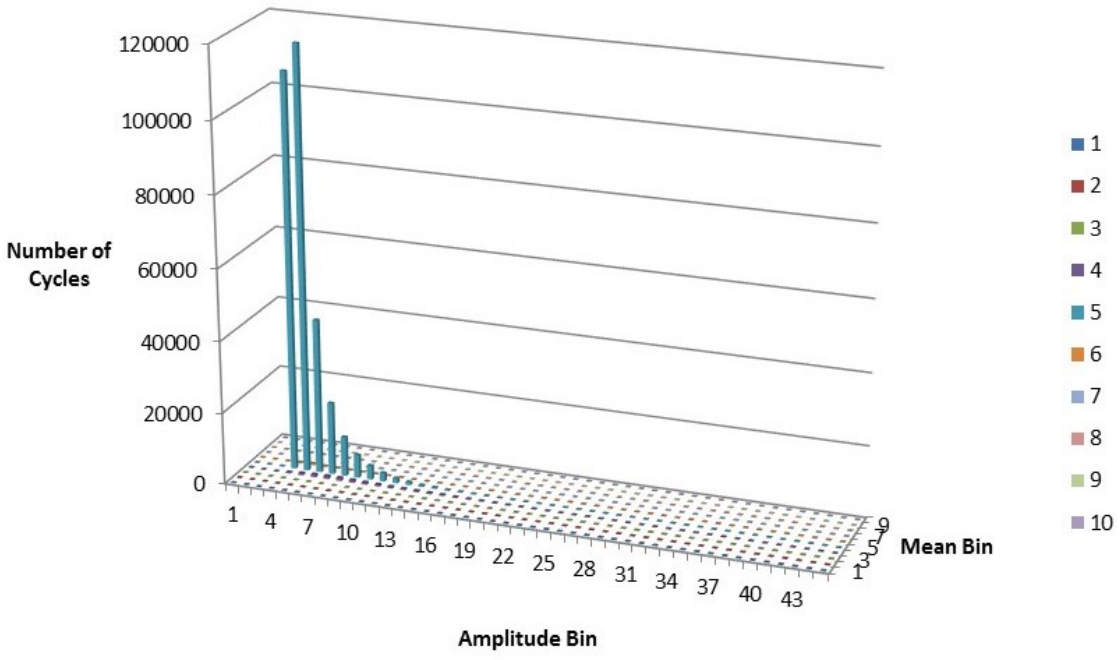

Figure F.2: A-04-2 gauge counts for 2013.

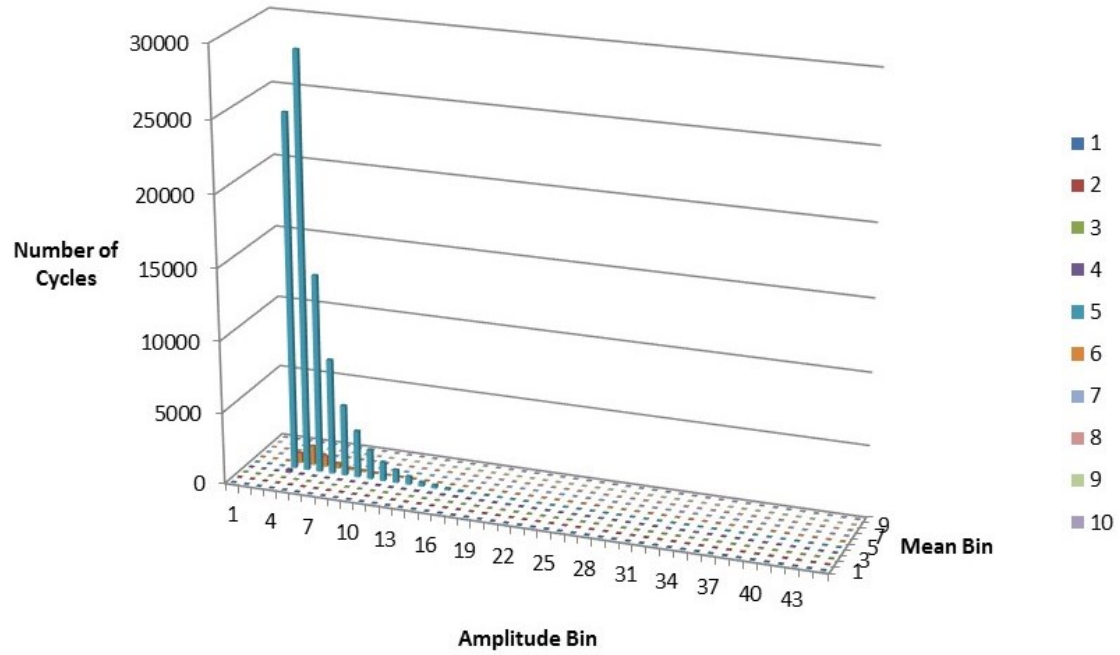

Figure F.3: A-06-1 gauge counts for 2013.

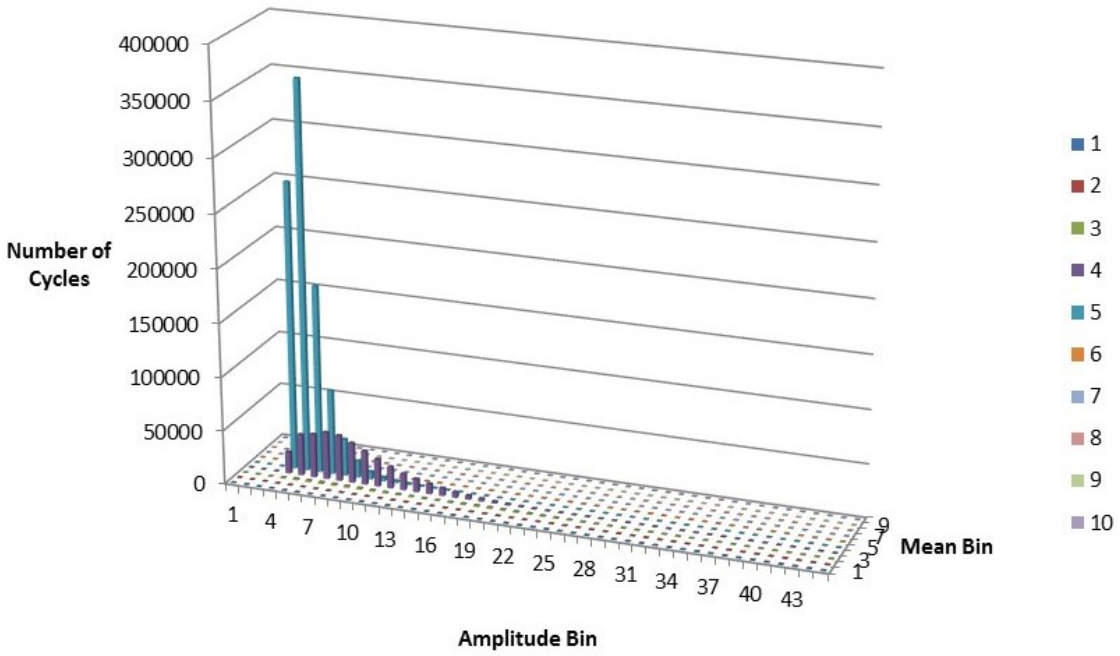

Figure F.4: A-06-2 gauge counts for 2013.

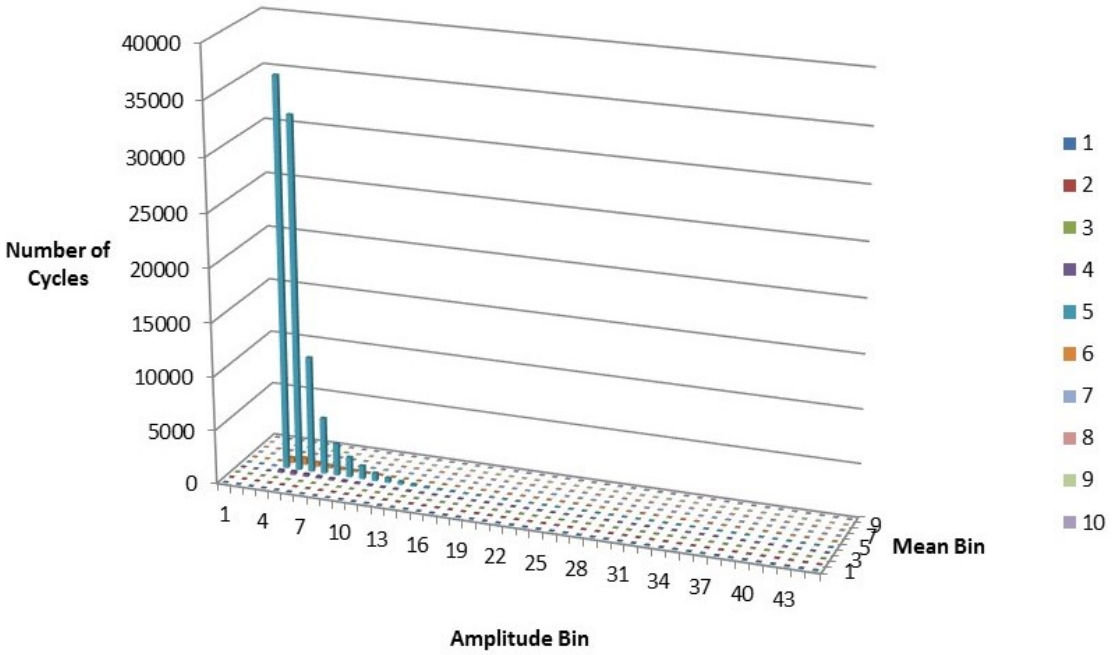

Figure F.5: A-10-2 gauge counts for 2013.

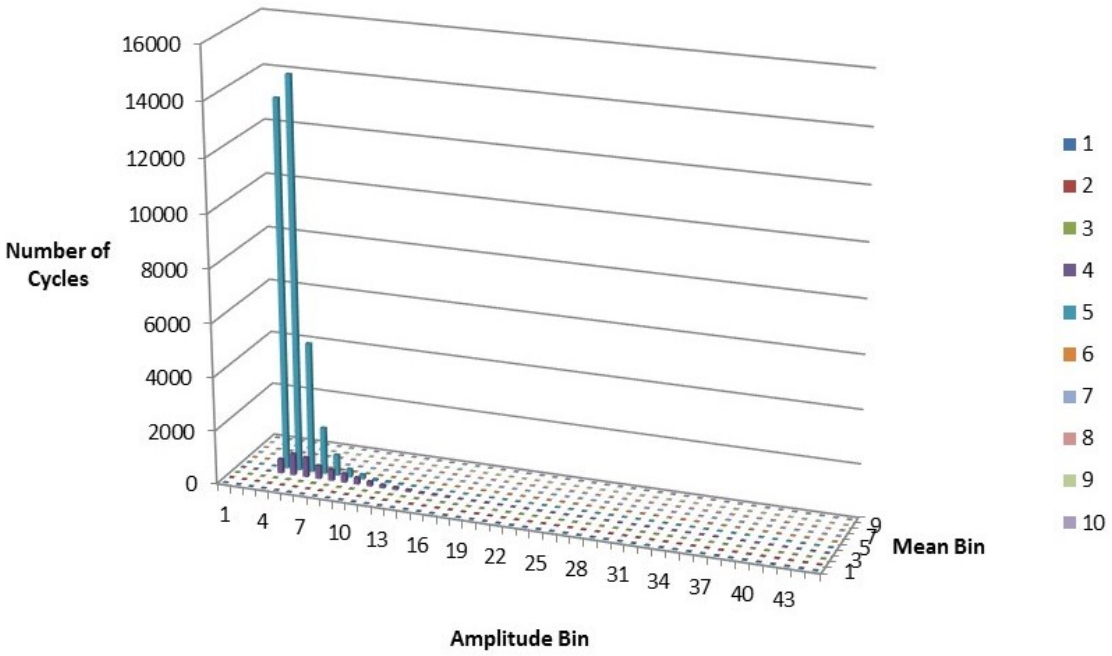

Figure F.6: A-11-1 gauge counts for 2013.

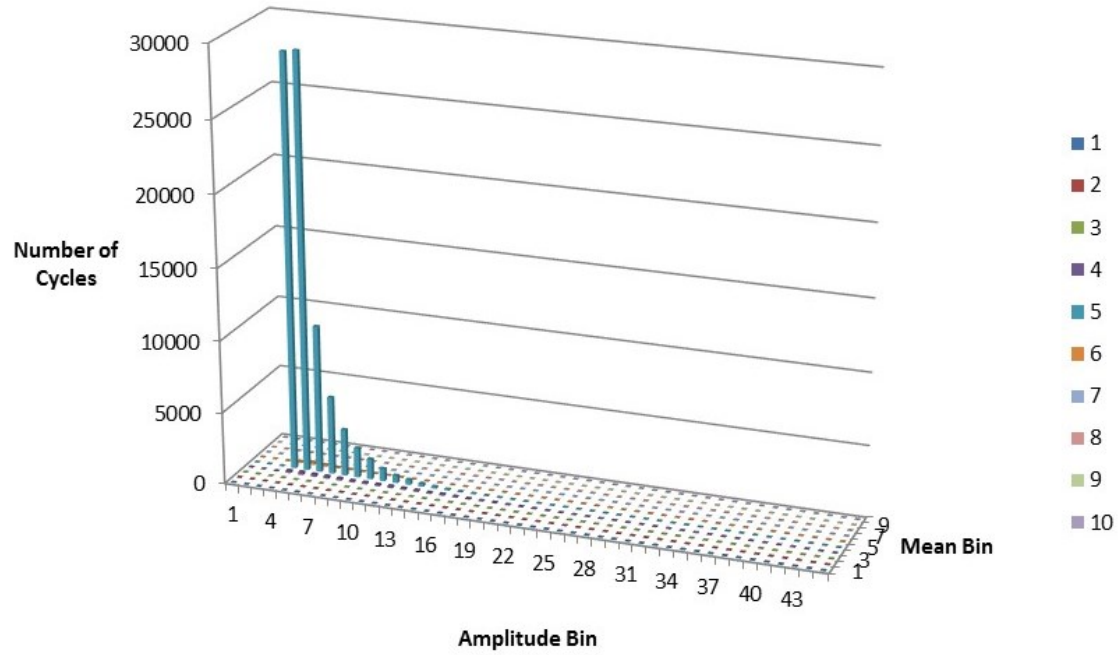

Figure F.7: A-12-1 gauge counts for 2013.

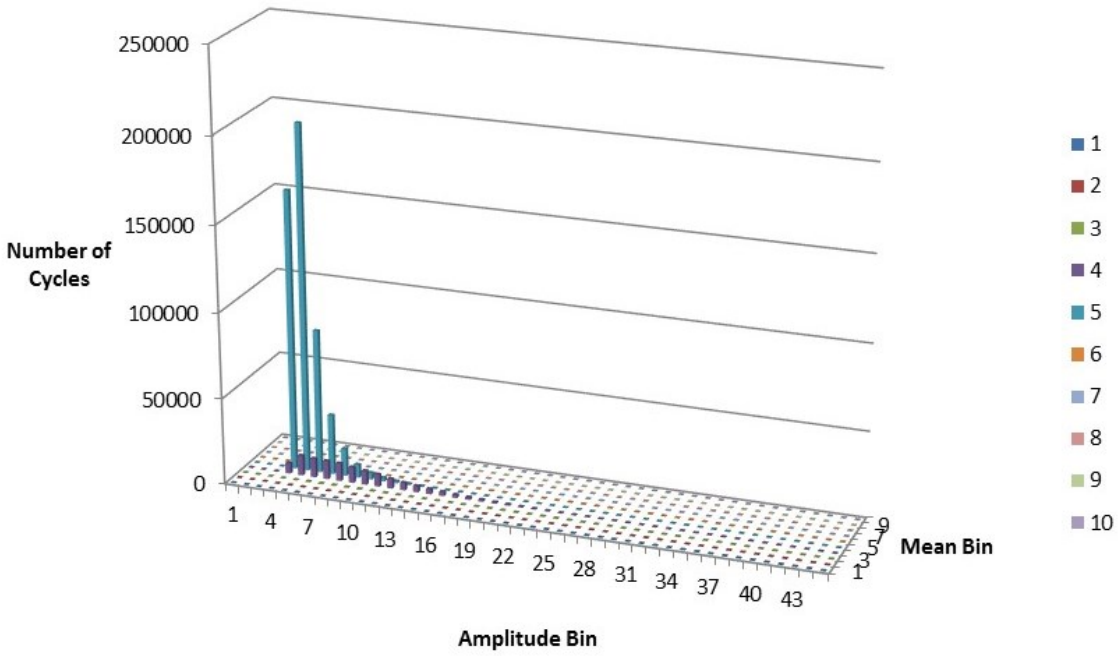

Figure F.8: A-12-2 gauge counts for 2013.

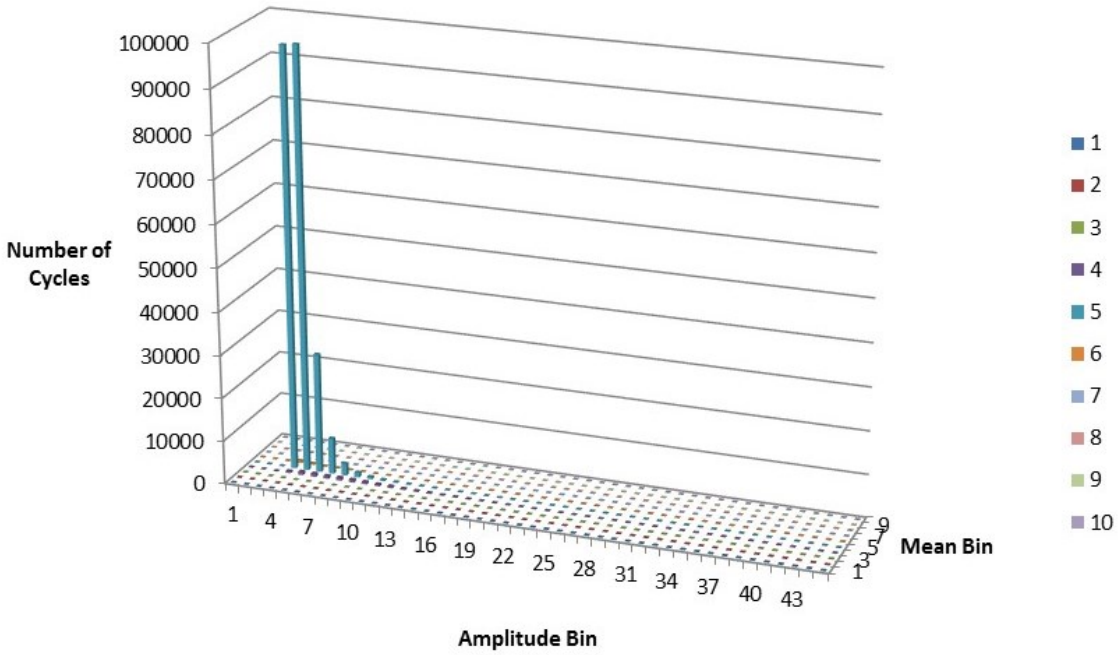

Figure F.9: A-16-1 gauge counts for 2013.

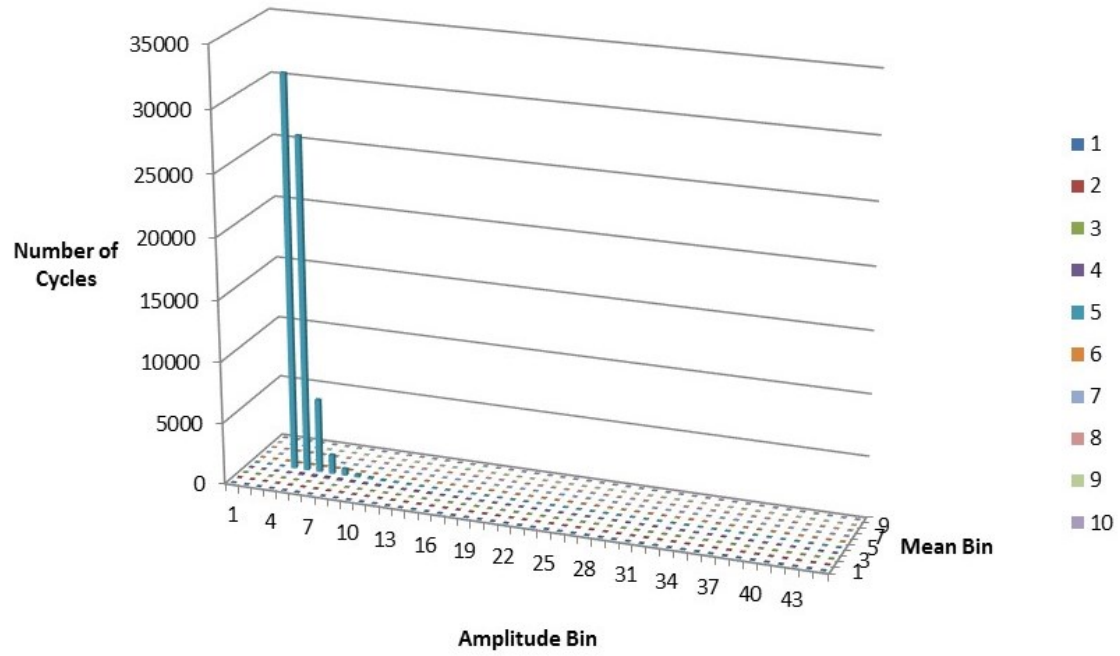

Figure F.10: A-16-2 gauge counts for 2013.

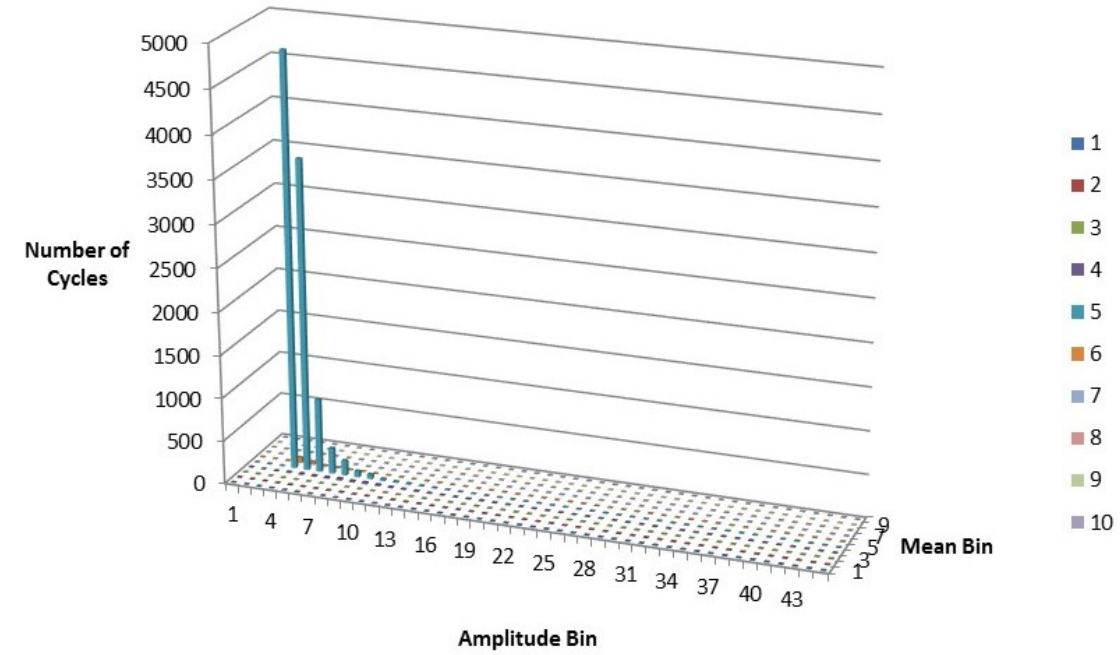

Figure F.11: A-18-1 gauge counts for 2013.

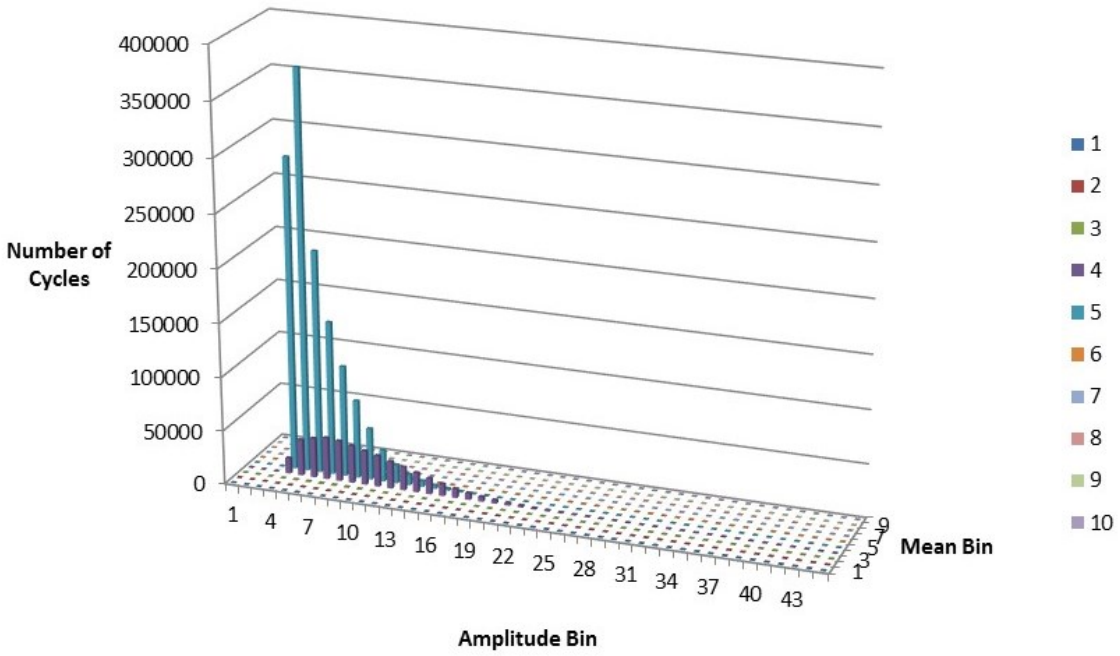

Figure F.12: A-21-2 gauge counts for 2013.

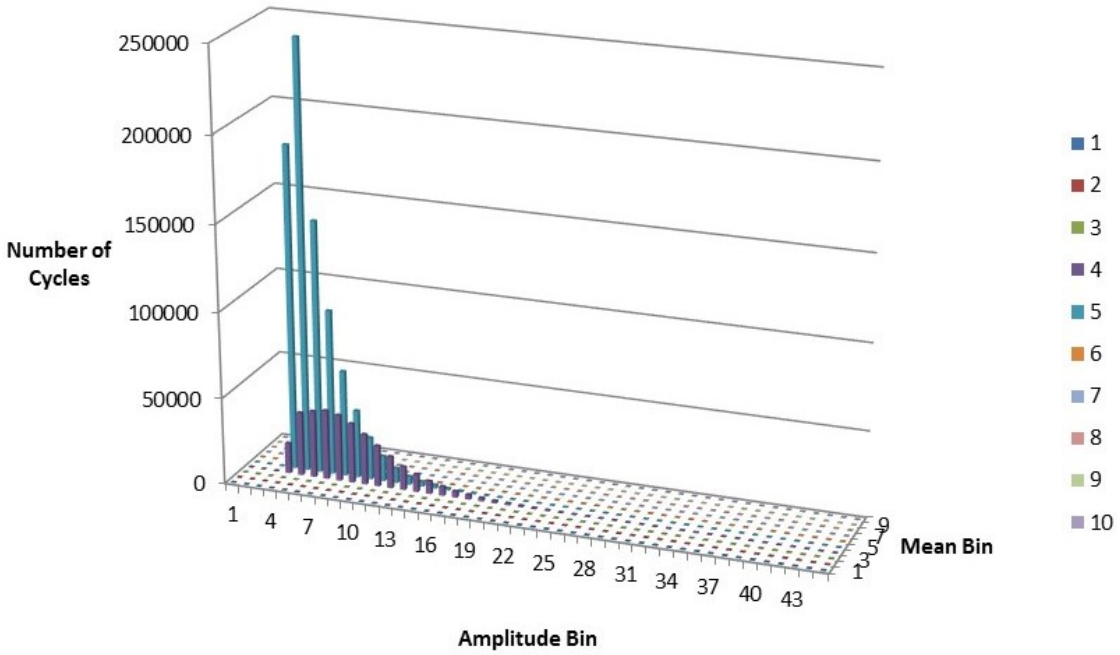

Figure F.13: A-24-1 gauge counts for 2013.

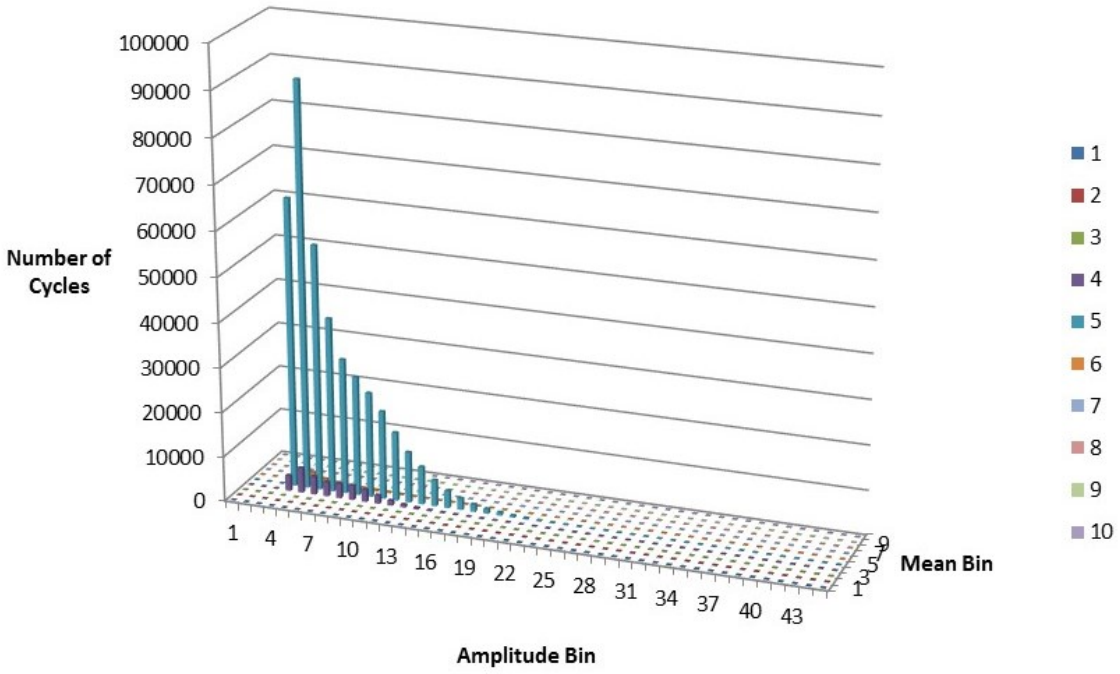

Figure F.14: B-04-1 gauge counts for 2013.

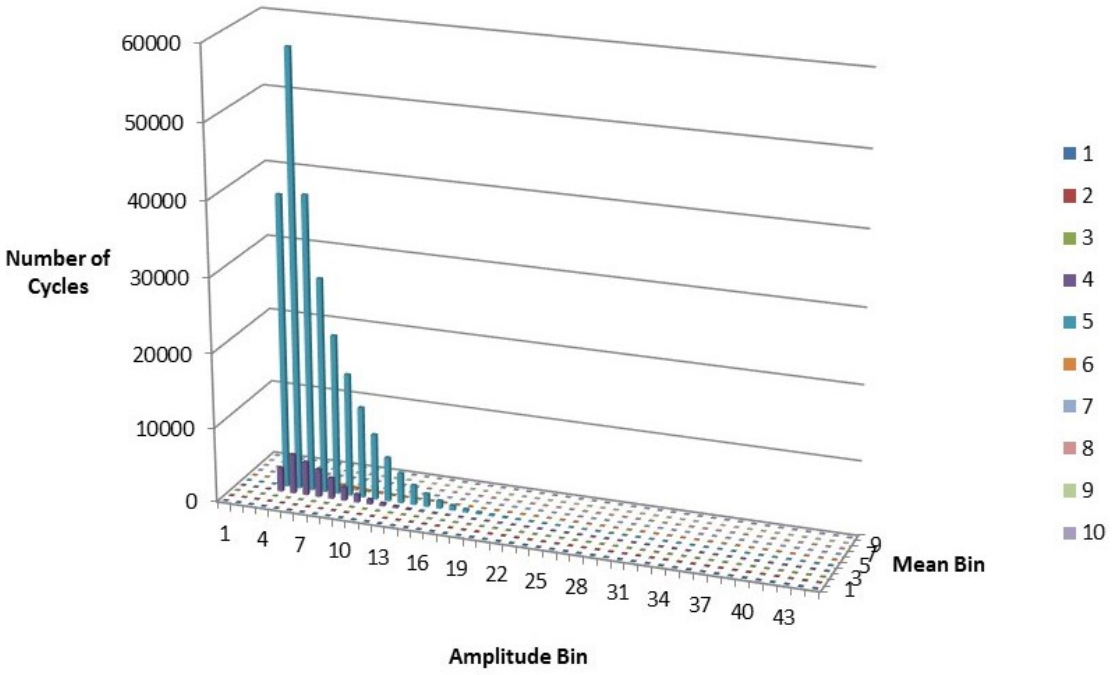

Figure F.15: B-06-1 gauge counts for 2013.

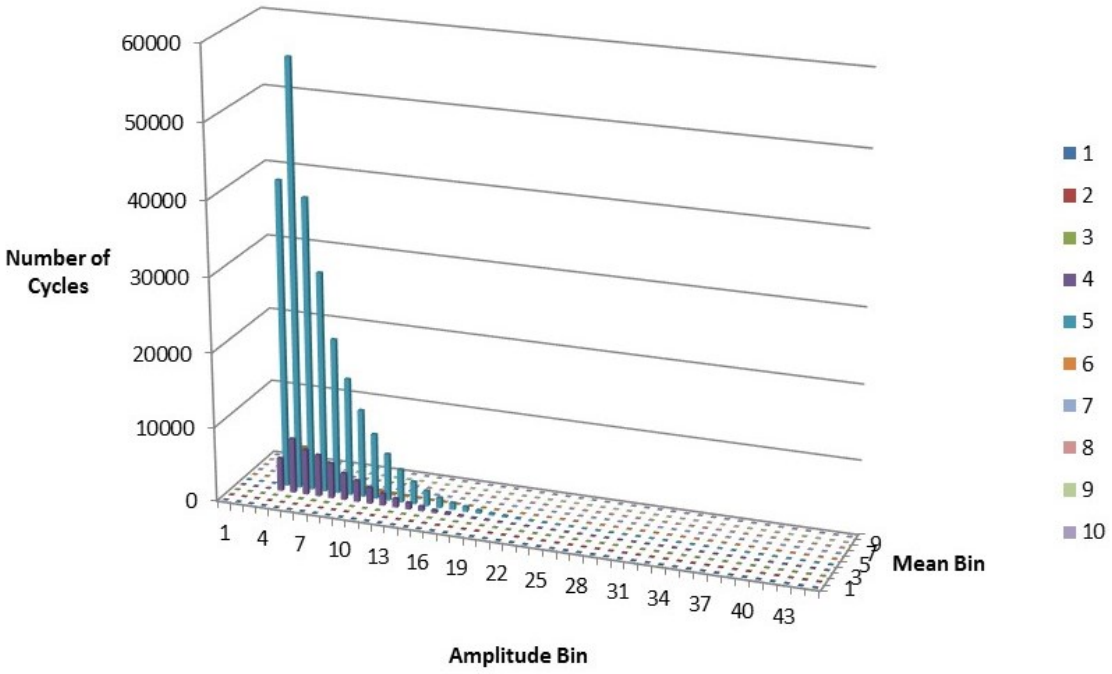

Figure F.16: B-06-2 gauge counts for 2013.

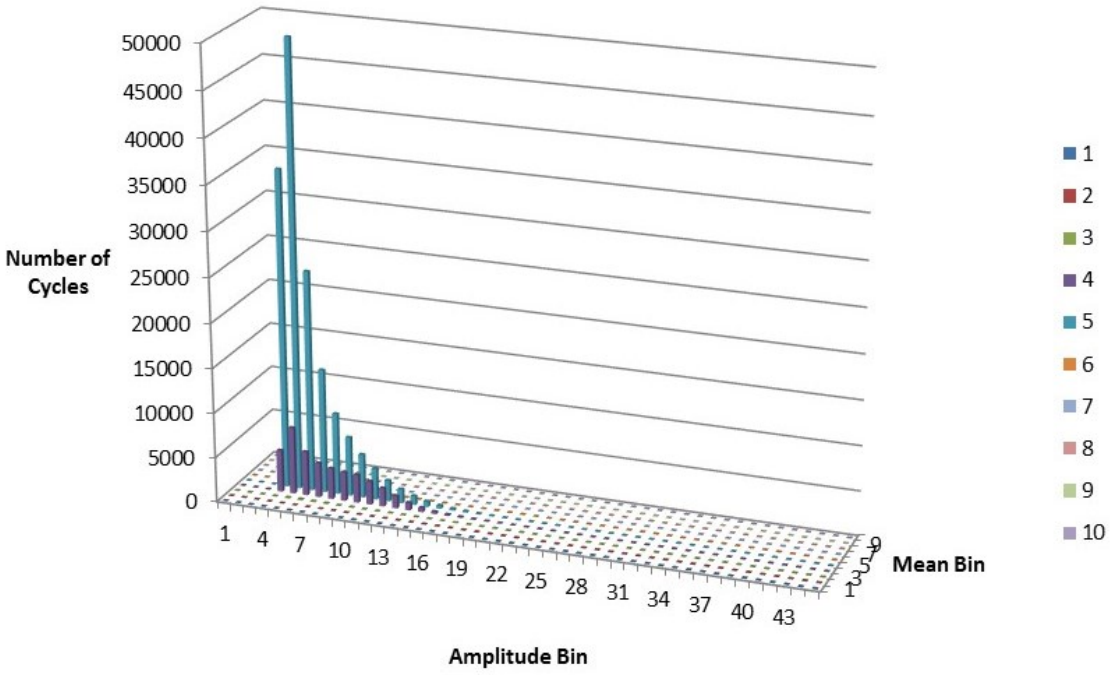

Figure F.17: B-10-2 gauge counts for 2013.

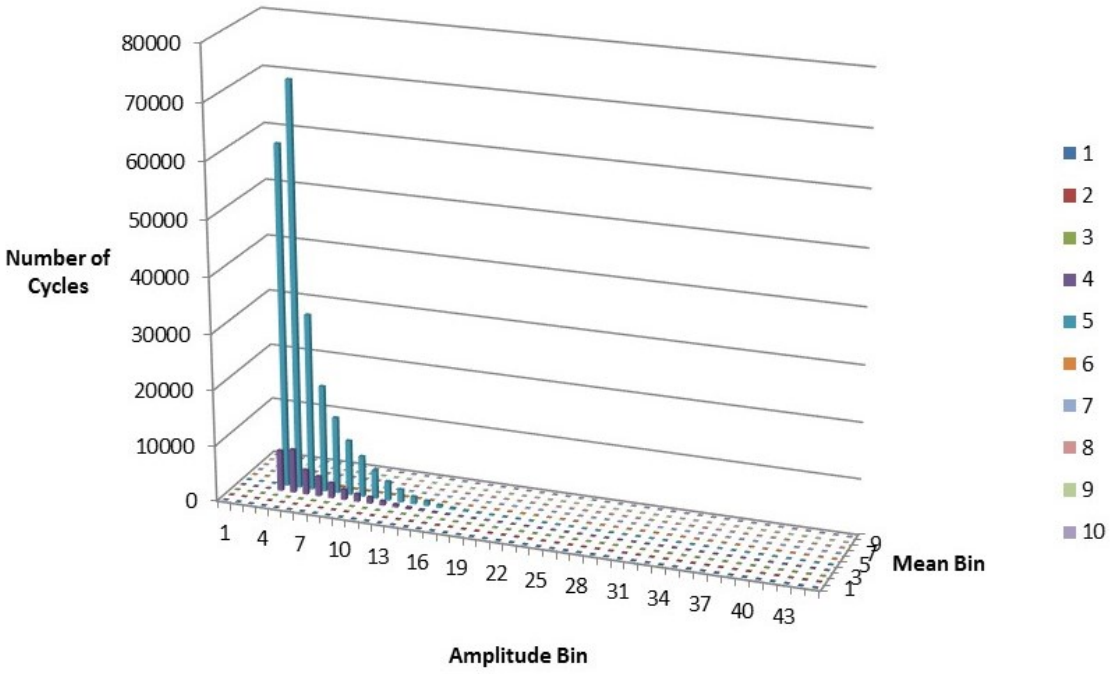

Figure F.18: B-12-1 gauge counts for 2013.

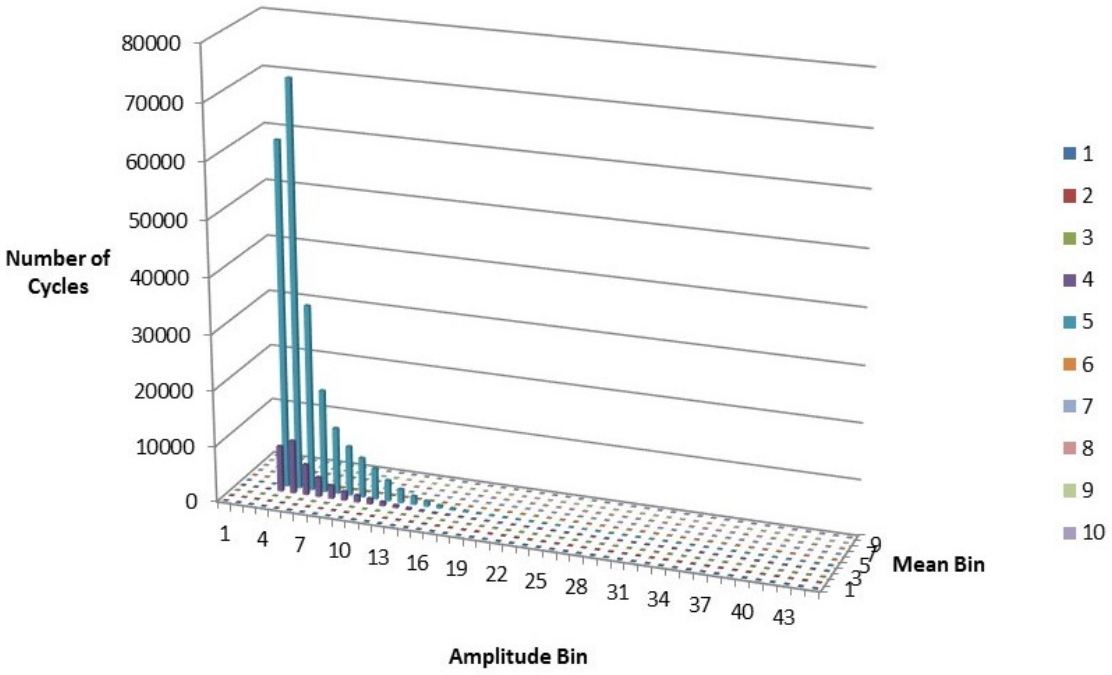

Figure F.19: B-12-2 gauge counts for 2013.

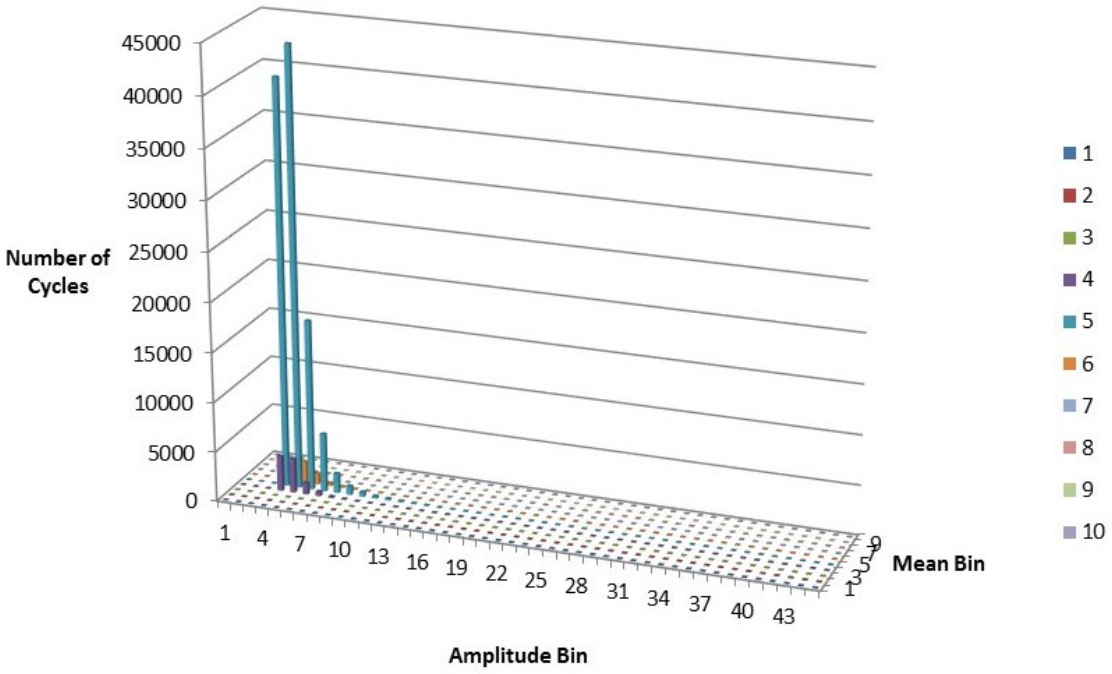

Figure F.20: B-16-1 gauge counts for 2013.

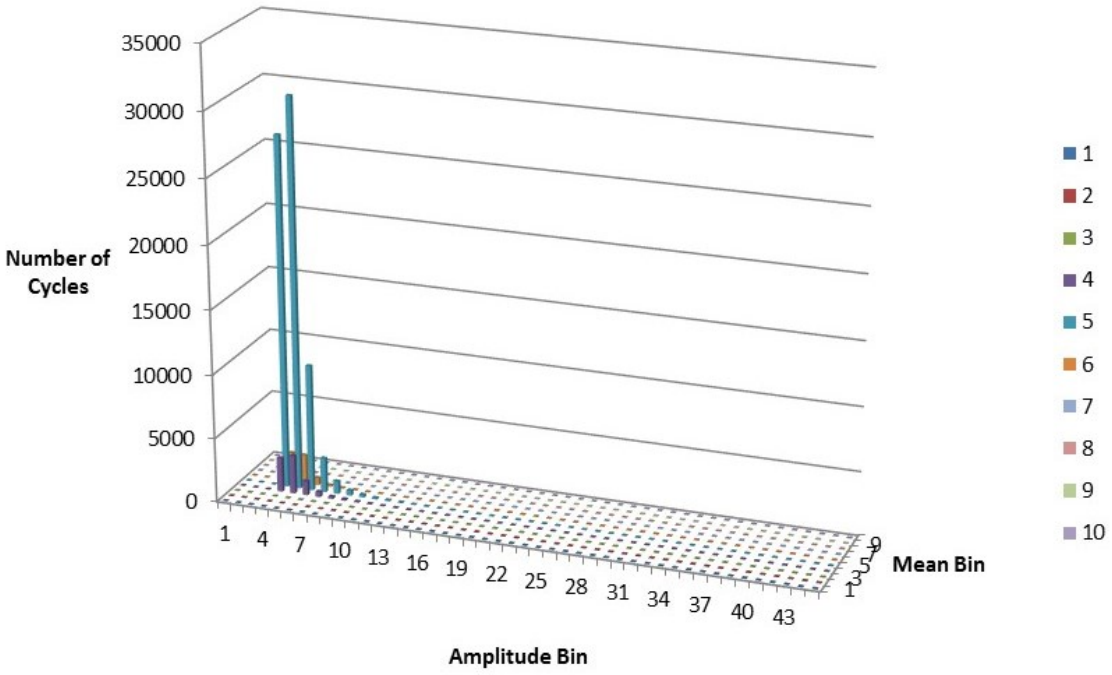

Figure F.21: B-16-2 gauge counts for 2013.

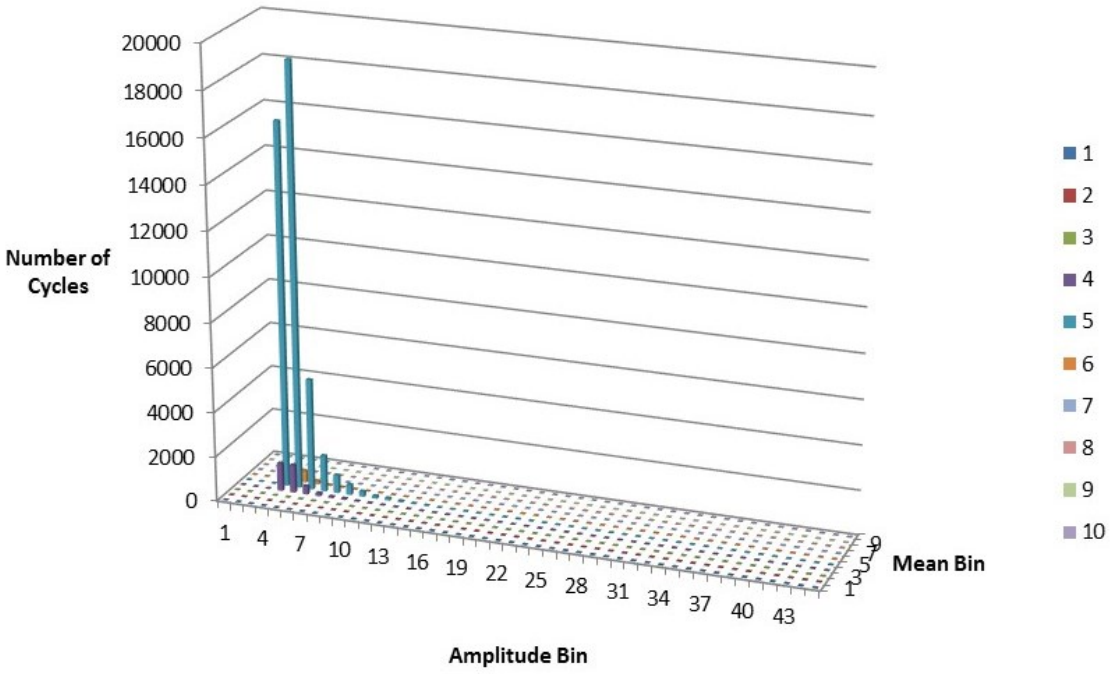

Figure F.22: B-18-1 gauge counts for 2013.

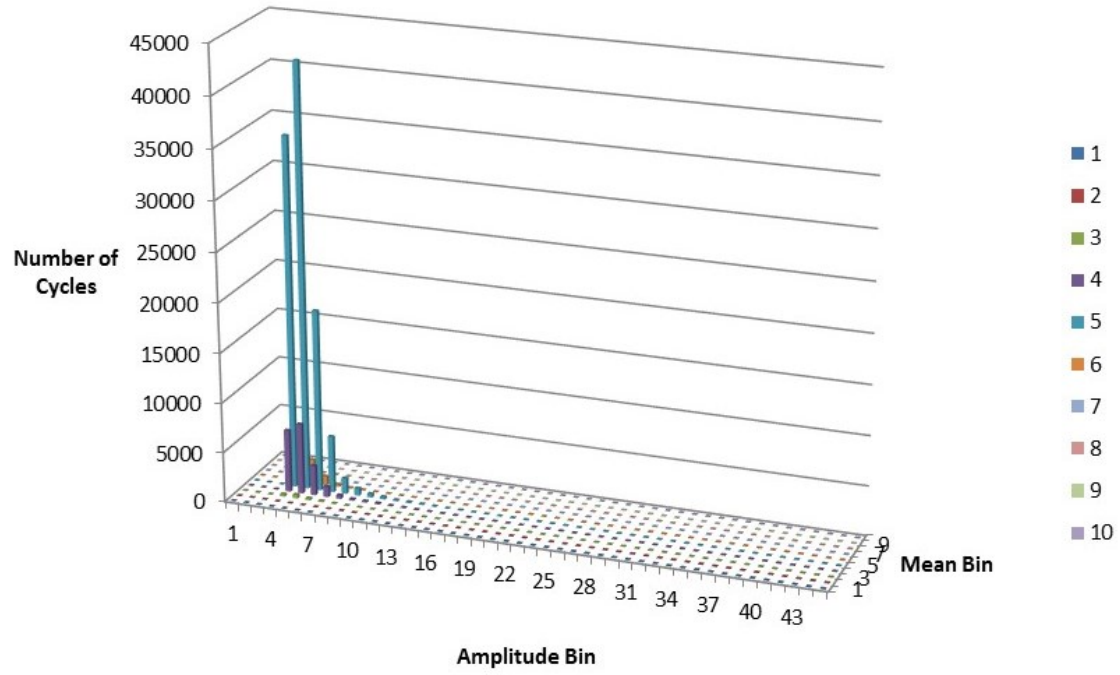

Figure F.23: B-18-2 gauge counts for 2013.

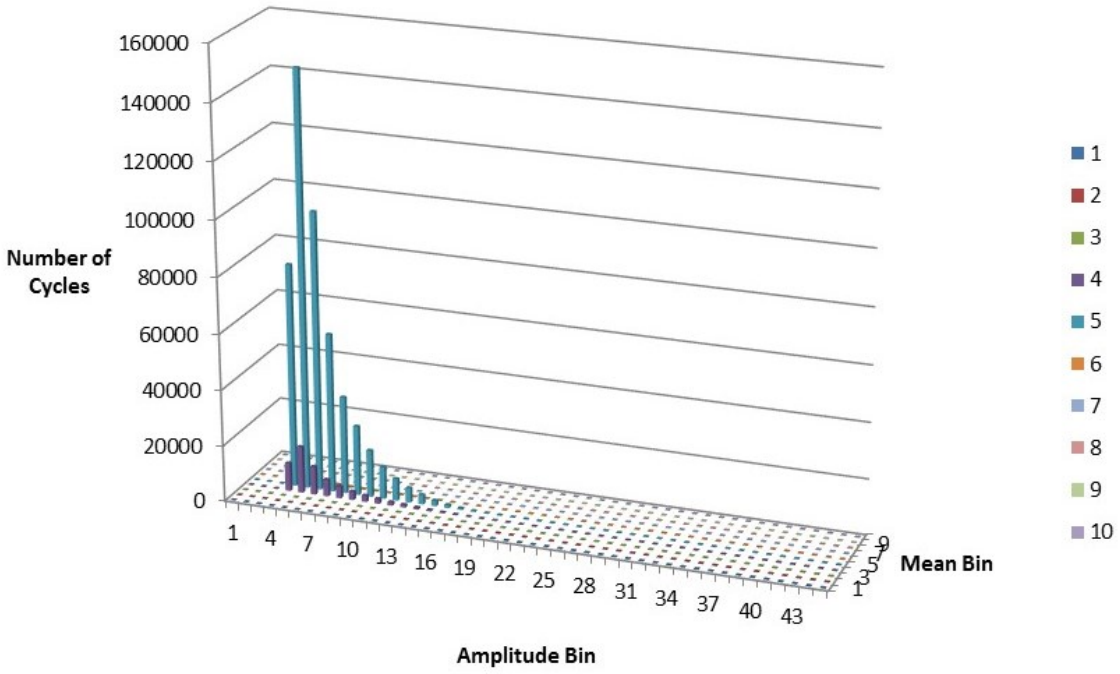

Figure F.24: B-21-1 gauge counts for 2013.

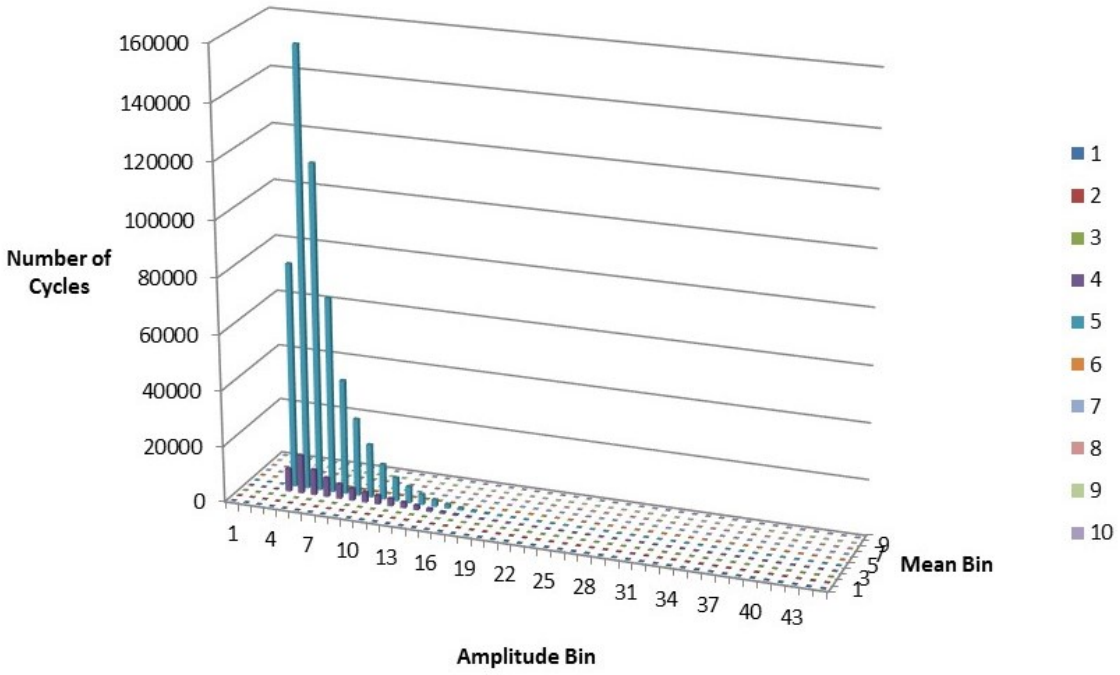

Figure F.25: B-21-2 gauge counts for 2013.

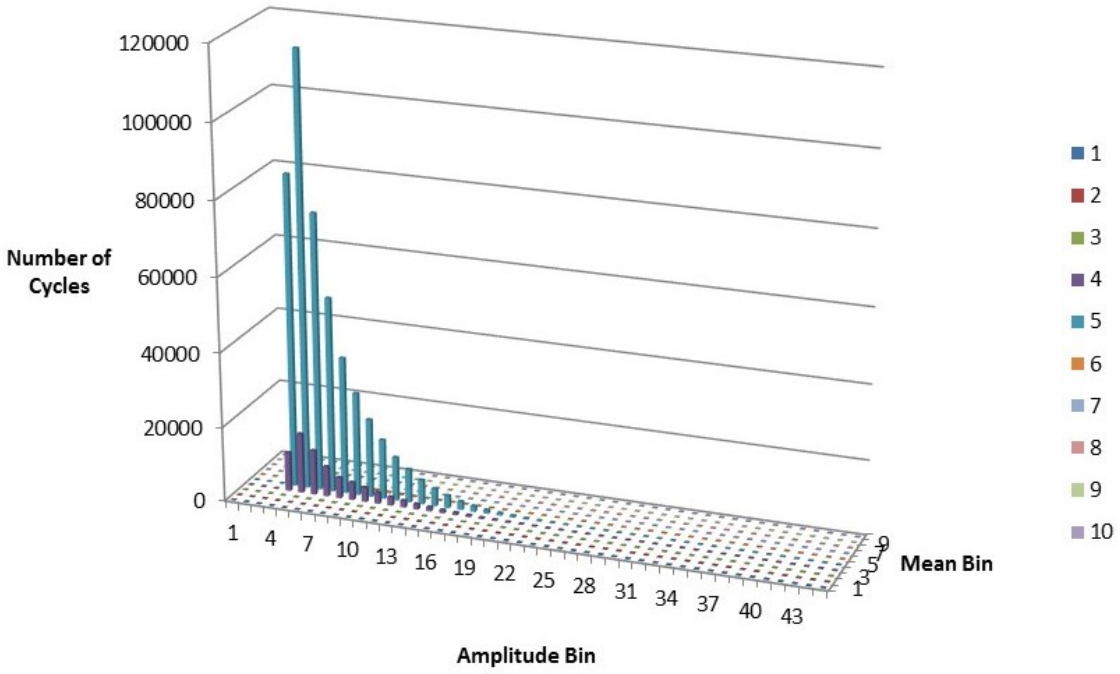

Figure F.26: B-24-1 gauge counts for 2013.

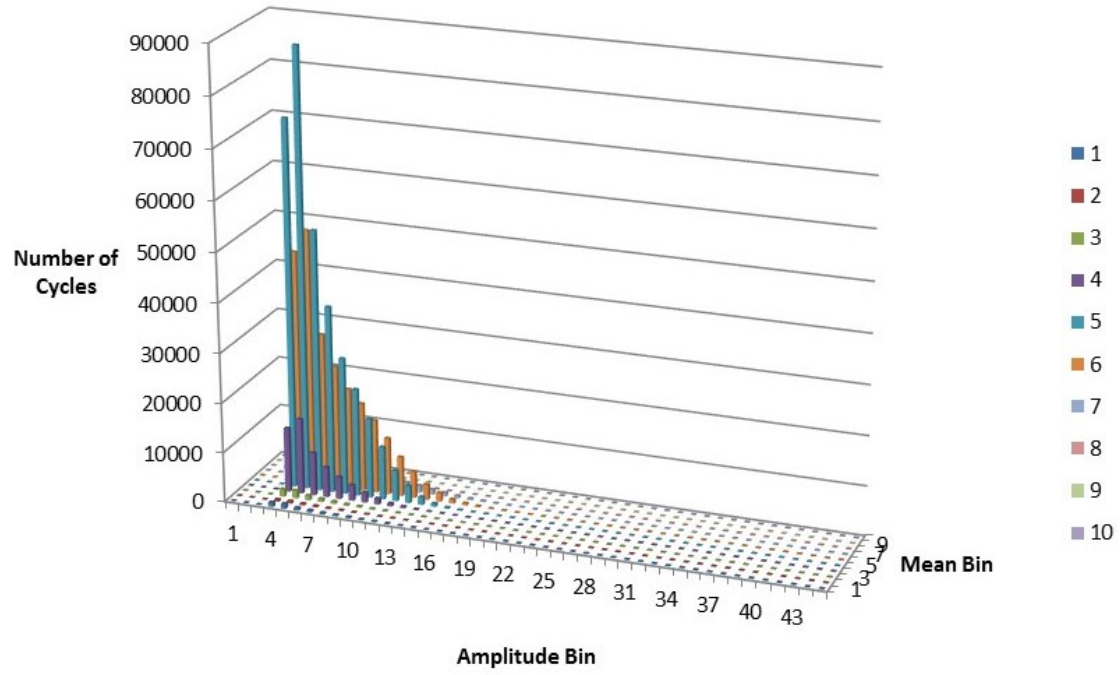

Figure F.27: C-04-1 gauge counts for 2013.

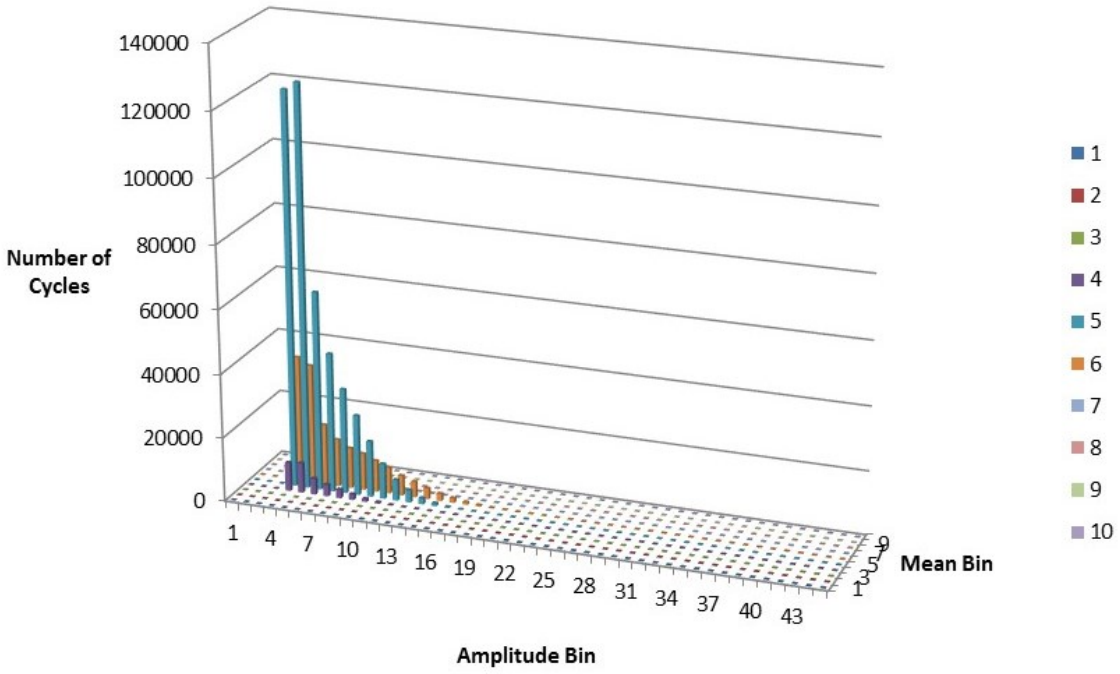

Figure F.28: C-04-4 gauge counts for 2013.

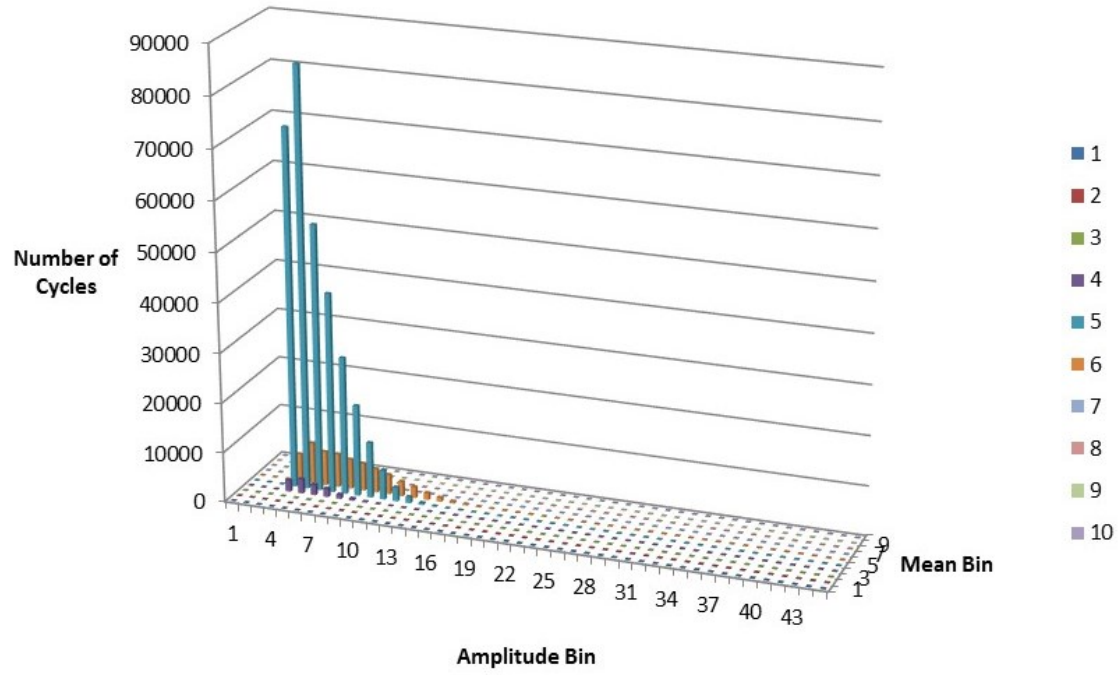

Figure F.29: C-06-1 gauge counts for 2013.

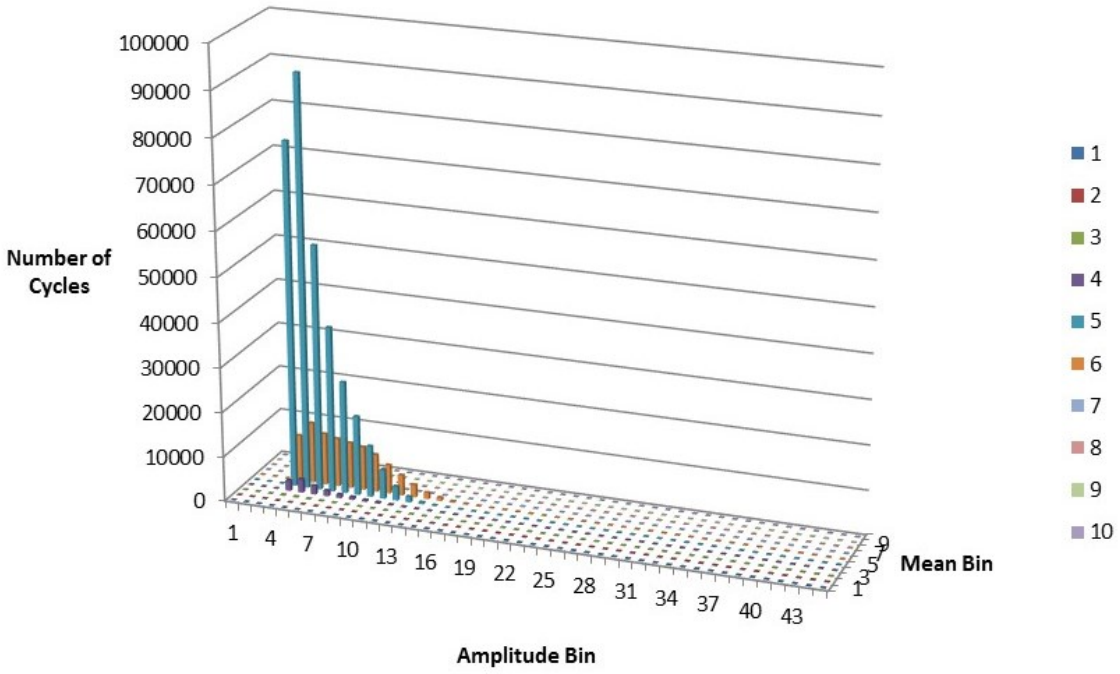

Figure F.30: C-06-4 gauge counts for 2013.

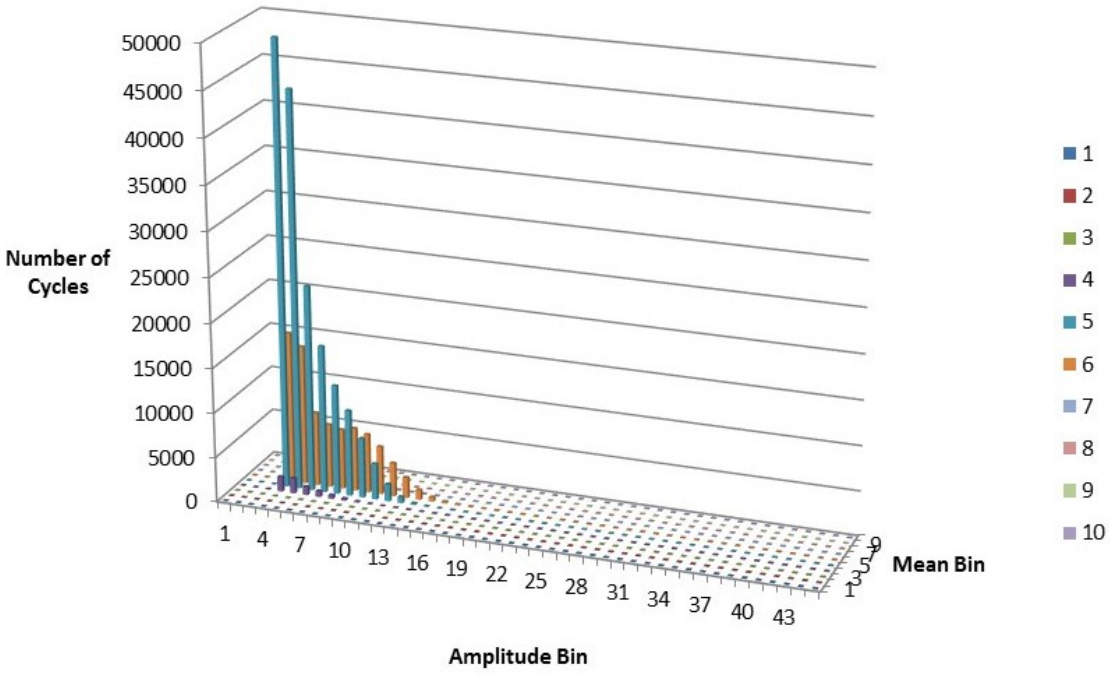

Figure F.31: C-10-1 gauge counts for 2013.

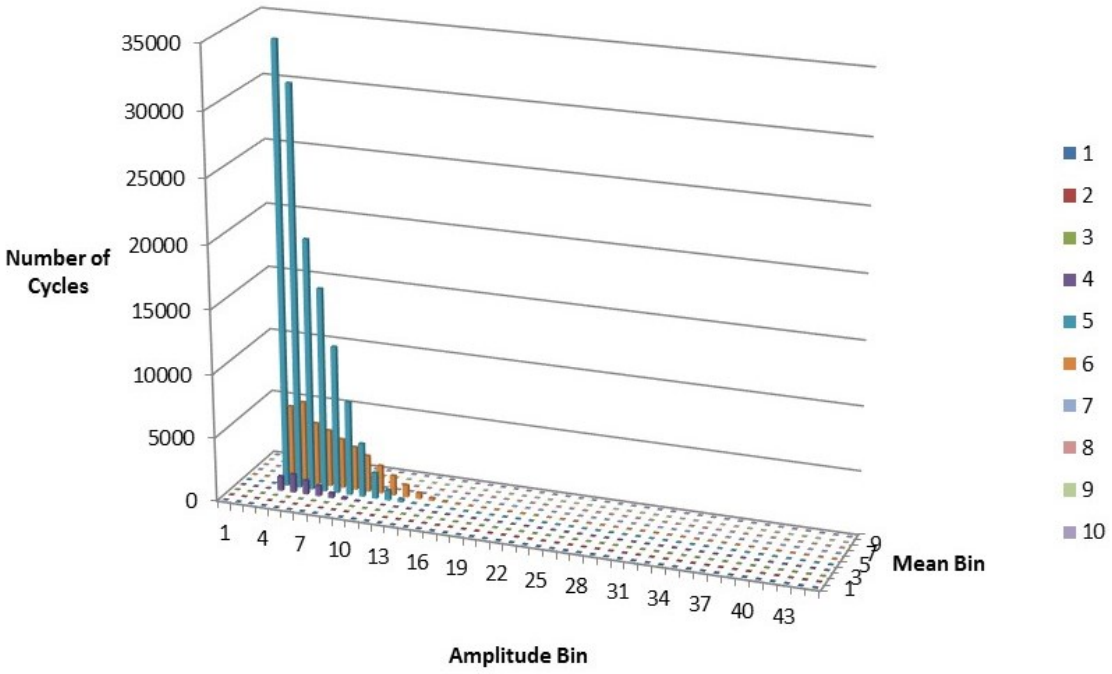

Figure F.32: C-10-4 gauge counts for 2013.

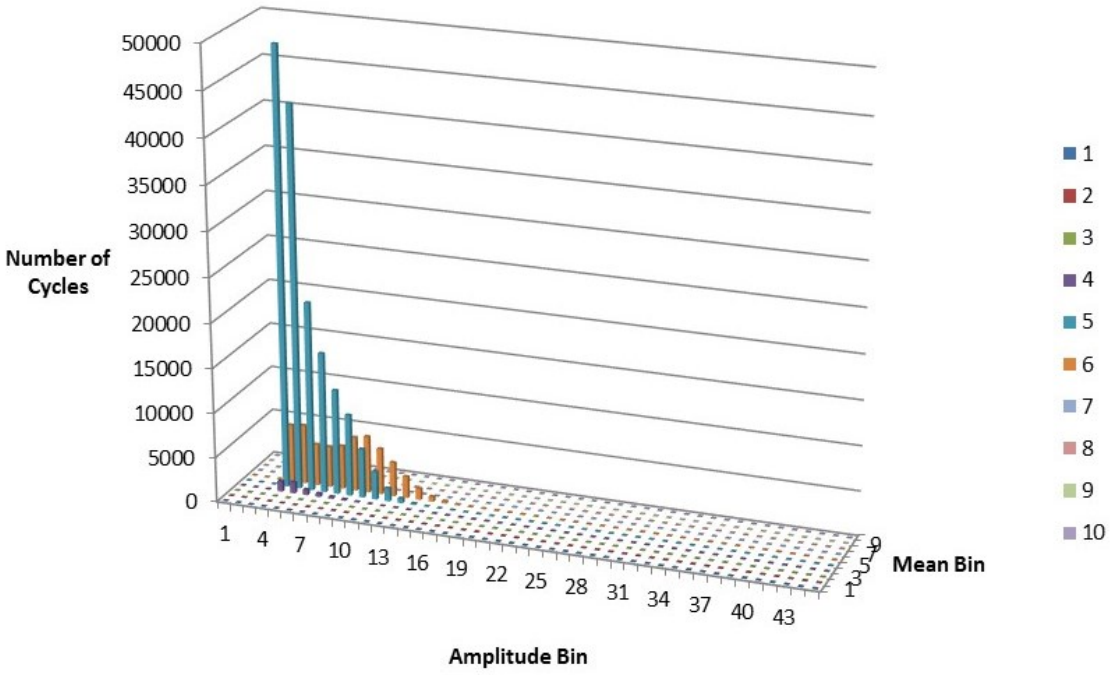

Figure F.33: C-12-4 gauge counts for 2013.

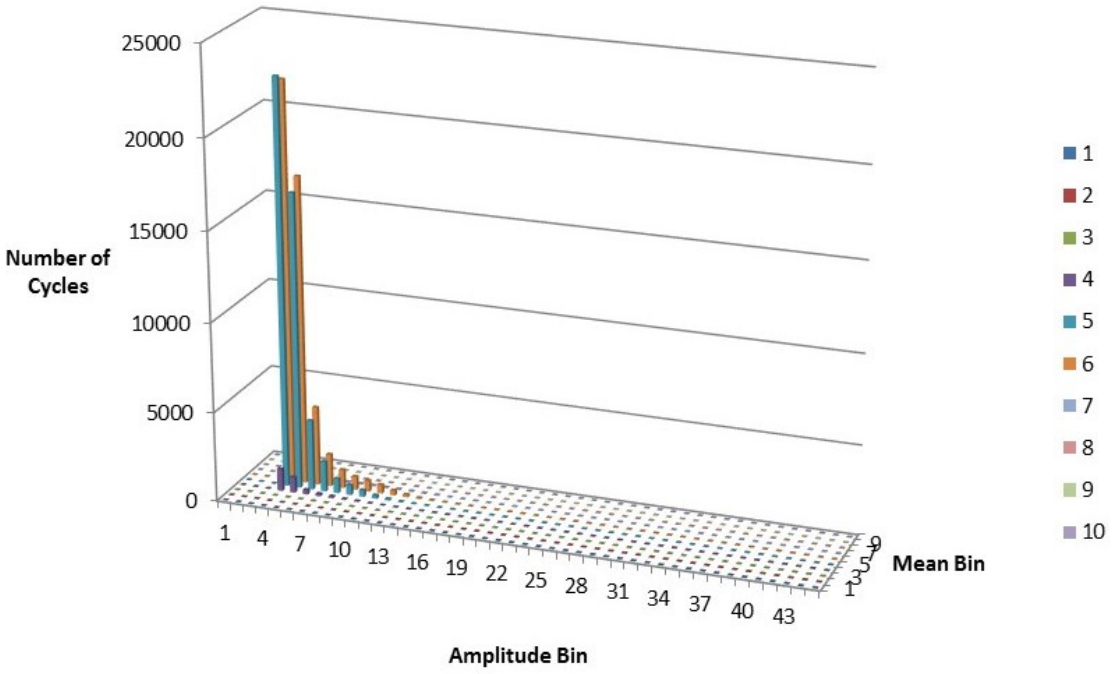

Figure F.34: C-16-1 gauge counts for 2013.

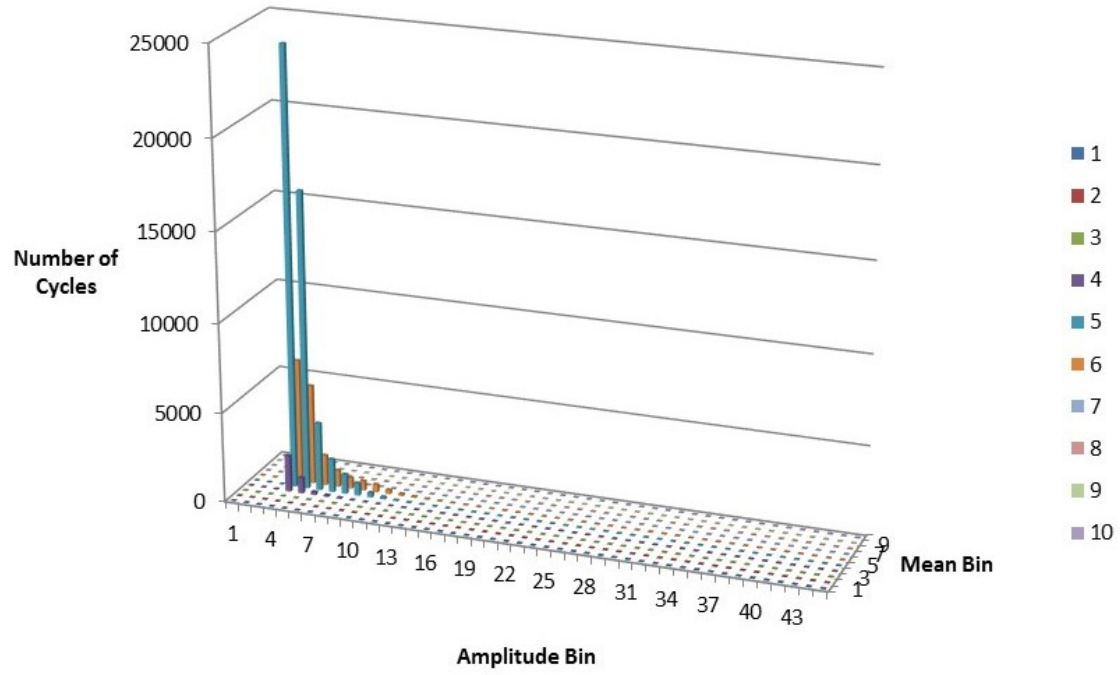

Figure F.35: C-18-4 gauge counts for 2013.

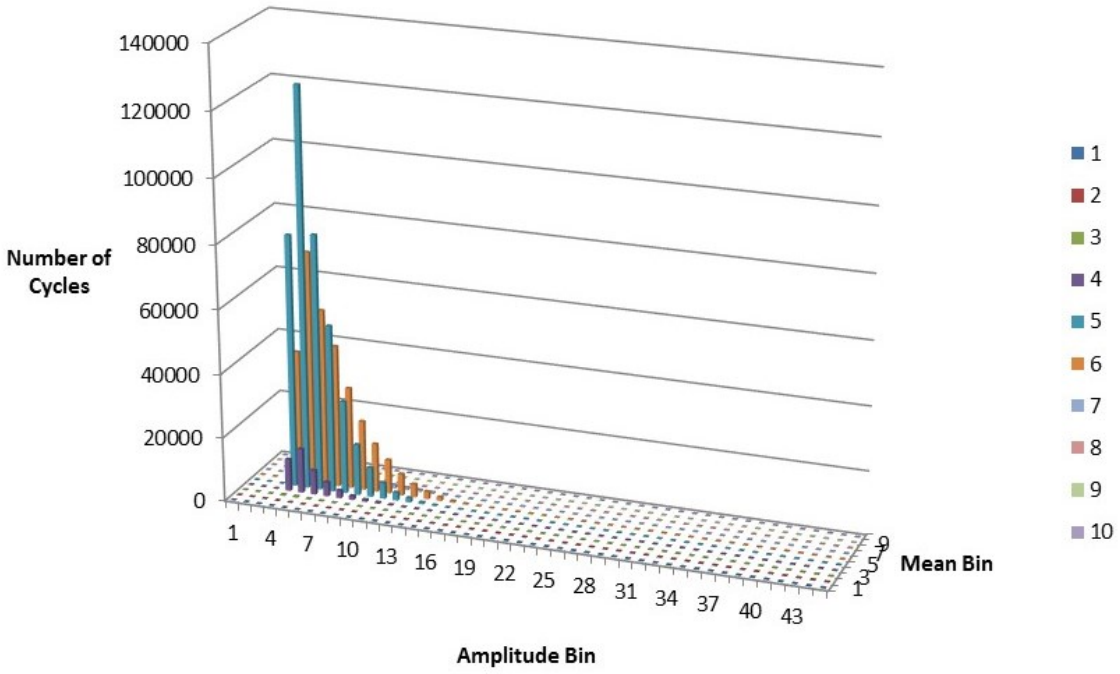

Figure F.36: C-21-1 gauge counts for 2013.

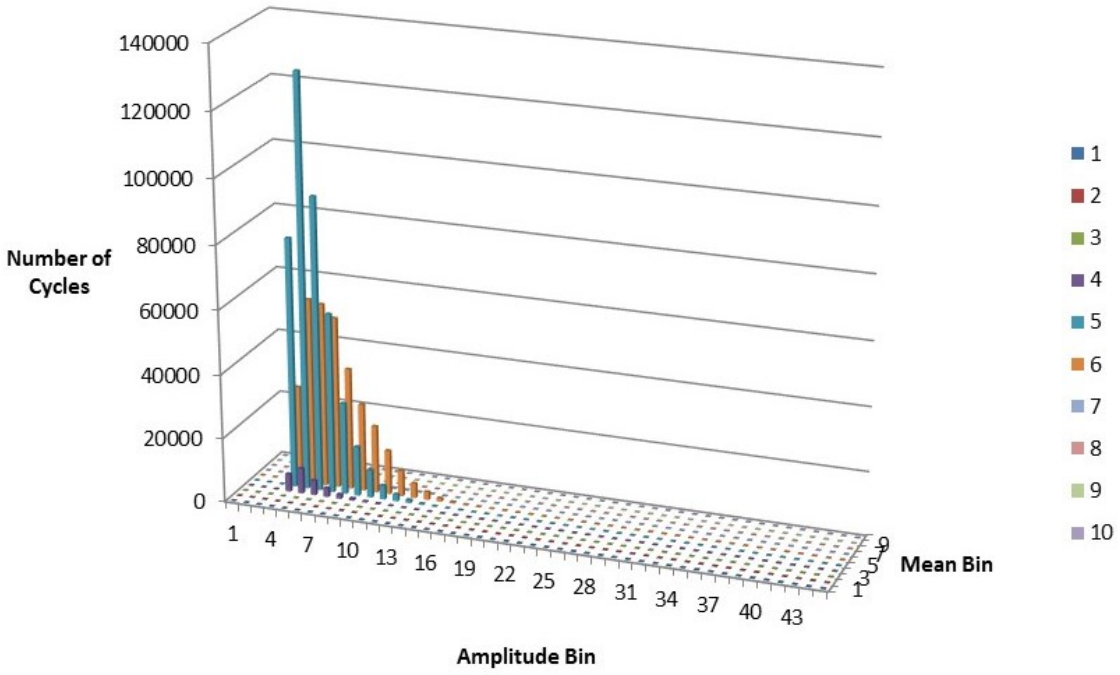

Figure F.37: C-21-4 gauge counts for 2013.

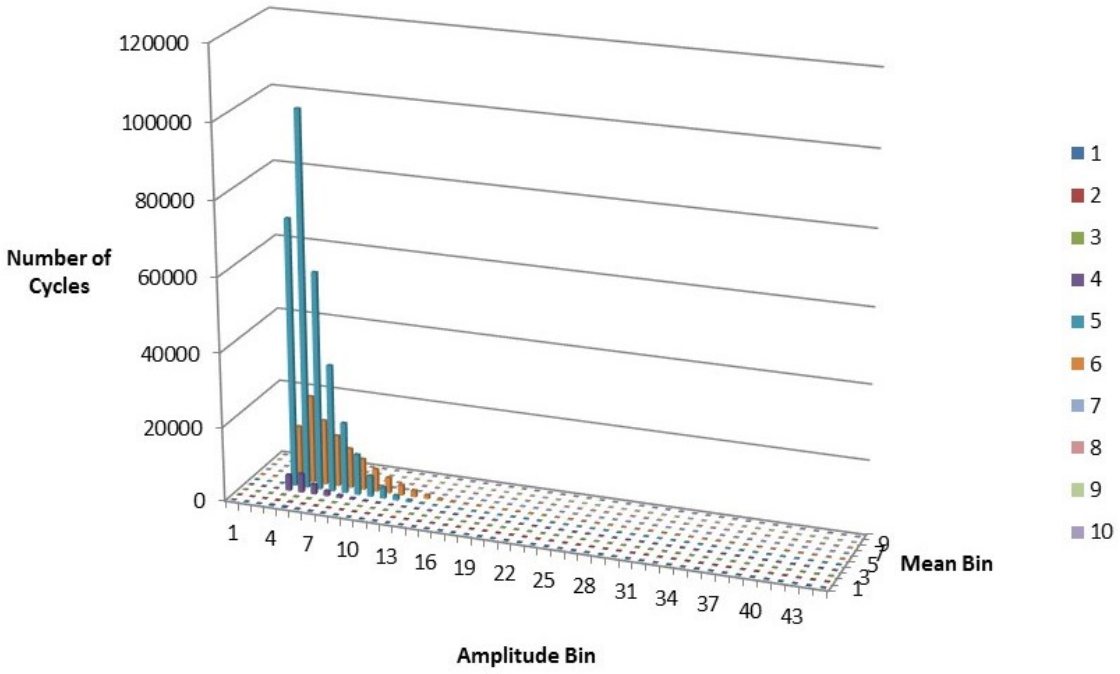

Figure F.38: C-24-1 gauge counts for 2013.

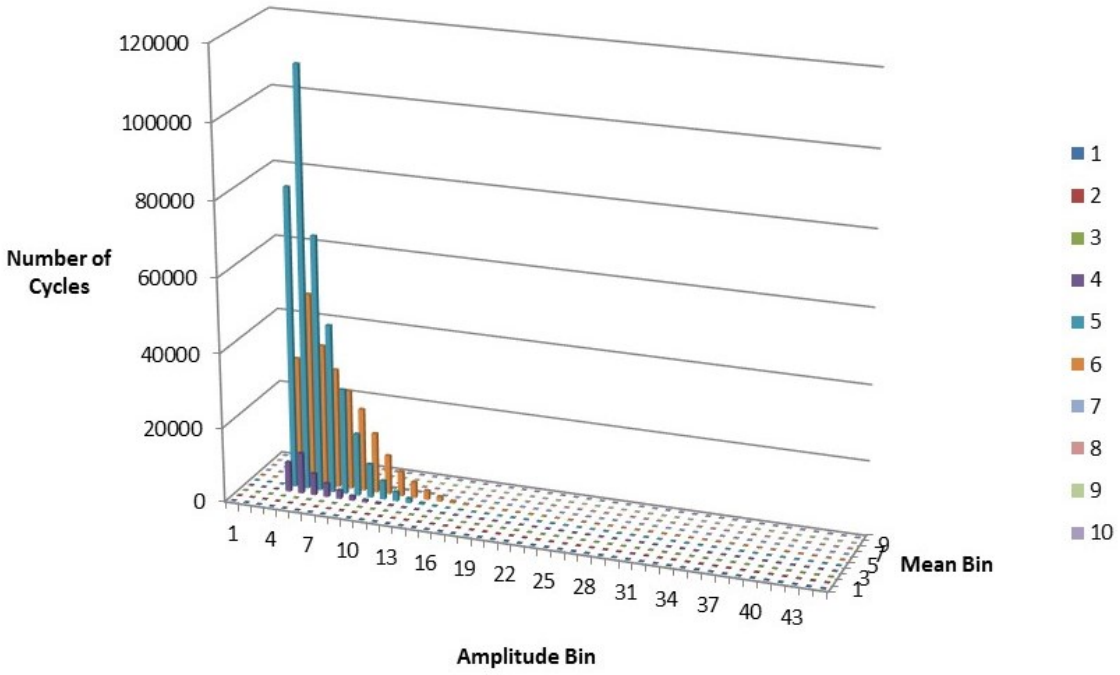

Figure F.39Figure AP F.1: C-24-4 gauge counts for 2013.

Appendix G : Gauge Reliability

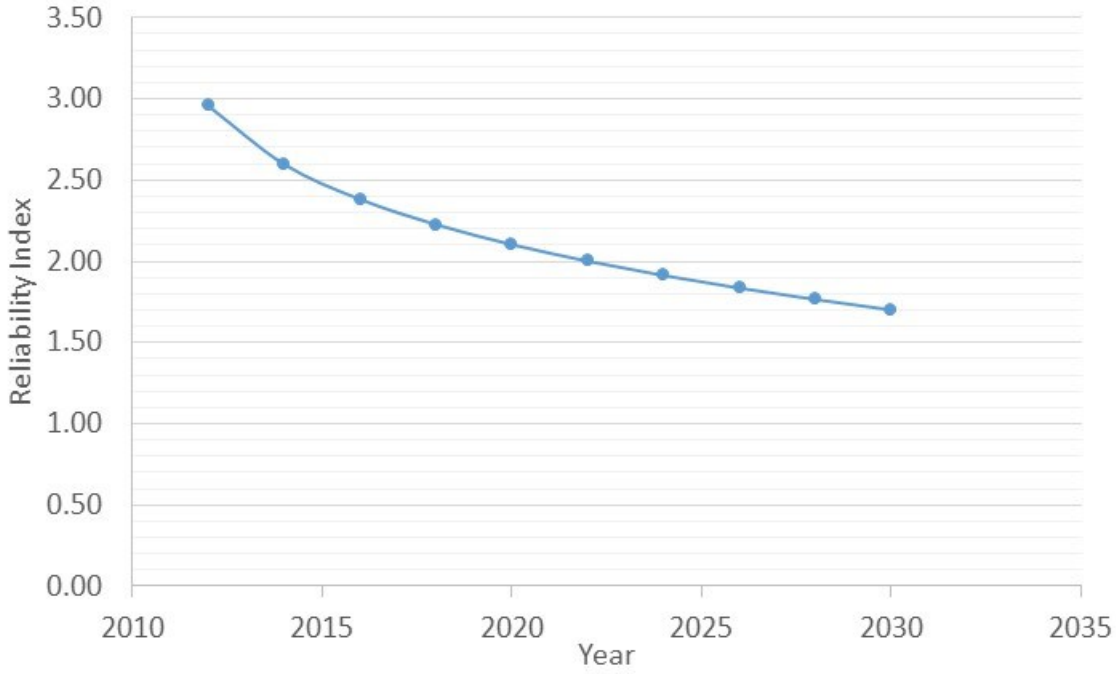

Figure G.1: A-04-1 gauge reliability over time.

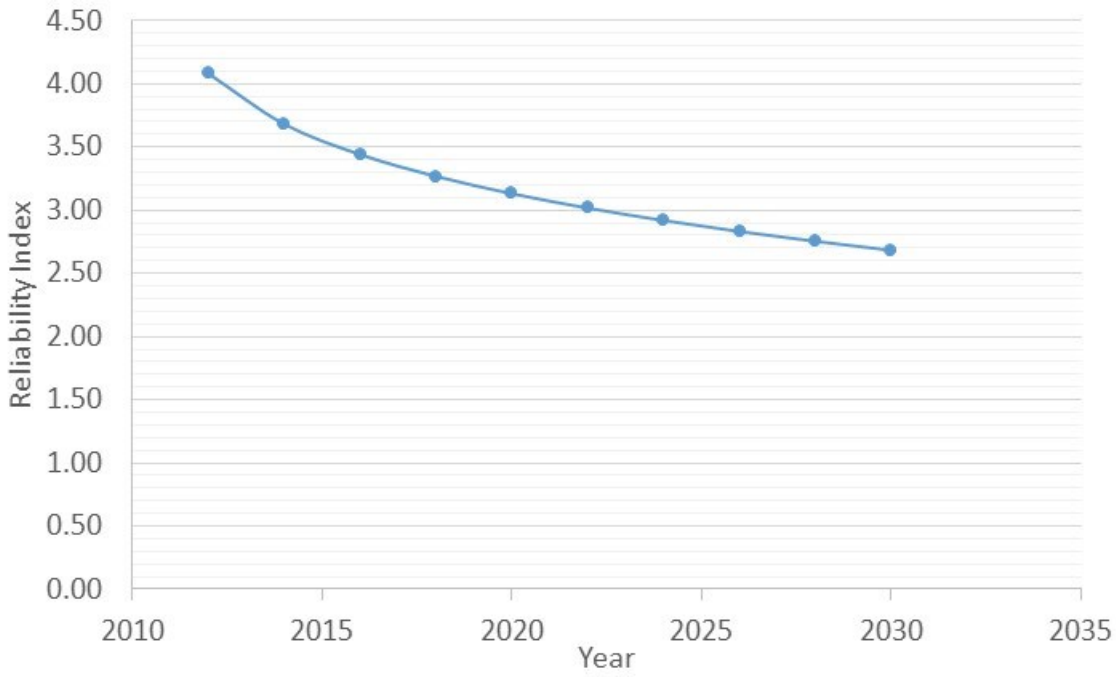

Figure G.2: A-04-2 gauge reliability over time.

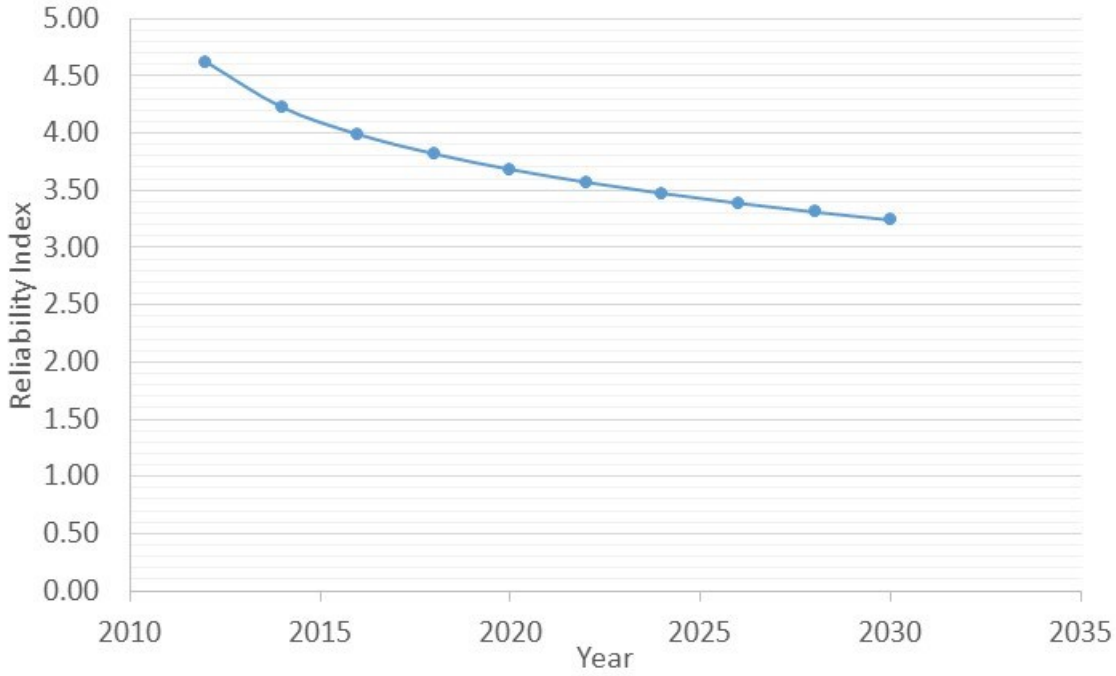

Figure G.3: A-06-1 gauge reliability over time.

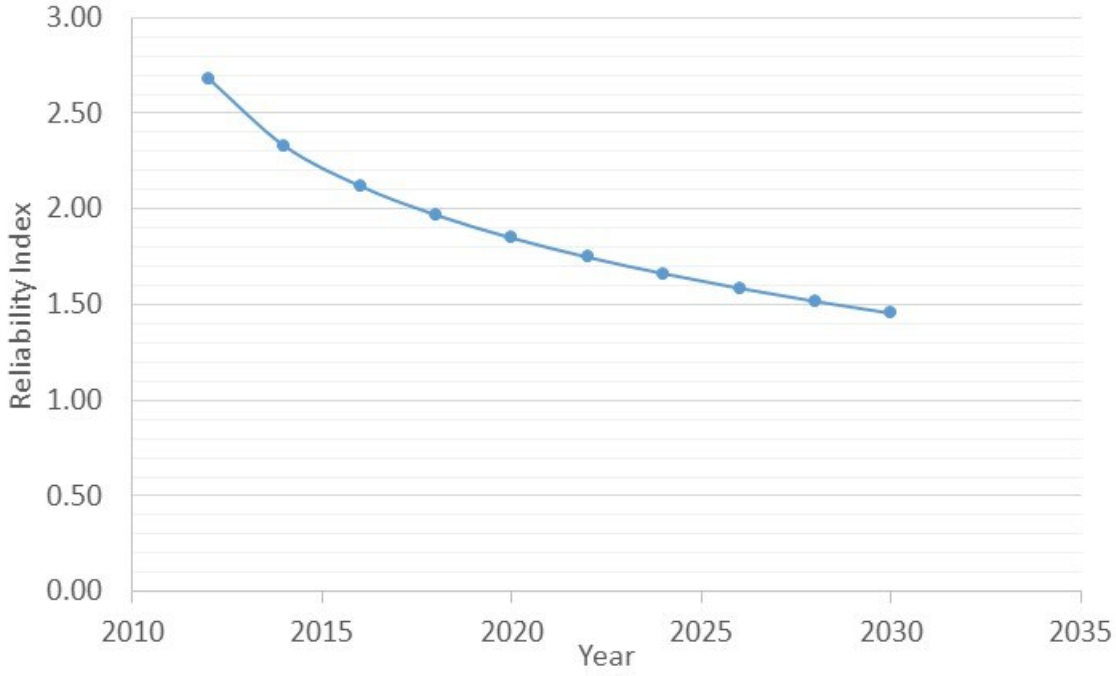

Figure G.4: A-06-2 gauge reliability over time.

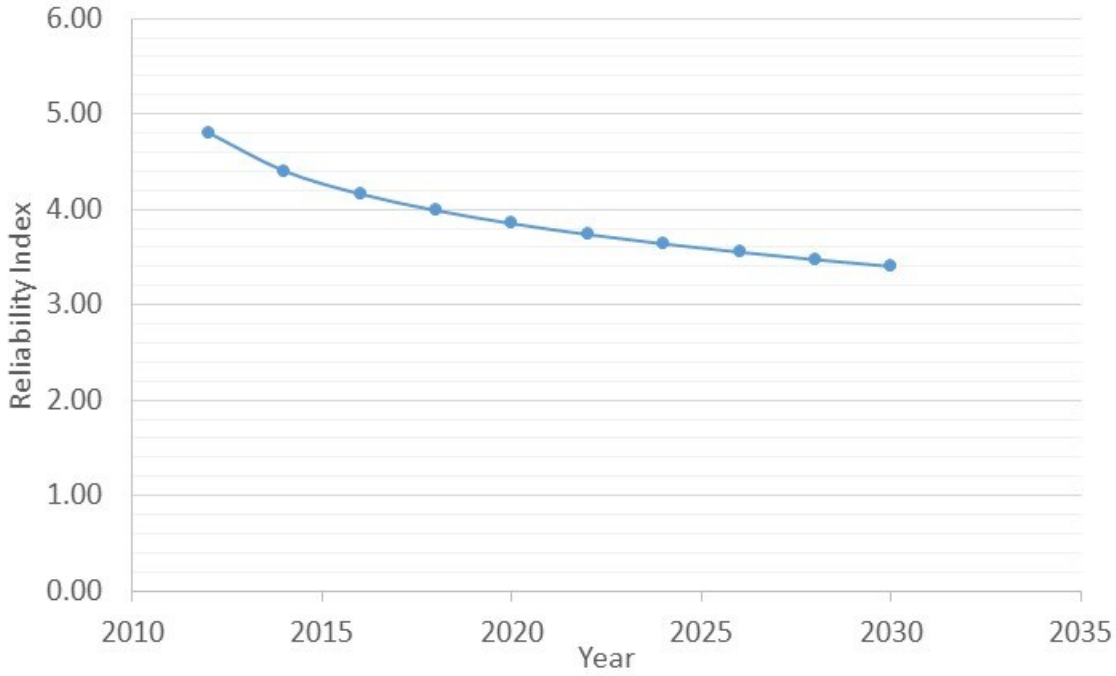

Figure G.5: A-10-2 gauge reliability over time.

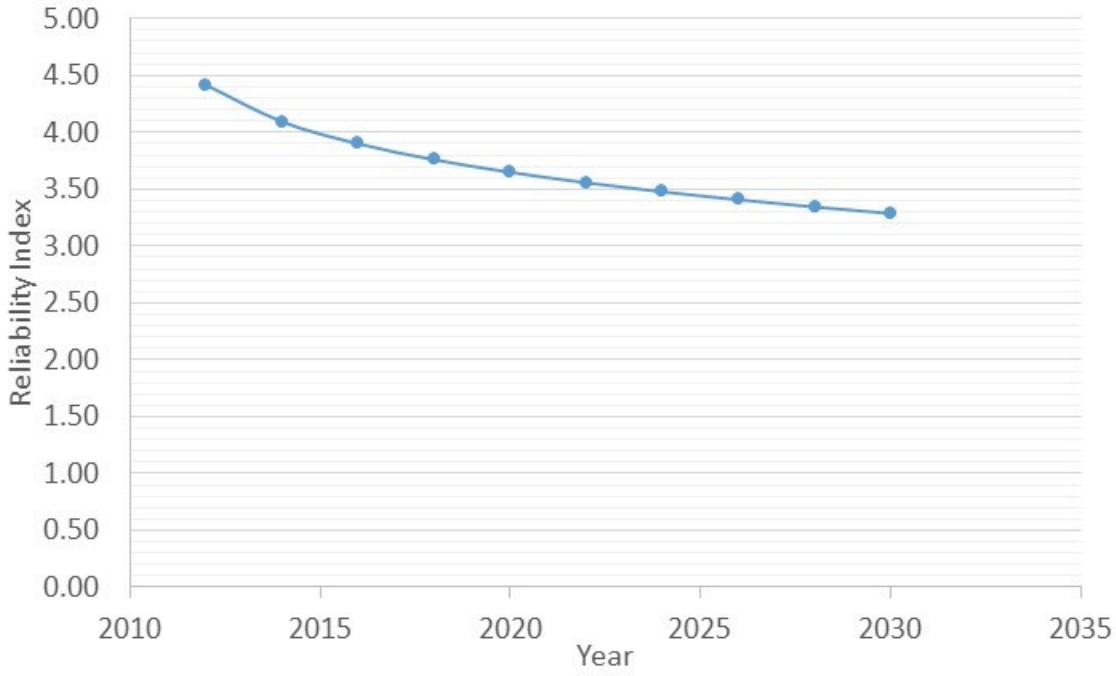

Figure G.6: A-11-1 gauge reliability over time.

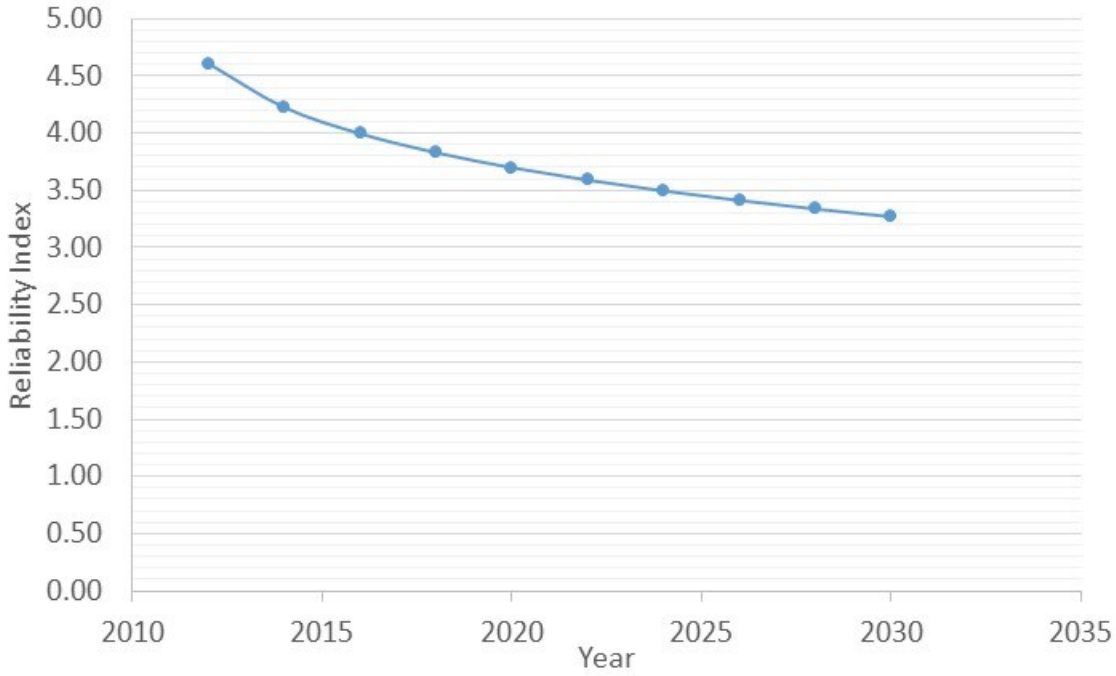

Figure G.7: A-12-1 gauge reliability over time.

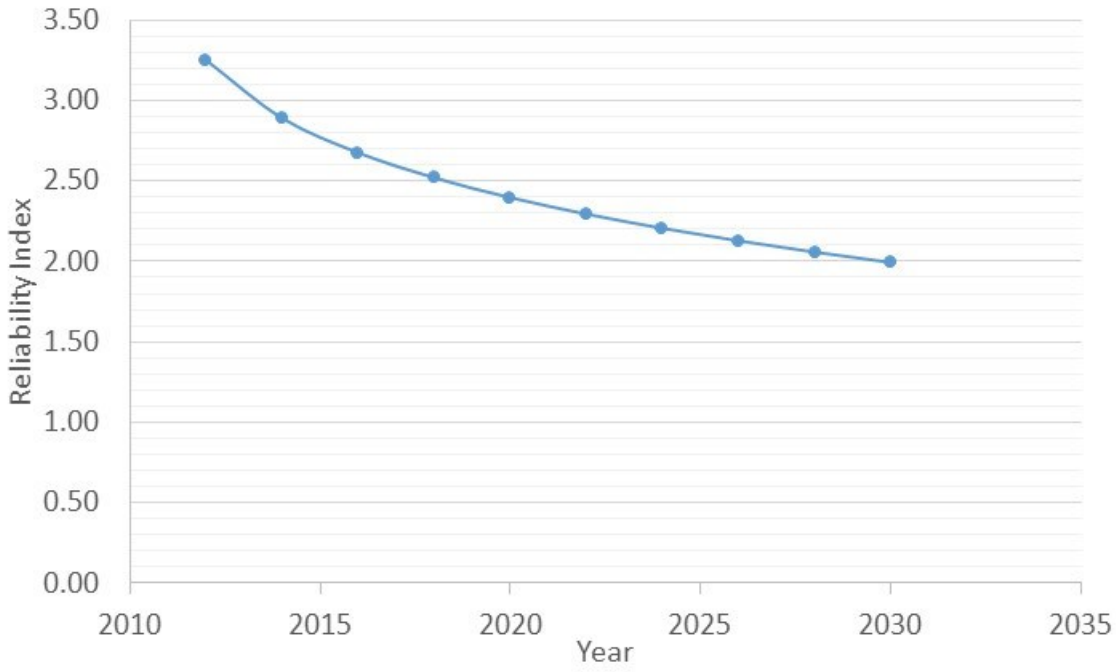

Figure G.8: A-12-2 gauge reliability over time.

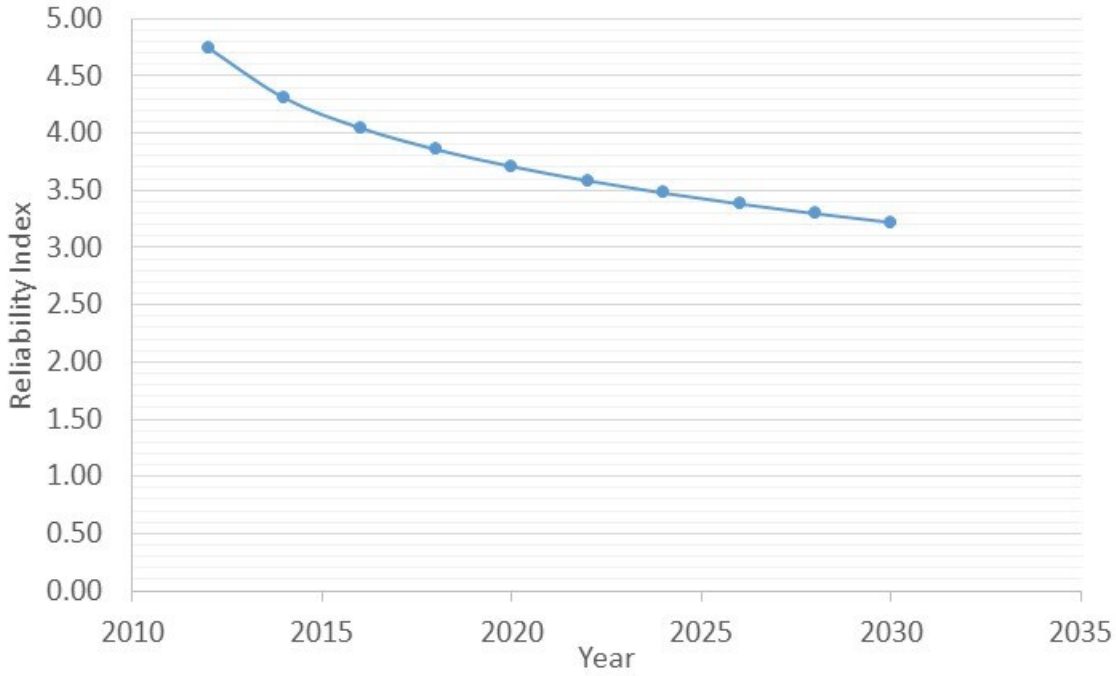

Figure G.9: A-16-1 gauge reliability over time.

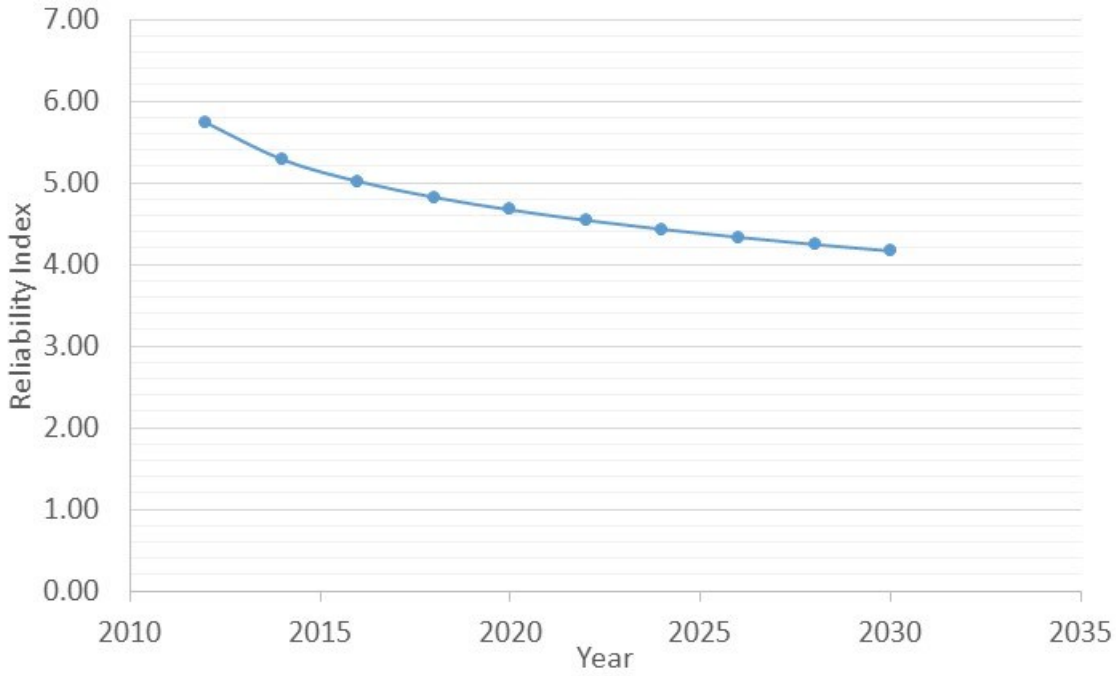

Figure G.10: A-16-2 gauge reliability over time.

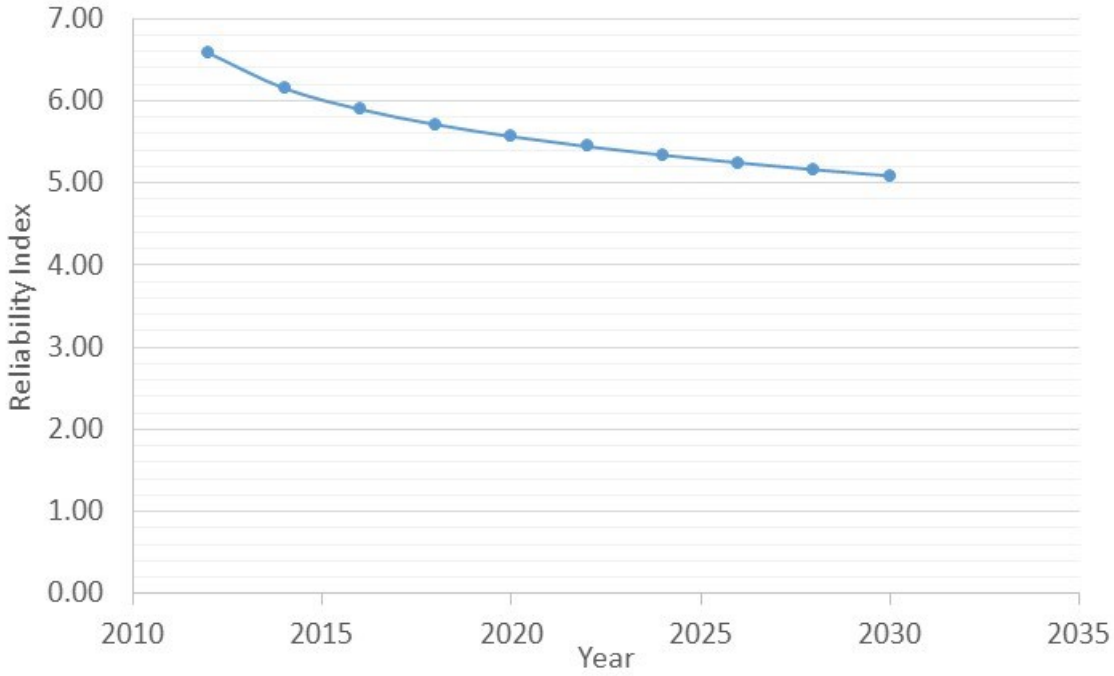

Figure G.11: A-18-1 gauge reliability over time.

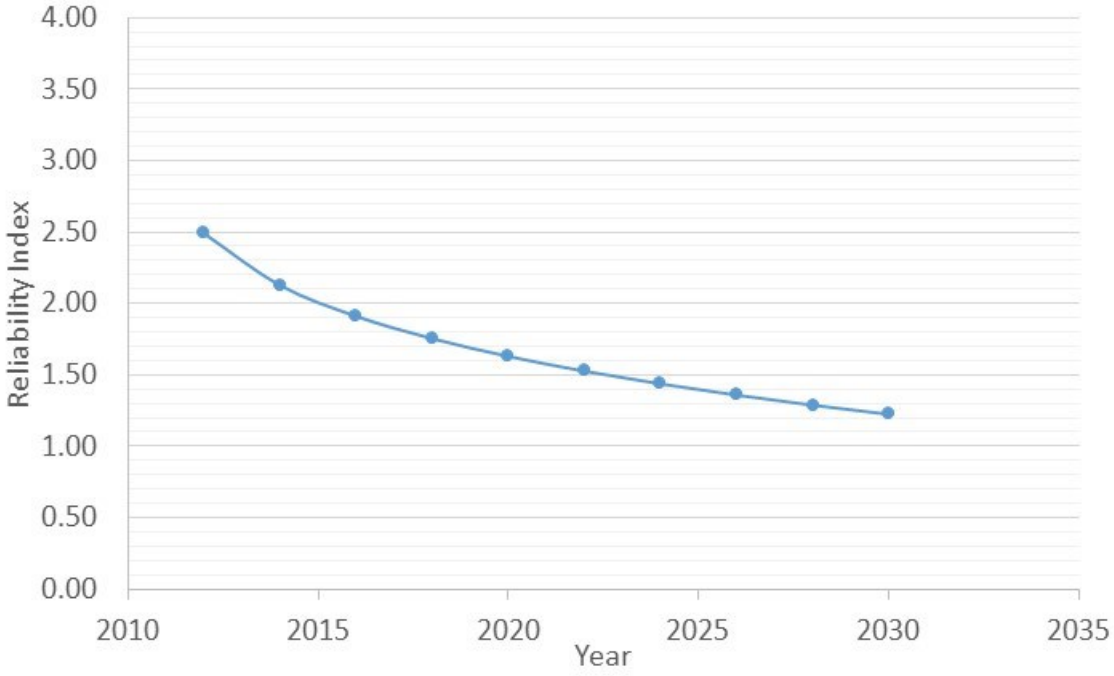

Figure G.12: A-21-2 gauge reliability over time.

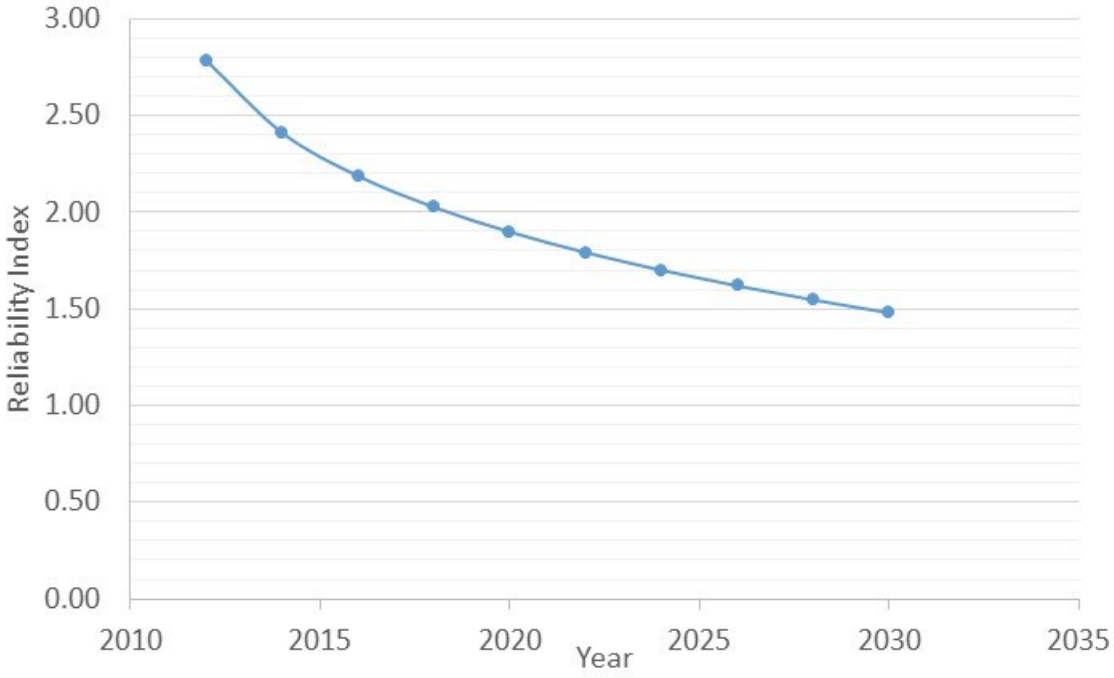

Figure G.13: A-24-1 gauge reliability over time.

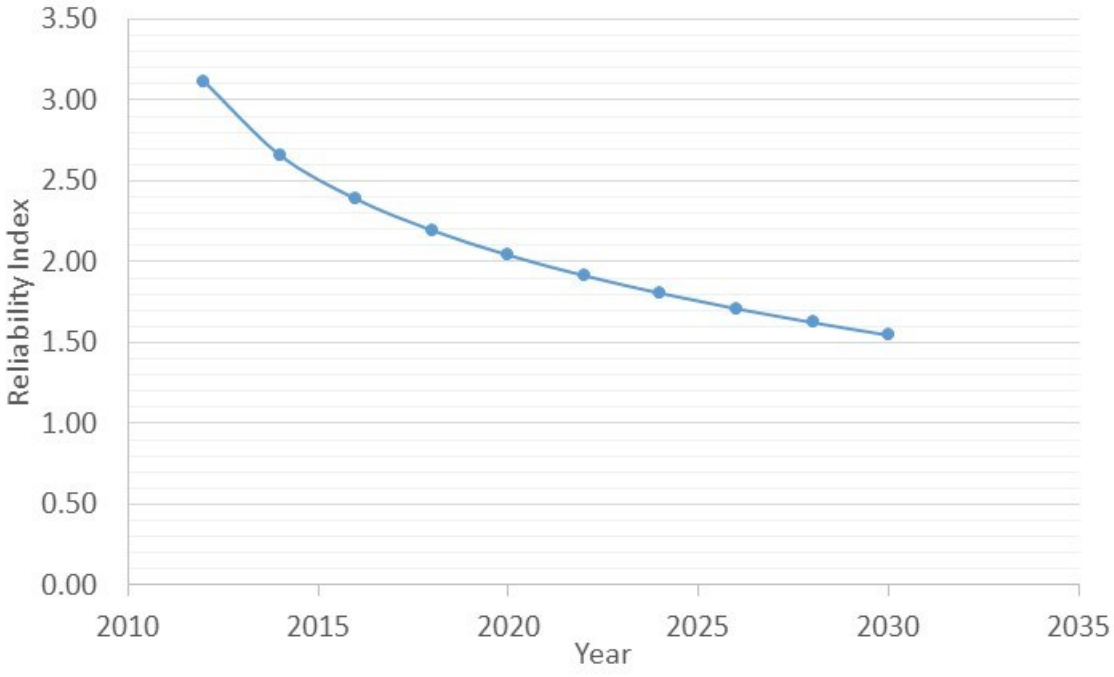

Figure G.14: B-04-1 gauge reliability over time.

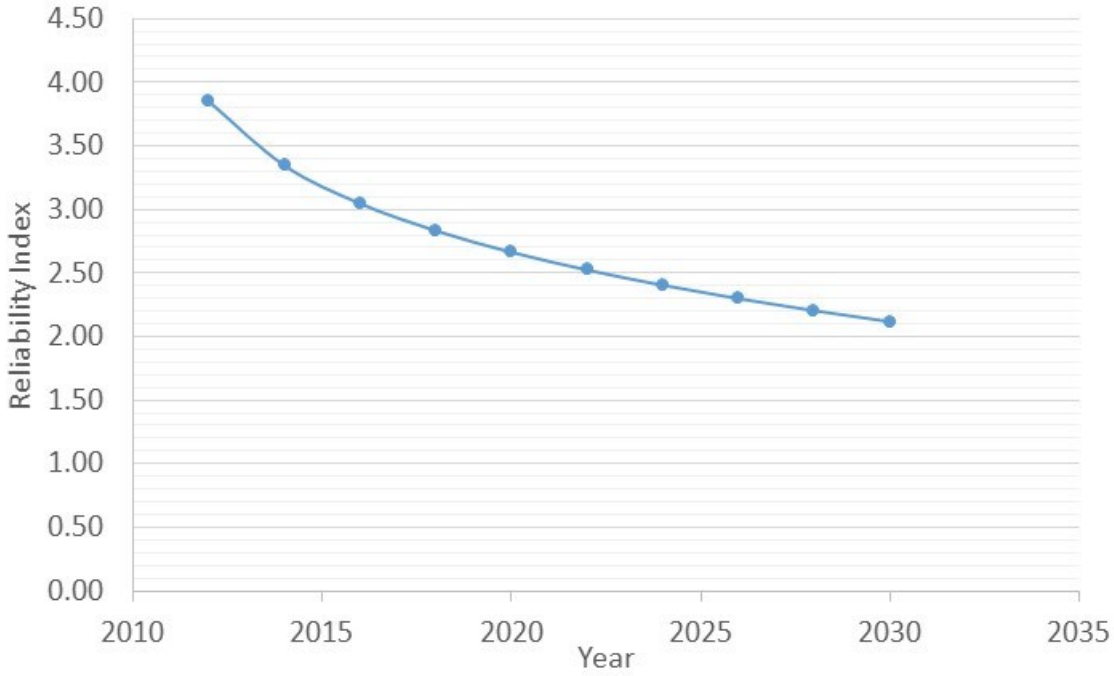

Figure G.15: B-06-1 gauge reliability over time.

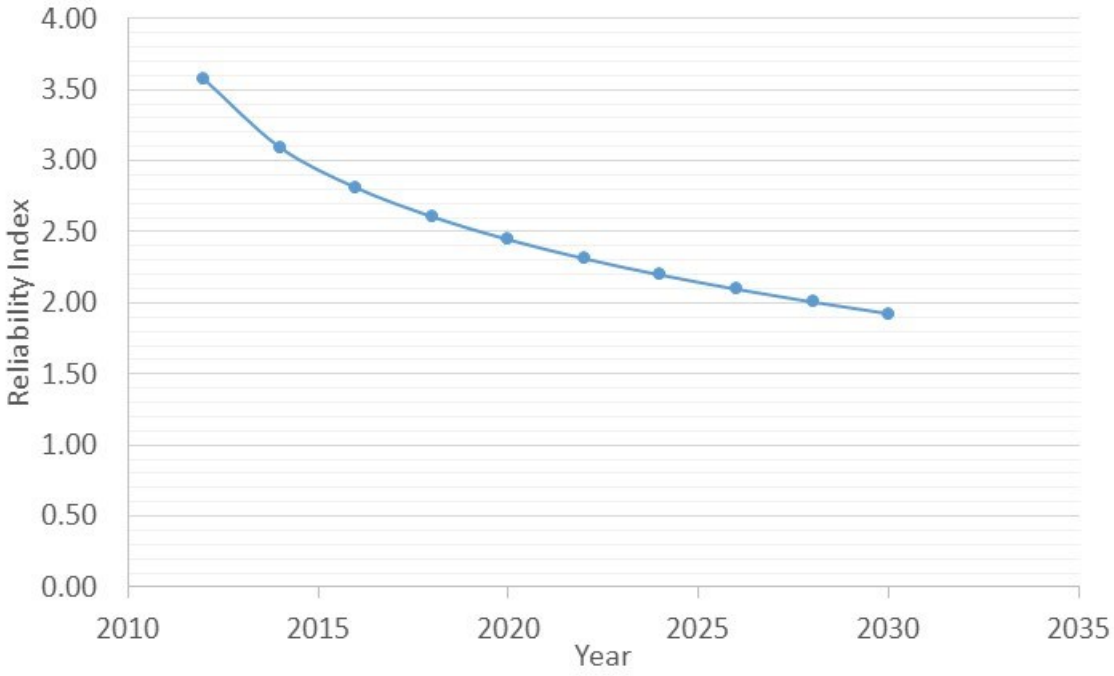

Figure G.16: B-06-2 gauge reliability over time.

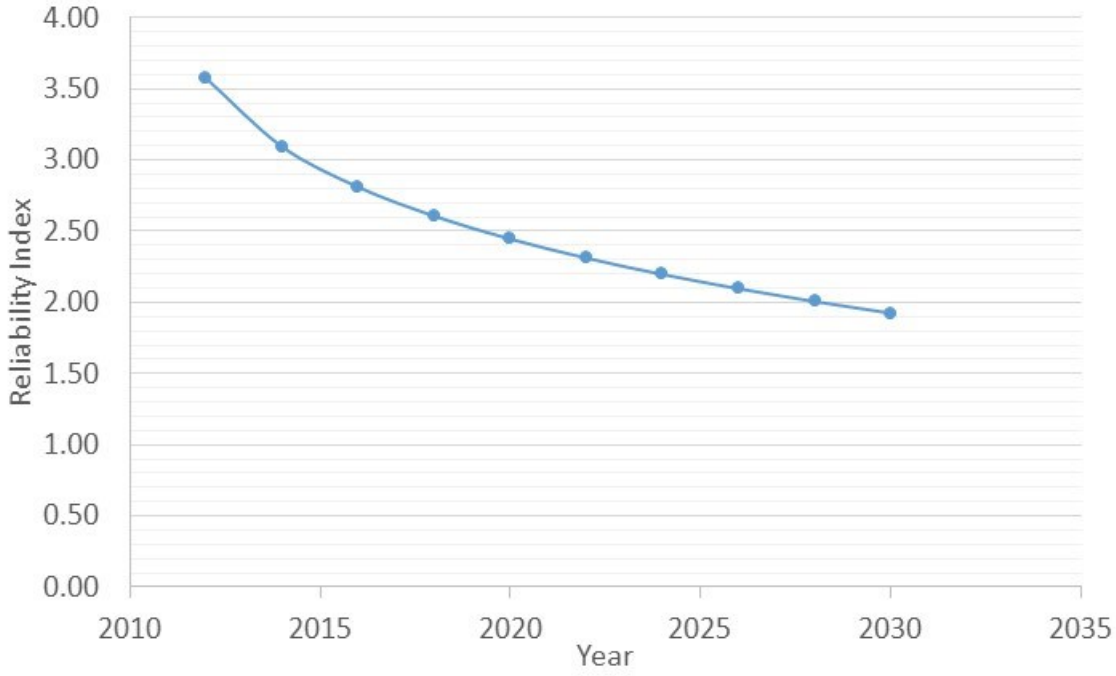

Figure G.17: B-10-2 gauge reliability over time.

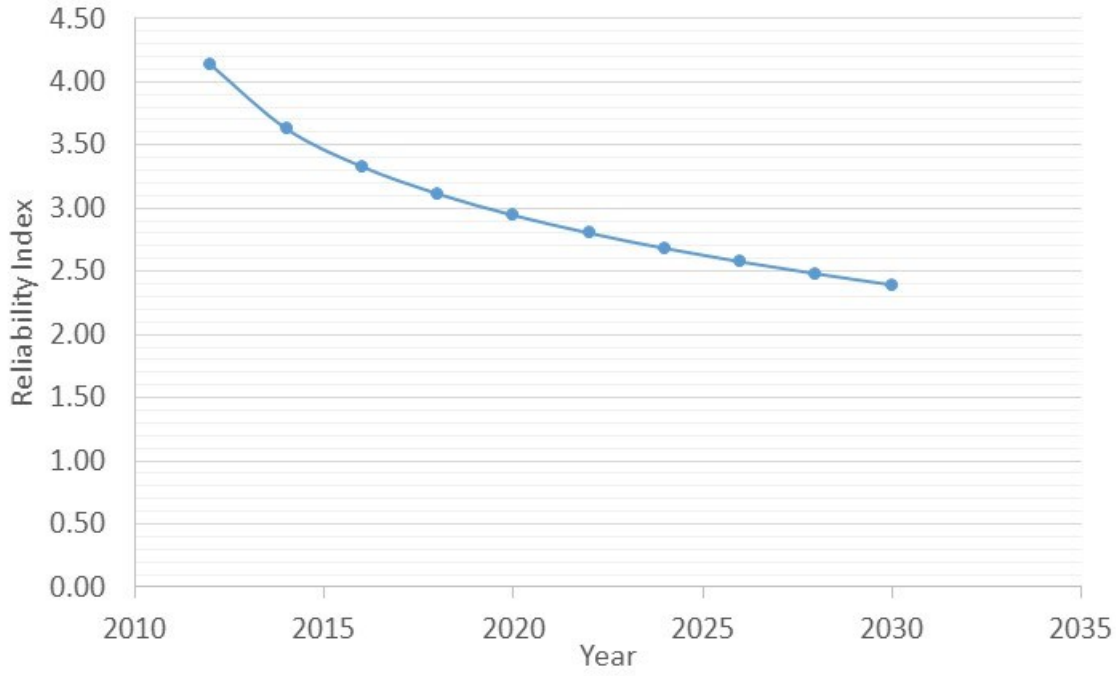

Figure G.18: B-12-1 gauge reliability over time.

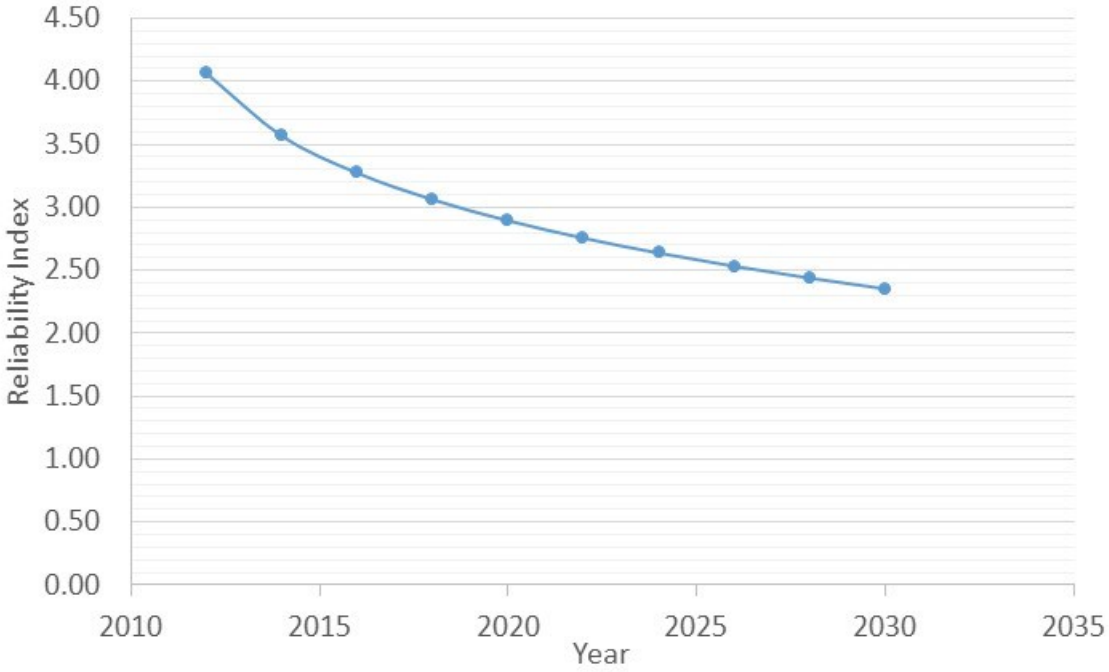

Figure G.19: B-12-2 gauge reliability over time.

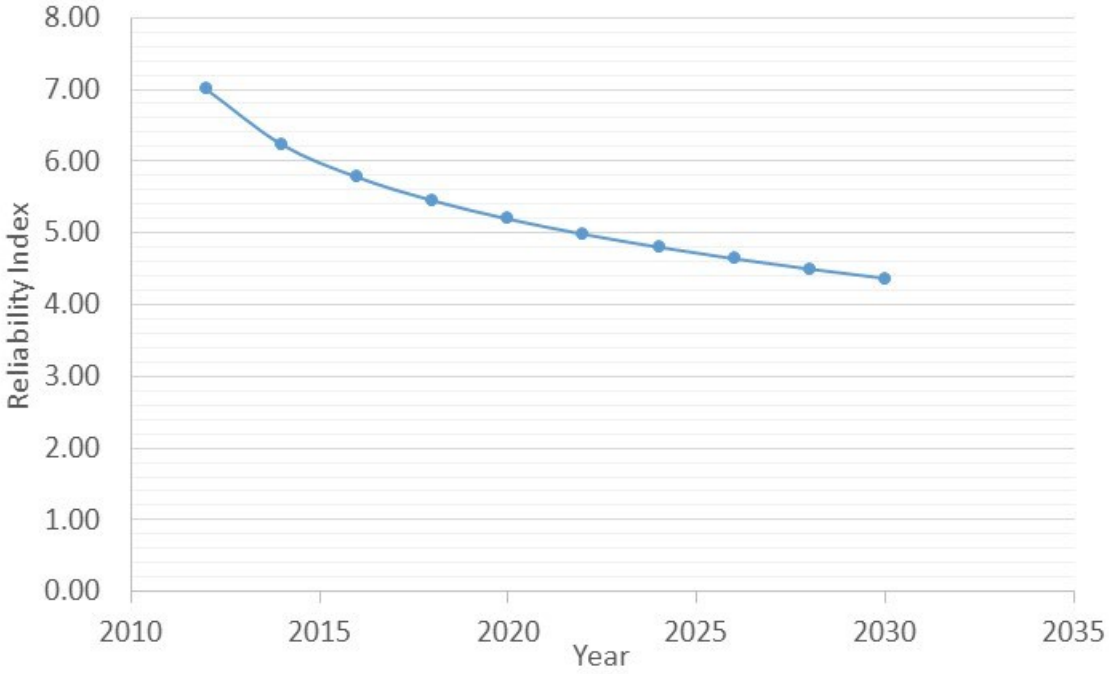

Figure G.20: B-16-1 gauge reliability over time.

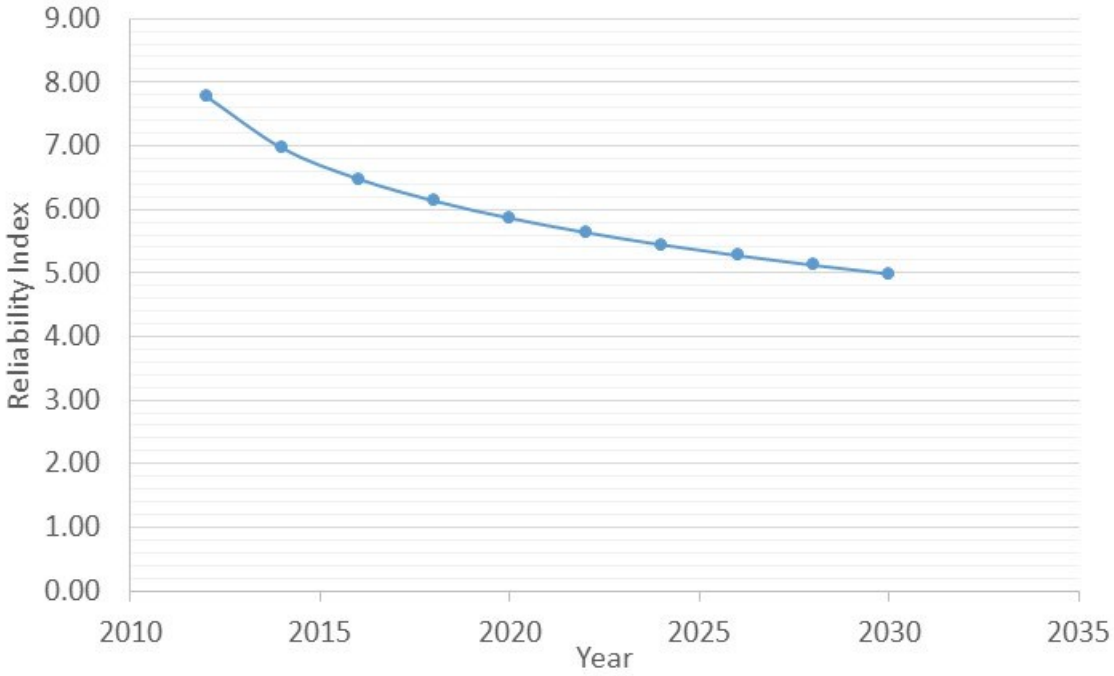

Figure G.21: B-16-2 gauge reliability over time.

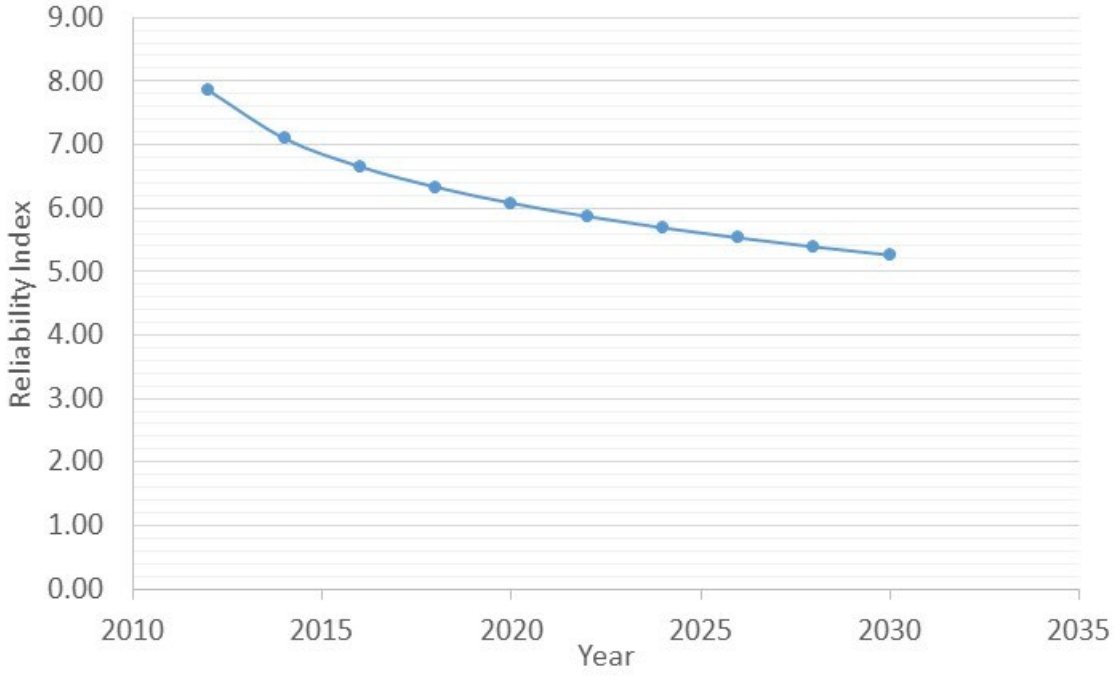

Figure G.22: B-18-1 gauge reliability over time.

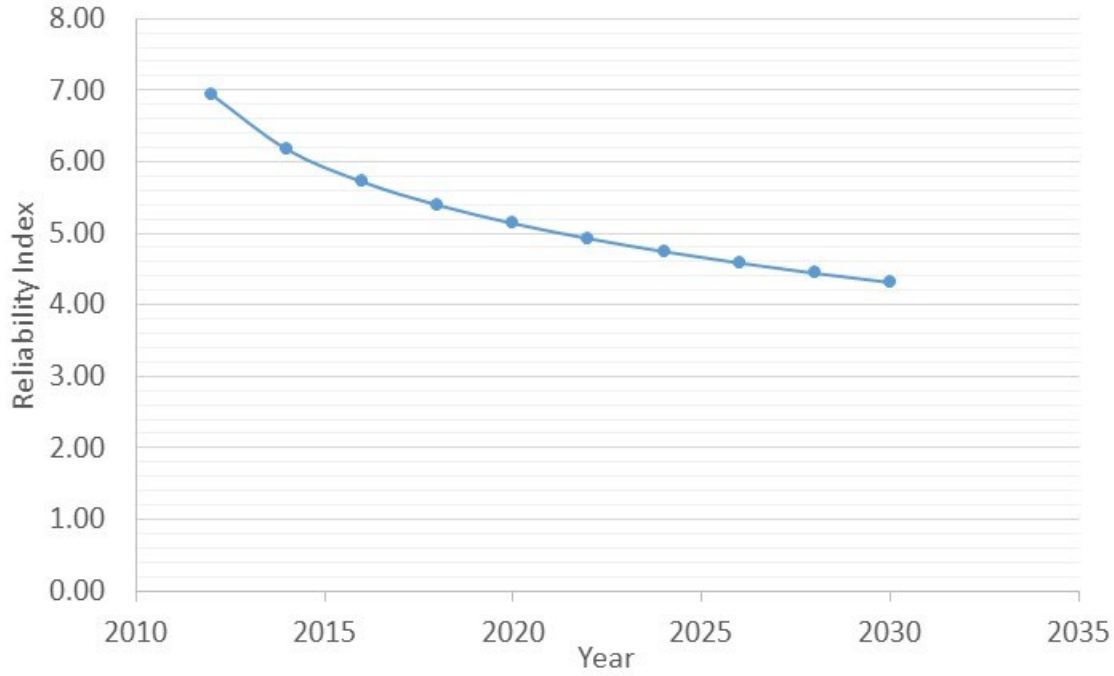

Figure G.23: B-18-2 gauge reliability over time.

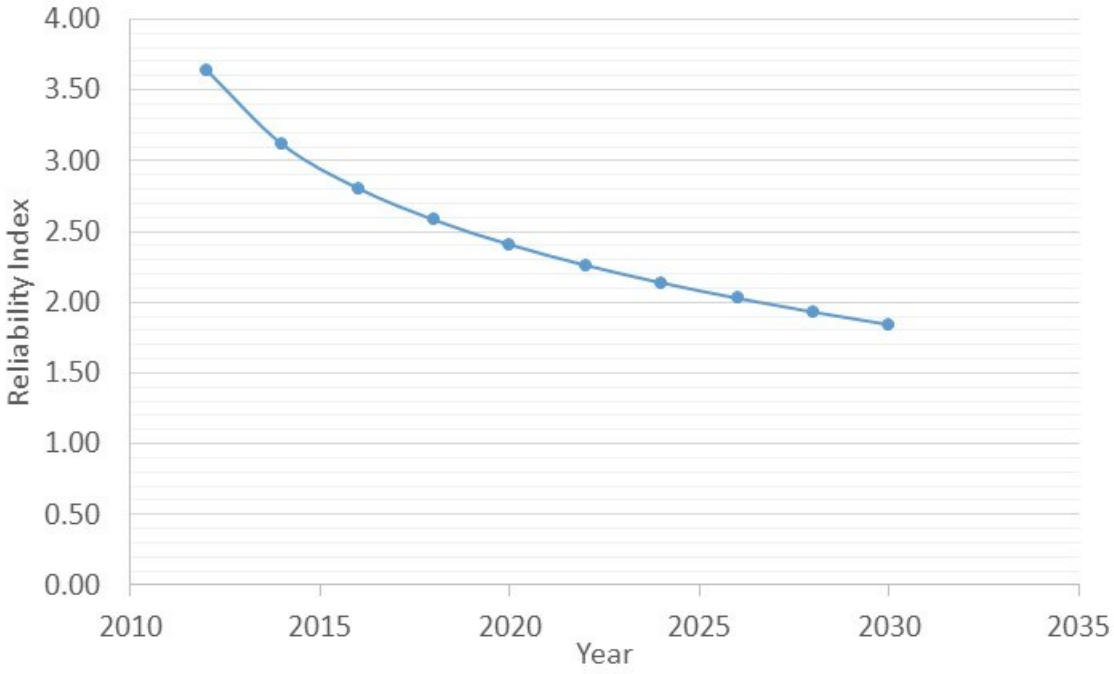

Figure G.24: B-21-1 gauge reliability over time.

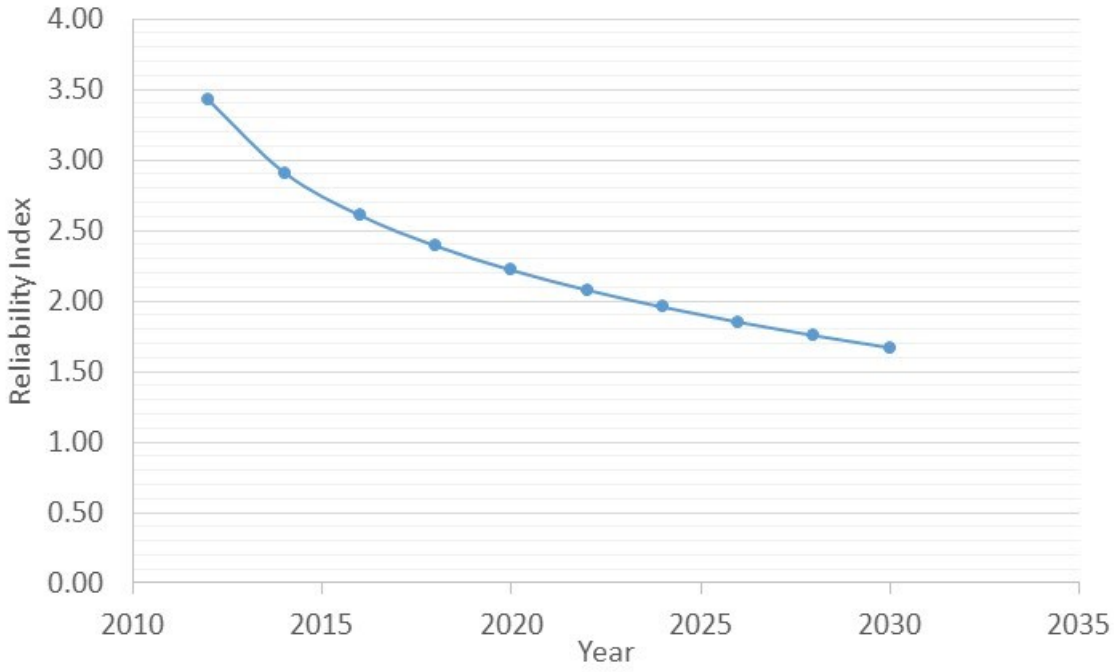

Figure G.25: B-21-2 gauge reliability over time.

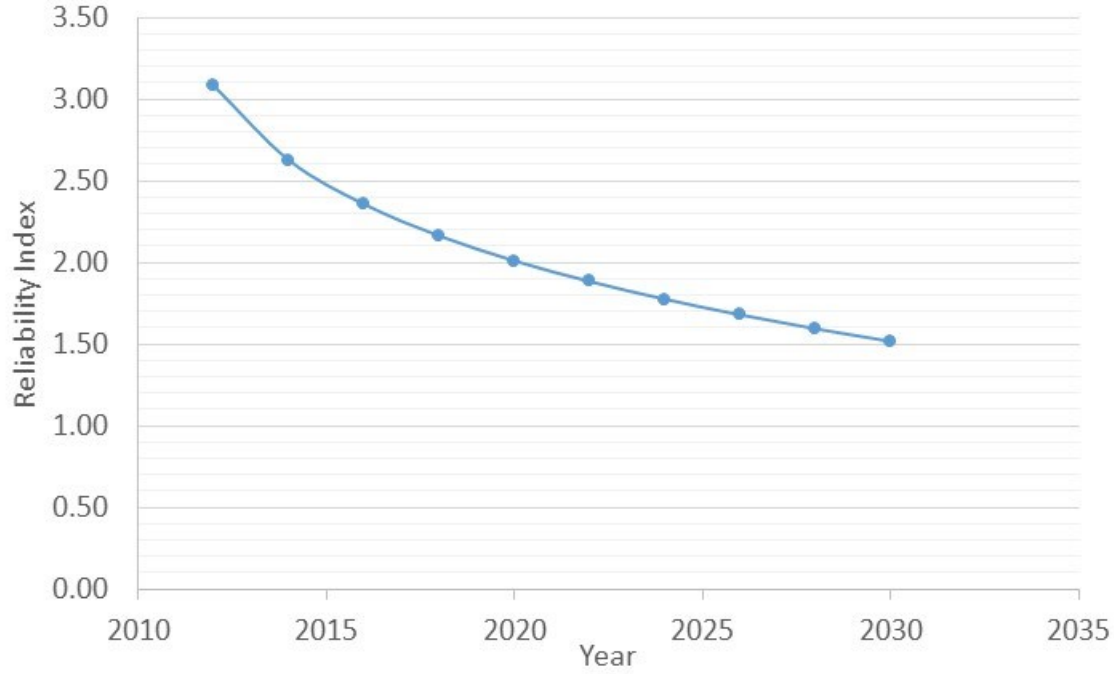

Figure G.26: B-24-1 gauge reliability over time.

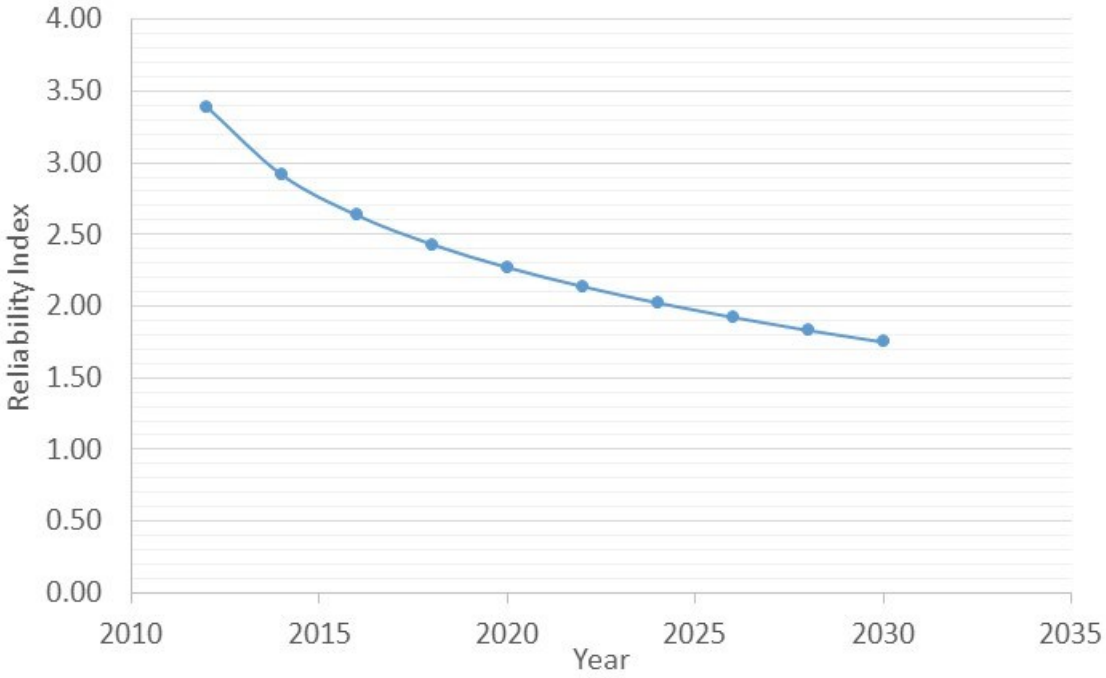

Figure G.27: C-04-1 gauge reliability over time.

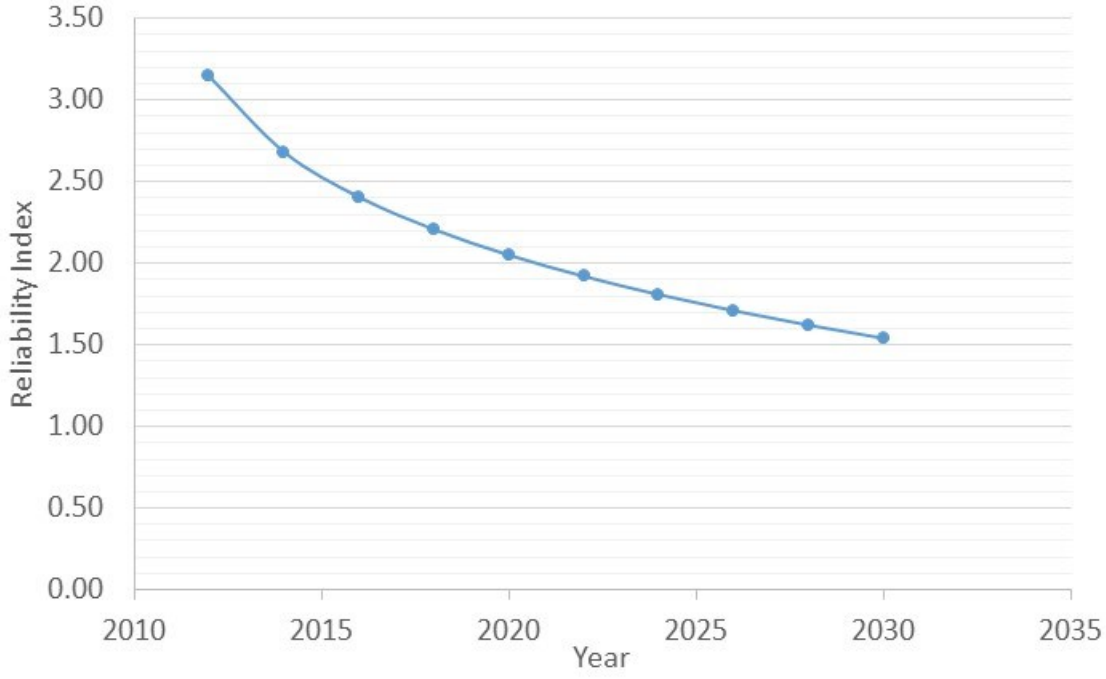

Figure G.28: C-04-4 gauge reliability over time.

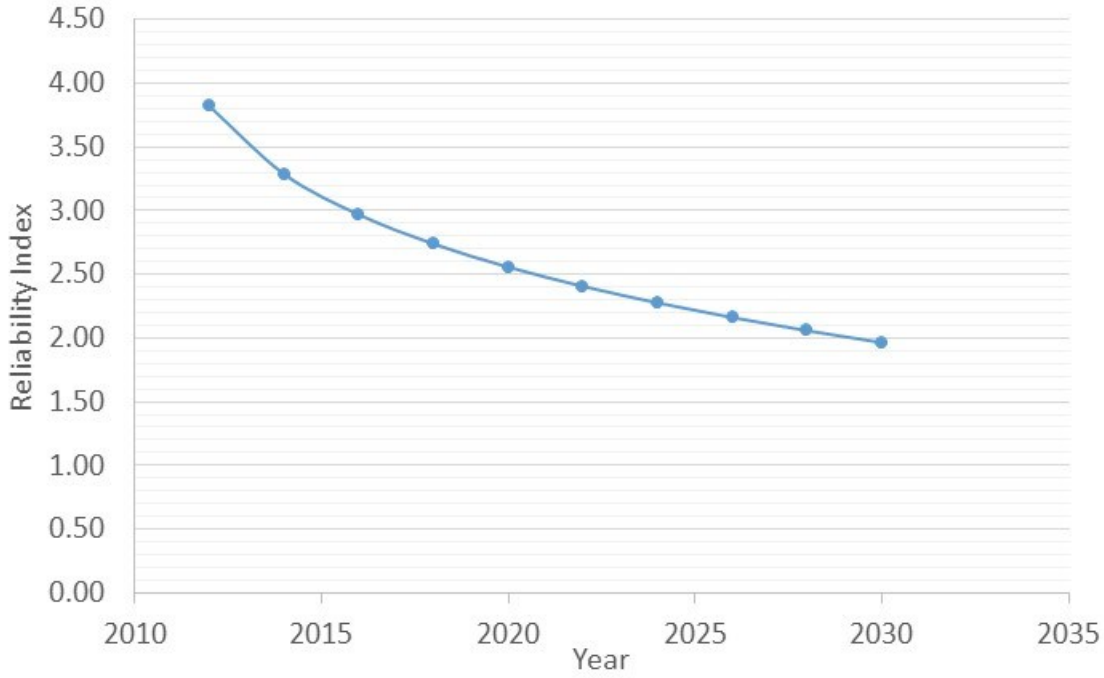

Figure G.29: C-06-1 gauge reliability over time.

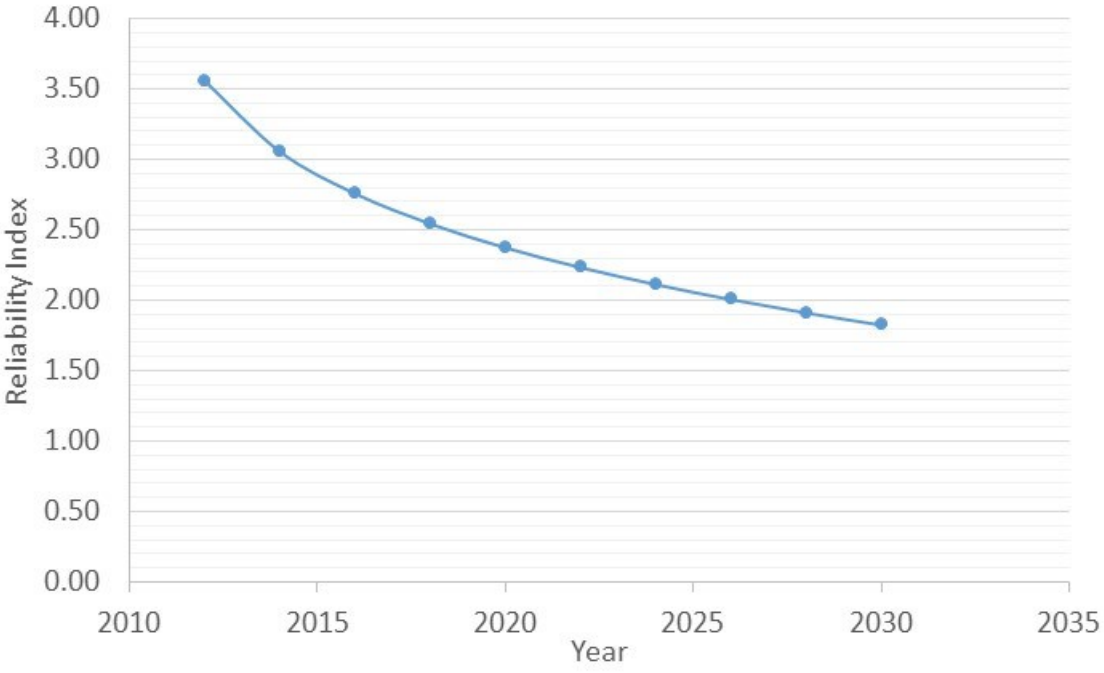

Figure G.30: C-06-4 gauge reliability over time.

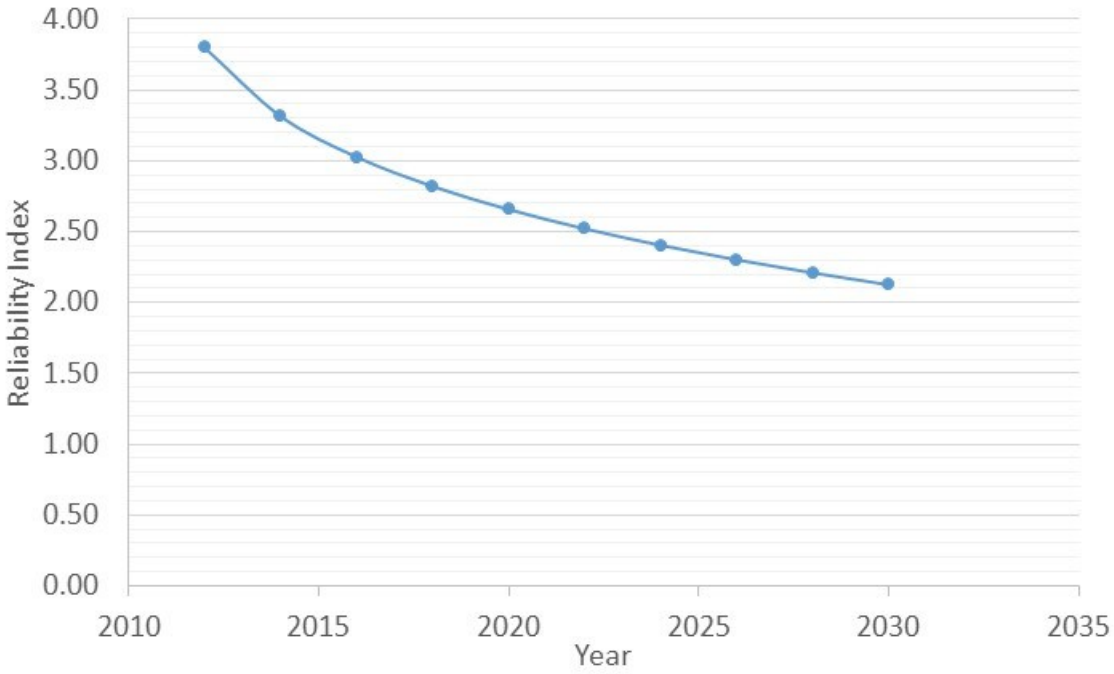

Figure G.31: C-10-1 gauge reliability over time.

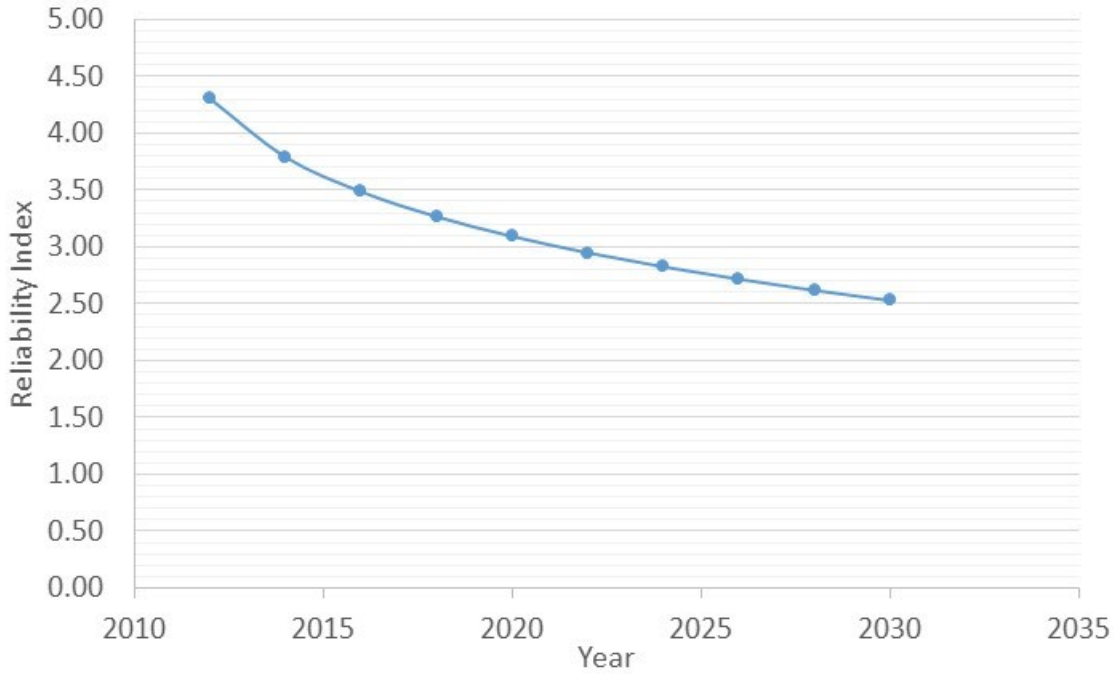

Figure G.32: C-10-4 gauge reliability over time.

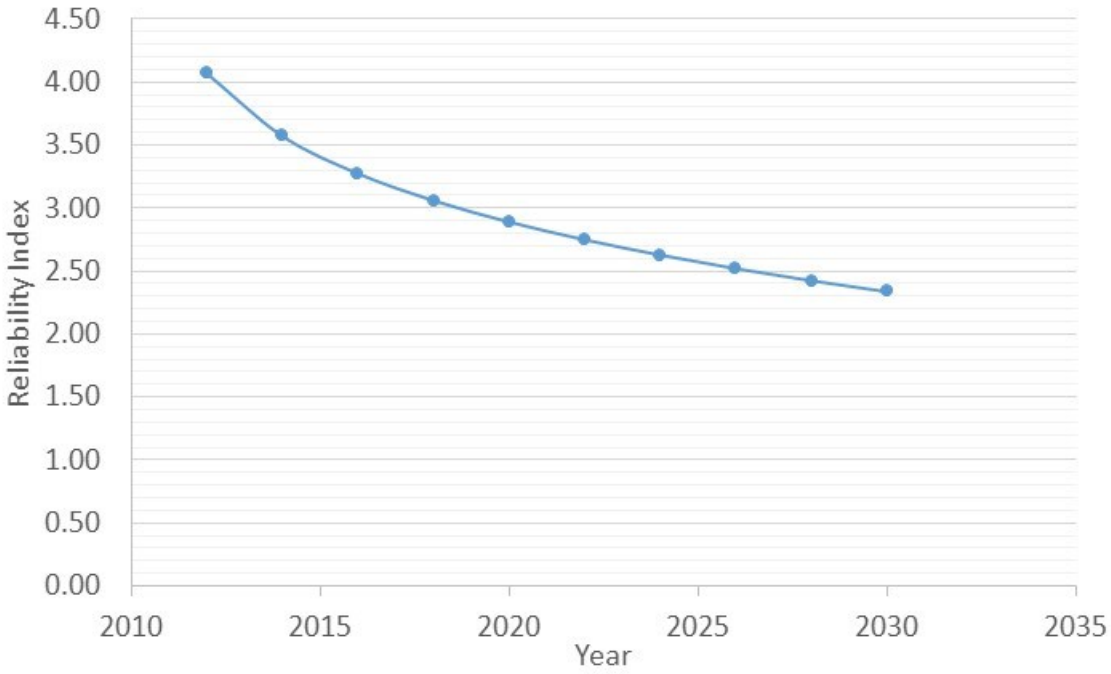

Figure G.33: C-12-4 gauge reliability over time.

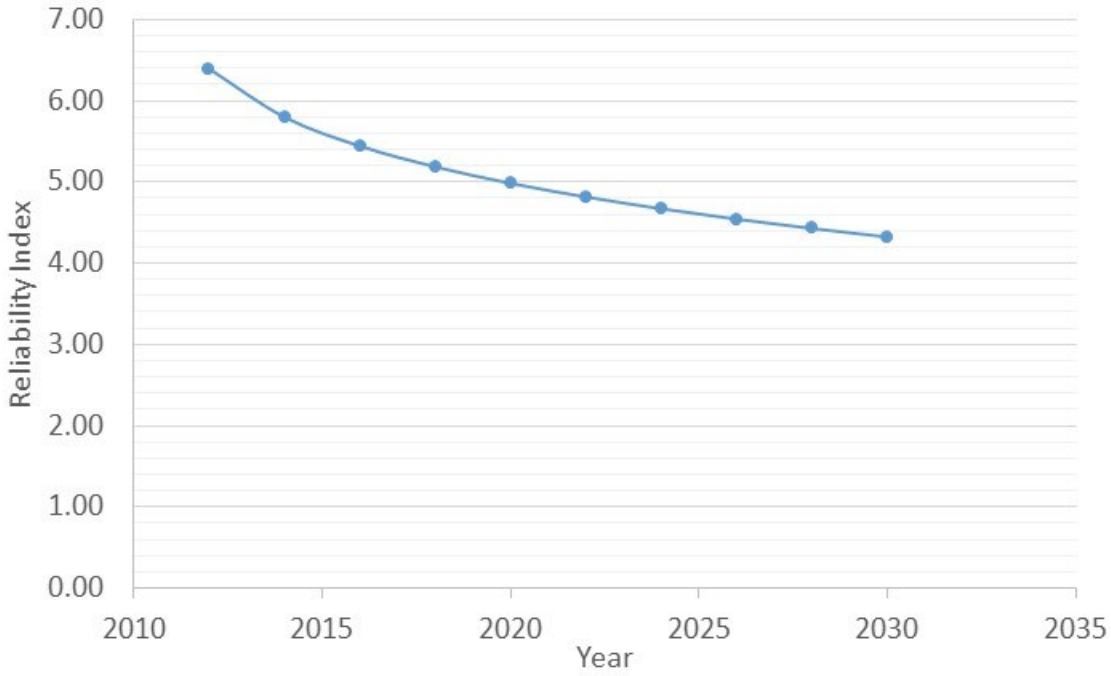

Figure G.34: C-16-1 gauge reliability over time.

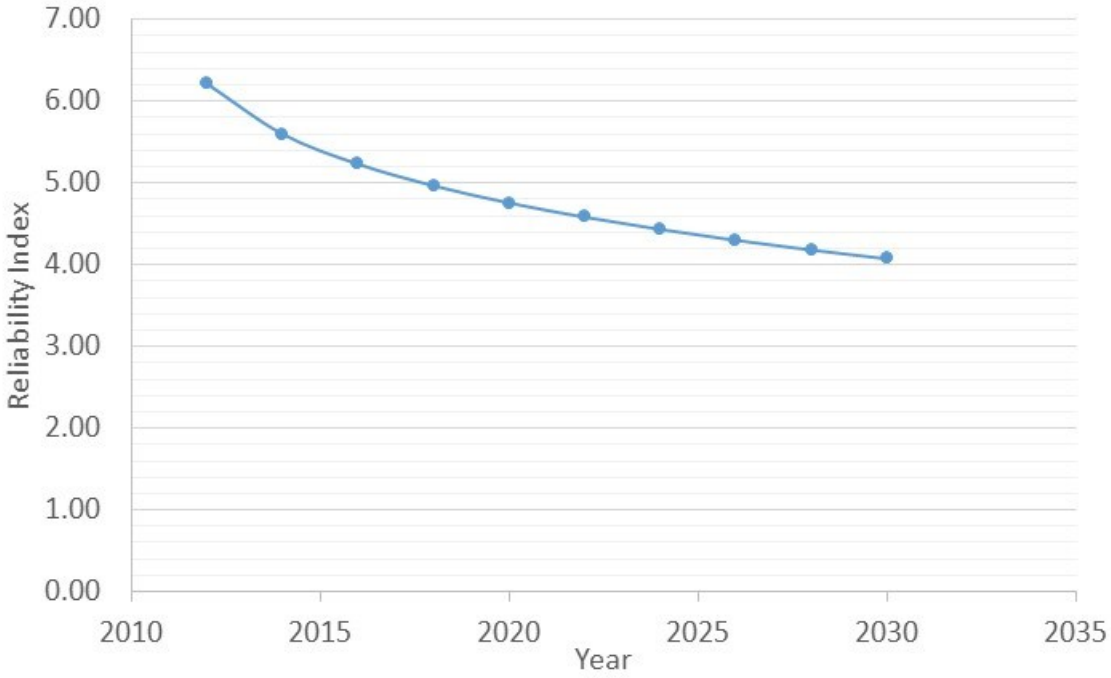

Figure G.35: C-18-4 gauge reliability over time.

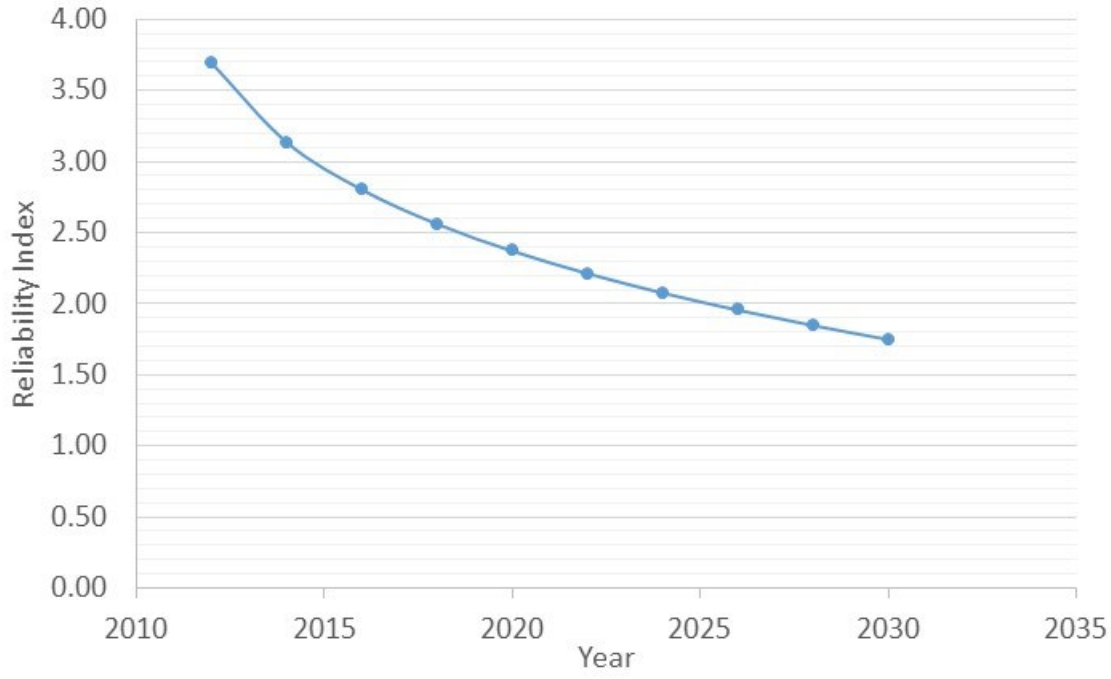

Figure G.36: C-21-1 gauge reliability over time.

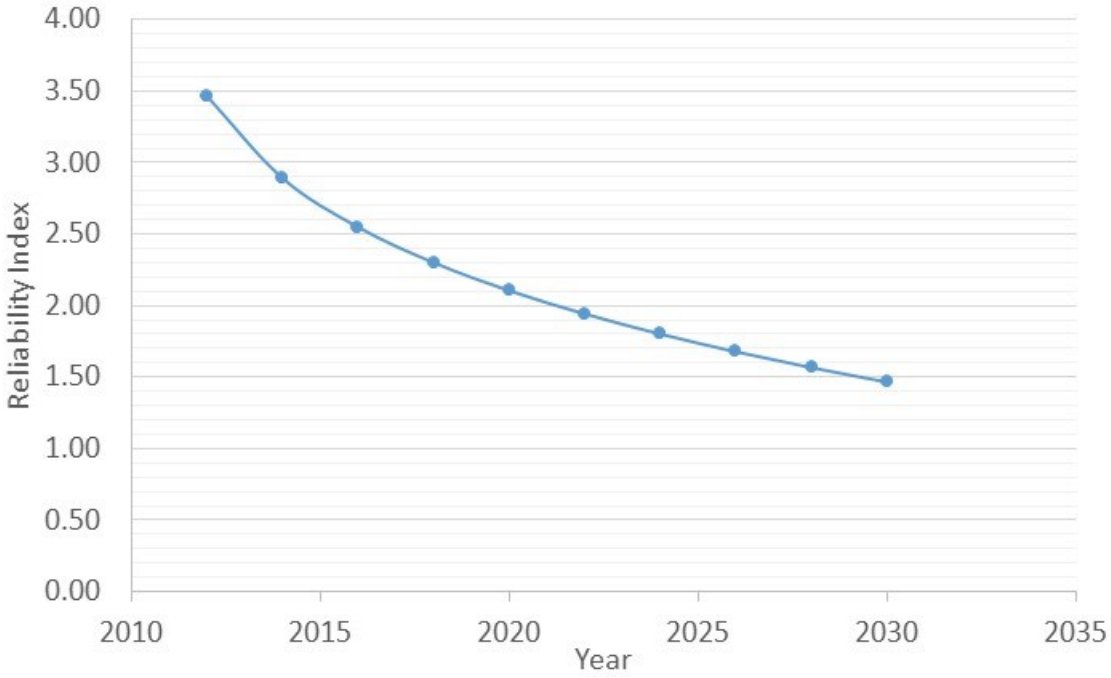

Figure G.37: C-21-4 gauge reliability over time.

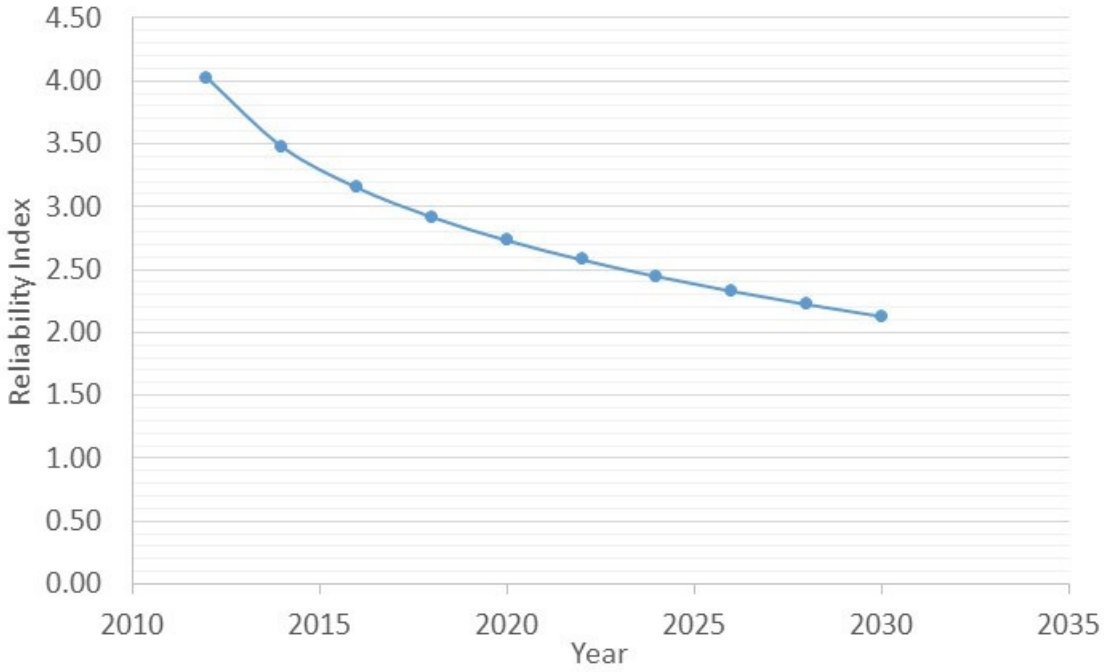

Figure G.38: C-24-1 gauge reliability over time.

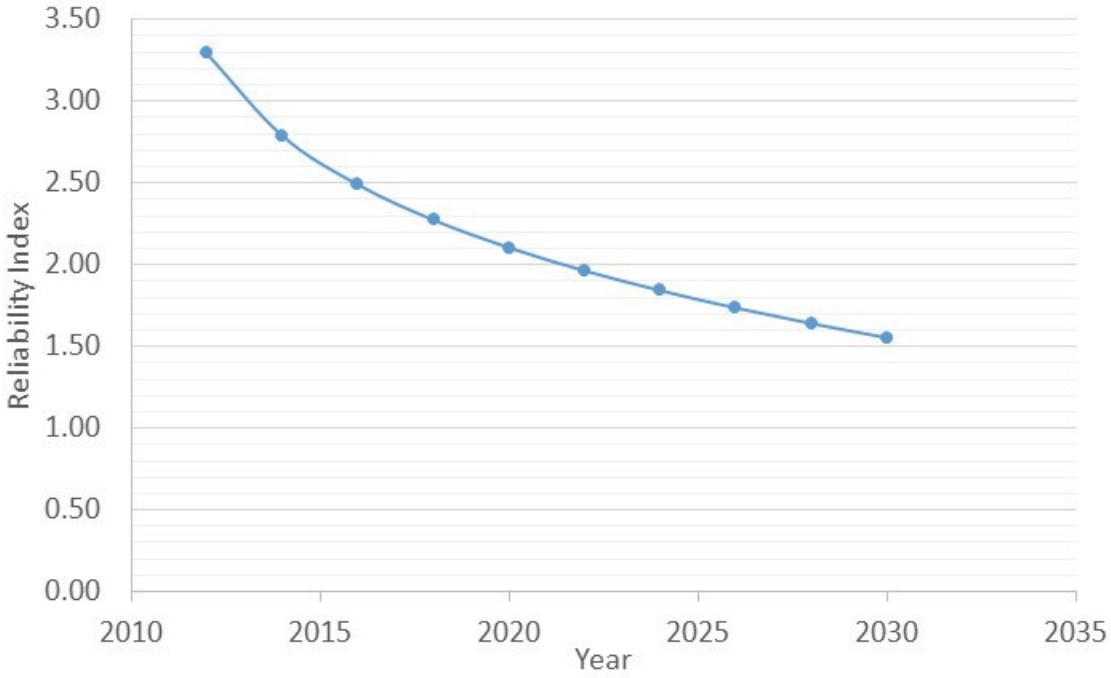

Figure G.39: C-24-4 gauge reliability over time.